DGK Veröffentlichungen der DGK

Ausschuss Geodäsie der Bayerischen Akademie der Wissenschaften

Reihe C | Dissertationen | Heft Nr. 928

Sven Weisbrich

On the Challenges of a Measurement- and Model-based Structural Analysis

München 2024

Bayerische Akademie der Wissenschaften

ISSN 0065-5325 ISBN 978-3-7696-5340-3

Diese Arbeit ist gleichzeitig veröffentlicht in:
DepositOnce – Forschungsdaten und Publikationen der Technischen Universität Berlin
https://doi.org/10.14279/depositonce-18428, Berlin 2023

DGK Veröffentlichungen der DGK

Ausschuss Geodäsie der Bayerischen Akademie der Wissenschaften

Reihe C Dissertationen Heft Nr. 928

On the Challenges of a Measurement- and Model-based Structural Analysis

Von der Fakultät VI – Planen Bauen Umwelt
der Technischen Universität Berlin
zur Erlangung des akademischen Grades
Doktor-Ingenieur (Dr.-Ing.)
genehmigte Dissertation

von

Dipl.-Ing. Sven Weisbrich

München 2024

Bayerische Akademie der Wissenschaften

ISSN 0065-5325 ISBN 978-3-7696-5340-3

Diese Arbeit ist gleichzeitig veröffentlicht in:

DepositOnce – Forschungsdaten und Publikationen der Technischen Universität Berlin
https://doi.org/10.14279/depositonce-18428, Berlin 2023

Adresse der DGK:

Ausschuss Geodäsie der Bayerischen Akademie der Wissenschaften (DGK)

Alfons-Goppel-Straße 11 ● D – 80 539 München

Telefon +49 - 331 - 6264 1685 ● E-Mail post@dgk.badw.de

http://www.dgk.badw.de

Prüfungskommission:

Vorsitzender: Prof. Dr.-Ing. Martin Kada

Referent: Prof. Dr.-Ing. Frank Neitzel

Korreferenten: Prof. Dr.-Ing. Andreas Eichhorn (TU Darmstadt)
Univ.-Prof. Dipl.-Ing. Dr. techn. Werner Lienhart (TU Graz)
Prof. Dipl.-Ing. Dr. techn. Wolf-Dieter Schuh (Universität Bonn)

Tag der mündlichen Prüfung: 21.02.2023

ISSN 0065-5325 ISBN 978-3-7696-5340-3

ABSTRACT

The Measurement– and Model–based Structural Analysis (MeMoS) project was initiated in 2013 with the aim to detect and localise damage to structures based on an integrated analysis of spatially and temporally distributed hybrid measurements. Therefore, a physical model of the structure is directly embedded as a functional model in the least squares adjustment, ensuring a rigorous and direct solution of the system parameters solely based on the measurements. This enables a damages analysis based on the estimated system parameters using well established geodetic deformation analysis methods. However, besides a detailed understanding of the applied sensors, a profound knowledge of the functional model is indispensable for a correct and successful data evaluation.

This thesis, therefore, provides new and in-depth insights into the characteristics of an integrated analysis using an embedded physical model and addresses the resulting challenges of a damage analysis via MeMoS using static measurements, such as, displacements, inclination or strain. Based on a detailed discussion on the approximation of univariate functions by polynomials from a geodetic point of view, the structural behaviour is not approximated by FEM as usual, but by a spectral method using Chebyshev polynomials. This ensures, in principle, that the functional model is always correct and complete, so that there are no systematic falsifications of the estimated system parameters due to approximation errors of the structural behaviour. The characteristics of the resulting inverse problem are discussed in detail and it is shown how the measurement noise affects the estimation of the system parameters and consequently the detection and localisation of damage. In addition, the impact of damage on the static measurements will be addressed, which provides insights into the extent to which damage can be reconstructed from measurements at all. Consequently, known statistical tests were adapted for the problem at hand and transferred to continuous functions, so that they can be effectively used for a damage analysis via MeMoS. Furthermore, new approaches for the localisation of damage have been developed, which are based on a data-driven regularisation of the least squares solution. The capabilities and limitations of a damage analysis via MeMoS are demonstrated by numerical and experimental studies on a four-point bending test.

ZUSAMMENFASSUNG

Das Measurement– and Model–based Structural Analysis (MeMoS) Projekt wurde 2013 mit dem Ziel initiiert, Schäden an Bauwerken auf Grundlage einer integrierten Analyse räumlich und zeitlich verteilter hybrider Messungen zu detektieren und zu lokalisieren. Zu diesem Zweck wird ein physikalisches Modell der zu untersuchenden Struktur direkt als funktionales Modell in eine Ausgleichung nach der Methode der kleinsten Quadrate eingebettet, wodurch eine strenge und direkte Lösung der Systemparameter allein auf der Grundlage der Messwerte gewährleistet wird. Dies ermöglicht eine Schädigungsanalyse anhand der geschätzten Systemparameter unter Verwendung etablierter geodätischer Methoden zur Deformationsanalyse. Für eine korrekte und erfolgreiche Datenauswertung ist jedoch neben einem detaillierten Verständnis der eingesetzten Sensoren auch eine fundierte Kenntnis des funktionalen Modells der Ausgleichung unabdingbar.

Diese Arbeit gibt daher neue und vertiefte Einblicke in die Charakteristiken einer integrierten Analyse unter Verwendung eines eingebetteten physikalischen Modells und adressiert die sich daraus ergebenden Herausforderungen einer Schadensanalyse mittels MeMoS unter Verwendung statischer Messungen, wie z.B. Verschiebungen, Neigungen oder Dehnungen. Ausgehend von einer ausführlichen Darlegung der Approximation univariater Funktionen durch Polynome aus geodätischer Sicht, wird das Strukturverhalten nicht wie üblich durch FEM, sondern durch eine Spektralmethode mit Tschebyscheff-Polynomen approximiert. Damit ist prinzipiell sichergestellt, dass das funktionale Modell immer korrekt und vollständig ist, so dass es keine systematischen Verfälschungen der geschätzten Systemparameter durch Approximationsfehler des Strukturverhaltens gibt. Die Eigenschaften des resultierenden inversen Problems werden ausführlich diskutiert und es wird gezeigt, wie sich das Messrauschen auf die Schätzung der Systemparameter und folglich auf die Detektion und Lokalisierung von Schäden auswirkt. Darüber hinaus wird der Einfluss von Schäden auf die statischen Messungen behandelt, was Aufschluss darüber gibt, inwieweit Schäden überhaupt aus Messungen rekonstruiert werden können. Folglich wurden bekannte statistische Tests für die vorliegende Problemstellung angepasst und auf kontinuierlichen Funktionen übertragen, so dass sie effektiv für eine Schädigungsanalyse mittels MeMoS genutzt werden können. Darüber hinaus wurden neue Ansätze zur Lokalisierung von Schäden entwickelt, die auf einer datengetriebenen Regularisierung der Kleinste-Quadrate-Lösung basieren. Die Einsatzmöglichkeiten und Grenzen einer Schädigungsanalyse mit MeMoS werden anhand von numerischen und experimentellen Untersuchungen an einem Vier-Punkt-Biegeversuch demonstriert.

CONTENTS

LIST OF FIGURES

LIST OF TABLES

LIST OF PROGRAMMES

ACRONYMS

BAM	Bundesanstalt für Materialforschung und -prüfung
BVP	boundary value problem
DM	Damage Modeller
DS	Damage Sniffer
EV	redundancy number
FEM	finite element method
FOS	fibre optic sensors
GI	Global Identifier
IA	Integrated Analysis
IaFB	Institut für angewandte Forschung im Bauwesen e.V
LI	Local Indicator
LS	Local Smoother
MCS	Monte Carlo simulation
MeMoS	Measurement– and Model–based Structural Analysis
MLS	method of least squares
NV	standardised residual
ODE	ordinary differential equation
PDE	partial differential equation
PS	Parameter Sifter
SHM	Structural Health Monitoring
TLS	terrestrial laser scanning

PROLOGUE

INTRODUCTION

The determination of the movement and deformation of an object is one of the main task in engineering geodesy, as stated in the foreword of (Heunecke *et al.* 2013, p. VI). For this purpose, numerous approaches have been developed in geodesy during the last decades, whereby the focus is essentially based on an evaluation of measurements using statistical methods. Such a data analysis in terms of precision and reliability by means of adjustment calculation is an integral part of engineering geodesy and one of its core competencies in general, see e.g. (Kuhlmann *et al.* 2014). For a correct and successful data evaluation, a detailed understanding of the applied sensors and also a profound knowledge of the mathematical relationships are playing a decisive role. Besides natural objects such as hillsides or glaciers, the main focus of a deformation analysis lies typically on structures such as tunnels, dams or bridges. The latter in particular has been the subject of numerous studies and scientific work for many years, especially in civil engineering, see e.g. (Koo *et al.* 2013), (Meng *et al.* 2004), (Lienhart *et al.* 2017) or (Omidalizarandi *et al.* 2020). Due to ageing structures and increasing traffic loads innovative approaches for a reliable damage assessment and predictions regarding the remaining service life of bridges are required.

One technology that has established itself in recent decades for the assessment of the integrity of structures is the Structural Health Monitoring (SHM), see (Boller *et al.* 2009), (Farrar and Worden 2013) or (Karbhari and Ansari 2011). The SHM covers the entire process from the characterisation of the structure, the selection of a suitable sensor technology and up to the statistical evaluation of the measurements, see (Daum 2013, p. 414 ff). Since in general "sensors cannot measure damage" (Worden *et al.* 2007, Axiom IVa), two main approaches are used in a SHM to extract information about damage from the measurements, namely the *inverse–problem* or *model–based* approach and the *data–based* approach (Farrar and Worden 2013, p. 9). The *data–based* approach is built on "intelligent feature extraction" and machine learning algorithms in order "to convert sensor data into damage information", see (Worden *et al.* 2007, Axiom IVa/b). A functional model does not have to be explicitly defined, but is rather estimated on the basis of training data and optimisation routines. In contrast, the *model–based* approach is built on a physical model of the structure under investigation, which is usually defined by a set of partial differential equations (PDEs) with boundary conditions and is often represented by a finite element model, see (Farrar and Worden 2013, p. 9). In general, this modelling must be very accurate, because even small deviations can sometimes have a large impact on the structural response. This requires not only the expert knowledge of different engineering sciences, but usually also an update of the model by measurements carried out on the real structure, see e.g. the standard literature on model update (Friswell and Mottershead 2011). The resulting model is also referred to as a *structural model* and is considered to represent the normal condition of the structure under investigation. The damage analysis is then based on deviations between the model and measurements from future monitoring epochs. Apart from this, there are also *modal models* which also belong to the *model–based* approach, although "the *modal model* does not contain specific information about the

Together with Condition Monitoring, which essentially relates to machines, the Structural Health Monitoring is summarised under the generic term Technical Diagnostics (Czichos 2013).

For detailed information about finite element method (FEM) in general please refer to standard literature such as (Bathe 2014), (Šolin 2006) or (Zienkiewicz *et al.* 2013).

structural connectivity or the geometric distribution of mass, structural damping and stiffness" (Chen and Ni 2018, Chapter 4.6). In this approach, the structural analysis is based on the dynamic behaviour of the structure represented by the modal parameters, i.e. eigenfrequencies, mode shapes and damping. One strategy that refers to modal models is the *ambient vibration monitoring*, see (Wenzel and Pichler 2005).

System identification

In general, the process to create a model from measured input and output data of a system is referred to as *system identification*. According to (Ljung 1998, p. 163), the entire process can be divided into the four steps:

- Measurement of the input and output data of a system.
- Choosing a set of candidate models.
- Estimation of the parameters of the model.
- Validation of the model.

"The single most important step in the identification process is to decide upon a model structure, i.e., a set of candidate models. In practice typically a whole lot of them are tried out and the process of identification really becomes the process of evaluating and choosing between the resulting models in these different structures" (Ljung 1998, p. 164). Generally, a distinction is made in the model structure between *black box*, *grey box* and *white box* models, for which the relationship according to (Heunecke *et al.* 2013, p. 81) is shown in Figure I.1.

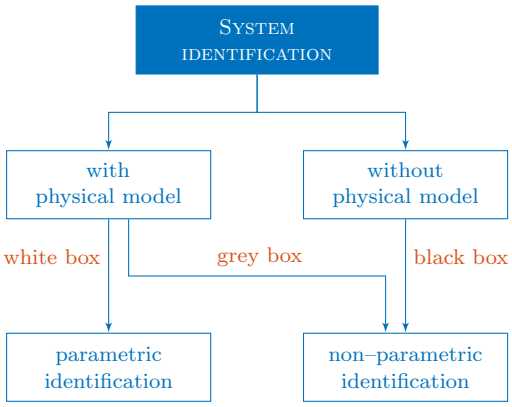

Figure I.1: Model structures according to (Heunecke *et al.* 2013, p. 81).

If the modelling of the system is based on a purely mathematical formulation without taking into account the physical relationship between input and output, then it is referred to as a *black box* model. In this case, the model parameters can only be interpreted mathematically and the process is referred to as *non-parametric identification*. In contrast, a *white box* model takes the physical relationship between input and output into account, and the model parameters can be interpreted physically. The process is referred to as *parametric identification*. Finally, *grey box* models are, as the name already implies, a mixture of both and are based on a semi-physical modelling, see (Ljung 1998, p. 165).

The classification of the system identification in the overall context of structural problems according to (Natke 1992, p. 3) is shown in Figure I.2.

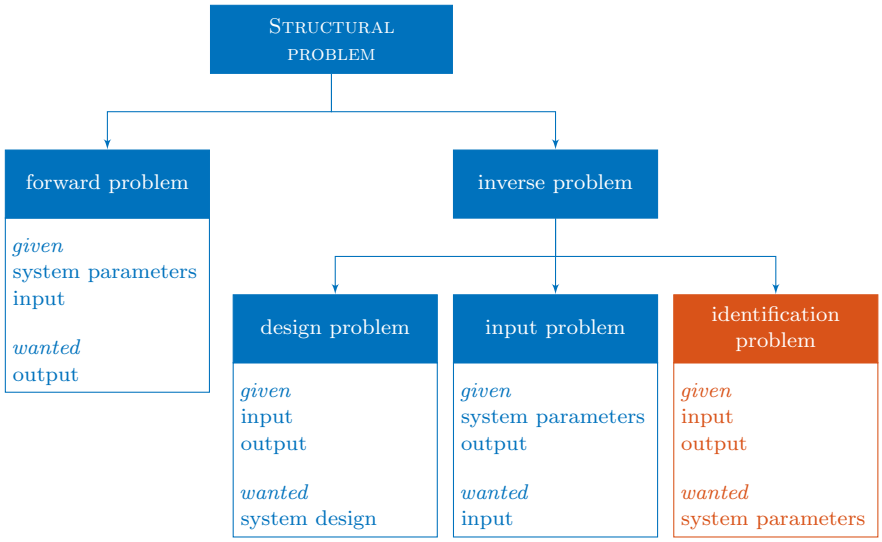

Figure I.2: Classification of the system identification according to (Natke 1992, p. 3).

Basically, structural problems can be divided into two main classes, namely the *forward* and the *inverse problem*. Whereas for *forward problems* with given input and system parameters the output can be calculated directly, this is typically not the case for *inverse problems*, as usually an infinite number of solutions exist. Especially for identification problems, therefore, in most cases only optimal sets of system parameters are determined by using optimisation routines and under consideration of additional information and/or search space constraints. However, for such problems there is usually no guarantee to find the best solution, which also corresponds to reality. In general, it can only be checked whether the determined system is reasonable and ideally provides the correct output for all input data of interest.

Deformation models for monitoring measurements

Engineering surveying is involved in all phases of the life cycle of a structure, from design/planning through construction and maintenance to reconstruction/demolition, see (Borrmann *et al.* 2015, p. 4). However, the monitoring measurements during the maintenance and operational phase have always been of particular interest in engineering geodesy. The focus thereby lies on a statistical analysis with regard to deformation affecting the stability and functionality of the structure under investigation. Depending on the problem/task, different models can be used for the deformation analysis of monitoring measurements, which can be classified according to (Heunecke *et al.* 2013, p. 77) as shown in Figure I.3.

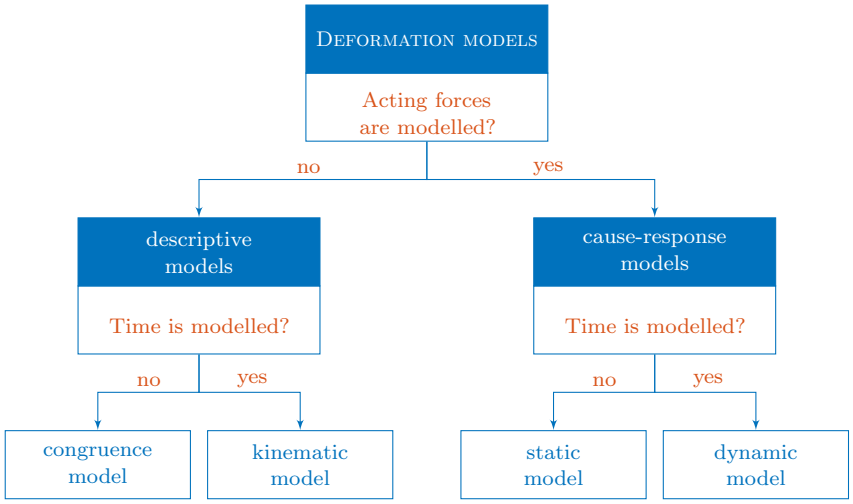

Figure I.3: Deformation models for monitoring measurements according to (Heunecke *et al.* 2013, p. 77).

Basically, the deformation models are classified in two steps. Firstly, whether the external forces acting on the structure are modelled or not and, in addition, if a movement of the structure over time is taken into account. Compared to *cause–response models*, the influence of external forces is not modelled for *descriptive models* and, consequently, deformation due to changes in these forces cannot be distinguished from actual deformation. Furthermore, if the movement of the structure as a function of time is not taken into account, the deformation analysis is based on a so-called *congruence model*. The *congruence model* is, therefore, the simplest modelling case and also the classical approach in engineering geodesy for the deformation analysis of structures. In this case, the deformation analysis is usually based on a purely geometric comparison of discrete points representing the structure under investigation. In contrast, *dynamic models* usually represent the real behaviour of structures in the best way, however, they are also often highly complex.

The measurement– and model–based structural analysis

Initiated by a project in cooperation with the Bundesanstalt für Materialforschung und -prüfung (BAM) and the Institut für angewandte Forschung im Bauwesen e.V (IaFB) on the detection of structural damage by an analysis of the Lagrange multipliers of adjustment calculation, the Measurement– and Model–based Structural Analysis (MeMoS) project was launched in 2013.

The functional model to adjust displacements and strain measurements for the Lagrange multiplier analysis was based on a mechanical model and allowed to detect damage, but rather based on a geometric comparison than on a deeper analysis of the model itself, see (Brandes *et al.* 2012). In addition, it was not possible at this stage to localise any damage with this first approach. These drawbacks and motivated by the work of (Lienhart 2007) this was to be changed with MeMoS. It was the unanimous opinion of all initiators at this time that MeMoS must be built on a *model–based* approach, or more precisely on a *structural model*. Because, the core of this approach shall be based on an all-embracing Integrated Analysis (IA) of spatially and temporally distributed hybrid measurements, observed e.g. by total stations, GNNS, terrestrial laser scanning (TLS), photogrammetry, radar interferometry, fibre optic sensors (FOS), strain gauges, accelerometers or inclination sensors. The

This expression has been adapted from the *Integrated Analysis Method* proposed by Lienhart (2007) and now describes the basic process for the least squares adjustment of measurements using a *structural model* within MeMoS.

aim of this IA is to ensure a rigorous and direct solution for the system parameters solely based on the measurements using the method of least squares. Consequently, a physical model of the structure must be embedded directly as a functional model in the least squares adjustment. The damage analysis is then based on these system parameters using well established geodetic deformation analysis methods, while the deformation model, thus, corresponds to a *cause-response model*.

The sheer number of publications in the field of civil engineering on damage assessment based on modal parameters demonstrates that such approaches are of great importance and that they can be used in a wide range of applications, while even some of these approaches are available to the user as a software package for several years now, see e.g. ARTeMIS Modal by STRUCTURAL VIBRATION SOLUTIONS A/S (2021). Thus, they can already be used directly for practical applications.

A general overview of the health monitoring of structures e.g. using modal parameters as well as their successful application in many examples can be found in standard literature such as (KARBHARI and ANSARI 2011), (CHEN and NI 2018), (FARRAR and WORDEN 2013) or (WENZEL 2009).

However, apart from basic studies in the analysis of vibration measurements using accelerometers or TLS, see (NEITZEL *et al.* 2011) and (NEITZEL *et al.* 2012), and the frequency analysis via the method of least squares, see (WEISBRICH and NEITZEL 2014), it was soon decided to focus first on static measurements such as displacements, inclinations and strains. This was necessary to keep the functional model for the IA as simple as possible and, therefore, to gain a better understanding of the *inverse problem*.

In contrast to the structural analysis using modal parameters, approaches based on *structural models* and static measurements are much less present in the literature. Although all these approaches are usually rely on an FEM, however, they roughly follow 3 different strategies for the structural analysis:

1. A geometrical comparison between model and measurements, see (BOLJEN 1983) or (MA 2019).
2. A determination of the system parameters using mainly black box FE programmes and an additional optimisation routine, see (LIENHART 2007), (EICHHORN 2005) or (KÜNZEL 2016).
3. An estimation of the system parameters, where both the model and the measurements are contributing to the objective function of the least squares adjustment, see (TESKY 1988) or (STEPHAN 2016).

In principle, the last strategy corresponds most closely to the actual requirement for the IA, but with the drawback that the estimation of the system parameters is not solely based on the measurements. Due to the formulation of the objective function for estimating the system parameters according to the method of least squares, both the model and the measurements have an impact on the solution. The *structural model* is not directly integrated as a functional model in the least squares adjustment. Therefore, a modified approach is developed for MeMoS.

In collaboration with my colleague Cheng-Chieh Wu from the BAM, we developed a preliminary version of the IA for a *parametric identification*, that allows a rigorous and direct solution for the system parameters solely based on the measurements, directly embedding a *structural model* represented by an FEM into the least squares adjustment, see e.g. (NEITZEL *et al.* 2014) or (WU *et al.* 2016). Furthermore, a substitute model for geometrical complex structures was derived, to drastically reduce the number of elements while keeping the behaviour of the model almost the same, see (WU *et al.* 2017).

Introducing a material parameter for each element enabled the localisation of damages within the structure based on statistical tests, which was to some extent successfully applied in two experimental tests, see (Wu 2020, Chapter 5). However, non-modelled residual stresses probably falsified the analysis and thus the localisation of small damages.

Introducing a material parameter for each element using the concept of observed unknowns, see (Wu 2020, Chapter 5.2), already had some disadvantages. Apart from a very large resulting equation system, prior knowledge about the material parameters must first be determined and the corresponding weights for the adjustment carefully chosen. The damage localisation is, therefore, not only based on the measurements, but also on the prior information about the material parameters. In addition, for many elements, i.e. for a high spatial resolution of the damage localisation, the least squares solution in practice no longer converges and the local material parameters can take numerical values up to $\pm\infty$ without changing the value of the objective function even in the last decimal place. In these cases, a solution can only be obtained by introducing high weights for the material parameters, which of course counteracts the localisation of damage.

After all, it remained unclear which part of the solution was due to the measurement noise and which was due to the functional model of the adjustment, i.e. the approximation of the structural behaviour by FEM. As already mentioned, a profound knowledge of the mathematical relationships, i.e. the functional model of the least squares adjustment, are playing a decisive role for a successful damage analysis, which was unfortunately not the case for this former approach and is the actual motivation for this thesis.

THE MAIN OBJECTIVE OF THIS THESIS

Several aspects are of great importance for a successful damage analysis with MeMoS. The most important one is certainly, that "it is very difficult to build an accurate model of a structure from first physical principles. Information or insight will be lacking in many areas, for example, and the exact nature of bonds, joints and so on can be difficult to specify. Another issue is that material properties may not be known with great accuracy" (Farrar and Worden 2013, p. 9). Consequently, modelling errors are usually present, which in general significantly affect the damage analysis, especially for complex structures.

For such problems, therefore, the expert knowledge of various engineering sciences is usually required and cannot be addressed within the scope of this thesis.

Furthermore, the physical model is usually defined by a set of PDEs with boundary conditions, for which the analytical solution is usually not known and can only be approximated, e.g. by means of FEM. Depending on the chosen approach, therefore, approximation errors are also present, which in the worst case also have a large impact on the damage analysis.

In addition to the error influences affecting the accuracy of measurements, the actual challenge of a damage analysis by means of MeMoS can be described, as shown in Figure I.4.

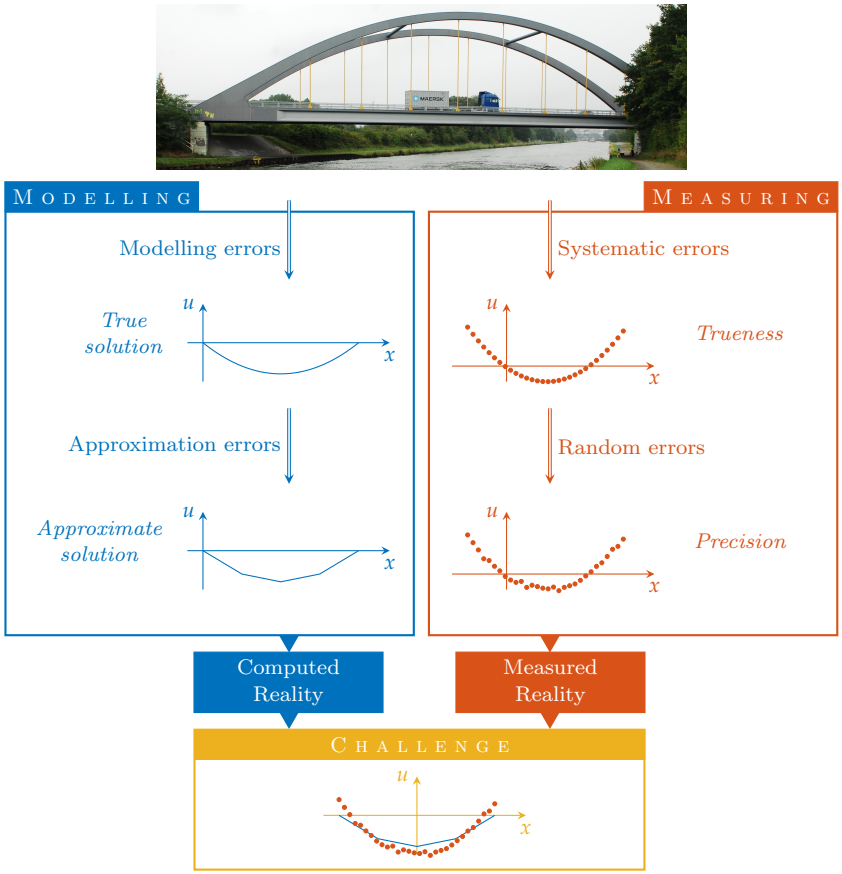

Figure I.4: Problems in modelling and measuring reality.

According to Figure I.4, the actual problem can be divided into two parts, namely in *modelling* and *measuring reality*. As already mentioned, the modelling and approximation errors are the two main error influences in the part of *modelling reality*, which mainly falsified the damage localisation in (Wu 2020, Chapter 5). On the part of *measuring reality*, two further important error influences are present affecting the accuracy of the measurements, namely the systematic and random errors, which basically cannot be avoided. In general, systematic errors have a similar influence as modelling errors and in the best case, their influence can be reduced by e.g. calibration of the sensors, a suitable measurement configuration or by mathematical compensation. At least it should be ensured that the influence of systematic errors is significantly smaller than the random errors, otherwise the damage analysis will be falsified. In the optimal case, a damage analysis would be based on an error-free model as well as on measurements that are only affected by random errors.

In addition, outliers or gross errors also occur, but they are not considered further in this case, as their influence often corresponds to damage itself. Therefore, it must be ensured that no outliers in the measurements are present.

Apart from the discussed problems in modelling and measuring reality, there is another issue for a damage analysis based on a physical model and measurements. In general, the model has a different reference frame than the measurements. Thus, each part has its own coordinate system and for a damage analysis, both have to be transferred into a common reference frame, which can usually only be done on the basis of additional measurements. If this transformation is not performed accurately, it will in turn falsify the damage analysis. However, it always has an influence.

Even worse, because usually each sensor has its own reference frame.

Before a damage analysis can be carried out at all, the challenge is to eliminate all error influences as far as possible, except for the unavoidable random errors, and to transform the model and the measurements into a common reference

frame. Only then is it ensured that a damage analysis using MeMoS has any significance at all. In this context, the following two main research topics are addressed in all detail in this thesis.

About the characteristics of basis functions on the approximation of functions

Especially for the least squares adjustment of observations of different physical quantities based on a complex functional relationship, undesired effects between the measurements and the model can easily be missed, which can distort the result and consequently make a successful damage analysis impossible. Therefore, the behaviour of the functional model must be clearly understood. For this purpose, the characteristics of different sets of basis functions for the approximation must be considered, since the functional model is based on an approximation of the unknown analytical solution of PDEs. Within the scope of this research topic, the following questions will also be addressed:

- What are the advantages and disadvantages of different approximation approaches, i.e. different sets of basis functions?
- Can it be ensured that the best approximation is always available?
- What about the numerical stability of the different approaches?
- How can approximations be transformed between different sets of basis functions?
- What problems generally arise in the transition from the approximation of univariate to multivariate functions?
- Is there a set of basis functions that always provides an optimal approximation for continuous functions?
- Which set of basis functions provides the best approximation of the analytical solution of PDEs for structures with simple geometry?
- Which set of basis functions is best suited for the analyses in the second research topic?

About the impact of random errors on the damage analysis using MeMoS

This research topic is essentially based on the results of the previous examinations with the actual aim of selecting the best set of basis functions for the damage analyses with MeMoS, which in this thesis is only based on static measurements, such as displacements, inclinations and strains. In this context, the following questions need to be answered first:

- What is the impact of measurement noise on the estimated unknown parameters?
- Are there any systematic effects between the chosen functional model and the measurements?
- What is the actual nature of the inverse problem?
- Does a numerically stable solution for the unknown parameters exist?

With regard to a damage analysis using MeMoS, the following questions must also be addressed.

- How does damage to the structure affect the measurements?
- To what extent can the effects of damage be measured at all?
- Is a damage analysis based on an IA possible, i.e. based solely on the measurements using the method of least squares?
- How can the information content of static measurements be optimally exploited for damage localisation using the method of least squares?

Based on the new insights, the potential of a Measurement– and Model–based Structural Analysis is finally re-evaluated using the example of the four-point bending test apparatus from (Wu 2020, Chapter 5.2).

OUTLINE OF THIS THESIS

Except for this and the last part, the thesis is divided into three main parts consisting of 9 chapters altogether. A short summary for each of these three parts is given below.

Fundamentals

The methodological background for the practical guide to the approximation of functions using the method of least squares in Part ii is given in Chapter 1. Afterwards, Chapter 2 presents the basics of adjustment calculation and shows how unknown parameters can be estimated from measurements using the method of least squares. In addition, the precision and reliability of adjustment results are briefly discussed. Both chapters provide the theoretical background for a Measurement– and Model–based Structural Analysis (MeMoS).

A practical guide to approximation of functions

In Chapter 3 the approximation of univariate functions in the monomial basis is discussed from a geodetic point of view in detail and then extended to an elementwise approximation. In addition, a transformation between different sets of basis functions is shown and how new basis functions with specific properties can be derived. At the end of this chapter an approximation with two sets of orthogonal basis functions is presented. These approaches are then extended to functions of two variables defined on a rectangular domain in Chapter 4. How bivariate functions in general can be approximated over any convex domain is outlined at the end of this chapter. Lastly, the approximation of boundary value problems (BVPs) using the method of least squares is briefly discussed in Chapter 5. Based on the insights gained in this part, we select an approximation approach which ensures that the approximation error of the functional model used for MeMoS in Part iii is zero within machine precision.

Measurement– and Model–based Structural Analysis

The challenges of MeMoS are clarified by the simple example of a statically bended Euler–Bernoulli beam. For this purpose, the mechanical model of a

four–point bending test is presented in Chapter 7. Subsequently, a numerical solution of the unknown function describing the bending line of the beam is derived. Then, this solution is implemented in Chapter 8 as the functional model of an Integrated Analysis (IA), which is the core of MeMoS. However, the derivation of the IA is limited to static measurements such as displacements, inclinations and/or strains, with the aim to detect and localise damage to the beam. Although this example is only a simple 1D problem and only static measurements are considered, there are already serious difficulties for a reliable damage analysis. Therefore, comprehensive numerical studies are carried out in Chapter 9 to highlight the actual nature of the inverse problem. First questions will be clarified, e.g. how the sensor position, the number of sensors or the measurement noise influence the estimated parameters and thus the damage analysis. Furthermore, it is shown how damage affects the static measurements and what can be expected from a damage analysis using MeMoS. The potential of a damage analysis via MeMoS is finally demonstrated in Chapter 10 by numerical and experimental studies, whereby some tools have been developed especially for this purpose.

At the end, the results of this thesis are summarized and evaluated. In addition, an outlook of MeMoS is given and future extensions and possibilities are addressed.

Part I

FUNDAMENTALS

1 APPROXIMATION THEORY

When we speak of an approximation in engineering geodesy, we usually mean an approximation using the method of least squares (MLS), as it is the most common method for the analysis of measured quantities. It is widely acknowledged that the first fundamental work on this method was published by LEGENDRE (1806), where he mainly "proposed [it] as a convenient method only", see (MERRIMAN 1877). Almost at the same time, ADRIAN (1809) and GAUSS (1809) presented a justification for the MLS based on normal distributed errors and the estimation of the most probable values for the unknown parameters. In addition, "Gauss had the temerity to claim that he had been using the method since 1795, and one of the most famous priority disputes in the history of science was off and running", see (STIGLER 1981). The circumstances and the contributions of all those involved in its development are still being discussed centuries later, see e.g. (PLACKETT 1972) or (SHEYNIN 2014). Apart from that, the derivation of the MLS shown by ADRIAN (1809) or GAUSS (1809), is the basic approach in statistical inference to estimate the most probable value for unknown parameters from a given sample of arbitrarily distributed observations, see e.g. (GENTLE 2009, Chapter 1.4) or (MONTGOMERY and RUNGER 2011, Chapter 7), and can also be found in standard literature on adjustment calculation, see e.g. (GHILANI 2018, Chapter 11.2). In addition, the relevant literature on measurement data analysis in general either simply refers to the least squares principle, see e.g. (MIKHAIL and ACKERMANN 1976, p. 104), (NIEMEIER 2008, p. 132) or (RADHAKRISHNA RAO and TOUTENBURG 1999, p. 24) , or also derives it via orthogonal projection, see (TEUNISSEN 2000, p. 6). The latter is generally also the common approach in approximation theory, which is essentially concerned with the approximation of functions. Thereby, complicated functions are usually approximated by a linear combination of simple basis functions, especially by polynomials. However, interpolation rather than MLS is typically used as it is faster to calculate in practice. But in order to understand the properties of different sets of basis functions, the MLS by means of orthogonal projection is well suited and will be discussed in more detail in this chapter. Therefore, we will only consider an approximation of functions using the method of least squares, while the basic structure and content of this chapter is essentially based on (LANGTANGEN 2016a) or (LANGTANGEN 2016b).

A comprehensive overview of the historical development of the MLS, including detailed summaries of the important contributions up to 1974, can be found in the series of articles (HARTER 1974a) (HARTER 1974b), (HARTER 1975a), (HARTER 1975b) and (HARTER 1975c).

The geometric interpretation of MLS via orthogonal projection is discussed in the geodetic literatur also by e.g. (ÁDÁM 1982), (BORRE 2006, p. 93 ff), (DERMANIS 1976, p. 30 ff), (MIKHAIL and ACKERMANN 1976, p. 131 ff) or (MORITZ and SÜNKEL 1978, pp. 134–148).

1.1 APPROXIMATION OF VECTORS

To illustrate an approximation of vectors, we consider a three–dimensional vector $\mathbf{L} \in \mathbb{R}^3$ with standard basis, as shown in Figure 1-1.

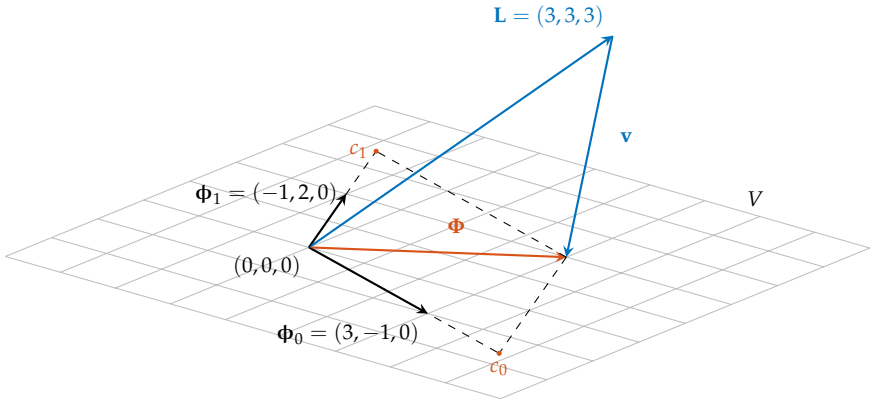

Figure 1-1: Approximation of a 3D vector $\mathbf{L}$ in a 2D vector space V spanned by the basis vectors $\boldsymbol{\Phi}_0$ and $\boldsymbol{\Phi}_1$.

In addition, we assume that we want to approximate $\mathbf{L}$ by another vector $\boldsymbol{\Phi}$, that lies in a two–dimensional vector space V spanned by the two *basis vectors* $\boldsymbol{\Phi}_0$ and $\boldsymbol{\Phi}_1$

$$V = \text{span}\{\boldsymbol{\Phi}_0, \boldsymbol{\Phi}_1\}\,. \tag{1-1}$$

Thus, vector $\boldsymbol{\Phi}$ can be written as a linear combination of these two basis vectors

$$\boldsymbol{\Phi} = \sum_{j=0}^{1} c_j\,\boldsymbol{\Phi}_j = c_0\boldsymbol{\Phi}_0 + c_1\boldsymbol{\Phi}_1\,, \tag{1-2}$$

with the two unknown parameters c_0 and c_1. As $\mathbf{L}$ is generally not in V, vector $\mathbf{L}$ is different from $\boldsymbol{\Phi}$ and this difference is known as *correction* or *residual* and is denoted by $\mathbf{v}$. Hence, we obtain the following relationship

$$\mathbf{L} + \mathbf{v} = \boldsymbol{\Phi}\,, \tag{1-3}$$

known in adjustment calculation as *observation equations*. Now the objective is to determine the unknown parameters in such a way that $\boldsymbol{\Phi}$ approximates $\mathbf{L}$ to the best possible extent. Usually the length of vector $\mathbf{v}$ is used as a measure for the best approximation, which is given by its Euclidian or L^2 norm

$$\|\mathbf{v}\|_2 = \sqrt{\langle \mathbf{v}, \mathbf{v}\rangle}\,, \tag{1-4}$$

with $\langle\cdot,\cdot\rangle$ being the *standard scalar product* of two vectors. The determination of the unknown coefficients under the condition that the length of $\mathbf{v}$ is minimal is known as the *method of least squares* and will be illustrated on the example presented in Figure 1-1.

1.1.1 *Method of least squares*

In the following we want to determine the unknown coefficients c_0 and c_1 from Figure 1-1 in such a way that the length of $\mathbf{v}$ is minimized. The length (1-4) is minimal, when

$$\Omega(c_0, c_1) = \langle \mathbf{v}, \mathbf{v}\rangle \rightarrow \min\,, \tag{1-5}$$

which is known as *objective*, *target* or *cost function*. Rearranging (1-3) and inserting into (1-5) yields

$$\Omega(c_0, c_1) = \langle \boldsymbol{\Phi} - \mathbf{L}, \boldsymbol{\Phi} - \mathbf{L}\rangle\,. \tag{1-6}$$

With (1-2) and since the scalar product is bilinear, equation (1-6) results in

$$\begin{aligned}\Omega(c_0,c_1) &= \langle c_0\boldsymbol{\Phi}_0 + c_1\boldsymbol{\Phi}_1 - \mathbf{L}, c_0\boldsymbol{\Phi}_0 + c_1\boldsymbol{\Phi}_1 - \mathbf{L}\rangle \\ &= \langle c_0\boldsymbol{\Phi}_0, c_0\boldsymbol{\Phi}_0\rangle + \langle c_0\boldsymbol{\Phi}_0, c_1\boldsymbol{\Phi}_1\rangle - \langle c_0\boldsymbol{\Phi}_0, \mathbf{L}\rangle \\ &\quad + \langle c_1\boldsymbol{\Phi}_1, c_0\boldsymbol{\Phi}_0\rangle + \langle c_1\boldsymbol{\Phi}_1, c_1\boldsymbol{\Phi}_1\rangle - \langle c_1\boldsymbol{\Phi}_1, \mathbf{L}\rangle \\ &\quad - \langle \mathbf{L}, c_0\boldsymbol{\Phi}_0\rangle - \langle \mathbf{L}, c_1\boldsymbol{\Phi}_1\rangle + \langle \mathbf{L}, \mathbf{L}\rangle\,. \end{aligned} \tag{1-7}$$

As the constant coefficients c_0 and c_1 can be extracted from the scalar product, the objective function (1-7) reads

$$\begin{aligned}\Omega(c_0,c_1) &= c_0^2\langle\boldsymbol{\Phi}_0,\boldsymbol{\Phi}_0\rangle + c_0c_1\langle\boldsymbol{\Phi}_0,\boldsymbol{\Phi}_1\rangle - c_0\langle\boldsymbol{\Phi}_0,\mathbf{L}\rangle \\ &\quad + c_0c_1\langle\boldsymbol{\Phi}_1,\boldsymbol{\Phi}_0\rangle + c_1^2\langle\boldsymbol{\Phi}_1,\boldsymbol{\Phi}_1\rangle - c_1\langle\boldsymbol{\Phi}_1,\mathbf{L}\rangle \\ &\quad - c_0\langle\mathbf{L},\boldsymbol{\Phi}_0\rangle - c_1\langle\mathbf{L},\boldsymbol{\Phi}_1\rangle + \langle\mathbf{L},\mathbf{L}\rangle\,. \end{aligned} \tag{1-8}$$

Introducing the necessary conditions for a minimum of the objective function (1-8)

$$\frac{1}{2}\frac{\partial\Omega(c_0,c_1)}{\partial c_0} = 0 \quad \text{and} \quad \frac{1}{2}\frac{\partial\Omega(c_0,c_1)}{\partial c_1} = 0 \tag{1-9}$$

and with $\langle\boldsymbol{\Phi}_0,\boldsymbol{\Phi}_1\rangle = \langle\boldsymbol{\Phi}_1,\boldsymbol{\Phi}_0\rangle$, equations (1-9) results in

$$\begin{aligned}\frac{1}{2}\frac{\partial\Omega(c_0,c_1)}{\partial c_0} &= c_0\langle\boldsymbol{\Phi}_0,\boldsymbol{\Phi}_0\rangle + c_1\langle\boldsymbol{\Phi}_0,\boldsymbol{\Phi}_1\rangle - \langle\boldsymbol{\Phi}_0,\mathbf{L}\rangle = 0\,, \\ \frac{1}{2}\frac{\partial\Omega(c_0,c_1)}{\partial c_1} &= c_0\langle\boldsymbol{\Phi}_1,\boldsymbol{\Phi}_0\rangle + c_1\langle\boldsymbol{\Phi}_1,\boldsymbol{\Phi}_1\rangle - \langle\boldsymbol{\Phi}_1,\mathbf{L}\rangle = 0\,. \end{aligned} \tag{1-10}$$

The resulting system of equations (1-10) are known as *normal equations* and can be written in matrix notation as follows

$$\mathbf{N}\mathbf{x} = \mathbf{n}$$

$$\begin{bmatrix}\langle\boldsymbol{\Phi}_0,\boldsymbol{\Phi}_0\rangle & \langle\boldsymbol{\Phi}_0,\boldsymbol{\Phi}_1\rangle \\ \langle\boldsymbol{\Phi}_1,\boldsymbol{\Phi}_0\rangle & \langle\boldsymbol{\Phi}_1,\boldsymbol{\Phi}_1\rangle\end{bmatrix}\begin{bmatrix}c_0\\c_1\end{bmatrix} = \begin{bmatrix}\langle\boldsymbol{\Phi}_0,\mathbf{L}\rangle\\ \langle\boldsymbol{\Phi}_1,\mathbf{L}\rangle\end{bmatrix}. \tag{1-11}$$

Since the basis vectors $\boldsymbol{\Phi}_0$ and $\boldsymbol{\Phi}_1$ are linear independent, the normal matrix $\mathbf{N}$ is invertible and the normal equation system (1-11) can be solved. For the example depicted in Figure 1-1, the normal equation system (1-11) reads

$$\begin{bmatrix}10 & -5\\ -5 & 5\end{bmatrix}\begin{bmatrix}c_0\\c_1\end{bmatrix} = \begin{bmatrix}6\\3\end{bmatrix} \tag{1-12}$$

and the coefficients are

$$\begin{bmatrix}c_0\\c_1\end{bmatrix} = \begin{bmatrix}1.8\\2.4\end{bmatrix}. \tag{1-13}$$

Inserting the coefficients (1-13) into (1-2) yields the least squares approximation of $\mathbf{L}$

$$\begin{aligned}\boldsymbol{\Phi} &= \sum_{j=0}^{1} c_j\,\boldsymbol{\Phi}_j = c_0\boldsymbol{\Phi}_0 + c_1\boldsymbol{\Phi}_1 = 1.8\,\boldsymbol{\Phi}_0 + 2.4\,\boldsymbol{\Phi}_1 \\ &= 1.8\begin{bmatrix}3\\-1\\0\end{bmatrix} + 2.4\begin{bmatrix}-1\\2\\0\end{bmatrix} = \begin{bmatrix}5.4\\-1.8\\0\end{bmatrix} + \begin{bmatrix}-2.4\\4.8\\0\end{bmatrix} = \begin{bmatrix}3\\3\\0\end{bmatrix}, \end{aligned} \tag{1-14}$$

which is depicted in Figure 1-2.

Throughout this thesis we only consider unknown functions as a linear combination of basis functions and since $\langle\mathbf{v},\mathbf{v}\rangle \geq 0$, it is ensured that the objective function has only one stationary point, which is a minimum.

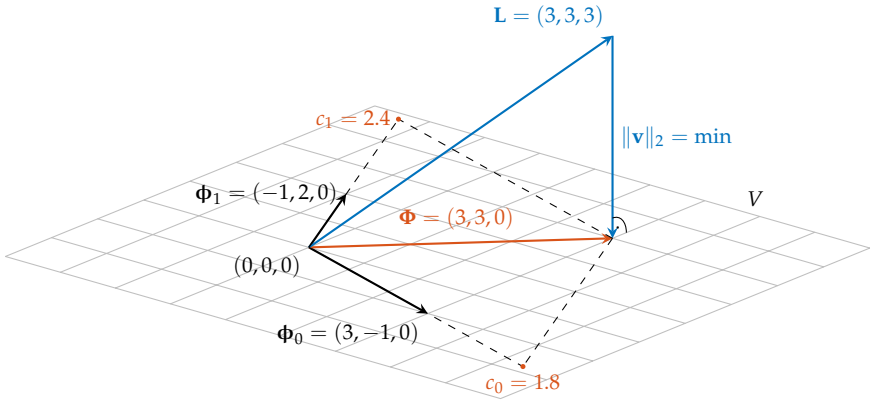

Figure 1-2: Least squares approximation of a 3D vector $\mathbf{L}$ in a 2D vector space V spanned by the basis vectors ϕ_0 and ϕ_1.

1.1.2 *Orthogonal projection*

As can be clearly seen in Figure 1-2, the length of $\mathbf{v}$ is minimal if it is orthogonal to V. Consequently, we can determine the unknown coefficients c_0 and c_1 of an least squares approximation of $\mathbf{L}$ by demanding that $\mathbf{v}$ must be orthogonal on V. From a geometrical point of view, this is only the case if $\mathbf{v}$ is orthogonal to the basis vectors and therefore the scalar products must be equal to zero

$$\langle \boldsymbol{\Phi}_i, \mathbf{v} \rangle = 0 \quad \text{for } i = 0,1\,. \tag{1-15}$$

However, this can also be shown in general, as done in (Langtangen 2016b, p. 10). Therefore, we consider an arbitrary vector $\mathbf{u} \in V$. If $\mathbf{v}$ is orthogonal to V, then it is also orthogonal to $\mathbf{u}$. Hence, the scalar product is equal to zero

$$\langle \mathbf{u}, \mathbf{v} \rangle = 0 \quad \forall \mathbf{u} \in V\,. \tag{1-16}$$

As all vectors $\mathbf{u}$ can be written as a linear combination of the two basis vectors

$$\mathbf{u} = \sum_{i=0}^{1} u_i\, \boldsymbol{\Phi}_i\,, \tag{1-17}$$

equation (1-16) results in

$$\langle \sum_{i=0}^{1} u_i\, \boldsymbol{\Phi}_i, \mathbf{v} \rangle = 0 \tag{1-18}$$

and rearranging yields

$$\begin{aligned} \sum_{i=0}^{1} u_i \langle \boldsymbol{\Phi}_i, \mathbf{v} \rangle &= 0 \\ u_0 \langle \boldsymbol{\Phi}_0, \mathbf{v} \rangle + u_1 \langle \boldsymbol{\Phi}_1, \mathbf{v} \rangle &= 0\,. \end{aligned} \tag{1-19}$$

Since (1-19) must hold true for all $\mathbf{u} \in V$ with arbitrary u_i, the two scalar products in (1-19) must be equal zero

$$\langle \boldsymbol{\Phi}_0, \mathbf{v} \rangle = 0 \quad \text{and} \quad \langle \boldsymbol{\Phi}_1, \mathbf{v} \rangle = 0\,, \tag{1-20}$$

which finally gives the same equations as from the geometric considerations in (1-15). Rearranging (1-3) and inserting into (1-20) yields

$$\begin{aligned} \langle \boldsymbol{\Phi}_0, \boldsymbol{\Phi} - \mathbf{L} \rangle &= 0 \\ \langle \boldsymbol{\Phi}_1, \boldsymbol{\Phi} - \mathbf{L} \rangle &= 0\,. \end{aligned} \tag{1-21}$$

Introducing (1-2) into (1-21) yields

$$\begin{aligned}\langle \boldsymbol{\Phi}_0, c_0\boldsymbol{\Phi}_0 + c_1\boldsymbol{\Phi}_1 - \mathbf{L}\rangle &= 0\\ \langle \boldsymbol{\Phi}_1, c_0\boldsymbol{\Phi}_0 + c_1\boldsymbol{\Phi}_1 - \mathbf{L}\rangle &= 0\end{aligned} \tag{1-22}$$

and results in

$$\begin{aligned}c_0\langle \boldsymbol{\Phi}_0, \boldsymbol{\Phi}_0\rangle + c_1\langle \boldsymbol{\Phi}_0, \boldsymbol{\Phi}_1\rangle - \langle \boldsymbol{\Phi}_0, \mathbf{L}\rangle &= 0\,,\\ c_0\langle \boldsymbol{\Phi}_1, \boldsymbol{\Phi}_0\rangle + c_1\langle \boldsymbol{\Phi}_1, \boldsymbol{\Phi}_1\rangle - \langle \boldsymbol{\Phi}_1, \mathbf{L}\rangle &= 0\,,\end{aligned} \tag{1-23}$$

which is the same equation system as already given by (1-10). To derive the normal equation system of a least squares approximation by demanding that $\mathbf{v}$ must be orthogonal to the basis vectors $\boldsymbol{\Phi}_j$ is known as *projection*.

1.1.3 *Least squares approximation of general vectors*

The presented least squares approximation of three–dimensional vectors in Section 1.1 can directly be transferred to vector spaces of any dimensions. Let us consider an arbitrary vector $\mathbf{L} \in \mathbb{R}^N$ to be approximated by $\boldsymbol{\Phi}$, that lies in a vector space V spanned by $p+1$ basis vectors

$$V = \text{span}\{\boldsymbol{\Phi}_0, \boldsymbol{\Phi}_1, \ldots, \boldsymbol{\Phi}_p\}\,, \tag{1-24}$$

with $N > p+1$ and

$$\boldsymbol{\Phi} = \sum_{j=0}^{p} c_j\,\boldsymbol{\Phi}_j = c_0\boldsymbol{\Phi}_0 + c_1\boldsymbol{\Phi}_1 + \ldots + c_p\boldsymbol{\Phi}_p\,. \tag{1-25}$$

According to Section 1.1.1 and 1.1.2 the length of $\mathbf{v}$ is minimal when

$$\Omega(c_0, c_1, \ldots, c_p) = \langle \mathbf{v}, \mathbf{v}\rangle \rightarrow \min\,, \tag{1-26}$$

or, when $\mathbf{v}$ is orthogonal to the basis vectors $\boldsymbol{\Phi}_i$ with

$$\langle \boldsymbol{\Phi}_i, \mathbf{v}\rangle = 0 \quad \text{for } i = 0, 1, \ldots, p\,. \tag{1-27}$$

Introducing $\mathbf{v} = \boldsymbol{\Phi} - \mathbf{L}$ into (1-27) yields

$$\langle \boldsymbol{\Phi}_i, \boldsymbol{\Phi} - \mathbf{L}\rangle = 0 \quad \text{for } i = 0, 1, \ldots, p \tag{1-28}$$

and as the scalar product is bilinear equation (1-28) reads

$$\langle \boldsymbol{\Phi}_i, \boldsymbol{\Phi}\rangle = \langle \boldsymbol{\Phi}_i, \mathbf{L}\rangle \quad \text{for } i = 0, 1, \ldots, p\,. \tag{1-29}$$

Inserting (1-25) results in

$$\langle \boldsymbol{\Phi}_i, \sum_{j=0}^{p} c_j\,\boldsymbol{\Phi}_j\rangle = \langle \boldsymbol{\Phi}_i, \mathbf{L}\rangle \quad \text{for } i = 0, 1, \ldots, p \tag{1-30}$$

and rearranging yields the $p+1$ normal equations

$$\sum_{j=0}^{p} c_j\langle \boldsymbol{\Phi}_i, \boldsymbol{\Phi}_j\rangle = \langle \boldsymbol{\Phi}_i, \mathbf{L}\rangle \quad \text{for } i = 0, 1, \ldots, p\,, \tag{1-31}$$

or in detail

$$c_0\langle \boldsymbol{\Phi}_i, \boldsymbol{\Phi}_0\rangle + c_1\langle \boldsymbol{\Phi}_i, \boldsymbol{\Phi}_1\rangle + \ldots + c_p\langle \boldsymbol{\Phi}_i, \boldsymbol{\Phi}_p\rangle = \langle \boldsymbol{\Phi}_i, \mathbf{L}\rangle \tag{1-32}$$

for $i = 0, 1, \ldots, p$. Writing the normal equation system (1-32) in matrix notation reads

$$\underbrace{\begin{bmatrix} \langle \boldsymbol{\Phi}_0, \boldsymbol{\Phi}_0 \rangle & \langle \boldsymbol{\Phi}_0, \boldsymbol{\Phi}_1 \rangle & \ldots & \langle \boldsymbol{\Phi}_0, \boldsymbol{\Phi}_p \rangle \\ \langle \boldsymbol{\Phi}_1, \boldsymbol{\Phi}_0 \rangle & \langle \boldsymbol{\Phi}_1, \boldsymbol{\Phi}_1 \rangle & \ldots & \langle \boldsymbol{\Phi}_1, \boldsymbol{\Phi}_p \rangle \\ \vdots & \vdots & \ddots & \vdots \\ \langle \boldsymbol{\Phi}_p, \boldsymbol{\Phi}_0 \rangle & \langle \boldsymbol{\Phi}_p, \boldsymbol{\Phi}_1 \rangle & \ldots & \langle \boldsymbol{\Phi}_p, \boldsymbol{\Phi}_p \rangle \end{bmatrix}}_{\mathbf{N}} \underbrace{\begin{bmatrix} c_0 \\ c_1 \\ \vdots \\ c_p \end{bmatrix}}_{\mathbf{x}} = \underbrace{\begin{bmatrix} \langle \boldsymbol{\Phi}_0, \mathbf{L} \rangle \\ \langle \boldsymbol{\Phi}_1, \mathbf{L} \rangle \\ \vdots \\ \langle \boldsymbol{\Phi}_p, \mathbf{L} \rangle \end{bmatrix}}_{\mathbf{n}} . \tag{1-33}$$

1.2 APPROXIMATION OF FUNCTIONS

For detailed information on the approximation of functions in general please refer to standard literature such as (BURDEN and FAIRES 2011, Chapter 8.2), (SÜLI and MAYERS 2003, Chapter 9) or (TREFETHEN 2013).

As already shown for vectors, functions can also be approximated by the method of least squares. For this purpose we consider an arbitrary function $f(x) \in L^2([a,b])$, the Hilbert space of square integrable functions. In addition, we assume that we want to approximate $f(x)$ by another function $\Phi(x)$, that lies in vector space V spanned by $p+1$ *basis functions*

$$V = \operatorname{span}\{\phi_0(x), \phi_1(x), \ldots, \phi_p(x)\} . \tag{1-34}$$

Thus, function $\Phi(x)$ can be written as a linear combination of these basis functions

$$\Phi(x) = \sum_{j=0}^{p} c_j \phi_j(x) = c_0\phi_0(x) + c_1\phi_1(x) + \ldots + c_p\phi_p(x) , \tag{1-35}$$

In the literature, the residual function is usually denoted by $R(x)$.

with the unknown parameters c_j. Since $f(x)$ is generally not in V, it is different from $\Phi(x)$ and this difference is known as *residual function*. As for vectors, we obtain the following relationship

$$f(x) + v(x) = \Phi(x) . \tag{1-36}$$

Now the objective is to determine the unknown parameters in such a way that $\Phi(x)$ approximates $f(x)$ to the best possible extent and as for vectors we use the length of $v(x)$ as a measure for the best approximation, which is given by the L^2 norm

$$\|v(x)\|_2 = \sqrt{\langle v, v \rangle} = \sqrt{\int_a^b \left(v(x)\right)^2 \mathrm{d}x} , \tag{1-37}$$

with $\langle \cdot, \cdot \rangle$ being the inner product of two functions, see for example (BRONSHTEIN *et al.* 2007, page 920) and

$$v(x) = \Phi(x) - f(x) = \sum_{j=0}^{p} c_j \phi_j(x) - f(x) . \tag{1-38}$$

1.2.1 *Method of least squares*

Like before, we want to determine the unknown coefficients c_j in such a way that the length of $v(x)$ is minimized and this is the case when

$$\Omega(c_0, c_1, \ldots, c_p) = \langle v, v \rangle \rightarrow \min . \tag{1-39}$$

Inserting (1-38) into (1-39) yields

$$\Omega(c_0, c_1, \ldots, c_p) = \langle \Phi - f, \Phi - f \rangle \tag{1-40}$$

and with (1-35) the target function (1-40) reads

$$\Omega(c_0, c_1, \ldots, c_p) = \langle \sum_{i=0}^{p} c_i \phi_i - f, \sum_{j=0}^{p} c_j \phi_j - f \rangle \,. \tag{1-41}$$

Since the inner product is bilinear, equation (1-41) results in

$$\Omega(c_0, c_1, \ldots, c_p) = \sum_{i=0}^{p} \sum_{j=0}^{p} c_i c_j \langle \phi_i, \phi_j \rangle - 2 \sum_{k=0}^{p} c_k \langle \phi_k, f \rangle + \langle f, f \rangle \,. \tag{1-42}$$

Introducing the necessary conditions for a minimum of the objective function (1-42) yields

$$\frac{1}{2} \frac{\partial \Omega(c_0, c_1, \ldots, c_p)}{\partial c_i} = \sum_{j=0}^{p} c_j \langle \phi_i, \phi_j \rangle - \langle \phi_i, f \rangle = 0 \,, \tag{1-43}$$

or rather

$$\sum_{j=0}^{p} c_j \langle \phi_i, \phi_j \rangle = \langle \phi_i, f \rangle \,, \tag{1-44}$$

for $i = 0, 1, \ldots, p$. The system of normal equations (1-44) can be written in matrix notation as follows

$$\mathbf{N}\mathbf{x} = \mathbf{n}$$

$$\begin{bmatrix} \langle \phi_0, \phi_0 \rangle & \langle \phi_0, \phi_1 \rangle & \ldots & \langle \phi_0, \phi_p \rangle \\ \langle \phi_1, \phi_0 \rangle & \langle \phi_1, \phi_1 \rangle & \ldots & \langle \phi_1, \phi_p \rangle \\ \vdots & \vdots & \ddots & \vdots \\ \langle \phi_p, \phi_0 \rangle & \langle \phi_p, \phi_1 \rangle & \ldots & \langle \phi_p, \phi_p \rangle \end{bmatrix} \begin{bmatrix} c_0 \\ c_1 \\ \vdots \\ c_p \end{bmatrix} = \begin{bmatrix} \langle \phi_0, f \rangle \\ \langle \phi_1, f \rangle \\ \vdots \\ \langle \phi_p, f \rangle \end{bmatrix} . \tag{1-45}$$

For a least squares approximation of $f(x)$ with respect to a certain set of basis functions $\phi_j(x)$ we only have to calculate the integrals

$$\begin{aligned} \langle \phi_i, \phi_j \rangle &= \int_a^b \phi_i(x)\, \phi_j(x)\, \mathrm{d}x \\ \langle \phi_i, f \rangle &= \int_a^b \phi_i(x)\, f(x)\, \mathrm{d}x \end{aligned} \tag{1-46}$$

for $i, j = 0, 1, \ldots, p$ and to solve (1-45) for the unknown coefficients c_j.

1.2.2 *Orthogonal projection*

As already shown in Section 1.1.2, we can also determine the unknown coefficients c_j of a least squares approximation of $f(x)$ by demanding that $v(x)$ must be orthogonal on V. This is only the case if $v(x)$ is orthogonal to the basis functions and therefore the inner products must be equal to zero

$$\langle \phi_i, v \rangle = 0 \,, \tag{1-47}$$

with $i = 0, 1, \ldots, p$. Inserting (1-36) into (1-47) yields

$$\langle \phi_i, \Phi - f \rangle = 0 \quad \text{for } i = 0, 1, \ldots, p \,, \tag{1-48}$$

and with (1-35) the system of normal equations reads

$$\langle \phi_i, \sum_{j=0}^{p} c_j \phi_j(x) - f \rangle = 0 \,. \tag{1-49}$$

Since the inner product if bilinear, equation (1-49) results in

$$\sum_{j=0}^{p} c_j \langle \phi_i, \phi_j \rangle = \langle \phi_i, f \rangle \,, \tag{1-50}$$

for $i = 0, 1, \ldots, p$ and is equal to (1-44).

The normal equation system (1-45) forms the basis for all kinds of approximations of functions or partial differential equations using the method of least squares. In addition to the norm and/or the vector space in which the residual function is orthogonally projected, the choice of a suitable basis is essential for a reasonable approximation. To clarify this issue, a practical guide to the approximation of functions for different sets of basis functions is given in Part ii.

2 ADJUSTMENT CALCULATION

In Chapter 1 we already discussed the method of least squares and demonstrated in general how functions can be approximated. In addition, we will present the basics of adjustment calculation in the following and show how unknown parameters can be estimated from measurements using the method of least squares. For detailed information about adjustment calculation in general please refer to standard literature such as (Ghilani 2018), (Mikhail and Ackermann 1976) or (Teunissen 2000). The notation used here is based on (Niemeier 2008).

2.1 MATHEMATICAL MODEL

As described in (Mikhail and Ackermann 1976, p. 5), for example, the mathematical model of adjustment calculation consists essentially of two parts: the *functional model* and *stochastic model*. While the stochastic model considers the non–deterministic properties of the observations, the functional model represents the deterministic properties that reflect the geometrical or physical situation to be investigated. A clear description of both parts is indispensable for the solution of an adjustment problem.

2.1.1 *Functional model*

An essential task in adjustment calculation is to formulate a mathematical relationship that connects the observations l with the unknown parameters x, which is known as the *functional model*. In general, this can be any implicit functional relationship

$$\Phi(l, x) = 0\,, \tag{2-1}$$

with $\Phi(l, x)$ being in general a nonlinear, differentiable function. A rigorous solution of adjustment problems resulting from such implicit functional relationships can be found in (Lenzmann and Lenzmann 2004) and (Neitzel 2010), for example. At this point, however, we only want to consider the special case that the observations l can be represented as a function of the unknown parameters x, which results in the following explicit functional relationship

$$l = \Phi(x)\,. \tag{2-2}$$

2.1.2 *Stochastic model*

While usually dealing with heterogeneous types of observations measuring different physical or geometrical quantities, we have to take their different stochastic properties into account. Usually this is done by specifying variances and covariances. In case n observations l_i with $i = 1, \ldots, n$ are given, their

stochastic properties can be combined in the variance–covariance matrix of the observations $\mathbf{\Sigma_{ll}}$, which is defined by

$$\mathbf{\Sigma_{ll}} = \begin{bmatrix} \sigma_{l_1}^2 & \sigma_{l_1 l_2} & \cdots & \sigma_{l_1 l_n} \\ \sigma_{l_2 l_1} & \sigma_{l_2}^2 & \cdots & \sigma_{l_2 l_n} \\ \vdots & \vdots & \ddots & \vdots \\ \sigma_{l_n l_1} & \sigma_{l_n l_2} & \cdots & \sigma_{l_n}^2 \end{bmatrix}, \tag{2-3}$$

with the standard deviation σ_{l_i} of the observations l_i being the positive square root of the variance $\sigma_{l_i}^2$. In addition, the correlation coefficient $\varrho_{l_i l_j}$ between two observations l_i and l_j can be calculated by

$$\varrho_{l_i l_j} = \frac{\sigma_{l_i l_j}}{\sigma_{l_i} \sigma_{l_j}}, \tag{2-4}$$

From a numerical point of view, one should always choose an appropriate value for σ_0.

with $\sigma_{l_i l_j}$ being the covariance. Choosing an arbitrary theoretical reference standard deviation σ_0 and scaling the variance–covariance matrix (2-3) yields the cofactor matrix

$$\mathbf{Q_{ll}} = \frac{1}{\sigma_0^2} \mathbf{\Sigma_{ll}}. \tag{2-5}$$

Assuming that $\mathbf{Q_{ll}}$ is a non-singular matrix, the weight matrix $\mathbf{P}$ represents the *stochastic model* and reads

$$\mathbf{P} = \mathbf{Q_{ll}}^{-1}. \tag{2-6}$$

2.2 OBSERVATION EQUATIONS

As already mentioned, we only consider a functional model according to Equation (2-2). Let us suppose that n observations l_i for $i = 1, \ldots, n$ are available to estimate m unknown parameters x_j for $j = 1, \ldots, m$, then the functional relationship is given by the equation system

$$\begin{aligned} l_1 &= \Phi_1(x_1, \ldots, x_m), \\ l_2 &= \Phi_2(x_1, \ldots, x_m), \\ &\vdots \\ l_n &= \Phi_n(x_1, \ldots, x_m). \end{aligned} \tag{2-7}$$

In general, only those cases will be considered in adjustment calculation where more observations than unknown parameters are given with $n > m$. Hence, the equation system (2-7) is usually not fulfilled as the true values for the observations are in principle not given. Thus, we introduce a residual v_i for each observation l_i and Equations (2-7) result in

$$\begin{aligned} l_1 + v_1 &= \Phi_1(x_1, \ldots, x_m), \\ l_2 + v_2 &= \Phi_2(x_1, \ldots, x_m), \\ &\vdots \\ l_n + v_n &= \Phi_n(x_1, \ldots, x_m), \end{aligned} \tag{2-8}$$

which are known as the *observation equations*. In addition, we only want to consider linear adjustment problems, so that the system of observation equations (2-8) can be written in matrix notation as follows

$$\mathbf{l} + \mathbf{v} = \mathbf{A}\mathbf{x}, \tag{2-9}$$

with the vector of observations

$$\mathbf{l} = \begin{bmatrix} l_1 & l_2 & \dots & l_n \end{bmatrix}^\mathsf{T}, \tag{2-10}$$

the vector of unknowns

$$\mathbf{x} = \begin{bmatrix} x_1 & x_2 & \dots & x_m \end{bmatrix}^\mathsf{T} \tag{2-11}$$

and the design matrix $\mathbf{A}$ containing the coefficients of the linear model.

2.3 LEAST SQUARES ADJUSTMENT

In the following we want to determine the vector of unknown parameters $\mathbf{x}$ from the linear observation equations (2-9) in such a way that the sum of weighted squared residuals is minimum. Hence, the target function reads

$$\Omega(\mathbf{x}) = \mathbf{v}^\mathsf{T}\mathbf{P}\mathbf{v} \rightarrow \min . \tag{2-12}$$

Solving (2-9) for $\mathbf{v}$ and inserting in (2-12) yields

$$\Omega(\mathbf{x}) = (\mathbf{A}\mathbf{x} - \mathbf{l})^\mathsf{T}\mathbf{P}(\mathbf{A}\mathbf{x} - \mathbf{l}) \tag{2-13}$$

and results after rearranging into

$$\begin{aligned} \Omega(\mathbf{x}) &= (\mathbf{x}^\mathsf{T}\mathbf{A}^\mathsf{T} - \mathbf{l}^\mathsf{T})\mathbf{P}(\mathbf{A}\mathbf{x} - \mathbf{l}), \\ &= \mathbf{x}^\mathsf{T}\mathbf{A}^\mathsf{T}\mathbf{P}\mathbf{A}\mathbf{x} - \mathbf{l}^\mathsf{T}\mathbf{P}\mathbf{A}\mathbf{x} - \mathbf{x}^\mathsf{T}\mathbf{A}^\mathsf{T}\mathbf{P}\mathbf{l} + \mathbf{l}^\mathsf{T}\mathbf{P}\mathbf{l}, \\ &= \mathbf{x}^\mathsf{T}\mathbf{A}^\mathsf{T}\mathbf{P}\mathbf{A}\mathbf{x} - 2\mathbf{x}^\mathsf{T}\mathbf{A}^\mathsf{T}\mathbf{P}\mathbf{l} + \mathbf{l}^\mathsf{T}\mathbf{P}\mathbf{l}. \end{aligned} \tag{2-14}$$

Introducing the necessary conditions for a minimum of the objective function (2-14)

$$\frac{1}{2}\frac{\partial \Omega(\mathbf{x})}{\partial \mathbf{x}^\mathsf{T}} = \mathbf{0} \tag{2-15}$$

results in

$$\mathbf{A}^\mathsf{T}\mathbf{P}\mathbf{A}\mathbf{x} - \mathbf{A}^\mathsf{T}\mathbf{P}\mathbf{l} = \mathbf{0} \tag{2-16}$$

and yields the normal equation system

$$\begin{aligned} \mathbf{A}^\mathsf{T}\mathbf{P}\mathbf{A}\mathbf{x} &= \mathbf{A}^\mathsf{T}\mathbf{P}\mathbf{l}, \\ \mathbf{N}\mathbf{x} &= \mathbf{n}, \end{aligned} \tag{2-17}$$

with the normal matrix $\mathbf{N} = \mathbf{A}^\mathsf{T}\mathbf{P}\mathbf{A}$ and the vector of the right hand side $\mathbf{n} = \mathbf{A}^\mathsf{T}\mathbf{P}\mathbf{l}$. Solving (2-17) yields the least squares estimate of the unknown parameters

Adjusted quantities are denoted by "ˆ ".

$$\begin{aligned} \hat{\mathbf{x}} &= \mathbf{N}^{-1}\mathbf{n}, \\ &= \mathbf{Q}_{\hat{\mathbf{x}}\hat{\mathbf{x}}}\mathbf{n}, \end{aligned} \tag{2-18}$$

with the cofactor matrix of the unknown parameters $\mathbf{Q}_{\hat{\mathbf{x}}\hat{\mathbf{x}}} = \mathbf{N}^{-1}$. The empirical reference standard deviation s_0 can be calculated by

$$s_0 = \sqrt{\frac{\mathbf{v}^\mathsf{T}\mathbf{P}\mathbf{v}}{n - m}}, \tag{2-19}$$

with

$$\mathbf{v} = \mathbf{A}\hat{\mathbf{x}} - \mathbf{l}. \tag{2-20}$$

The variance–covariance matrix of the unknown parameters is given by

$$\mathbf{\Sigma}_{\hat{\mathbf{x}}\hat{\mathbf{x}}} = s_0^2\,\mathbf{Q}_{\hat{\mathbf{x}}\hat{\mathbf{x}}}, \tag{2-21}$$

providing the standard deviations $s_{\hat{x}_j}$ of the adjusted unknown parameters $\hat{x}_j$ on the main diagonal of $\mathbf{\Sigma}_{\hat{\mathbf{x}}\hat{\mathbf{x}}}$.

2.4 LEAST SQUARES ADJUSTMENT WITH CONSTRAINTS

Let us assume that in addition to the observation equations in (2-9), the following n_c linear constraints between the unknown parameters $\mathbf{x}$ are given

$$\mathbf{C}\mathbf{x} = \mathbf{0}\,, \tag{2-22}$$

This problem can also be solved by eliminating unknown parameters, which is not covered here.

with matrix $\mathbf{C}$ containing the coefficients of the linear constraints. The least squares solution of such a problem can be determined by formulating the Lagrange function

$$L(\mathbf{x},\boldsymbol{\lambda}) = \mathbf{v}^\mathsf{T}\mathbf{P}\mathbf{v} + 2\boldsymbol{\lambda}^\mathsf{T}\mathbf{C}\mathbf{x}\,, \tag{2-23}$$

with the vector of Langrangian multiplier $\boldsymbol{\lambda}$, see (BRONSHTEIN *et al.* 2007, p. 403). For linear adjustment problems the Lagrange function in (2-23) has only a saddle point, see e.g. (BRONSHTEIN *et al.* 2007, p. 862), that can be found by introducing the necessary conditions

$$\begin{aligned} \frac{1}{2}\frac{\partial L(\mathbf{x},\boldsymbol{\lambda})}{\partial \mathbf{x}^\mathsf{T}} &= \mathbf{0}\,, \\ \frac{1}{2}\frac{\partial L(\mathbf{x},\boldsymbol{\lambda})}{\partial \boldsymbol{\lambda}^\mathsf{T}} &= \mathbf{0}\,, \end{aligned} \tag{2-24}$$

which in the end results in the extended normal equation system

$$\begin{bmatrix} \mathbf{A}^\mathsf{T}\mathbf{P}\mathbf{A} & \mathbf{C}^\mathsf{T} \\ \mathbf{C} & \mathbf{0} \end{bmatrix} \begin{bmatrix} \mathbf{x} \\ \boldsymbol{\lambda} \end{bmatrix} = \begin{bmatrix} \mathbf{A}^\mathsf{T}\mathbf{P}\mathbf{l} \\ \mathbf{0} \end{bmatrix}\,, \tag{2-25}$$

or in short

$$\begin{bmatrix} \mathbf{N} & \mathbf{C}^\mathsf{T} \\ \mathbf{C} & \mathbf{0} \end{bmatrix} \begin{bmatrix} \mathbf{x} \\ \boldsymbol{\lambda} \end{bmatrix} = \begin{bmatrix} \mathbf{n} \\ \mathbf{0} \end{bmatrix}\,. \tag{2-26}$$

Solving (2-26) yields the least squares estimate of the unknown parameters

$$\begin{aligned} \begin{bmatrix} \hat{\mathbf{x}} \\ \boldsymbol{\lambda} \end{bmatrix} &= \begin{bmatrix} \mathbf{N} & \mathbf{C}^\mathsf{T} \\ \mathbf{C} & \mathbf{0} \end{bmatrix}^{-1} \begin{bmatrix} \mathbf{n} \\ \mathbf{0} \end{bmatrix}\,, \\ &= \begin{bmatrix} \mathbf{Q}_{\hat{\mathbf{x}}\hat{\mathbf{x}}} & \mathbf{Q}_{\hat{\mathbf{x}}\boldsymbol{\lambda}} \\ \mathbf{Q}_{\boldsymbol{\lambda}\hat{\mathbf{x}}} & \mathbf{Q}_{\boldsymbol{\lambda}\boldsymbol{\lambda}} \end{bmatrix} \begin{bmatrix} \mathbf{n} \\ \mathbf{0} \end{bmatrix}\,, \end{aligned} \tag{2-27}$$

under the requirement that the constraints (2-22) must be fulfilled. The empirical reference standard deviation s_0 can be calculated by

$$s_0 = \sqrt{\frac{\mathbf{v}^\mathsf{T}\mathbf{P}\mathbf{v}}{n - m + n_c}} \tag{2-28}$$

and the standard deviations $s_{\hat{x}_j}$ of the adjusted unknown parameters $\hat{x}_j$ can be determined from the variance–covariance matrix of the unknowns $\boldsymbol{\Sigma}_{\hat{\mathbf{x}}\hat{\mathbf{x}}}$, which can be calculated according to Section 2.3.

2.5 QUALITY ASSESSMENT OF ADJUSTMENT RESULTS

So far, we have mainly dealt with the estimation of unknown parameters, however, it is indispensable to assess the quality of the adjustment result. In general, conclusions about the quality of adjustment results are based on measures

referring to *precision* and *reliability*. The precision describes the reproducibility or repeatability of the unknown parameters estimated from measurements acquired under the same conditions and under the assumption that the functional and stochastic model is appropriate and that measurements are only affected by random errors. Only if this is the case, it makes sense to provide measures describing the precision, because otherwise the result can be strongly falsified by, for example, possible outliers in the observations. Therefore, measures for the reliability are describing to what extent outliers can be detected, how large their impact on the estimation of the unknown parameters is and how well the observations control each other. A common measure describing the precision is the standard deviation of the unknown parameters $s_{\hat{x}_j}$, which is derived from the cofactor matrix of the unknowns $\mathbf{Q}_{\hat{\mathbf{x}}\hat{\mathbf{x}}}$ and has already been discussed in Section 2.3 or 2.4. In contrast, all measures describing the reliability are derived from the cofactor matrix of the residuals $\mathbf{Q}_{\mathbf{vv}}$, which can be calculated by

$$\mathbf{Q}_{\mathbf{vv}} = \mathbf{Q}_{\mathbf{ll}} - \mathbf{Q}_{\hat{\mathbf{l}}\hat{\mathbf{l}}}\,, \tag{2-29}$$

with the cofactor matrix of the adjusted observations

$$\mathbf{Q}_{\hat{\mathbf{l}}\hat{\mathbf{l}}} = \mathbf{A}\mathbf{Q}_{\hat{\mathbf{x}}\hat{\mathbf{x}}}\mathbf{A}^{\mathsf{T}}\,. \tag{2-30}$$

However, the measures known from literature to describe the internal and external reliability are not discussed here, further information can be found e.g. in (NIEMEIER 2008, Chapter 8.3). In the following we only want to consider the redundancy numbers (EVs), the global test of the adjustment calculation and the standardised residuals (NVs) in more detail.

2.5.1 *Redundancy numbers*

The redundancy number r_i can be regarded as a transfer factor indicating the extent to which an error in an observation l_i is transferred to its corresponding residual v_i and is given by

$$r_i = \left(\mathbf{Q}_{\mathbf{vv}}\mathbf{P}\right)_{ii}\,. \tag{2-31}$$

The redundancy number r_i can take values between 0 and 1, where $r_i = 1$ means that an error in the observation l_i is to be found completely in its residual v_i and hence is detectable. While for $r_i = 0$ the error can not be found in its residual at all and therefore is not detectable. The redundancy number r_i thus indicates how well an observation l_i is controlled by the others and can be given in percentage by EV_i with

German: *Einfluss auf die Verbesserung.*

$$EV_i = 100\,\%\; r_i\,. \tag{2-32}$$

In practice, the following rating scale for the evaluation of the redundancy numbers is used:

0 %	$\leq$	EV_i	$<$	1 %	observation is not controlled,
1 %	$\leq$	EV_i	$<$	10 %	observation is poorly controlled,
10 %	$\leq$	EV_i	$<$	30 %	observation is sufficiently controlled,
30 %	$\leq$	EV_i	$<$	70 %	observation is well controlled,
70 %	$\leq$	EV_i	$<$	100 %	observation can be removed without loss of reliability.

2.5.2 *Global test*

After an adjustment, a global test is usually performed first. Assuming that the functional and stochastic model was chosen appropriately and the observations are well controlled, this test can indicate if outliers may be present in the observations. Thereby it is checked whether the empirical reference standard deviation s_0 corresponds to the theoretical reference standard deviation σ_0 chosen before the adjustment. This is done by a χ^2–test with the null hypothesis

$$H_0 : \boldsymbol{\mathcal{E}}\{s_0^2\} = \sigma_0^2\,, \tag{2-33}$$

while $\boldsymbol{\mathcal{E}}\{\cdot\}$ being the expectation operator. The alternative hypothesis results in

$$H_A : \boldsymbol{\mathcal{E}}\{s_0^2\} > \sigma_0^2. \tag{2-34}$$

The test statistic is given by

$$\chi^2 = f\frac{s_0^2}{\sigma_0^2} \tag{2-35}$$

and the critical value of the χ^2–distribution for a degree of freedom f and error level α is denoted by $\chi^2_{f,\alpha}$. The null hypothesis H_0 will be rejected in favour of the alternative hypothesis H_A if

$$\chi^2 > \chi^2_{f,\alpha}\,. \tag{2-36}$$

In case the null hypothesis will be rejected and under the aforementioned assumptions it can be concluded that outliers are present in the observations.

2.5.3 *Standardised residuals*

If the null hypothesis of the global test must be rejected, we have to check the observations for outliers and remove them from the adjustment. The following approach for the localisation of outliers was developed by Baarda (1968) and is referred to as *Data Snooping*. The measure for the localisation of outliers is called standardised residual NV_i and is defined by

German: *Normierte Verbesserung.*

$$NV_i = \frac{|v_i|}{\sigma_{v_i}} = \frac{|v_i|}{\sigma_0\sqrt{q_{v_iv_i}}}\,, \tag{2-37}$$

where $q_{v_iv_i}$ is the cofactor from $\mathbf{Q_{vv}}$ for observation l_i. In practice, the following rating scale for the evaluation of the standardised residual can be applied:

$$\begin{aligned} & & NV_i & < & 2.5 & \text{no outlier identifiable,} \\ 2.5 & \leq & NV_i & < & 4 & \text{outlier is possible,} \\ 4 & \leq & NV_i & & & \text{outlier is very likely.} \end{aligned}$$

The outliers must be eliminated iteratively, whereby the observation with the largest NV is always removed from the adjustment.

Part II

A PRACTICAL GUIDE TO APPROXIMATION OF FUNCTIONS

At first we give a general practical introduction to the approximation of univariate functions using different sets of basis functions and discuss the main advantages as well as the disadvantages. Here, the main focus is on the extent to which a best approximation can be realised at all and, therefore, the numerical stability of the different sets is also briefly discussed and compared. One aim of this work is to obtain a comprehensive understanding of the general behaviour of approximations, which is fundamental for a successful damage analysis using MeMoS, since the functional model is based on an approximation of the unknown analytical solution of the physical model, represented usually by a set of PDEs. In accordance to Figure I.4, this part also deals with the approximation error within *modelling reality*, see Figure S.1.

Best in the sense of how close it fits the function, i.e. L^∞ norm $\rightarrow$ min.

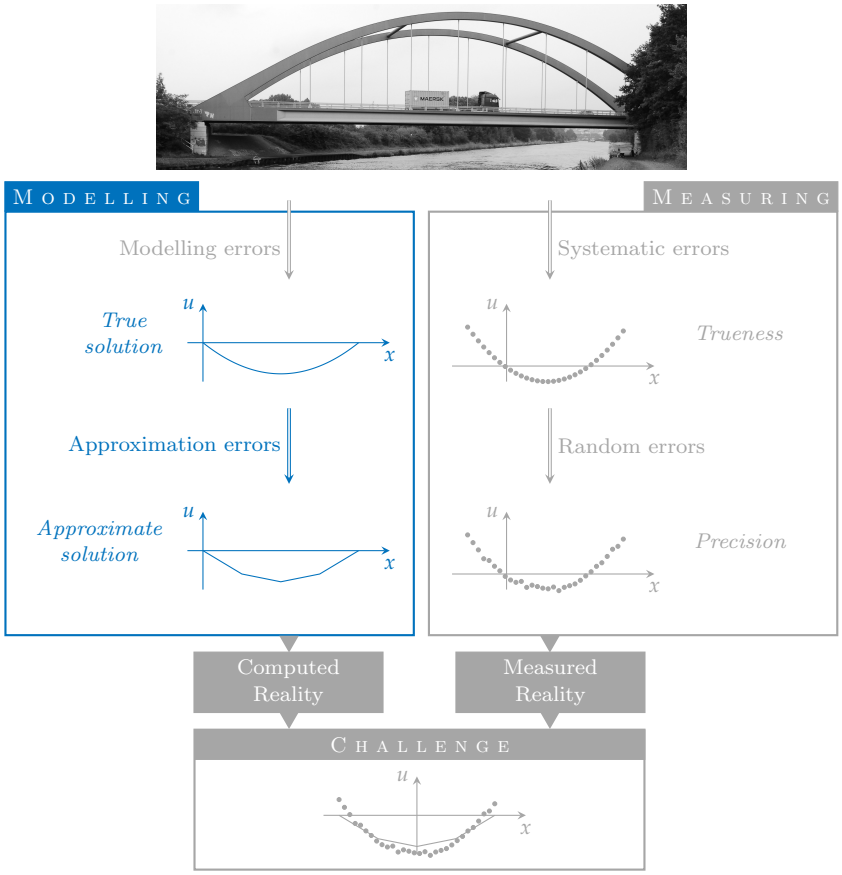

Figure S.1: Addressed error source in modelling and measuring reality within Part ii. Elements in grey are not considered

Furthermore, we will also consider the transformation between different sets of basis functions und briefly discuss the challenges arising for the approximation of multivariate functions. In addition, a set of basis functions for approximation is presented, which is apparently best suited for the approximation of continuous functions and the determination of the optimal degree is solely based on its coefficients. In practice, it has been shown that this approach works very well and in general always guarantees that the deviations from the true function are within machine precision. Consequently, one can assume

that basically no approximation errors are present any more. Finally, we will briefly demonstrate how the unknown solution of PDEs can be approximated, which, therefore, is the basis for the examinations of the second research topic using MeMoS.

3 APPROXIMATION OF FUNCTIONS IN ONE DIMENSION

Any polynomial can be written in the well known form

$$P_p(x) = \sum_{j=0}^{p} c_j \, \phi_j(x) = \sum_{j=0}^{p} c_j \, x^j = c_0 + c_1 x + c_2 x^2 + \cdots + c_p x^p \tag{3-1}$$

with the linear independent basis functions 1, x, x^2, …, x^p, which are called *monomials*. Let us choose a polynomial of 3rd degree to approximate the following continuous real function

The choice of a 3rd degree is a compromise between a "good fit" and a small equation system as an example.

$$f(x) = \sin(3x) \tag{3-2}$$

on the interval $x \in [-1, 1]$. While choosing monomials x^j as basis functions $\phi_j(x)$, the least squares approximation of (3-2), according to (1-45), yields the following normal equation system

$$\begin{bmatrix} \langle x^0, x^0 \rangle & \langle x^1, x^0 \rangle & \langle x^2, x^0 \rangle & \langle x^3, x^0 \rangle \\ \langle x^0, x^1 \rangle & \langle x^1, x^1 \rangle & \langle x^2, x^1 \rangle & \langle x^3, x^1 \rangle \\ \langle x^0, x^2 \rangle & \langle x^1, x^2 \rangle & \langle x^2, x^2 \rangle & \langle x^3, x^2 \rangle \\ \langle x^0, x^3 \rangle & \langle x^1, x^3 \rangle & \langle x^2, x^3 \rangle & \langle x^3, x^3 \rangle \end{bmatrix} \begin{bmatrix} c_0 \\ c_1 \\ c_2 \\ c_3 \end{bmatrix} = \begin{bmatrix} \langle x^0, \sin(3x) \rangle \\ \langle x^1, \sin(3x) \rangle \\ \langle x^2, \sin(3x) \rangle \\ \langle x^3, \sin(3x) \rangle \end{bmatrix}. \tag{3-3}$$

Solving the integrals

$$\langle x^i, x^j \rangle = \int_{-1}^{1} x^i \, x^j \, \mathrm{d}x = \frac{1}{i+j+1} \left(1 - (-1)^{i+j+1} \right) \quad \text{with } i, j = 0, 1, 2, 3$$

and

$$\langle x^i, \sin(3x) \rangle = \int_{-1}^{1} x^i \, \sin(3x) \, \mathrm{d}x \quad \text{with } i = 0, 1, 2, 3$$

yields

$$\begin{bmatrix} 2 & 0 & 2/3 & 0 \\ 0 & 2/3 & 0 & 2/5 \\ 2/3 & 0 & 2/5 & 0 \\ 0 & 2/5 & 0 & 2/7 \end{bmatrix} \begin{bmatrix} c_0 \\ c_1 \\ c_2 \\ c_3 \end{bmatrix} = \begin{bmatrix} 0.000\,000\,000\,000\,000 \\ 0.691\,354\,999\,524\,712 \\ 0.000\,000\,000\,000\,000 \\ 0.293\,171\,670\,090\,401 \end{bmatrix}. \tag{3-4}$$

The solution of the normal equation system yields the unknown coefficients

$$\begin{bmatrix} c_0 \\ c_1 \\ c_2 \\ c_3 \end{bmatrix} = \begin{bmatrix} 0.000\,000\,000\,000\,000 \\ 2.633\,574\,950\,607\,669 \\ 0.000\,000\,000\,000\,000 \\ -2.660\,904\,085\,534\,336 \end{bmatrix} \tag{3-5}$$

for a polynomial approximation of 3rd degree. The resulting approximation and the residual function are depicted in Figure 3-1.

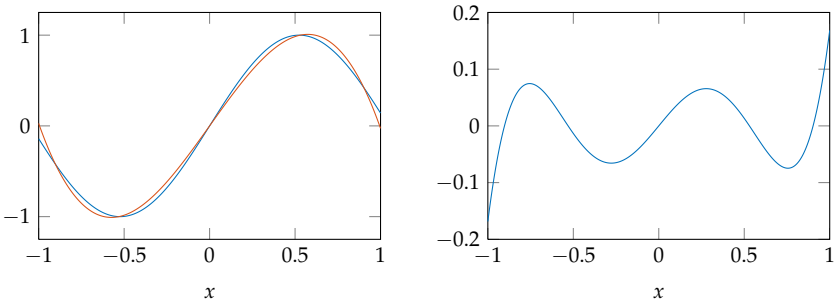

Figure 3-1: Given function (3-2) in blue and it's polynomial approximation $P_3(x)$ in red (left). Residual function $v(x) = \sin(3x) - P_3(x)$ (right).

The polynomial $P_3(x)$ approximates (3-2) within roughly ± 0.1 and only exceeds it at the limits of the interval. The residual function for this and all upcoming examples have been determined by discretising the function using at least 1 million equispaced points. For the plots, these points have been reduced in such a way that the main characteristic of the residual function and especially their extreme values have been preserved.

The computations have been done with the MATLAB code in Programme 3-1. While the integrals in the normal matrix can be easily solved directly, the integrals for the right hand side have been solved numerically using a global adaptive quadrature. Parts of the MATLAB built-in function *integral* are based on (SHAMPINE 2008). Furthermore, all entries in the symmetric normal matrix have been calculated individually, so the performance of the code is not optimal.

It has been verified that the results of numerical integration for the monomial basis are within machine precision.

Programme 3-1: Code for polynomial approximation in the monomial basis.

```
%Approximation of f(x) on [-1, 1]
a=-1; b=1;

%Polynomial degree
p=3;

%Preallocate matrices
N=zeros(p+1); n=zeros(p+1,1);

%Normal equation system
for j=0:p
    for i=0:p
        N(j+1,i+1)=1/(i+j+1)*(1-a^(i+j+1));
    end
    n(j+1)=integral(@(x) sin(3*x).*x.^j,a,b);
end

%Solution
c=N\n;
```

Depending on the problem it might be already a sufficient approximation or not. Nevertheless the question might arise, which polynomial degree is needed to approximate function (3-2) to roughly machine precision, about 15 digits of relative accuracy?

The interested reader who wants to refresh his knowledge on conditioning is referred to (TREFETHEN and BAU 1997, pp. 89-96).

To answer this question, different polynomials are fitted while increasing the polynomial degree up to 50. For each polynomial degree the maximum absolute difference $\max|\sin(3x) - P_p(x)|$ and the 2-norm condition number κ of the normal matrix $\mathbf{N}$ was calculated and the results are depicted in Figure 3-2.

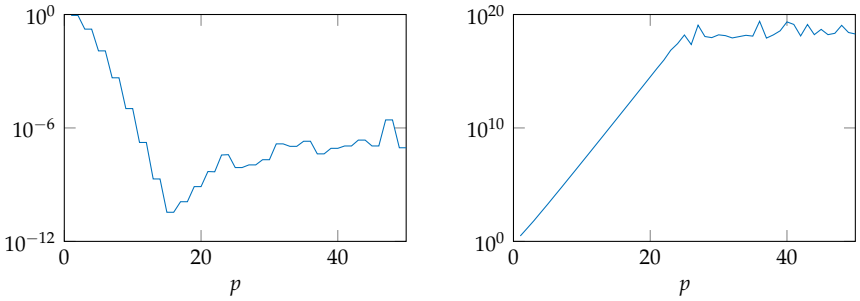

Figure 3-2: Logarithmic plot for $\max|\sin(3x) - P_p(x)|$ (left) and 2-norm condition number $\kappa(\mathbf{N})$ (right) for different polynomial degree p. For better visibility, the discrete points are usually represented by a line plot.

As shown in Figure (3-2) (left) the best fitting polynomial is of 15^{th} degree. A further increase of the degree results in a worse approximation. A closer look at the condition number in Figure 3-2 (right) reveals an exponential increase with growing polynomial degree. From a polynomial of 25^{th} degree onwards, MATLAB also displays a warning that the normal matrix is close to singular and the result may be inaccurate. According to TREFETHEN and BAU (1997, p. 95)

Best in terms of $\max|\sin(3x) - P_p(x)| \to \min$.

> *If a problem $Ax = b$ contains an ill-conditioned matrix A, one must expect to "lose $\log_{10}\kappa(A)$ digits" in computing the solution, except under very special circumstances.*

The condition number of the normal matrix for fitting a polynomial 15^{th} degree is in this case $\kappa(\mathbf{N}) \approx 5 \cdot 10^{10}$, which already corresponds to roughly 10 digits. Fitting polynomials in the monomial basis is in general an ill-conditioned problem. The determination of the unknown coefficients is inaccurate. The resulting normal matrix $\mathbf{N}$ corresponds to the HILBERT matrix, defined on an interval $[0, 1]$, which is a well known example of an ill-conditioned matrix.

A comprehensive insight into this very interesting topic about the accuracy of numerical algorithms can be found in (HIGHAM 2002).

In order to illustrate the extent of this numerical ill-conditioned problem of polynomial approximation in the monomial basis, we will consider the following function

$$f(x) = \sin(30x^2). \tag{3-6}$$

Also in this case we fitted different polynomials while increasing the polynomial degree up to 200.

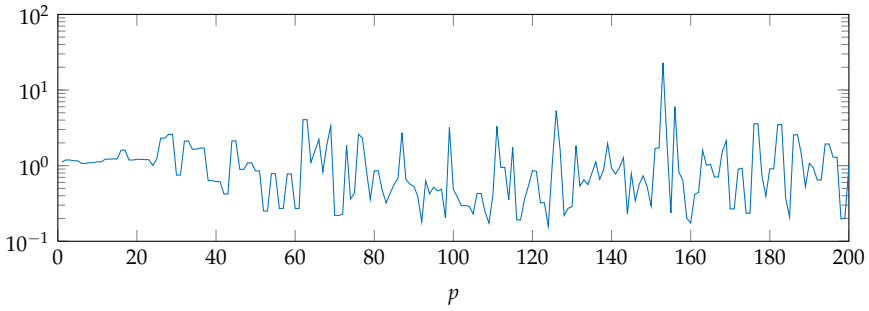

Figure 3-3: Logarithmic plot of $\max|\sin(30x^2) - P_p(x)|$ for different polynomial degree.

Figure 3-3 clearly reveals, that an increase of the polynomial degree will not necessarily improve the approximation itself. It is also not possible to clearly identify the degree for the best fitting polynomial. In this case a polynomial of 124^{th} degree leads to the smallest value for $\max|\sin(30x^2) - P_p(x)|$ and is depicted in Figure 3-4 (left).

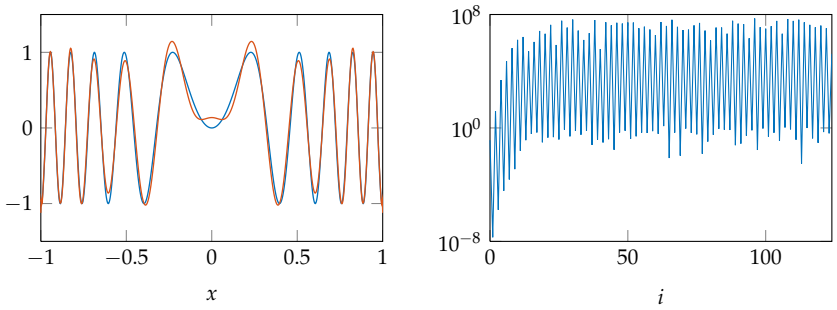

Figure 3-4: Given function (3-6) in blue and it's polynomial approximation $P_{124}(x)$ in red (left). Logarithmic plot for the coefficients $|c_i|$ of $P_{124}(x)$ (right).

As one can see from this graph the largest deviations between (3-6) and its approximation $P_{124}(x)$ are around zero and at the two peaks to the left and right. Even a polynomial of 1000^{th} or higher degree will not reduce these deviations significantly.

Figure 3-4 (right) depicts the absolute values of the coefficients for the best fitting polynomial $P_{124}(x)$. Due to the symmetry of (3-6) the coefficients for the monomials of odd degree are very small in comparison to the even ones, which are up to 10^8. The increase in values with increasing degree and these very large values are typical for such polynomials of higher degree.

Another property of polynomial approximation in the monomial basis will be illustrated by the approximations $P_{123}(x)$ and $P_{126}(x)$ of the same function (3-6) as depicted in Figure 3-4 (left). The difference of these two polynomials with respect to the best fit $P_{124}(x)$ and the coefficients for all three polynomials are depicted in Figure 3-5.

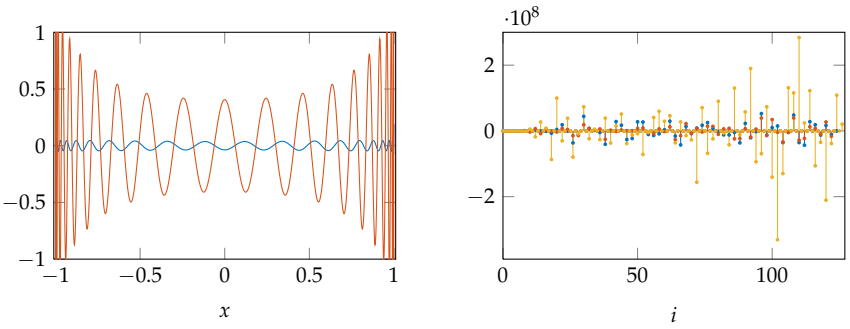

Figure 3-5: The difference of $P_{124}(x) - P_{123}(x)$ in blue and $P_{124}(x) - P_{126}(x)$ in red (left). Coefficients c_i for $P_{124}(x)$ in blue, $P_{123}(x)$ in red and $P_{126}(x)$ in yellow (right).

Although $P_{123}(x)$ and $P_{124}(x)$ are very similar and only differ by $\approx 5\%$, their coefficients deviate significantly from each other in values up to $\approx 10^7$ and sometimes even change their sign. In addition the approximation $P_{126}(x)$ consists only of two more terms than $P_{124}(x)$ but results in a completely different set of coefficients as can be seen in Figure 3-5 (right). While $P_{124}(x)$ preserves at least the main characteristics of the function (3-6), Figure 3-5 (left) reveals that $P_{126}(x)$ is extremely different from $P_{124}(x)$ and therefore is not coinciding with function (3-6) depicted in (3-4). One can say that $P_{126}(x)$ is a very bad approximation of (3-6).

Before one might conclude that polynomial approximation in the monomial basis might be not suitable for wiggly functions like (3-6), but obviously suitable for smooth functions like (3-2), we will consider the following function

$$f(x) = \exp(-100x^2). \tag{3-7}$$

Following the same procedure as before we find out that a polynomial of 108^{th} leads to the smallest value for $\max|\exp(-100x^2) - P_p(x)|$. Function (3-7) and $P_{108}(x)$ are depicted in Figure 3-6 (left).

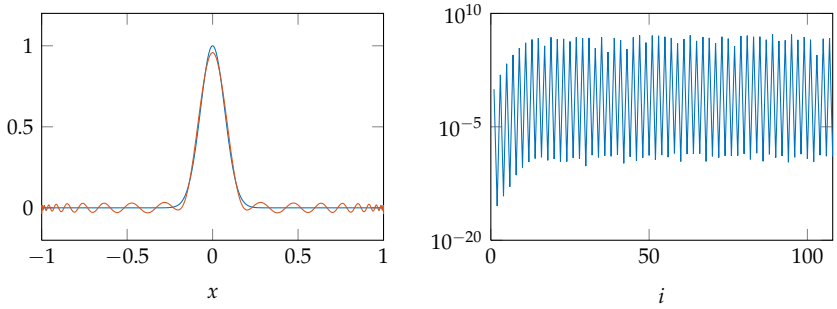

Figure 3-6: Given function (3-7) in blue and it is polynomial approximation $P_{108}(x)$ in red (left). Logarithmic plot for the coefficients $|c_i|$ of $P_{108}(x)$ (right).

The plot of $P_{108}(x)$ clearly reveals the oscillatory behaviour with increasing frequency at the limits. This is characteristic for a least squares approximation. On closer inspection this behaviour is also visible in Figure 3-1 and Figure 3-4. For polynomial approximation in the monomial basis this behaviour can also cause huge deviations at limits or jump discontinuities.

In order to intensify this behaviour we change (3-7) to

$$f(x) = \exp(-1000x^2), \tag{3-8}$$

which amplifies the spike in the function. We found $P_{172}(x)$ as a best fitting polynomial, which is depicted in Figure 3-7.

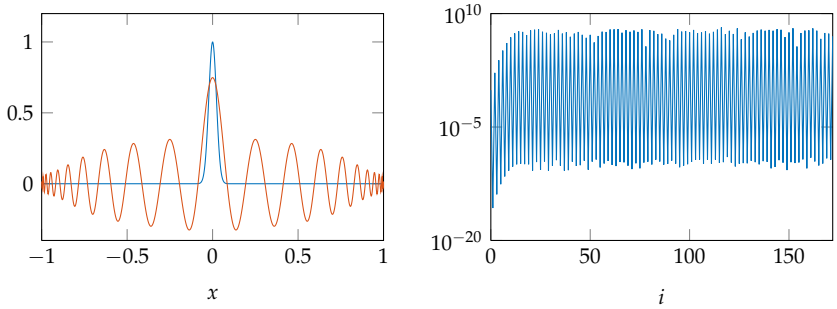

Figure 3-7: Given function (3-8) in blue and it is polynomial approximation $P_{172}(x)$ in red (left). Logarithmic plot for the coefficients $|c_i|$ of $P_{172}(x)$ (right).

In Figure 3-7 (left) it is clearly visible that $P_{172}(x)$ as a best fitting polynomial is a very bad approximation of (3-8). It is not possible to find a polynomial approximation in the monomial basis that, at least, preserves the main shape of the given function (3-8).

Best in terms of $\max|\exp(-1000x^2) - P_p(x)| \to \min$.

In general, we can conclude that polynomial approximation in the monomial basis is not a good idea, especially for higher degrees. Based on the previous examples we can identify the following drawbacks:

- Normal matrix $\mathbf{N}$ is usually a full matrix. This means that the coefficients cannot be determined independently of each other. Each time the polynomial degree will be altered, a new normal equation system needs to be solved again.
- The condition number of $\mathbf{N}$ grows exponentially with increasing polynomial degree. Therefore, it is an ill-conditioned problem and the coefficients for polynomials of higher degree cannot be determined accurately.

The coefficients tend to take extremely large values and a small change in the polynomial degree usually leads to a completely different set of coefficients.

- Only in some cases it is possible to find a suitable polynomial approximation for a given function. In most cases the polynomial is inadequate as an approximation.

But why is it such an ill-conditioned problem?

The reason for this ill-conditioning is due to the chosen basis functions, the monomials. Figure 3-8 depicts the first 11 monomial basis functions.

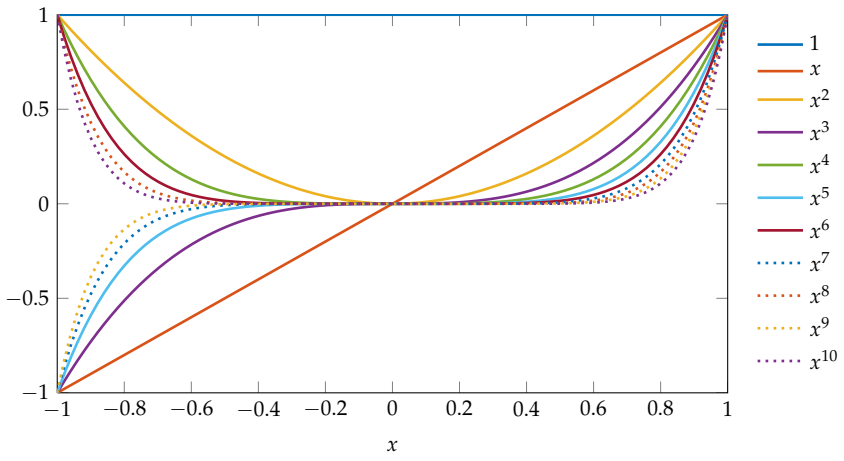

Figure 3-8: Basis functions x^j for $j = 0, \cdots, 10$.

While the first three monomials can easily be distinguished, the monomials for higher even or odd degree become more and more similar. To get an impression of the impact of this similarity onto an approximation, it is of great advantage to understand the method of least squares as an orthogonal projection, as already described in Section 1.2.2. A least squares approximation of a function is its orthogonal projection into the vector space V spanned by these monomials

$$V = \text{span}\{\phi_j(x)\} = \text{span}\{x^j\}. \tag{3-9}$$

The set of basis functions $\phi_j(x)$ are basis vectors in space V. Figure 3-8 illustrates that monomials become more and more similar with increasing degree, as a consequence the basis functions become more and more similar. This implies, that from a certain polynomial degree onwards, the basis functions are showing nearly in the same or opposite direction.

To illustrate this problem, we calculate the angle between two basis functions $\phi_i(x)$ and $\phi_j(x)$. The inner product of two functions reads

$$\langle \phi_i, \phi_j \rangle = \|\phi_i\|_2 \, \|\phi_j\|_2 \cos(\alpha_{i,j}), \tag{3-10}$$

where $\alpha_{i,j}$ is the angle between the two basis functions and $\|\cdot\|_2$ is the $L^2([-1,1])$ norm. Rearranging (3-10) and with (1-37) yields

$$\alpha_{i,j} = \arccos\left(\frac{\langle \phi_i, \phi_j \rangle}{\left(\langle \phi_i, \phi_i \rangle \langle \phi_j, \phi_j \rangle \right)^{1/2}} \right). \tag{3-11}$$

The angle $\alpha_{i,j}$ between all 11 basis vectors depicted in Figure 3-8 has been calculated according to (3-11) and is listed in the following table.

	1	x	x^2	x^3	x^4	x^5	x^6	x^7	x^8	x^9	x^{10}
1	0	100	46.5	100	59.0	100	65.6	100	69.7	100	72.6
x		0	100	26.2	100	38.7	100	46.5	100	51.8	100
x^2			0	100	18.4	100	29.3	100	36.7	100	42.2
x^3				0	100	14.3	100	23.7	100	30.5	100
x^4					0	100	11.6	100	19.9	100	26.2
x^5						0	100	9.8	100	17.2	100
x^6							0	100	8.5	100	15.1
x^7								0	100	7.5	100
x^8									0	100	6.7
x^9										0	100

Table 3-1: Angle $\alpha_{i,j}$ in [gon] between the first 11 monomial basis functions. Due to symmetry only the upper triangular part is presented.

As one can see, monomials of even degree are orthogonal to those of odd degree and vice versa, which was already visible in the normal matrix in (3-4) while the corresponding entries are zero. Table 3-1 shows, that monomials of higher even or odd degree are nearly showing in the same direction. The angle $\alpha_{8,10}$ between $\phi_8(x) = x^8$ and $\phi_{10}(x) = x^{10}$ is only 6.7 gon. Furthermore, the length of the basis vectors x^j will decrease with increasing degree j. The basis vector x^{10} is already nearly 5 times shorter than x^0, which is shown in Figure 3-9.

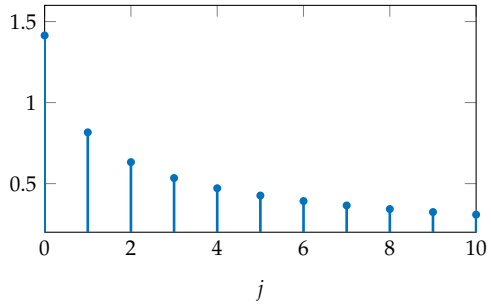

Figure 3-9: The length $\|x^j\|_2$ of the first 11 monomial basis functions.

Both properties, the angle between the basis vectors and their length ratios, are illustrating, from a geometrical point of view, the reason why a polynomial approximation in the monomial basis is an ill-conditioned problem. Figure 3-10 clarifies this matter.

While we approximate functions on $x \in [-1, 1]$ the length of the basis vectors are not playing such an important role. Yet this will be dependent on the chosen interval, while the length ratios between the monomials can be huge.

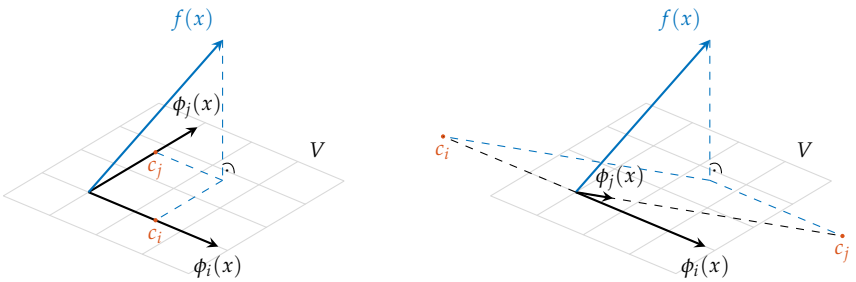

Figure 3-10: Orthogonal projection of $f(x)$ into vector space V spanned by orthogonal basis vectors with equal length (left) and non-orthogonal basis vectors with different lengths (right).

A geometrical interpretation of an orthogonal projection of a function $f(x)$ into a vector space V spanned by orthogonal basis vectors $\phi_i(x)$ and $\phi_j(x)$ with equal length is given in Figure 3-10 (left). For an approximation of $f(x)$

we need to determine the unknown coefficients c_i and c_j. Hence, we need to determine the intersection of two straight lines. While the basis vectors are orthogonal, these two lines will also intersect orthogonally. For a polynomial approximation of $f(x)$ in the monomial basis, the vectors $\phi_i(x) = x^i$ and $\phi_j(x) = x^j$ are usually not orthogonal, as depicted in Figure 3-10 (right). In most cases they are nearly showing in the same or opposite direction. Furthermore, these basis vectors have different lengths. Once again we need to determine the intersection of two straight lines, while this time these lines will intersect in a very acute angle. From a geometrical point of view it is quite obvious, that the determination of an intersection of two lines is more accurate for orthogonal than for non-orthogonal basis vectors, like monomials.

Since the approximation in the monomial basis is an ill-conditioned problem, numerous approaches have been developed for various fields of application in order to obtain suitable approximations for arbitrary functions. One approach already arises from Figure 3-10, namely the approximation using orthogonal basis functions. Another approach frequently used in engineering sciences is based on an elementwise approximation with polynomials of low degree. Both approaches will be addressed in more detail in the following sections.

3.1 ELEMENTWISE APPROXIMATION IN THE MONOMIAL BASIS

As it has been already shown in the previous section, polynomial approximation in the monomial basis leads to numerical problems for even small polynomial degrees. However, the normal matrix for a polynomial of low degree is well conditioned, so the coefficients can be determined accurately. Thus, one might conclude that monomials are still suitable for polynomial approximation and an accurate solution can be still computed with the following strategy. The whole domain where one wants to approximate any given function can be divided into several sub domains and each sub domain will be approximated by a polynomial of low degree. Hence, the accuracy of the approximation can be increased by introducing more sub domains.

Following the same terminology with the well known finite element method (FEM) we will also call these sub domains elements and we will call the point connecting two successive elements a node.

3.1.1 *Elementwise non continuous approximation*

To illustrate the procedure of an elementwise non continuous approximation we approximate function (3-2) by dividing the whole domain into $N = 3$ equispaced elements and each element will be approximated by a straight line. Before we set-up the normal equation system for each element, it is of great advantage to introduce a unique identifier for the nodes ν and elements ζ, which can be stored in the following tables.

Table 3-2: Coordinates for all nodes ν and the nodes for all three elements ζ.

ν	x_ν
1	-1
2	$-1/3$
3	$1/3$
4	1

and

ζ	ν_1	ν_2
1	1	2
2	2	3
3	3	4

Based on the definition of nodes and elements in Table 3-2 and the two basis functions of a straight line we can set-up for each element ζ the normal equation system

$$ {}^{\zeta}\mathbf{N}\,{}^{\zeta}\mathbf{x} = {}^{\zeta}\mathbf{n}\,, \tag{3-12} $$

which reads

$$ \begin{bmatrix} {}^{\zeta}\langle x^0, x^0\rangle & {}^{\zeta}\langle x^1, x^0\rangle \\ {}^{\zeta}\langle x^0, x^1\rangle & {}^{\zeta}\langle x^1, x^1\rangle \end{bmatrix} \begin{bmatrix} {}^{\zeta}c_0 \\ {}^{\zeta}c_1 \end{bmatrix} = \begin{bmatrix} {}^{\zeta}\langle x^0, \sin(3x)\rangle \\ {}^{\zeta}\langle x^1, \sin(3x)\rangle \end{bmatrix} \tag{3-13} $$

with $\zeta = 1,2,3$. Solving the integrals in (3-13)

$$ {}^{\zeta}\langle x^i, x^j\rangle = \int_{{}^{\zeta}x_{\nu_1}}^{{}^{\zeta}x_{\nu_2}} x^i\, x^j \,\mathrm{d}x = \frac{1}{i+j+1}\left(\left({}^{\zeta}x_{\nu_2}\right)^{i+j+1} - \left({}^{\zeta}x_{\nu_1}\right)^{i+j+1}\right) $$

and

$$ {}^{\zeta}\langle x^i, \sin(3x)\rangle = \int_{{}^{\zeta}x_{\nu_1}}^{{}^{\zeta}x_{\nu_2}} x^i\, \sin(3x)\,\mathrm{d}x\,, $$

for $i,j = 0,1$ results in the following three normal equation systems

$$ \begin{aligned} \begin{bmatrix} 2/3 & -4/9 \\ -4/9 & 26/81 \end{bmatrix} \begin{bmatrix} {}^{1}c_0 \\ {}^{1}c_1 \end{bmatrix} &= \begin{bmatrix} -0.510\,098\,267\,489\,528 \\ 0.312\,214\,313\,213\,494 \end{bmatrix}, \\ \begin{bmatrix} 2/3 & 0 \\ 0 & 2/81 \end{bmatrix} \begin{bmatrix} {}^{2}c_0 \\ {}^{2}c_1 \end{bmatrix} &= \begin{bmatrix} 0.000\,000\,000\,000\,000 \\ 0.066\,926\,373\,097\,724 \end{bmatrix}, \\ \begin{bmatrix} 2/3 & 4/9 \\ 4/9 & 26/81 \end{bmatrix} \begin{bmatrix} {}^{3}c_0 \\ {}^{3}c_1 \end{bmatrix} &= \begin{bmatrix} 0.510\,098\,267\,489\,528 \\ 0.312\,214\,313\,213\,494 \end{bmatrix}, \end{aligned} \tag{3-14} $$

which can be solved individually. The solution of these equation systems yields the unknown parameters of a straight line for each element

$$ \begin{aligned} \begin{bmatrix} {}^{1}c_0 \\ {}^{1}c_1 \end{bmatrix} &= \begin{bmatrix} -1.517\,129\,759\,281\,461 \\ -1.127\,973\,537\,070\,754 \end{bmatrix}, \\ \begin{bmatrix} {}^{2}c_0 \\ {}^{2}c_1 \end{bmatrix} &= \begin{bmatrix} 0.000\,000\,000\,000\,000 \\ 2.710\,518\,110\,457\,811 \end{bmatrix}, \\ \begin{bmatrix} {}^{3}c_0 \\ {}^{3}c_1 \end{bmatrix} &= \begin{bmatrix} 1.517\,129\,759\,281\,465 \\ -1.127\,973\,537\,070\,758 \end{bmatrix}. \end{aligned} \tag{3-15} $$

All computations have been done with Programme 3-2.

Programme 3-2: Code for elementwise non continuous polynomial approximation in the monomial basis.

```
%Approximation of f(x) on [-1, 1]
a=-1; b=1;

%polynomial degree for each element
p=1;

%number of elements
num_elements=3;

%Position of the equispaced nodes
nodes=linspace(a,b,num_elements+1);

%Preallocate matrices
N=zeros(p+1); n=zeros(p+1,1); c=zeros(p+1,num_elements);

for zeta=1:num_elements
  for i=0:p
    for j=0:p
      N(i+1,j+1)=1/(i+j+1)*(nodes(zeta+1)^(i+j+1)-nodes(
          zeta)^(i+j+1));
    end
    n(i+1)=integral(@(x) sin(3*x).*x.^i,nodes(zeta),nodes(
        zeta+1));
  end
  c(:,zeta)=N\n;
end
```

The solution of the elementwise approximation of (3-2) and the resulting residual function are depicted in Figure 3-11.

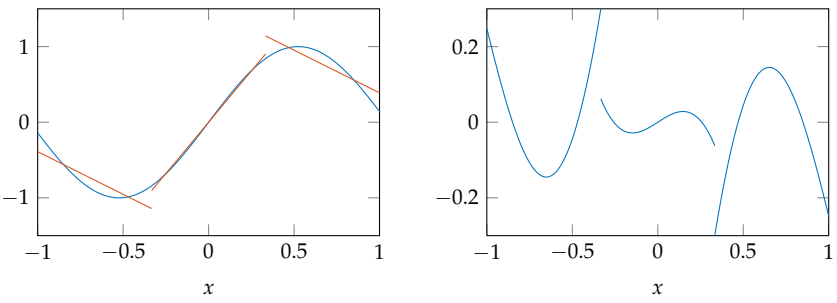

Figure 3-11: Given function (3-2) in blue and it's elementwise linear approximation in red (left). Residual function $v(x) = \sin(3x) - \sum_{\zeta=1}^{3} {}^{\zeta}P_1(x)$ (right).

Figure 3-11 clearly reveals that the resulting approximation is not continuous, which is the major drawback of this approach. In case continuity is not required, one can achieve suitable approximations for even complex functions. The question might arise, how many elements are needed to approximate (3-2) within machine precision? Therefore, the number of elements was increased up to $N = 20\,000$ and we determined the maximum absolute deviation between (3-2) and each elementwise approximation. Furthermore, each element was approximated by a polynomial of 1^{st}, 2^{nd} and 3^{rd} degree. The result is depicted in Figure 3-12.

At least better approximations as depicted in Figure 3-4 (left) or Figure 3-7 (left).

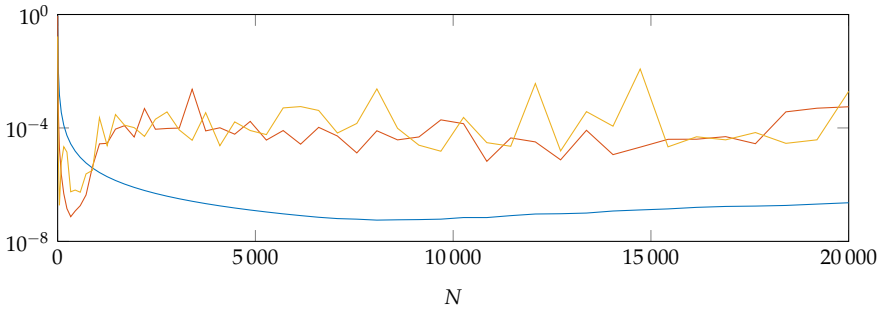

Figure 3-12: Logarithmic plot of $\max|\sin(3x) - \sum_{\zeta=1}^{N} {}^{\zeta}P_p(x)|$ for an elementwise linear (blue), quadratic (red) and cubic (yellow) polynomial approximation of function (3-2).

For the presented elementwise approximation computed by Programme 3-2 and based on the results depicted in Figure 3-12, the following conclusions can be made:

- It is not possible to approximate (3-2) within machine precision.
- In comparison to a linear polynomial approximation (blue curve), using quadratic (red) or cubic (yellow) polynomials will dramatically reduce the number of elements, while $\max|v(x)|$ is nearly equal. A best approximation of (3-2) can be achieved while using roughly 8000 elements for a linear, 350 for a quadratic and 50 for a cubic approximation. But this also implies that $\approx 16\,000$ (linear) resp. ≈ 1050 (quadratic) or ≈ 200 (cubic) parameters are needed in order to approximate (3-2) only within $\approx 10^{-7}$.

  Which is even worse than the solution using a polynomial of 15^{th} degree from Figure 3-2 (left).
- A further increase of elements will always lead to a worse approximation than the presented one. For an elementwise quadratic or cubic polynomial approximation this is even much worse.

Although the resulting normal matrix ${}^{\zeta}\mathbf{N}$ of an elementwise linear, quadratic and cubic polynomial approximation is well conditioned for a small amount of elements, it will dramatically change with increasing N. To gain a better understanding of this issue, we will have a closer look at the angles between the basis vectors and their length ratios for each element. In addition, we also consider their change, while increasing the number of elements.

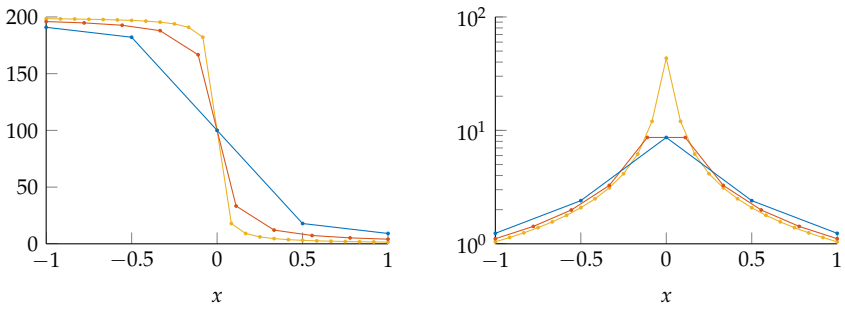

Figure 3-13: Angle ${}^{\zeta}\alpha_{0,1}$ in [gon] between the two basis vectors ${}^{\zeta}\phi_0(x) = 1$ and ${}^{\zeta}\phi_1(x) = x$ (left) and length ratio $\|{}^{\zeta}\phi_0\|_2 / \|{}^{\zeta}\phi_1\|_2$ (right) for 5 elements in blue, 10 in red and 25 in yellow.

Figure 3-13 (left) shows the angle ${}^{\zeta}\alpha_{0,1}$ between the two basis vectors ${}^{\zeta}\phi_0(x) = 1$ and ${}^{\zeta}\phi_1(x) = x$, depending on the location of the element, reaching from $0 - 200\,\text{gon}$. In case we want to approximate a function within the first element, starting at $x = -1$, the angle between both basis vectors is nearly 200 gon, no matter if we have 5, 10 or 25 elements. This means that both vectors are showing nearly in an opposite direction. For elements close to $x = 1$ it is the other way round, both basis vectors will nearly show in the same

direction, while the angle between them is nearly 0 gon. Only for an element with a symmetric interval around $x = 0$ the angle ${}^{\zeta}\alpha_{0,1}$ between the two basis vectors will be exactly 100 gon. In this case, both basis vectors are orthogonal. However, Figure 3-13 (left) reveals that the length ratio $\|{}^{\zeta}\phi_0\|_2/\|{}^{\zeta}\phi_1\|_2$ for this element in the middle is $\approx 9:1$, while using 5 elements. This means that ${}^{\zeta}\phi_0(x) = 1$ is roughly nine times longer than ${}^{\zeta}\phi_1(x) = x$. While using 25 elements (yellow curve) it is even worse. These effects of a changing angle or length ratio between basis functions for an element will be amplified, while using more elements and/or higher polynomial degree.

To illustrate this issue, we determined the 2-norm condition number $\kappa({}^1\mathbf{N})$ always for the normal matrix of the first element for each approximation for up to $N = 1000$ elements. This was done for an elementwise linear, quadratic and cubic approximation and is depicted in Figure 3-14.

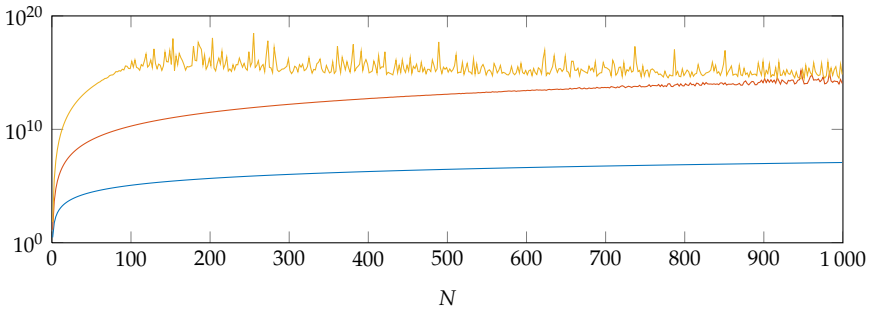

Figure 3-14: Logarithmic plot of 2-norm condition number $\kappa({}^1\mathbf{N})$ for an elementwise linear (blue), quadratic (red) and cubic (yellow) polynomial approximation of function (3-2) for N elements.

Figure 3-14 clearly shows, that $\kappa({}^1\mathbf{N})$ increases very fast and highly depends on the number of elements and polynomial degree. The normal matrices of a cubic polynomial approximation with only 100 elements are nearly singular. Using quadratic polynomials with roughly 800 elements will also yield nearly singular normal matrices. This problem is not as serious for an elementwise linear approximation, but the normal matrices are still far from being numerically well-conditioned.

Just for the sake of completeness.

Although the approximation is non-continuous and is usually not used in engineering science and other fields, we will also present the best approximation for the functions (3-6) and (3-8). Based on previous considerations, we will use quadratic polynomials, as a compromise between a good approximation and not too many elements.

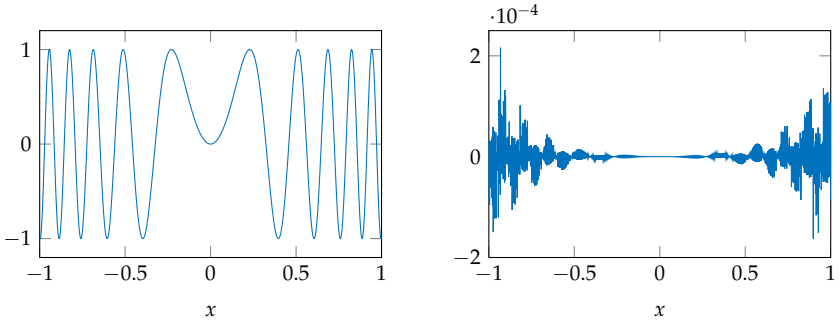

Figure 3-15: A best approximation of function (3-6) with 470 elements using quadratic polynomials (left). Residual function $v(x) = \sin(30x^2) - \sum_{\zeta=1}^{470} {}^{\zeta}P_2(x)$ (right).

Figure 3-15 (left) depicts the best non-continuous approximation of (3-6) with 470 elements using quadratic polynomials, which is quite similar to the original function (3-6) depicted in Figure 3-4 (left) in blue. The largest deviation between both functions is in the range of $2 \cdot 10^{-4}$ and is much smaller than

an approximation with one single polynomial of high degree, as depicted in Figure 3-4 (right). It is also possible to achieve a similarly good approximation of function (3-8) as can bee seen in Figure 3-16.

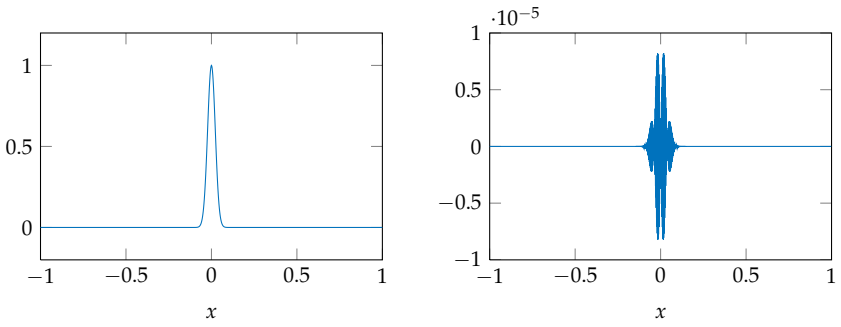

Figure 3-16: An approximation of function (3-6) with 1000 elements using quadratic polynomials (left). Residual function $v(x) = \exp(-1000x^2) - \sum_{\zeta=1}^{1000} {}^{\zeta}P_2(x)$ (right).

For the presented approximation in Figure 3-16 (left) we have limited ourselves to 1000 elements using quadratic polynomials. The difference between the original function (3-8) and the chosen approximation is smaller than 10^{-5}, but only around the peak within the interval $x \in [-0.1, 0.1]$. Outside the peak, the residual function is zero within machine precision. In a direct comparison to the approximation $P_{172}(x)$ depicted in Figure 3-7 (left) we can see a big improvement. While introducing more elements the residual function can be further reduced, but only to a certain extent. With this approach it is possible to obtain non continuous approximations, that can preserve at least the shape of even complex functions. But usually a large number of elements are needed.

The computational effort to determine an optimal number of elements and polynomial degree for the best possible approximation is enormos, especially in contrast to the resulting residual function, which will only be smaller by a factor of $10 - 100$.

3.1.2 *Elementwise continuous approximation*

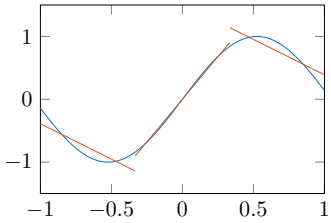

As already mentioned in the previous section, the presented approximation is not continuous. An approximation with N elements will have $N-1$ discontinuities located at the inner nodes. Thus, we will focus on the question of how to remove these discontinuities at the inner nodes in order to obtain an elementwise approximation which is continuous. While we still use monomials as basis functions, we can enforce continuity by introducing a constraint at each inner node, namely

$$ {}^{\zeta}P_1({}^{\zeta}x_{\nu_2}) = {}^{\zeta+1}P_1({}^{\zeta+1}x_{\nu_1}). \tag{3-16} $$

Based on the previous example of approximating (3-2) using 3 elements, we have to introduce the following two constraints

$$ \begin{aligned} {}^1c_0 + {}^1c_1 {}^1x_{\nu_2} - ({}^2c_0 + {}^2c_1 {}^2x_{\nu_1}) &= 0\,, \\ {}^2c_0 + {}^2c_1 {}^2x_{\nu_2} - ({}^3c_0 + {}^3c_1 {}^3x_{\nu_1}) &= 0\,. \end{aligned} \tag{3-17} $$

Each constraint depends always on the unknown parameters of two successive elements. These constraints induce a dependency between the unknown parameters of the elements and the three normal equation systems (3-14) can not be solved individually any more. In order to solve this issue we combine the three normal equation systems of the non continuous approach to a single one as follows

$$ \begin{bmatrix} {}^1\mathbf{N} & \mathbf{0} & \mathbf{0} \\ \mathbf{0} & {}^2\mathbf{N} & \mathbf{0} \\ \mathbf{0} & \mathbf{0} & {}^3\mathbf{N} \end{bmatrix} \begin{bmatrix} {}^1\mathbf{x} \\ {}^2\mathbf{x} \\ {}^3\mathbf{x} \end{bmatrix} = \begin{bmatrix} {}^1\mathbf{n} \\ {}^2\mathbf{n} \\ {}^3\mathbf{n} \end{bmatrix}, \tag{3-18} $$

or in a shorter notation

$$\mathbf{N}\,\mathbf{x} = \mathbf{n}\,, \tag{3-19}$$

and rewrite the constraints (3-17) in matrix notation

$$\mathbf{C}\,\mathbf{x} = \mathbf{0} \tag{3-20}$$

with

$$\mathbf{C} = \begin{bmatrix} 1 & {}^{1}x_{\nu_2} & -1 & -{}^{2}x_{\nu_1} & 0 & 0 \\ 0 & 0 & 1 & {}^{2}x_{\nu_2} & -1 & -{}^{3}x_{\nu_1} \end{bmatrix}. \tag{3-21}$$

Now with (3-19) and (3-20) we obtain an equation system with constraints between the unknown parameters. As shown in Section 2.4 a solution of such a problem can be obtained by solving the following extended normal equation system

$$\begin{bmatrix} \mathbf{N} & \mathbf{C}^{\mathsf{T}} \\ \mathbf{C} & \mathbf{0} \end{bmatrix} \begin{bmatrix} \mathbf{x} \\ \boldsymbol{\lambda} \end{bmatrix} = \begin{bmatrix} \mathbf{n} \\ \mathbf{0} \end{bmatrix}, \tag{3-22}$$

which reads in this case

$$\begin{bmatrix} 2/3 & -4/9 & 0 & 0 & 0 & 0 & 1 & 0 \\ -4/9 & 26/81 & 0 & 0 & 0 & 0 & -1/3 & 0 \\ 0 & 0 & 2/3 & 0 & 0 & 0 & -1 & 1 \\ 0 & 0 & 0 & 2/81 & 0 & 0 & 1/3 & 1/3 \\ 0 & 0 & 0 & 0 & 2/3 & 4/9 & 0 & -1 \\ 0 & 0 & 0 & 0 & 4/9 & 26/81 & 0 & -1/3 \\ 1 & -1/3 & -1 & 1/3 & 0 & 0 & 0 & 0 \\ 0 & 0 & 1 & 1/3 & -1 & -1/3 & 0 & 0 \end{bmatrix} \begin{bmatrix} {}^{1}c_0 \\ {}^{1}c_1 \\ {}^{2}c_0 \\ {}^{2}c_1 \\ {}^{3}c_0 \\ {}^{3}c_1 \\ \lambda_1 \\ \lambda_2 \end{bmatrix} = \begin{bmatrix} -0.510\,098\,267\,489\,528 \\ 0.312\,214\,313\,213\,494 \\ 0.000\,000\,000\,000\,000 \\ 0.066\,926\,373\,097\,724 \\ 0.510\,098\,267\,489\,528 \\ 0.312\,214\,313\,213\,494 \\ 0.000\,000\,000\,000\,000 \\ 0.000\,000\,000\,000\,000 \end{bmatrix}. \tag{3-23}$$

The solution of the extended normal equation (3-23) system yields the unknown parameters of a straight line for each element

$$\begin{bmatrix} {}^{1}c_0 \\ {}^{1}c_1 \\ {}^{2}c_0 \\ {}^{2}c_1 \\ {}^{3}c_0 \\ {}^{3}c_1 \end{bmatrix} = \begin{bmatrix} -1.350\,786\,978\,874\,439 \\ -0.914\,104\,247\,976\,010 \\ 0.000\,000\,000\,000\,000 \\ 3.138\,256\,688\,647\,309 \\ 1.350\,786\,978\,874\,442 \\ -0.914\,104\,247\,976\,016 \end{bmatrix}. \tag{3-24}$$

These results have been obtained with the code listed in Programme 3-3.

Programme 3-3: Code for an elementwise continuous polynomial approximation in the monomial basis.

```
%Approximation of f(x) on [-1, 1]
a=-1; b=1;

%polynomial degree for each element
p=1;

%number of elements
num_elements=3;

%Position of the equispaced nodes
nodes=linspace(a,b,num_elements+1);

%Preallocate matrices
N=zeros((p+1)*num_elements); n=zeros((p+1)*num_elements,1);
C=zeros(num_elements-1,(p+1)*num_elements);

%Normal matrix and right hand side
for zeta=1:num_elements
  index=(p+1)*zeta-p;
  for i=0:p
    for j=0:p
      N(index+i,index+j)=1/(i+j+1)*(nodes(zeta+1)^(i+j+1)
          -...
           nodes(zeta)^(i+j+1));
    end
    n(index+i)=integral(@(x)  sin(3*x).*x.^i,nodes(zeta),
        nodes(zeta+1));
  end
end

%Matrix for the conditions
for zeta=2:length(nodes)-1
   index=(p+1)*(zeta-1)-p;
   C(zeta-1,index:index+2*(p+1)-1)=...
       [nodes(zeta).^(0:p) -nodes(zeta).^(0:p)];
end

%Extended normal equation system
N_ext=[N C';C zeros(num_elements-1)]; n_ext=[n; zeros(
    num_elements-1,1)];
c=N_ext\n_ext;

%Deleting the Lagrangian multipliers
c(end-num_elements+2:end)=[];
```

Function (3-2), the resulting approximation and the residual function are depicted in Figure 3-17 and it can clearly be seen that the approximation is continuous. The straight lines (red) of the elements are connected at the inner nodes ${}^{2}x_{\nu_1} = -1/3$ and ${}^{3}x_{\nu_1} = 1/3$ and therefore the residual function in (3-17) (right) is continuous.

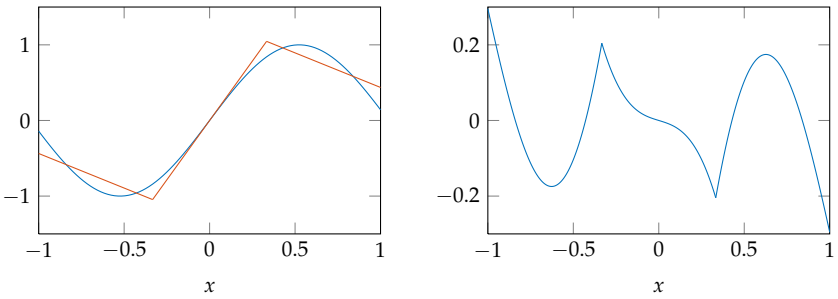

Figure 3-17: Given function (3-2) in blue and it's continuous approximation with 3 elements using linear polynomials in red (left). Residual function $v(x) = \sin(3x) - \sum_{\zeta=1}^{3} \zeta P_1(x)$ (right).

Now we can obtain an elementwise continuous approximations of any real-valued function $f(x)$, but one might wonder what happens if we will increase the number of elements and polynomial degree. Is it possible to achieve more accurate approximations than using the non-continuous approximation from the previous section, or will it be even worse? In the continuous case we have to solve one large equation system, while in the non-continuous case we have to solve many small equation systems. In both cases, the normal matrix is badly conditioned for a larger amount of elements or higher polynomial degree. Based on Figure 3-12 we determine the non-continuous and continuous approximations of function (3-2) with 350 elements using quadratic polynomials. The resulting residual functions of the two approximations are depicted in Figure 3-18.

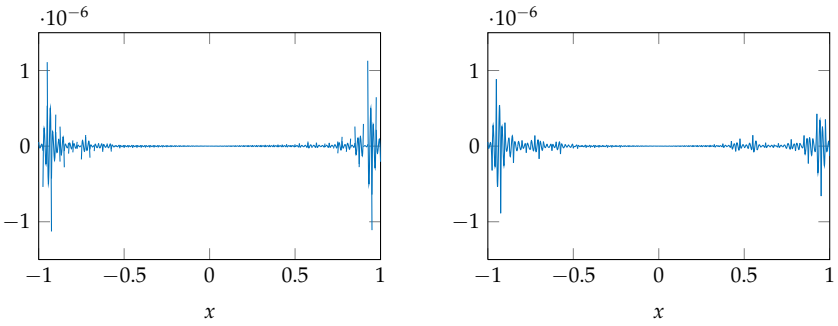

Figure 3-18: Residual function $v(x) = \sin(3x) - \sum_{\zeta=1}^{350} \zeta P_2(x)$ of a non-continuous (right) and continuous (left) approximation.

Since the normal equation system is ill-conditioned, an exact symmetrical distribution of the residual function is usually not resulting.

The residual functions of the non-continuous and continuous approximation of (3-2) are very similar and do not differ significantly. Also if we choose a different number of elements and/or polynomial degree even for some other functions, we always obtain very similar results. In most cases the continuous approximation yields slightly smaller values for the residual function, with the only advantage that the resulting approximation is continuous. However, the following figure reveals a small drawback so far.

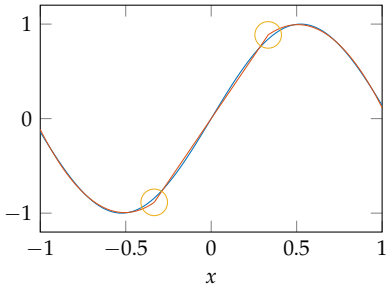

Figure 3-19: An approximation of function (3-2) with 3 elements using quadratic polynomials.

The approximation of function (3-2) with 3 elements using quadratic polynomials in Figure 3-19 is continuous but reveals a kink (yellow circle) at the inner nodes $x_2 = -1/3$ and $x_3 = 1/3$. The approximation is continuous but only piecewise smooth. To remove these kinks, we can enforce continuity in the first and second derivative by introducing the following two additional constraints for each inner node

A function $f(x)$ is said to be C^n continuous if its first n derivatives $\frac{\mathrm{d}^n f(x)}{\mathrm{d}x^n}$ are continuous.

$$\begin{aligned} {}^{\zeta}P_1'({}^{\zeta}x_{\nu_2}) &= {}^{\zeta+1}P_1'({}^{\zeta+1}x_{\nu_1}), \\ {}^{\zeta}P_1''({}^{\zeta}x_{\nu_2}) &= {}^{\zeta+1}P_1''({}^{\zeta+1}x_{\nu_1}), \end{aligned} \tag{3-25}$$

which implies that the second derivative ${}^{\zeta+1}P_1''$ must be at least a constant. Therefore, we will now focus on cubic polynomials and approximate (3-2) with 3 elements. In this case each normal matrix ${}^{\zeta}\mathbf{N}$ in (3-18) is larger and refers to 4 unknown parameters. For the constraints (3-17) and (3-25) we obtain three matrices enforcing continuity in the functional value

Such an approximation is known as a cubic spline, with the only difference that we use monomials as basis functions. The approach shown was also presented by (EZHOV *et al.* 2018).

$$\mathbf{C}_1 = \begin{bmatrix} 1 & {}^1x_{\nu_2} & {}^1x_{\nu_2}^2 & {}^1x_{\nu_2}^3 & -1 & -{}^2x_{\nu_1} & -{}^2x_{\nu_1}^2 & -{}^2x_{\nu_1}^3 & 0 & 0 & 0 & 0 \\ 0 & 0 & 0 & 0 & 1 & {}^2x_{\nu_2} & {}^2x_{\nu_2}^2 & {}^2x_{\nu_2}^3 & -1 & -{}^3x_{\nu_1} & -{}^3x_{\nu_1}^2 & -{}^3x_{\nu_1}^3 \end{bmatrix}, \tag{3-26}$$

in the first derivative

$$\mathbf{C}_2 = \begin{bmatrix} 0 & 1 & 2\,{}^1x_{\nu_2} & 3\,{}^1x_{\nu_2}^2 & 0 & -1 & -2\,{}^2x_{\nu_1} & -3\,{}^2x_{\nu_1}^2 & 0 & 0 & 0 & 0 \\ 0 & 0 & 0 & 0 & 0 & 1 & 2\,{}^2x_{\nu_2} & 3\,{}^2x_{\nu_2}^2 & 0 & -1 & -2\,{}^3x_{\nu_1} & -3\,{}^3x_{\nu_1}^2 \end{bmatrix} \tag{3-27}$$

and in the second derivative

$$\mathbf{C}_3 = \begin{bmatrix} 0 & 0 & 2 & 6\,{}^1x_{\nu_2} & 0 & 0 & -2 & -6\,{}^2x_{\nu_1} & 0 & 0 & 0 & 0 \\ 0 & 0 & 0 & 0 & 0 & 0 & 2 & 6\,{}^2x_{\nu_2} & 0 & 0 & -2 & -6\,{}^3x_{\nu_1} \end{bmatrix}. \tag{3-28}$$

These three matrices can be combined to

$$\mathbf{C} = \begin{bmatrix} \mathbf{C}_1 \\ \mathbf{C}_2 \\ \mathbf{C}_3 \end{bmatrix} \tag{3-29}$$

and will be inserted in (3-22). Extending the code in Programme 3-3 by a couple of lines for $\mathbf{C}_2$ and $\mathbf{C}_3$, we obtain the following smooth approximation without any kinks at the inner nodes.

We say an approximation is smooth, if it is C^2 continuous.

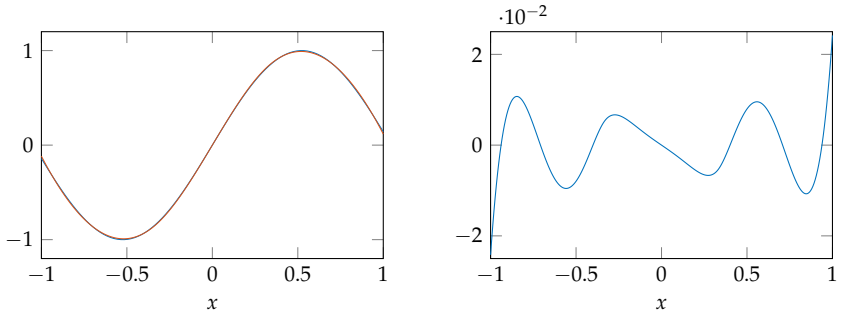

Figure 3-20: Given function (3-2) in blue and it's smooth approximation with 3 elements using cubic polynomials in red (left). Residual function $v(x) = \sin(3x) - \sum_{\zeta=1}^{3} {}^{\zeta}P_3(x)$ (right).

Figure 3-20 (left) shows a very smooth and already quite good approximation of (3-2) while using only 3 elements. The smoothness is also visible in the

residual function in Figure 3-20 (right) as no kinks are noticeable. While the computational effort to find the best approximation of (3-2) is huge we only present a near best fit in Figure 3-21. Based on numerical investigations it is very likely that the difference to the best approximation is small.

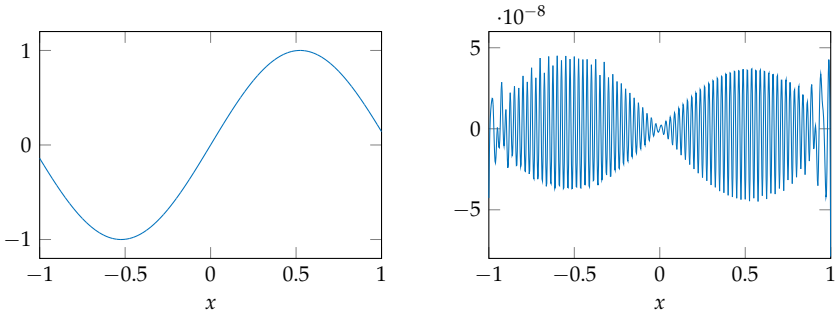

Figure 3-21: A near best smooth approximation of (3-2) with 80 elements using cubic polynomials (left). Residual function $v(x) = \sin(3x) - \sum_{\zeta=1}^{80} \zeta P_3(x)$ (right).

Figure 3-21 (right) shows, that the residual function for the near best smooth approximation of (3-2) is in a range of $\approx 5 \cdot 10^{-8}$ and is, in that case, not really better or worse than an approximation without the constraints (3-25). The same applies for the near best smooth approximation of function (3-6), which is depicted in Figure 3-22.

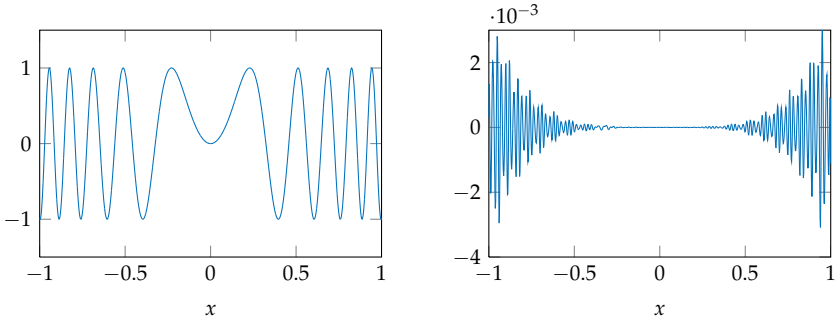

Figure 3-22: A near best smooth approximation of (3-6) with 100 elements using cubic polynomials (left). Residual function $v(x) = \sin(30x^2) - \sum_{\zeta=1}^{100} \zeta P_3(x)$ (right).

The residual function in Figure 3-22 (right) is a bit worse than the one of a non-continuous approximation in Figure 3-15. The main benefit of such approximations is, that they are continuous in the 1st and 2nd derivative, so they are smooth. But this benefit has also a downside while dealing with monomials as basis functions. The constraints (3-25) are having a big impact on the solution of the unknown parameters and while we deal with an ill-posed problem, a small change in the parameters of one element can have a huge impact on the unknown parameters of neighboured elements. Such a numerical effect on the solution of the unknown parameters can be seen in Figure 3-23.

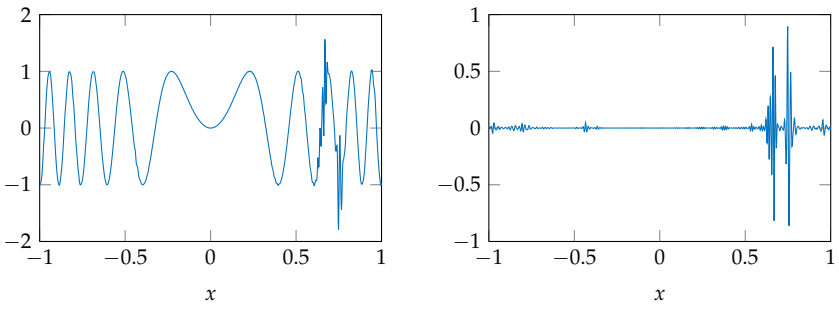

Figure 3-23: A smooth approximation of (3-6) with 300 elements using cubic polynomials (left). Residual function $v(x) = \sin(30x^2) - \sum_{\zeta=1}^{300} \zeta P_3(x)$ (right).

Figure 3-23 (left) shows some strange oscillations around $x = 0.7$, which are caused by the solution of the ill-conditioned normal matrix. This effect should not be confused with RUNGE's phenomenon.

For sake of completeness, we also present a near best smooth approximation of function (3-8), which is depicted in Figure 3-24.

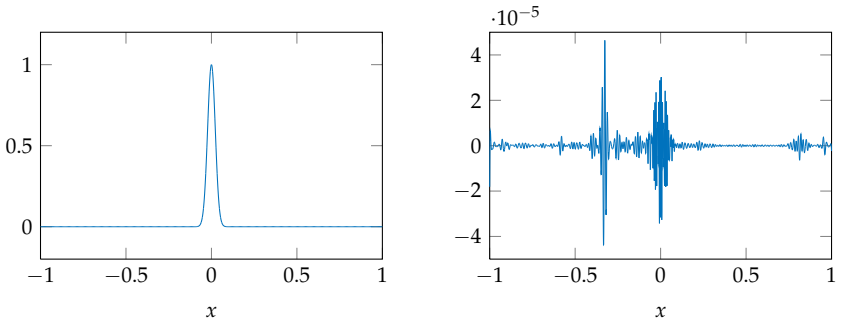

Figure 3-24: A near best smooth approximation of (3-8) with 300 elements using cubic polynomials (left). Residual function $v(x) = \exp(-1000x^2) - \sum_{\zeta=1}^{300} {}^{\zeta}P_3(x)$ (right).

While the residual function of the elementwise non-continuous approximation in Figure 3-16 is zero within machine precision off site the peak, the smooth approximation also shows large deviations in these areas as illustrated in Figure 3-24 (right). Once again, these deviations are caused by the constraints and the ill-conditioned normal matrix.

Like a butterfly effect - a small error in one element, can disturbe the whole approximation.

At the end of this section we can conclude that polynomial approximation in the monomial basis is still an ill-conditioned problem. Significant improvements have been achieved, while we divided the whole domain into elements and introduced constraints in order to obtain smooth approximations. So far we only focused on equispaced elements, probably the easiest case. For sure it can be further improved, like implementing strategies to identify the optimal number of elements and especially where the nodes must be located, etc. But in the end, it is still an ill-conditioned problem. We are familiar with the monomials basis and it is easy for us to handle it, but nevertheless it should never be used for numerical work. Only for didactic reasons or maybe in case that a low polynomial degree is needed.

3.2 ELEMENTWISE APPROXIMATION IN AN ALTERNATIVE BASIS

An elementwise continuous polynomial approximation can also be obtained without the necessity of introducing constraints at the inner nodes. The basic idea shall be exemplified on an elementwise linear approximation, as depicted in Figure 3-25.

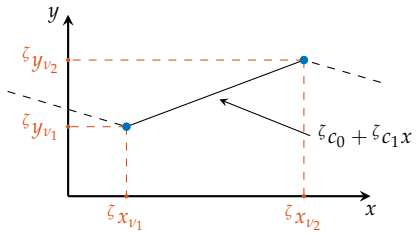

Figure 3-25: Illustration of an element for a linear approximation.

Figure 3-25 illustrates one single element of an elementwise polynomial approximation, while the elements must be connected at the inner nodes. The

previous and successive elements are only indicated by a black dashed line. The straight line of the depicted element is uniquely described by the two parameters ${}^{\zeta}c_0$ and ${}^{\zeta}c_1$. In the previous sections, these parameters were estimated for each element under the constraint, that the elements must be connected at the inner nodes. However, the same straight line is also uniquely described by the two nodes (blue dots) and while we set ${}^{\zeta}x_{\nu_1}$ and ${}^{\zeta}x_{\nu_2}$ only the $y-$coordinates ${}^{\zeta}y_{\nu_1}$ and ${}^{\zeta}y_{\nu_2}$ of the two nodes are unknown. The basic idea is now to substitute the two unknown parameters ${}^{\zeta}c_0$ and ${}^{\zeta}c_1$ by the two $y-$coordinates ${}^{\zeta}y_{\nu_1}$ and ${}^{\zeta}y_{\nu_2}$. Hence, we have the following two equivalent representations of the same polynomial

$$ {}^{\zeta}P_1(x) = \sum_{j=0}^{1} {}^{\zeta}c_j \, \phi_j(x) = \sum_{j=0}^{1} {}^{\zeta}d_j \, \psi_j(x) \,, \tag{3-30} $$

with the monomial basis $\phi_j(x) = x^j$ and the new unknown parameters ${}^{\zeta}d_j$, containing the $y-$coordinates ${}^{\zeta}y_{\nu_1}$ and ${}^{\zeta}y_{\nu_2}$. Now the question arises, how to determine the two new basis functions $\psi_j(x)$? First of all we rewrite (3-30) in matrix notation

$$ \begin{bmatrix} \phi_0 & \phi_1 \end{bmatrix} \begin{bmatrix} {}^{\zeta}c_0 \\ {}^{\zeta}c_1 \end{bmatrix} = \begin{bmatrix} \psi_0 & \psi_1 \end{bmatrix} \begin{bmatrix} {}^{\zeta}d_0 \\ {}^{\zeta}d_1 \end{bmatrix} \,. \tag{3-31} $$

Furthermore, we know the following two equations based on Figure 3-25

$$ \begin{aligned} {}^{\zeta}c_0 + {}^{\zeta}c_1 \, {}^{\zeta}x_{\nu_1} &= {}^{\zeta}y_{\nu_1} \,, \\ {}^{\zeta}c_0 + {}^{\zeta}c_1 \, {}^{\zeta}x_{\nu_2} &= {}^{\zeta}y_{\nu_2} \,. \end{aligned} \tag{3-32} $$

Substituting the $y-$coordinates ${}^{\zeta}y_{\nu_1}$ and ${}^{\zeta}y_{\nu_2}$ in (3-32) with the new unknown parameters ${}^{\zeta}d_j$ yields

$$ \begin{aligned} {}^{\zeta}c_0 + {}^{\zeta}c_1 \, {}^{\zeta}x_{\nu_1} &= {}^{\zeta}d_0 \,, \\ {}^{\zeta}c_0 + {}^{\zeta}c_1 \, {}^{\zeta}x_{\nu_2} &= {}^{\zeta}d_1 \,, \end{aligned} \tag{3-33} $$

which can be written in matrix notation

$$ \begin{bmatrix} 1 & {}^{\zeta}x_{\nu_1} \\ 1 & {}^{\zeta}x_{\nu_2} \end{bmatrix} \begin{bmatrix} {}^{\zeta}c_0 \\ {}^{\zeta}c_1 \end{bmatrix} = \begin{bmatrix} {}^{\zeta}d_0 \\ {}^{\zeta}d_1 \end{bmatrix} \,. \tag{3-34} $$

Solving (3-34) for the unknown coefficients ${}^{\zeta}c_0$ and ${}^{\zeta}c_1$ reads

$$ \begin{bmatrix} {}^{\zeta}c_0 \\ {}^{\zeta}c_1 \end{bmatrix} = \frac{1}{{}^{\zeta}x_{\nu_2} - {}^{\zeta}x_{\nu_1}} \begin{bmatrix} {}^{\zeta}x_{\nu_2} & -{}^{\zeta}x_{\nu_1} \\ -1 & 1 \end{bmatrix} \begin{bmatrix} {}^{\zeta}d_0 \\ {}^{\zeta}d_1 \end{bmatrix} \,. \tag{3-35} $$

Inserting (3-35) into the left hand side of (3-31) results in

$$ \begin{aligned} \frac{1}{{}^{\zeta}x_{\nu_2} - {}^{\zeta}x_{\nu_1}} \begin{bmatrix} \phi_0 & \phi_1 \end{bmatrix} \begin{bmatrix} {}^{\zeta}x_{\nu_2} & -{}^{\zeta}x_{\nu_1} \\ -1 & 1 \end{bmatrix} \begin{bmatrix} {}^{\zeta}d_0 \\ {}^{\zeta}d_1 \end{bmatrix} &= \begin{bmatrix} \psi_0 & \psi_1 \end{bmatrix} \begin{bmatrix} {}^{\zeta}d_0 \\ {}^{\zeta}d_1 \end{bmatrix} \,, \\ \frac{1}{{}^{\zeta}x_{\nu_2} - {}^{\zeta}x_{\nu_1}} \begin{bmatrix} \phi_0 \, {}^{\zeta}x_{\nu_2} - \phi_1 & \phi_1 - \phi_0 \, {}^{\zeta}x_{\nu_1} \end{bmatrix} \begin{bmatrix} {}^{\zeta}d_0 \\ {}^{\zeta}d_1 \end{bmatrix} &= \begin{bmatrix} \psi_0 & \psi_1 \end{bmatrix} \begin{bmatrix} {}^{\zeta}d_0 \\ {}^{\zeta}d_1 \end{bmatrix} \,. \end{aligned} \tag{3-36} $$

Equating the coefficients in (3-36) yields the two new basis functions

$$ \psi_0(x) = \frac{\phi_0 \, {}^{\zeta}x_{\nu_2} - \phi_1}{{}^{\zeta}x_{\nu_2} - {}^{\zeta}x_{\nu_1}} \qquad \text{and} \qquad \psi_1(x) = \frac{\phi_1 - \phi_0 \, {}^{\zeta}x_{\nu_1}}{{}^{\zeta}x_{\nu_2} - {}^{\zeta}x_{\nu_1}} \,. \tag{3-37} $$

Inserting the monomial basis $\phi_j(x) = x^j$ in (3-37) yields

In FEM these basis functions are known as the *hat functions*.

$$\psi_0(x) = \frac{{}^{\zeta}x_{\nu_2} - x}{{}^{\zeta}x_{\nu_2} - {}^{\zeta}x_{\nu_1}} \qquad \text{and} \qquad \psi_1(x) = \frac{x - {}^{\zeta}x_{\nu_1}}{{}^{\zeta}x_{\nu_2} - {}^{\zeta}x_{\nu_1}}\,. \tag{3-38}$$

Introducing a new variable

$$\tilde{x} = \frac{x - {}^{\zeta}x_{\nu_1}}{{}^{\zeta}x_{\nu_2} - {}^{\zeta}x_{\nu_1}}\,, \tag{3-39}$$

with $\tilde{x} \in [0,1]$ for all elements, the two basis functions (3-38) are

These basis functions are equal to the Bernstein polynomials $B_{0,1}$ and $B_{1,1}$, see e.g. (Piegl and Tiller 1997, p. 16).

$$\tilde{\psi}_0(\tilde{x}) = 1 - \tilde{x} \qquad \text{and} \qquad \tilde{\psi}_1(\tilde{x}) = \tilde{x}\,, \tag{3-40}$$

and are depicted in Figure 3-26.

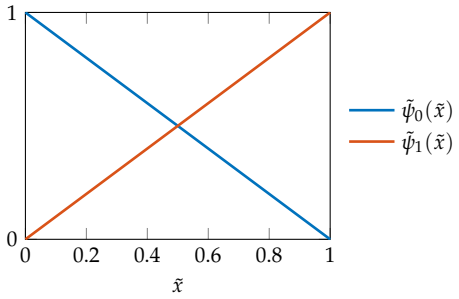

Figure 3-26: Alternative basis functions for a straight line, while the two $y-$coordinates ${}^{\zeta}y_{\nu_1}$ and ${}^{\zeta}y_{\nu_2}$ of the nodes are unknown parameters.

The basis functions (3-40) are referring to a generalised element and therefore, are always equal for all elements. The angle between $\tilde{\psi}_0(\tilde{x})$ and $\tilde{\psi}_1(\tilde{x})$ is $\alpha_{0,1} = 66.67\,\text{gon}$ and both are of equal length. In contrast to monomials, the angle between these basis functions and their length do not depend on the position of the element, but are always equal. These facts are of great advantage from a numerical point of view, as we shall see in the following example.

To illustrate an elementwise linear approximation in the derived alternative basis (3-40), we approximate function (3-2) by dividing the whole domain into $N = 3$ equispaced elements. Based on the definition of nodes and elements in Table 3-2 and the two alternative basis functions of a straight line we can set-up the normal equation system for each element

$$\begin{bmatrix} {}^{\zeta}\langle\psi_0,\psi_0\rangle & {}^{\zeta}\langle\psi_1,\psi_0\rangle \\ {}^{\zeta}\langle\psi_0,\psi_1\rangle & {}^{\zeta}\langle\psi_1,\psi_1\rangle \end{bmatrix} \begin{bmatrix} {}^{\zeta}d_0 \\ {}^{\zeta}d_1 \end{bmatrix} = \begin{bmatrix} {}^{\zeta}\langle\psi_0,\sin(3x)\rangle \\ {}^{\zeta}\langle\psi_1,\sin(3x)\rangle \end{bmatrix}\,, \tag{3-41}$$

with $\zeta = 1,2,3$. Using the definition of the basis function in (3-38), the integrals in the normal matrix are expressed by

$${}^{\zeta}\langle\psi_i,\psi_j\rangle = \int_{{}^{\zeta}x_{\nu_1}}^{{}^{\zeta}x_{\nu_2}} \psi_i(x),\psi_j(x)\,\mathrm{d}x \tag{3-42}$$

with $i,j = 0,1$. But it is more feasible to solve the integral for the generalised coordinate $\tilde{x}$, which is always within the interval $[0,1]$ for all elements. Inserting (3-40) and adopting the limits of the integrals yields

$${}^{\zeta}\langle\psi_i,\psi_j\rangle = \int_0^1 \tilde{\psi}_i(\tilde{x})\tilde{\psi}_j(\tilde{x})\,\mathrm{d}x \qquad \text{for} \qquad i,j = 0,1\,. \tag{3-43}$$

In order to change $\mathrm{d}x$ we take the derivative of the generalised coordinate (3-39)

$$\frac{\mathrm{d}\tilde{x}}{\mathrm{d}x} = \frac{\mathrm{d}}{\mathrm{d}x}\left(\frac{x - {}^{\zeta}x_{\nu_1}}{{}^{\zeta}x_{\nu_2} - {}^{\zeta}x_{\nu_1}}\right) = \frac{1}{{}^{\zeta}x_{\nu_2} - {}^{\zeta}x_{\nu_1}} \tag{3-44}$$

and after rearranging we obtain

$$\mathrm{d}x = ({}^{\zeta}x_{\nu_2} - {}^{\zeta}x_{\nu_1})\,\mathrm{d}\tilde{x}\,. \tag{3-45}$$

Inserting (3-45) with ${}^{\zeta}J = {}^{\zeta}x_{\nu_2} - {}^{\zeta}x_{\nu_1}$ into (3-43) yields

$${}^{\zeta}\langle\psi_i, \psi_j\rangle = {}^{\zeta}J \int_0^1 \tilde{\psi}_i(\tilde{x})\tilde{\psi}_j(\tilde{x})\,\mathrm{d}\tilde{x} \qquad \text{for} \qquad i,j = 0,1\,. \tag{3-46}$$

Solving the integrals in the generalised coordinate is of great advantage, while the integrals simplify to

$${}^{\zeta}\langle\psi_i, \psi_j\rangle = {}^{\zeta}J\langle\tilde{\psi}_i, \tilde{\psi}_j\rangle \qquad \text{for} \qquad i,j = 0,1. \tag{3-47}$$

The integrals

$$\langle\tilde{\psi}_i, \tilde{\psi}_j\rangle = \int_0^1 \tilde{\psi}_i(\tilde{x})\tilde{\psi}_j(\tilde{x})\,\mathrm{d}\tilde{x} \qquad \text{for} \qquad i,j = 0,1 \tag{3-48}$$

are referring to a generalised element and therefore, they only needs to be solved once. The integrals for the normal matrix only have to be scaled by the factor ${}^{\zeta}J$

$${}^{\zeta}\mathbf{N} = {}^{\zeta}J\,\mathbf{N}_{\text{element}} \tag{3-49}$$

with

$$\mathbf{N}_{\text{element}} = \begin{bmatrix} 1/3 & 1/6 \\ 1/6 & 1/3 \end{bmatrix}, \tag{3-50}$$

which saves a lot of computational time. In case of equispaced elements, ${}^{\zeta}J$ is also constant for all elements. The integrals for the right hand side will also be solved for the generalised coordinate $\tilde{x}$ and yields

$${}^{\zeta}\langle\psi_i, \sin(3x)\rangle = {}^{\zeta}J \int_0^1 \tilde{\psi}_i(\tilde{x})\,\sin(3x)\,\mathrm{d}\tilde{x} \qquad \text{for} \qquad i = 0,1\,. \tag{3-51}$$

Rearranging (3-39) as

$$x = ({}^{\zeta}x_{\nu_2} - {}^{\zeta}x_{\nu_1})\,\tilde{x} + {}^{\zeta}x_{\nu_1} = {}^{\zeta}J\,\tilde{x} + {}^{\zeta}x_{\nu_1} \tag{3-52}$$

and inserting into (3-51) results in

$${}^{\zeta}\langle\psi_i, \sin(3x)\rangle = {}^{\zeta}J \int_0^1 \tilde{\psi}_i(\tilde{x})\,\sin\left(3({}^{\zeta}J\,\tilde{x} + {}^{\zeta}x_{\nu_1})\right)\,\mathrm{d}\tilde{x} \tag{3-53}$$

for $i = 0,1$. The linear approximation of (3-41) using 3 elements yields the three normal equation systems

$$\begin{aligned}
\begin{bmatrix} 2/9 & 1/9 \\ 1/9 & 2/9 \end{bmatrix} \begin{bmatrix} {}^{1}y_{\nu_1} \\ {}^{1}y_{\nu_2} \end{bmatrix} &= \begin{bmatrix} -0.213\,272\,336\,075\,477 \\ -0.296\,825\,931\,414\,051 \end{bmatrix}, \\
\begin{bmatrix} 2/9 & 1/9 \\ 1/9 & 2/9 \end{bmatrix} \begin{bmatrix} {}^{2}y_{\nu_1} \\ {}^{2}y_{\nu_2} \end{bmatrix} &= \begin{bmatrix} -0.100\,389\,559\,646\,586 \\ 0.100\,389\,559\,646\,586 \end{bmatrix}, \\
\begin{bmatrix} 2/9 & 1/9 \\ 1/9 & 2/9 \end{bmatrix} \begin{bmatrix} {}^{3}y_{\nu_1} \\ {}^{3}y_{\nu_2} \end{bmatrix} &= \begin{bmatrix} 0.296\,825\,931\,414\,052 \\ 0.213\,272\,336\,075\,477 \end{bmatrix}.
\end{aligned} \tag{3-54}$$

Based on Table 3-2, two elements share the same node, namely

$$ {}^{1}x_{\nu_2} = {}^{2}x_{\nu_1} = x_2 \tag{3-55} $$

and

$$ {}^{2}x_{\nu_2} = {}^{3}x_{\nu_1} = x_3\,. \tag{3-56} $$

Substituting ${}^{\zeta}y_{\nu_1}$ and ${}^{\zeta}y_{\nu_2}$ in (3-54) by the unique identifier for the nodes, the normal equation system can be written as

$$ \begin{aligned} \begin{bmatrix} 2/9 & 1/9 \\ 1/9 & 2/9 \end{bmatrix} \begin{bmatrix} y_1 \\ y_2 \end{bmatrix} &= \begin{bmatrix} -0.213\,272\,336\,075\,477 \\ -0.296\,825\,931\,414\,051 \end{bmatrix}, \\ \begin{bmatrix} 2/9 & 1/9 \\ 1/9 & 2/9 \end{bmatrix} \begin{bmatrix} y_2 \\ y_3 \end{bmatrix} &= \begin{bmatrix} -0.100\,389\,559\,646\,586 \\ 0.100\,389\,559\,646\,586 \end{bmatrix}, \\ \begin{bmatrix} 2/9 & 1/9 \\ 1/9 & 2/9 \end{bmatrix} \begin{bmatrix} y_3 \\ y_4 \end{bmatrix} &= \begin{bmatrix} 0.296\,825\,931\,414\,052 \\ 0.213\,272\,336\,075\,477 \end{bmatrix}. \end{aligned} \tag{3-57} $$

While two elements share the same nodes, the three normal equation systems can not be solved individually. To solve for the unknowns parameters, the normal equation systems needs to be combined as follows

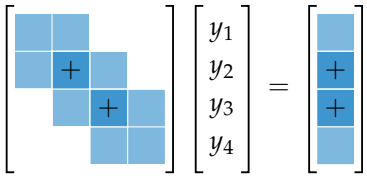

(3-58)

and will read

$$ \begin{bmatrix} 2/9 & 1/9 & 0 & 0 \\ 1/9 & 4/9 & 1/9 & 0 \\ 0 & 1/9 & 4/9 & 1/9 \\ 0 & 0 & 1/9 & 2/9 \end{bmatrix} \begin{bmatrix} y_1 \\ y_2 \\ y_3 \\ y_4 \end{bmatrix} = \begin{bmatrix} -0.213\,272\,336\,075\,477 \\ -0.397\,215\,491\,060\,637 \\ 0.397\,215\,491\,060\,637 \\ 0.213\,272\,336\,075\,477 \end{bmatrix}. \tag{3-59} $$

Solving (3-59) yields the unknown parameters

$$ \begin{bmatrix} y_1 \\ y_2 \\ y_3 \\ y_4 \end{bmatrix} = \begin{bmatrix} -0.436\,682\,730\,898\,429 \\ -1.046\,085\,562\,882\,435 \\ 1.046\,085\,562\,882\,435 \\ 0.436\,682\,730\,898\,429 \end{bmatrix}. \tag{3-60} $$

The resulting elementwise continuous linear approximation of (3-2) is depicted in Figure 3-27 and is equivalent to the approximation in the monomial basis depicted in Figure 3-17.

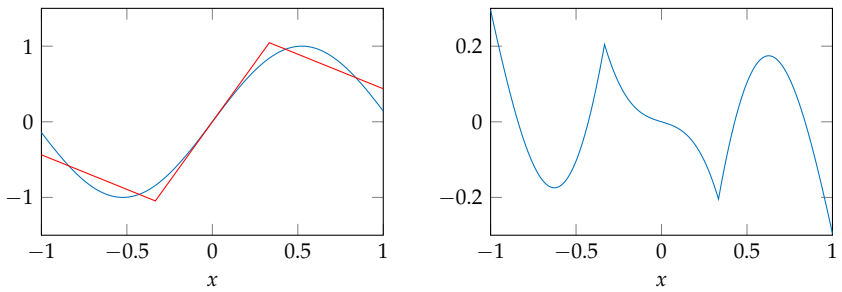

Figure 3-27: Given function (3-2) in blue and it's continuous approximation with 3 elements using the derived alternative linear polynomials in red (left). Residual function $v(x) = \sin(3x) - \sum_{\zeta=1}^{3} {}^{\zeta}P_1(x)$ (right).

In order to prove that the result is really equal to the one in the monomial basis (3-24), we insert the result from (3-60) into (3-35) and determine the parameters ${}^{\zeta}c_0$ and ${}^{\zeta}c_1$ for all three lines from the $y-$coordinates of nodes. The derived coefficients and the coefficients from (3-24) are listed in Table 3-3.

Table 3-3: Comparison of derived coefficients based on the solution for the $y-$coordinates of the nodes in (3-60) and the solution from an elementwise continuous approximation in the monomial basis in (3-24). Deviations are due to rounding errors.

	Derived from (3-60)	Monomial basis
${}^{1}c_0$	−1.350 786 978 874 438	−1.350 786 978 874 439
${}^{1}c_1$	−0.914 104 247 976 009	−0.914 104 247 976 010
${}^{2}c_0$	0.000 000 000 000 000	0.000 000 000 000 000
${}^{2}c_1$	3.138 256 688 647 305	3.138 256 688 647 309
${}^{3}c_0$	1.350 786 978 874 438	1.350 786 978 874 442
${}^{3}c_1$	−0.914 104 247 976 009	−0.914 104 247 976 016

Table 3-3 shows, that the elementwise approximation in the alternative basis (3-40) is equivalent to an elementwise continuous approximation in the monomial basis, while we introduce constraints at inner nodes, as described in Section 3.1.2.

The presented linear approximation in the alternative basis (3-40) has been performed with the MATLAB code in Programme 3-4.

Programme 3-4: Code for an elementwise continuous polynomial approximation in the derived alternative basis (3-40).

```
%Approximation of L(x) on [-1, 1]
a=-1; b=1;

%number of elements
elements=3;

%Position of the equispaced nodes
nodes=linspace(a,b,elements+1);

%Initilisation of the matrices
N=zeros(elements+1); n=zeros(elements+1,1);

%Normal matrix for a generalised element
N_element=[1/3 1/6;1/6 1/3];

for zeta=1:elements
    J=nodes(zeta+1)-nodes(zeta);
    N(zeta:zeta+1,zeta:zeta+1)=N(zeta:zeta+1,zeta:zeta+1)+J
        *N_element;
    n(zeta)=n(zeta)+J*integral(@(x) sin(3*(J*x+nodes(zeta))
        ).*(1-x),0,1);
    n(zeta+1)=n(zeta+1)+J*integral(@(x) sin(3*(J*x+nodes(
        zeta))).*x,0,1);
end
c=N\n;
```

In direct comparison to the code for an equivalent approximation in the monomial basis in Programme 3-3, the one in the alternative basis is shorter and also faster. Furthermore, an approximation in the alternative basis is numerically more stable and also applicable for a large amount of elements. For

the monomial basis, the condition number of the normal matrix increases rapidly with increasing number of elements, in contrast to the derived alternative basis, as illustrated in Figure 3-28.

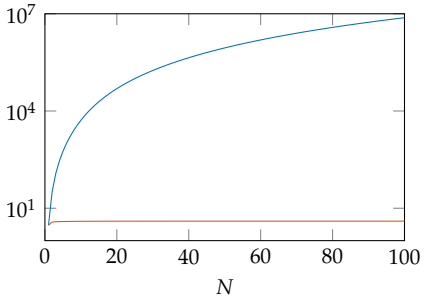

Figure 3-28: Logarithmic plot of the condition number of the normal matrix of an elementwise continuous linear approximation in the monomial basis (blue) and in the alternative basis (red) for increasing number of elements N.

Figure 3-28 depicts the condition number of the normal matrix for the monomial (blue) and alternative basis (red) with increasing number of elements N. The difference between both is huge. While the condition number of the normal matrix for the monomial basis grows rapidly towards 10^7 with increasing number of elements, the one for the normal matrix in the derived alternative basis tends towards 4. Another difference between both sets of basis vectors is the size of the normal equation system in dependence to the number of elements N. While the normal matrix in the alternative basis is only of size $N+1$, the normal matrix in the monomial basis is already of size $3N-1$. For the presented approximation of functions in one dimension this difference is not huge, but this changes for approximations of functions in two or more dimensions.

3.2.1 *The generalised 1D element*

In the previous section we derived an alternative basis for a linear approximation. While introducing $\tilde{x}$ we transformed each element onto a generalised element, which allows an easy and fast way to set-up the normal matrix. The derived basis functions are always equal and are not depending on the elements any more. To define basis functions of a more complex approximation, than for the presented one in Section 3.2, it is sometimes of great advantage to distinguish between the transformation of the element and the transformation of the coefficients between different basis functions. This allows to determine the new basis function directly for the generalised element, which is usually very simple. Therefore, we will introduce two different transformations:

1. Transformation of the elements.
2. Transformation of the coefficients.

The application of these two transformations will be illustrated on the derivation of an alternative basis for a cubic elementwise approximation, as illustrated in Figure 3-29.

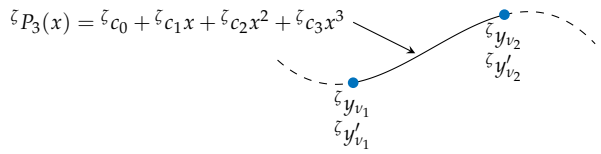

Figure 3-29: Illustration of an element for a cubic approximation.

Like in the previous section, we substitute the four unknown parameters ${}^{\zeta}c_i$ by the two $y-$coordinates ${}^{\zeta}y_{\nu_1}$ and ${}^{\zeta}y_{\nu_2}$ of the nodes and the two derivatives of the approximation at the nodes

$$\begin{aligned} \left.\frac{\mathrm{d}^{\zeta}P_3(x)}{\mathrm{d}x}\right|_{x={}^{\zeta}x_{\nu_1}} &= {}^{\zeta}y'_{\nu_1}\,, \\ \left.\frac{\mathrm{d}^{\zeta}P_3(x)}{\mathrm{d}x}\right|_{x={}^{\zeta}x_{\nu_2}} &= {}^{\zeta}y'_{\nu_2}\,. \end{aligned} \tag{3-61}$$

Thus, we have the following two equivalent representations of the same polynomial

$${}^{\zeta}P_3(x) = \sum_{j=0}^{3} {}^{\zeta}c_j\,\phi_j(x) = \sum_{j=0}^{3} {}^{\zeta}d_j\,\psi_j(x)\,, \tag{3-62}$$

with the monomial basis $\phi_j(x) = x^j$ and the new unknown parameters

$$\begin{bmatrix} {}^{\zeta}d_0 \\ {}^{\zeta}d_1 \\ {}^{\zeta}d_2 \\ {}^{\zeta}d_3 \end{bmatrix} = \begin{bmatrix} {}^{\zeta}y_{\nu_1} \\ {}^{\zeta}y'_{\nu_1} \\ {}^{\zeta}y_{\nu_1} \\ {}^{\zeta}y'_{\nu_2} \end{bmatrix}\,. \tag{3-63}$$

Choosing these parameters ensures an approximation, that is also continuous in its first derivative. In the following we will present the derivation of the new basis functions $\psi_j(x)$ for an elementwise cubic approximation, while introducing the aforementioned two transformations.

3.2.1.1 *Transformation of a 1D element*

Although this transformation is very simple and obvious for a 1D element, it is a bit different for a 2D or 3D element. Therefore, we will address this issue also for a 1D element in more detail. Consider the following transformation of an arbitrary 1D element, depicted in Figure 3-30.

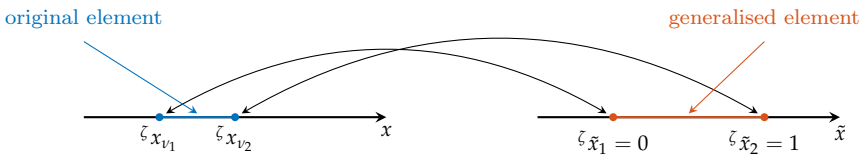

Figure 3-30: Transformation of a 1D element.

We parameterise x.

The problem is to define a transformation that maps an element (blue) onto the generalised element (red) and vice versa. In general, this can be done by any functional relationship

$$\begin{aligned} x &= \tilde{f}(\tilde{x})\,, \\ \tilde{x} &= f(x)\,. \end{aligned} \tag{3-64}$$

For convenience and to ensure a unique transformation, we will focus on a linear combination of some arbitrary basis functions

$$x = \sum_{j=0}^{p} {}^{\zeta}a_j\,\xi_j(\tilde{x}) \tag{3-65}$$

and choose monomials $\xi_j(\tilde{x}) = \tilde{x}^j$. While an element is defined by its two nodes ${}^{\zeta}x_{\nu_1}$ and ${}^{\zeta}x_{\nu_2}$, we define a linear combination of two basis functions in order

to ensure a unique solution for the unknown parameters for each element ${}^{\zeta}a_j$. Finally, the linear transformation reads

$$x = {}^{\zeta}a_0 + {}^{\zeta}a_1\tilde{x}\,, \tag{3-66}$$

with the two unknown parameters ${}^{\zeta}a_0$ and ${}^{\zeta}a_1$. To compute the unknown parameters we set-up the following equation system based on the two nodes of each element

$$\begin{bmatrix} {}^{\zeta}x_{\nu_1} \\ {}^{\zeta}x_{\nu_2} \end{bmatrix} = \begin{bmatrix} 1 & 0 \\ 1 & 1 \end{bmatrix} \begin{bmatrix} {}^{\zeta}a_0 \\ {}^{\zeta}a_1 \end{bmatrix}, \tag{3-67}$$

and obtain

$$\begin{bmatrix} {}^{\zeta}a_0 \\ {}^{\zeta}a_1 \end{bmatrix} = \begin{bmatrix} {}^{\zeta}x_{\nu_1} \\ {}^{\zeta}x_{\nu_2} - {}^{\zeta}x_{\nu_1} \end{bmatrix}. \tag{3-68}$$

The transformation reads

$$x = {}^{\zeta}x_{\nu_1} + \left({}^{\zeta}x_{\nu_2} - {}^{\zeta}x_{\nu_1}\right)\tilde{x}\,, \tag{3-69}$$

which is exactly the same as (3-39). The basic concept of the presented transformation is directly extendible for 2D or 3D elements, as shown in Section 4.4.

The transformation is equivalent to a parameterisation.

3.2.1.2 *Transformation of the coefficients*

The transformation of coefficients between different sets of basis functions has already been briefly discussed. However, to easily solve the integrals of the normal matrix for any kind of basis functions or to convert a set of coefficients into a different basis or to convert different basis functions, it is necessary to get a better understanding of this issue. Figure 3-31 illustrates the four main transformations between different basis on the original and generalised element.

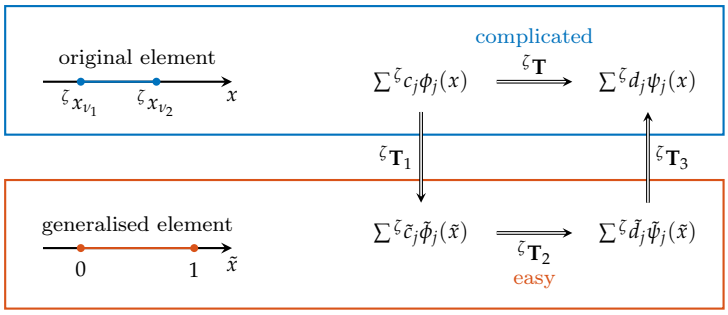

Figure 3-31: Transformation of the coefficients between different basis functions.

For the example of an elemetwise cubic approximation, the blue box in Figure 3-31 represents a polynomial on the original element

$${}^{\zeta}P_3(x) = \sum_{j=0}^{3} {}^{\zeta}c_j\phi_j(x) = \sum_{j=0}^{3} {}^{\zeta}d_j\psi_j(x) \tag{3-70}$$

and the red box represents the same polynomial on a generalised element

$${}^{\zeta}\tilde{P}_3(\tilde{x}) = \sum_{j=0}^{3} {}^{\zeta}\tilde{c}_j\tilde{\phi}_j(\tilde{x}) = \sum_{j=0}^{3} {}^{\zeta}\tilde{d}_j\tilde{\psi}_j(\tilde{x})\,. \tag{3-71}$$

Both polynomials are describing exactly the same curve only on different intervals, thus

$$ {}^{\zeta}P_3(x) = {}^{\zeta}\tilde{P}_3(\tilde{x})\,. \tag{3-72} $$

The derivative of the polynomials in (3-72) reads

$$ \frac{\mathrm{d}^{\zeta}P_3(x)}{\mathrm{d}x} = \frac{\mathrm{d}^{\zeta}\tilde{P}_3(\tilde{x})}{\mathrm{d}x} = \frac{\mathrm{d}^{\zeta}\tilde{P}_3(\tilde{x})}{\mathrm{d}\tilde{x}}\frac{\mathrm{d}\tilde{x}}{\mathrm{d}x}\,, \tag{3-73} $$

with

$$ \frac{\mathrm{d}\tilde{x}}{\mathrm{d}x} = \frac{1}{{}^{\zeta}x_{\nu_2} - {}^{\zeta}x_{\nu_1}} = \frac{1}{{}^{\zeta}J}\,. \tag{3-74} $$

Based on these relationships we can determine the four different transformations illustrated in Figure 3-31.

1. Determination of the transformation matrix ${}^{\zeta}\mathbf{T}$ to convert ${}^{\zeta}c_j$ into ${}^{\zeta}d_j$.

   Based on Figure 3-29 and Equation (3-61) we know the following four equations

   $$ \begin{aligned} {}^{\zeta}c_0 + {}^{\zeta}c_1\,{}^{\zeta}x_{\nu_1} + {}^{\zeta}c_2\,{}^{\zeta}x_{\nu_1}^2 + {}^{\zeta}c_3\,{}^{\zeta}x_{\nu_1}^3 &= {}^{\zeta}y_{\nu_1}\,,\\ {}^{\zeta}c_1 + 2\,{}^{\zeta}c_2\,{}^{\zeta}x_{\nu_1} + 3\,{}^{\zeta}c_3\,{}^{\zeta}x_{\nu_1}^2 &= {}^{\zeta}y'_{\nu_1}\,,\\ {}^{\zeta}c_0 + {}^{\zeta}c_1\,{}^{\zeta}x_{\nu_2} + {}^{\zeta}c_2\,{}^{\zeta}x_{\nu_2}^2 + {}^{\zeta}c_3\,{}^{\zeta}x_{\nu_2}^3 &= {}^{\zeta}y_{\nu_2}\,,\\ {}^{\zeta}c_1 + 2\,{}^{\zeta}c_2\,{}^{\zeta}x_{\nu_2} + 3\,{}^{\zeta}c_3\,{}^{\zeta}x_{\nu_2}^2 &= {}^{\zeta}y'_{\nu_2}\,, \end{aligned} \tag{3-75} $$

   which can be written in matrix notation as

   $$ \begin{bmatrix} 1 & {}^{\zeta}x_{\nu_1} & {}^{\zeta}x_{\nu_1}^2 & {}^{\zeta}x_{\nu_1}^3\\ 0 & 1 & 2\,{}^{\zeta}x_{\nu_1} & 3\,{}^{\zeta}x_{\nu_1}^2\\ 1 & {}^{\zeta}x_{\nu_2} & {}^{\zeta}x_{\nu_2}^2 & {}^{\zeta}x_{\nu_2}^3\\ 0 & 1 & 2\,{}^{\zeta}x_{\nu_2} & 3\,{}^{\zeta}x_{\nu_2}^2 \end{bmatrix} \begin{bmatrix} {}^{\zeta}c_0\\ {}^{\zeta}c_1\\ {}^{\zeta}c_2\\ {}^{\zeta}c_3 \end{bmatrix} = \begin{bmatrix} {}^{\zeta}d_0\\ {}^{\zeta}d_1\\ {}^{\zeta}d_2\\ {}^{\zeta}d_3 \end{bmatrix}\,, \tag{3-76} $$

   or,

   $$ {}^{\zeta}\mathbf{T}\,{}^{\zeta}\mathbf{c} = {}^{\zeta}\mathbf{d}\,. \tag{3-77} $$

2. Determination of the transformation matrix ${}^{\zeta}\mathbf{T}_1$ to convert ${}^{\zeta}c_j$ into ${}^{\zeta}\tilde{c}_j$.

   First of all, we need to find four equations in order to solve for ${}^{\zeta}\mathbf{T}_1$. In general, these can be any kind of relationship between both coefficients, as long as they are linear independent. Due to simplicity, we chose the same kind of equations as in (3-75). Based on the nodes of the generalised element in Figure 3-29 and under consideration of (3-72) – (3-74), we obtain

   $$ \begin{aligned} {}^{\zeta}c_0 + {}^{\zeta}c_1\,{}^{\zeta}x_{\nu_1} + {}^{\zeta}c_2\,{}^{\zeta}x_{\nu_1}^2 + {}^{\zeta}c_3\,{}^{\zeta}x_{\nu_1}^3 &= {}^{\zeta}\tilde{c}_0\,,\\ {}^{\zeta}c_1 + 2\,{}^{\zeta}c_2\,{}^{\zeta}x_{\nu_1} + 3\,{}^{\zeta}c_3\,{}^{\zeta}x_{\nu_1}^2 &= \frac{1}{{}^{\zeta}J}\left({}^{\zeta}\tilde{c}_1\right),\\ {}^{\zeta}c_0 + {}^{\zeta}c_1\,{}^{\zeta}x_{\nu_2} + {}^{\zeta}c_2\,{}^{\zeta}x_{\nu_2}^2 + {}^{\zeta}c_3\,{}^{\zeta}x_{\nu_2}^3 &= {}^{\zeta}\tilde{c}_0 + {}^{\zeta}\tilde{c}_1 + {}^{\zeta}\tilde{c}_2 + {}^{\zeta}\tilde{c}_3\,,\\ {}^{\zeta}c_1 + 2\,{}^{\zeta}c_2\,{}^{\zeta}x_{\nu_2} + 3\,{}^{\zeta}c_3\,{}^{\zeta}x_{\nu_2}^2 &= \frac{1}{{}^{\zeta}J}\left({}^{\zeta}\tilde{c}_0 + {}^{\zeta}\tilde{c}_1 + {}^{\zeta}\tilde{c}_2 + {}^{\zeta}\tilde{c}_3\right). \end{aligned} \tag{3-78} $$

   Writing (3-78) in matrix notation yields

   $$ \begin{bmatrix} 1 & {}^{\zeta}x_{\nu_1} & {}^{\zeta}x_{\nu_1}^2 & {}^{\zeta}x_{\nu_1}^3\\ 0 & 1 & 2\,{}^{\zeta}x_{\nu_1} & 3\,{}^{\zeta}x_{\nu_1}^2\\ 1 & {}^{\zeta}x_{\nu_2} & {}^{\zeta}x_{\nu_2}^2 & {}^{\zeta}x_{\nu_2}^3\\ 0 & 1 & 2\,{}^{\zeta}x_{\nu_2} & 3\,{}^{\zeta}x_{\nu_2}^2 \end{bmatrix} \begin{bmatrix} {}^{\zeta}c_0\\ {}^{\zeta}c_1\\ {}^{\zeta}c_2\\ {}^{\zeta}c_3 \end{bmatrix} = \begin{bmatrix} 1 & 0 & 0 & 0\\ 0 & 1/{}^{\zeta}J & 0 & 0\\ 1 & 1 & 1 & 1\\ 0 & 1/{}^{\zeta}J & 2/{}^{\zeta}J & 3/{}^{\zeta}J \end{bmatrix} \begin{bmatrix} {}^{\zeta}\tilde{c}_0\\ {}^{\zeta}\tilde{c}_1\\ {}^{\zeta}\tilde{c}_2\\ {}^{\zeta}\tilde{c}_3 \end{bmatrix} \tag{3-79} $$

and rearranging gives the transformation matrix

$$
{}^{\zeta}\mathbf{T}_1 = \begin{bmatrix} 1 & 0 & 0 & 0 \\ 0 & 1/{}^{\zeta}J & 0 & 0 \\ 1 & 1 & 1 & 1 \\ 0 & 1/{}^{\zeta}J & 2/{}^{\zeta}J & 3/{}^{\zeta}J \end{bmatrix}^{-1} \begin{bmatrix} 1 & {}^{\zeta}x_{\nu_1} & {}^{\zeta}x_{\nu_1}^2 & {}^{\zeta}x_{\nu_1}^3 \\ 0 & 1 & 2\,{}^{\zeta}x_{\nu_1} & 3\,{}^{\zeta}x_{\nu_1}^2 \\ 1 & {}^{\zeta}x_{\nu_2} & {}^{\zeta}x_{\nu_2}^2 & {}^{\zeta}x_{\nu_2}^3 \\ 0 & 1 & 2\,{}^{\zeta}x_{\nu_2} & 3\,{}^{\zeta}x_{\nu_2}^2 \end{bmatrix} . \tag{3-80}
$$

Finally, the transformation matrix reads

$$
{}^{\zeta}\mathbf{T}_1 = \begin{bmatrix} 1 & {}^{\zeta}x_{\nu_1} & {}^{\zeta}x_{\nu_1}^2 & {}^{\zeta}x_{\nu_1}^3 \\ 0 & {}^{\zeta}x_{\nu_2} - {}^{\zeta}x_{\nu_1} & 2\,{}^{\zeta}x_{\nu_1}\left({}^{\zeta}x_{\nu_2} - {}^{\zeta}x_{\nu_1}\right) & 3\,{}^{\zeta}x_{\nu_1}^2\left({}^{\zeta}x_{\nu_2} - {}^{\zeta}x_{\nu_1}\right) \\ 0 & 0 & \left({}^{\zeta}x_{\nu_2} - {}^{\zeta}x_{\nu_1}\right)^2 & 3\,{}^{\zeta}x_{\nu_1}^3\left({}^{\zeta}x_{\nu_2} - {}^{\zeta}x_{\nu_1}\right)^2 \\ 0 & 0 & 0 & \left({}^{\zeta}x_{\nu_2} - {}^{\zeta}x_{\nu_1}\right)^3 \end{bmatrix} , \tag{3-81}
$$

which can be used to convert the coefficients

$$
{}^{\zeta}\mathbf{T}_1\,{}^{\zeta}\mathbf{c} = {}^{\zeta}\tilde{\mathbf{c}} . \tag{3-82}
$$

3. Determination of the transformation matrix ${}^{\zeta}\mathbf{T}_2$ to convert ${}^{\zeta}\tilde{c}_j$ into ${}^{\zeta}\tilde{d}_j$.

The transformation matrix ${}^{\zeta}\mathbf{T}_2$ can be determined in exactly the same way as ${}^{\zeta}\mathbf{T}$, with the only difference that it refers to the generalised element and therefore, only depends on $\tilde{x}$. ${}^{\zeta}\mathbf{T}_2$ is completely independent of x and hence we obtain the following four equations

$$
\begin{aligned}
{}^{\zeta}\tilde{c}_0 &= {}^{\zeta}\tilde{y}_{\nu_1} , \\
{}^{\zeta}\tilde{c}_1 &= {}^{\zeta}\tilde{y}'_{\nu_1} , \\
{}^{\zeta}\tilde{c}_0 + {}^{\zeta}\tilde{c}_1 + {}^{\zeta}\tilde{c}_2 + {}^{\zeta}\tilde{c}_3 &= {}^{\zeta}\tilde{y}_{\nu_2} , \\
{}^{\zeta}\tilde{c}_1 + 2\,{}^{\zeta}\tilde{c}_2 + 3\,{}^{\zeta}\tilde{c}_3 &= {}^{\zeta}\tilde{y}'_{\nu_2} ,
\end{aligned} \tag{3-83}
$$

which can be written in matrix notation as

$$
\begin{bmatrix} 1 & 0 & 0 & 0 \\ 0 & 1 & 0 & 0 \\ 1 & 1 & 1 & 1 \\ 0 & 1 & 2 & 3 \end{bmatrix} \begin{bmatrix} {}^{\zeta}\tilde{c}_0 \\ {}^{\zeta}\tilde{c}_1 \\ {}^{\zeta}\tilde{c}_2 \\ {}^{\zeta}\tilde{c}_3 \end{bmatrix} = \begin{bmatrix} {}^{\zeta}\tilde{d}_0 \\ {}^{\zeta}\tilde{d}_1 \\ {}^{\zeta}\tilde{d}_2 \\ {}^{\zeta}\tilde{d}_3 \end{bmatrix} , \tag{3-84}
$$

or,

$$
{}^{\zeta}\mathbf{T}_2\,{}^{\zeta}\tilde{\mathbf{c}} = {}^{\zeta}\tilde{\mathbf{d}} . \tag{3-85}
$$

4. Determination of the transformation matrix ${}^{\zeta}\mathbf{T}_3$ to convert ${}^{\zeta}\tilde{d}_j$ into ${}^{\zeta}d_j$.

The determination of the last transformation matrix is based on (3-72) and (3-73). The following four relationships between ${}^{\zeta}\tilde{d}_j$ and ${}^{\zeta}d_j$ can be derived

$$
\begin{aligned}
{}^{\zeta}\tilde{y}_{\nu_1} &= {}^{\zeta}y_{\nu_1} , \\
\frac{1}{{}^{\zeta}J}\,{}^{\zeta}\tilde{y}'_{\nu_1} &= {}^{\zeta}y'_{\nu_1} , \\
{}^{\zeta}\tilde{y}_{\nu_2} &= {}^{\zeta}y_{\nu_2} , \\
\frac{1}{{}^{\zeta}J}\,{}^{\zeta}\tilde{y}'_{\nu_2} &= {}^{\zeta}y'_{\nu_2} .
\end{aligned} \tag{3-86}
$$

Writing (3-86) in matrix notation results in

$$\begin{bmatrix} 1 & 0 & 0 & 0 \\ 0 & 1/{}^{\zeta}J & 0 & 0 \\ 0 & 0 & 1 & 0 \\ 0 & 0 & 0 & 1/{}^{\zeta}J \end{bmatrix} \begin{bmatrix} {}^{\zeta}\tilde{d}_0 \\ {}^{\zeta}\tilde{d}_1 \\ {}^{\zeta}\tilde{d}_2 \\ {}^{\zeta}\tilde{d}_3 \end{bmatrix} = \begin{bmatrix} {}^{\zeta}d_0 \\ {}^{\zeta}d_1 \\ {}^{\zeta}d_2 \\ {}^{\zeta}d_3 \end{bmatrix}, \tag{3-87}$$

or equivalently

$${}^{\zeta}\mathbf{T}_3\,{}^{\zeta}\tilde{\mathbf{d}} = {}^{\zeta}\mathbf{d}\,. \tag{3-88}$$

All four transformation matrices are regular and can be used to transform one arbitrary set of coefficients into another one and vice versa. The transformation matrix ${}^{\zeta}\mathbf{T}$ can also be derived by

$${}^{\zeta}\mathbf{T} = {}^{\zeta}\mathbf{T}_3\,{}^{\zeta}\mathbf{T}_2\,{}^{\zeta}\mathbf{T}_1\,. \tag{3-89}$$

Furthermore, these transformation matrices allows us to easily convert the basis functions.

3.2.1.3 *Transformation of the basis functions*

The basic methodology for the transformation of the basis functions can be found in e.g. (Gander 2005).

To determine the new basis function $\psi_j(x)$ we rewrite (3-70) in matrix notation

$${}^{\zeta}P_3(x) = \boldsymbol{\phi}\,{}^{\zeta}\mathbf{c} = \boldsymbol{\psi}\,{}^{\zeta}\mathbf{d} \tag{3-90}$$

with the monomial basis

$$\boldsymbol{\phi} = \begin{bmatrix} 1 & x & x^2 & x^3 \end{bmatrix}. \tag{3-91}$$

Solving (3-77) for ${}^{\zeta}\mathbf{c}$ and inserting in (3-90) yields

$$\boldsymbol{\phi}\,{}^{\zeta}\mathbf{T}^{-1}\,{}^{\zeta}\mathbf{d} = \boldsymbol{\psi}\,{}^{\zeta}\mathbf{d}\,. \tag{3-92}$$

Equating the coefficients of (3-92) yields the new basis

$$\boldsymbol{\psi} = \boldsymbol{\phi}\,{}^{\zeta}\mathbf{T}^{-1}, \tag{3-93}$$

with

$$\begin{aligned} \psi_0 &= \frac{(x - {}^{\zeta}x_{\nu_2})^2 (2x - 3\,{}^{\zeta}x_{\nu_1} + {}^{\zeta}x_{\nu_2})}{({}^{\zeta}x_{\nu_2} - {}^{\zeta}x_{\nu_1})^3}, \\ \psi_1 &= \frac{(x - {}^{\zeta}x_{\nu_1})(x - {}^{\zeta}x_{\nu_2})^2}{({}^{\zeta}x_{\nu_2} - {}^{\zeta}x_{\nu_1})^2}, \\ \psi_2 &= -\frac{(x - {}^{\zeta}x_{\nu_2})^2 (2x + {}^{\zeta}x_{\nu_1} - 3\,{}^{\zeta}x_{\nu_2})}{({}^{\zeta}x_{\nu_2} - {}^{\zeta}x_{\nu_1})^3}, \\ \psi_3 &= \frac{(x - {}^{\zeta}x_{\nu_1})^2 (x - {}^{\zeta}x_{\nu_1})}{({}^{\zeta}x_{\nu_2} - {}^{\zeta}x_{\nu_1})^2}. \end{aligned} \tag{3-94}$$

It is usually quite complicated to derive the new basis functions for the original element, while we need to substitute the generalised coordinate (3-69) in (3-94) and rearrange the equations in a suitable way. As already mentioned, it is

easier to determine $\tilde{\psi}_j(\tilde{x})$ directly on the generalised element. Therefore, we write (3-71) in matrix notation

$$ {}^{\zeta}\tilde{P}_3(\tilde{x}) = \tilde{\boldsymbol{\Phi}}\,{}^{\zeta}\tilde{\mathbf{c}} = \tilde{\boldsymbol{\Psi}}\,{}^{\zeta}\tilde{\mathbf{d}} \tag{3-95} $$

with the generalised monomial basis

$$ \tilde{\boldsymbol{\Phi}} = \begin{bmatrix} 1 & \tilde{x} & \tilde{x}^2 & \tilde{x}^3 \end{bmatrix} . \tag{3-96} $$

Solving (3-85) for ${}^{\zeta}\tilde{\mathbf{c}}$ and inserting in (3-95) yields

$$ \tilde{\boldsymbol{\Phi}}\,{}^{\zeta}\mathbf{T}_2^{-1}\,{}^{\zeta}\tilde{\mathbf{d}} = \tilde{\boldsymbol{\Psi}}\,{}^{\zeta}\tilde{\mathbf{d}} . \tag{3-97} $$

Equating the coefficients of (3-97) directly yields the new basis for the generalised element

$$ \tilde{\boldsymbol{\Psi}} = \tilde{\boldsymbol{\Phi}}\,{}^{\zeta}\mathbf{T}_2^{-1} , \tag{3-98} $$

with

$$ \begin{aligned} \tilde{\psi}_0 &= 2\tilde{x}^3 - 3\tilde{x}^2 + 1 , \\ \tilde{\psi}_1 &= \tilde{x}^3 - 2\tilde{x}^2 + \tilde{x} , \\ \tilde{\psi}_2 &= -2\tilde{x}^3 + 3\tilde{x}^2 , \\ \tilde{\psi}_3 &= \tilde{x}^3 - \tilde{x}^2 . \end{aligned} \tag{3-99} $$

The derived basis functions (3-99) are known as Hermite basis functions and they are defining the basis of a cubic Hermite spline. The basis functions (3-99) can be converted into (3-94) according to

$$ \boldsymbol{\Psi} = \tilde{\boldsymbol{\Psi}}\,{}^{\zeta}\mathbf{T}_3^{-1} , \tag{3-100} $$

The Hermite basis functions are depicted in Figure 3-32.

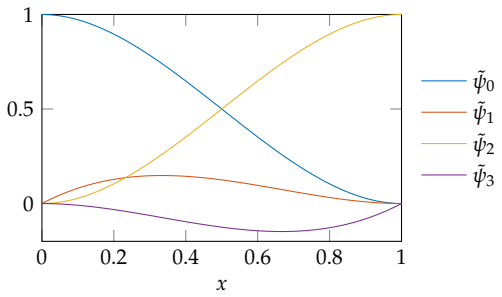

Figure 3-32: Cubic Hermite basis functions

As we have seen in the previous section, an elementwise continuous linear approximation in the derived alternative basis outperformes the one in the monomial basis, in both, computational speed and numerical stability. Therefore, we will also have a closer look at the four Hermite basis functions depicted in Figure 3-32. The angle $\alpha_{i,j}$ between these basis functions has been calculated according to (3-11) and is listed in the Table 3-4.

	$\tilde{\psi}_0$	$\tilde{\psi}_1$	$\tilde{\psi}_2$	$\tilde{\psi}_3$
$\tilde{\psi}_0$	0	31.4	77.5	134.8
$\tilde{\psi}_1$		0	65.2	153.0
$\tilde{\psi}_2$			0	168.6

Table 3-4: Angle $\alpha_{i,j}$ in [gon] between the four Hermite basis vectors (3-99). Due to symmetry only the upper triangular part is presented.

Table 3-4 shows, that the Hermite basis is not an orthogonal one and hence, is not optimal. The angle between $\tilde{\psi}_0$ and $\tilde{\psi}_1$ is only 31.4 gon and 168.64 gon

between $\tilde{\psi}_2$ and $\tilde{\psi}_3$. In both cases, the vectors are tending to show in the same/or opposite direction. Furthermore, the Hermite basis functions are also of different lengths, which are

$$\begin{aligned} \|\tilde{\psi}_0\|_2 &= \|\tilde{\psi}_2\|_2 = 0.6094\,, \\ \|\tilde{\psi}_1\|_2 &= \|\tilde{\psi}_3\|_2 = 0.0976. \end{aligned} \tag{3-101}$$

As already mentioned, for the numerical computation of the unknown coefficients of an approximation, the angle between the basis functions and their length ratios are playing an important role. In contrast to monomial basis, the aforementioned geometric properties of the Hermite basis do not depend on the position of an element. It can therefore be assumed that the computation of the unknown coefficients in the Hermite basis yields numerically more accurate results than using monomials.

In general, it has been shown that it is easier to derive a new set of basis functions on the generalised element directly. The coefficients can always be converted into a different basis as depicted in Figure 3-31. An approximation in the Hermite basis and how to easily solve the integrals for the normal matrix will be shown in following section.

3.2.2 *Elementwise approximation in the Hermite basis*

The Hermite basis should not be confused with Hermite polynomials. It refers to a cubic Hermite spline.

In the previous section, we derived an alternative basis for an elementwise cubic approximation, which is C^1 continuous. To illustrate an approximation in the cubic Hermite basis, we approximate function (3-2) by dividing the whole domain into $N = 3$ equispaced elements. Based on the definition of nodes and elements in Table 3-2 and the four basis functions (3-94), we can set-up the normal equation system for each element

$$\begin{bmatrix} {}^{\zeta}\langle\psi_0,\psi_0\rangle & {}^{\zeta}\langle\psi_1,\psi_0\rangle & {}^{\zeta}\langle\psi_2,\psi_0\rangle & {}^{\zeta}\langle\psi_3,\psi_0\rangle \\ {}^{\zeta}\langle\psi_0,\psi_1\rangle & {}^{\zeta}\langle\psi_1,\psi_1\rangle & {}^{\zeta}\langle\psi_2,\psi_1\rangle & {}^{\zeta}\langle\psi_3,\psi_1\rangle \\ {}^{\zeta}\langle\psi_0,\psi_2\rangle & {}^{\zeta}\langle\psi_1,\psi_2\rangle & {}^{\zeta}\langle\psi_2,\psi_2\rangle & {}^{\zeta}\langle\psi_3,\psi_2\rangle \\ {}^{\zeta}\langle\psi_0,\psi_3\rangle & {}^{\zeta}\langle\psi_1,\psi_3\rangle & {}^{\zeta}\langle\psi_2,\psi_3\rangle & {}^{\zeta}\langle\psi_3,\psi_3\rangle \end{bmatrix} \begin{bmatrix} {}^{\zeta}d_0 \\ {}^{\zeta}d_1 \\ {}^{\zeta}d_2 \\ {}^{\zeta}d_3 \end{bmatrix} = \begin{bmatrix} {}^{\zeta}\langle\psi_0,\sin(3x)\rangle \\ {}^{\zeta}\langle\psi_1,\sin(3x)\rangle \\ {}^{\zeta}\langle\psi_2,\sin(3x)\rangle \\ {}^{\zeta}\langle\psi_3,\sin(3x)\rangle \end{bmatrix} \tag{3-102}$$

for $\zeta = 1,2,3$. To solve the integrals based on the generalised element, we introduce

$$\boldsymbol{\psi} = \begin{bmatrix} \psi_0(x) & \psi_1(x) & \psi_2(x) & \psi_3(x) \end{bmatrix} \tag{3-103}$$

and rewrite the normal matrix of an element (3-102) as

$${}^{\zeta}\mathbf{N} = {}^{\zeta}\langle\boldsymbol{\psi}^{\mathsf{T}},\boldsymbol{\psi}\rangle = \int_{{}^{\zeta}x_{v_1}}^{{}^{\zeta}x_{v_2}} \boldsymbol{\psi}^{\mathsf{T}}\,\boldsymbol{\psi}\,\mathrm{d}x\,. \tag{3-104}$$

Inserting (3-45) and (3-100) into (3-104) and adopting the limits of the integral yields

$${}^{\zeta}\mathbf{N} = {}^{\zeta}\langle\boldsymbol{\psi}^{\mathsf{T}},\boldsymbol{\psi}\rangle = {}^{\zeta}J \int_0^1 {}^{\zeta}\mathbf{T}_3^{-\mathsf{T}}\,\tilde{\boldsymbol{\psi}}^{\mathsf{T}}\,\tilde{\boldsymbol{\psi}}\,{}^{\zeta}\mathbf{T}_3^{-1}\,\mathrm{d}\tilde{x}\,, \tag{3-105}$$

with

$$ {}^{\zeta}\mathbf{T}_3^{-\mathsf{T}} = \begin{bmatrix} 1 & 0 & 0 & 0 \\ 0 & 1/{}^{\zeta}J & 0 & 0 \\ 0 & 0 & 1 & 0 \\ 0 & 0 & 0 & 1/{}^{\zeta}J \end{bmatrix} \tag{3-106} $$

and ${}^{\zeta}J = {}^{\zeta}x_{\nu_2} - {}^{\zeta}x_{\nu_1}$. While ${}^{\zeta}\mathbf{T}_3^{-\mathsf{T}}$ only contains constant values, we can extract it from the integral and the normal matrix reads

$$ {}^{\zeta}\mathbf{N} = {}^{\zeta}\langle \boldsymbol{\psi}^{\mathsf{T}}, \boldsymbol{\psi} \rangle = {}^{\zeta}J \, {}^{\zeta}\mathbf{T}_3^{-\mathsf{T}} \int_0^1 \tilde{\boldsymbol{\psi}}^{\mathsf{T}} \, \tilde{\boldsymbol{\psi}} \, \mathrm{d}\tilde{x} \, {}^{\zeta}\mathbf{T}_3^{-1} \, . \tag{3-107} $$

Introducing

$$ \mathbf{N}_{\text{element}} = \int_0^1 \tilde{\boldsymbol{\psi}}^{\mathsf{T}} \, \tilde{\boldsymbol{\psi}} \, \mathrm{d}\tilde{x} \, , \tag{3-108} $$

with

$$ \mathbf{N}_{\text{element}} = \begin{bmatrix} \langle \tilde{\psi}_0, \tilde{\psi}_0 \rangle & \langle \tilde{\psi}_1, \tilde{\psi}_0 \rangle & \langle \tilde{\psi}_2, \tilde{\psi}_0 \rangle & \langle \tilde{\psi}_3, \tilde{\psi}_0 \rangle \\ \langle \tilde{\psi}_0, \tilde{\psi}_1 \rangle & \langle \tilde{\psi}_1, \tilde{\psi}_1 \rangle & \langle \tilde{\psi}_2, \tilde{\psi}_1 \rangle & \langle \tilde{\psi}_3, \tilde{\psi}_1 \rangle \\ \langle \tilde{\psi}_0, \tilde{\psi}_2 \rangle & \langle \tilde{\psi}_1, \tilde{\psi}_2 \rangle & \langle \tilde{\psi}_2, \tilde{\psi}_2 \rangle & \langle \tilde{\psi}_3, \tilde{\psi}_2 \rangle \\ \langle \tilde{\psi}_0, \tilde{\psi}_3 \rangle & \langle \tilde{\psi}_1, \tilde{\psi}_3 \rangle & \langle \tilde{\psi}_2, \tilde{\psi}_3 \rangle & \langle \tilde{\psi}_3, \tilde{\psi}_3 \rangle \end{bmatrix} . \tag{3-109} $$

Solving the integrals in (3-109) with the Hermite basis functions (3-99) yields the normal matrix for the generalised element

$$ \mathbf{N}_{\text{element}} = \begin{bmatrix} 13/35 & 11/210 & 9/70 & -13/420 \\ 11/210 & 1/105 & 13/420 & -1/140 \\ 9/70 & 13/420 & 13/35 & -11/210 \\ -13/420 & -1/140 & -11/210 & 1/105 \end{bmatrix} . \tag{3-110} $$

Inserting $\mathbf{N}_{\text{element}}$ into (3-107) yields the normal matrix for each element

$$ {}^{\zeta}\mathbf{N} = {}^{\zeta}\langle \boldsymbol{\psi}^{\mathsf{T}}, \boldsymbol{\psi} \rangle = {}^{\zeta}J \, {}^{\zeta}\mathbf{T}_3^{-\mathsf{T}} \, \mathbf{N}_{\text{element}} \, {}^{\zeta}\mathbf{T}_3^{-1} \, . \tag{3-111} $$

In the same way we can solve the integrals for the right hand side

$$ {}^{\zeta}\mathbf{n} = {}^{\zeta}\langle \boldsymbol{\psi}^{\mathsf{T}}, f \rangle = \int_{{}^{\zeta}x_1}^{{}^{\zeta}x_2} \boldsymbol{\psi}^{\mathsf{T}} \, f(x) \, \mathrm{d}x \, . \tag{3-112} $$

Inserting (3-45) and (3-100) into (3-112) and adopting the limits of the integral yields

$$ {}^{\zeta}\mathbf{n} = {}^{\zeta}\langle \boldsymbol{\psi}^{\mathsf{T}}, f \rangle = {}^{\zeta}J \int_0^1 {}^{\zeta}\mathbf{T}_3^{-T} \tilde{\boldsymbol{\psi}}^{\mathsf{T}} \, f(x) \, \mathrm{d}\tilde{x} \, . \tag{3-113} $$

After rearranging (3-113) the right hand side can be expressed by

$$ {}^{\zeta}\mathbf{n} = {}^{\zeta}\langle \boldsymbol{\psi}^{\mathsf{T}}, f \rangle = {}^{\zeta}J {}^{\zeta}\mathbf{T}_3^{-T} \int_0^1 \tilde{\boldsymbol{\psi}}^{\mathsf{T}} \, f\big({}^{\zeta}x_1 + ({}^{\zeta}x_2 - {}^{\zeta}x_1)\tilde{x}\big) \, \mathrm{d}\tilde{x} \, . \tag{3-114} $$

The cubic approximation of (3-102) with 3 elements yields the following three normal equation systems

$$\begin{bmatrix} 26/105 & 22/945 & 3/35 & -13/945 \\ 22/945 & 8/2835 & 13/945 & -2/945 \\ 3/35 & 13/945 & 26/105 & -22/945 \\ -13/945 & -2/945 & -22/945 & 8/2835 \end{bmatrix} \begin{bmatrix} {}^1y_0 \\ {}^1y'_0 \\ {}^1y_1 \\ {}^1y'_1 \end{bmatrix} = \begin{bmatrix} -0.204\,667\,105\,858\,953 \\ -0.027\,559\,579\,350\,093 \\ -0.305\,431\,161\,630\,575 \\ 0.033\,296\,399\,494\,442 \end{bmatrix},$$

$$\begin{bmatrix} 26/105 & 22/945 & 3/35 & -13/945 \\ 22/945 & 8/2835 & 13/945 & -2/945 \\ 3/35 & 13/945 & 26/105 & -22/945 \\ -13/945 & -2/945 & -22/945 & 8/2835 \end{bmatrix} \begin{bmatrix} {}^2y_0 \\ {}^2y'_0 \\ {}^2y_1 \\ {}^2y'_1 \end{bmatrix} = \begin{bmatrix} -0.121\,067\,910\,317\,044 \\ -0.006\,892\,783\,556\,819 \\ 0.121\,067\,910\,317\,043 \\ -0.006\,892\,783\,556\,819 \end{bmatrix},$$

$$\begin{bmatrix} 26/105 & 22/945 & 3/35 & -13/945 \\ 22/945 & 8/2835 & 13/945 & -2/945 \\ 3/35 & 13/945 & 26/105 & -22/945 \\ -13/945 & -2/945 & -22/945 & 8/2835 \end{bmatrix} \begin{bmatrix} {}^3y_0 \\ {}^3y'_0 \\ {}^3y_1 \\ {}^3y'_1 \end{bmatrix} = \begin{bmatrix} 0.305\,431\,161\,630\,575 \\ 0.033\,296\,399\,494\,442 \\ 0.204\,667\,105\,858\,953 \\ -0.027\,559\,579\,350\,093 \end{bmatrix}. \tag{3-115}$$

The three normal matrices in (3-115) are equal, while we introduced equispaced elements, thus, ${}^\zeta J$ and also ${}^\zeta \mathbf{T}_3$ are equal for all elements. Based on Table 3-2 two elements share the same node, namely

$${}^1x_{\nu_2} = {}^2x_{\nu_1} = x_2 \tag{3-116}$$

and

$${}^2x_{\nu_2} = {}^3x_{\nu_1} = x_3\,. \tag{3-117}$$

Substituting ${}^\zeta y_i$ and ${}^\zeta y'_i$ in (3-115) by the unique identifier for the nodes, the normal equation system (3-115) reads

$$\begin{bmatrix} 26/105 & 22/945 & 3/35 & -13/945 \\ 22/945 & 8/2835 & 13/945 & -2/945 \\ 3/35 & 13/945 & 26/105 & -22/945 \\ -13/945 & -2/945 & -22/945 & 8/2835 \end{bmatrix} \begin{bmatrix} y_1 \\ y'_1 \\ y_2 \\ y'_2 \end{bmatrix} = \begin{bmatrix} -0.204\,667\,105\,858\,953 \\ -0.027\,559\,579\,350\,093 \\ -0.305\,431\,161\,630\,575 \\ 0.033\,296\,399\,494\,442 \end{bmatrix},$$

$$\begin{bmatrix} 26/105 & 22/945 & 3/35 & -13/945 \\ 22/945 & 8/2835 & 13/945 & -2/945 \\ 3/35 & 13/945 & 26/105 & -22/945 \\ -13/945 & -2/945 & -22/945 & 8/2835 \end{bmatrix} \begin{bmatrix} y_2 \\ y'_2 \\ y_3 \\ y'_3 \end{bmatrix} = \begin{bmatrix} -0.121\,067\,910\,317\,044 \\ -0.006\,892\,783\,556\,819 \\ 0.121\,067\,910\,317\,043 \\ -0.006\,892\,783\,556\,819 \end{bmatrix},$$

$$\begin{bmatrix} 26/105 & 22/945 & 3/35 & -13/945 \\ 22/945 & 8/2835 & 13/945 & -2/945 \\ 3/35 & 13/945 & 26/105 & -22/945 \\ -13/945 & -2/945 & -22/945 & 8/2835 \end{bmatrix} \begin{bmatrix} y_3 \\ y'_3 \\ y_4 \\ y'_4 \end{bmatrix} = \begin{bmatrix} 0.305\,431\,161\,630\,575 \\ 0.033\,296\,399\,494\,442 \\ 0.204\,667\,105\,858\,953 \\ -0.027\,559\,579\,350\,093 \end{bmatrix}. \tag{3-118}$$

To solve for the unknown parameters, the three normal equation systems need to be combined as follows

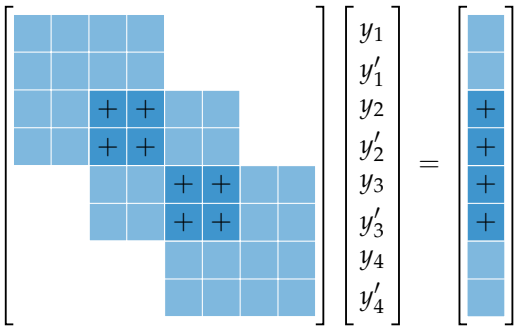

$$= \begin{bmatrix} \\ \\ + \\ + \\ + \\ + \\ \\ \end{bmatrix}. \tag{3-119}$$

Solving the combined equation system

$$\mathbf{N}\,\mathbf{x} = \mathbf{n}\,, \tag{3-120}$$

with

$$\mathbf{N} = \begin{bmatrix} 26/105 & 22/945 & 3/35 & -13/945 & 0 & 0 & 0 & 0 \\ 22/945 & 8/2835 & 13/945 & -2/945 & 0 & 0 & 0 & 0 \\ 3/35 & 13/945 & 52/105 & 0 & 3/35 & -13/945 & 0 & 0 \\ -13/945 & -2/945 & 0 & 16/2835 & 13/945 & -2/945 & 0 & 0 \\ 0 & 0 & 3/35 & 13/945 & 52/105 & 0 & 3/35 & -13/945 \\ 0 & 0 & -13/945 & -2/945 & 0 & 16/2835 & 13/945 & -2/945 \\ 0 & 0 & 0 & 0 & 3/35 & 13/945 & 26/105 & -22/945 \\ 0 & 0 & 0 & 0 & -13/945 & -2/945 & -22/945 & 8/2835 \end{bmatrix} \tag{3-121}$$

and

$$\mathbf{n} = \begin{bmatrix} -0.204\,667\,105\,858\,953 \\ -0.027\,559\,579\,350\,093 \\ -0.426\,499\,071\,947\,619 \\ 0.026\,403\,615\,937\,623 \\ 0.426\,499\,071\,947\,618 \\ 0.026\,403\,615\,937\,623 \\ 0.204\,667\,105\,858\,953 \\ -0.027\,559\,579\,350\,093 \end{bmatrix} \tag{3-122}$$

yields the solution for the unknown parameters

$$\begin{bmatrix} y_1 \\ y_1' \\ y_2 \\ y_2' \\ y_3 \\ y_3' \\ y_4 \\ y_4' \end{bmatrix} = \begin{bmatrix} -0.127\,892\,892\,631\,587 \\ -3.310\,672\,567\,507\,778 \\ -0.846\,388\,475\,928\,077 \\ 1.699\,324\,240\,428\,790 \\ 0.846\,388\,475\,928\,077 \\ 1.699\,324\,240\,428\,787 \\ 0.127\,892\,892\,631\,591 \\ -3.310\,672\,567\,507\,737 \end{bmatrix}. \tag{3-123}$$

The resulting cubic approximation of (3-2) in the Hermite basis is depicted in Figure 3-33.

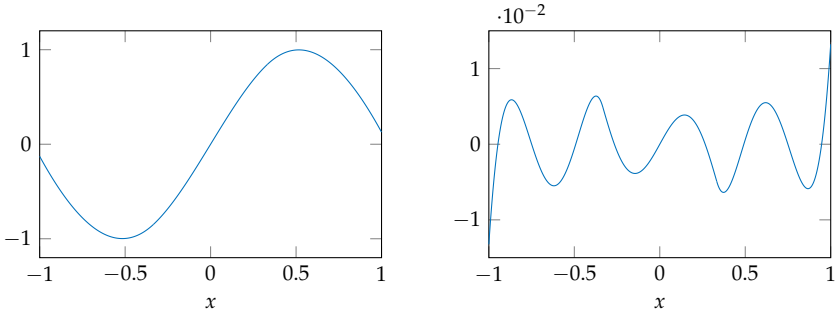

Figure 3-33: Cubic approximation of (3-2) with 3 elements using Hermite basis functions (3-99) (left). Residual function $v(x) = \sin(3x) - \sum_{\zeta=1}^{3} {}^{\zeta}P_3(x)$ (right).

Figure 3-20 (left) shows a very smooth and already quite good approximation of (3-2) while only 3 elements are used. The residual function in Figure 3-20 (right) is within the range of 10^{-2}. Figure 3-34 shows that the cubic approximation in the Hermite basis is also continuous in its first derivative. But of course reveals a kink at the inner nodes $x_2 = -1/3$ and $x_3 = 1/3$, as indicated by a yellow circle in the residual plot in Figure 3-34 (right).

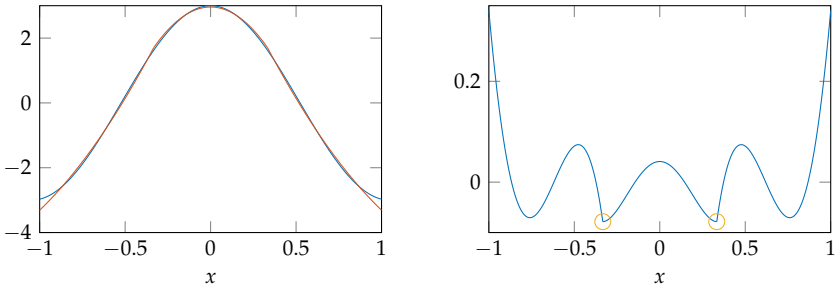

Figure 3-34: First derivative of the given function $f(x) = \sin(3x)$ in blue and its approximation with 3 elements using Hermite basis functions (3-99) in red (left). Residual function $v(x) = \frac{\mathrm{d}\sin(3x)}{\mathrm{d}x} - \sum_{\zeta=1}^{3} \frac{\mathrm{d}^{\zeta}P_3(x)}{\mathrm{d}x}$ (right).

All calculations of a cubic approximation in the Hermite basis have been done with the MATLAB code in Programme 3-5.

Programme 3-5: Code for an elementwise cubic polynomial approximation in the Hermite basis (3-99).

```
%Given function
f=@(x) sin(3*x);

%Approximation of f(x) on [-1, 1]
a=-1; b=1;

%number of elements
elements=3;

%Position of the equispaced nodes
nodes=linspace(a,b,elements+1);

%Initilisation of the matrices
N=zeros(2*(elements+1)); n=zeros(2*(elements+1),1);
n_element=zeros(4,1);

%Hermite basis functions
phi{1}=@(x)  2*x.^3 - 3*x.^2 + 1;
phi{2}=@(x)    x.^3 - 2*x.^2 + x;
phi{3}=@(x) -2*x.^3 + 3*x.^2;
phi{4}=@(x)    x.^3 -   x.^2;

%Normal matrix of the generalised Element
N_element=[13/35 11/210 9/70 -13/420; 11/210 1/105 13/420
    -1/140;
       9/70 13/420 13/35 -11/210;-13/420 -1/140 -11/210
           1/105];

for k=1:elements
    J=nodes(k+1)-nodes(k); T_3=diag([1 J 1 J]);
    %Index for the normal matrix
    from=2*k-1; to=2*(k+1);
    N(from:to,from:to)=N(from:to,from:to)+J.*T_3'*N_element
        *T_3;
    %right hand side
    for l=1:4
        n_element(l)=integral(@(x) f(J*x+nodes(k)).*phi{l}(
            x),0,1);
    end
    n(from:to)=n(from:to)+J*T_3'*n_element;
end
c=N\n;
```

When deriving the Hermite basis, we have recognized that it is not orthogonal and therefore not an optimal basis. Consequently, we determine the condition number of the related normal matrix for increasing N, which is depicted Figure 3-35.

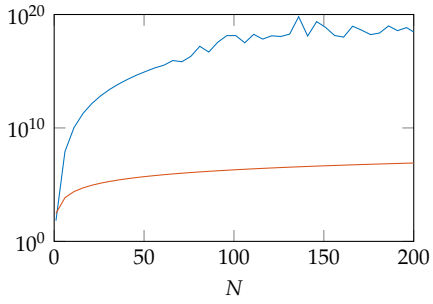

Figure 3-35: Logarithmic plot of the condition number of the normal matrix of an elementwise continuous cubic approximation in the monomial basis (blue) and in the Hermite basis (red) for increasing number of elements N.

The red curve in Figure 3-35 represents the condition number of the normal matrix for a cubic approximation in the Hermite basis. The blue curve represents the condition number of the normal matrix for an equivalent cubic approximation in the monomial basis. In the previous chapter we noticed that the Hermite basis is not optimal, while we addressed the angles between the basis functions and their length. This is also reflected by the condition number for the normal matrix, while it is already $\approx 10^7$ for 200 elements. However, this is significantly smaller than the condition number of the normal matrix for the same approximation in the monomial basis, which is already $\approx 10^{17}$ for only 100 elements.

That an approximation in the Hermite basis is numerically more stable than in the monomial basis can also be seen in the approximation of function (3-6) using 10 000 elements, which is depicted in Figure 3-36.

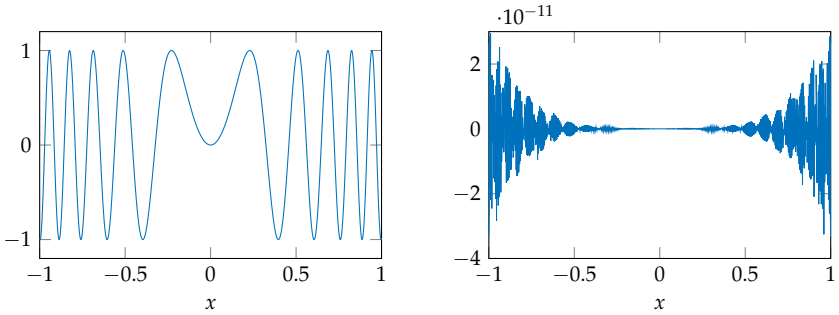

Figure 3-36: Cubic approximation of (3-6) with 10 000 elements using Hermite basis functions (left). Residual function $v(x) = \sin(30x^2) - \sum_{\zeta=1}^{10\,000} \zeta P_3(x)$ (right).

Figure 3-36 (left) shows a smooth and very good approximation of (3-6). The residual function indicates deviations in a range of $\approx 10^{-11}$. In the same way function (3-8) can be approximated by 10 000 elements, as it is illustrated in Figure 3-37.

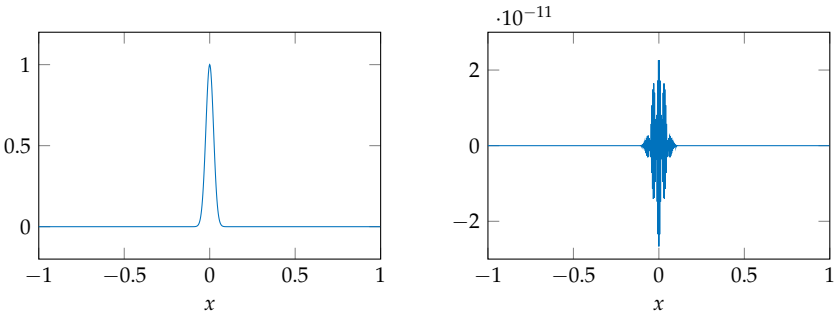

Figure 3-37: Cubic approximation of (3-8) with 10 000 elements using Hermite basis functions (left). Residual function $v(x) = \exp(-1000x^2) - \sum_{\zeta=1}^{10\,000} \zeta P_3(x)$ (right).

Off site the peak, the residual function in Figure 3-37 (right) is zero within machine precision and only reveals deviations of $\approx 10^{-11}$ around the peak at

$x = 0$. Numerical effects, as presented for the cubic approximation in the monomial basis with only ≈ 300 elements as depicted in Figure 3-23 or Figure 3-24, are not apparent so far. A further increase up to 15 000 elements only reduces the residual function by a factor of 2, while using 20 000 elements the residual function starts to increase again and get worse. The condition number of the normal matrix for 20 000 elements is already $\approx 10^{11}$. The computational effort for an improvement of the approximation is huge. To emphasize once again, both approximations in Figure 3-36 and Figure 3-37 are functions of 20 002 parameters.

3.3 APPROXIMATION USING ORTHOGONAL BASIS FUNCTIONS

As shown before, polynomial approximation in the monomial basis is an ill-posed problem and has hardly any relevance for practical applications. In many engineering sciences, an elementwise approximation with polynomials of low degree is used for various tasks, whereby the choice of a suitable basis is decisive. In this way, depending on the task at hand, approximations can be achieved that are sufficiently accurate for most applications, as demonstrated in Section 3.2.2. However, depending on the selected basis, the accuracy of the approximation can usually not be increased arbitrarily and also the number of required parameters increases very quickly. Therefore, we also will discuss a further approach for the approximation of functions.

Having a closer look on especially the angle between the basis functions allows a simple geometrical interpretation of the aforementioned ill-conditioned problem and gives the motivation to use another set of basis functions, which are orthogonal. In the broad literature one will find a variety of orthogonal polynomials, such as

- Chebyshev polynomial of the first kind,
- Chebyshev polynomial of the second kind,
- Gegenbauer polynomial,
- Hermite polynomial,
- Jacobi polynomial,
- Laguerre polynomial and
- Legendre polynomial,

just to name a few important ones. But in approximation theory in general *one will encounter two closely related sets of orthogonal basis functions associated with the names of Chebyshev and Fourier*, slightly rephrasing (TREFETHEN 2013, p. 12). Reason enough to introduce Chebyshev polynomials of the first kind and Fourier series as a basis for the approximation of functions and whenever we use the expression "Chebyshev polynomial" we refer exclusively to the Chebyshev polynomial of the first kind $T_j(x)$.

3.3.1 *Approximation in the Chebyshev basis*

The Chebyshev polynomial $T_j(x)$ of degree $j \geq 0$ is defined by

$$T_j(x) = \cos(j \arccos(x)) \qquad \text{for } x \in [-1, 1]. \tag{3-124}$$

A comprehensive overview on Chebyshev polynomials can be found in MASON and HANDSCOMB (2003) and RIVLIN (1974).

These polynomials satisfy the three term recurrence relation

$$T_j(x) = 2xT_{j-1}(x) - T_{j-2}(x) \qquad \text{for } j \geq 2 \tag{3-125}$$

with the initial conditions

$$T_0(x) = 1 \qquad \text{and} \qquad T_1(x) = x. \tag{3-126}$$

The Chebyshev polynomials are orthogonal with respect to a weighted inner product

$$\langle T_i, T_j \rangle = \int_{-1}^{1} \frac{T_i(x)\, T_j(x)}{\sqrt{1-x^2}}\, \mathrm{d}x = \begin{cases} \pi, & i = j = 0, \\ \pi/2, & i = j \geq 1, \\ 0, & i \neq j. \end{cases} \tag{3-127}$$

The first 11 Chebyshev polynomials are depicted in Figure 3-38.

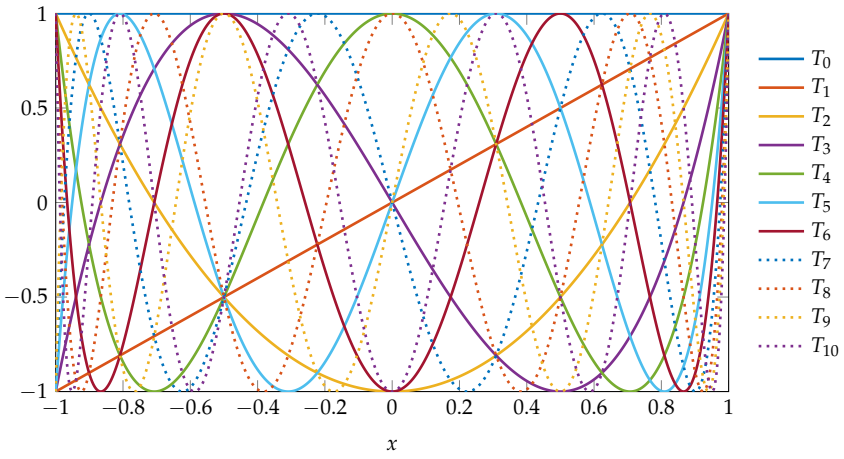

Figure 3-38: Basis functions $T_j(x)$ for $j = 0, \cdots, 10$.

In direct comparison to the first 11 monomials depicted in Figure 3-8, the Chebyshev polynomials in Figure 3-38 can easily be distinguished.

As for the monomial basis, we will first approximate function (3-2) on the interval $x \in [-1, 1]$ by a polynomial of 3^{rd} degree. According to (1-45), the least squares approximation in the Chebyshev basis of (3-2) yields the following normal equation system

$$\begin{bmatrix} \langle T_0, T_0 \rangle & \langle T_1, T_0 \rangle & \langle T_2, T_0 \rangle & \langle T_3, T_0 \rangle \\ \langle T_0, T_1 \rangle & \langle T_1, T_1 \rangle & \langle T_2, T_1 \rangle & \langle T_3, T_1 \rangle \\ \langle T_0, T_2 \rangle & \langle T_1, T_2 \rangle & \langle T_2, T_2 \rangle & \langle T_3, T_2 \rangle \\ \langle T_0, T_3 \rangle & \langle T_1, T_3 \rangle & \langle T_2, T_3 \rangle & \langle T_3, T_3 \rangle \end{bmatrix} \begin{bmatrix} c_0 \\ c_1 \\ c_2 \\ c_3 \end{bmatrix} = \begin{bmatrix} \langle T_0, \sin(3x) \rangle \\ \langle T_1, \sin(3x) \rangle \\ \langle T_2, \sin(3x) \rangle \\ \langle T_3, \sin(3x) \rangle \end{bmatrix} \tag{3-128}$$

and while choosing orthogonal basis functions, the normal equation system simplifies to

$$\begin{bmatrix} \langle T_0, T_0 \rangle & 0 & 0 & 0 \\ 0 & \langle T_1, T_1 \rangle & 0 & 0 \\ 0 & 0 & \langle T_2, T_2 \rangle & 0 \\ 0 & 0 & 0 & \langle T_3, T_3 \rangle \end{bmatrix} \begin{bmatrix} c_0 \\ c_1 \\ c_2 \\ c_3 \end{bmatrix} = \begin{bmatrix} \langle T_0, \sin(3x) \rangle \\ \langle T_1, \sin(3x) \rangle \\ \langle T_2, \sin(3x) \rangle \\ \langle T_3, \sin(3x) \rangle \end{bmatrix}. \tag{3-129}$$

Thus, the normal matrix $\mathbf{N}$ is diagonal and the unknown coefficients can directly be determined by

$$c_j = \frac{\langle T_j, \sin(3x) \rangle}{\langle T_j, T_j \rangle} \tag{3-130}$$

with

$$\langle T_j, \sin(3x)\rangle = \int_{-1}^{1} \frac{T_j \sin(3x)}{\sqrt{1-x^2}}\,\mathrm{d}x \quad \text{for } j = 0,1,2,3. \tag{3-131}$$

The coefficients for a polynomial approximation in the Chebyshev basis of 3rd degree are

$$\begin{bmatrix} c_0 \\ c_1 \\ c_2 \\ c_3 \end{bmatrix} = \begin{bmatrix} 0.000\,000\,000\,000\,000 \\ 0.678\,117\,917\,051\,832 \\ 0.000\,000\,000\,000\,000 \\ -0.618\,125\,444\,510\,544 \end{bmatrix}. \tag{3-132}$$

Due to the symmetry of (3-2) the even coefficients are zero. The resulting approximation and the residual function are depicted in Figure 3-39.

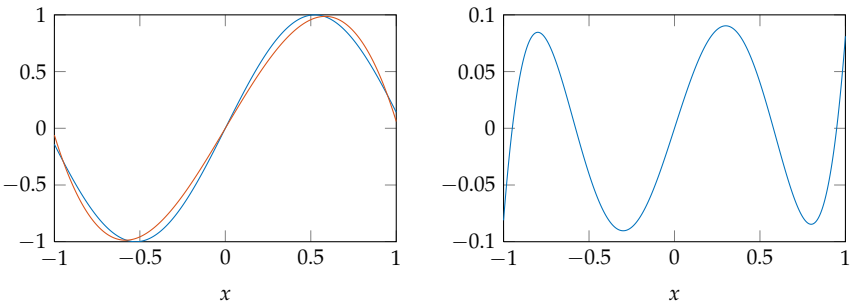

Figure 3-39: Given function (3-2) in blue and it's polynomial approximation in the Chebyshev basis $P_3(x)$ in red (left). Residual function $v(x) = \sin(3x) - P_3(x)$ (right).

The polynomial approximation in the Chebyshev basis in Figure 3-39 (left) is very similar to the one in the monomial basis depicted in Figure 3-1 (left), but they are not equal. The residual function in Figure 3-39 (right) shows deviations smaller than ±0.1.

The least squares approximation in the Chebyshev basis is a near-minimax or near-L_∞ approximation, see Mason and Handscomb (2003, Chapter 5.5).

The Matlab code for the presented polynomial approximation in the Chebyshev basis is given in Programme 3-6.

Programme 3-6: Code for polynomial approximation in the Chebyshev basis.

```
%Approximation of f(x) on [-1, 1]
a=-1; b=1;

%degree of approximation
p=3;

%Initialization of the matrices
c=zeros(p+1,1);

%First coefficient
c(1)=1/pi*integral(@(x) sin(3*x)./sqrt(1-x.^2),a,b);

%Remaining coefficients
for i=1:p
 c(i+1)=2/pi*integral(@(x) sin(3*x).*cos(i*acos(x))./sqrt
     (1-x.^2),a,b);
end
```

Like in the previous sections, we want to know which polynomial degree is needed to approximate (3-2) within roughly machine precision. Therefore, we iteratively determine the coefficients up to c_{50} and calculate the maximum

absolute difference between function (3-2) and it's approximation. The result is depicted in Figure 3-40.

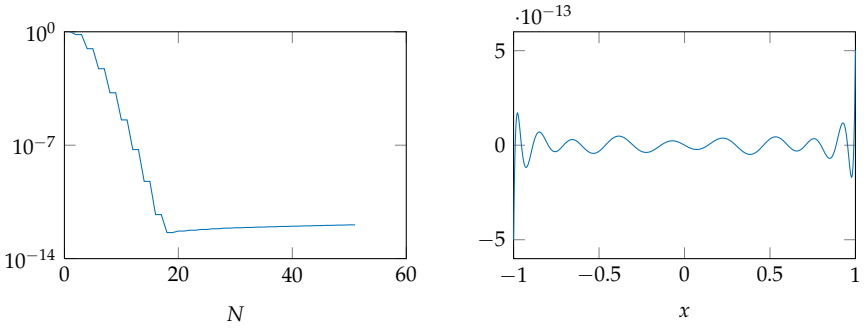

Figure 3-40: Logarithmic plot of $\max|\sin(3x) - P_N(x)|$ for different polynomial degree (left). Residual function $v(x) = \sin(3x) - P_{19}(x)$ for the best fitting polynomial (right).

The residual function for the best fitting polynomial $P_{19}(x)$ in Figure 3-40 (right) shows an oscillatory behaviour with an amplitude of about 10^{-13} and is not within machine precision. Increasing the polynomial degree will not improve the approximation and reduce the residual function. The reason why it is not possible to approximate (3-2) within machine precision is due to the numerical integration of the right hand side (3-131), while the last two or three digits are wrong. These inaccuracies are leading to the presented residual function and can be avoided while using the following analytic solution for the integrals of the right hand side of (3-131)

For all examples presented here, the analytical solutions have been derived using (WOLFRAM RESEARCH, INC. 2021).

$$\langle \sin(3x), T_j \rangle = \begin{cases} (-1)^{j-1/2}\,\pi\, J_j(3), & \text{if } j \text{ is odd,} \\ 0, & \text{if } j \text{ is even,} \end{cases} \tag{3-133}$$

with $J_j(x)$ being the BESSEL function of the first kind. As a result we found a polynomial of 21^{st} degree which approximates (3-2) within machine precision. The residual function is depicted in Figure 3-41 and reveals deviations smaller than $\pm 10^{-15}$.

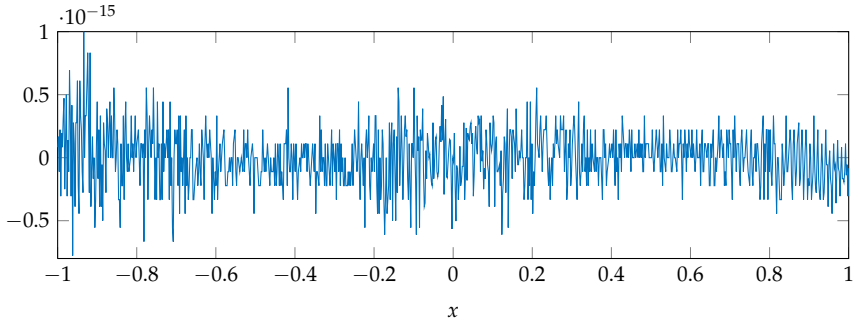

Figure 3-41: Residual function $v(x) = \sin(3x) - P_{21}(x)$ for the best fitting polynomial using the analytic solution (3-133) for the integrals of the right hand side.

The non zero coefficients of $P_{21}(x)$ are

$$\begin{bmatrix} c_1 \\ c_3 \\ c_5 \\ c_7 \\ c_9 \\ c_{11} \\ c_{13} \\ c_{15} \\ c_{17} \\ c_{19} \\ c_{21} \end{bmatrix} = \begin{bmatrix} 0.678\,117\,917\,051\,873\,0 \\ -0.618\,125\,444\,510\,503\,2 \\ 0.086\,056\,869\,754\,095\,2 \\ -0.005\,094\,588\,903\,609\,4 \\ 0.000\,168\,790\,042\,618\,2 \\ -0.000\,003\,587\,979\,324\,7 \\ 0.000\,000\,053\,181\,392\,6 \\ -0.000\,000\,000\,581\,529\,0 \\ 0.000\,000\,000\,004\,887\,0 \\ -0.000\,000\,000\,000\,032\,6 \\ 0.000\,000\,000\,000\,000\,2 \end{bmatrix} \tag{3-134}$$

and revealing a very interesting and important property of polynomial approximation in the Chebyshev basis. According to MASON and HANDSCOMB (2003, Chapter 5.3.2) the Chebyshev series expansion will converge to $f(x)$ as long as $f(x)$ satisfies the Dini-Lipschitz condition, thus if $f(x)$ is Lipschitz continuous. The truncation error of this approximation is in the same order-of-magnitude as the absolute value of the last coefficient, see (BOYD 2002, Chapter 2.12). This is of great advantage to approximate functions within machine precision.

In simplified terms, this means that the slope of $f(x)$ cannot become arbitrarily large.

A rule-of-thumb.

Right now we are facing the problem that the numerical integration of the right hand side (3-131) is not very accurate and to use its analytic solution is also not really feasible, as it is usually very hard to derive. While it is quite comfortable to integrate the right hand side numerically, we can obtain a numerical more accurate representation of

Due to singularities of the weighting function at $x = \pm 1$.

$$\int_{-1}^{1} \frac{f(x)\ T_j(x)}{\sqrt{1-x^2}}\,\mathrm{d}x = \int_{-1}^{1} \frac{f(x)\cos\left(j\ \arccos(x)\right)}{\sqrt{1-x^2}}\,\mathrm{d}x \tag{3-135}$$

by the following change of variable

$$x = \cos(\theta) \tag{3-136}$$

and with

$$\frac{\mathrm{d}x}{\mathrm{d}\theta} = \frac{\mathrm{d}\cos(\theta)}{\mathrm{d}\theta} = -\sin(\theta) \tag{3-137}$$

we obtain

$$\mathrm{d}x = -\sin(\theta)\,\mathrm{d}\theta. \tag{3-138}$$

Inserting (3-136) and (3-138) in the right hand side of (3-135) and changing the limits according to $\cos(\pi) = -1$ and $\cos(0) = 1$ yields

$$\begin{aligned} \int_{-1}^{1} \frac{f(x)\ T_j(x)}{\sqrt{1-x^2}}\,\mathrm{d}x &= -\int_{\pi}^{0} \frac{f\big(\cos(\theta)\big)\ \cos(j\,\theta)}{\sqrt{1-\cos^2(\theta)}}\sin(\theta)\,\mathrm{d}\theta \\ &= -\int_{\pi}^{0} \frac{f\big(\cos(\theta)\big)\ \cos(j\,\theta)}{\sin(\theta)}\sin(\theta)\,\mathrm{d}\theta \\ &= \int_{0}^{\pi} f\big(\cos(\theta)\big)\cos(j\,\theta)\,\mathrm{d}\theta. \end{aligned} \tag{3-139}$$

The derived integral (3-139) as a function of θ yields more accurate results for the numerical integration of the right hand side (3-131). Figure 3-42 depicts

the resulting residual function of the best approximation of (3-2), while using (3-139) for the numerical integration of (3-131).

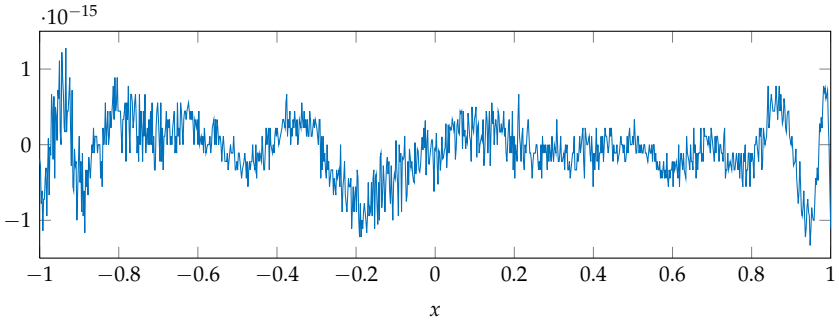

Figure 3-42: Residual function $v(x) = \sin(3x) - P_{21}(x)$ for the best fitting polynomial using (3-139) for the integrals of the right hand side.

Although the residual function in Figure 3-42 is slightly different than the one for the analytic solution in Figure 3-41, it also only shows deviations within $\pm 10^{-15}$. Thus, the numerical integration using (3-139) nearly gives the same results as the analytic solution (3-133).

Let us now consider the other two examples from Chapter 3, while this time we shift function (3-8) a bit to the right in order to avoid symmetry. The two functions are depicted in Figure 3-43.

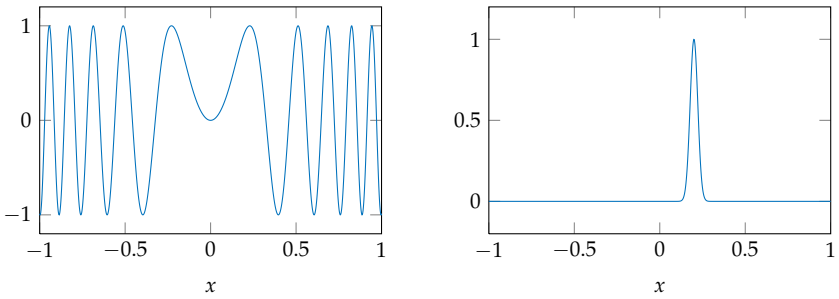

Figure 3-43: The two examples from the previous sections, $f(x) = \sin(30x^2)$ (left) and the shifted function $f(x) = \exp(-1000(x - 0.2)^2)$ (right).

Function $f(x) = \sin(30x^2)$ can be approximated within 10^{-14} by a polynomial of 85^{th} degree, as can be seen in the residual plot in Figure 3-44 (left).

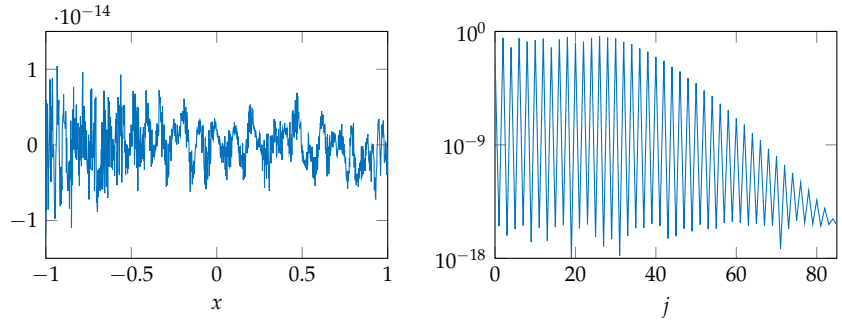

Figure 3-44: Residual function $v(x) = \sin(30x^2) - P_{85}(x)$ (left) and logarithmic plot for the coefficients $|c_j|$ (right).

The absolute value of the coefficients are illustrated in Figure 3-44 (right) and due to the symmetry of the function the odd coefficients are zero within machine precision. The even coefficients are rapidly converging to zero, while

the last one is $\approx 10^{-15}$. Even the exact solution for the integral of the right hand side

$$\langle \sin(30x^2), T_j \rangle = \begin{cases} -\cos\left(\left(\frac{j}{4} + \frac{1}{2}\right)\pi + 15\right) \pi J_{j/2}(15), & \text{if } j \text{ is even,} \\ 0, & \text{if } j \text{ is odd,} \end{cases} \tag{3-140}$$

will yield nearly the same result as depicted in Figure 3-44. The polynomial approximation $P_{85}(x)$ of function (3-6) is within machine precision. The same occurs for the shifted function

$$f(x) = \exp\left(-1000(x-0.2)^2\right). \tag{3-141}$$

The residual plot and the absolute values of the coefficients are depicted in Figure 3-45.

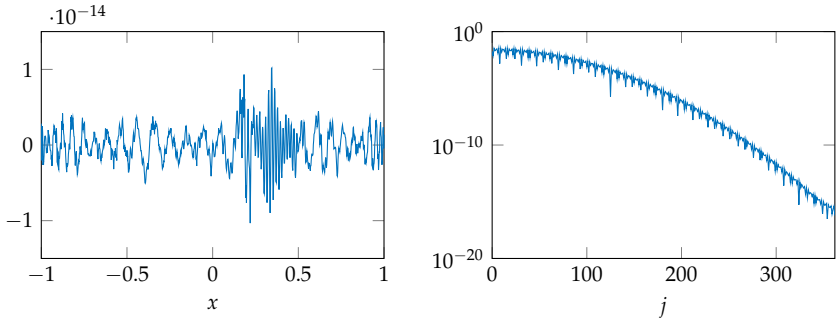

Figure 3-45: Residual function $v(x) = \exp(-1000(x-0.2)^2) - P_{362}(x)$ (left) and logarithmic plot for the coefficients $|c_j|$ (right).

A polynomial of 362nd degree approximates (3-141) within 10^{-14} and while the function depicted in Figure 3-43 (right) is not symmetric with respect to $x = 0$, neither the even nor odd coefficients are zero, except the last ones which are $\approx 10^{-16}$.

In direct comparison to the approximation in the monomial basis presented in Chapter 3 the approximation in the Chebyshev basis is more accurate, much faster and easier to implement. The only problem so far is the numerical integration of the right hand side. Using the integral (3-139) instead of (3-135) usually yields more accurate results for the numerical integration, but only to a certain extent. Until now the limitation of a least squares approximation in the Chebyshev basis is the solution of the integrals of the right hand side in both accuracy and computational time.

3.3.2 *Approximation in the Fourier basis*

As the Chebyshev series are closely related to the Fourier series, we will also present an approximation in the Fourier basis. According to BRONSHTEIN *et al.* (2007, p. 420 ff.) the Fourier series is given by

I intentionally omitted the term *periodic function*.

$$S_p(x) = \frac{1}{2}a_0 + \sum_{j=1}^{p} a_j \cos(j\omega x) + \sum_{j=1}^{p} b_j \sin(j\omega x) \tag{3-142}$$

with the angular frequency $\omega = 2\pi/T$ and period T. The complex representation of (3-142) is given by

$$S_p(x) = \sum_{j=-p}^{p} c_j \exp(\imath j\omega x) \tag{3-143}$$

with the imaginary unit $\imath = \sqrt{-1}$. The coefficients a_j and b_j can be converted into c_j as follows

$$c_j = \begin{cases} \frac{1}{2}a_0, & j = 0, \\ \frac{1}{2}(a_j - \imath b_j), & j > 0, \\ \frac{1}{2}(a_{-j} + \imath b_{-j}), & j < 0. \end{cases} \tag{3-144}$$

As in the previous chapters we will approximate function (3-2) by a Fourier series with $p = 3$, while using the complex representation (3-143). The basis functions $\phi_j = \exp(\imath j\omega x)$ satisfy the orthogonality condition

$$\langle \phi_i, \phi_j \rangle = \int_{-1}^{1} \exp(\imath i\omega x) \exp(\imath j\omega x)\, \mathrm{d}x = \begin{cases} T, & i = -j, \\ 0, & \text{else.} \end{cases} \tag{3-145}$$

and hence, the normal equation system of a least squares approximation of (3-2) in the Fourier basis reads

$$\begin{bmatrix} 0 & 0 & 0 & 0 & 0 & 0 & T \\ 0 & 0 & 0 & 0 & 0 & T & 0 \\ 0 & 0 & 0 & 0 & T & 0 & 0 \\ 0 & 0 & 0 & T & 0 & 0 & 0 \\ 0 & 0 & T & 0 & 0 & 0 & 0 \\ 0 & T & 0 & 0 & 0 & 0 & 0 \\ T & 0 & 0 & 0 & 0 & 0 & 0 \end{bmatrix} \begin{bmatrix} c_{-3} \\ c_{-2} \\ c_{-1} \\ c_0 \\ c_1 \\ c_2 \\ c_3 \end{bmatrix} = \begin{bmatrix} \langle \exp(-3\imath\omega x), \sin(3x) \rangle \\ \langle \exp(-2\imath\omega x), \sin(3x) \rangle \\ \langle \exp(-1\imath\omega x), \sin(3x) \rangle \\ \langle \exp(0\imath\omega x), \sin(3x) \rangle \\ \langle \exp(1\imath\omega x), \sin(3x) \rangle \\ \langle \exp(2\imath\omega x), \sin(3x) \rangle \\ \langle \exp(3\imath\omega x), \sin(3x) \rangle \end{bmatrix}. \tag{3-146}$$

While the normal matrix $\mathbf{N}$ is anti-diagonal, the coefficients can be directly determined by

$$c_j = \frac{1}{T} \int_{-1}^{1} \sin(3x) \exp(-\imath j\omega x)\, \mathrm{d}x\,, \tag{3-147}$$

for $j = -3, -2, -1, 0, 1, 2, 3$ and $T = 2$. This solution can also be found in Bronshtein *et al.* (2007, pp. 421) and yields the coefficients

$$\begin{bmatrix} c_{-3} \\ c_{-2} \\ c_{-1} \\ c_0 \\ c_1 \\ c_2 \\ c_3 \end{bmatrix} = \begin{bmatrix} 0 + 0.016\,661\,456\,383\,217\imath \\ 0 - 0.029\,092\,165\,239\,709\imath \\ 0 + 0.509\,819\,844\,563\,844\imath \\ 0 + 0.000\,000\,000\,000\,000\imath \\ 0 - 0.509\,819\,844\,563\,844\imath \\ 0 + 0.029\,092\,165\,239\,709\imath \\ 0 - 0.016\,661\,456\,383\,217\imath \end{bmatrix}. \tag{3-148}$$

Due to the symmetry of (3-2) the real part of the coefficients are zero. The resulting approximation and the residual function are depicted in Figure 3-46.

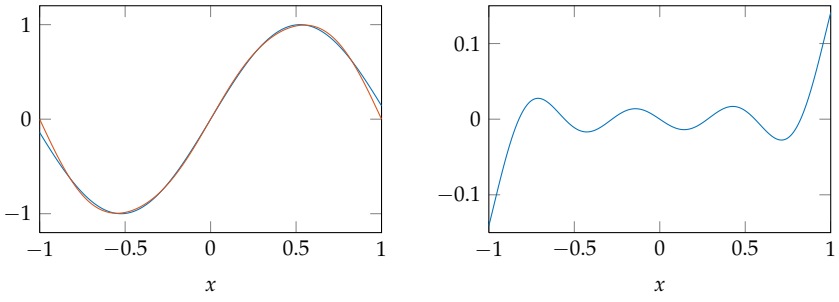

Figure 3-46: Given function (3-2) in blue and it's approximation in the Fourier basis $S_3(x)$ in red (left). Residual function $v(x) = \sin(3x) - S_3(x)$ (right).

The Matlab code for the presented approximation in the Fourier basis is given in Programme 3-7.

Programme 3-7: Code for an approximation in the Fourier basis.

```
%Approximation of sin(x) on [-1, 1]
a=-1; b=1;

%angular frequency and period T
omega=2*pi/(b-a); T=b-a;

%degree of approximation (number of harmonic ascillations)
p=3;

%Initialization of the matrix
c=zeros(p+1,1);

%Calcutaion of the coefficients
for j=-p:p
   c(j+p+1)=1/T*integral(@(x) sin(3*x).*exp(1i*j*omega*x),a
       ,b);
end

%Flipping the coefficients due to anti-diagonal normal
    matrix
c=flipud(c);
```

Increasing the number of terms to $p = 50$ will generally reduce the residual function, but will still keep the large deviation at the limits as depicted in Figure 3-47.

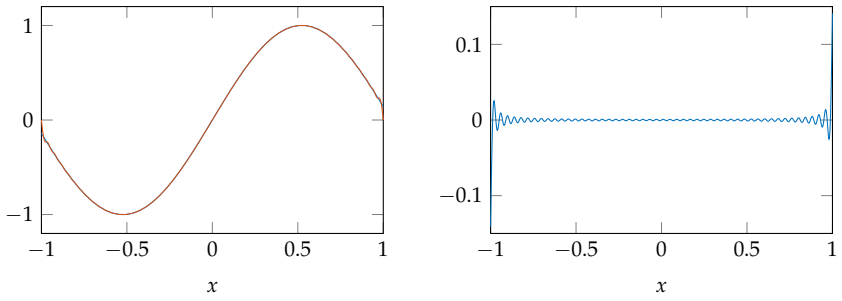

Figure 3-47: Given function (3-2) in blue and it's approximation in the Fourier basis $S_{50}(x)$ in red (left). Residual function $v(x) = \sin(3x) - S_{50}(x)$ (right).

These deviations at the limits will not vanish while increasing the number of harmonic oscillations. Although it is mentioned in BRONSHTEIN *et al.* (2007, pp. 420), and probably also in most books about Fourier series expansion, that we can

> *...represent a given periodic function $f(x)$ with period T exactly or approximatively by a sum of trigonometric functions...*

So far we have neglected the term *periodic*. But this is very important, because a representation of a function in the Fourier basis can only be exact in case we use an interval equal to an integral multiple of the period. While we approximated (3-2) on the interval $x \in [-1, 1]$ we implicitly assumed a period of $T = 2$, whereas the exact period is $T_{\text{exact}} = 2\pi/3$. This is the reason why it is not possible to achieve an approximation in the Fourier basis within machine precision. The resulting approximation will always preserve an implied

periodicity of function (3-2) with a period of $T = 2$. Figure 3-48 illustrates this issue.

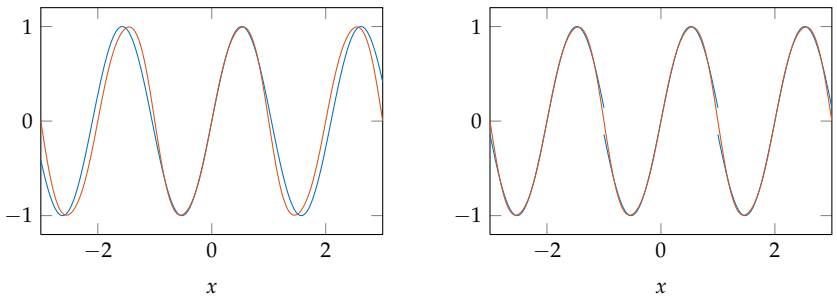

Figure 3-48: Given function (3-2) in blue and it's least squares approximation on the interval $x \in [-1, 1]$ in the Fourier basis $S_3(x)$ in red. We extended the interval to $x \in [-3, 3]$ in order to illustrate what we wanted to approximate (left) and what we actually did (right).

The different periods of the given function and the least squares approximation in the Fourier basis can be seen in Figure 3-48 (left), but this plot does not illustrate the actual situation of the performed adjustment. While we approximated function (3-2) on the interval $x \in [-1, 1]$, we implicitly defined that this function has a period of $T = 2$. As we already know this period is not the exact one. Hence, the actually performed least squares approximation in the Fourier basis is depicted in Figure 3-48 (right), which clearly reveals jump discontinuities at the limits $x = -1$ and $x = 1$. The approximation is not only a best to fit of function (3-2), it also tries to approximate these jumps as best as possible, which is also the reason for the large oscillations of the residual function in Figure 3-47 (right). This oscillating behaviour of the approximation in the vicinity of the jump discontinuities is known as Gibbs phenomenon.

Or, in other words, we tried to approximate a non continuous function by a continuous one.

Let's consider the last two examples depicted in Figure 3-43. An approximation of function (3-6) is given in Figure 3-49.

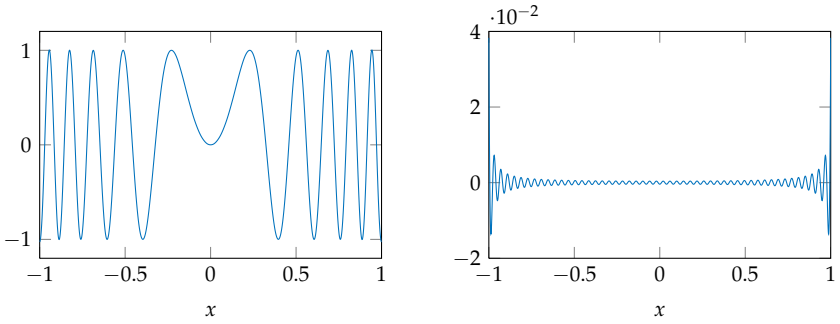

Figure 3-49: Approximation in the Fourier basis $S_{50}(x)$ of function (3-6) (left). Residual function $v(x) = \sin(30x^2) - S_{50}(x)$ (right).

Although it seems like function (3-6) is periodic on the interval $x \in [-1, 1]$, it is not. Once again we have jump discontinuities at the limits, which causes large deviations, as depicted in the residual plot Figure 3-49 (right). The coefficients of $S_{50}(x)$ are illustrated in Figure 3-50.

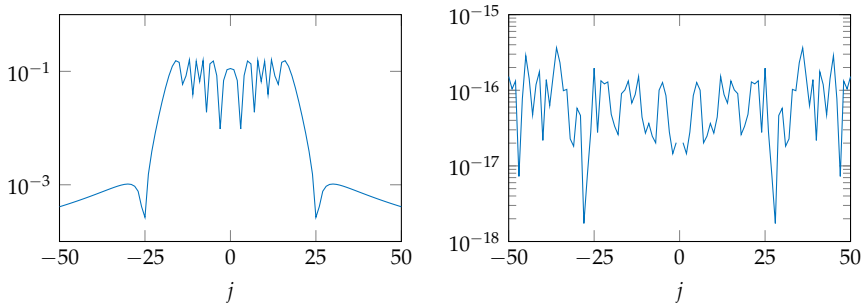

Figure 3-50: Logarithmic plot of the absolute values for the real (left) and imaginary part (right) of the complex coefficients c_j of $S_{50}(x)$.

Due to the symmetry of the function the imaginary part of the complex coefficients c_j is zero, as can be seen in Figure 3-50 (right). The imaginary part of the coefficient for the offset c_0 is always equal to zero and hence always a gap at $j = 0$ appears in these plots. The real part of the coefficients are decreasing with increasing j. However, they will not converge to zero, due to the wrong period or to the resulting jump discontinuities at the limits.

The last example depicted in Figure 3-43 (right) is also not periodic, but it is possible to approximate function (3-141) within machine precision with $p = 112$ terms. $S_{112}(x)$ and the residual function are depicted in Figure 3-51.

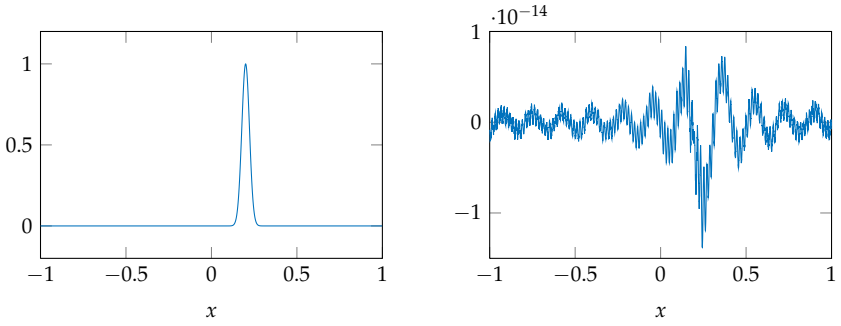

Figure 3-51: Best approximation in the Fourier basis $S_{117}(x)$ of function (3-141) (left). Residual function $v(x) = \exp(-1000(x-0.2)^2) - S_{112}(x)$ (right).

The largest deviations of $\approx 10^{-14}$ are appearing at the position of the peak of the function, as can be seen in Figure 3-51 (right). The coefficients of $S_{112}(x)$ are illustrated in Figure 3-52.

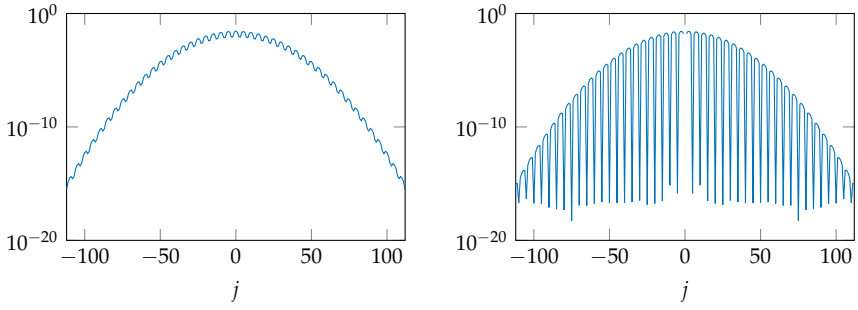

Figure 3-52: Logarithmic plot of the absolute values for the real (left) and imaginary part (right) of the complex coefficients c_j of $S_{112}(x)$.

The logarithmic plot of the absolute values in Figure 3-52 shows that the coefficients rapidly converging to zero within machine precision with increasing j. Although function (3-141) is not a periodic function we can approximate it within machine precision using the Fourier basis. But this is only due to the nature of this exponential function. The functional value at the limits is only $f(x = \pm 1) \approx 10^{-277}$ and its first k derivatives are only increasing by a factor

$\approx 1000^k$. And while we only deal with roughly 15 digits of relative accuracy we can conclude, that function (3-141) is an almost periodic function. At least from a numerical point of view.

3.3.3 *Chebyshev vs. Fourier*

This section is essentially based on (TREFETHEN 2013, Chapter 3 & 4), while mainly focussing on the integrals instead of the series expansion.

As already mentioned in Section 3.3, the Chebyshev and Fourier basis are two closely related sets of orthogonal basis functions. To illustrate this relationship, we will consider a least squares approximation of a Lipschitz continuous function $f(x)$ on $[-1,1]$ in the Chebyshev basis according to (3-130). The coefficients can be calculated by

$$c_{\text{Cheby}_j} = \frac{1}{\langle T_j, T_j \rangle} \int_{-1}^{1} \frac{f(x)\, T_j}{\sqrt{1-x^2}}\, \mathrm{d}x\,, \tag{3-149}$$

or by introducing the change in variables (3-136), the coefficients can also be determined by

$$\begin{aligned} c_{\text{Cheby}_j} &= \frac{1}{\langle T_j, T_j \rangle} \int_0^{\pi} f\big(\cos(\theta)\big) \cos(j\,\theta)\, \mathrm{d}\theta \\ &= \frac{1}{\langle T_j, T_j \rangle} \int_0^{\pi} F(\theta) \cos(j\,\theta)\, \mathrm{d}\theta\,. \end{aligned} \tag{3-150}$$

This change in the variables can also be interpreted as a mapping of $f(x)$ onto the upper half of the unit circle, which is depicted in Figure 3-53.

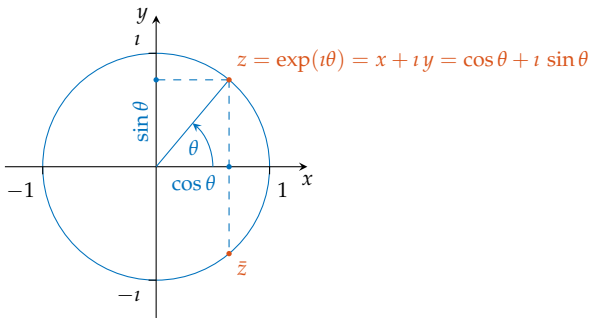

Figure 3-53: Unit circle in the complex plane with the imaginary unit $\imath = \sqrt{-1}$.

An arbitrary point z on the unit circle is uniquely defined by its coordinates (x, y), satisfying

$$x^2 + y^2 = 1\,, \tag{3-151}$$

or an angle θ, with

$$\begin{aligned} \mathrm{Re}(z) &= x = \cos\theta\,, \\ \mathrm{Im}(z) &= y = \sin\theta\,, \end{aligned} \tag{3-152}$$

while the upper equation in (3-152) is the introduced change in variables (3-136). Due to

$$x = \mathrm{Re}(z) = \mathrm{Re}(\bar{z}) \tag{3-153}$$

it follows

$$F(\theta) = F(-\theta) \tag{3-154}$$

and the integral in (3-150) can also be written as

$$c_{\text{Cheby}_j} = \frac{1}{2}\frac{1}{\langle T_j, T_j \rangle} \int_{-\pi}^{\pi} F(\theta) \cos(j\,\theta)\, \mathrm{d}\theta\,. \tag{3-155}$$

While mapping $f(x)$ onto the unit circle we obtain a so-called transplanted function $F(\theta)$ for $\theta \in [-\pi, \pi]$ which is an infinitely differentiable, even, periodic function, see ORSZAG 1971. Therefore, $F(\theta)$ has a Fourier cosine series expansion

For a non-periodic function $f(x)$ we obtain a periodic function $F(\theta)$ only after the change of variable (3-136).

$$F(\theta) = \frac{1}{2}a_0 + \sum_{j=1}^{\infty} a_j \cos(j\omega\theta)\,. \tag{3-156}$$

A least squares approximation of the periodic function $F(\theta)$ on $[-\pi, \pi]$ in the Fourier basis according to Section 3.3.2 results in the coefficients

$$c_{\text{Fourier}_j} = \frac{1}{2\pi}\int_{-\pi}^{\pi} F(\theta)\exp(-\imath j\omega\theta)\,\mathrm{d}\theta\,. \tag{3-157}$$

Using Euler's equation

$$\exp(\pm\imath\,\theta) = \cos\theta \pm \imath\,\sin\theta \tag{3-158}$$

and with $\omega = {}^{2\pi}/_{T} = 1$ the integral in (3-157) can be written in the form

$$\begin{aligned} c_{\text{Fourier}_j} &= \frac{1}{2\pi}\int_{-\pi}^{\pi} F(\theta)\left[\cos(j\,\theta) - \imath\,\sin(j\,\theta)\right]\mathrm{d}\theta \\ &= \frac{1}{2\pi}\int_{-\pi}^{\pi} F(\theta)\cos(j\,\theta)\,\mathrm{d}\theta - \imath\,\frac{1}{2\pi}\int_{-\pi}^{\pi} F(\theta)\sin(j\,\theta)\,\mathrm{d}\theta\,. \end{aligned} \tag{3-159}$$

While $F(\theta)$ is an even function

$$\int_{-\pi}^{\pi} F(\theta)\sin(j\,\theta)\,\mathrm{d}\theta = 0 \tag{3-160}$$

and Equation (3-159) simplifies to

$$c_{\text{Fourier}_j} = \frac{1}{2\pi}\int_{-\pi}^{\pi} F(\theta)\cos(j\,\theta)\,\mathrm{d}\theta\,. \tag{3-161}$$

Now it is quite obvious that the Chebyshev coefficients c_{Cheby_j} in (3-155) are equal to the Fourier coefficients c_{Fourier_j} in (3-161), only scaled by a constant factor. An approximation of $f(x)$ on $[-1, 1]$ in the Chebyshev basis is directly related to an approximation of a transplanted function $F(\theta)$ on $[-\pi, \pi]$ in the Fourier basis.

As we have seen in Section 3.3.1, solving the integrals (3-150) using the MATLAB built-in function *integral* is slow and also not very accurate. But in case $F(\theta)$ is known only at equally spaced points θ_k, the integrals in (3-159) can be approximated by the Fast Fourier Transformation (FFT), see (BRONSHTEIN *et al.* 2007, Section 19.6.4). Using FFT is very fast and in case a sufficient amount of points are given, it is also accurate down to the last digit. Let us consider some equally spaced points on the upper half of the unit circle as depicted in Figure 3-54.

According to (TREFETHEN 2013, p. 15) this was probably observed around 1970, see (AHMED and FISHER 1970) or (ORSZAG 1971).

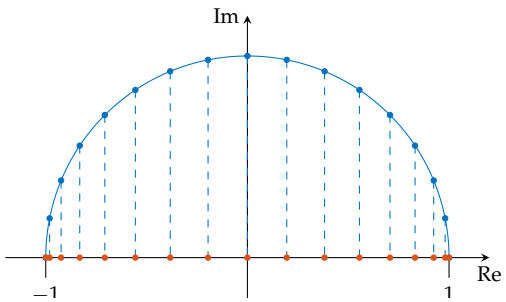

Figure 3-54: Equispaced points on the upper half on the unit circle in blue and Chebyshev points in red.

In the following we call them only Chebyshev points.

The projection of these equally spaced points onto the real axis are known as *Chebyshev points of the second kind*, *Chebyshev extreme points*, or *Chebyshev-Lobatto points* and are given by

$$x_k = \cos\left(\frac{k\pi}{n}\right), \quad 0 \leq k \leq n\,. \tag{3-162}$$

And if we discretize $f(x)$ at the Chebyshev points we obtain

$$f(x_k) = F(\theta_k)\,, \tag{3-163}$$

which can directly be evaluated using FFT. The basic procedure for an efficient approximation of $f(x)$ with the aid of the FFT is illustrated in Figure 3-55.

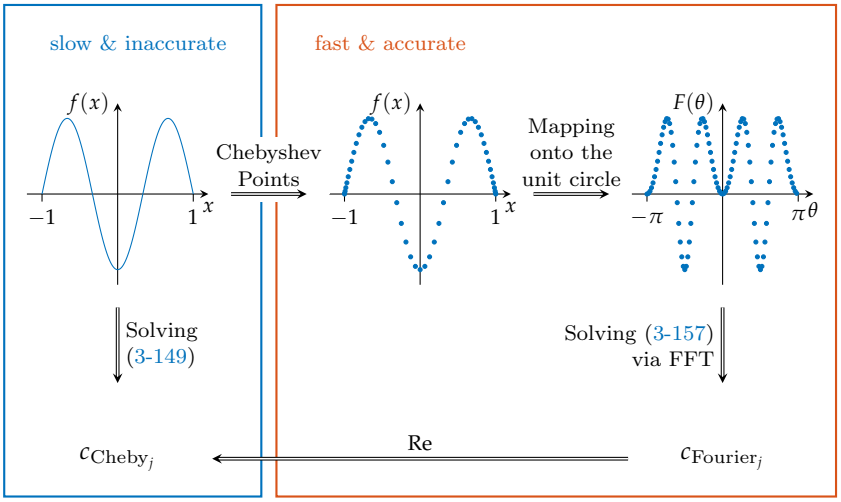

Figure 3-55: Procedure for a fast and accurate approximation of $f(x)$ in the Chebyshev basis via FFT.

The Chebyshev coefficients c_{Cheby_j} are the real part of c_{Fourier_j}, only scaled by a constant factor. While for Part ii the coefficents are determined by using the MATLAB built-in function *integral*, FFT is used for the practical applications Measurement– and Model–based Structural Analysis (MeMoS) in Part iii.

4

APPROXIMATION OF FUNCTIONS IN TWO DIMENSIONS

The basic methodology for the least squares approximation of univariate functions shown in Chapter 3 can in principle be directly extended to bivariate or multivariate functions, as already remarked in (Langtangen 2016a, Chapter 8). For detailed information about multivariate approximation of functions in general please refer to standard literature such as (Atkinson and Han 2009, Chapter 14) or (Reimer 2003). A general overview of different methods and/or different sets of basis functions can be found in (Schaback 2015).

Therefore, hardly any additional literature has been used throughout this chapter.

For the approximation of univariate functions we in general only considered the domain $[a,b]$ mapped onto $[-1,1]$. But we have not considered the other two domains, namely $[a,\infty)$ and $(-\infty,\infty)$, and have not discussed the resulting problems in solving the integrals in the normal equations system (1-45). However, there are many different types of domains for the approximation of bivariate functions. Solving the integrals of the normal equation system, therefore, turns out to be the main problem in the computation of a least square approximation of bivariate functions. Thus, we restrict ourselves in this thesis only to functions defined on the unit square $[-1,1]^2$ and we only briefly discuss the mapping of simple arbitrary convex domains on the unit square in Section 4.4.

For practical application and since any function can be discretised, we would also like to refer to standard literature on the approximation of scattered data, such as e.g. (Buhmann 2003), (Lancaster and Salkauskas 1988), (Piegl and Tiller 1997) or (Wendland 2004).

Any bivariate polynomial of degree p can be written in the form

$$P_p(x,y) = \sum_{i=0}^{p}\sum_{j=0}^{p} c_{ij}\,\phi_{ij}(x,y) = \sum_{i=0}^{p}\sum_{j=0}^{p} c_{ij}\,x^i y^j \tag{4-1}$$

while $i+j \le p$. The advantage of this representation of a bivariate polynomial is, that the indices of the unknown coefficients c_{ij} are directly referring to the corresponding basis function $\phi_{ij}(x,y) = x^i y^j$. Storing these coefficients in a matrix allows an easy way for a visual inspection and further interpretation. Using (4-1) for the implementation of a least squares approximation in accordance to (1-45), might lead to some confusion. Therefore, it is better to rewrite the two sums in Equation (4-1) into a single one and use the following equivalent representation of (4-1) for a bivariate polynomial of degree p

$$P_p(x,y) = \sum_{k=0}^{p_\mathrm{n}} c_k\,\phi_k(x,y) = \sum_{k=0}^{p_\mathrm{n}} c_k\,x^i y^j \qquad i+j \le p, \tag{4-2}$$

with $p_\mathrm{n} = \frac{1}{2}(p+1)(p+2)$ and where i,j permute accordingly. An appropriate way to illustrate the terms of a bivariate polynomial is by the usage of the Pascal triangle as depicted in Figure 4-1.

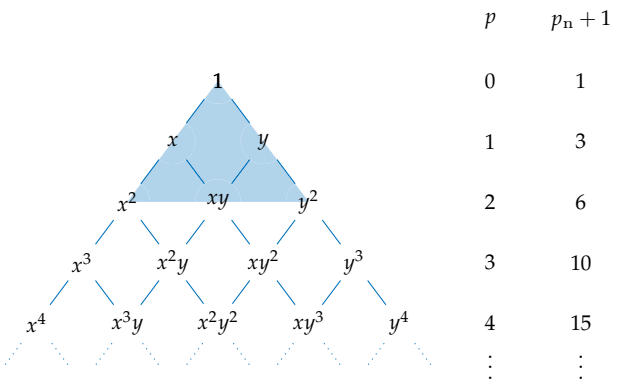

Figure 4-1: Pascal triangle for the terms of a bivariate polynomial of degree p. Including the number of terms $p_n + 1$ for each degree. The terms for a polynomial of 2nd degree are shaded in light blue. The illustration was adopted from Zienkiewicz *et al.* (2013, p. 153) and slightly modified.

For a least square approximation of a function in two dimensions, the representation (4-2) with only one sum can be used in the same way as already done in Chapter 3. To illustrate the procedure we will approximate the continuous real function

$$f(x,y) = \cos\left(\frac{x}{y+1.5}\right), \qquad (x,y) \in [-1,1]^2, \tag{4-3}$$

by a polynomial of 2nd degree with $p_n + 1 = 6$ unknown coefficients. Function (4-3) is depicted in Figure 4-2.

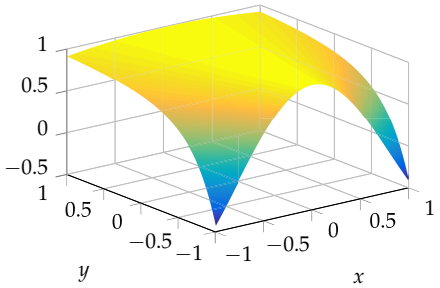

Figure 4-2: Given function $f(x,y) = \cos\left(x/(y+1.5)\right)$.

In order to approximate (4-3) the 6 basis functions $\phi_k = x^i y^j$ of a polynomial of 2nd degree are defined as listed in Table 4-1.

k	i	j	$\phi_k = x^i y^j$
0	0	0	1
1	0	1	y
2	0	2	y^2
3	1	0	x
4	1	1	xy
5	2	0	x^2

Table 4-1: All $p_n + 1$ permutations of i and j under the condition $i + j \leq p$ for polynomial degree $p = 2$ and resulting basis functions $\phi_k = x^i y^j$.

The normal equation system

$$\mathbf{N}\,\mathbf{x} = \mathbf{n}$$

of a least squares approximation of (4-3) by a polynomial of 2nd degree results in

$$\begin{bmatrix} \langle\phi_0,\phi_0\rangle & \langle\phi_1,\phi_0\rangle & \cdots & \langle\phi_{p_n},\phi_0\rangle \\ \langle\phi_0,\phi_1\rangle & \langle\phi_1,\phi_1\rangle & \cdots & \langle\phi_{p_n},\phi_1\rangle \\ \vdots & \vdots & \ddots & \vdots \\ \langle\phi_0,\phi_{p_n}\rangle & \langle\phi_1,\phi_{p_n}\rangle & \cdots & \langle\phi_{p_n},\phi_{p_n}\rangle \end{bmatrix} \begin{bmatrix} c_0 \\ c_1 \\ \vdots \\ c_{p_n} \end{bmatrix} = \begin{bmatrix} \langle\phi_0, \cos\left(x/(y+1.5)\right)\rangle \\ \langle\phi_1, \cos\left(x/(y+1.5)\right)\rangle \\ \vdots \\ \langle\phi_{p_n}, \cos\left(x/(y+1.5)\right)\rangle \end{bmatrix}, \tag{4-4}$$

with the integrals

$$\langle \phi_k, \phi_l \rangle = \int_{-1}^{1} \int_{-1}^{1} \phi_k \phi_l \, \mathrm{d}x \, \mathrm{d}y \quad \text{for } k, l = 0, 1, 2, \ldots, p_\mathrm{n}$$

and

$$\langle \phi_l, \cos\left(x/(y+1.5)\right) \rangle = \int_{-1}^{1} \int_{-1}^{1} \phi_l \, \cos\left(x/(y+1.5)\right) \, \mathrm{d}x \, \mathrm{d}y$$

for $l = 0, 1, 2, \ldots, p_\mathrm{n}$. Based on the basis functions ϕ_k listed in Table 4-1 the normal matrix in (4-4) reads

$$\mathbf{N} = \begin{bmatrix} \langle 1,1 \rangle & \langle y,1 \rangle & \langle y^2,1 \rangle & \langle x,1 \rangle & \langle xy,1 \rangle & \langle x^2,1 \rangle \\ \langle 1,y \rangle & \langle y,y \rangle & \langle y^2,y \rangle & \langle x,y \rangle & \langle xy,y \rangle & \langle x^2,y \rangle \\ \langle 1,y^2 \rangle & \langle y,y^2 \rangle & \langle y^2,y^2 \rangle & \langle x,y^2 \rangle & \langle xy,y^2 \rangle & \langle x^2,y^2 \rangle \\ \langle 1,x \rangle & \langle y,x \rangle & \langle y^2,x \rangle & \langle x,x \rangle & \langle xy,x \rangle & \langle x^2,x \rangle \\ \langle 1,xy \rangle & \langle y,xy \rangle & \langle y^2,xy \rangle & \langle x,xy \rangle & \langle xy,xy \rangle & \langle x^2,xy \rangle \\ \langle 1,x^2 \rangle & \langle y,x^2 \rangle & \langle y^2,x^2 \rangle & \langle x,x^2 \rangle & \langle xy,x^2 \rangle & \langle x^2,x^2 \rangle \end{bmatrix}. \tag{4-5}$$

The integrals in (4-5) can be solved directly and yields the following normal matrix

$$\mathbf{N} = \begin{bmatrix} 4 & 0 & 4/3 & 0 & 0 & 4/3 \\ 0 & 4/3 & 0 & 0 & 0 & 0 \\ 4/3 & 0 & 4/5 & 0 & 0 & 4/9 \\ 0 & 0 & 0 & 4/3 & 0 & 0 \\ 0 & 0 & 0 & 0 & 4/9 & 0 \\ 4/3 & 0 & 4/9 & 0 & 0 & 4/5 \end{bmatrix}. \tag{4-6}$$

As in the previous sections we solve the integrals of the right hand side numerically using the MATLAB built-in function *integral2* for double integrals. The right hand side reads

$$\mathbf{n} = \begin{bmatrix} \langle 1, \cos\left(x/(y+1.5)\right) \rangle \\ \langle y, \cos\left(x/(y+1.5)\right) \rangle \\ \langle y^2, \cos\left(x/(y+1.5)\right) \rangle \\ \langle x, \cos\left(x/(y+1.5)\right) \rangle \\ \langle xy, \cos\left(x/(y+1.5)\right) \rangle \\ \langle x^2, \cos\left(x/(y+1.5)\right) \rangle \end{bmatrix} = \begin{bmatrix} 3.508\,314\,674\,752\,977 \\ 0.231\,521\,135\,845\,772 \\ 1.104\,046\,536\,710\,792 \\ -3.951\,960\,286\,796\,56 \cdot 10^{-14} \\ -8.604\,228\,440\,844\,96 \cdot 10^{-16} \\ 1.042\,930\,815\,846\,090 \end{bmatrix}. \tag{4-7}$$

The solution of the normal equation system (4-4) yields the unknown coefficients

$$\begin{bmatrix} c_0 \\ c_1 \\ c_2 \\ c_3 \\ c_4 \\ c_5 \end{bmatrix} = \begin{bmatrix} 1.056\,984\,072\,386\,777 \\ 0.173\,640\,851\,884\,329 \\ -0.183\,914\,123\,081\,812 \\ -2.963\,970\,215\,097\,42 \cdot 10^{-14} \\ -1.935\,951\,399\,190\,12 \cdot 10^{-15} \\ -0.355\,802\,088\,013\,786 \end{bmatrix}. \tag{4-8}$$

for a bivariate polynomial approximation of 2nd degree. The resulting approximation and the residual function are depicted in Figure 4-3.

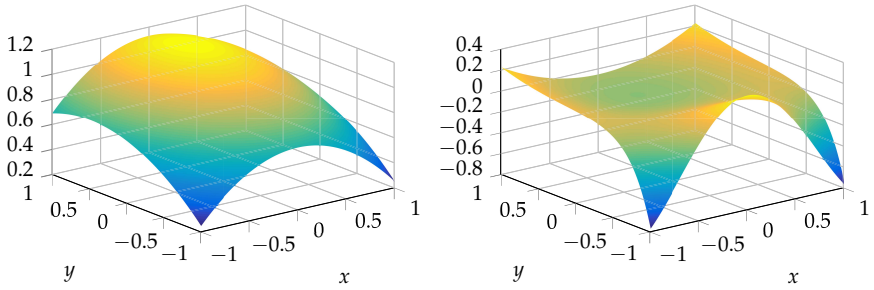

Figure 4-3: Polynomial approximation $P_2(x,y)$ of function (4-3) (left). Residual function $v(x,y) = \cos\left(x/(y+1.5)\right) - P_2(x,y)$ (right).

As Figure 4-3 illustrates, $P_2(x,y)$ is only a very coarse approximation of function (4-3) with the largest deviations at the two corners for $y = -1$. The best approximation can be achieved by using a polynomial of 14^{th} degree, which yields a residual function smaller than 10^{-3}, as depicted in Figure 4-4.

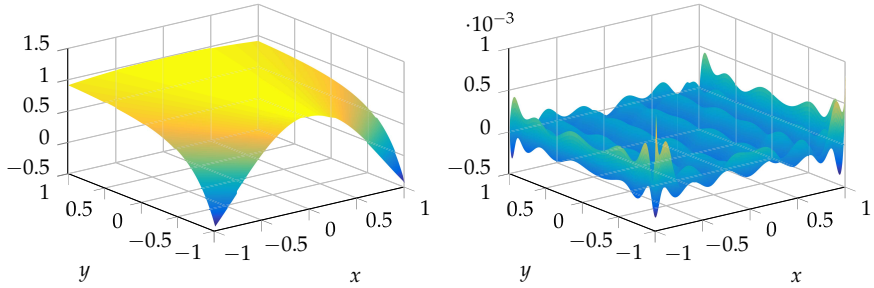

Figure 4-4: Best polynomial approximation $P_{14}(x,y)$ of function (4-3) (left). Residual function $v(x,y) = \cos\left(x/(y+1.5)\right) - P_{14}(x,y)$ (right).

A further increase of the polynomial degree leads to a larger residual function and therefore, to a worse approximation. A polynomial of 22^{nd} degree already yields a residual function which is slightly smaller than for $P_2(x,y)$, as depicted in Figure 4-5 (right).

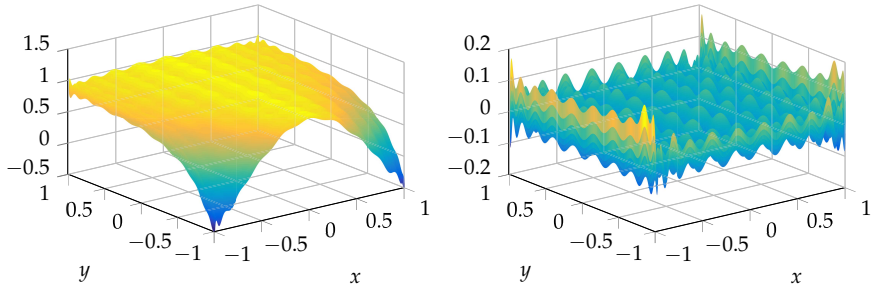

Figure 4-5: Polynomial approximation $P_{22}(x,y)$ of function (4-3) (left). Residual function $v(x,y) = \cos\left(x/(y+1.5)\right) - P_{22}(x,y)$ (right).

As already mentioned, polynomial approximation in the monomial basis is an ill-conditioned problem. The condition number of the normal matrix for a polynomial of 20^{th} degree is $\approx 10^{14}$ and exponentially increases with increasing degree. A polynomial approximation of 24^{th} degree has already no similarities to function (4-3) any more, as Figure 4-6 illustrates.

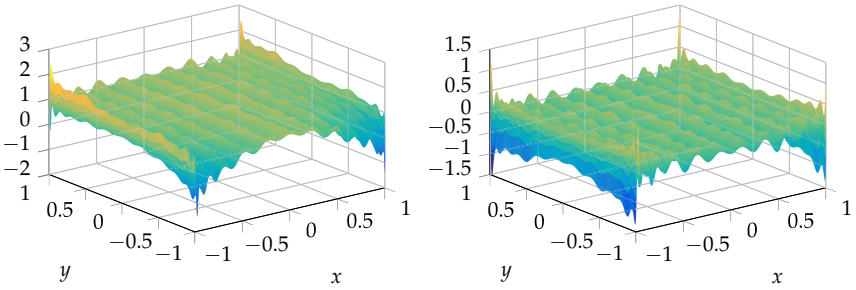

Figure 4-6: Polynomial approximation $P_{24}(x,y)$ of function (4-3) (left). Residual function $v(x,y) = \cos\left(x/(y+1.5)\right) - P_{24}(x,y)$ (right).

In order to visualise the coefficients it is convenient to convert the column wise representation c_k into a matrix c_{ij}. The coefficients of $P_{24}(x,y)$ are depicted in Figure 4-7 and are offering the same characteristics as in the one-dimensional case.

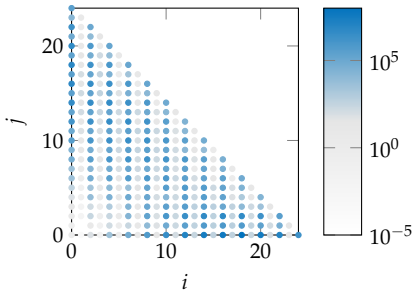

Figure 4-7: Colour coded visualisation of the absolute values for the coefficients c_{ij} of $P_{24}(x,y)$ on a logarithmic scale.

Each point in Figure 4-7 represents the coefficients c_{ij} corresponding to the basis function $\phi_{ij}(x,y) = x^i y^j$. The absolute value for each coefficient is visualised by a colour on a logarithmic scale. Due to the symmetry of function (4-3) with respect to $x = 0$ the coefficients for odd i, are very small in comparison to the ones for even i, which takes values up to $\approx 10^7$ with increasing degree i and j. Due to the condition $i + j \leq p$ in the definition of a bivariate polynomial of degree p, the upper triangular part in Figure 4-7 is always empty.

The MATLAB code for the presented polynomial approximation of functions in two dimensions is given in Programme 4-1. Due to the symmetry of the normal matrix only the upper triangular part has been determined and mirrored to the lower one. Further optimisation of the source code has been avoided in favour of readability.

Programme 4-1: Code for an approximation in the monomial basis for bivariate functions.

```
%Approximation of f(x) on x,y in [-1, 1]
a=-1; b=1;

%polynomial degree
p=2; p_n=(p+1)*(p+2)/2;

%Preallocation of the matrices
N=zeros(p_n); n=zeros(p_n,1);

%Permutation of i and j for i+j<=p
[ii,jj]=meshgrid(0:p);
ii=reshape(ii,[],1); jj=reshape(jj,[],1);

%index for i+j>k and deleting entries
out=(ii+jj)>p; ii(out)=[]; jj(out)=[];

%Basis function
phi=@(x,y,i,j) x.^i.*y.^j;

%Integral for the product of two Basis functions
int_phi=@(i,j,a,b) 1/(i+j+1)*(b^(i+j+1)-a^(i+j+1));

for k=1:p_n
    for l=k:p_n
        N(k,l)=int_phi(ii(k),ii(l),a,b)*int_phi(jj(k),jj(l)
            ,a,b);
    end
    n(k)=integral2(@(x,y) cos(x.*y).*phi(x,y,ii(k),jj(k)),a
        ,b,a,b);
end
%Adding the lower triangular part
N=N+triu(N,1)';

c=N\n;
```

4.1 ELEMENTWISE APPROXIMATION IN THE MONOMIAL BASIS

As in Section 3.1 we improve the approximation by dividing the whole domain into elements and approximate each element by a polynomial of low degree. Furthermore, we enforce continuity at connecting nodes in order to achieve a continuous approximation on the whole domain. The division of the domain into elements can be done arbitrarily, but for convenience we will now focus on quadratic elements, while their edges are aligned parallel to the $x-$ and $y-$axis as illustrated in Figure 4-8.

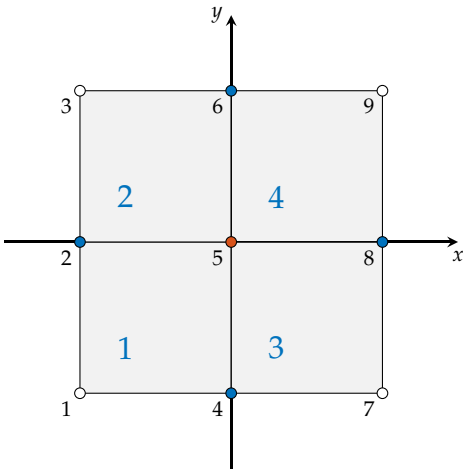

Figure 4-8: Alignment of the elements and position of the nodes. Elements are highlighted in light grey and numbered in blue and nodes in black. The colour of the circles indicates the number of constraints of each node in order to enforce continuity at the nodes, with white = 0, blue = 1 and red = 3 constraints.

The choice of quadratic elements as aligned in Figure 4-8 allows an easy determination of the integrals for all elements only based on the coordinates of the corner nodes. In order to illustrate the procedure we approximate function (4-3) by dividing the whole domain into $N = 4$ elements using polynomials of 2^{nd} degree. Before we set-up the normal equation system in accordance to (3-18) we need an unique identifier for the nodes ν and the elements ζ, which can be stored in tables as follows.

Nodes

ν	x_ν	y_ν
1	−1.0	−1.0
2	−1.0	0.0
3	−1.0	1.0
4	0.0	−1.0
5	0.0	0.0
6	0.0	1.0
7	1.0	−1.0
8	1.0	0.0
9	1.0	1.0

Elements

ζ	ν_1	ν_2	ν_3	ν_4
1	1	2	4	5
2	2	3	5	6
3	4	5	7	8
4	5	6	8	9

Table 4-2: Coordinates for all nodes ν and the corner nodes for all four element ζ as illustrated in Figure 4-8.

Based on the definition of nodes and elements in Table 4-2 and the basis functions of a quadratic polynomial in Table 4-1 we can set-up the normal equation system for each element ζ

$$ {}^{\zeta}\mathbf{N}\,{}^{\zeta}\mathbf{x} = {}^{\zeta}\mathbf{n} \tag{4-9} $$

which reads in accordance to (4-4)

$$ \begin{bmatrix} {}^{\zeta}\langle\phi_0,\phi_0\rangle & {}^{\zeta}\langle\phi_1,\phi_0\rangle & \cdots & {}^{\zeta}\langle\phi_{p_n},\phi_0\rangle \\ {}^{\zeta}\langle\phi_0,\phi_1\rangle & {}^{\zeta}\langle\phi_1,\phi_1\rangle & \cdots & {}^{\zeta}\langle\phi_{p_n},\phi_1\rangle \\ \vdots & \vdots & \ddots & \vdots \\ {}^{\zeta}\langle\phi_0,\phi_{p_n}\rangle & {}^{\zeta}\langle\phi_0,\phi_{p_n}\rangle & \cdots & {}^{\zeta}\langle\phi_{p_n},\phi_{p_n}\rangle \end{bmatrix} \begin{bmatrix} {}^{\zeta}c_0 \\ {}^{\zeta}c_1 \\ \vdots \\ {}^{\zeta}c_{p_n} \end{bmatrix} = \begin{bmatrix} {}^{\zeta}\langle\cos\left(x/(y+1.5)\right),\phi_0\rangle \\ {}^{\zeta}\langle\cos\left(x/(y+1.5)\right),\phi_1\rangle \\ \vdots \\ {}^{\zeta}\langle\cos\left(x/(y+1.5)\right),\phi_{p_n}\rangle \end{bmatrix}. \tag{4-10} $$

Due to the alignment of the elements depicted Figure 4-8 and the order of the corner nodes for each element in Table 4-2, the limits for the integrals in

(4-10) are defined by the coordinates of ν_1 and ν_4 for each element. For the integrals in the normal matrices we get

$$ {}^{\zeta}\langle \phi_k, \phi_l \rangle = \int_{{}^{\zeta}y_{\nu_1}}^{{}^{\zeta}y_{\nu_4}} \int_{{}^{\zeta}x_{\nu_1}}^{{}^{\zeta}x_{\nu_4}} \phi_k \phi_l \, \mathrm{d}x \, \mathrm{d}y \quad \text{for } k, l = 0, 1, 2, \ldots, p_\mathrm{n} $$

and for the right hand side

$$ {}^{\zeta}\langle \cos\left({}^{x}/_{(y+1.5)}\right), \phi_l \rangle = \int_{{}^{\zeta}y_{\nu_1}}^{{}^{\zeta}y_{\nu_4}} \int_{{}^{\zeta}x_{\nu_1}}^{{}^{\zeta}x_{\nu_4}} \cos\left({}^{x}/_{(y+1.5)}\right) \phi_l \, \mathrm{d}x \, \mathrm{d}y, $$

with $l = 0, 1, 2, \ldots, p_\mathrm{n}$ and $\zeta = 1, 2, 3, 4$. Approximating each element by a polynomial of 2^{nd} degree leads to $p_\mathrm{n} = 6$ basis functions. Inserting the basis functions from Table 4-1 in (4-10) the normal matrix for each element reads

$$ {}^{\zeta}\mathbf{N} = \begin{bmatrix} {}^{\zeta}\langle 1,1\rangle & {}^{\zeta}\langle y,1\rangle & {}^{\zeta}\langle y^2,1\rangle & {}^{\zeta}\langle x,1\rangle & {}^{\zeta}\langle xy,1\rangle & {}^{\zeta}\langle x^2,1\rangle \\ {}^{\zeta}\langle 1,y\rangle & {}^{\zeta}\langle y,y\rangle & {}^{\zeta}\langle y^2,y\rangle & {}^{\zeta}\langle x,y\rangle & {}^{\zeta}\langle xy,y\rangle & {}^{\zeta}\langle x^2,y\rangle \\ {}^{\zeta}\langle 1,y^2\rangle & {}^{\zeta}\langle y,y^2\rangle & {}^{\zeta}\langle y^2,y^2\rangle & {}^{\zeta}\langle x,y^2\rangle & {}^{\zeta}\langle xy,y^2\rangle & {}^{\zeta}\langle x^2,y^2\rangle \\ {}^{\zeta}\langle 1,x\rangle & {}^{\zeta}\langle y,x\rangle & {}^{\zeta}\langle y^2,x\rangle & {}^{\zeta}\langle x,x\rangle & {}^{\zeta}\langle xy,x\rangle & {}^{\zeta}\langle x^2,x\rangle \\ {}^{\zeta}\langle 1,xy\rangle & {}^{\zeta}\langle y,xy\rangle & {}^{\zeta}\langle y^2,xy\rangle & {}^{\zeta}\langle x,xy\rangle & {}^{\zeta}\langle xy,xy\rangle & {}^{\zeta}\langle x^2,xy\rangle \\ {}^{\zeta}\langle 1,x^2\rangle & {}^{\zeta}\langle y,x^2\rangle & {}^{\zeta}\langle y^2,x^2\rangle & {}^{\zeta}\langle x,x^2\rangle & {}^{\zeta}\langle xy,x^2\rangle & {}^{\zeta}\langle x^2,x^2\rangle \end{bmatrix} \tag{4-11} $$

and the right hand side yields

$$ {}^{\zeta}\mathbf{n} = \begin{bmatrix} {}^{\zeta}\langle 1, \cos\left({}^{x}/_{(y+1.5)}\right)\rangle \\ {}^{\zeta}\langle y, \cos\left({}^{x}/_{(y+1.5)}\right)\rangle \\ {}^{\zeta}\langle y^2, \cos\left({}^{x}/_{(y+1.5)}\right)\rangle \\ {}^{\zeta}\langle x, \cos\left({}^{x}/_{(y+1.5)}\right)\rangle \\ {}^{\zeta}\langle xy, \cos\left({}^{x}/_{(y+1.5)}\right)\rangle \\ {}^{\zeta}\langle x^2, \cos\left({}^{x}/_{(y+1.5)}\right)\rangle \end{bmatrix}. \tag{4-12} $$

Due to the the alignment of the elements with respect to $x = 0$ and $y = 0$, the entries in all four normal matrices have the same absolute values and only their algebraic sign changes. For the normal matrices these values are

$$ |{}^{\zeta}\mathbf{N}| = \begin{bmatrix} 1 & 1/2 & 1/3 & 1/2 & 1/4 & 1/3 \\ 1/2 & 1/3 & 1/4 & 1/4 & 1/6 & 1/6 \\ 1/3 & 1/4 & 1/5 & 1/6 & 1/8 & 1/9 \\ 1/2 & 1/4 & 1/6 & 1/3 & 1/6 & 1/4 \\ 1/4 & 1/6 & 1/8 & 1/6 & 1/9 & 1/8 \\ 1/3 & 1/6 & 1/9 & 1/4 & 1/8 & 1/5 \end{bmatrix} \tag{4-13} $$

While the given function (4-3) is symmetric with respect to $x = 0$ the absolute values for the entries in the right hand side are also equal for elements mirrored at $x = 0$, with

$$ |{}^{1}\mathbf{n}| = |{}^{3}\mathbf{n}| = \begin{bmatrix} 0.797\,961\,310\,921\,639 \\ 0.365\,984\,483\,528\,582 \\ 0.229\,825\,889\,790\,003 \\ 0.350\,103\,493\,838\,381 \\ 0.150\,796\,269\,875\,836 \\ 0.214\,341\,565\,866\,359 \end{bmatrix} \tag{4-14} $$

and

$$|^2\mathbf{n}| = |^4\mathbf{n}| = \begin{bmatrix} 0.956\,196\,026\,034\,606 \\ 0.481\,745\,052\,176\,112 \\ 0.322\,197\,377\,003\,143 \\ 0.467\,200\,192\,747\,361 \\ 0.236\,326\,734\,438\,577 \\ 0.307\,123\,841\,908\,079 \end{bmatrix}. \tag{4-15}$$

The algebraic sign for each entry of the right hand sides are as follows

$$^1\mathbf{n}_{\text{sign}} = \begin{bmatrix} + \\ - \\ + \\ - \\ + \\ + \end{bmatrix}, \; ^2\mathbf{n}_{\text{sign}} = \begin{bmatrix} + \\ + \\ + \\ - \\ - \\ + \end{bmatrix}, \; ^3\mathbf{n}_{\text{sign}} = \begin{bmatrix} + \\ - \\ + \\ + \\ - \\ + \end{bmatrix}, \; ^4\mathbf{n}_{\text{sign}} = \begin{bmatrix} + \\ + \\ + \\ + \\ + \\ + \end{bmatrix} \tag{4-16}$$

and for the entries in the normal matrices (4-13) the algebraic signs are given by

$$^\zeta\mathbf{N}_{\text{sign}} = {}^\zeta\mathbf{n}_{\text{sign}} {}^\zeta\mathbf{n}_{\text{sign}}^\mathsf{T}. \tag{4-17}$$

The four normal equation systems are combined to a single one as follows

$$\begin{bmatrix} ^1\mathbf{N} & \mathbf{0} & \mathbf{0} & \mathbf{0} \\ \mathbf{0} & ^2\mathbf{N} & \mathbf{0} & \mathbf{0} \\ \mathbf{0} & \mathbf{0} & ^3\mathbf{N} & \mathbf{0} \\ \mathbf{0} & \mathbf{0} & \mathbf{0} & ^4\mathbf{N} \end{bmatrix} \begin{bmatrix} ^1\mathbf{x} \\ ^2\mathbf{x} \\ ^3\mathbf{x} \\ ^3\mathbf{x} \end{bmatrix} = \begin{bmatrix} ^1\mathbf{n} \\ ^2\mathbf{n} \\ ^3\mathbf{n} \\ ^4\mathbf{n} \end{bmatrix} \tag{4-18}$$

or in shorter notation

$$\mathbf{N}\,\mathbf{x} = \mathbf{n}\,, \tag{4-19}$$

while $\mathbf{x}$ contains the unknowns parameters of a polynomial of 2nd degree for all four elements. In order to obtain a continuous approximation, we introduce constraints at nodes connecting two or more elements as already described in (3.1.2). As the colour for the nodes in Figure 4-8 indicates the number of constraints, we have to introduce for nodes in white = 0, for nodes in blue = 1 and for nodes in red = 3 constraints. According to Figure 4-8 and Table 4-2 the constraints between the polynomials (4-2) at these nodes are

$\nu = 2$:

$$^1P_2(^1x_{\nu_2}, {}^1y_{\nu_2}) - {}^2P_2(^2x_{\nu_1}, {}^2y_{\nu_1}) = 0\,, \tag{4-20}$$

$\nu = 4$:

$$^1P_2(^1x_{\nu_3}, {}^1y_{\nu_3}) - {}^3P_2(^3x_{\nu_1}, {}^3y_{\nu_1}) = 0\,, \tag{4-21}$$

$\nu = 5$:

$$\begin{aligned} ^1P_2(^1x_{\nu_4}, {}^1y_{\nu_4}) - {}^2P_2(^2x_{\nu_3}, {}^2y_{\nu_3}) &= 0\,, \\ ^1P_2(^1x_{\nu_4}, {}^1y_{\nu_4}) - {}^3P_2(^3x_{\nu_2}, {}^3y_{\nu_2}) &= 0\,, \\ ^1P_2(^1x_{\nu_4}, {}^1y_{\nu_4}) - {}^4P_2(^4x_{\nu_1}, {}^4y_{\nu_1}) &= 0\,, \end{aligned} \tag{4-22}$$

$\nu = 6$:

$$^2P_2(^2x_{\nu_4}, {}^2y_{\nu_4}) - {}^4P_2(^4x_{\nu_2}, {}^4y_{\nu_2}) = 0\,, \tag{4-23}$$

and for $\nu = 8$:

$$ {}^{3}P_2({}^{3}x_{\nu_4}, {}^{3}y_{\nu_4}) - {}^{4}P_2({}^{4}x_{\nu_3}, {}^{4}y_{\nu_3}) = 0\,. \tag{4-24} $$

As an example the costraint for (4-20) explicitly reads

$$ \begin{aligned} &{}^{1}c_0 + {}^{1}c_1\,{}^{1}y_{\nu_2} + {}^{1}c_2\,{}^{1}y_{\nu_2}^2 + {}^{1}c_3\,{}^{1}x_{\nu_2} + {}^{1}c_4\,{}^{1}x_{\nu_2}\,{}^{1}y_{\nu_2} + {}^{1}c_5\,{}^{1}x_{\nu_2}^2 \\ &\quad - \left({}^{2}c_0 + {}^{2}c_1\,{}^{2}y_{\nu_1} + {}^{2}c_2\,{}^{2}y_{\nu_1}^2 + {}^{2}c_3\,{}^{2}x_{\nu_1} + {}^{2}c_4\,{}^{2}x_{\nu_1}\,{}^{2}y_{\nu_1} + {}^{2}c_5\,{}^{2}x_{\nu_1}^2\right) = 0\,. \end{aligned} \tag{4-25} $$

Rewriting the seven constraints (4-20) to (4-24) in matrix notation

$$ \mathbf{C}\,\mathbf{x} = \mathbf{c} \qquad \text{with} \qquad \mathbf{c} = \mathbf{0} \tag{4-26} $$

and inserting the coordinates of nodes from Table 4-2 yields

$$ \mathbf{C} = \begin{bmatrix} 1 & 0 & 0 & -1 & 0 & 1 & -1 & 0 & 0 & 1 & 0 & -1 & 0 & 0 & 0 & 0 & 0 & 0 & 0 & 0 & 0 & 0 & 0 \\ 1 & -1 & 1 & 0 & 0 & 0 & 0 & 0 & 0 & 0 & 0 & 0 & -1 & 1 & -1 & 0 & 0 & 0 & 0 & 0 & 0 & 0 & 0 \\ 0 & 0 & 0 & 0 & 0 & 0 & 0 & 0 & 0 & 0 & 0 & 0 & 1 & 0 & 0 & 0 & 0 & 0 & -1 & 0 & 0 & 0 & 0 \\ 0 & 0 & 0 & 0 & 0 & 0 & 1 & 0 & 0 & 0 & 0 & 0 & 0 & 0 & 0 & 0 & 0 & 0 & -1 & 0 & 0 & 0 & 0 \\ 1 & 0 & 0 & 0 & 0 & 0 & 0 & 0 & 0 & 0 & 0 & 0 & 0 & 0 & 0 & 0 & 0 & 0 & -1 & 0 & 0 & 0 & 0 \\ 0 & 0 & 0 & 0 & 0 & 0 & 1 & 1 & 1 & 0 & 0 & 0 & 0 & 0 & 0 & 0 & 0 & 0 & -1 & -1 & -1 & 0 & 0 \\ 0 & 0 & 0 & 0 & 0 & 0 & 0 & 0 & 0 & 0 & 0 & 0 & 1 & 0 & 0 & 1 & 0 & 1 & -1 & 0 & 0 & -1 & 0 \end{bmatrix} \tag{4-27} $$

Extending the normal equation system (4-19)

$$ \begin{bmatrix} \mathbf{N} & \mathbf{C}^{\mathsf{T}} \\ \mathbf{C} & \mathbf{0} \end{bmatrix} \begin{bmatrix} \mathbf{x} \\ \boldsymbol{\lambda} \end{bmatrix} = \begin{bmatrix} \mathbf{n} \\ \mathbf{0} \end{bmatrix} \tag{4-28} $$

and its solution yields the unknown parameters of a two-dimensional polynomial of 2nd degree for all elements

$$ \begin{aligned} \begin{bmatrix} {}^{1}c_0 \\ {}^{1}c_1 \\ {}^{1}c_2 \\ {}^{1}c_3 \\ {}^{1}c_4 \\ {}^{1}c_5 \end{bmatrix} &= \begin{bmatrix} 0.918\,692\,574\,762\,579 \\ -0.554\,136\,455\,301\,609 \\ -0.473\,688\,826\,744\,928 \\ -0.290\,392\,910\,713\,106 \\ -0.991\,210\,870\,907\,134 \\ -0.402\,288\,988\,764\,597 \end{bmatrix}, \quad \begin{bmatrix} {}^{2}c_0 \\ {}^{2}c_1 \\ {}^{2}c_2 \\ {}^{2}c_3 \\ {}^{2}c_4 \\ {}^{2}c_5 \end{bmatrix} = \begin{bmatrix} 0.918\,692\,574\,762\,579 \\ 0.189\,589\,873\,414\,247 \\ -0.128\,719\,468\,646\,491 \\ -0.111\,985\,010\,531\,353 \\ -0.004\,195\,617\,695\,992 \\ -0.223\,881\,088\,582\,844 \end{bmatrix}, \\ \begin{bmatrix} {}^{3}c_0 \\ {}^{3}c_1 \\ {}^{3}c_2 \\ {}^{3}c_3 \\ {}^{3}c_4 \\ {}^{3}c_5 \end{bmatrix} &= \begin{bmatrix} 0.918\,692\,574\,762\,579 \\ -0.554\,136\,455\,301\,626 \\ -0.473\,688\,826\,744\,945 \\ 0.290\,392\,910\,713\,097 \\ 0.991\,210\,870\,907\,132 \\ -0.402\,288\,988\,764\,592 \end{bmatrix}, \quad \begin{bmatrix} {}^{4}c_0 \\ {}^{4}c_1 \\ {}^{4}c_2 \\ {}^{4}c_3 \\ {}^{4}c_4 \\ {}^{4}c_5 \end{bmatrix} = \begin{bmatrix} 0.918\,692\,574\,762\,579 \\ 0.189\,589\,873\,414\,254 \\ -0.128\,719\,468\,646\,497 \\ 0.111\,985\,010\,531\,362 \\ 0.004\,195\,617\,695\,991 \\ -0.223\,881\,088\,582\,857 \end{bmatrix}. \end{aligned} \tag{4-29} $$

The resulting approximation of (4-3) with $N = 4$ elements using quadratic polynomials and the residual function is depicted Figure 4-9.

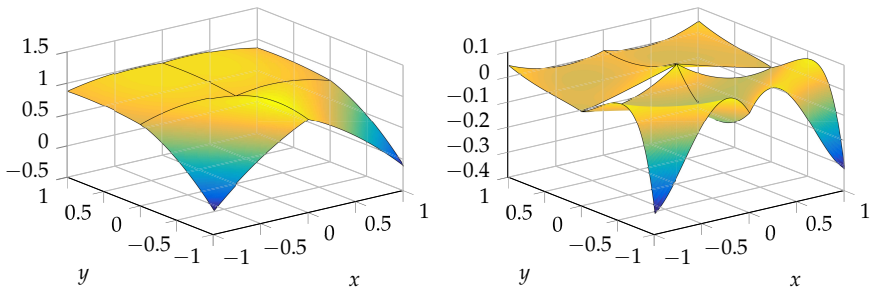

Figure 4-9: Polynomial approximation of function (4-3) with $N = 4$ elements using quadratic polynomials (left). Residual function $v(x, y) = \cos\left(x/(y+1.5)\right) - \sum_{\zeta=1}^{4} {}^{\zeta}P_2(x, y)$ (right).

As one can see in Figure 4-9 (left), $\sum_{\zeta=1}^{4} {}^{\zeta}P_2(x,y)$ is only a very coarse approximation of function (4-3) with the largest deviations at the two corners for $y = -1$. The nodes of neighboured elements are connected but the residual function in Figure 4-9 (right) also shows discontinuities along their edges for $y = 0$.

While dealing with an elementwise approximation of two-dimensional functions we face some problems which do not occur in the one-dimensional case. To introduce constraints at nodes in order to obtain a C^n continuous approximation, as we did for the one-dimensional case, is no longer sufficient. In general, a continuous approximation for any number of elements and arbitrary polynomial degree can not be guaranteed any more. In this way, one must always define a suitable polynomial for a certain element, for instance, triangle or rectangle and desired C^n continuity. In the presented example of using rectangular elements and introducing constraints to enforce C^0 continuity only

$$ {}^{\zeta}P_1 = {}^{\zeta}c_0 + {}^{\zeta}c_1 x + {}^{\zeta}c_2 y + {}^{\zeta}c_3 xy \tag{4-30} $$

would always yield a continuous approximation for any number of elements. One loses the flexibility of choosing an arbitrary number of rectangular elements and of any polynomial degree.

4.2 ELEMENTWISE CONTINUOUS APPROXIMATION

As we have seen in the previous section, introducing constraints at nodes to achieve an elementwise C^n continuous approximation is only suitable for a certain typ of element and an appropriate polynomial. In order to keep the flexibility of choosing any typ of element and an arbitrary polynomial degree, two slightly different approaches for defining appropriate constraints will be presented and are referred in this thesis as

- Node based and
- Edge based approach.

The node based approach is simply an extension of the concept to enforce continuity by introducing constraints at nodes connecting elements, as already shown in Section 3.1.2. The basic idea of this approach is also widely used in the finite element method to derive higher order elements, see e.g. (ZIENKIEWICZ *et al.* 2013, p. 153). In contrast, the edge based approach has been developed in this thesis only out of pure curiosity. The motivation behind this was to obtain continuity between elements not by introducing constraints at discrete points, but rather continuously along common edges. Both approaches are discussed in detail in the following sections.

4.2.1 *Node based approach*

Perhaps the simplest way to obtain a continuous approximation is to introduce additional constraints at auxiliary nodes along an edge connecting two elements. As an illustration we consider the same example as in Section 4.1, while approximating function (4-3) by $N = 4$ elements using polynomials of 2^{nd} degree. The curve along an edge connecting two elements is a cross section of ${}^{\zeta}P_2(x,y)$ and therefore also a polynomial of 2^{nd} degree. So far, two connec-

ted elements are sharing two nodes and while any polynomial of 2nd degree is uniquely described by three different points, we only have to introduce one further auxiliary node on the edge connecting two elements. For convenience we introduced the auxiliary nodes in the middle on the edges as depicted in Figure 4-10 (left).

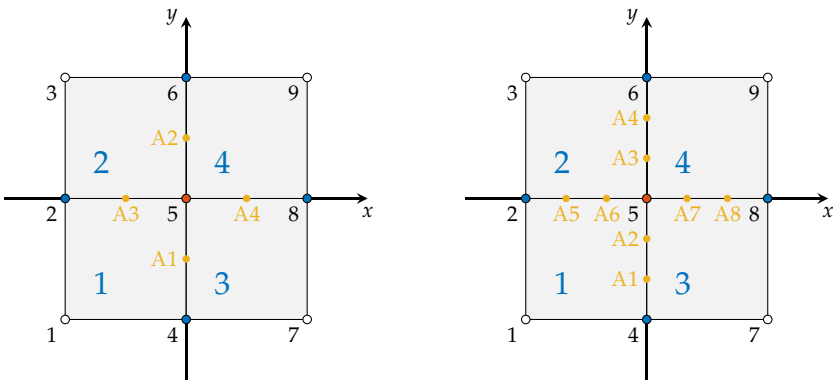

Figure 4-10: Placement of the auxiliary nodes (yellow) for an continuous elementwise polynomial approximation. For polynomials of 2nd degree we have to introduce four auxiliary nodes (left) and for polynomials of 3rd degree eight auxiliary nodes (right). Elements are highlighted in light grey and numbered in blue and nodes in black

Figure 4-10 illustrates the placement of the auxiliary nodes while using polynomials of 2nd degree (left) and also for 3rd degree (right). With increasing polynomial degree we have to introduce more auxiliary nodes accordingly. For our example we only need to introduce four auxiliary nodes as depicted in Figure 4-10 (left). The coordinates of these nodes are listed in Table 4-3.

Table 4-3: Tables for the coordinates of the auxiliary nodes as illustrated in Figure 4-10 (left).

Auxiliary nodes

ν	x_ν	y_ν
A1	0.0	−0.5
A2	0.0	0.5
A3	−0.5	0.0
A4	0.5	0.0

For each of these auxiliary nodes we have to introduce one additional constraint and according to Table 4-3 and Figure 4-10 these constraints are

$\nu = \text{A1}$:

$$ {}^1P_2(x_{\text{A1}}, y_{\text{A1}}) - {}^3P_2(x_{\text{A1}}, y_{\text{A1}}) = 0\,, \tag{4-31} $$

$\nu = \text{A2}$:

$$ {}^2P_2(x_{\text{A2}}, y_{\text{A2}}) - {}^4P_2(x_{\text{A2}}, y_{\text{A2}}) = 0\,, \tag{4-32} $$

$\nu = \text{A3}$:

$$ {}^1P_2(x_{\text{A3}}, y_{\text{A3}}) - {}^2P_2(x_{\text{A3}}, y_{\text{A3}}) = 0\,, \tag{4-33} $$

$\nu = \text{A4}$:

$$ {}^3P_3(x_{\text{A4}}, y_{\text{A4}}) - {}^4P_2(x_{\text{A4}}, y_{\text{A4}}) = 0\,. \tag{4-34} $$

As an example the constraint for (4-31) explicitly reads

$$ \begin{aligned} &\left[{}^1c_0 + {}^1c_1\, y_{\text{A1}} + {}^1c_2\, y_{\text{A1}}^2 + {}^1c_3\, x_{\text{A1}} + {}^1c_4\, x_{\text{A1}}\, y_{\text{A1}} + {}^1c_5\, x_{\text{A1}}^2\right] - \\ &\quad - \left[{}^3c_0 + {}^3c_1\, y_{\text{A1}} + {}^3c_2\, y_{\text{A1}}^2 + {}^3c_3\, x_{\text{A1}} + {}^3c_4\, x_{\text{A1}}\, y_{\text{A1}} + {}^3c_5\, x_{\text{A1}}^2\right] = 0, \end{aligned} \tag{4-35} $$

Rewriting the four constraints (4-31) to (4-34) in matrix notation

$$ \mathbf{C}_{\text{A}}\, \mathbf{x} = \mathbf{c}_{\text{A}} \qquad \text{with} \qquad \mathbf{c}_{\text{A}} = \mathbf{0} \tag{4-36} $$

and inserting the coordinates of nodes from Table 4-2 yields

$$\mathbf{C}_\mathrm{A} = \begin{bmatrix} 1 & -\frac{1}{2} & \frac{1}{4} & 0 & 0 & 0 & 0 & 0 & 0 & 0 & 0 & -1 & \frac{1}{2} & -\frac{1}{4} & 0 & 0 & 0 & 0 & 0 & 0 & 0 & 0 & 0 \\ 0 & 0 & 0 & 0 & 0 & 0 & 1 & \frac{1}{2} & \frac{1}{4} & 0 & 0 & 0 & 0 & 0 & 0 & 0 & 0 & -1 & -\frac{1}{2} & -\frac{1}{4} & 0 & 0 & 0 \\ 1 & 0 & 0 & -\frac{1}{2} & 0 & \frac{1}{4} & -1 & 0 & 0 & \frac{1}{2} & 0 & -\frac{1}{4} & 0 & 0 & 0 & 0 & 0 & 0 & 0 & 0 & 0 & 0 & 0 \\ 0 & 0 & 0 & 0 & 0 & 0 & 0 & 0 & 0 & 0 & 0 & 1 & 0 & 0 & \frac{1}{2} & 0 & \frac{1}{4} & -1 & 0 & 0 & -\frac{1}{2} & 0 & -\frac{1}{4} \end{bmatrix} \tag{4-37}$$

Adding the constraints (4-37) to (4-27)

$$\mathbf{C}_\mathrm{ext} = \begin{bmatrix} \mathbf{C} \\ \mathbf{C}_\mathrm{A} \end{bmatrix} \tag{4-38}$$

yields in total 11 constraints, which can be used to extend the normal equation system (4-19)

$$\begin{bmatrix} \mathbf{N} & \mathbf{C}_\mathrm{ext}^\mathsf{T} \\ \mathbf{C}_\mathrm{ext} & \mathbf{0} \end{bmatrix} \begin{bmatrix} \mathbf{x} \\ \boldsymbol{\lambda} \end{bmatrix} = \begin{bmatrix} \mathbf{n} \\ \mathbf{0} \end{bmatrix} . \tag{4-39}$$

Solving (4-39) yields the unknowns parameters of ${}^{\zeta}P_2(x,y)$ for each element of an continuous approximation of function (4-3)

$$\begin{bmatrix} {}^1c_0 \\ {}^1c_1 \\ {}^1c_2 \\ {}^1c_3 \\ {}^1c_4 \\ {}^1c_5 \end{bmatrix} = \begin{bmatrix} 0.918\,692\,574\,762\,582 \\ -0.613\,605\,755\,362\,188 \\ -0.523\,246\,576\,795\,413 \\ -0.201\,188\,960\,622\,225 \\ -0.991\,210\,870\,907\,130 \\ -0.313\,085\,038\,673\,720 \end{bmatrix}, \begin{bmatrix} {}^2c_0 \\ {}^2c_1 \\ {}^2c_2 \\ {}^2c_3 \\ {}^2c_4 \\ {}^2c_5 \end{bmatrix} = \begin{bmatrix} 0.918\,692\,574\,762\,582 \\ 0.130\,120\,573\,353\,657 \\ -0.079\,161\,718\,596\,000 \\ -0.201\,188\,960\,622\,225 \\ -0.004\,195\,617\,695\,996 \\ -0.313\,085\,038\,673\,719 \end{bmatrix},$$

$$\begin{bmatrix} {}^3c_0 \\ {}^3c_1 \\ {}^3c_2 \\ {}^3c_3 \\ {}^3c_4 \\ {}^3c_5 \end{bmatrix} = \begin{bmatrix} 0.918\,692\,574\,762\,582 \\ -0.613\,605\,755\,362\,188 \\ -0.523\,246\,576\,795\,412 \\ 0.201\,188\,960\,622\,226 \\ 0.991\,210\,870\,907\,130 \\ -0.313\,085\,038\,673\,721 \end{bmatrix}, \begin{bmatrix} {}^4c_0 \\ {}^4c_1 \\ {}^4c_2 \\ {}^4c_3 \\ {}^4c_4 \\ {}^4c_5 \end{bmatrix} = \begin{bmatrix} 0.918\,692\,574\,762\,582 \\ 0.130\,120\,573\,353\,656 \\ -0.079\,161\,718\,595\,999 \\ 0.201\,188\,960\,622\,226 \\ 0.004\,195\,617\,695\,996 \\ -0.313\,085\,038\,673\,721 \end{bmatrix} . \tag{4-40}$$

The resulting continuous approximation of (4-3) with $N = 4$ elements using quadratic polynomials and the residual function is depicted Figure 4-11.

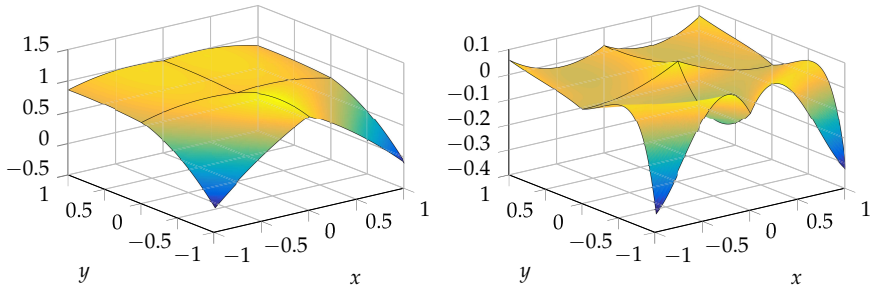

Figure 4-11: Continuous approximation of function (4-3) with $N = 4$ elements using quadratic polynomials (left). Residual function $v(x,y) = \cos\left({}^{x}/_{(y+1.5)}\right) - \sum_{\zeta=1}^{4} {}^{\zeta}P_2(x,y)$ (right).

In direct comparison to Figure 4-9 (right) the residual function depicted in Figure 4-11 (right) does not reveal any discontinuities. In addition, it has also been proven numerically that two connected elements are always describing exactly the same curve along their edge. The approximation is C^0 continuous within machine precision.

4.2.2 *Edge based approach*

In the following we will derive a continuous approximation of functions in two dimensions, while introducing constraints for edges connecting two elements. To illustrated the procedure we use the same example as in Section 4.1 and approximate function (4-3) by $N = 4$ elements using polynomials of 2^{nd} degree. The alignment of the elements is depicted in Figure 4-12.

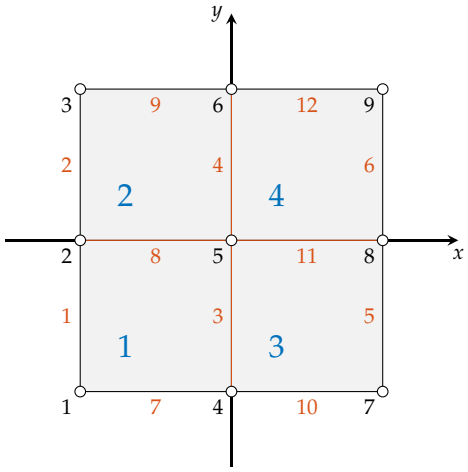

Figure 4-12: Alignment of the elements and position of the nodes. Elements are highlighted in light grey and numbered in blue, edges in red and nodes in black. To enforce continuity between elements, we need to introduce constraints for edges coloured in red.

Based on Figure 4-12 we define a unique identifier for nodes, edges and elements, which can be stored in the following tables.

Table 4-4: Tables for the nodes, edges and elements as illustrated in Figure 4-12.

Nodes

ν	x_ν	y_ν
1	−1.0	−1.0
2	−1.0	0.0
3	−1.0	1.0
4	0.0	−1.0
5	0.0	0.0
6	0.0	1.0
7	1.0	−1.0
8	1.0	0.0
9	1.0	1.0

Edges

ϵ	ν_1	ν_2
1	1	2
2	2	3
3	4	5
4	5	6
5	7	8
6	8	9
7	1	4
8	2	5
9	3	6
10	4	7
11	5	8
12	6	9

Elements

ζ	ϵ_1	ϵ_2	ϵ_3	ϵ_4
1	1	3	7	8
2	2	4	8	9
3	3	5	10	11
4	4	6	11	12

The alignment of the elements as well as the definition of the nodes is exactly the same as for the example in Section 4.1. Therefore, we can also use the same normal equation system (4-18) and we only have to introduce constraints for edges connecting two elements in order to achieve a C^0 continuous approximation. For this example we have to introduce constraints for the four edges coloured in red in Figure 4-12.

The basic idea is to enforce connected elements to share the same curve along their edge. Each edge ϵ is uniquely defined by its starting and end node ${}^{\epsilon}\nu_1$ and ${}^{\epsilon}\nu_2$ according to Table 4-4. The curve is in general a cross section of ${}^{\zeta}P_p(x, y)$ and therefore a univariate function. In order to describe the curve

we transform each edge onto a generalised edge, represented by a single generalised coordinate u. This can be done in the same way as for the transformation of a 1D element, described in Section 3.2.1.1. Figure 4-13 illustrates the transformation.

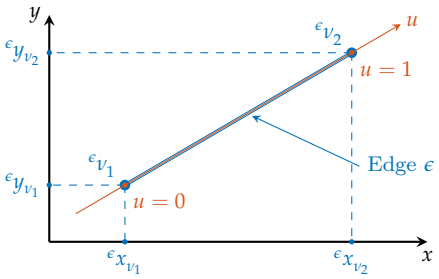

Figure 4-13: Transformation of the coordinates of the edge

Each edge ϵ within the $x,y-$plane is described by its coordinates ${}^{\epsilon}x_{\mathrm{e}}$ and ${}^{\epsilon}y_{\mathrm{e}}$, which can be expressed as a function of the generalised coordinate u by applying transformation (3-69). These coordinates are

$$\begin{aligned} {}^{\epsilon}x_{\mathrm{e}} &= {}^{\epsilon}x_{\nu_1} + \left({}^{\epsilon}x_{\nu_2} - {}^{\epsilon}x_{\nu_1}\right)u\,, \\ {}^{\epsilon}y_{\mathrm{e}} &= {}^{\epsilon}y_{\nu_1} + \left({}^{\epsilon}y_{\nu_2} - {}^{\epsilon}y_{\nu_1}\right)u\,, \end{aligned} \tag{4-41}$$

with $u \in [0,1]$. Let us assume that two neighboured elements ζ_1 and ζ_2 are sharing the same edge ϵ_1. The curve along this edge described by element ζ_1 for a polynomial of 2^{nd} degree reads

$$\begin{aligned} {}^{\zeta_1}P_2\left({}^{\epsilon_1}x_{\mathrm{e}}, {}^{\epsilon_1}y_{\mathrm{e}}\right) = {}^{\zeta_1}c_0 + {}^{\zeta_1}c_1\,{}^{\epsilon_1}y_{\mathrm{e}} + {}^{\zeta_1}c_2\,{}^{\epsilon_1}y_{\mathrm{e}}^2 + {}^{\zeta_1}c_3\,{}^{\epsilon_1}x_{\mathrm{e}} + \\ + {}^{\zeta_1}c_4\,{}^{\epsilon_1}x_{\mathrm{e}}\,{}^{\epsilon_1}y_{\mathrm{e}} + {}^{\zeta_1}c_5\,{}^{\epsilon_1}x_{\mathrm{e}}^2\,. \end{aligned} \tag{4-42}$$

Inserting (4-41) into (4-42) yields

$$\begin{aligned} {}^{\zeta_1}P_2(u) = {}^{\zeta_1}c_0 + {}^{\zeta_1}c_1 \left({}^{\epsilon_1}y_{\nu_1} + \left({}^{\epsilon_1}y_{\nu_2} - {}^{\epsilon_1}y_{\nu_1}\right)u\right) + \\ + {}^{\zeta_1}c_2 \left({}^{\epsilon_1}y_{\nu_1} + \left({}^{\epsilon_1}y_{\nu_2} - {}^{\epsilon_1}y_{\nu_1}\right)u\right)^2 + \\ + {}^{\zeta_1}c_3 \left({}^{\epsilon_1}x_{\nu_1} + \left({}^{\epsilon_1}x_{\nu_2} - {}^{\epsilon_1}x_{\nu_1}\right)u\right) + \\ + {}^{\zeta_1}c_4 \left({}^{\epsilon_1}x_{\nu_1} + \left({}^{\epsilon_1}x_{\nu_2} - {}^{\epsilon_1}x_{\nu_1}\right)u\right)\left({}^{\epsilon_1}y_{\nu_1} + \left({}^{\epsilon_1}y_{\nu_2} - {}^{\epsilon_1}y_{\nu_1}\right)u\right) + \\ + {}^{\zeta_1}c_5 \left({}^{\epsilon_1}x_{\nu_1} + \left({}^{\epsilon_1}x_{\nu_2} - {}^{\epsilon_1}x_{\nu_1}\right)u\right)^2. \end{aligned} \tag{4-43}$$

While the coordinates of the starting and end node of edge ϵ_1 are constants the polynomial in (4-43) is only a function of u and simplifies to

$${}^{\zeta_1}P_2(u) = {}^{\zeta_1}d_0 + {}^{\zeta_1}d_1\,u + {}^{\zeta_1}d_2\,u^2\,, \tag{4-44}$$

with

$$\begin{aligned} {}^{\zeta_1}d_0 &= {}^{\zeta_1}c_0 + {}^{\zeta_1}c_1\,{}^{\epsilon_1}y_{\nu_1} + {}^{\zeta_1}c_2\,{}^{\epsilon_1}y_{\nu_1}^2 + {}^{\zeta_1}c_3\,{}^{\epsilon_1}x_{\nu_1} + \\ &\quad + {}^{\zeta_1}c_4\,{}^{\epsilon_1}x_{\nu_1}\,{}^{\epsilon_1}y_{\nu_1} + {}^{\zeta_1}c_5\,{}^{\epsilon_1}x_{\nu_1}^2\,, \\ {}^{\zeta_1}d_1 &= {}^{\zeta_1}c_1\left({}^{\epsilon_1}y_{\nu_2} - {}^{\epsilon_1}y_{\nu_1}\right) + 2\,{}^{\zeta_1}c_2\,{}^{\epsilon_1}y_{\nu_1}\left({}^{\epsilon_1}y_{\nu_2} - {}^{\epsilon_1}y_{\nu_1}\right) + \\ &\quad + {}^{\zeta_1}c_3\left({}^{\epsilon_1}x_{\nu_2} - {}^{\epsilon_1}x_{\nu_1}\right) + {}^{\zeta_1}c_4\,{}^{\epsilon_1}y_{\nu_1}\left({}^{\epsilon_1}x_{\nu_2} - {}^{\epsilon_1}x_{\nu_1}\right) + \\ &\quad + {}^{\zeta_1}c_4\,{}^{\epsilon_1}x_{\nu_1}\left({}^{\epsilon_1}y_{\nu_2} - {}^{\epsilon_1}y_{\nu_1}\right) + 2\,{}^{\zeta_1}c_5\,{}^{\epsilon_1}x_{\nu_1}\left({}^{\epsilon_1}x_{\nu_2} - {}^{\epsilon_1}x_{\nu_1}\right), \\ {}^{\zeta_1}d_2 &= {}^{\zeta_1}c_2\left({}^{\epsilon_1}y_{\nu_2} - {}^{\epsilon_1}y_{\nu_1}\right)^2 + {}^{\zeta_1}c_4\left({}^{\epsilon_1}x_{\nu_2} - {}^{\epsilon_1}x_{\nu_1}\right)\left({}^{\epsilon_1}y_{\nu_2} - {}^{\epsilon_1}y_{\nu_1}\right) + \\ &\quad + {}^{\zeta_1}c_5\left({}^{\epsilon_1}x_{\nu_2} - {}^{\epsilon_1}x_{\nu_1}\right)^2. \end{aligned} \tag{4-45}$$

The same curve along edge ϵ_1 described by element ζ_2 reads

$$\begin{aligned}{}^{\zeta_2}P_2\left({}^{\epsilon_1}x_\mathrm{e}, {}^{\epsilon_1}y_\mathrm{e}\right) = {}^{\zeta_2}c_0 + {}^{\zeta_2}c_1\,{}^{\epsilon_1}y_\mathrm{e} + {}^{\zeta_2}c_2\,{}^{\epsilon_1}y_\mathrm{e}^2 + {}^{\zeta_2}c_3\,{}^{\epsilon_1}x_\mathrm{e} + \\ + {}^{\zeta_2}c_4\,{}^{\epsilon_1}x_\mathrm{e}\,{}^{\epsilon_1}y_\mathrm{e} + {}^{\zeta_2}c_5\,{}^{\epsilon_1}x_\mathrm{e}^2\,.\end{aligned} \tag{4-46}$$

Inserting (4-41) into (4-46) and rearranging yields

$${}^{\zeta_2}P_2(u) = {}^{\zeta_2}d_0 + {}^{\zeta_2}d_1\,u + {}^{\zeta_2}d_2\,u^2\,, \tag{4-47}$$

with

$$\begin{aligned}{}^{\zeta_2}d_0 &= {}^{\zeta_2}c_0 + {}^{\zeta_2}c_1\,{}^{\epsilon_1}y_{\nu_1} + {}^{\zeta_2}c_2\,{}^{\epsilon_1}y_{\nu_1}^2 + {}^{\zeta_2}c_3\,{}^{\epsilon_1}x_{\nu_1} + \\ &\quad + {}^{\zeta_2}c_4\,{}^{\epsilon_1}x_{\nu_1}\,{}^{\epsilon_1}y_{\nu_1} + {}^{\zeta_2}c_5\,{}^{\epsilon_1}x_{\nu_1}^2\,, \\ {}^{\zeta_2}d_1 &= {}^{\zeta_2}c_1\left({}^{\epsilon_1}y_{\nu_2} - {}^{\epsilon_1}y_{\nu_1}\right) + 2\,{}^{\zeta_2}c_2\,{}^{\epsilon_1}y_{\nu_1}\left({}^{\epsilon_1}y_{\nu_2} - {}^{\epsilon_1}y_{\nu_1}\right) + \\ &\quad + {}^{\zeta_2}c_3\left({}^{\epsilon_1}x_{\nu_2} - {}^{\epsilon_1}x_{\nu_1}\right) + {}^{\zeta_2}c_4\,{}^{\epsilon_1}y_{\nu_1}\left({}^{\epsilon_1}x_{\nu_2} - {}^{\epsilon_1}x_{\nu_1}\right) + \\ &\quad + {}^{\zeta_2}c_4\,{}^{\epsilon_1}x_{\nu_1}\left({}^{\epsilon_1}y_{\nu_2} - {}^{\epsilon_1}y_{\nu_1}\right) + 2\,{}^{\zeta_2}c_5\,{}^{\epsilon_1}x_{\nu_1}\left({}^{\epsilon_1}x_{\nu_2} - {}^{\epsilon_1}x_{\nu_1}\right), \\ {}^{\zeta_2}d_2 &= {}^{\zeta_2}c_2\left({}^{\epsilon_1}y_{\nu_2} - {}^{\epsilon_1}y_{\nu_1}\right)^2 + {}^{\zeta_2}c_4\left({}^{\epsilon_1}x_{\nu_2} - {}^{\epsilon_1}x_{\nu_1}\right)\left({}^{\epsilon_1}y_{\nu_2} - {}^{\epsilon_1}y_{\nu_1}\right) + \\ &\quad + {}^{\zeta_2}c_5\left({}^{\epsilon_1}x_{\nu_2} - {}^{\epsilon_1}x_{\nu_1}\right)^2.\end{aligned} \tag{4-48}$$

To enforce continuity between element ζ_1 and ζ_2 along edge ϵ_1 the two polynomials (4-44) and (4-47) must be equal

$$\begin{aligned}{}^{\zeta_1}P_2(u) &= {}^{\zeta_2}P_2(u)\,, \\ {}^{\zeta_1}d_0 + {}^{\zeta_1}d_1\,u + {}^{\zeta_1}d_2\,u^2 &= {}^{\zeta_2}d_0 + {}^{\zeta_2}d_1\,u + {}^{\zeta_2}d_2\,u^2\,.\end{aligned} \tag{4-49}$$

This is fulfilled, if their coefficients are equal. Hence, we get the following three constraints

$$\begin{aligned}{}^{\zeta_1}d_0 - {}^{\zeta_2}d_0 &= 0\,, \\ {}^{\zeta_1}d_1 - {}^{\zeta_2}d_1 &= 0\,, \\ {}^{\zeta_1}d_2 - {}^{\zeta_2}d_2 &= 0\,.\end{aligned} \tag{4-50}$$

For the example of approximating function (4-3) by $N = 4$ elements as aligned in Figure 4-12 and based on the tables for nodes, edges and elements in Table 4-4 the constraints (4-50) with (4-45) and (4-48) have to be introduced for each edge connecting two elements. For edge $\epsilon = 3$ these constraints are

$$\begin{aligned}{}^{1}d_0 - {}^{3}d_0 &= 0\,, \\ {}^{1}d_1 - {}^{3}d_1 &= 0\,, \\ {}^{1}d_2 - {}^{3}d_2 &= 0\end{aligned} \tag{4-51}$$

and inserting (4-45) and (4-48) yields

$$\begin{aligned}&\left[{}^{1}c_0 + {}^{1}c_1\,{}^{3}y_{\nu_1} + {}^{1}c_2\,{}^{3}y_{\nu_1}^2 + {}^{1}c_3\,{}^{3}x_{\nu_1} + {}^{1}c_4\,{}^{3}x_{\nu_1}\,{}^{3}y_{\nu_1} + {}^{1}c_5\,{}^{3}x_{\nu_1}^2\right] - \\ &\quad - \left[{}^{3}c_0 + {}^{3}c_1\,{}^{3}y_{\nu_1} + {}^{3}c_2\,{}^{3}y_{\nu_1}^2 + {}^{3}c_3\,{}^{3}x_{\nu_1} + {}^{3}c_4\,{}^{3}x_{\nu_1}\,{}^{3}y_{\nu_1} + {}^{3}c_5\,{}^{3}x_{\nu_1}^2\right] = 0,\end{aligned} \tag{4-52}$$

$$\begin{aligned}&\left[{}^{1}c_1\left({}^{3}y_{\nu_2} - {}^{3}y_{\nu_1}\right) + 2\,{}^{1}c_2\,{}^{3}y_{\nu_1}\left({}^{3}y_{\nu_2} - {}^{3}y_{\nu_1}\right) + {}^{1}c_3\left({}^{3}x_{\nu_2} - {}^{3}x_{\nu_1}\right) + \right. \\ &\quad + {}^{1}c_4\,{}^{3}y_{\nu_1}\left({}^{3}x_{\nu_2} - {}^{3}x_{\nu_1}\right) + {}^{1}c_4\,{}^{3}x_{\nu_1}\left({}^{3}y_{\nu_2} - {}^{3}y_{\nu_1}\right) + 2\,{}^{1}c_5\,{}^{3}x_{\nu_1}\left({}^{3}x_{\nu_2} - {}^{3}x_{\nu_1}\right)\Big] - \\ &\quad - \Big[{}^{3}c_1\left({}^{3}y_{\nu_2} - {}^{3}y_{\nu_1}\right) + 2\,{}^{3}c_2\,{}^{3}y_{\nu_1}\left({}^{3}y_{\nu_2} - {}^{3}y_{\nu_1}\right) + {}^{3}c_3\left({}^{3}x_{\nu_2} - {}^{3}x_{\nu_1}\right) + \\ &\quad \left. + {}^{3}c_4\,{}^{3}y_{\nu_1}\left({}^{3}x_{\nu_2} - {}^{3}x_{\nu_1}\right) + {}^{3}c_4\,{}^{3}x_{\nu_1}\left({}^{3}y_{\nu_2} - {}^{3}y_{\nu_1}\right) + 2\,{}^{3}c_5\,{}^{3}x_{\nu_1}\left({}^{3}x_{\nu_2} - {}^{3}x_{\nu_1}\right)\right] = 0\end{aligned} \tag{4-53}$$

and

$$\left[{}^{1}c_2\left({}^{3}y_{\nu_2}-{}^{3}y_{\nu_1}\right)^2+{}^{1}c_4\left({}^{3}x_{\nu_2}-{}^{3}x_{\nu_1}\right)\left({}^{3}y_{\nu_2}-{}^{3}y_{\nu_1}\right)+{}^{1}c_5\left({}^{3}x_{\nu_2}-{}^{3}x_{\nu_1}\right)^2\right]- \\ -\left[{}^{3}c_2\left({}^{3}y_{\nu_2}-{}^{3}y_{\nu_1}\right)^2+{}^{3}c_4\left({}^{3}x_{\nu_2}-{}^{3}x_{\nu_1}\right)\left({}^{3}y_{\nu_2}-{}^{3}y_{\nu_1}\right)+{}^{3}c_5\left({}^{3}x_{\nu_2}-{}^{3}x_{\nu_1}\right)^2\right]=0. \tag{4-54}$$

Rewriting these constraints in matrix notation

$${}^{\epsilon}\mathbf{C}\,\mathbf{x}={}^{\epsilon}\mathbf{c} \qquad \text{with} \qquad {}^{\epsilon}\mathbf{c}=\mathbf{0} \tag{4-55}$$

and inserting the coordinates for the nodes ν_1 and ν_2 of edge $\epsilon=3$ results in

$${}^{3}\mathbf{C}=\begin{bmatrix} 1 & -1 & 1 & 0 & 0 & 0 & 0 & 0 & 0 & 0 & 0 & 0 & -1 & 1 & -1 & 0 & 0 & 0 & 0 & 0 & 0 & 0 & 0 & 0 \\ 0 & 1 & -2 & 0 & 0 & 0 & 0 & 0 & 0 & 0 & 0 & 0 & 0 & -1 & 2 & 0 & 0 & 0 & 0 & 0 & 0 & 0 & 0 & 0 \\ 0 & 0 & 1 & 0 & 0 & 0 & 0 & 0 & 0 & 0 & 0 & 0 & 0 & 0 & -1 & 0 & 0 & 0 & 0 & 0 & 0 & 0 & 0 & 0 \end{bmatrix}. \tag{4-56}$$

The constraints for the other three edges can be derived accordingly and are reading

$${}^{4}\mathbf{C}=\begin{bmatrix} 0 & 0 & 0 & 0 & 0 & 0 & 1 & 0 & 0 & 0 & 0 & 0 & 0 & 0 & 0 & 0 & 0 & 0 & -1 & 0 & 0 & 0 & 0 & 0 \\ 0 & 0 & 0 & 0 & 0 & 0 & 0 & 1 & 0 & 0 & 0 & 0 & 0 & 0 & 0 & 0 & 0 & 0 & 0 & -1 & 0 & 0 & 0 & 0 \\ 0 & 0 & 0 & 0 & 0 & 0 & 0 & 0 & 1 & 0 & 0 & 0 & 0 & 0 & 0 & 0 & 0 & 0 & 0 & 0 & -1 & 0 & 0 & 0 \end{bmatrix}, \tag{4-57}$$

$${}^{8}\mathbf{C}=\begin{bmatrix} 1 & 0 & 0 & -1 & 0 & 1 & -1 & 0 & 0 & 1 & 0 & -1 & 0 & 0 & 0 & 0 & 0 & 0 & 0 & 0 & 0 & 0 & 0 & 0 \\ 0 & 0 & 0 & 1 & 0 & -2 & 0 & 0 & 0 & -1 & 0 & 2 & 0 & 0 & 0 & 0 & 0 & 0 & 0 & 0 & 0 & 0 & 0 & 0 \\ 0 & 0 & 0 & 0 & 0 & 1 & 0 & 0 & 0 & 0 & 0 & -1 & 0 & 0 & 0 & 0 & 0 & 0 & 0 & 0 & 0 & 0 & 0 & 0 \end{bmatrix}, \tag{4-58}$$

$${}^{11}\mathbf{C}=\begin{bmatrix} 0 & 0 & 0 & 0 & 0 & 0 & 0 & 0 & 0 & 0 & 0 & 0 & 1 & 0 & 0 & 0 & 0 & 0 & -1 & 0 & 0 & 0 & 0 & 0 \\ 0 & 0 & 0 & 0 & 0 & 0 & 0 & 0 & 0 & 0 & 0 & 0 & 0 & 0 & 0 & 1 & 0 & 0 & 0 & 0 & 0 & -1 & 0 & 0 \\ 0 & 0 & 0 & 0 & 0 & 0 & 0 & 0 & 0 & 0 & 0 & 0 & 0 & 0 & 0 & 0 & 0 & 1 & 0 & 0 & 0 & 0 & 0 & -1 \end{bmatrix}. \tag{4-59}$$

While combing (4-56) to (4-59) into

$$\mathbf{C}=\begin{bmatrix} {}^{3}\mathbf{C} \\ {}^{4}\mathbf{C} \\ {}^{8}\mathbf{C} \\ {}^{11}\mathbf{C} \end{bmatrix} \qquad \text{and} \qquad \mathbf{c}=\mathbf{0} \tag{4-60}$$

yields in total 12 constraints. As we have seen in Section 4.2.1 only 11 constraints are necessary to obtain an elementwise continuous approximation with $N=4$ elements using polynomials of 2^{nd} degree. Therefore, matrix $\mathbf{C}\in\mathbb{R}^{12\times 24}$ has a rank deficiency of one with

$$\operatorname{rank}(\mathbf{C})=11\,, \tag{4-61}$$

which means that one row in $\mathbf{C}$ can be represented by a linear combination of all other rows. Before we proceed we need to remove this rank deficiency by choosing any 11 linear independent rows of matrix $\mathbf{C}$ in such a way that $\mathbf{C}\in\mathbb{R}^{11\times 24}$ is of full rank. The remaining 11 constraints are used to extend the normal equation system (4-19)

$$\begin{bmatrix} \mathbf{N} & \mathbf{C}^{\mathsf{T}} \\ \mathbf{C} & \mathbf{0} \end{bmatrix}\begin{bmatrix} \mathbf{x} \\ \boldsymbol{\lambda} \end{bmatrix}=\begin{bmatrix} \mathbf{n} \\ \mathbf{0} \end{bmatrix}. \tag{4-62}$$

Solving (4-62) yields the unknown parameters of a two-dimensional polynomial of 2nd degree for each element

$$\begin{bmatrix} {}^1c_0 \\ {}^1c_1 \\ {}^1c_2 \\ {}^1c_3 \\ {}^1c_4 \\ {}^1c_5 \end{bmatrix} = \begin{bmatrix} 0.918\,692\,574\,762\,579 \\ -0.613\,605\,755\,362\,192 \\ -0.523\,246\,576\,795\,415 \\ -0.201\,188\,960\,622\,233 \\ -0.991\,210\,870\,907\,130 \\ -0.313\,085\,038\,673\,726 \end{bmatrix}, \begin{bmatrix} {}^2c_0 \\ {}^2c_1 \\ {}^2c_2 \\ {}^2c_3 \\ {}^2c_4 \\ {}^2c_5 \end{bmatrix} = \begin{bmatrix} 0.918\,692\,574\,762\,579 \\ 0.130\,120\,573\,353\,666 \\ -0.079\,161\,718\,596\,009 \\ -0.201\,188\,960\,622\,233 \\ -0.004\,195\,617\,695\,995 \\ -0.313\,085\,038\,673\,726 \end{bmatrix},$$
$$\begin{bmatrix} {}^3c_0 \\ {}^3c_1 \\ {}^3c_2 \\ {}^3c_3 \\ {}^3c_4 \\ {}^3c_5 \end{bmatrix} = \begin{bmatrix} 0.918\,692\,574\,762\,579 \\ -0.613\,605\,755\,362\,192 \\ -0.523\,246\,576\,795\,415 \\ 0.201\,188\,960\,622\,234 \\ 0.991\,210\,870\,907\,131 \\ -0.313\,085\,038\,673\,728 \end{bmatrix}, \begin{bmatrix} {}^4c_0 \\ {}^4c_1 \\ {}^4c_2 \\ {}^4c_3 \\ {}^4c_4 \\ {}^4c_5 \end{bmatrix} = \begin{bmatrix} 0.918\,692\,574\,762\,579 \\ 0.130\,120\,573\,353\,666 \\ -0.079\,161\,718\,596\,009 \\ 0.201\,188\,960\,622\,234 \\ 0.004\,195\,617\,695\,995 \\ -0.313\,085\,038\,673\,728 \end{bmatrix}, \tag{4-63}$$

while the approximation is continuous along edges connecting two elements. The coefficients derived from node based (4-40) and edge based (4-63) approach only differ by $\approx 10^{-14}$. The resulting approximation of the edge based approach is depicted in Figure 4-14 and does not differ from the result of the node based approach in Figure 4-11.

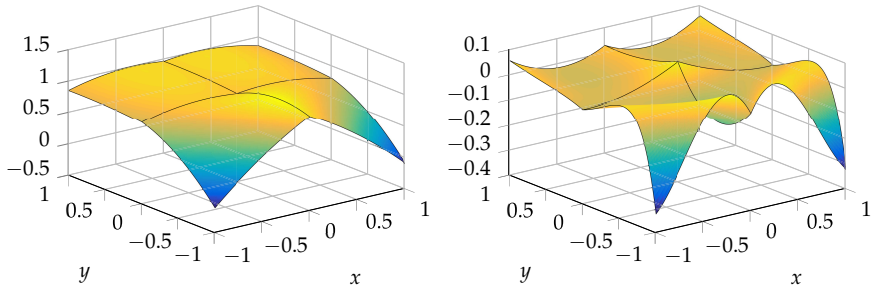

Figure 4-14: Polynomial approximation of function (4-3) with $N = 4$ elements using quadratic polynomials (left). Residual function $v(x,y) = \cos\left({}^{x}/_{(y+1.5)}\right) - \sum_{\zeta=1}^{4} {}^{\zeta}P_2(x,y)$ (right).

It has also been proven numerically that two connected elements are always describing exactly the same curve along their edge. The presented edge based approach yields also an approximation, which is C^0 continuous.

Figure 4-15 depicts an approximation with $N = 25$ elements using quadratic polynomials, which is already quite similar to function (4-3).

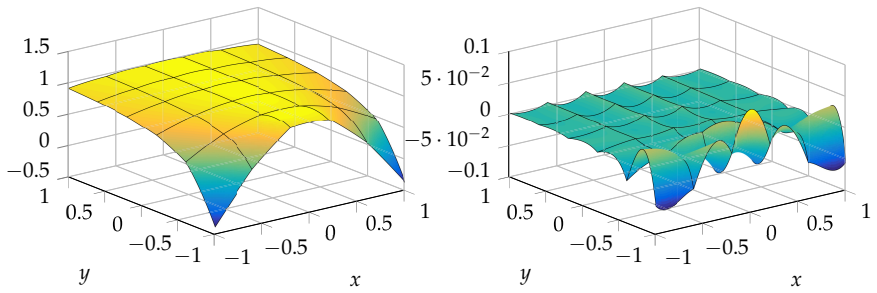

Figure 4-15: Polynomial approximation of function (4-3) with $N = 25$ elements using quadratic polynomials (left). Residual function $v(x,y) = \cos\left({}^{x}/_{(y+1.5)}\right) - \sum_{\zeta=1}^{25} {}^{\zeta}P_2(x,y)$ (right).

The computational effort to find the best continuous elementwise approximation of function (4-3) is tremendous.

The residual function in depicted Figure 4-15 (right) reveals deviation in a range of ≈ 0.1. An approximation with $N = 100$ elements using polynomials of 4th degree is depicted in Figure 4-16 and reveals a residual function, which is overall just slightly smaller than the best polynomial approximation $P_{14}(x,y)$ depicted in Figure 4-4.

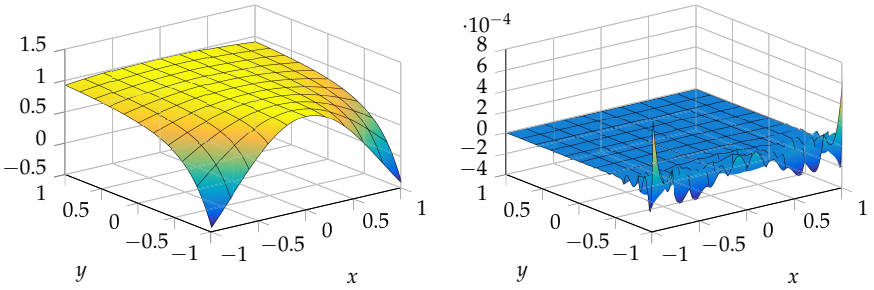

Figure 4-16: Polynomial approximation of function (4-3) with $N = 100$ elements using polynomials of 4^{th} degree (left). Residual function $v(x,y) = \cos\left(x/(y+1.5)\right) - \sum_{\zeta=1}^{100} {}^{\zeta}P_4(x,y)$ (right).

But one should remember that for the best approximation $P_{14}(x,y)$ depicted in Figure 4-4 only 120 parameters are needed, while for the approximation $\sum_{\zeta=1}^{100} {}^{\zeta}P_4(x,y)$ in Figure 4-16 (left) already 1500 parameters are needed. An enormous increase of unknown parameters with hardly any improvement.

At first glance, the introduced edge based approach seems to be very complex and difficult in comparison to the node based approach presented in Section 4.2.1. However, the edge based approach is almost as easy to implement as the node based one and also the rank deficiency can be removed very easily. Furthermore, the basic concept of the presented edge based approach illustrates how to obtain approximations with certain characteristics along borders or arbitrary cross sections. These characteristics can be any given function expressed as polynomial coefficients, which can directly be imposed in the constraints without the necessity of defining proper auxiliary nodes as needed for the node based approach.

4.2.3 *Elementwise smooth approximation*

In this section we will briefly show how to obtain an elementwise C^2 continuous approximation of functions in two dimensions. A smooth approximation can be achieved, while introducing additional constraints for the partial derivatives in the same way as already shown for a C^0 continuous approximation as described in Section 4.2. In this section, however, we will only focus on the edge based approach and exemplify the derivation of the additional constraints for the same example as in Section 4.2.2. According to Equation (4-42) the polynomial of 2^{nd} degree for an edge ϵ of an element ζ is given by

$$\begin{aligned} {}^{\zeta}P_2\left({}^{\epsilon}x_{\mathrm{e}}, {}^{\epsilon}y_{\mathrm{e}}\right) = {}^{\zeta}c_0 + {}^{\zeta}c_1\,{}^{\epsilon}y_{\mathrm{e}} + {}^{\zeta}c_2\,{}^{\epsilon}y_{\mathrm{e}}^2 + {}^{\zeta}c_3\,{}^{\epsilon}x_{\mathrm{e}} + \\ + {}^{\zeta}c_4\,{}^{\epsilon}x_{\mathrm{e}}\,{}^{\epsilon}y_{\mathrm{e}} + {}^{\zeta}c_5\,{}^{\epsilon}x_{\mathrm{e}}^2\,, \end{aligned} \tag{4-64}$$

with the coordinates of the edge ϵ

$$\begin{aligned} {}^{\epsilon}x_{\mathrm{e}} &= {}^{\epsilon}x_{\nu_1} + \left({}^{\epsilon}x_{\nu_2} - {}^{\epsilon}x_{\nu_1}\right)u\,, \\ {}^{\epsilon}y_{\mathrm{e}} &= {}^{\epsilon}y_{\nu_1} + \left({}^{\epsilon}y_{\nu_2} - {}^{\epsilon}y_{\nu_1}\right)u\,. \end{aligned} \tag{4-65}$$

In order to obtain a smooth approximation between two neighboured arbitrary elements ζ_1 and ζ_2, the polynomials of both elements must be equal along their connecting edge ϵ_1, as already shown in Section 4.2.2, and they must also be equal in their first-order

$$\frac{\partial\,{}^{\zeta_1}P_2\left({}^{\epsilon_1}x_{\mathrm{e}}, {}^{\epsilon_1}y_{\mathrm{e}}\right)}{\partial\,{}^{\epsilon_1}x_{\mathrm{e}}} = \frac{\partial\,{}^{\zeta_2}P_2\left({}^{\epsilon_1}x_{\mathrm{e}}, {}^{\epsilon_1}y_{\mathrm{e}}\right)}{\partial\,{}^{\epsilon_1}x_{\mathrm{e}}}\,, \tag{4-66}$$

$$\frac{\partial\,{}^{\zeta_1}P_2\left({}^{\epsilon_1}x_{\mathrm{e}}, {}^{\epsilon_1}y_{\mathrm{e}}\right)}{\partial\,{}^{\epsilon_1}y_{\mathrm{e}}} = \frac{\partial\,{}^{\zeta_2}P_2\left({}^{\epsilon_1}x_{\mathrm{e}}, {}^{\epsilon_1}y_{\mathrm{e}}\right)}{\partial\,{}^{\epsilon_1}y_{\mathrm{e}}} \tag{4-67}$$

and in their second-order partial derivatives

$$\frac{\partial^2\, {}^{\zeta_1}P_2\left({}^{\epsilon_1}x_\mathrm{e}, {}^{\epsilon_1}y_\mathrm{e}\right)}{\partial\, {}^{\epsilon_1}x_\mathrm{e}^2} = \frac{\partial^2\, {}^{\zeta_2}P_2\left({}^{\epsilon_1}x_\mathrm{e}, {}^{\epsilon_1}y_\mathrm{e}\right)}{\partial\, {}^{\epsilon_1}x_\mathrm{e}^2}\,, \tag{4-68}$$

$$\frac{\partial^2\, {}^{\zeta_1}P_2\left({}^{\epsilon_1}x_\mathrm{e}, {}^{\epsilon_1}y_\mathrm{e}\right)}{\partial\, {}^{\epsilon_1}y_\mathrm{e}^2} = \frac{\partial^2\, {}^{\zeta_2}P_2\left({}^{\epsilon_1}x_\mathrm{e}, {}^{\epsilon_1}y_\mathrm{e}\right)}{\partial\, {}^{\epsilon_1}y_\mathrm{e}^2}\,, \tag{4-69}$$

$$\frac{\partial^2\, {}^{\zeta_1}P_2\left({}^{\epsilon_1}x_\mathrm{e}, {}^{\epsilon_1}y_\mathrm{e}\right)}{\partial\, {}^{\epsilon_1}x_\mathrm{e}\;\partial\, {}^{\epsilon_1}y_\mathrm{e}} = \frac{\partial^2\, {}^{\zeta_2}P_2\left({}^{\epsilon_1}x_\mathrm{e}, {}^{\epsilon_1}y_\mathrm{e}\right)}{\partial\, {}^{\epsilon_1}y_\mathrm{e}\;\partial\, {}^{\epsilon_1}y_\mathrm{e}}\,. \tag{4-70}$$

The derivation of the constraints for fulfilling Equations (4-66) to (4-70) is done in the same way as described in Section 4.2.2 and will be exemplified for (4-66). The partial derivative of (4-66) for element ζ_1 reads

$$\frac{\partial\, {}^{\zeta_1}P_2\left({}^{\epsilon_1}x_\mathrm{e}, {}^{\epsilon_1}y_\mathrm{e}\right)}{\partial\, {}^{\epsilon_1}x_\mathrm{e}} = {}^{\zeta_1}P_\mathrm{x}\left({}^{\epsilon_1}x_\mathrm{e}, {}^{\epsilon_1}y_\mathrm{e}\right) = {}^{\zeta}c_3 + {}^{\zeta}c_4\, {}^{\epsilon_1}y_\mathrm{e} + 2\, {}^{\zeta}c_5\, {}^{\epsilon_1}x_\mathrm{e}\,. \tag{4-71}$$

Inserting (4-65) into (4-71) yields

$$\begin{aligned} {}^{\zeta_1}P_\mathrm{x}(u) = {}^{\zeta_1}c_3 + {}^{\zeta_1}c_4 \left({}^{\epsilon_1}y_{\nu_1} + \left({}^{\epsilon_1}y_{\nu_2} - {}^{\epsilon_1}y_{\nu_1}\right)u\right) + \\ + 2\, {}^{\zeta_1}c_5 \left({}^{\epsilon_1}x_{\nu_1} + \left({}^{\epsilon_1}x_{\nu_2} - {}^{\epsilon_1}x_{\nu_1}\right)u\right). \end{aligned} \tag{4-72}$$

While the coordinates starting and end node of edge ϵ_1 are constants, the resulting polynomial of the first derivative in (4-72) is only a function of u and simplifies to

$${}^{\zeta_1}P_\mathrm{x}(u) = {}^{\zeta_1}d_0 + {}^{\zeta_1}d_1\, u\,, \tag{4-73}$$

with

$$\begin{aligned} {}^{\zeta_1}d_0 &= {}^{\zeta_1}c_3 + {}^{\zeta_1}c_4\, {}^{\epsilon_1}y_{\nu_1} + 2\, {}^{\zeta_1}c_5\, {}^{\epsilon_1}x_{\nu_1}\,, \\ {}^{\zeta_1}d_1 &= {}^{\zeta_1}c_4 \left({}^{\epsilon_1}y_{\nu_2} - {}^{\epsilon_1}y_{\nu_1}\right) + 2\, {}^{\zeta_1}c_5 \left({}^{\epsilon_1}x_{\nu_2} - {}^{\epsilon_1}x_{\nu_1}\right). \end{aligned} \tag{4-74}$$

Analogous to the above, the partial derivative of (4-66) for element ζ_2 results in

$$\frac{\partial\, {}^{\zeta_2}P_2\left({}^{\epsilon_1}x_\mathrm{e}, {}^{\epsilon_1}y_\mathrm{e}\right)}{\partial\, {}^{\epsilon_1}x_\mathrm{e}} = {}^{\zeta_2}P_\mathrm{x}(u) = {}^{\zeta_2}d_0 + {}^{\zeta_2}d_1\, u\,, \tag{4-75}$$

with

$$\begin{aligned} {}^{\zeta_2}d_0 &= {}^{\zeta_2}c_3 + {}^{\zeta_2}c_4\, {}^{\epsilon_1}y_{\nu_1} + 2\, {}^{\zeta_2}c_5\, {}^{\epsilon_1}x_{\nu_1}\,, \\ {}^{\zeta_2}d_1 &= {}^{\zeta_2}c_4 \left({}^{\epsilon_1}y_{\nu_2} - {}^{\epsilon_1}y_{\nu_1}\right) + 2\, {}^{\zeta_2}c_5 \left({}^{\epsilon_1}x_{\nu_2} - {}^{\epsilon_1}x_{\nu_1}\right). \end{aligned} \tag{4-76}$$

Inserting (4-73) and (4-75) into the first-order partial derivative (4-66) yields

$${}^{\zeta_1}d_0 + {}^{\zeta_1}d_1\, u = {}^{\zeta_2}d_0 + {}^{\zeta_2}d_1\, u\,. \tag{4-77}$$

Equation (4-77) is fulfilled, if the coefficients of both polynomials are equal. Hence, we get the following two constraints

$$\begin{aligned} {}^{\zeta_1}d_0 - {}^{\zeta_2}d_0 = 0\,, \\ {}^{\zeta_1}d_1 - {}^{\zeta_2}d_1 = 0\,. \end{aligned} \tag{4-78}$$

For the example of approximating function (4-3) by $N = 4$ elements as aligned in Figure 4-12 and based on the tables for nodes, edges and elements in Table 4-4 the constraints (4-78) with (4-74) and (4-76) have to be introduced for each edge connecting two elements. For edge $\epsilon = 3$ these constraints are

$$\begin{aligned} {}^{1}d_0 - {}^{3}d_0 = 0\,, \\ {}^{1}d_1 - {}^{3}d_1 = 0 \end{aligned} \tag{4-79}$$

and inserting (4-74) and (4-76) yields

$$\left[{}^{1}c_3 + {}^{1}c_4\,{}^{3}y_{\nu_1} + 2\,{}^{1}c_5\,{}^{3}x_{\nu_1}\right] - \left[{}^{3}c_3 + {}^{3}c_4\,{}^{3}y_{\nu_1} + 2\,{}^{3}c_5\,{}^{3}x_{\nu_1}\right] = 0 \tag{4-80}$$

and

$$\left[{}^{1}c_4\left({}^{3}y_{\nu_2} - {}^{3}y_{\nu_1}\right) + 2\,{}^{1}c_5\left({}^{3}x_{\nu_2} - {}^{3}x_{\nu_1}\right)\right] - \\ - \left[{}^{3}c_4\left({}^{3}y_{\nu_2} - {}^{3}y_{\nu_1}\right) + 2\,{}^{3}c_5\left({}^{3}x_{\nu_2} - {}^{3}x_{\nu_1}\right)\right] = 0\,. \tag{4-81}$$

Rewriting these two constraints in matrix notation

$${}^{\epsilon}\mathbf{C}_{\mathrm{x}}\,\mathbf{x} = {}^{\epsilon}\mathbf{c}_{\mathrm{x}} \qquad \text{with} \qquad {}^{\epsilon}\mathbf{c}_{\mathrm{x}} = \mathbf{0} \tag{4-82}$$

and inserting the coordinates for the nodes ν_1 and ν_2 of edge $\epsilon = 3$ yields

$${}^{3}\mathbf{C}_{\mathrm{x}} = \begin{bmatrix} 0&0&0&1&-1&0&0&0&0&0&0&0&0&0&0&-1&1&0&0&0&0&0&0&0 \\ 0&0&0&0&1&0&0&0&0&0&0&0&0&0&0&0&-1&0&0&0&0&0&0&0 \end{bmatrix}. \tag{4-83}$$

The constraints for the other three edges can be derived accordingly and are reading

$${}^{4}\mathbf{C}_{\mathrm{x}} = \begin{bmatrix} 0&0&0&0&0&0&0&0&0&1&0&0&0&0&0&0&0&0&0&0&0&-1&0&0 \\ 0&0&0&0&0&0&0&0&0&0&1&0&0&0&0&0&0&0&0&0&0&0&-1&0 \end{bmatrix}, \tag{4-84}$$

$${}^{8}\mathbf{C}_{\mathrm{x}} = \begin{bmatrix} 0&0&0&1&0&-2&0&0&0&-1&0&2&0&0&0&0&0&0&0&0&0&0&0&0 \\ 0&0&0&0&0&2&0&0&0&0&0&-2&0&0&0&0&0&0&0&0&0&0&0&0 \end{bmatrix}, \tag{4-85}$$

$${}^{11}\mathbf{C}_{\mathrm{x}} = \begin{bmatrix} 0&0&0&0&0&0&0&0&0&0&0&0&0&0&0&0&1&0&0&0&0&0&-1&0&0 \\ 0&0&0&0&0&0&0&0&0&0&0&0&0&0&0&0&0&2&0&0&0&0&0&-2 \end{bmatrix}. \tag{4-86}$$

Combing (4-83) to (4-86) into

$$\mathbf{C}_{\mathrm{x}} = \begin{bmatrix} {}^{3}\mathbf{C}_{\mathrm{x}} \\ {}^{4}\mathbf{C}_{\mathrm{x}} \\ {}^{8}\mathbf{C}_{\mathrm{x}} \\ {}^{11}\mathbf{C}_{\mathrm{x}} \end{bmatrix} \qquad \text{and} \qquad \mathbf{c}_{\mathrm{x}} = \mathbf{0} \tag{4-87}$$

yields in total 8 constraints in order to enforce continuity in the first derivative (4-66) along the four connecting edges. In the same way, constraints for the remaining partial derivatives can be derived and yields the following matrix for the first-order partial derivative (4-67)

$$\mathbf{C}_{\mathrm{y}} = \begin{bmatrix} 0&1&-2&0&0&0&0&0&0&0&0&0&0&-1&2&0&0&0&0&0&0&0&0&0 \\ 0&0&2&0&0&0&0&0&0&0&0&0&0&0&-2&0&0&0&0&0&0&0&0&0 \\ 0&0&0&0&0&0&0&1&0&0&0&0&0&0&0&0&0&0&0&-1&0&0&0&0 \\ 0&0&0&0&0&0&0&0&2&0&0&0&0&0&0&0&0&0&0&0&-2&0&0&0 \\ 0&1&0&0&-1&0&0&-1&0&0&1&0&0&0&0&0&0&0&0&0&0&0&0&0 \\ 0&0&0&0&1&0&0&0&0&0&-1&0&0&0&0&0&0&0&0&0&0&0&0&0 \\ 0&0&0&0&0&0&0&0&0&0&0&0&0&1&0&0&0&0&0&-1&0&0&0&0 \\ 0&0&0&0&0&0&0&0&0&0&0&0&0&0&0&0&1&0&0&0&0&0&-1&0 \end{bmatrix}, \tag{4-88}$$

while the order of the rows in (4-88) is the same as in (4-87). Each of the three remaining second-order partial derivatives (4-68) to (4-70) yields only one constraint for each edge. These constraints are

$$\mathbf{C}_{xx} = \begin{bmatrix} 0 & 0 & 0 & 0 & 0 & 2 & 0 & 0 & 0 & 0 & 0 & 0 & 0 & 0 & 0 & 0 & -2 & 0 & 0 & 0 & 0 & 0 & 0 \\ 0 & 0 & 0 & 0 & 0 & 0 & 0 & 0 & 0 & 0 & 0 & 2 & 0 & 0 & 0 & 0 & 0 & 0 & 0 & 0 & 0 & 0 & -2 \\ 0 & 0 & 0 & 0 & 0 & 2 & 0 & 0 & 0 & 0 & 0 & -2 & 0 & 0 & 0 & 0 & 0 & 0 & 0 & 0 & 0 & 0 & 0 \\ 0 & 0 & 0 & 0 & 0 & 0 & 0 & 0 & 0 & 0 & 0 & 0 & 0 & 0 & 0 & 0 & 0 & 2 & 0 & 0 & 0 & 0 & -2 \end{bmatrix}, \tag{4-89}$$

$$\mathbf{C}_{yy} = \begin{bmatrix} 0 & 0 & 2 & 0 & 0 & 0 & 0 & 0 & 0 & 0 & 0 & 0 & 0 & -2 & 0 & 0 & 0 & 0 & 0 & 0 & 0 & 0 & 0 \\ 0 & 0 & 0 & 0 & 0 & 0 & 0 & 0 & 2 & 0 & 0 & 0 & 0 & 0 & 0 & 0 & 0 & 0 & 0 & -2 & 0 & 0 & 0 \\ 0 & 0 & 2 & 0 & 0 & 0 & 0 & 0 & -2 & 0 & 0 & 0 & 0 & 0 & 0 & 0 & 0 & 0 & 0 & 0 & 0 & 0 & 0 \\ 0 & 0 & 0 & 0 & 0 & 0 & 0 & 0 & 0 & 0 & 0 & 0 & 0 & 0 & 2 & 0 & 0 & 0 & 0 & 0 & -2 & 0 & 0 \end{bmatrix} \tag{4-90}$$

and

$$\mathbf{C}_{xy} = \begin{bmatrix} 0 & 0 & 0 & 0 & 1 & 0 & 0 & 0 & 0 & 0 & 0 & 0 & 0 & 0 & 0 & 0 & -1 & 0 & 0 & 0 & 0 & 0 & 0 & 0 \\ 0 & 0 & 0 & 0 & 0 & 0 & 0 & 0 & 0 & 0 & 1 & 0 & 0 & 0 & 0 & 0 & 0 & 0 & 0 & 0 & 0 & 0 & -1 & 0 \\ 0 & 0 & 0 & 0 & 1 & 0 & 0 & 0 & 0 & 0 & -1 & 0 & 0 & 0 & 0 & 0 & 0 & 0 & 0 & 0 & 0 & 0 & 0 & 0 \\ 0 & 0 & 0 & 0 & 0 & 0 & 0 & 0 & 0 & 0 & 0 & 0 & 0 & 0 & 0 & 0 & 1 & 0 & 0 & 0 & 0 & 0 & -1 & 0 \end{bmatrix}. \tag{4-91}$$

Combining the constraints (4-87) to (4-91) with (4-60) into

$$\mathbf{C}_{ext} = \begin{bmatrix} \mathbf{C} \\ \mathbf{C}_x \\ \mathbf{C}_y \\ \mathbf{C}_{xx} \\ \mathbf{C}_{yy} \\ \mathbf{C}_{xy} \end{bmatrix} \tag{4-92}$$

I want to point out that this approach is not well thought out so far and has some weaknesses. Its derivation and implementation was just pretty straight forward and it works.

yields in total 40 constraints, while only 18 are necessary in order to obtain a C^2 continuous approximation using polynomials of 2^{nd} degree. To remove this rank deficiency, we choose any 18 linear independent rows of matrix $\mathbf{C}_{ext}$ in such a way that $\mathbf{C}_{ext} \in \mathbb{R}^{18\times 24}$ is of full rank. The remaining 18 constraints are used to extend the normal equation system (4-19)

$$\begin{bmatrix} \mathbf{N} & \mathbf{C}_{ext}^T \\ \mathbf{C}_{ext} & \mathbf{0} \end{bmatrix} \begin{bmatrix} \mathbf{x} \\ \boldsymbol{\lambda} \end{bmatrix} = \begin{bmatrix} \mathbf{n} \\ \mathbf{0} \end{bmatrix}. \tag{4-93}$$

Solving (4-93) yields the unknowns parameters of ${}^{\zeta}P_2(x,y)$ for each element of an C^2 continuous approximation of function (4-3)

$$\begin{bmatrix} {}^1c_0 \\ {}^1c_1 \\ {}^1c_2 \\ {}^1c_3 \\ {}^1c_4 \\ {}^1c_5 \end{bmatrix} = \begin{bmatrix} 1.056\,984\,074\,859\,209 \\ 0.173\,640\,852\,971\,296 \\ -0.183\,914\,131\,081\,515 \\ -2.656\,963\,858\,023\,53 \cdot 10^{-18} \\ 0 \\ -0.355\,802\,088\,061\,745 \end{bmatrix}, \begin{bmatrix} {}^2c_0 \\ {}^2c_1 \\ {}^2c_2 \\ {}^2c_3 \\ {}^2c_4 \\ {}^2c_5 \end{bmatrix} = \begin{bmatrix} 1.056\,984\,074\,859\,209 \\ 0.173\,640\,852\,971\,296 \\ -0.183\,914\,131\,081\,515 \\ -2.656\,963\,858\,023\,53 \cdot 10^{-18} \\ 0 \\ -0.355\,802\,088\,061\,745 \end{bmatrix},$$

$$\begin{bmatrix} {}^3c_0 \\ {}^3c_1 \\ {}^3c_2 \\ {}^3c_3 \\ {}^3c_4 \\ {}^3c_5 \end{bmatrix} = \begin{bmatrix} 1.056\,984\,074\,859\,209 \\ 0.173\,640\,852\,971\,296 \\ -0.183\,914\,131\,081\,515 \\ -2.656\,963\,858\,023\,53 \cdot 10^{-18} \\ 0 \\ -0.355\,802\,088\,061\,745 \end{bmatrix}, \begin{bmatrix} {}^4c_0 \\ {}^4c_1 \\ {}^4c_2 \\ {}^4c_3 \\ {}^4c_4 \\ {}^4c_5 \end{bmatrix} = \begin{bmatrix} 1.056\,984\,074\,859\,209 \\ 0.173\,640\,852\,971\,296 \\ -0.183\,914\,131\,081\,515 \\ -2.656\,963\,858\,023\,53 \cdot 10^{-18} \\ 0 \\ -0.355\,802\,088\,061\,745 \end{bmatrix}. \quad (4\text{-}94)$$

As can be seen easily, the coefficients are equal for all elements and almost identical to those in (4-8). While the second order derivative of a polynomial of 2nd degree is only a constant value, the presented elementwise smooth approximation yields the only possible solution referring to one single polynomial defined for the whole domain, as already derived in Chapter 4. Polynomials of 2nd degree have only been chosen in order to illustrate the derivation of the constraints for a smooth approximation, while using higher order polynomials would have led to very large equations that would have filled several pages.

A smooth approximation with $N = 100$ elements using polynomials of 4th degree is depicted in Figure 4-17.

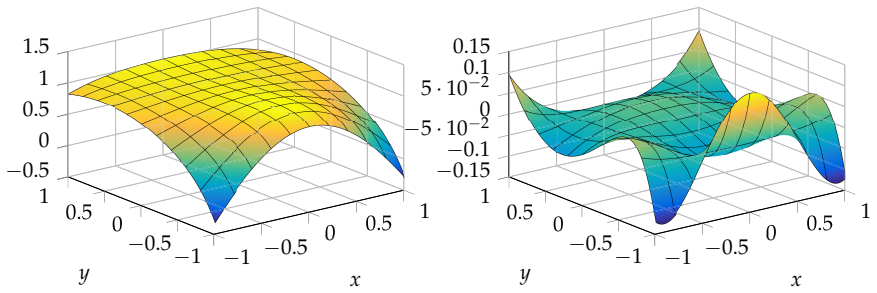

Figure 4-17: Polynomial smooth approximation of function (4-3) with $N = 100$ elements using polynomials of 4th degree (left). Residual function $v(x,y) = \cos\left({}^{x}/_{(y+1.5)}\right) - \sum_{\zeta=1}^{100} {}^{\zeta}P_4(x,y)$ (right).

In comparison to the C^0 continuous approximation depicted in Figure 4-16, the resulting smooth approximation in Figure 4-17 shows huge differences. The residual function in Figure 4-17 (right) shows deviations within a range of ≈ 0.15 and are nearly 1000 times larger than the one for the C^0 continuous approximation in Figure 4-16 (right). The introduced constraints for a C^2 continuous approximation are having a huge impact on the solution of the unknown parameters. To increase the number of elements will hardly improve the residual function in Figure 4-17 (right). The chosen polynomial of 4th degree with 15 parameters is not flexible enough to approximate the function in a suitable way under the requirement that the constraints must be full filled. Even a polynomial of 5th degree with 21 parameters is not suitable as illustrated in Figure 4-18.

This would not be different if we had chosen the node based approach to obtain an elementwise smooth approximation.

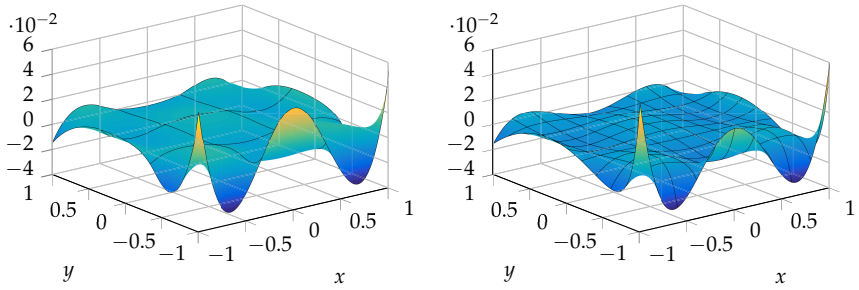

Figure 4-18: Residual functions of a smooth approximation of function (4-3) with $N = 9$ (left) and $N = 100$ (right) elements using polynomials of 5^{th} degree.

As can be seen in Figure 4-18, the residual function of a smooth approximation using polynomials of 5^{th} degree with only $N = 9$ elements hardly differs from the one using $N = 100$ elements. This will not change even if more elements are used. The only way to improve the approximation for the presented approach is to introduce more parameters, so to increase the polynomial degree. Figure 4-19 depicts the residual functions of a smooth approximation using polynomials of 6^{th} degree.

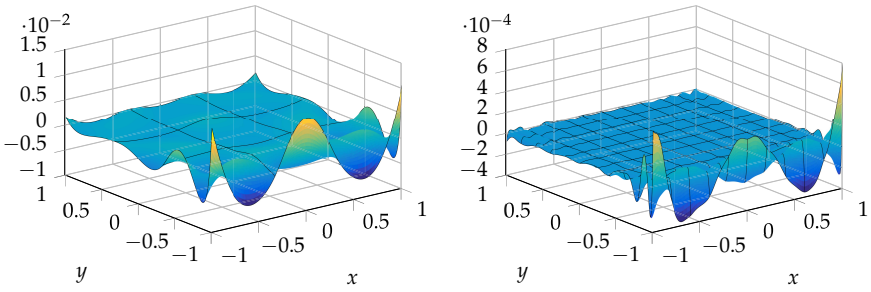

Figure 4-19: Residual functions of a smooth approximation of function (4-3) with $N = 9$ (left) and $N = 100$ (right) elements using polynomials of 6^{th} degree.

The residual function of a smooth approximation using polynomials of 6^{th} degree with $N = 100$ elements, shown in Figure 4-19 (right), is nearly 100 times smaller than the one with only $N = 9$ elements (left). The residual function decreases with increasing number of elements, therefore, the constraints no longer have an unwanted impact on the approximation, as before. The chosen polynomial of 6^{th} degree with 28 parameters is now flexible enough to full fill the constraints and still be able to approximate the function in a proper way. The already mentioned polynomial smooth approximation of function (4-3) with $N = 100$ elements using polynomials of 6^{th} degree is depicted in Figure 4-20.

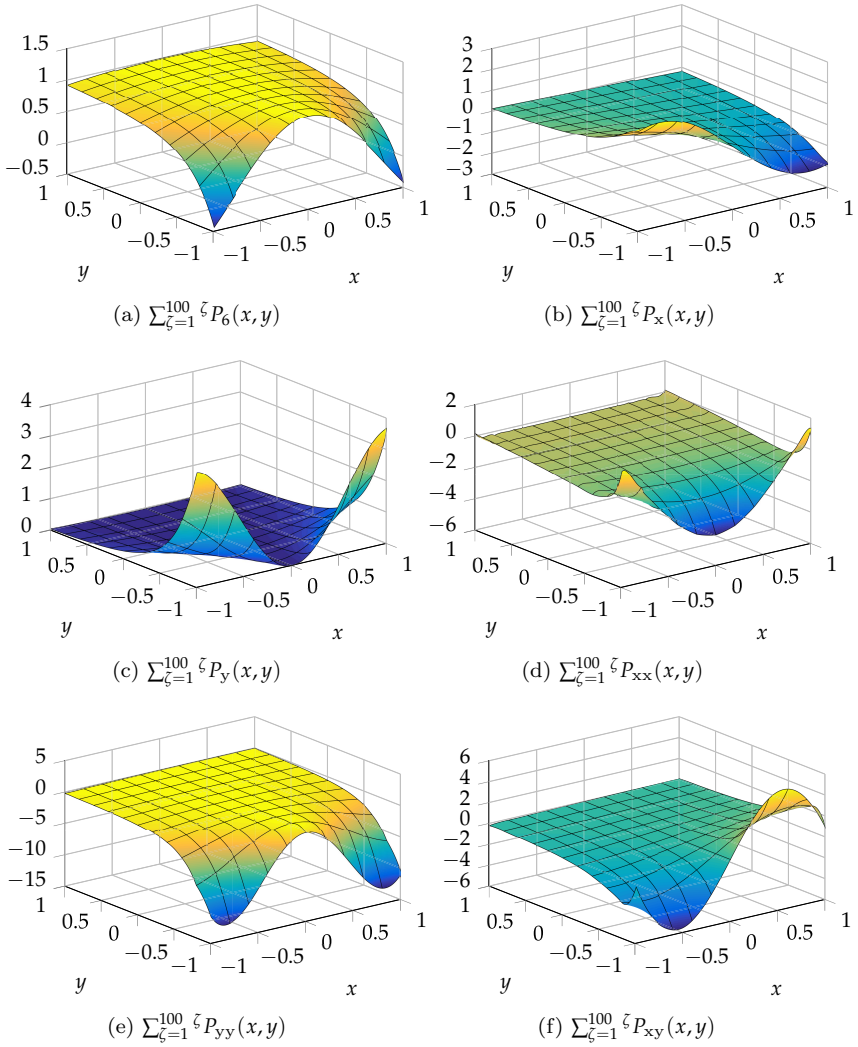

Figure 4-20: Polynomial smooth approximation of function (4-3) with $N = 100$ elements using polynomials of 6^{th} degree and its first and second order partial derivatives.

Furthermore, Figure 4-20 also illustrates the first and second order partial derivatives given in Equations (4-66) to (4-70), to show that the smooth approximation in (a) is really C^2 continuous. It has also been proven numerically that two connected elements are always describing exactly the same curve along their edge for all its partial derivatives.

Nevertheless, the presented smooth approximation in the monomial basis using polynomials of 6^{th} degree is an ill-conditioned problem. The extended normal matrix in Equation (4-93) is nearly singular for only $N = 25$ elements. In summary, a smooth approximation in the monomial basis as presented in this section is hardly applicable for the approximation of complex functions.

It should be noted that, according to the definition in Figure 4-1, a polynomial of 6^{th} degree already consists of 28 basis functions. That is why the normal matrix becomes nearly singular even for small polynomial degrees.

4.3 APPROXIMATION IN THE CHEBYSHEV BASIS

A bivariate polynomial of degree p in the Chebyshev basis can be formed in the same way as for the monomial basis and reads

$$P_p(x,y) = \sum_{i=0}^{p} \sum_{j=0}^{p} c_{ij}\, \phi_{ij}(x,y) = \sum_{i=0}^{p} \sum_{j=0}^{p} c_{ij}\, T_i(x) T_j(y) \tag{4-95}$$

A sophisticated approach for the approximation of bivariate functions using Chebshev polynomials is presented by (TOWNSEND 2014).

while $i+j \leq p$. Rewriting the two sums in Equation (4-95) into a single one yields its equivalent representation

$$P_p(x,y) = \sum_{k=0}^{p_n} c_k \, \phi_k(x,y) = \sum_{k=0}^{p_n} c_k \, T_i(x) T_j(y) \quad \text{for} \quad i+j \leq p, \tag{4-96}$$

with $p_n = \frac{1}{2}(p+1)(p+2)$ and where i,j permute accordingly. To illustrate a least squares approximation in the Chebyshev basis, we also approximate function (4-3) by a polynomial of 2^{nd} degree and the resulting 6 basis functions $\phi_k = T_i(x)T_j(y)$ of a polynomial of 2^{nd} degree are listed in Table 4-5.

Table 4-5: All $p_n + 1$ permutations of i and j under the condition $i + j \leq p$ for polynomial degree $p = 2$ and resulting basis functions $\phi_k = T_i(x)T_j(y)$.

k	i	j	$\phi_k = T_i(x)T_j(y)$
0	0	0	$T_0(x)T_0(y)$
1	0	1	$T_0(x)T_1(y)$
2	0	2	$T_0(x)T_2(y)$
3	1	0	$T_1(x)T_0(y)$
4	1	1	$T_1(x)T_1(y)$
5	2	0	$T_2(x)T_0(y)$

The normal equation system

$$\mathbf{N}\,\mathbf{x} = \mathbf{n}$$

for a least squares approximation of (4-3) by a polynomial of 2^{nd} degree results in

$$\begin{bmatrix} \langle\phi_0,\phi_0\rangle & \langle\phi_1,\phi_0\rangle & \cdots & \langle\phi_{p_n},\phi_0\rangle \\ \langle\phi_0,\phi_1\rangle & \langle\phi_1,\phi_1\rangle & \cdots & \langle\phi_{p_n},\phi_1\rangle \\ \vdots & \vdots & \ddots & \vdots \\ \langle\phi_0,\phi_{p_n}\rangle & \langle\phi_1,\phi_{p_n}\rangle & \cdots & \langle\phi_{p_n},\phi_{p_n}\rangle \end{bmatrix} \begin{bmatrix} c_0 \\ c_1 \\ \vdots \\ c_{p_n} \end{bmatrix} = \begin{bmatrix} \langle\cos\left(x/(y+1.5)\right),\phi_0\rangle \\ \langle\cos\left(x/(y+1.5)\right),\phi_1\rangle \\ \vdots \\ \langle\cos\left(x/(y+1.5)\right),\phi_{p_n}\rangle \end{bmatrix}. \tag{4-97}$$

While Chebyshev polynomials are orthogonal with respect to a weighted inner product, the basis functions ϕ_k are also orthogonal and for integrals offside the main diagonal it holds

$$\langle\phi_k,\phi_l\rangle = \int_{-1}^{1}\int_{-1}^{1} \frac{\phi_k\,\phi_l}{\sqrt{1-x^2}\sqrt{1-y^2}}\,\mathrm{d}x\,\mathrm{d}y = 0 \quad \text{for } k \neq l \tag{4-98}$$

and $k,l = 0,1,2,\cdots,p_n$. Hence, the normal matrix $\mathbf{N}$ is diagonal

$$\begin{bmatrix} \langle\phi_0,\phi_0\rangle & 0 & \cdots & 0 \\ 0 & \langle\phi_1,\phi_1\rangle & \cdots & 0 \\ \vdots & \vdots & \ddots & \vdots \\ 0 & 0 & \cdots & \langle\phi_{p_n},\phi_{p_n}\rangle \end{bmatrix} \begin{bmatrix} c_0 \\ c_1 \\ \vdots \\ c_{p_n} \end{bmatrix} = \begin{bmatrix} \langle\phi_0,\cos\left(x/(y+1.5)\right)\rangle \\ \langle\phi_1,\cos\left(x/(y+1.5)\right)\rangle \\ \vdots \\ \langle\phi_{p_n},\cos\left(x/(y+1.5)\right)\rangle \end{bmatrix} \tag{4-99}$$

and the unknown coefficients can be determined directly by

$$c_k = \frac{\langle\phi_k,\cos\left(x/(y+1.5)\right)\rangle}{\langle\phi_k,\phi_k\rangle}, \tag{4-100}$$

with

$$\langle\phi_k,\cos\left(x/(y+1.5)\right)\rangle = \int_{1}^{1}\int_{-1}^{1} \frac{\phi_k\,\cos\left(x/(y+1.5)\right)}{\sqrt{1-x^2}\sqrt{1-y^2}}\,\mathrm{d}x\,\mathrm{d}y \tag{4-101}$$

for $k = 0, 1, 2, \cdots, p_n$. For the implementation it is convenient to determine the coefficients c_{ij} of (4-95) by

$$c_{ij} = \frac{\langle T_i(x)T_j(y), \cos\left(x/(y+1.5)\right)\rangle}{\langle T_i(x)T_j(y), T_i(x)T_j(y)\rangle} \tag{4-102}$$

with

$$\begin{aligned}\langle T_i(x)T_j(y), T_i(x)T_j(y)\rangle &= \int_1^1 \int_{-1}^1 \frac{T_i(x)T_j(y)\; T_i(x)T_j(y)}{\sqrt{1-x^2}\sqrt{1-y^2}}\; \mathrm{d}x\; \mathrm{d}y \\ &= \begin{cases} \pi^2, & i, j = 0, \\ \pi^2/2, & i = 0 \text{ or } j = 0, \\ \pi^2/4, & i, j \neq 0. \end{cases}\end{aligned} \tag{4-103}$$

and

$$\langle T_i(x)T_j(y), \cos\left(x/(y+1.5)\right)\rangle = \int_1^1 \int_{-1}^1 \frac{T_i(x)T_j(y)\; \cos\left(x/(y+1.5)\right)}{\sqrt{1-x^2}\sqrt{1-y^2}}\; \mathrm{d}x\; \mathrm{d}y \tag{4-104}$$

The integrals for the right hand side (4-104) are solved numerically and as we have seen in Section 3.3.1, it is more accurate to solve its equivalent representation derived by a change of variables

$$\begin{aligned} x &= \theta_1 \\ y &= \theta_2\,. \end{aligned} \tag{4-105}$$

According to (3-139) the right hand side in general reads

$$\langle f(x,y), T_i(x)T_j(y)\rangle = \int_0^\pi \int_0^\pi f\big(\cos(\theta_1), \cos(\theta_2)\big)\; \cos(i\theta_1)\cos(j\theta_2)\; \mathrm{d}\theta_1\, \mathrm{d}\theta_2\,. \tag{4-106}$$

The coefficients c_{ij} of a least squares adjustment of function (4-3) by a polynomial of 2nd degree in the Chebyshev basis are

$$c_{ij} = \begin{bmatrix} c_{00} \\ c_{01} \\ c_{02} \\ c_{10} \\ c_{11} \\ c_{20} \end{bmatrix} = \begin{bmatrix} 0.768\,628\,045\,269\,019 \\ 0.292\,411\,417\,653\,142 \\ -0.146\,557\,372\,362\,098 \\ 2.999\,709\,625\,653\,26 \cdot 10^{-17} \\ -1.406\,113\,887\,024\,97 \cdot 10^{-17} \\ -0.219\,584\,736\,147\,031 \end{bmatrix}. \tag{4-107}$$

The Matlab code for the presented polynomial approximation in the Chebyshev basis is given in Programme 4-2.

Programme 4-2: Code for 2D polynomial approximation in the Chebyshev basis.

```
%Function f(x)
f=@(x,y) cos((x)./(y+1.5));

%Polynomial degree
p=2; c=zeros(p+1);

for i=0:p
    for j=0:p-i
        c(i+1,j+1)=(2/pi)^2*integral2(@(t1,t2) f(cos(t1),
            cos(t2))...
          .*cos(i*t1).*cos(j*t2),0,pi,0,pi,'Method','
             iterated');
    end
end
%Correcting c due to the different weighted inner product
    of N
c(1,:)=c(1,:)/2; c(:,1)=c(:,1)/2;
```

The resulting approximation and the residual function are depicted in Figure 4-21.

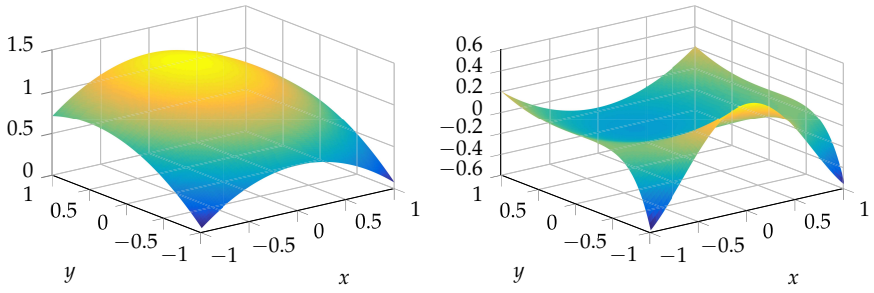

Figure 4-21: Polynomial approximation $P_2(x,y)$ in the Chebyshev basis of function (4-3) (left). Residual function $v(x,y) = \cos\left(x/(y+1.5)\right) - P_2(x,y)$ (right).

The residual function in Figure 4-21 (right) of a polynomial approximation in the Chebyshev basis is quite similar to the one in the monomial basis in Figure 4-3 (right). Both residual functions are nearly within the same range and also share the same characteristic. But as before, this dramatically changes for increasing polynomial degree. The polynomial in the monomial basis of 24^{th} degree depicted Figure 4-6 has already no similarities with function (4-3) any more. In contrast to the polynomial in the Chebyshev basis depicted in Figure 4-22, which approximates function (4-3) very well.

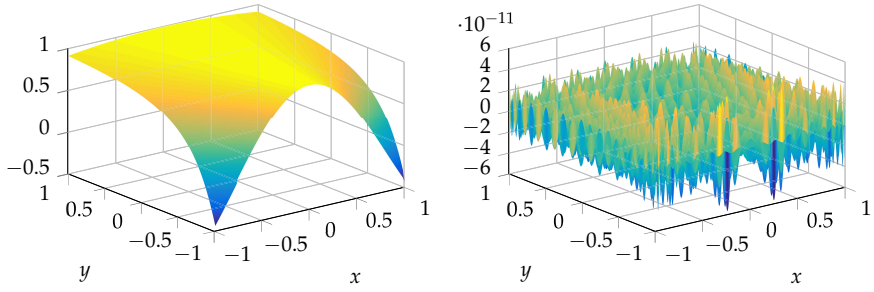

Figure 4-22: Polynomial approximation $P_{50}(x,y)$ in the Chebyshev basis of function (4-3) (left). Residual function $v(x,y) = \cos\left(x/(y+1.5)\right) - P_{50}(x,y)$ (right).

The residual function for a polynomial approximation in the Chebyshev basis of 50^{th} degree in Figure 4-22 (right) is already within $\approx 10^{-11}$. But having a closer look at the coefficients c_{ij} depicted in Figure 4-23 reveals a drawback so far.

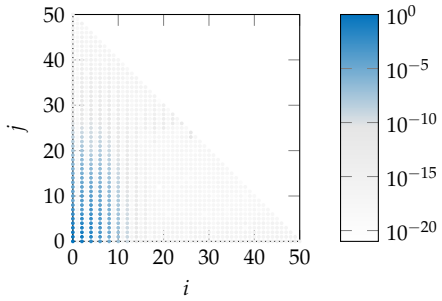

Figure 4-23: Colour coded visualisation of the absolute values for the coefficients c_{ij} of $P_{50}(x,y)$ on a logarithmic scale.

Each point in Figure 4-23 represents the coefficients c_{ij} corresponding to the basis function $\phi_{ij}(x,y) = T_i(x)T_j(y)$. The absolute value for each coefficient is visualised by a colour on a logarithmic scale and are offering the same characteristic as in the one-dimensional case. The coefficients c_{ij} rapidly converging to $\approx 10^{-16}$ for increasing i and j. But Figure 4-23 also shows that for the $x-$ and $y-$direction a different polynomial degree is needed, while the coefficients converge much faster to zero for i than for j. This is also the reason not to use a polynomial based on a single parameter p with $i+j \leq p$ as defined in (4-95). Usually too many coefficients have to be determined, although they are already zero within machine precision. In general, it is better to introduce for the $x-$ and $y-$direction a separate polynomial degree. For a polynomial approximation in the Chebyshev basis the bivariate polynomial reads

$$P_{p_x,p_y}(x,y) = \sum_{i=0}^{p_x} \sum_{j=0}^{p_y} c_{ij}\, T_i(x)T_j(y) \tag{4-108}$$

and it is more suitable than as defined by (4-95). Introducing a different polynomial degree for the $x-$ and $y-$direction reduces the amount of coefficients to be calculated and also allows an easy implementation of a break-off condition in order to find the best approximation of a given function. For the former example we find $P_{18,42}(x,y)$ as the best polynomial approximation in the Chebyshev basis of function (4-3), which is depicted in Figure 4-24.

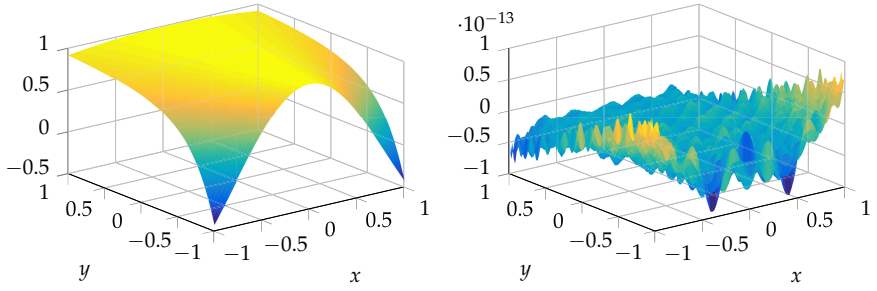

Figure 4-24: Best polynomial approximation in the Chebyshev basis $P_{18,42}(x,y)$ of function (4-3) (left). Residual function $v(x,y) = \cos\left(x/(y+1.5)\right) - P_{18,42}(x,y)$ (right).

The residual function in Figure 4-24 (right) is $\approx 10^{-13}$ but obviously not zero within machine precision. Due to the numerical integration of the right hand side, the last $2-3$ digits of these values are inaccurate. This results in the residual function depicted in Figure 4-24 (right), which can not be reduced by a further increase of the polynomial degree any more.

As in the previous chapter, the advantages of an approximation of bivariate functions in the Chebyshev basis in direct comparison with the results of an elementwise continuous approximation in the monomial basis from Section 4.2 are also clearly evident. The optimal polynomial degree for the $x-$ and

$y-$direction can be easily determined and usually significantly fewer coefficients are needed to represent the function with sufficient accuracy. However, there is also a considerable drawback. While an elementwise approximation can be performed quite easily on arbitrary domains, this is no longer so easy for an approximation in the Chebyshev basis as the whole domain must be mapped on the unit square $[-1,1]^2$.

To illustrate the general problem of mapping arbitrary domains, the next section will demonstrate how an approximation of bivariate functions can be performed for an arbitrary convex tetragon.

4.4 THE GENERALISED 2D ELEMENT

For further information about affine or isoparemetric mapping in general please refere to standard literature, such as e.g. (LANGTANGEN 2016a, p. 88 ff.), (LOGG *et al.* 2012, Chapter 2.4) or (ZIENKIEWICZ *et al.* 2013, Chapter 6.5).

Until now we focussed on quadratic elements, while their edges are aligned parallel to the $x-$ and $y-$axis. Using such elements allows an easy determination of the integrals in the normal equation system. But it is not always convenient to use such elements and in general it would be easier to use any convex tetragon as elements. To illustrate the procedure, we consider the following transformation for arbitrary convex tetragons, depicted in Figure 4-25.

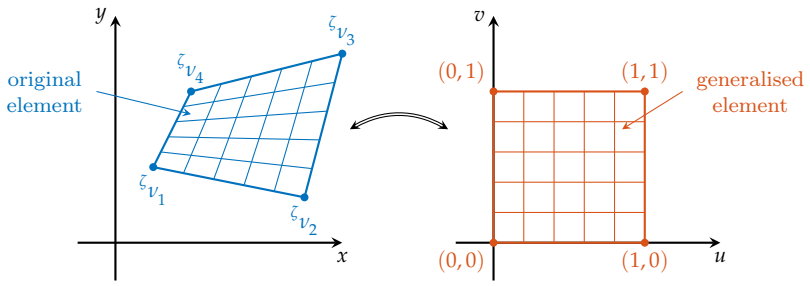

Figure 4-25: Transformation of a convex 2D element.

This mapping can also be solved by a projective transformation, e.g. (HARTLEY and ZISSERMAN 2003, pp. 87).

A transformation that maps an element (blue) onto the generalised element (red), can be any two dimensional functional relationship. For convenience we define two independent transformations

$$\begin{aligned} x_\mathrm{e} &= x(u,v)\,, \\ y_\mathrm{e} &= y(u,v)\,. \end{aligned} \tag{4-109}$$

While the procedure to derive the transformation of x_e is exactly the same as for y_e, we will now only consider the derivation of the transformation for x_e.

In order to ensure an unique transformation, we once again chose a linear combination of some arbitrary basis functions

$$x_\mathrm{e} = \sum_{j=0}^{p} {}^{\zeta}a_j\, \xi_j(u,v) \tag{4-110}$$

and we also chose monomials, as given in Figure 4-1. While an element is defined by its four nodes ${}^{\zeta}\nu_1$ to ${}^{\zeta}\nu_4$, we define a linear combination of four basis functions in order to ensure an unique solution for the unknown parameters ${}^{\zeta}a_j$ for each element. The linear transformation for x reads

$$x_\mathrm{e} = {}^{\zeta}a_0 + {}^{\zeta}a_1 u + {}^{\zeta}a_2 v + {}^{\zeta}a_3 uv\,, \tag{4-111}$$

To solve for the unknown parameters we set-up the following equation system based on the four nodes of each element as illustrated in Figure 4-25

$$\begin{bmatrix} {}^{\zeta}x_{\nu_1} \\ {}^{\zeta}x_{\nu_2} \\ {}^{\zeta}x_{\nu_3} \\ {}^{\zeta}x_{\nu_4} \end{bmatrix} = \begin{bmatrix} 1 & 0 & 0 & 0 \\ 1 & 1 & 0 & 0 \\ 1 & 1 & 1 & 1 \\ 1 & 0 & 1 & 0 \end{bmatrix} \begin{bmatrix} {}^{\zeta}a_0 \\ {}^{\zeta}a_1 \\ {}^{\zeta}a_2 \\ {}^{\zeta}a_3 \end{bmatrix}, \tag{4-112}$$

and obtain

$$\begin{bmatrix} {}^{\zeta}a_0 \\ {}^{\zeta}a_1 \\ {}^{\zeta}a_2 \\ {}^{\zeta}a_3 \end{bmatrix} = \begin{bmatrix} {}^{\zeta}x_{\nu_1} \\ {}^{\zeta}x_{\nu_2} - {}^{\zeta}x_{\nu_1} \\ {}^{\zeta}x_{\nu_4} - {}^{\zeta}x_{\nu_1} \\ {}^{\zeta}x_{\nu_1} - {}^{\zeta}x_{\nu_2} + {}^{\zeta}x_{\nu_3} - {}^{\zeta}x_{\nu_4} \end{bmatrix}. \tag{4-113}$$

The transformation for the x_e reads

$$x_e = {}^{\zeta}x_{\nu_1} + ({}^{\zeta}x_{\nu_2} - {}^{\zeta}x_{\nu_1})u + ({}^{\zeta}x_{\nu_4} - {}^{\zeta}x_{\nu_1})v + ({}^{\zeta}x_{\nu_1} - {}^{\zeta}x_{\nu_2} + {}^{\zeta}x_{\nu_3} - {}^{\zeta}x_{\nu_4})uv. \tag{4-114}$$

The transformation of the y_e can be derived accordingly and yields

$$y_e = {}^{\zeta}y_{\nu_1} + ({}^{\zeta}y_{\nu_2} - {}^{\zeta}y_{\nu_1})u + ({}^{\zeta}y_{\nu_4} - {}^{\zeta}y_{\nu_1})v + ({}^{\zeta}y_{\nu_1} - {}^{\zeta}y_{\nu_2} + {}^{\zeta}y_{\nu_3} - {}^{\zeta}y_{\nu_4})uv. \tag{4-115}$$

Based on the transformations (4-114) and (4-115) the integrals of the normal equation system can also be solved for the generalised elements, as already shown in Section 3.2.2. This allows to use any arbitrary convex tetragon as elements. To illustrate this we will approximate the following continuous real function

$$f(x, y) = \sin(xy) \tag{4-116}$$

by a polynomial in the monomial basis of 2^{nd} degree on the convex element ζ depicted in Figure 4-26.

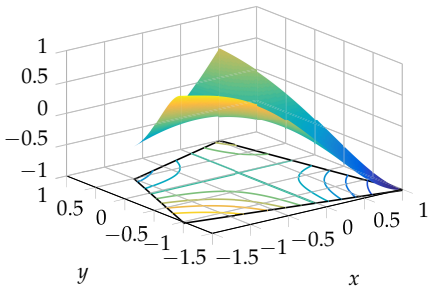

Figure 4-26: $f(x, y) = \sin(xy)$ on an arbitrary convex element ζ.

The coordinates of the four corner nodes of the element are listed in Table 4-6.

Nodes

ν	x_ν	y_ν
1	−1.5	−1.0
2	1.0	−1.5
3	0.5	1.0
4	−1.0	0.5

Table 4-6: Coordinates for the corner nodes of the element ζ in Figure 4-26. The labelling is in accordance to Figure 4-25 (left).

The least squares approximation of (4-116) by a polynomial of 2nd degree results in the normal equation system

$$\mathbf{N}\,\mathbf{x} = \mathbf{n}$$

$$\begin{bmatrix} \langle\phi_0,\phi_0\rangle & \langle\phi_1,\phi_0\rangle & \cdots & \langle\phi_5,\phi_0\rangle \\ \langle\phi_0,\phi_1\rangle & \langle\phi_1,\phi_1\rangle & \cdots & \langle\phi_5,\phi_1\rangle \\ \vdots & \vdots & \ddots & \vdots \\ \langle\phi_0,\phi_5\rangle & \langle\phi_1,\phi_5\rangle & \cdots & \langle\phi_5,\phi_5\rangle \end{bmatrix} \begin{bmatrix} c_0 \\ c_1 \\ \vdots \\ c_5 \end{bmatrix} = \begin{bmatrix} \langle\phi_0,\sin(xy)\rangle \\ \langle\phi_1,\sin(xy)\rangle \\ \vdots \\ \langle\phi_5,\sin(xy)\rangle \end{bmatrix} \tag{4-117}$$

and with the 6 basis functions $\phi_k = x^i y^j$ listed in Table 4-1 the normal matrix reads

$$\mathbf{N} = \begin{bmatrix} \langle 1,1\rangle & \langle y,1\rangle & \langle y^2,1\rangle & \langle x,1\rangle & \langle xy,1\rangle & \langle x^2,1\rangle \\ \langle 1,y\rangle & \langle y,y\rangle & \langle y^2,y\rangle & \langle x,y\rangle & \langle xy,y\rangle & \langle x^2,y\rangle \\ \langle 1,y^2\rangle & \langle y,y^2\rangle & \langle y^2,y^2\rangle & \langle x,y^2\rangle & \langle xy,y^2\rangle & \langle x^2,y^2\rangle \\ \langle 1,x\rangle & \langle y,x\rangle & \langle y^2,x\rangle & \langle x,x\rangle & \langle xy,x\rangle & \langle x^2,x\rangle \\ \langle 1,xy\rangle & \langle y,xy\rangle & \langle y^2,xy\rangle & \langle x,xy\rangle & \langle xy,xy\rangle & \langle x^2,xy\rangle \\ \langle 1,x^2\rangle & \langle y,x^2\rangle & \langle y^2,x^2\rangle & \langle x,x^2\rangle & \langle xy,x^2\rangle & \langle x^2,x^2\rangle \end{bmatrix}. \tag{4-118}$$

Accordingly the right hand side in (4-117) results in

$$\mathbf{n} = \begin{bmatrix} \langle 1,\sin(xy)\rangle \\ \langle y,\sin(xy)\rangle \\ \langle y^2,\sin(xy)\rangle \\ \langle x,\sin(xy)\rangle \\ \langle xy,\sin(xy)\rangle \\ \langle x^2,\sin(xy)\rangle \end{bmatrix}. \tag{4-119}$$

In order to determine the unknown coefficients c_k we need to solve the following integrals

$$\langle\phi_k,\phi_l\rangle = \iint_\zeta \phi_k\phi_l \,\mathrm{d}x\,\mathrm{d}y \quad \text{for } k,l = 0,1,2,\ldots,5 \tag{4-120}$$

and

$$\langle\phi_k,\sin(xy)\rangle = \iint_\zeta \phi_k \sin(xy)\,\mathrm{d}x\,\mathrm{d}y \tag{4-121}$$

for $k = 0,1,2,\ldots,5$ over the element ζ depicted in Figure 4-26. While this is quite complicated we will map the element on the generalised element using the two transformations (4-114) and (4-115). Inserting the coordinates of the corner nodes into these two transformations results in

$$\begin{aligned} x(u,v) &= -\frac{3}{2} + \frac{5}{2}u + \frac{1}{2}v - uv \\ y(u,v) &= -1 - \frac{1}{2}u + \frac{3}{2}v + uv\,. \end{aligned} \tag{4-122}$$

According to (Bronshtein *et al.* 2007, p. 473-474) and with (4-122) the integrals of the normal matrix (4-120) can be solved for the generalised element as follows

$$\iint_\zeta \phi_k(x,y)\,\phi_l(x,y)\,\mathrm{d}x\,\mathrm{d}y = \int_0^1\int_0^1 \phi_k\big(x(u,v),y(u,v)\big)\,\phi_l\big(x(u,v),y(u,v)\big)\,|J|\,\mathrm{d}u\,\mathrm{d}v\,, \tag{4-123}$$

while $|J|$ being the absolute value of the Jacobian determinant

$$J = \begin{vmatrix} \frac{\partial x}{\partial u} & \frac{\partial x}{\partial v} \\ \frac{\partial y}{\partial u} & \frac{\partial y}{\partial v} \end{vmatrix} . \tag{4-124}$$

Inserting the partial derivatives of (4-122) into (4-124) yields

$$J = \begin{vmatrix} 5/2 - v & 1/2 - u \\ v - 1/2 & u + 3/2 \end{vmatrix} = 4 + 2u - 2v . \tag{4-125}$$

The integrals for the right hand side (4-121) can be solved in the same way and are reading

$$\iint_{\zeta} \sin(xy)\, \phi_l(x,y)\, \mathrm{d}x\, \mathrm{d}y = \int_0^1 \int_0^1 \sin\left(x(u,v)y(u,v)\right) \phi_l\left(x(u,v), y(u,v)\right) |J|\, \mathrm{d}u\, \mathrm{d}v . \tag{4-126}$$

The integrals for the normal matrix (4-125) and right hand side (4-126) can easily be solved numerically and results in

$$\mathbf{N} = \begin{bmatrix} 4 & -4/3 & 11/6 & -2/3 & 1/6 & 3/2 \\ -4/3 & 11/6 & -7/5 & 1/6 & -1/20 & -7/10 \\ 11/6 & -7/5 & 7/4 & -1/20 & -1/20 & 259/360 \\ -2/3 & 1/6 & -1/20 & 3/2 & -7/10 & -17/20 \\ 1/6 & -1/20 & -1/20 & -7/10 & 259/360 & 41/120 \\ 3/2 & -7/10 & 259/360 & -17/20 & 41/120 & 77/60 \end{bmatrix} \tag{4-127}$$

and

$$\mathbf{n} = \begin{bmatrix} 0.145\,756\,487\,141\,373 \\ -0.042\,846\,463\,368\,636 \\ -0.042\,499\,116\,708\,621 \\ -0.612\,543\,848\,627\,254 \\ 0.631\,791\,937\,468\,570 \\ 0.291\,378\,751\,245\,651 \end{bmatrix} . \tag{4-128}$$

The solution of the normal equation system (4-117) yields the unknown coefficients

$$\begin{bmatrix} c_0 \\ c_1 \\ c_2 \\ c_3 \\ c_4 \\ c_5 \end{bmatrix} = \begin{bmatrix} 0.003\,253\,362\,989\,749 \\ 0.000\,736\,886\,760\,280 \\ 0.005\,069\,718\,055\,172 \\ -0.005\,888\,389\,584\,868 \\ 0.880\,390\,318\,592\,853 \\ -0.017\,484\,163\,373\,636 \end{bmatrix} . \tag{4-129}$$

for a polynomial approximation in the monomial basis of 2^{nd} degree on the convex element ζ depicted in Figure 4-26. The resulting approximation and the residual function are depicted in Figure 4-27.

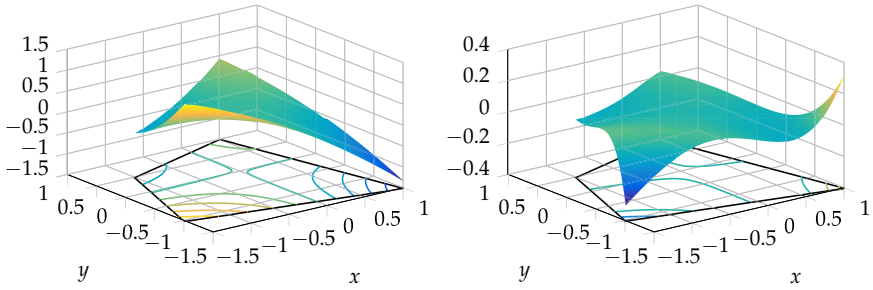

Figure 4-27: Polynomial approximation $P_2(x,y)$ of function (4-116) on the convex element ζ (left). Residual function $v(x,y) = \sin(xy) - P_2(x,y)$ (right).

As Figure 4-27 illustrates, $P_2(x,y)$ is only a very coarse approximation of function (4-116) with the largest deviations at the two nodes $\nu = 1$ and $\nu = 2$. Whereas a polynomial of 8^{th} degree approximates function (4-116) already within $\approx 10^{-4}$ as illustrated in Figure 4-28.

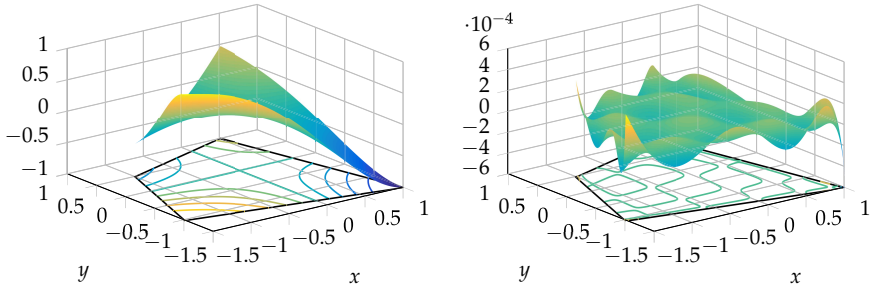

Figure 4-28: Polynomial approximation $P_8(x,y)$ of function (4-116) on the convex element ζ (left). Residual function $v(x,y) = \sin(xy) - P_8(x,y)$ (right).

With the presented transformation we are able to solve the integrals of the normal equation system for any kind of convex element. Implementing this transformation into the elementwise approximation shown in Section 4.1 allows us to approximate any given function over an arbitrary domain. This results in the following two different approximations.

- The approximation of the function by polynomials, as already shown in this part.
- The approximation of the domain by elements.

The presented transformation is also valid for triangular elements, while we only have to introduce the same coordinates for two neighboured nodes, and it can easily be adopted for 3D or higher dimensional elements.

The MATLAB code for the presented polynomial approximation of two-dimensional functions on an arbitrary convex element is given in Programme 4-3.

Programme 4-3: Code for an approximation in the monomial basis for two-dimensional functions on arbitrary convex elements.

```
%Function
f=@(x,y) sin(x.*y);

%Transformation to the generalised element
fx=@(u,v) -3/2+5/2*u+1/2*v-u.*v; fy=@(u,v) -1-1/2*u+3/2*v+u.*v;
detJ=@(u,v) abs(4+2*u-2*v);

%Polynomial degree of approximation
p=2; p_n=1/2*(p+1)*(p+2);

%Permutation of i and j for i+j<=p
[ii,jj]=meshgrid(0:p);
ii=reshape(ii,[],1); jj=reshape(jj,[],1);

%index for i+j>p and deleting entries
out=(ii+jj)>p; ii(out)=[]; jj(out)=[];

%Basis functions
phi=@(x,y,i,j) x.^i.*y.^j;

%Preallocation of the matrices
N=zeros(p_n); n=zeros(p_n,1);

for k=1:p_n
 for l=k:p_n
  N(k,l)=integral2(@(u,v) detJ(u,v).*phi(fx(u,v),fy(u,v),ii(k),jj(k))...
      .*phi(fx(u,v),fy(u,v),ii(l),jj(l)),0,1,0,1,'Method','iterated');
 end
 n(k)=integral2(@(u,v) detJ(u,v).*f(fx(u,v),fy(u,v)).*phi(fx(u,v),...
     fy(u,v),ii(k),jj(k)),0,1,0,1,'Method','iterated');
end

%Adding the lower triangular part
N=N+triu(N,1)';

c=N\n;
```

5

A GLIMPSE ON THE APPROXIMATION OF BOUNDARY VALUE PROBLEMS

To illustrate how to solve some BVPs we consider a linear ordinary differential equation (ODE), for example,

$$\frac{\mathrm{d}^2\,\Phi(x)}{\mathrm{d}x^2} = f(x) \tag{5-1}$$

for $x \in [-1,1]$, with some boundary conditions

$$\Phi(x = \pm 1) = \text{const.}\,. \tag{5-2}$$

In general, an analytic solution of a boundary value problem is unknown and usually too complicated to derive. For many problems that arise in different engineering sciences only an approximate solution can be found so far. In the literature, e.g. (Atkinson and Han 2009), (Burden and Faires 2011) or (Quarteroni and Rozza 2014), one can find many different methods for solving such boundary value problems, for instance, the FEM or spectral methods.
We only mentioned these two methods, because FEM is based on the concept of the described elementwise continuous approximation in Section 3.1.2 and the class of spectral methods are mainly using orthogonal basis functions, as explained in Section 3.3. This means that the basic idea of FEM and of the spectral methods have already been discussed in Part ii.

For further information about FEM in general please refer to standard literature such as (Bathe 2014), (Šolin 2006) or (Zienkiewicz *et al.* 2013) and for spectral methods, see e.g. (Boyd 2002), (Kopriva 2009) or (Trefethen 2008).

In the following, we do not explicitly apply any of the aforementioned two methods, but rather derive a solution that is based on the presented least squares approximation of functions in Part ii.

To solve a given boundary value problem numerically, we approximate the unknown solution $\Phi(x)$ in (5-1) by a finite linear combination of basis functions

$$\Phi(x) \approx \hat{\Phi}_p(x) = \sum_{j=0}^{p} c_j\,\phi_j(x)\,, \tag{5-3}$$

with its second derivative

$$\frac{\mathrm{d}^2\,\hat{\Phi}_p(x)}{\mathrm{d}x^2} = \hat{\Phi}_p''(x) = \sum_{j=0}^{p} c_j\,\phi_j''(x)\,. \tag{5-4}$$

Inserting (5-4) into (5-1) and rearranging yields the residual function

$$v(x) = \sum_{j=0}^{p} c_j\,\phi_j''(x) - f(x)\,, \tag{5-5}$$

which has the same structure as (1-38), with the only difference that the second derivatives of the basis functions are used. Therefore, the normal equation

system of a least squares approximation of the linear ODE (5-1) can be derived in exactly the same way as described in Section 1.2 and results in

$$\begin{bmatrix} \langle \phi_0'', \phi_0'' \rangle & \langle \phi_1'', \phi_0'' \rangle & \cdots & \langle \phi_p'', \phi_0'' \rangle \\ \langle \phi_0'', \phi_1'' \rangle & \langle \phi_1'', \phi_1'' \rangle & \cdots & \langle \phi_p'', \phi_1'' \rangle \\ \vdots & \vdots & \ddots & \vdots \\ \langle \phi_0'', \phi_p'' \rangle & \langle \phi_1'', \phi_p'' \rangle & \cdots & \langle \phi_p'', \phi_p'' \rangle \end{bmatrix} \begin{bmatrix} c_0 \\ c_1 \\ \vdots \\ c_p \end{bmatrix} = \begin{bmatrix} \langle \phi_0'', f(x) \rangle \\ \langle \phi_1'', f(x) \rangle \\ \vdots \\ \langle \phi_p'', f(x) \rangle \end{bmatrix} \tag{5-6}$$

with the integrals

$$\langle \phi_i'', \phi_j'' \rangle = \int_{-1}^{1} \phi_i'' \phi_j'' \, \mathrm{d}x \quad \text{for } i, j = 0, 1, 2, \ldots, p$$

and

$$\langle \phi_i'', f(x) \rangle = \int_{-1}^{1} \phi_i'' f(x) \, \mathrm{d}x \quad \text{for } i = 0, 1, 2, \ldots, p \, .$$

To demonstrate a least squares approximation of an unknown solution $\Phi(x)$, we consider the following boundary value problem

$$\frac{\mathrm{d}^2 \Phi(x)}{\mathrm{d}x^2} = \sin(3x) + \frac{1}{10}\pi \quad \text{with} \quad \Phi(x = \pm 1) = 0 \, , \tag{5-7}$$

for $x \in [-1, 1]$. The analytical solution is given by

$$\Phi(x) = \frac{1}{20}\pi(x^2 - 1) + \frac{1}{9} x \sin(3) - \frac{1}{9}\sin(3x) \tag{5-8}$$

and is depicted in Figure 5-1.

Figure 5-1: Analytical solution (5-8) of the boundary value problem (5-7).

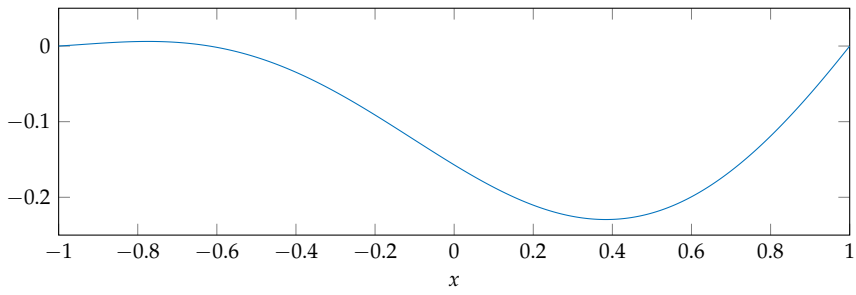

In the following we will determine an approximation of the unknown solution $\Phi(x)$ by a polynomial in the monomial basis of 3rd degree

$$\Phi(x) \approx \hat{\Phi}_3(x) = \sum_{j=0}^{3} c_j \, \phi_j(x) = \sum_{j=0}^{3} c_j \, x^j = c_0 + c_1 x + c_2 x^2 + c_3 x^3 \, . \tag{5-9}$$

The second derivative of (5-9) reads

$$\frac{\mathrm{d}^2 \hat{\Phi}_3(x)}{\mathrm{d}x^2} = \hat{\Phi}_3''(x) = \sum_{j=0}^{3} c_j \, \phi_j''(x) = 2c_2 + 6c_3 x \, , \tag{5-10}$$

with the second derivatives of the basis functions

$$\phi_0''(x) = 0 \, , \; \phi_1''(x) = 0 \, , \; \phi_2''(x) = 2 \text{ and } \phi_3''(x) = 6x \, . \tag{5-11}$$

Inserting (5-11) into (5-6) yields

$$\begin{bmatrix} \langle 0, 0 \rangle & \langle 0, 0 \rangle & \langle 2, 0 \rangle & \langle 6x, 0 \rangle \\ \langle 0, 0 \rangle & \langle 0, 0 \rangle & \langle 2, 0 \rangle & \langle 6x, 0 \rangle \\ \langle 0, 2 \rangle & \langle 0, 2 \rangle & \langle 2, 2 \rangle & \langle 6x, 2 \rangle \\ \langle 0, 6x \rangle & \langle 0, 6x \rangle & \langle 2, 6x \rangle & \langle 6x, 6x \rangle \end{bmatrix} \begin{bmatrix} c_0 \\ c_1 \\ c_2 \\ c_3 \end{bmatrix} = \begin{bmatrix} \langle 0, \sin(3x) + 1/10 \, \pi \rangle \\ \langle 0, \sin(3x) + 1/10 \, \pi \rangle \\ \langle 2, \sin(3x) + 1/10 \, \pi \rangle \\ \langle 6x, \sin(3x) + 1/10 \, \pi \rangle \end{bmatrix} . \tag{5-12}$$

Solving the integrals in (5-12) results in the following normal equation system

$$\begin{bmatrix} 0 & 0 & 0 & 0 \\ 0 & 0 & 0 & 0 \\ 0 & 0 & 8 & 0 \\ 0 & 0 & 0 & 24 \end{bmatrix} \begin{bmatrix} c_0 \\ c_1 \\ c_2 \\ c_3 \end{bmatrix} = \begin{bmatrix} 0.000\,000\,000\,000\,000 \\ 0.000\,000\,000\,000\,000 \\ 1.256\,637\,061\,435\,917 \\ 4.148\,129\,997\,148\,272 \end{bmatrix} . \tag{5-13}$$

In order to be able to distinguish between the normal equation system for an approximation of functions, as used in Part ii, and of PDEs, we will introduce the following notation widely used in FEM for the normal matrix and the vector of right hand side

However, in this case $\mathbf{K}$ does not correspond to the stiffness matrix.

$$\mathbf{K}\,\mathbf{c} = \mathbf{f} . \tag{5-14}$$

It is easy to see that the normal matrix in (5-13) is singular and has a rank deficiency of 2. To obtain a unique solution for (5-13) we have to impose the two linear boundary conditions given in (5-9). For a polynomial of 3rd degree, these two conditions result in

$$\begin{aligned} \hat{\Phi}_3(x = -1) &= c_0 - c_1 + c_2 - c_3 = 0 , \\ \hat{\Phi}_3(x = 1) &= c_0 + c_1 + c_2 + c_3 = 0 . \end{aligned} \tag{5-15}$$

Expressing (5-15) in matrix notation yields

$$\begin{bmatrix} 1 & -1 & 1 & -1 \\ 1 & 1 & 1 & 1 \end{bmatrix} \begin{bmatrix} c_0 \\ c_1 \\ c_2 \\ c_3 \end{bmatrix} = \begin{bmatrix} 0 \\ 0 \end{bmatrix} , \tag{5-16}$$

or in a shorter notation

$$\mathbf{C}\,\mathbf{c} = \mathbf{0} . \tag{5-17}$$

Extending the normal equation system (5-13) with (5-17) results in

Usually, these two conditions are imposed by substituting the first two rows in the normal matrix $\mathbf{N}$ by $\mathbf{C}$ and changing the first two entries in the right hand side accordingly.

$$\begin{bmatrix} \mathbf{K} & \mathbf{C}^\mathsf{T} \\ \mathbf{C} & \mathbf{0} \end{bmatrix} \begin{bmatrix} \mathbf{c} \\ \boldsymbol{\lambda} \end{bmatrix} = \begin{bmatrix} \mathbf{f} \\ \mathbf{0} \end{bmatrix} . \tag{5-18}$$

Solving (5-18) yields the coefficients of a polynomial of 3rd degree

$$\begin{bmatrix} c_0 \\ c_1 \\ c_2 \\ c_3 \end{bmatrix} = \begin{bmatrix} -0.157\,079\,632\,679\,490 \\ -0.172\,838\,749\,881\,178 \\ 0.157\,079\,632\,679\,490 \\ 0.172\,838\,749\,881\,178 \end{bmatrix} . \tag{5-19}$$

The resulting polynomial approximation for the unknown solution $\Phi(x)$ of the boundary value problem (5-7) is depicted in Figure 5-2.

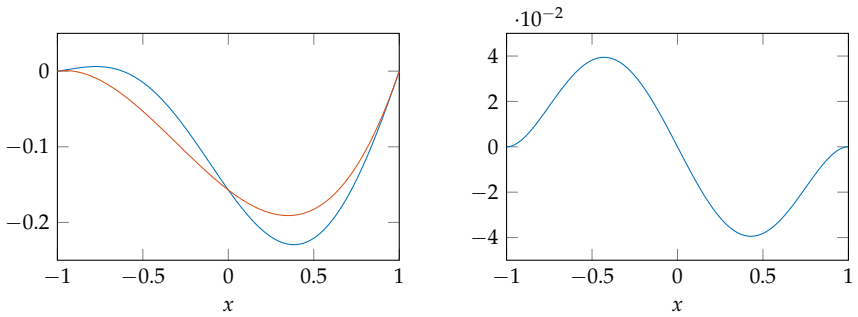

Figure 5-2: Analytical solution (5-8) in blue and its polynomial approximation of 3rd degree in red (left). Residual function $v(x) = \Phi(x) - \hat{\Phi}_3(x)$ (right).

The residual function in Figure 5-2 (right) shows deviations in the range of ≈ 0.04 and can be further decreased by increasing the polynomial degree. The best polynomial approximation for the unknown solution $\Phi(x)$ in the monomial basis is a polynomial of 21^{st} degree and is depicted in Figure 5-3.

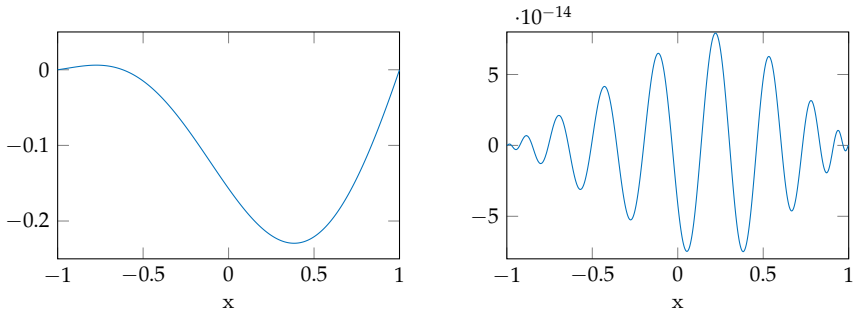

Figure 5-3: Polynomial approximation of 21^{st} degree (left). Residual function $v(x) = \Phi(x) - \hat{\Phi}_{21}(x)$ (right).

5.1 LEAST SQUARES APPROXIMATION OF BVP IN MATRIX NOTATION

The basic concept was taken from (TOWNSEND and OLVER 2015) and (TREFETHEN 2008) and adopted in this section to derive a solution via the method of least squares.

In the previous sections we have solved a given boundary value problem in exactly the same way as we did for the approximation of functions. The only difference was that we used the second derivatives of the basis functions and that we had to impose boundary conditions to ensure a unique solution. However, while using certain basis functions for the approximation of boundary value problems, such as monomials or Chebyshev polynomials, it is convenient to use matrix notation from the beginning.Therefore, the least squares approximation in matrix notation of an unknown solution $\Phi(x)$ for a given boundary value problem will be illustrated in detail.

A linear ODE bounded on the domain $x \in [a, b]$ can be written in the form

$$\mathfrak{L}\,\Phi(x) = f(x) \tag{5-20}$$

with the linear differential operator

$$\mathfrak{L} = \sum_{j=0}^{N} l_j(x) \frac{\mathrm{d}^N}{\mathrm{d}x^N} \tag{5-21}$$

where N is the differential order of $\mathfrak{L}$, $f(x)$ and $l_j(x)$ are functions defined on $[a, b]$ and $\Phi(x)$ is the unknown solution. Moreover, linear boundary conditions are given as

$$\mathfrak{B}\,\Phi(x) = g(x) \tag{5-22}$$

to ensure a unique solution. The approximation of the unknown solution $\Phi(x)$ is given by a finite linear combination of basis functions

$$\Phi(x) \approx \hat{\Phi}_p(x) = \sum_{j=0}^{p} c_j\, \phi_j(x)\,, \tag{5-23}$$

or in matrix notation

$$\hat{\Phi}_p(x) = \boldsymbol{\Phi}\mathbf{c}\,, \tag{5-24}$$

with

$$\boldsymbol{\Phi} = \begin{bmatrix} \phi_0(x) & \phi_1(x) & \cdots & \phi_p(x) \end{bmatrix} \tag{5-25}$$

and

$$\mathbf{c}^{\mathsf{T}} = \begin{bmatrix} c_0 & c_1 & \cdots & c_p \end{bmatrix}. \tag{5-26}$$

Based on (5-24) the left hand side of the ODE (5-20) can be approximated by

$$\mathfrak{L}\,\Phi(x) \approx \boldsymbol{\phi}\boldsymbol{\mathcal{L}}\,\mathbf{c}\,, \tag{5-27}$$

with the differential operator $\boldsymbol{\mathcal{L}}$, which is unknown so far. Inserting (5-27) into (5-20) and rearranging yields the residual function

$$v(x) = \boldsymbol{\phi}\boldsymbol{\mathcal{L}}\,\mathbf{c} - f(x)\,. \tag{5-28}$$

To derive a least squares solution for the vector of unknown coefficients $\mathbf{c}$ we need to find the minimum of the target function

$$\Omega = \int_a^b \Big(\boldsymbol{\phi}\boldsymbol{\mathcal{L}}\,\mathbf{c} - f(x)\Big)^2\,\mathrm{d}x \to \min\,. \tag{5-29}$$

Taking the first order derivative of (5-29) and setting it to zero yields the normal equation system

$$\frac{1}{2}\frac{\mathrm{d}\Omega}{\mathrm{d}\mathbf{c}} = \int_a^b \boldsymbol{\mathcal{L}}^{\mathsf{T}}\boldsymbol{\phi}^{\mathsf{T}}\Big(\boldsymbol{\phi}\boldsymbol{\mathcal{L}}\,\mathbf{c} - f(x)\Big)\,\mathrm{d}x = 0\,. \tag{5-30}$$

Rearranging (5-30) results in

$$\int_a^b \boldsymbol{\mathcal{L}}^{\mathsf{T}}\boldsymbol{\phi}^{\mathsf{T}}\boldsymbol{\phi}\boldsymbol{\mathcal{L}}\,\mathbf{c}\,\mathrm{d}x = \int_a^b \boldsymbol{\mathcal{L}}^{\mathsf{T}}\boldsymbol{\phi}^{\mathsf{T}} f(x)\,\mathrm{d}x\,. \tag{5-31}$$

For basis functions, such as monomials or Chebyshev polynomials, the differential operator $\boldsymbol{\mathcal{L}}$ contains only constant values and therefore we can extract the operator from the integral. Thus, the normal equation system (5-31) can be equivalently written as

$$\boldsymbol{\mathcal{L}}^{\mathsf{T}}\int_a^b \boldsymbol{\phi}^{\mathsf{T}}\boldsymbol{\phi}\,\mathrm{d}x\;\boldsymbol{\mathcal{L}}\,\mathbf{c} = \boldsymbol{\mathcal{L}}^{\mathsf{T}}\int_a^b \boldsymbol{\phi}^{\mathsf{T}} f(x)\,\mathrm{d}x\,, \tag{5-32}$$

with

$$\mathbf{N} = \int_a^b \boldsymbol{\phi}^{\mathsf{T}}\boldsymbol{\phi}\,\mathrm{d}x = \langle\phi_i,\phi_j\rangle = \begin{bmatrix} \langle\phi_0,\phi_0\rangle & \langle\phi_1,\phi_0\rangle & \cdots & \langle\phi_p,\phi_0\rangle \\ \langle\phi_0,\phi_1\rangle & \langle\phi_1,\phi_1\rangle & \cdots & \langle\phi_p,\phi_1\rangle \\ \vdots & \vdots & \ddots & \vdots \\ \langle\phi_0,\phi_p\rangle & \langle\phi_1,\phi_p\rangle & \cdots & \langle\phi_p,\phi_p\rangle \end{bmatrix} \tag{5-33}$$

and

$$\mathbf{n} = \int_a^b \boldsymbol{\phi}^{\mathsf{T}} f(x)\,\mathrm{d}x = \langle\phi_i, f(x)\rangle = \begin{bmatrix} \langle\phi_0, f(x)\rangle \\ \langle\phi_1, f(x)\rangle \\ \vdots \\ \langle\phi_p, f(x)\rangle \end{bmatrix} \tag{5-34}$$

being the normal matrix and the vector of the right hand side of a least squares approximation of functions, as widely used in the previous chapters. The normal equation system (5-32) simplifies to

$$\begin{aligned} \boldsymbol{\mathcal{L}}^{\mathsf{T}}\mathbf{N}\,\boldsymbol{\mathcal{L}}\,\mathbf{c} &= \boldsymbol{\mathcal{L}}^{\mathsf{T}}\mathbf{n} \\ \mathbf{K}\,\mathbf{c} &= \mathbf{f}\,. \end{aligned} \tag{5-35}$$

That the operator $\boldsymbol{\mathcal{L}}$ is independent of x is of great advantage for solving BVPs, while using monomials or Chebyshev polynomials, as basis functions. Instead of solving the integrals for the derivatives of the basis functions, as illustrated in Chapter 5, we can solve them for the basis functions directly and do the conversion by applying the differential operator $\boldsymbol{\mathcal{L}}$. This idea is clearly illustrated in the following section.

5.1.1 *Approximation of BVP in the monomial basis*

In this section we will determine the least squares approximation of the unknown solution $\Phi(x)$ of the given boundary value problem

$$\frac{\mathrm{d}^2\,\Phi(x)}{\mathrm{d}x^2} = \sin(3x) + \frac{1}{10}\pi\,, \quad \Phi(x = \pm 1) = 0\,, \tag{5-36}$$

for $x \in [-1, 1]$, which was already solved in Chapter 5. The analytical solution is depicted in Figure 5-1. As before, we will determine an approximation of the unknown solution $\Phi(x)$ by a polynomial in the monomial basis of 3^{rd} degree

$$\Phi(x) \approx \hat{\Phi}_3(x) = \sum_{j=0}^{3} c_j\,\phi_j(x) = \sum_{j=0}^{3} c_j\,x^j = c_0 + c_1 x + c_2 x^2 + c_3 x^3\,, \tag{5-37}$$

or in matrix notation

$$\hat{\Phi}_3(x) = \boldsymbol{\phi}\mathbf{c} = \begin{bmatrix} 1 & x & x^2 & x^3 \end{bmatrix} \begin{bmatrix} c_0 \\ c_1 \\ c_2 \\ c_3 \end{bmatrix}. \tag{5-38}$$

The first derivative of the approximation $\hat{\Phi}_3(x)$ with respect to x is

$$\frac{\mathrm{d}\hat{\Phi}_3(x)}{\mathrm{d}x} = c_1 + 2c_2 x + 3c_3 x^2 \tag{5-39}$$

and can be written in matrix notation by

$$\hat{\Phi}_x(x) = \boldsymbol{\phi}\boldsymbol{\mathcal{L}}_{\mathrm{x}}\,\mathbf{c} = \begin{bmatrix} 1 & x & x^2 & x^3 \end{bmatrix} \boldsymbol{\mathcal{L}}_{\mathrm{x}} \begin{bmatrix} c_0 \\ c_1 \\ c_2 \\ c_3 \end{bmatrix}, \tag{5-40}$$

with the differential operator

$$\boldsymbol{\mathcal{L}}_{\mathrm{x}} = \begin{bmatrix} 0 & 1 & 0 & 0 \\ 0 & 0 & 2 & 0 \\ 0 & 0 & 0 & 3 \\ 0 & 0 & 0 & 0 \end{bmatrix}. \tag{5-41}$$

Furthermore, the second derivative results in

$$\hat{\Phi}_{xx}(x) = \boldsymbol{\phi}\boldsymbol{\mathcal{L}}_{\mathrm{xx}}\,\mathbf{c}\,, \tag{5-42}$$

with

$$\boldsymbol{\mathcal{L}}_{\mathrm{xx}} = \boldsymbol{\mathcal{L}}_{\mathrm{x}}^2 = \begin{bmatrix} 0 & 0 & 2 & 0 \\ 0 & 0 & 0 & 6 \\ 0 & 0 & 0 & 0 \\ 0 & 0 & 0 & 0 \end{bmatrix}. \tag{5-43}$$

The normal equation system according to (5-32) reads

$$\boldsymbol{\mathcal{L}}_{\mathrm{xx}}^{\mathsf{T}} \int_{-1}^{1} \boldsymbol{\phi}^{\mathsf{T}}\boldsymbol{\phi}\,\mathrm{d}x\;\boldsymbol{\mathcal{L}}_{\mathrm{xx}}\,\mathbf{c} = \boldsymbol{\mathcal{L}}_{\mathrm{xx}}^{\mathsf{T}} \int_{-1}^{1} \boldsymbol{\phi}^{\mathsf{T}}\left(\sin(3x) + {}^{1}\!/_{10}\,\pi\right)\mathrm{d}x\,, \tag{5-44}$$

with

$$\mathbf{N} = \int_{-1}^{1} \boldsymbol{\phi}^{\mathsf{T}} \boldsymbol{\phi} \, \mathrm{d}x = \langle \phi_i, \phi_j \rangle = \begin{bmatrix} \langle x^0, x^0 \rangle & \langle x^1, x^0 \rangle & \langle x^2, x^0 \rangle & \langle x^3, x^0 \rangle \\ \langle x^0, x^1 \rangle & \langle x^1, x^1 \rangle & \langle x^2, x^1 \rangle & \langle x^3, x^1 \rangle \\ \langle x^0, x^2 \rangle & \langle x^1, x^2 \rangle & \langle x^2, x^2 \rangle & \langle x^3, x^2 \rangle \\ \langle x^0, x^3 \rangle & \langle x^1, x^3 \rangle & \langle x^2, x^3 \rangle & \langle x^3, x^3 \rangle \end{bmatrix} \tag{5-45}$$

and

$$\begin{aligned} \mathbf{n} &= \int_{-1}^{1} \boldsymbol{\phi}^{\mathsf{T}} \left(\sin(3x) + 1/10\pi \right) \mathrm{d}x = \langle \phi_i, \sin(3x) + 1/10\pi \rangle \\ &= \begin{bmatrix} \langle 1, \sin(3x) + \pi/10 \rangle \\ \langle x, \sin(3x) + \pi/10 \rangle \\ \langle x^2, \sin(3x) + \pi/10 \rangle \\ \langle x^3, \sin(3x) + \pi/10 \rangle \end{bmatrix} . \end{aligned} \tag{5-46}$$

Solving the integrals in (5-45) results in exactly the same matrix as for the very first example (3-4)

$$\mathbf{N} = \begin{bmatrix} 2 & 0 & 2/3 & 0 \\ 0 & 2/3 & 0 & 2/5 \\ 2/3 & 0 & 2/5 & 0 \\ 0 & 2/5 & 0 & 2/7 \end{bmatrix} \tag{5-47}$$

and $\mathbf{n}$ reads

$$\mathbf{n} = \begin{bmatrix} 0.628\,318\,530\,717\,959 \\ 0.691\,354\,999\,524\,712 \\ 0.209\,439\,510\,239\,320 \\ 0.293\,171\,670\,090\,401 \end{bmatrix} . \tag{5-48}$$

Inserting (5-47), (5-48) and the differential operator (5-43) into (5-44) yields the normal equation system

$$\begin{gathered} \mathbf{K}\,\mathbf{c} = \mathbf{f}\,, \\ \mathcal{L}^{\mathsf{T}} \mathbf{N}\, \mathcal{L}\, \mathbf{c} = \mathcal{L}^{\mathsf{T}} \mathbf{n}\,, \\ \begin{bmatrix} 0 & 0 & 0 & 0 \\ 0 & 0 & 0 & 0 \\ 0 & 0 & 8 & 0 \\ 0 & 0 & 0 & 24 \end{bmatrix} \begin{bmatrix} c_0 \\ c_1 \\ c_2 \\ c_3 \end{bmatrix} = \begin{bmatrix} 0.000\,000\,000\,000\,000 \\ 0.000\,000\,000\,000\,000 \\ 1.256\,637\,061\,435\,917 \\ 4.148\,129\,997\,148\,272 \end{bmatrix} , \end{gathered} \tag{5-49}$$

which, of course, is identical to (5-13). Introducing the same constraints (5-16) for the given boundary conditions in (5-36) and solving the extended normal equation system (5-18) results in the exactly the same solution for the coefficients (5-19) of a polynomial of 3rd degree as was to be expected. All presented calculations have been done with Programme 5-1.

Programme 5-1: Code for polynomial approximation of BVPs in the monomial basis.

```
%Approximation of Phi(x) on [-1, 1]
a=-1; b=1;

%Polynomial degree
p=3;

%Differential operator
Lx=diag(1:p,1); Lxx=Lx^2;

%Preallocate matrices
N=zeros(p+1); n=zeros(p+1,1);

%Normal equation system for Phi=f(x)
for j=0:p
    for i=0:p
        N(j+1,i+1)=1/(i+j+1)*(1-a^(i+j+1));
    end
    n(j+1)=integral(@(x) (sin(3*x)+1/10*pi).*x.^j,a,b);
end

%Applying Lxx to obtain the normal equation system for Phi
    ''=f(x)
K=Lxx'*N*Lxx; f=Lxx'*n;

%Boundary conditions
C=zeros(2,p+1); C(1,:)=(-1).^(0:p)'; C(2,:)=1.^(0:p)';

%Extended normal equation system
K_ext=[K C';C zeros(2)]; f_ext=[f;zeros(2,1)];

%Solution
c=K_ext\f_ext;

%Deleting the Lagrangian multipliers
c(end-1:end)=[];
```

As we have seen in this section, we can easily determine an approximation for the unknown solution of certain boundary value problems, which is mainly based on Programme 3-1 and with the aid of a differential operator.

5.1.2 *Approximation of BVP in the Chebyshev basis*

The presented least squares approximation of BVPs in matrix notation in Section 5.1 can directly be applied for the Chebyshev basis, which will be illustrated on the approximation of the unknown solution $\Phi(x)$ of the already given boundary value problem

$$\frac{\mathrm{d}^2\Phi(x)}{\mathrm{d}x^2} = \sin(3x) + \frac{1}{10}\pi\,, \quad \Phi(x=\pm 1) = 0\,, \tag{5-50}$$

for $x \in [-1,1]$. The unknown solution $\Phi(x)$ will be approximated by a polynomial in the Chebyshev basis

$$\Phi(x) \approx \hat{\Phi}_p(x) = \sum_{j=0}^{p} c_j\,\phi_j(x) = \sum_{j=0}^{p} c_j\,T_j(x)\,, \tag{5-51}$$

or in matrix notation

$$\hat{\Phi}_p(x) = \boldsymbol{\Phi}\,\mathbf{c} = \begin{bmatrix} T_0(x) & T_1(x) & \cdots & T_p(x) \end{bmatrix} \begin{bmatrix} c_0 \\ c_1 \\ \vdots \\ c_p \end{bmatrix} . \tag{5-52}$$

The first derivative of the approximation $\hat{\Phi}_p(x)$ with respect to x reads

$$\frac{\mathrm{d}\hat{\Phi}_p(x)}{\mathrm{d}x} = \sum_{j=0}^{p} c_j \frac{\mathrm{d}T_j(x)}{\mathrm{d}x} . \tag{5-53}$$

According to MASON and HANDSCOMB (2003, p. 34) the derivative of $T_j(x)$ is given by

$$\frac{\mathrm{d}T_j(x)}{\mathrm{d}x} = j\,U_{j-1}(x) , \tag{5-54}$$

with the Chebyshev polynomials of the second-kind $U_j(x)$. The differentiation operator reads

$$\boldsymbol{\mathcal{D}} = \begin{bmatrix} 0 & 1 & & & \\ & & 2 & & \\ & & & 3 & \\ & & & & \ddots \end{bmatrix} \tag{5-55}$$

and is identical to the differential operator in the monomial basis (5-41). But, applying $\boldsymbol{\mathcal{D}}$ changes the basis of the series from $T_j(x)$ into $U_j(x)$.

The Chebyshev polynomials of the second-kind $U_j(x)$ satisfy the recurrence relation

$$U_j(x) = 2xU_{j-1}(x) - U_{j-2}(x) \qquad \text{for } j \geq 2 \tag{5-56}$$

with the initial conditions

$$U_0(x) = 1 \qquad \text{and} \qquad U_1(x) = 2x . \tag{5-57}$$

The relationship between the Chebyshev polynomials of the first-kind and second-kind is given by

$$T_j(x) = \frac{1}{2}\left(U_j(x) - U_{j-2}(x)\right) \qquad \text{for } j \geq 2 , \tag{5-58}$$

see (MASON and HANDSCOMB 2003, p. 4). Therefore, a series in the Chebyshev basis $T_j(x)$ can be represented by $U_j(x)$ as follows

$$\hat{\Phi}_p(x) = \sum_{j=0}^{p} c_j\,T_j(x) = c_0U_0(x) + \frac{1}{2}c_1U_1(x) + \frac{1}{2}\sum_{j=2}^{p} c_j\left(U_j(x) - U_{j-2}(x)\right) . \tag{5-59}$$

Resorting the right hand side of (5-59) yields

$$\hat{\Phi}_p(x) = \sum_{j=0}^{p} c_j\,T_j(x) = \left(c_0 - \frac{1}{2}c_2\right)U_0(x) + \sum_{j=1}^{p} \frac{1}{2}\left(c_j - c_{j-2}\right)U_j(x) , \tag{5-60}$$

see also OLVER and TOWNSEND (2013). Based on (5-60) we can define the following conversion operator that maps the coefficients of a series in $T_j(x)$ into $U_j(x)$

$$\boldsymbol{\mathcal{S}} = \begin{bmatrix} 1 & & -1/2 & & & \\ & 1/2 & & -1/2 & & \\ & & 1/2 & & -1/2 & \\ & & & \ddots & & \ddots \end{bmatrix} \tag{5-61}$$

Finally, the differential operator results in

$$\boldsymbol{\mathcal{L}}_{\mathrm{x}} = \boldsymbol{\mathcal{S}}^{-1}\boldsymbol{\mathcal{D}}\,, \tag{5-62}$$

which is an upper triangular sparse matrix. Now we have everything to approximate the unknown solution $\Phi(x)$ of the given BVP (5-50) by a polynomial in the Chebyshev basis of 3rd degree

$$\Phi(x) \approx \hat{\Phi}_3(x) = \sum_{j=0}^{3} c_j\,\phi_j(x) = \sum_{j=0}^{3} c_j\,T_j(x)\,, \tag{5-63}$$

or in matrix notation

$$\hat{\Phi}_3(x) = \boldsymbol{\phi}\,\mathbf{c} = \begin{bmatrix} T_0(x) & T_1(x) & T_2(x) & T_3(x) \end{bmatrix} \begin{bmatrix} c_0 \\ c_1 \\ c_2 \\ c_3 \end{bmatrix}. \tag{5-64}$$

The differential operator for a polynomial of 3rd degree results in

$$\boldsymbol{\mathcal{L}}_{\mathrm{x}} = \boldsymbol{\mathcal{S}}^{-1}\boldsymbol{\mathcal{D}} = \begin{bmatrix} 1 & 0 & -1/2 & 0 \\ 0 & 1/2 & 0 & -1/2 \\ 0 & 0 & 1/2 & 0 \\ 0 & 0 & 0 & 1/2 \end{bmatrix}^{-1} \begin{bmatrix} 0 & 1 & 0 & 0 \\ 0 & 0 & 2 & 0 \\ 0 & 0 & 0 & 3 \\ 0 & 0 & 0 & 0 \end{bmatrix} = \begin{bmatrix} 0 & 1 & 0 & 3 \\ 0 & 0 & 4 & 0 \\ 0 & 0 & 0 & 6 \\ 0 & 0 & 0 & 0 \end{bmatrix} \tag{5-65}$$

and the second derivative of the approximation $\hat{\Phi}_3(x)$ with respect to x reads

$$\hat{\Phi}_{\mathrm{xx}}(x) = \boldsymbol{\phi}\,\boldsymbol{\mathcal{L}}_{\mathrm{xx}}\,\mathbf{c}\,, \tag{5-66}$$

with $\boldsymbol{\mathcal{L}}_{\mathrm{xx}} = \boldsymbol{\mathcal{L}}_{\mathrm{x}}^2$. The normal equation system according to (5-32) reads

$$\begin{aligned} \boldsymbol{\mathcal{L}}_{\mathrm{xx}}^{\mathsf{T}} \int_{-1}^{1} \boldsymbol{\phi}^{\mathsf{T}}\boldsymbol{\phi}\,\mathrm{d}x\;\boldsymbol{\mathcal{L}}_{\mathrm{xx}}\,\mathbf{c} &= \boldsymbol{\mathcal{L}}_{\mathrm{xx}}^{\mathsf{T}} \int_{-1}^{1} \boldsymbol{\phi}^{\mathsf{T}}\left(\sin(3x) + 1/10\,\pi\right)\mathrm{d}x\,, \\ \boldsymbol{\mathcal{L}}_{\mathrm{xx}}^{\mathsf{T}}\,\mathbf{N}\,\boldsymbol{\mathcal{L}}_{\mathrm{xx}}\,\mathbf{c} &= \boldsymbol{\mathcal{L}}_{\mathrm{xx}}^{\mathsf{T}}\,\mathbf{n}\,. \end{aligned} \tag{5-67}$$

While Chebyshev polynomials are orthogonal with respect to a weighted inner product, the matrix $\mathbf{N}$ in (5-67) results in

$$\begin{aligned} \mathbf{N} = \int_{-1}^{1} \boldsymbol{\phi}^{\mathsf{T}}\boldsymbol{\phi}\,\mathrm{d}x = \langle T_i, T_j\rangle &= \begin{bmatrix} \langle T_0, T_0\rangle & 0 & 0 & 0 \\ 0 & \langle T_1, T_1\rangle & 0 & 0 \\ 0 & 0 & \langle T_2, T_2\rangle & 0 \\ 0 & 0 & 0 & \langle T_3, T_3\rangle \end{bmatrix} \\ &= \begin{bmatrix} \pi & 0 & 0 & 0 \\ 0 & \pi/2 & 0 & 0 \\ 0 & 0 & \pi/2 & 0 \\ 0 & 0 & 0 & \pi/2 \end{bmatrix} \end{aligned} \tag{5-68}$$

and for the integrals of the right hand side we get

$$\begin{aligned} \mathbf{n} = \int_{-1}^{1} \boldsymbol{\phi}^{\mathsf{T}}\left(\sin(3x) + 1/10\pi\right)\mathrm{d}x &= \langle T_i, \sin(3x) + 1/10\pi\rangle \\ &= \begin{bmatrix} \langle T_0, \sin(3x) + 1/10\pi\rangle \\ \langle T_1, \sin(3x) + 1/10\pi\rangle \\ \langle T_2, \sin(3x) + 1/10\pi\rangle \\ \langle T_3, \sin(3x) + 1/10\pi\rangle \end{bmatrix} = \begin{bmatrix} 0.986\,960\,440\,108\,936 \\ 1.065\,185\,133\,238\,888 \\ 0.000\,000\,000\,000\,000 \\ -0.970\,949\,177\,735\,561 \end{bmatrix}. \end{aligned} \tag{5-69}$$

Inserting (5-68), (5-69) and the differential operator (5-65) into (5-67) yields the normal equation system

$$\mathbf{K}\,\mathbf{c} = \mathbf{f}\,,$$

$$\begin{bmatrix} 0 & 0 & 0 & 0 \\ 0 & 0 & 0 & 0 \\ 0 & 0 & 16\pi & 0 \\ 0 & 0 & 0 & 288\pi \end{bmatrix} \begin{bmatrix} c_0 \\ c_1 \\ c_2 \\ c_3 \end{bmatrix} = \begin{bmatrix} 0.000\,000\,000\,000\,000 \\ 0.000\,000\,000\,000\,000 \\ 3.947\,841\,760\,435\,742 \\ 25.564\,443\,197\,733\,318 \end{bmatrix}. \tag{5-70}$$

Introducing the same constraints (5-16) for the given boundary conditions in (5-50) and solving the extended normal equation system

$$\begin{bmatrix} \mathbf{K} & \mathbf{C}^\mathsf{T} \\ \mathbf{C} & \mathbf{0} \end{bmatrix} \begin{bmatrix} \mathbf{c} \\ \boldsymbol{\lambda} \end{bmatrix} = \begin{bmatrix} \mathbf{f} \\ \mathbf{0} \end{bmatrix}, \tag{5-71}$$

yields the coefficients a polynomial in the Chebyshev basis of 3$^{\text{rd}}$ degree

$$\begin{bmatrix} c_0 \\ c_1 \\ c_2 \\ c_3 \end{bmatrix} = \begin{bmatrix} -0.078\,539\,816\,339\,745 \\ -0.028\,254\,913\,210\,495 \\ 0.078\,539\,816\,339\,745 \\ 0.028\,254\,913\,210\,495 \end{bmatrix}. \tag{5-72}$$

The resulting polynomial approximation for the unknown solution $\Phi(x)$ of the boundary value problem (5-50) is depicted in Figure 5-4.

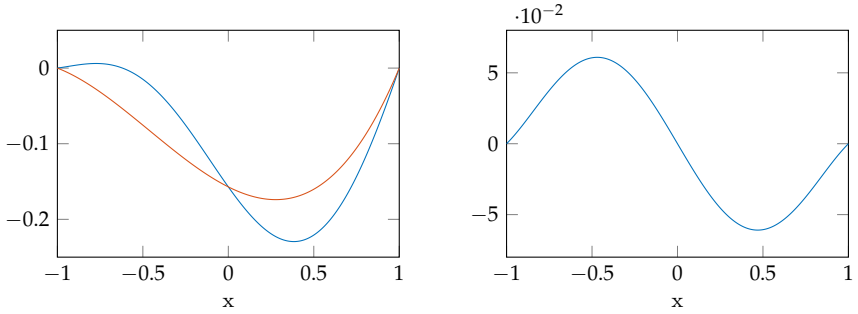

Figure 5-4: Analytical solution (5-8) in blue and its polynomial approximation in the Chebyshev basis of 3$^{\text{rd}}$ degree in red (left). Residual function $v(x) = \Phi(x) - \hat{\Phi}_3(x)$ (right).

The residual function illustrated in Figure 5-4 (right) shows deviation within a range of ≈ 0.05 and can be further decreased while increasing the polynomial degree. The best approximation is depicted in Figure 5-5.

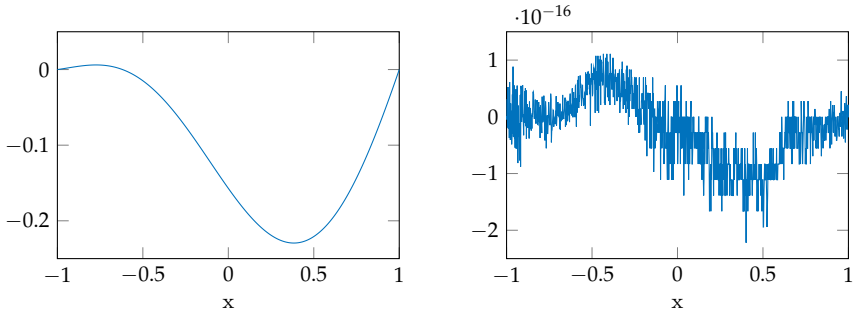

Figure 5-5: Polynomial approximation in the Chebyshev basis of 21$^{\text{st}}$ degree (left). Residual function $v(x) = \Phi(x) - \hat{\Phi}_{21}(x)$ (right).

Figure 5-5 (right) shows that a polynomial in the Chebyshev basis of 21$^{\text{st}}$ degree approximates the unknown solution $\Phi(x)$ of the BVP in (5-50) within

machine precision. In comparison to Section 3.3.1, an approximation of the unknown solution of BVPs in the Chebyshev basis leads to a dense normal matrix **K**. The advantage of orthogonal basis functions is no longer given for solving boundary value problems. The presented least squares approximation of BVPs in the Chebyshev basis leads also to an ill-conditioned extended normal matrix in (5-71). However, this is even worse for the resulting extended normal matrix in the monomial basis.

All calculations have been done with Programme 5-2.

Programme 5-2: Code for a polynomial approximation of BVPs in the Chebyshev basis.

```
%Approximation of Phi(x) on [-1, 1]
a=-1; b=1;

%Polynomial degree
p=3;

%Differentiation operator dT/dx -> U
D=diag(1:p,1);

%Conversion operator T -> U
S=diag(1/2*ones(p+1,1))-diag(1/2*ones(p-1,1),2);
S(1,1)=1;

%Differential operator
Lx=S\D; Lxx=Lx^2;

%Solution of the normal matrix N = int T_i * T_j
N=diag([pi; pi/2*ones(p,1)]);

%Preallocation
n=zeros(p+1,1);

%right hand side n
for i=0:p
    n(i+1)=integral(@(x) (sin(3*cos(x))+1/10*pi).*cos(i*x)
        ,0,pi);
end

%Applying Lxx to obtain the normal equation system for Phi
    ''=f(x)
K=Lxx'*N*Lxx; f=Lxx'*n;

%Boundary conditions
C=zeros(2,p+1); C(1,:)=(-1).^(0:p)'; C(2,:)=1.^(0:p)';

%Extended normal equation system
K_ext=[K C';C zeros(2)]; f_ext=[f;zeros(2,1)];

%Solution
c=K_ext\f_ext;

%Deleting the Lagrangian multipliers
c(end-1:end)=[];
```

5.1.3 *Alternative approximation of BVP in the Chebyshev basis*

As already mentioned in Section 3.3.1 and according to TREFETHEN (2013, Theorem 3.1), if $\Phi(x)$ is Lipschitz continuous, then it has an absolutely and uniformly convergent Chebyshev series

$$\Phi(x) = \sum_{j=0}^{\infty} c_j \, T_j(x) \, . \tag{5-73}$$

Thus, we can determine the coefficients c_j of a least squares approximation in a faster and numerical more stable way, which is mainly used for the numerical solution of BVPs by spectral methods as described in, for example, (TREFETHEN 2008), (OLVER and TOWNSEND 2013), (TOWNSEND 2014). To illustrate this procedure we will consider the same example from the previous section

$$\frac{\mathrm{d}^2 \Phi(x)}{\mathrm{d}x^2} = \sin(3x) + \frac{1}{10}\pi \, , \quad \Phi(x = \pm 1) = 0 \, , \tag{5-74}$$

for $x \in [-1, 1]$. Let us rewrite the differential equation (5-74) into

$$\Phi_{xx}(x) = g(x), \tag{5-75}$$

with

$$g(x) = \sin(3x) + \frac{1}{10}\pi. \tag{5-76}$$

As shown in Section 3.3.1 function $g(x)$ can easily be approximated within machine precision by a truncated Chebyshev series

$$g(x) \approx \hat{g}(x) = \sum_{j=0}^{p} g_j \, T_j(x) \tag{5-77}$$

or in matrix notation

$$\hat{g}(x) = \boldsymbol{\Phi} \, \mathbf{g} = \begin{bmatrix} T_0(x) & T_1(x) & \cdots & T_p(x) \end{bmatrix} \begin{bmatrix} g_0 \\ g_1 \\ \vdots \\ g_p \end{bmatrix} . \tag{5-78}$$

The second derivative of the unknown solution $\Phi_{xx}(x)$ is given by (5-66) and Equation (5-75) reads

$$\boldsymbol{\Phi} \boldsymbol{\mathcal{L}}_{xx} \, \mathbf{c} = \boldsymbol{\Phi} \, \mathbf{g} \, . \tag{5-79}$$

Equating the coefficients with respect to $\boldsymbol{\Phi}$ yields

$$\boldsymbol{\mathcal{L}}_{xx} \, \mathbf{c} = \mathbf{g} \, . \tag{5-80}$$

Introducing the constraints (5-16) for the given boundary conditions and solving the extended normal equation system

$$\begin{bmatrix} \boldsymbol{\mathcal{L}}_{xx} & \mathbf{C}^{\mathsf{T}} \\ \mathbf{C} & \mathbf{0} \end{bmatrix} \begin{bmatrix} \mathbf{c} \\ \boldsymbol{\lambda} \end{bmatrix} = \begin{bmatrix} \mathbf{g} \\ \mathbf{0} \end{bmatrix} . \tag{5-81}$$

yields the coefficients a polynomial in the Chebyshev basis. In case $g(x)$ and $\Phi(x)$ are approximated within machine precision, these coefficients will be exactly the same as using the extended normal equation system (5-71) of a least squares approximation. The first column in Table 5-1 shows the 21 coefficients $\mathbf{c}_{\mathrm{LS}}$ of a least squares approximation of the BVP (5-74) according to

(5-71). While the other three columns are showing the coefficients c_p determined by (5-81) for different polynomial degree p.

Table 5-1: Coefficients c_j.

$\mathbf{c}_{\mathrm{LS}}$	$\mathbf{c}_p$		
	$p = 5$	$p = 12$	$p = 21$
-0.078 539 816 339 745	-0.078 539 816 339 745	-0.078 539 816 339 745	-0.078 539 816 339 745
-0.059 666 434 332 445	−0.059 878 326 017 304	−0.059 666 433 281 276	-0.059 666 434 332 445
0.078 539 816 339 745	0.078 539 816 339 745	0.078 539 816 339 745	0.078 539 816 339 745
0.068 680 604 945 611	0.068 680 604 945 611	0.068 680 604 945 611	0.068 680 604 945 611
-0.000 000 000 000 000	-0.000 000 000 000 000	0.000 000 000 000 000	0.000 000 000 000 000
-0.009 561 874 417 122	0.008 802 278 928 307	-0.009 561 874 417 122	-0.009 561 874 417 122
0.000 000 000 000 000		-0.000 000 000 000 000	-0.000 000 000 000 000
0.000 566 065 433 734		0.000 566 065 433 734	0.000 566 065 433 734
-0.000 000 000 000 000		-0.000 000 000 000 000	-0.000 000 000 000 000
-0.000 018 754 449 180		-0.000 018 754 449 180	-0.000 018 754 449 180
-0.000 000 000 000 000		0.000 000 000 000 000	0.000 000 000 000 000
0.000 000 398 664 369		0.000 000 391 768 232	0.000 000 398 664 369
0.000 000 000 000 000		-0.000 000 000 000 000	-0.000 000 000 000 000
-0.000 000 005 909 044			-0.000 000 005 909 044
-0.000 000 000 000 000			-0.000 000 000 000 000
0.000 000 000 064 614			0.000 000 000 064 614
0.000 000 000 000 000			0.000 000 000 000 000
-0.000 000 000 000 543			-0.000 000 000 000 543
-0.000 000 000 000 000			-0.000 000 000 000 000
0.000 000 000 000 004			0.000 000 000 000 004
0.000 000 000 000 000			-0.000 000 000 000 000
-0.000 000 000 000 000			-0.000 000 000 000 000

As one can see, some of the coefficients for $p = 5$ and $p = 12$ are significantly differing from $\mathbf{c}_{\mathrm{LS}}$, while the coefficients for $p = 21$ are equal down to the last digit to those a least squares approximation $\mathbf{c}_{\mathrm{LS}}$. As already mentioned, solving (5-81) for the unknown coefficients is faster and more accurate than solving the extended normal equation system (5-71) of a least squares approximation. The extended normal matrix in (5-71) is nearly singular for a polynomial of 140^{th} degree, while using (5-81) allows to approximate the unknown solution by a polynomial of even more than 2000^{th} degree.

A sophisticated approach for solving PDEs using a spectral method is presented by (Townsend and Olver 2015), which can approximate the unknown solution by a polynomial over a millionth degree within seconds.

6

SUMMARY

In Chapter 3, we discussed in detail the drawbacks of an approximation in the monomial basis and its reasons. Afterwards we attempted to avoid the drawbacks by an elementwise approximation in the monomial basis in Section 3.1. Although better results could be achieved, the actual problem of the monomial basis remains. As shown in Section 3.2, an elementwise approximation is only feasible by an appropriate change of the basis, whereby the unknown parameters have new properties. This approach enables numerically stable and efficient solutions, which are often used in many engineering sciences. However, with the big disadvantage that usually a lot of unknown parameters are needed. Then, an approximation using orthogonal basis functions was presented in Section 3.3, while we only focused on the Chebyshev and Fourier basis. The advantages of an approximation in the Chebyshev basis were clearly shown by some examples and although an approximation of non-periodic functions in the Fourier basis is already per definition not suitable, it was nevertheless shown for illustrative reasons in Section 3.3.2 as both sets of orthogonal basis functions are closely related. Based on the relationship between these two bases addressed in Section 3.3.3, the Chebyshev coefficients can be determined very efficiently using FFT, which finally leads to a very powerful approach for the approximation of continuous functions.

In Chapter 4 we have extended the approaches shown to the approximation of functions in two dimensions. The problem that arises for an elementwise continuous approximation for arbitrary polynomial degree was addressed in Section 4.1 and two possible solutions were presented in Section 4.2. Then the advantages of an approximation in the Chebyshev basis were again demonstrated and the approach extended to arbitrary convex tetragons as elements.

Finally, Chapter 5 briefly described how the unknown solution of some BVPs can be approximated in the monomial and Chebyshev basis as it was done in the previous chapters. In addition, an alternative approach for calculating the Chebyshev coefficients of a least squares approximation was described in Section 5.1.3. Following this approach, the functional model for MeMoS is derived in the following part. Thus, it is guaranteed that the functional model at least for all numerical studies is always complete and the results are not falsified by any approximation errors, cf. Figure I.4.

Part III

MEASUREMENT– AND MODEL–BASED STRUCTURAL ANALYSIS

SYNOPSIS

In the previous part we got a general insight into the approximation of functions and focused mainly on polynomials in the Chebyshev basis. It was shown that for at least simple geometric domains this set of basis functions has substantial advantages and basically always provides an approximation of the function in the range of the machine precision. The approximation in the Chebyshev basis also offers the possibility to easily and quickly perform numerical computations with functions, such as computing derivatives, integrals or root finding using of the open-source package Chebfun (2021), which was introduced by Battles and Trefethen (2004). This is of particular advantage for the tools developed in Chapter 10.1.

With respect to the experimental studies, the mechanical model of a four-point bending test is derived first and its analytical solution is approximated by a polynomial in the Chebyshev basis. Afterwards, the approximation is directly embedded as the functional model in a least squares adjustment of static measurements, such as displacements, inclinations and strains using a physical model. Based on this so-called Integrated Analysis (IA) detailed numerical studies are carried out to analyse the impact of random errors on the estimated unknown parameters and also clarify the question of how damage affects the measurements at all. Thus, a detailed insight into the nature of the inverse problem is provided. In accordance to Figure I.4, the considered

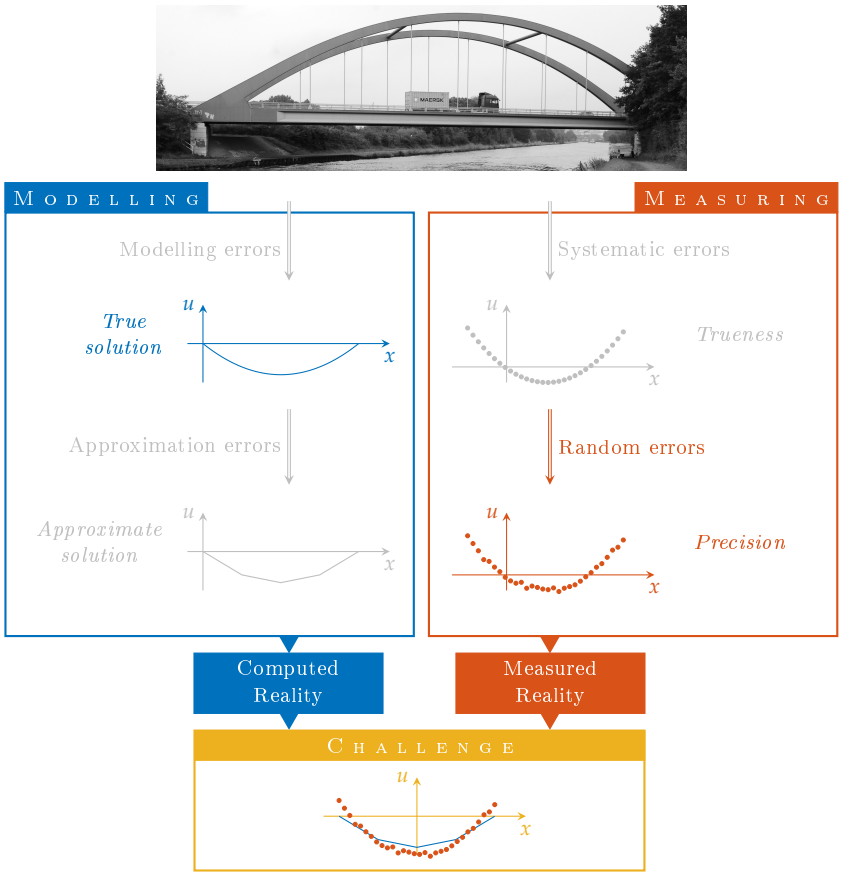

Figure S.2: Current scenario for the numerical studies concerning the damage analysis using MeMoS addressed in Chapter 9. Elements in grey are not considered or present.

error sources for the numerical studies in Chapter 9 are shown in Figure S.2. Based on the insights gained from the numerical studies, some tools for the damage analysis using Measurement– and Model–based Structural Analysis (MeMoS) are developed first and their potential for the detection and localisation of damage is demonstrated by numerical studies. Finally, a comprehensive damage analysis using MeMoS, from the model update to the evaluation of individual epochs up to the localisation of damage, is presented in an experimental example. In accordance to Figure I.4, the considered error sources for the experimental studies in Chapter 10.3 are shown in Figure S.3.

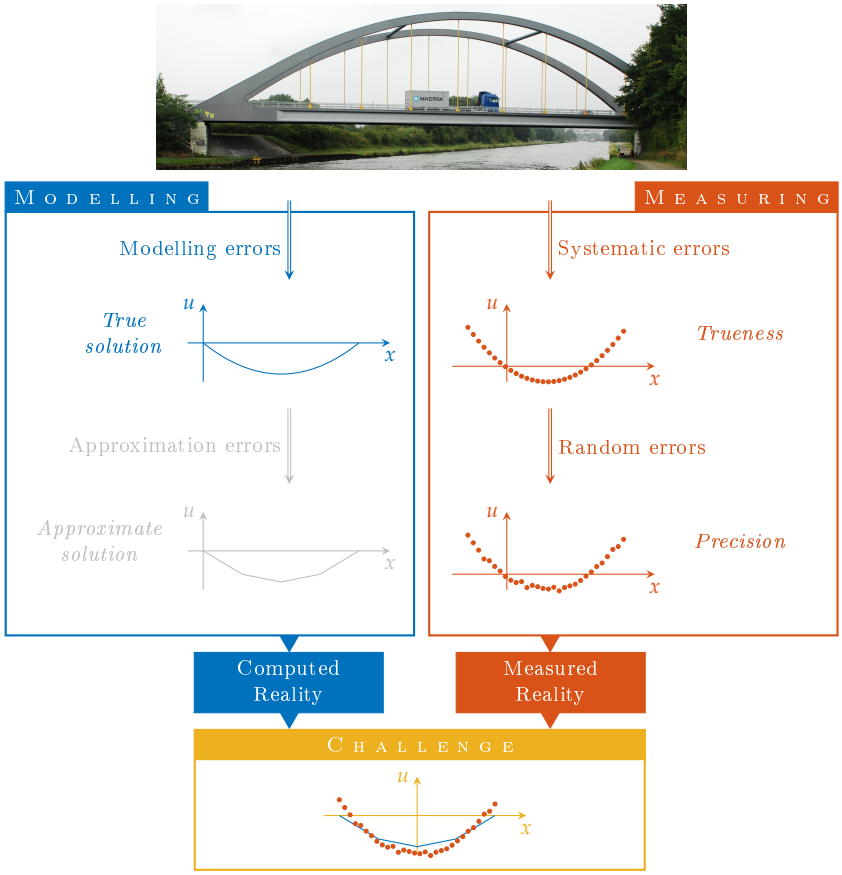

Figure S.3: Current scenario for the experimental studies concerning the damage analysis using MeMoS addressed in Chapter 10.3. Elements in grey are not present.

7 MECHANICAL MODEL

To illustrate the basic idea of a Measurement– and Model–based Structural Analysis (MeMoS) and the arising challenges, we will use a simple example in one dimension. In order to ensure that the results also corresponds to real problems, we choose a four-point bending test as an example, which is briefly presented in Section 7.1. Afterwards, we discuss the requirements of the functional model for MeMoS in Section 7.2 and in Section 7.3 we derive the solution of the BVP in the Chebyshev basis, as shown in Section 5.1.3.

7.1 FOUR-POINT BENDING TEST

The basic idea of MeMoS will be illustrated on the following simple problem. Let us consider a four-point bending test as depicted in Figure 7-1,

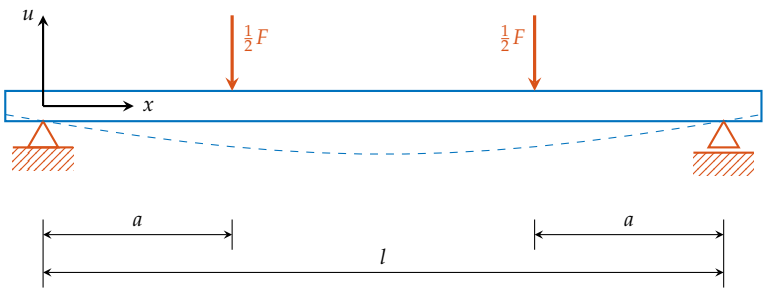

Figure 7-1: Four-point bending test

with force $F/2$ applied at the positions $x = a$ and $x = l - a$. The deformational behaviour of such a beam can be approximately described by the Euler-Bernoulli beam equation

For Euler-Bernoulli beam theory in general, please refer to standard literature such as e.g. (Carrera *et al.* 2011, Chapter 2.1) or (Öchsner 2021, Chapter 2).

$$\frac{\mathrm{d}^2 u(x)}{\mathrm{d}x^2} = -\frac{M(x)}{EI} \tag{7-1}$$

with the internal bending moment $M(x)$, elastic modulus E and the area moment of inertia I. Assuming a beam with a constant rectangular cross section along its length l, I is a constant factor given by

$$I = \frac{1}{12} w h^3 , \tag{7-2}$$

with h being the height and w the width of the beam. Due to the bearings on both sides of the beam, the Dirichtlet boundary conditions are as follows

$$u(x = 0) = 0 \qquad \text{and} \qquad u(x = l) = 0 . \tag{7-3}$$

For the illustrated four-point bending test in Figure 7-1 the internal bending moment results in

$$M(x) = \begin{cases} \frac{1}{2}Fx, & \text{for } 0 \geq x \geq a, \\ \frac{1}{2}Fa, & \text{for } a \geq x \geq (l-a), \\ \frac{1}{2}F(l-x), & \text{for } (l-a) \geq x \geq l. \end{cases} \tag{7-4}$$

and is depicted in Figure 7-2

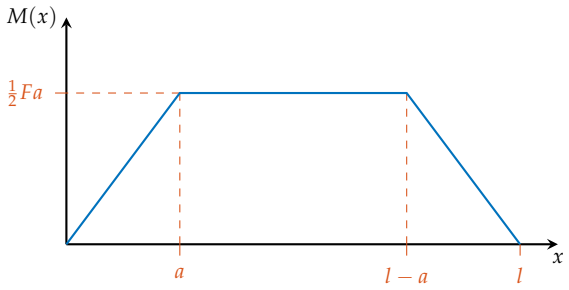

Figure 7-2: Internal bending moment $M(x)$ for the four-point bending test depicted in Figure 7-1.

7.2 OBJECTIVE

For the simple problem of a four-point bending test presented above, we need to derive a functional model that is capable of analysing different types of measurements in order to detect and localise damage to the beam. In this thesis we will only consider the following three types of measurements:

- Displacement,
- Inclination and
- Strain.

Furthermore, we need to define an unknown quantity that can be used for damage detection and localisation. Within beam theory, the elastic modulus E and the area moment of inertia I are coupled multiplicatively in (7-1). Therefore, damage caused by a change in geometry cannot be distinguished from damage caused by a change in the material, as shown in Figure 7-3.

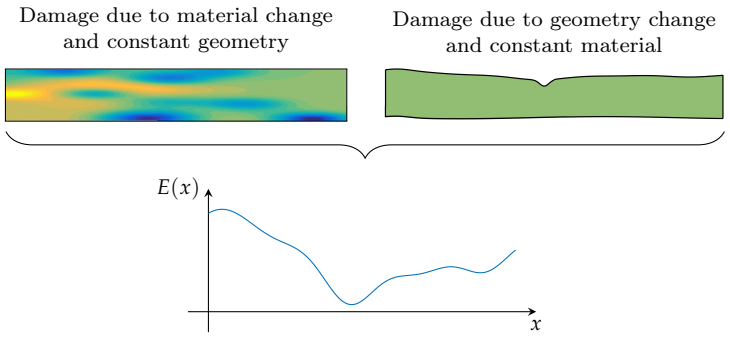

Figure 7-3: Damage due to changes in the material (upper left) or geometry (upper right) are represented by elastic modulus $E(x)$ (lower middle).

As a consequence, we chose the elastic modulus as an unknown quantity, as already shown in (Neitzel *et al.* 2014) or (Wu 2020, Chapter 5.2). But, estimating a single constant value E might be sufficient to detect damage, but it does not allow any damage localisation. Therefore, we introduce the elastic modulus as a continuous function along the beam $E(x)$. The whole process of damage detection and localisation is based on a detailed analysis of the estimated function $E(x)$.

7.3 SOLUTION OF THE BVP IN THE CHEBYSHEV BASIS

Let us consider the slightly modified Euler-Bernoulli beam equation

$$\frac{\mathrm{d}^2 u(x)}{\mathrm{d}x^2} = -\frac{M(x)}{E(x)\,I} = -\frac{M(x)}{I}\frac{1}{E(x)}\,, \tag{7-5}$$

with the elastic modulus $E(x)$ being a continuous function along the beam. At first, we express the unknown solution $u(x)$ and the internal bending moment $M(x)$ in terms of their Chebyshev series expansion

$$u(x) = \sum_{j=0}^{\infty} u_j\, T_j(x) = \boldsymbol{\Phi}\mathbf{u} \tag{7-6}$$

and

$$M(x) = \sum_{j=0}^{\infty} m_j\, T_j(x) = \boldsymbol{\Phi}\mathbf{m}\,, \tag{7-7}$$

with

$$\boldsymbol{\Phi} = \begin{bmatrix} T_0(x) & T_1(x) & T_2(x) & T_3(x) & \dots \end{bmatrix}. \tag{7-8}$$

In order to avoid $1/E(x)$ in Equation (7-5) we express this fraction by the Chebyshev series

$$\frac{1}{E(x)} = E^*(x) = \sum_{j=0}^{\infty} e_j\, T_j(x) = \boldsymbol{\Phi}\mathbf{e}\,. \tag{7-9}$$

Estimating $E(x)$ instead of $E^*(x)$ would result in a non-linear adjustment problem of a more complex functional model.

To handle the product of two functions $M(x)E^*(x)$ in terms of their Chebyshev series we introduce the following multiplication operator according to (OLVER and TOWNSEND 2013)

$$\boldsymbol{\mathcal{M}}[\mathbf{m}] = \frac{1}{2}\left[\begin{bmatrix} 2m_0 & m_1 & m_2 & m_3 & \cdots \\ m_1 & 2m_0 & m_1 & m_2 & \ddots \\ m_2 & m_1 & 2m_0 & m_1 & \ddots \\ m_3 & m_2 & m_1 & 2m_0 & \ddots \\ \vdots & \ddots & \ddots & \ddots & \ddots \end{bmatrix} + \begin{bmatrix} 0 & 0 & 0 & 0 & \cdots \\ m_1 & m_2 & m_3 & m_4 & \iddots \\ m_2 & m_3 & m_4 & m_5 & \iddots \\ m_3 & m_4 & m_5 & m_6 & \iddots \\ \vdots & \iddots & \iddots & \iddots & \iddots \end{bmatrix}\right], \tag{7-10}$$

where $\boldsymbol{\mathcal{M}}[\mathbf{m}]$ is a Toeplitz plus almost Hankel operator. According to Section 5.1.3, with the differential operator (5-62) and the multiplication operator (7-10), the modified Euler-Bernoulli beam equation (7-5) can be written as

$$\boldsymbol{\mathcal{L}}_{xx}\mathbf{u} = -\frac{1}{I}\boldsymbol{\mathcal{M}}[\mathbf{m}]\mathbf{e}\,. \tag{7-11}$$

As can be seen in Figure 7-2, the curve of the internal bending moment $M(x)$ is not a continuously differentiable function. The first derivative of $M(x)$ has two jump discontinuities located at $x = a$ and $x = l - a$ and we would need a polynomial of very high degree in order to approximate the given BVP with sufficient accuracy. Therefore, we divide the beam into 3 elements and introduce nodes at these two jump discontinuities. The resulting unique identifier for the nodes ν and elements ζ are listed Table 7-1.

ν	x_ν
1	0
2	a
3	$l-a$
4	l

and

ζ	ν_1	ν_2
1	1	2
2	2	3
3	3	4

Table 7-1: Coordinates for all nodes ν and the nodes for all three elements ζ.

Dividing the beam into three elements and according to Section 3.1, Equation 7-11 reads

$$\begin{bmatrix} \boldsymbol{\mathcal{L}}_{xx} & \mathbf{0} & \mathbf{0} \\ \mathbf{0} & \boldsymbol{\mathcal{L}}_{xx} & \mathbf{0} \\ \mathbf{0} & \mathbf{0} & \boldsymbol{\mathcal{L}}_{xx} \end{bmatrix} \begin{bmatrix} {}^1\mathbf{u} \\ {}^2\mathbf{u} \\ {}^3\mathbf{u} \end{bmatrix} = -\frac{1}{I} \begin{bmatrix} \boldsymbol{\mathcal{M}}[{}^1\mathbf{m}] & \mathbf{0} & \mathbf{0} \\ \mathbf{0} & \boldsymbol{\mathcal{M}}[{}^2\mathbf{m}] & \mathbf{0} \\ \mathbf{0} & \mathbf{0} & \boldsymbol{\mathcal{M}}[{}^3\mathbf{m}] \end{bmatrix} \begin{bmatrix} {}^1\mathbf{e} \\ {}^2\mathbf{e} \\ {}^3\mathbf{e} \end{bmatrix}. \tag{7-12}$$

So far we have not yet addressed the issue that Equation (7-5) is defined on the interval $x \in [0, l]$, while the presented approximation in the Chebyshev basis is defined on $[-1, 1]$. Therefore, we have to introduce a generalised coordinate t and map each element onto the interval $t \in [-1, 1]$. Equation (7-5) is defined on $x \in [0, l]$ and all Chebyshev series expansions are defined on $t \in [-1, 1]$. According to Section 3.2.1 the mapping for each element ζ reads

$${}^{\zeta}x = f_x\left(t, {}^{\zeta}x_{\nu_1}, {}^{\zeta}x_{\nu_2}\right) = \frac{1}{2}\left({}^{\zeta}x_{\nu_1} + {}^{\zeta}x_{\nu_2}\right) + \frac{1}{2}\left({}^{\zeta}x_{\nu_2} - {}^{\zeta}x_{\nu_1}\right)t \tag{7-13}$$

and

$${}^{\zeta}J = \frac{\mathrm{d}\,{}^{\zeta}x}{\mathrm{d}t} = \frac{1}{2}\left({}^{\zeta}x_{\nu_2} - {}^{\zeta}x_{\nu_1}\right). \tag{7-14}$$

Taking this mapping into account and analogously to Section 3.2 Equation (7-12) reads

$$\begin{bmatrix} {}^1J^2\boldsymbol{\mathcal{L}}_{xx} & \mathbf{0} & \mathbf{0} \\ \mathbf{0} & {}^2J^2\boldsymbol{\mathcal{L}}_{xx} & \mathbf{0} \\ \mathbf{0} & \mathbf{0} & {}^3J^2\boldsymbol{\mathcal{L}}_{xx} \end{bmatrix} \begin{bmatrix} {}^1\mathbf{u} \\ {}^2\mathbf{u} \\ {}^3\mathbf{u} \end{bmatrix} = -\frac{1}{I} \begin{bmatrix} \boldsymbol{\mathcal{M}}[{}^1\mathbf{m}] & \mathbf{0} & \mathbf{0} \\ \mathbf{0} & \boldsymbol{\mathcal{M}}[{}^2\mathbf{m}] & \mathbf{0} \\ \mathbf{0} & \mathbf{0} & \boldsymbol{\mathcal{M}}[{}^3\mathbf{m}] \end{bmatrix} \begin{bmatrix} {}^1\mathbf{e} \\ {}^2\mathbf{e} \\ {}^3\mathbf{e} \end{bmatrix}, \tag{7-15}$$

or in shorter notation

$$\boldsymbol{\mathcal{L}}\mathbf{u} = -\frac{1}{I}\boldsymbol{\mathcal{M}}\mathbf{e}, \tag{7-16}$$

with

$$\boldsymbol{\mathcal{L}} = \begin{bmatrix} {}^1J^2\boldsymbol{\mathcal{L}}_{xx} & \mathbf{0} & \mathbf{0} \\ \mathbf{0} & {}^2J^2\boldsymbol{\mathcal{L}}_{xx} & \mathbf{0} \\ \mathbf{0} & \mathbf{0} & {}^3J^2\boldsymbol{\mathcal{L}}_{xx} \end{bmatrix}, \tag{7-17}$$

$$\boldsymbol{\mathcal{M}} = \begin{bmatrix} \boldsymbol{\mathcal{M}}[{}^1\mathbf{m}] & \mathbf{0} & \mathbf{0} \\ \mathbf{0} & \boldsymbol{\mathcal{M}}[{}^2\mathbf{m}] & \mathbf{0} \\ \mathbf{0} & \mathbf{0} & \boldsymbol{\mathcal{M}}[{}^3\mathbf{m}] \end{bmatrix}, \tag{7-18}$$

$$\mathbf{u} = \begin{bmatrix} {}^1\mathbf{u} \\ {}^2\mathbf{u} \\ {}^3\mathbf{u} \end{bmatrix} \quad \text{and} \quad \mathbf{e} = \begin{bmatrix} {}^1\mathbf{e} \\ {}^2\mathbf{e} \\ {}^3\mathbf{e} \end{bmatrix}. \tag{7-19}$$

In order to solve the equation system (7-16) for $\mathbf{u}$ we have to introduce the Dirichtlet boundary conditions (7-3), namely

$$\begin{aligned} u(x = 0) &= \boldsymbol{\phi}(-1)\ {}^1\mathbf{u} = 0, \\ u(x = l) &= \boldsymbol{\phi}(1)\ {}^3\mathbf{u} = 0, \end{aligned} \tag{7-20}$$

with

$$\boldsymbol{\phi}(-1) = \begin{bmatrix} T_0(t=-1) & T_1(t=-1) & T_2(t=-1) & T_3(t=-1) & \dots \end{bmatrix} \tag{7-21}$$

and $\boldsymbol{\phi}(1)$ analogously. Writing these two constraints in matrix notation yields

$$\begin{bmatrix} \boldsymbol{\phi}(-1) & \mathbf{0} & \mathbf{0} \\ \mathbf{0} & \mathbf{0} & \boldsymbol{\phi}(1) \end{bmatrix} \begin{bmatrix} {}^1\mathbf{u} \\ {}^2\mathbf{u} \\ {}^3\mathbf{u} \end{bmatrix} = \begin{bmatrix} 0 \\ 0 \end{bmatrix}, \tag{7-22}$$

or in a shorter notation

$$\mathbf{C}_{\mathrm{BC}}\,\mathbf{u} = \mathbf{0}. \tag{7-23}$$

Furthermore, we introduce additional constraints at the inner nodes to ensure a C^2 continuous approximation of the unknown function $u(x)$ as described in Section 3.1.2. For the inner nodes these constraints are

$$\begin{aligned} \boldsymbol{\phi}(1)\ {}^{\zeta}\mathbf{u} &= \boldsymbol{\phi}(-1)\ {}^{\zeta+1}\mathbf{u}\,, \\ {}^{\zeta}J\ \boldsymbol{\phi}(1)\ \boldsymbol{\mathcal{L}}_{\mathrm{x}}\ {}^{\zeta}\mathbf{u} &= {}^{\zeta+1}J\ \boldsymbol{\phi}(-1)\ \boldsymbol{\mathcal{L}}_{\mathrm{x}}\ {}^{\zeta+1}\mathbf{u}\,, \\ {}^{\zeta}J^2\ \boldsymbol{\phi}(1)\ \boldsymbol{\mathcal{L}}_{\mathrm{xx}}\ {}^{\zeta}\mathbf{u} &= {}^{\zeta+1}J^2\ \boldsymbol{\phi}(-1)\ \boldsymbol{\mathcal{L}}_{\mathrm{xx}}\ {}^{\zeta+1}\mathbf{u}\,. \end{aligned} \tag{7-24}$$

Expressing the constraints (7-24) in matrix notation results in

$$\begin{bmatrix} \boldsymbol{\phi}(1) & -\boldsymbol{\phi}(-1) & \mathbf{0} \\ {}^1J\ \boldsymbol{\phi}(1)\ \boldsymbol{\mathcal{L}}_{\mathrm{x}} & -{}^2J\ \boldsymbol{\phi}(-1)\ \boldsymbol{\mathcal{L}}_{\mathrm{x}} & \mathbf{0} \\ {}^1J^2\ \boldsymbol{\phi}(1)\ \boldsymbol{\mathcal{L}}_{\mathrm{xx}} & -{}^2J^2\ \boldsymbol{\phi}(-1)\ \boldsymbol{\mathcal{L}}_{\mathrm{xx}} & \mathbf{0} \\ \mathbf{0} & \boldsymbol{\phi}(1) & -\boldsymbol{\phi}(-1) \\ \mathbf{0} & {}^2J\ \boldsymbol{\phi}(1)\ \boldsymbol{\mathcal{L}}_{\mathrm{x}} & -{}^3J\ \boldsymbol{\phi}(-1)\ \boldsymbol{\mathcal{L}}_{\mathrm{x}} \\ \mathbf{0} & {}^2J^2\ \boldsymbol{\phi}(1)\ \boldsymbol{\mathcal{L}}_{\mathrm{xx}} & -{}^3J^2\ \boldsymbol{\phi}(-1)\ \boldsymbol{\mathcal{L}}_{\mathrm{xx}} \end{bmatrix} \begin{bmatrix} {}^1\mathbf{u} \\ {}^2\mathbf{u} \\ {}^3\mathbf{u} \end{bmatrix} = \begin{bmatrix} 0 \\ 0 \\ 0 \\ 0 \\ 0 \\ 0 \end{bmatrix}, \tag{7-25}$$

or in short

$$\mathbf{C}_{\mathrm{conti}}\,\mathbf{u} = \mathbf{0}. \tag{7-26}$$

Combing (7-23) and (7-26) into

$$\mathbf{C}\,\mathbf{u} = \mathbf{0} \tag{7-27}$$

with

$$\mathbf{C} = \begin{bmatrix} \mathbf{C}_{\mathrm{BC}} \\ \mathbf{C}_{\mathrm{conti}} \end{bmatrix} \tag{7-28}$$

and solving the extended equation system

$$\begin{bmatrix} \boldsymbol{\mathcal{L}} & \mathbf{C}^{\mathsf{T}} \\ \mathbf{C} & \mathbf{0} \end{bmatrix} \begin{bmatrix} \mathbf{u} \\ \boldsymbol{\lambda} \end{bmatrix} = \begin{bmatrix} -\frac{1}{I}\boldsymbol{\mathcal{M}}\mathbf{e} \\ \mathbf{0} \end{bmatrix} \tag{7-29}$$

yields the coefficients $\mathbf{u}$ of the unknown solution $u(x)$ in the Chebyshev basis as a function of the internal bending moment $M(x)$ and the elastic modulus $E(x)$. The extended system of equations (7-29) serves as the basis for the functional model, which will be derived in the following section.

8 INTEGRATED ANALYSIS

Based on the solution (7-29) of the modified Euler-Bernoulli beam equation we derive a functional model that allows to adjust displacement, inclination and strain measurements by means of a least squares adjustment to estimate the elastic modulus $E(x)$ represented in its Chebyshev series expansion. The functional model is developed for the following two different types of observations.

- Discrete measurements as observations.
- Functions as observations.

The latter was mainly developed for the evaluation of quasi continuous measurements using for example terrestrial laser scanning (TLS), fibre optic sensors (FOS) or photogrammetry. At the end of this chapter, the results of both approaches will be compared and discussed.

8.1 DISCRETE MEASUREMENTS AS OBSERVATIONS

In order to derive the functional model, we need to exclude the elastic modulus $\mathbf{e}$ from the solution (7-29) of the modified Euler-Bernoulli beam equation. Hence, we obtain a new system of equations with two new unknown variables. Instead of the unknown solution $\mathbf{u}$ and Lagrangian multiplier $\boldsymbol{\lambda}$ in (7-29) we obtain $\mathbf{U}$ and $\boldsymbol{\Lambda}$ and the system of equations reads

$$\begin{bmatrix} \boldsymbol{\mathcal{L}} & \mathbf{C}^{\mathsf{T}} \\ \mathbf{C} & \mathbf{0} \end{bmatrix} \begin{bmatrix} \mathbf{U} \\ \boldsymbol{\Lambda} \end{bmatrix} = \begin{bmatrix} -\frac{1}{I}\boldsymbol{\mathcal{M}} \\ \mathbf{0} \end{bmatrix} \tag{8-1}$$

and solving for $\mathbf{U}$ yields

$$\begin{bmatrix} \mathbf{U} \\ \boldsymbol{\Lambda} \end{bmatrix} = \begin{bmatrix} \boldsymbol{\mathcal{L}} & \mathbf{C}^{\mathsf{T}} \\ \mathbf{C} & \mathbf{0} \end{bmatrix}^{-1} \begin{bmatrix} -\frac{1}{I}\boldsymbol{\mathcal{M}} \\ \mathbf{0} \end{bmatrix}, \tag{8-2}$$

with

$$\mathbf{u} = \mathbf{U}\mathbf{e} \tag{8-3}$$

and

$$\boldsymbol{\lambda} = \boldsymbol{\Lambda}\mathbf{e}\,. \tag{8-4}$$

Since we divided the whole beam into three elements matrix $\mathbf{U}$ also contains three parts one for each element and reads

$$\mathbf{U} = \begin{bmatrix} {}^{1}\mathbf{U} \\ {}^{2}\mathbf{U} \\ {}^{3}\mathbf{U} \end{bmatrix}. \tag{8-5}$$

8.1.1 *Functional model*

Based on (8-3) we derive the functional model for an integrated analysis of displacement, inclination and strain measurements as follows.

Displacement

Before we can set up the functional model for a displacement measurement L_{disp_i} at a position x_{disp_i} along the beam, we need to check to which element a measurement at a position x_{disp_i} belongs to and map it onto the interval $[-1, 1]$ of the corresponding element ζ applying the inverse function of (7-13), which reads

$$t = f_{\text{t}}\left(x, {}^{\zeta}x_{\nu_1}, {}^{\zeta}x_{\nu_2}\right) = \frac{2x - {}^{\zeta}x_{\nu_1} - {}^{\zeta}x_{\nu_2}}{{}^{\zeta}x_{\nu_2} - {}^{\zeta}x_{\nu_1}}\,. \tag{8-6}$$

Based on (7-6), with (8-3) and applying the mapping (8-6) the functional model for a displacement measurement L_{disp_i} at a position x_{disp_i} reads

$$\begin{aligned} L_{\text{disp}_i} &= \sum_{j=0}^{\infty} {}^{\zeta}u_j \; T_j\Big(f_{\text{t}}\Big(x_{\text{disp}_i}, {}^{\zeta}x_{\nu_1}, {}^{\zeta}x_{\nu_2}\Big)\Big) = \sum_{j=0}^{\infty} {}^{\zeta}u_j \; T_j\big(t_{\text{disp}_i}\big) \\ &= \boldsymbol{\phi}\big(t_{\text{disp}_i}\big)\,{}^{\zeta}\mathbf{u} \\ &= \boldsymbol{\phi}\big(t_{\text{disp}_i}\big)\,{}^{\zeta}\mathbf{U}\mathbf{e}\,, \end{aligned} \tag{8-7}$$

or in a shorter notation

$$L_{\text{disp}_i} = \mathbf{A}_{\text{disp}_i}\,\mathbf{e}\,, \tag{8-8}$$

with the design matrix

$$\mathbf{A}_{\text{disp}_i} = \boldsymbol{\phi}\big(t_{\text{disp}_i}\big)\,{}^{\zeta}\mathbf{U}\,, \tag{8-9}$$

containing the coefficients of the unknown parameters $\mathbf{e}$.

Inclination

The inclination of the bending line $u(x)$ is described by its first spatial derivative

$$\tan(\alpha) = \frac{\mathrm{d}u(x)}{\mathrm{d}x}\,, \tag{8-10}$$

see Müller and Ferber (2012, Chapter 2.6.1). The deflection $u(x)$ is usually quite small in comparison to the geometry of the beam and hence, the inclination of the bending line is very small. Therefore, for most problems the assumption

Besides this, the Euler-Bernoulli beam equation is also just an approximation.

$$\tan(\alpha) \approx \alpha \tag{8-11}$$

is justified. Nevertheless, instead of using α we will use $\tan(\alpha)$ as an observation for the adjustment and the functional model for a inclination measurement L_{inc_i} at a position x_{inc_i} results in

$$\begin{aligned} L_{\text{inc}_i} &= {}^{\zeta}J \sum_{j=0}^{\infty} {}^{\zeta}u_j \; \frac{\mathrm{d}T_j\Big(f_{\text{t}}\Big(x_{\text{inc}_i}, {}^{\zeta}x_{\nu_1}, {}^{\zeta}x_{\nu_2}\Big)\Big)}{\mathrm{d}t} = {}^{\zeta}J \sum_{j=0}^{\infty} {}^{\zeta}u_j \; \frac{\mathrm{d}T_j\big(t_{\text{inc}_i}\big)}{\mathrm{d}t} \\ &= {}^{\zeta}J\;\boldsymbol{\phi}\big(t_{\text{inc}_i}\big)\;\boldsymbol{\mathcal{L}}_{\text{x}}\;{}^{\zeta}\mathbf{u} \\ &= {}^{\zeta}J\;\boldsymbol{\phi}\big(t_{\text{inc}_i}\big)\;\boldsymbol{\mathcal{L}}_{\text{x}}\;{}^{\zeta}\mathbf{U}\mathbf{e}\,, \end{aligned} \tag{8-12}$$

or in a shorter notation

$$L_{\text{inc}_i} = \mathbf{A}_{\text{inc}_i}\,\mathbf{e}\,, \tag{8-13}$$

with

$$\mathbf{A}_{\text{inc}_i} = {}^{\zeta}J\;\boldsymbol{\phi}\big(t_{\text{inc}_i}\big)\;\boldsymbol{\mathcal{L}}_{\text{x}}\;{}^{\zeta}\mathbf{U}\,. \tag{8-14}$$

Strain

According to GERE and GOODNO (2013, Chapter 5.4) or MÜLLER and FERBER (2012, Chapter 2.6.1) the longitudinal strain ϵ is closely related to the second derivative of the deflection $u(x)$ and is given by

$$\epsilon = -e_{\mathrm{u}} \frac{\mathrm{d}^2 u(x)}{\mathrm{d}x^2}\,, \tag{8-15}$$

with e_{u} being the orthogonal distance to the neutral surface. While measuring the strain at the bottom or top of the beam and assuming the neutral surface to be located in the middle of the beam yields

$$e_{\mathrm{u}} = \frac{1}{2} h\,. \tag{8-16}$$

The functional model for a strain measurement L_{strain_i} at a position x_{strain_i} results in

$$\begin{aligned} L_{\mathrm{strain}_i} &= \frac{1}{2} h\, {}^{\zeta}J^2 \sum_{j=0}^{\infty} {}^{\zeta}u_j \, \frac{\mathrm{d}^2\, T_j\Big(f_{\mathrm{t}}\Big(x_{\mathrm{strain}_i}, {}^{\zeta}x_{\nu_1}, {}^{\zeta}x_{\nu_2}\Big)\Big)}{\mathrm{d}t^2} \\ &= \frac{1}{2} h\, {}^{\zeta}J^2 \sum_{j=0}^{\infty} {}^{\zeta}u_j \, \frac{\mathrm{d}^2\, T_j\big(t_{\mathrm{strain}_i}\big)}{\mathrm{d}t^2} \\ &= \frac{1}{2} h\, {}^{\zeta}J^2\, \boldsymbol{\phi}\big(t_{\mathrm{strain}_i}\big)\, \boldsymbol{\mathcal{L}}_{\mathrm{xx}}\, {}^{\zeta}\mathbf{u} \\ &= \frac{1}{2} h\, {}^{\zeta}J^2\, \boldsymbol{\phi}\big(t_{\mathrm{strain}_i}\big)\, \boldsymbol{\mathcal{L}}_{\mathrm{xx}}\, {}^{\zeta}\mathbf{U}\mathbf{e}\,, \end{aligned} \tag{8-17}$$

or in a shorter notation

$$L_{\mathrm{strain}_i} = \mathbf{A}_{\mathrm{strain}_i}\, \mathbf{e}\,, \tag{8-18}$$

with

$$\mathbf{A}_{\mathrm{strain}_i} = \frac{1}{2} h\, {}^{\zeta}J^2\, \boldsymbol{\phi}\big(t_{\mathrm{strain}_i}\big)\, \boldsymbol{\mathcal{L}}_{\mathrm{xx}}\, {}^{\zeta}\mathbf{U}\,. \tag{8-19}$$

8.1.2 *Observation equations*

The derivation of the observation equations for displacement, inclination and strain measurements are based on the following assumptions:

We're considering the simplest case now.

- The geometry of the beam is fixed and hence, the width w, height h and length l are error free values.
- The force F is an error free value.
- The positions the forces are applied to the beam are error free values, hence a is a fixed value.
- The sensor position x is error free.
- No movements at the bearings.

Let us assume that we have n displacement measurements along the beam with their positions given by

$$\mathbf{x}_{\mathrm{disp}} = \begin{bmatrix} x_{\mathrm{disp}_1} \\ x_{\mathrm{disp}_2} \\ \vdots \\ x_{\mathrm{disp}_n} \end{bmatrix}. \tag{8-20}$$

The functional model for a displacement measurement is given by (8-8) and based on the assumptions we made, only L_{disp_i} are observations subject to random errors and all entries in the design matrix $\mathbf{A}_{\text{disp}_i}$ are constant values (error free). Introducing the corresponding residuals v_{disp_i} results in the observation equations for all displacement measurements

$$\begin{bmatrix} L_{\text{disp}_1} \\ L_{\text{disp}_2} \\ \vdots \\ L_{\text{disp}_n} \end{bmatrix} + \begin{bmatrix} v_{\text{disp}_1} \\ v_{\text{disp}_2} \\ \vdots \\ v_{\text{disp}_n} \end{bmatrix} = \begin{bmatrix} \mathbf{A}_{\text{disp}_1} \\ \mathbf{A}_{\text{disp}_2} \\ \vdots \\ \mathbf{A}_{\text{disp}_n} \end{bmatrix} \mathbf{e}\,, \tag{8-21}$$

or in short

$$\mathbf{L}_{\text{disp}} + \mathbf{v}_{\text{disp}} = \mathbf{A}_{\text{disp}}\,\mathbf{e}\,, \tag{8-22}$$

with the vector of unknown parameters $\mathbf{e}$

$$\mathbf{e} = \begin{bmatrix} {}^1\mathbf{e} \\ {}^2\mathbf{e} \\ {}^3\mathbf{e} \end{bmatrix}\,, \tag{8-23}$$

containing the coefficients of a Chebyshev series for each element representing the inverse of elastic modulus $E(x)$ as a function along the beam. Analogously, the observation equations according to (8-13) for all inclination measurements are given by

$$\mathbf{L}_{\text{inc}} + \mathbf{v}_{\text{inc}} = \mathbf{A}_{\text{inc}}\,\mathbf{e} \tag{8-24}$$

and based on the functional model (8-18) the system of observation equations for all strain measurements results in

$$\mathbf{L}_{\text{strain}} + \mathbf{v}_{\text{strain}} = \mathbf{A}_{\text{strain}}\,\mathbf{e}\,. \tag{8-25}$$

The observation equations (8-22), (8-24) and (8-25) can be combined into

$$\mathbf{L} + \mathbf{v} = \mathbf{A}\,\mathbf{e}\,, \tag{8-26}$$

with the vector of observations $\mathbf{L}$, vector of residuals $\mathbf{v}$ and design matrix $\mathbf{A}$ beeing

$$\mathbf{L} = \begin{bmatrix} \mathbf{L}_{\text{disp}} \\ \mathbf{L}_{\text{inc}} \\ \mathbf{L}_{\text{strain}} \end{bmatrix}\,, \qquad \mathbf{v} = \begin{bmatrix} \mathbf{v}_{\text{disp}} \\ \mathbf{v}_{\text{inc}} \\ \mathbf{v}_{\text{strain}} \end{bmatrix}\,, \qquad \mathbf{A} = \begin{bmatrix} \mathbf{A}_{\text{disp}} \\ \mathbf{A}_{\text{inc}} \\ \mathbf{A}_{\text{strain}} \end{bmatrix}\,. \tag{8-27}$$

8.1.3 *Least squares adjustment*

Based on the observation equations (8-26) and the stochastic model represented by the weight matrix $\mathbf{P}$, the normal equation system for a least squares adjustment according to Section 2.3 results in

$$\begin{aligned} \mathbf{N}\,\mathbf{e} &= \mathbf{n} \\ \mathbf{A}^\mathsf{T}\mathbf{P}\mathbf{A}\,\mathbf{e} &= \mathbf{A}^\mathsf{T}\mathbf{P}\mathbf{L}\,, \end{aligned} \tag{8-28}$$

with the design matrix $\mathbf{A}$ and vector of observations $\mathbf{L}$ from (8-27). To ensure that $E^*(x)$ represented by its coefficients $\mathbf{e}$ in the Chebyshev basis is C^2 continuous along the whole beam, we have to introduce constraints at the two

inner nodes listed in Table 7-1 (left). In accordance to (7-24) these constraints are

$$\mathbf{C}_{\text{conti}}\,\mathbf{e} = \mathbf{0}\,, \tag{8-29}$$

with $\mathbf{C}_{\text{conti}}$ being exactly the same matrix as in (7-25). Solving the extended normal equation system

$$\begin{bmatrix} \mathbf{N} & \mathbf{C}_{\text{conti}}^{\mathsf{T}} \\ \mathbf{C}_{\text{conti}} & \mathbf{0} \end{bmatrix} \begin{bmatrix} \mathbf{e} \\ \boldsymbol{\lambda} \end{bmatrix} = \begin{bmatrix} \mathbf{n} \\ \mathbf{0} \end{bmatrix} \tag{8-30}$$

yields the unknown coefficients $\mathbf{e}$ of a Chebyshev series for each element representing the inverse of elastic modulus $E(x)$ as a C^2 continuous function along the beam.

8.2 FUNCTIONS AS OBSERVATIONS

Let us now consider the case that measurements with a high point density are available, e.g. recorded by TLS, photogrammetry or FOS. Of course, it is possible to analyse such measurements with the functional model derived in Section 8.1, but if, for example, outliers are present in the measurements, they would falsify the solution of the normal equation system. The elimination of outliers by data snooping according to (BAARDA 1968) is an iterative process and is maybe not really feasible for complex structures and/or the huge amount of observations. Therefore, it can sometimes be useful to eliminate outliers and also to reduce the dataset by a pre-processing of the measurements.

But for now, let us assume that a suitable approximation in the Chebyshev basis of measurements along the whole beam is available, as depicted for displacement measurements in Figure 8-1.

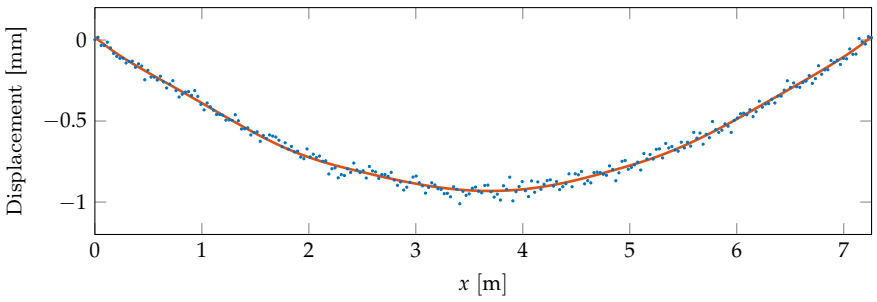

Figure 8-1: Displacement measurements (blue dots) and its C^2 continuous approximation in the Chebyshev basis (red line).

Instead of using all displacement measurements (blue dots) in Figure 8-1 to estimate $E(x)$ according to Section 8.1, we can also use its approximation in the Chebyshev basis (red line) represented by the coefficients

$$\mathbf{u} = \begin{bmatrix} {}^{1}\mathbf{u} \\ {}^{2}\mathbf{u} \\ {}^{3}\mathbf{u} \end{bmatrix}\,. \tag{8-31}$$

Furthermore, we also assume that the variances and covariances of the coefficients $\mathbf{u}$ are also given by the variance-covariance matrix $\boldsymbol{\Sigma}_{LL}$. Thus everything is provided to estimate $E(x)$ from the approximation $\mathbf{u}$. The same applies for inclination and strain measurements.

8.2.1 *Functional model*

The functional model for an adjustment of displacement, inclination and strain measurements as a function represented in its Chebyshev series expansion is also based on the solution (7-29) of the modified Euler-Bernoulli beam equation. Therefore, the functional models are as follows.

Displacement

As the solution of the BVP and the approximation of the measurements are given in the same basis, the functional for displacement measurements represented by a function in its Chebyshev series expansion is already given by (8-3), namely

$$\mathbf{u} = \mathbf{U}\mathbf{e}\,, \tag{8-32}$$

or

$$\begin{bmatrix} {}^1\mathbf{u} \\ {}^2\mathbf{u} \\ {}^3\mathbf{u} \end{bmatrix} = \begin{bmatrix} {}^1\mathbf{U} \\ {}^2\mathbf{U} \\ {}^3\mathbf{U} \end{bmatrix} \begin{bmatrix} {}^1\mathbf{e} \\ {}^2\mathbf{e} \\ {}^3\mathbf{e} \end{bmatrix}\,. \tag{8-33}$$

Hence, the functional model for an adjustment of displacement measurements represented by the coefficients $\mathbf{u}$ reads

$$\mathbf{L}_\mathrm{u} = \mathbf{A}_\mathrm{u}\,\mathbf{e}\,, \tag{8-34}$$

with

$$\mathbf{L}_\mathrm{u} = \begin{bmatrix} {}^1\mathbf{u} \\ {}^2\mathbf{u} \\ {}^3\mathbf{u} \end{bmatrix} \quad \text{and} \quad \mathbf{A}_\mathrm{u} = \begin{bmatrix} {}^1\mathbf{U} \\ {}^2\mathbf{U} \\ {}^3\mathbf{U} \end{bmatrix}\,. \tag{8-35}$$

Inclination

The inclination of the bending line $u(x)$ is described by its first spatial derivative and due to the assumption (8-11) we have the following functional relationship

$$\alpha(x) \approx \frac{\mathrm{d}u(x)}{\mathrm{d}x}\,. \tag{8-36}$$

The approximation of $\alpha(x)$ in the Chebyshev basis from inclination measurements along the whole beam is given by the coefficients

$$\boldsymbol{\alpha} = \begin{bmatrix} {}^1\boldsymbol{\alpha} \\ {}^2\boldsymbol{\alpha} \\ {}^3\boldsymbol{\alpha} \end{bmatrix}\,. \tag{8-37}$$

Thus, the functional model reads

$$\begin{aligned} \begin{bmatrix} {}^1\boldsymbol{\alpha} \\ {}^2\boldsymbol{\alpha} \\ {}^3\boldsymbol{\alpha} \end{bmatrix} &= \begin{bmatrix} {}^1J\,\boldsymbol{\mathcal{L}}_\mathrm{x} & \mathbf{0} & \mathbf{0} \\ \mathbf{0} & {}^2J\,\boldsymbol{\mathcal{L}}_\mathrm{x} & \mathbf{0} \\ \mathbf{0} & \mathbf{0} & {}^3J\,\boldsymbol{\mathcal{L}}_\mathrm{x} \end{bmatrix} \begin{bmatrix} {}^1\mathbf{u} \\ {}^2\mathbf{u} \\ {}^3\mathbf{u} \end{bmatrix} \\ &= \begin{bmatrix} {}^1J\,\boldsymbol{\mathcal{L}}_\mathrm{x} & \mathbf{0} & \mathbf{0} \\ \mathbf{0} & {}^2J\,\boldsymbol{\mathcal{L}}_\mathrm{x} & \mathbf{0} \\ \mathbf{0} & \mathbf{0} & {}^3J\,\boldsymbol{\mathcal{L}}_\mathrm{x} \end{bmatrix} \begin{bmatrix} {}^1\mathbf{U} \\ {}^2\mathbf{U} \\ {}^3\mathbf{U} \end{bmatrix} \begin{bmatrix} {}^1\mathbf{e} \\ {}^2\mathbf{e} \\ {}^3\mathbf{e} \end{bmatrix}\,, \end{aligned} \tag{8-38}$$

or

$$\mathbf{L}_\alpha = \mathbf{A}_\alpha\,\mathbf{e}\,, \tag{8-39}$$

with

$$\mathbf{L}_\alpha = \begin{bmatrix} {}^1\boldsymbol{\alpha} \\ {}^2\boldsymbol{\alpha} \\ {}^3\boldsymbol{\alpha} \end{bmatrix} \quad \text{and} \quad \mathbf{A}_\alpha = \begin{bmatrix} {}^1J\,\boldsymbol{\mathcal{L}}_x & \mathbf{0} & \mathbf{0} \\ \mathbf{0} & {}^2J\,\boldsymbol{\mathcal{L}}_x & \mathbf{0} \\ \mathbf{0} & \mathbf{0} & {}^3J\,\boldsymbol{\mathcal{L}}_x \end{bmatrix} \begin{bmatrix} {}^1\mathbf{U} \\ {}^2\mathbf{U} \\ {}^3\mathbf{U} \end{bmatrix}. \tag{8-40}$$

Strain

The longitudinal strain $\epsilon(x)$ is closely related to the second derivative of the deflection $u(x)$ and assuming the neutral surface to be located in the middle of the beam, yields the following functional relationship

$$\epsilon(x) = -\frac{1}{2}h\frac{\mathrm{d}^2u(x)}{\mathrm{d}x^2}. \tag{8-41}$$

An approximation of $\epsilon(x)$ in the Chebyshev basis from strain measurements along the whole beam is given by the coefficients

$$\boldsymbol{\epsilon} = \begin{bmatrix} {}^1\boldsymbol{\epsilon} \\ {}^2\boldsymbol{\epsilon} \\ {}^3\boldsymbol{\epsilon} \end{bmatrix}. \tag{8-42}$$

This results in the following functional model.

$$\begin{aligned} \begin{bmatrix} {}^1\boldsymbol{\epsilon} \\ {}^2\boldsymbol{\epsilon} \\ {}^3\boldsymbol{\epsilon} \end{bmatrix} &= \begin{bmatrix} {}^1J^2\,\boldsymbol{\mathcal{L}}_{xx} & \mathbf{0} & \mathbf{0} \\ \mathbf{0} & {}^2J^2\,\boldsymbol{\mathcal{L}}_{xx} & \mathbf{0} \\ \mathbf{0} & \mathbf{0} & {}^3J^2\,\boldsymbol{\mathcal{L}}_{xx} \end{bmatrix} \begin{bmatrix} {}^1\mathbf{u} \\ {}^2\mathbf{u} \\ {}^3\mathbf{u} \end{bmatrix} \\ &= \begin{bmatrix} {}^1J^2\,\boldsymbol{\mathcal{L}}_{xx} & \mathbf{0} & \mathbf{0} \\ \mathbf{0} & {}^2J^2\,\boldsymbol{\mathcal{L}}_{xx} & \mathbf{0} \\ \mathbf{0} & \mathbf{0} & {}^3J^2\,\boldsymbol{\mathcal{L}}_{xx} \end{bmatrix} \begin{bmatrix} {}^1\mathbf{U} \\ {}^2\mathbf{U} \\ {}^3\mathbf{U} \end{bmatrix} \begin{bmatrix} {}^1\mathbf{e} \\ {}^2\mathbf{e} \\ {}^3\mathbf{e} \end{bmatrix}, \end{aligned} \tag{8-43}$$

or

$$\mathbf{L}_\epsilon = \mathbf{A}_\epsilon\,\mathbf{e}, \tag{8-44}$$

with

$$\mathbf{L}_\epsilon = \begin{bmatrix} {}^1\boldsymbol{\epsilon} \\ {}^2\boldsymbol{\epsilon} \\ {}^3\boldsymbol{\epsilon} \end{bmatrix} \text{ and } \mathbf{A}_\epsilon = \begin{bmatrix} {}^1J^2\,\boldsymbol{\mathcal{L}}_{xx} & \mathbf{0} & \mathbf{0} \\ \mathbf{0} & {}^2J^2\,\boldsymbol{\mathcal{L}}_{xx} & \mathbf{0} \\ \mathbf{0} & \mathbf{0} & {}^3J^2\,\boldsymbol{\mathcal{L}}_{xx} \end{bmatrix} \begin{bmatrix} {}^1\mathbf{U} \\ {}^2\mathbf{U} \\ {}^3\mathbf{U} \end{bmatrix}. \tag{8-45}$$

Finally, we derived a functional model for an integrated analysis of functions as observations in order to estimate the inverse of the elastic modulus $E^*(x)$ represented by its coefficients $\mathbf{e}$ in the Chebyshev basis.

8.2.2 *Observation equations*

Under the same assumptions as listed in Section 8.1.2, we can set up the observation equations for the aforementioned functional models to adjust displacement, inclination and strain measurements as a function represented in its Chebyshev series expansion by means of a least squares adjustment.

The functional model for displacement measurements is given by (8-34) and only the coefficients in $\mathbf{L}_\mathrm{u}$ are regarded as observations subject to random

errors and all entries in the design matrix $\mathbf{A}_\mathrm{u}$ are constant values (error free). Introducing the corresponding residuals $\mathbf{v}_\mathrm{u}$ results in the observation equations for displacement measurements

$$\mathbf{L}_\mathrm{u} + \mathbf{v}_\mathrm{u} = \mathbf{A}_\mathrm{u}\,\mathbf{e}\,, \tag{8-46}$$

with the vector of unknown parameters $\mathbf{e}$

$$\mathbf{e} = \begin{bmatrix} {}^1\mathbf{e} \\ {}^2\mathbf{e} \\ {}^3\mathbf{e} \end{bmatrix}\,, \tag{8-47}$$

containing the coefficients of a Chebyshev series for each element representing the inverse of elastic modulus $E(x)$ as a function along the beam. Analogously, the observation equations according to (8-39) for inclination measurements are given by

$$\mathbf{L}_\alpha + \mathbf{v}_\alpha = \mathbf{A}_\alpha\,\mathbf{e} \tag{8-48}$$

and based on the functional model (8-44) the system of observation equations for strain measurements results in

$$\mathbf{L}_\epsilon + \mathbf{v}_\epsilon = \mathbf{A}_\epsilon\,\mathbf{e}\,. \tag{8-49}$$

The observation equations (8-46), (8-48) and (8-49) can be combined into

$$\mathbf{L} + \mathbf{v} = \mathbf{A}\,\mathbf{e}\,, \tag{8-50}$$

with the vector of observations $\mathbf{L}$, vector of residuals $\mathbf{v}$ and design matrix $\mathbf{A}$ beeing

$$\mathbf{L} = \begin{bmatrix} \mathbf{L}_\mathrm{u} \\ \mathbf{L}_\alpha \\ \mathbf{L}_\epsilon \end{bmatrix}\,, \qquad \mathbf{v} = \begin{bmatrix} \mathbf{v}_\mathrm{u} \\ \mathbf{v}_\alpha \\ \mathbf{v}_\epsilon \end{bmatrix}\,, \qquad \mathbf{A} = \begin{bmatrix} \mathbf{A}_\mathrm{u} \\ \mathbf{A}_\alpha \\ \mathbf{A}_\epsilon \end{bmatrix}\,. \tag{8-51}$$

8.2.3 *Least squares adjustment*

The least squares adjustment of functions as observations based on the observation equations (8-50) and a stochastic model represented by a weight matrix $\mathbf{P}$ is analogous to the least squares adjustment of discrete measurements as observations in Section 8.1.3 and the normal equation system reads

$$\begin{aligned} \mathbf{N}\,\mathbf{e} &= \mathbf{n} \\ \mathbf{A}^\mathsf{T}\mathbf{P}\mathbf{A}\,\mathbf{e} &= \mathbf{A}^\mathsf{T}\mathbf{P}\mathbf{L}\,, \end{aligned} \tag{8-52}$$

with the design matrix $\mathbf{A}$ and vector of observations $\mathbf{L}$ from (8-51). In order to ensure that $E^*(x)$ represented by its coefficients $\mathbf{e}$ in the Chebyshev basis is C^2 continuous along the whole beam, we have to introduce constraints at the two inner nodes listed in Table 7-1 (left). In accordance to (7-24) these constraints are

$$\mathbf{C}_\mathrm{conti}\,\mathbf{e} = \mathbf{0}\,, \tag{8-53}$$

with $\mathbf{C}_\mathrm{conti}$ being exactly the same matrix as in (7-25). Solving the extended normal equation system

$$\begin{bmatrix} \mathbf{N} & \mathbf{C}_\mathrm{conti}^\mathsf{T} \\ \mathbf{C}_\mathrm{conti} & \mathbf{0} \end{bmatrix} \begin{bmatrix} \mathbf{e} \\ \boldsymbol{\lambda} \end{bmatrix} = \begin{bmatrix} \mathbf{n} \\ \mathbf{0} \end{bmatrix} \tag{8-54}$$

yields the unknown coefficients $\mathbf{e}$ of a Chebyshev series for each element representing the inverse of elastic modulus $E(x)$ as a C^2 continuous function along the beam.

8.2.4 *Discrete measurements vs. functions*

Introducing coefficients of an approximation of displacement, inclination or strain measurements as observations into a least squares adjustment in order to estimate the unknown coefficients $\mathbf{e}$ may appear unusual at first glance. However, that this approach generally leads to the same result for the unknown coefficients $\mathbf{e}$ as inserting the measurements directly according to Section 8.1, will now be demonstrated only for displacement measurements, since it can be shown for inclination or strain measurements in the same way.

First step

Let us assume that the bending line of a beam has been observed by TLS and thus a profile is available represented by n displacement measurements L_{disp_i} at positions x_{disp_i} with $i = 1, \ldots, n$, as illustrated in Figure 8-1 (blue dots). To use the approximation of the points as an observation for an integrated analysis according to Section 8.2, they will be approximated by a C^2 continuous polynomial in the Chebyshev basis using 3 elements in accordance to Table 7-1. The mapping of the positions x_{disp_i} of the displacement measurements on the interval $[-1, 1]$ of the corresponding element ζ is done by Equation (8-6) and the functional model for the resulting approximation is already given by (8-7) and reads

$$\begin{aligned} L_{\mathrm{disp}_i} &= \sum_{j=0}^{\infty} {}^{\zeta}u_j \; T_j\Big(f_{\mathrm{t}}\Big(x_{\mathrm{disp}_i}, {}^{\zeta}x_{\nu_1}, {}^{\zeta}x_{\nu_2}\Big)\Big) = \sum_{j=0}^{\infty} {}^{\zeta}u_j \; T_j\big(t_{\mathrm{disp}_i}\big) \\ &= \boldsymbol{\phi}\big(t_{\mathrm{disp}_i}\big)\, {}^{\zeta}\mathbf{u}\,, \end{aligned} \tag{8-55}$$

or in short

$$L_{\mathrm{disp}_i} = \mathbf{A}_{\phi_i}\, \mathbf{u}\,, \tag{8-56}$$

for $i = 1, \ldots, n$ and with the design matrix

$$\mathbf{A}_{\phi_i} = \boldsymbol{\phi}\big(t_{\mathrm{disp}_i}\big)\,. \tag{8-57}$$

Writing (8-56) in matrix notation yields

$$\begin{bmatrix} L_{\mathrm{disp}_1} \\ L_{\mathrm{disp}_2} \\ \vdots \\ L_{\mathrm{disp}_n} \end{bmatrix} = \begin{bmatrix} \mathbf{A}_{\phi_1} \\ \mathbf{A}_{\phi_2} \\ \vdots \\ \mathbf{A}_{\phi_n} \end{bmatrix} \mathbf{u}\,, \tag{8-58}$$

or

$$\mathbf{L}_{\mathrm{disp}} = \mathbf{A}_{\phi}\, \mathbf{u}\,. \tag{8-59}$$

Based on the assumptions in Section 8.1.2, only L_{disp_i} is an observation and all entries in the design matrix $\mathbf{A}_{\phi_i}$ are constant values (error free). Therefore, the observation equations for all n displacement measurements results in

$$\mathbf{L}_{\mathrm{disp}} + \mathbf{v}_{\mathrm{disp}} = \mathbf{A}_{\phi}\, \mathbf{u}\,, \tag{8-60}$$

with the vector of unknown parameters $\mathbf{u}$

$$\mathbf{u} = \begin{bmatrix} {}^{1}\mathbf{u} \\ {}^{2}\mathbf{u} \\ {}^{3}\mathbf{u} \end{bmatrix}\,, \tag{8-61}$$

containing the coefficients of a Chebyshev series for each element representing the approximation of the displacement measurements as a function along the beam. For the observation equations (8-60) and the stochastic model of the displacement measurements represented by the weight matrix $\mathbf{P}_{\text{disp}}$, the normal equation system for a least squares adjustment results in

$$\begin{aligned} \mathbf{N}\,\mathbf{u} &= \mathbf{n} \\ \mathbf{A}_\phi^\mathsf{T}\,\mathbf{P}_{\text{disp}}\,\mathbf{A}_\phi\,\mathbf{u} &= \mathbf{A}_\phi^\mathsf{T}\,\mathbf{P}_{\text{disp}}\,\mathbf{L}_{\text{disp}}\,. \end{aligned} \tag{8-62}$$

Introducing the constraints (7-24) at the two inner nodes results in the extended normal equation system

$$\begin{bmatrix} \mathbf{A}_\phi^\mathsf{T}\,\mathbf{P}_{\text{disp}}\,\mathbf{A}_\phi & \mathbf{C}_{\text{conti}}^\mathsf{T} \\ \mathbf{C}_{\text{conti}} & \mathbf{0} \end{bmatrix} \begin{bmatrix} \mathbf{u} \\ \boldsymbol{\lambda} \end{bmatrix} = \begin{bmatrix} \mathbf{A}_\phi^\mathsf{T}\,\mathbf{P}_{\text{disp}}\,\mathbf{L}_{\text{disp}} \\ \mathbf{0} \end{bmatrix} \tag{8-63}$$

and solving (8-63) yields the unknown coefficients $\mathbf{u}$ for the approximation of the displacement measurements and their stochastic properties represented by the co-factor matrix $\mathbf{Q}_{\text{u}}$ with

$$\mathbf{Q}_{\text{u}} = \mathbf{Q}_{11} \tag{8-64}$$

and

$$\begin{bmatrix} \mathbf{A}_\phi^\mathsf{T}\,\mathbf{P}_{\text{disp}}\,\mathbf{A}_\phi & \mathbf{C}_{\text{conti}}^\mathsf{T} \\ \mathbf{C}_{\text{conti}} & \mathbf{0} \end{bmatrix}^{-1} = \begin{bmatrix} \mathbf{Q}_{11} & \mathbf{Q}_{12} \\ \mathbf{Q}_{21} & \mathbf{Q}_{22} \end{bmatrix}. \tag{8-65}$$

Second step

Now we want to use the approximation of the displacement measurements $\mathbf{u}$ to estimate the inverse of the elastic modulus $\mathbf{e}$ according to Section 8.2.1. The functional model is given by (8-32) and under the same assumptions as before, the observation equations are given by (8-46), namely

$$\mathbf{L}_{\text{u}} + \mathbf{v}_{\text{u}} = \mathbf{A}_{\text{u}}\,\mathbf{e}\,. \tag{8-66}$$

For the observation equations (8-66) and the stochastic model represented by the weight matrix $\mathbf{P}_{\text{u}}$, the normal equation system for a least squares adjustment results in

$$\mathbf{A}_{\text{u}}^\mathsf{T}\,\mathbf{P}_{\text{u}}\,\mathbf{A}_{\text{u}}\,\mathbf{e} = \mathbf{A}_{\text{u}}^\mathsf{T}\,\mathbf{P}_{\text{u}}\,\mathbf{L}_{\text{u}}\,. \tag{8-67}$$

As the weight matrix $\mathbf{P}_{\text{u}}$ is the inverse of the cofactor matrix $\mathbf{Q}_{\text{u}}$ and with (8-64), the weight matrix $\mathbf{P}_{\text{u}}$ reads

$$\mathbf{P}_{\text{u}} = \mathbf{A}_\phi^\mathsf{T}\,\mathbf{P}_{\text{disp}}\,\mathbf{A}_\phi\,. \tag{8-68}$$

Substituting $\mathbf{P}_{\text{u}}$ in (8-67) by (8-68) yields

$$\mathbf{A}_{\text{u}}^\mathsf{T}\,\mathbf{A}_\phi^\mathsf{T}\,\mathbf{P}_{\text{disp}}\,\mathbf{A}_\phi\,\mathbf{A}_{\text{u}}\,\mathbf{e} = \mathbf{A}_{\text{u}}^\mathsf{T}\,\mathbf{A}_\phi^\mathsf{T}\,\mathbf{P}_{\text{disp}}\,\mathbf{A}_\phi\,\mathbf{L}_{\text{u}}\,. \tag{8-69}$$

If we insert the functional model of the second step (8-34) into the functional model of the first step (8-59) we obtain

$$\mathbf{L}_{\text{disp}} = \mathbf{A}_\phi\,\mathbf{A}_{\text{u}}\,\mathbf{e}\,, \tag{8-70}$$

which is exactly the same functional model as for discrete displacements measurements (8-7) in Section 8.1 and this results in the following relationship between the design matrices

$$\mathbf{A}_{\text{disp}} = \mathbf{A}_\phi\,\mathbf{A}_{\text{u}}\,. \tag{8-71}$$

Inserting (8-71) in (8-69) with

$$\mathbf{A}_{\text{disp}}^{\mathsf{T}} = \left(\mathbf{A}_{\phi}\,\mathbf{A}_{\text{u}}\right)^{\mathsf{T}} = \mathbf{A}_{\text{u}}^{\mathsf{T}}\,\mathbf{A}_{\phi}^{\mathsf{T}} \tag{8-72}$$

and with

$$\mathbf{L}_{\text{disp}} = \mathbf{A}_{\phi}\,\mathbf{L}_{\text{u}}\,, \tag{8-73}$$

according to (8-56), the normal equation system (8-69) results in

$$\mathbf{A}_{\text{disp}}^{\mathsf{T}}\,\mathbf{P}_{\text{disp}}\,\mathbf{A}_{\text{disp}}\,\mathbf{e} = \mathbf{A}_{\text{disp}}^{\mathsf{T}}\,\mathbf{P}_{\text{disp}}\,\mathbf{L}_{\text{disp}}\,, \tag{8-74}$$

which is basically the same normal equation system as (8-28) that results when using discrete displacements measurements as observations according to Section 8.1. As has been shown, using the coefficients of an approximation of displacement measurements as observations in order to estimate the unknown coefficients $\mathbf{e}$ generally provides the same result as using the displacement measurements directly according to Section 8.1. Therefore, the correct stochastic model must be considered, which is also shown in more detail in the numerical studies in Section 9.1.

9 NUMERICAL STUDIES

To gain a better understanding of the inverse problem (8-30), for example, how measurement noise affects the solution $E(x)$, we will first conduct some numerical studies. This is essential while the strategy for MeMoS depends on the solution for $E(x)$ or more precisely on $E^*(x)$. All presented numerical studies are based on the same specification of the four-point bending test set-up and beam specimen as already used in (Wu 2020, p. 89), which is listed in Table 9-1.

beam length l	7.26 m	beam elastic modulus	70 GPa
beam width w	0.20 m	load F	7460 N
beam height h	0.36 m	loading position a	2.42 m

Table 9-1: Specification of the four-point bending set-up and beam specimen for the numerical studies.

For these parameters, the true solution $\tilde{L}_{\text{type}}$ for the displacement, inclination and strain along the beam can be calculated using (7-29) and is depicted in Figure 9-1.

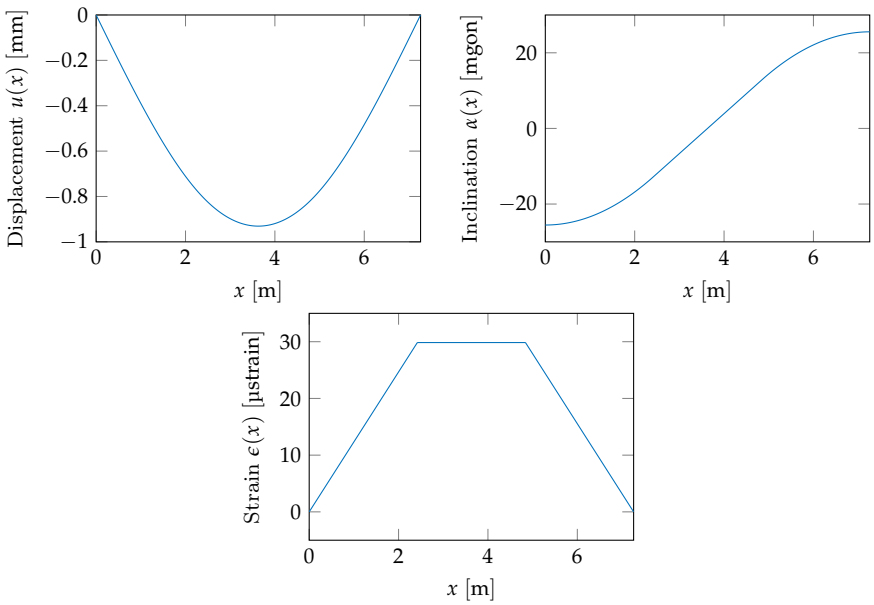

Figure 9-1: True solution $\tilde{L}_{\text{type}}$ for displacement, inclination and strain measurement along the beam.

To ensure the comparability of the results, all numerical studies are based on sensor precisions relative to the true measured values as depicted in Figure 9-1. Throughout these studies we consider three different sensor precisions, which we will refer to as low, medium and high precision according to Table 9-2.

Table 9-2: Used sensor precisions for the numerical studies based on the maximum absolute value for the true solutions depicted in Figure 9-1.

	$\max \lvert \check{L}_{\text{type}} \rvert$	Sensor precision $\sigma_{L_{\text{type}}}$		
		low [10 %]	medium [1 %]	high [0.1 %]
Displacement [mm]	≈ 0.93	$9.3 \cdot 10^{-2}$	$9.3 \cdot 10^{-3}$	$9.3 \cdot 10^{-4}$
Inclination [mgon]	≈ 25.0	2.5	$2.5 \cdot 10^{-1}$	$2.5 \cdot 10^{-2}$
Strain [µstrain]	≈ 30.0	3.0	$3.0 \cdot 10^{-1}$	$3.0 \cdot 10^{-2}$

Based on the true solutions in Figure 9-1 for the presented four-point bending test set-up and the different sensor precisions listed in Table 9-2 we will perform a sensitivity analysis in order to get a better understanding of the inverse problem (8-30). Therefore, we will answer the following questions, among others.

- What is the impact of the sensor position on the precision of $E(x)$?
- What is the impact of the measurement noise on the estimation of $E(x)$?
- What is the impact of the number of measurements on the estimation of $E(x)$?
- What is the impact of the polynomial degree of $E^*(x)$ on the estimation of $E(x)$?

Since the sensitivity analysis in Section 9.2 is only based on discrete measurements as observations, we will first of all also show numerically that both integrated analyses based on discrete measurements and functions as observations are equivalent, which in principle guarantees the transferability of the results.

9.1 DISCRETE MEASUREMENTS VS. FUNCTIONS

As we have already seen in Section 8.2.4, the integrated analysis using discrete measurements as observations, as described in Section 8.1, is in general equivalent to the integrated analysis of functions as observations, presented in Section 8.2. In the following we will also show this numerically and outline the impact of different weight matrices $\mathbf{P}_{\text{u}}$ on the unknowns $\mathbf{e}$.

Therefore, we consider the 24 equidistant and uncorrelated displacement measurements of high precision listed in Table 9-3, with 8 measurements for each of the three elements according to the beam specification listed in Table 9-1.

Table 9-3: 24 equidistant displacement measurements of high precision.

1st element			2nd element			3rd element		
i	x_i [m]	L_{disp_i} [µm]	i	x_i [m]	L_{disp_i} [µm]	i	x_i [m]	L_{disp_i} [µm]
1	0.0000	−0.6	9	2.5252	−829.7	17	5.0504	−765.4
2	0.3157	−125.2	10	2.8409	−878.5	18	5.3661	−683.7
3	0.6313	−251.2	11	3.1565	−912.9	19	5.6817	−587.4
4	0.9470	−371.4	12	3.4722	−927.9	20	5.9974	−481.8
5	1.2626	−484.5	13	3.7878	−930.1	21	6.3130	−370.6
6	1.5783	−589.0	14	4.1035	−911.3	22	6.6287	−249.9
7	1.8939	−683.0	15	4.4191	−879.3	23	6.9443	−124.7
8	2.2096	−763.4	16	4.7348	−829.4	24	7.2600	1.6

Based on the solution (8-2) of the beam equation for the specification listed in Table 9-1 we use these measurements to determine the unknown solution $\mathbf{e}$ for a polynomial degree $p_e = 3$ for each element. The standard deviation of the 24 uncorrelated displacement measurements of high precision according to Table 9-2 is $\sigma_{L_{disp}} = 0.93\,\mu m$ and choosing the same value for the theoretical reference standard deviation σ_0 results in an identity matrix for the weight matrix $\mathbf{P}_{disp}$, see Section 2.1.2. Thus, $\mathbf{e}$ can now be determined in two ways:

- Using the 24 displacement measurements as observations according to Section 8.1.
- Approximating the 24 displacement measurements and using the coefficients $\mathbf{u}$ as observations according to Section 8.2.

That both approaches generally lead to the same solution for $\mathbf{e}$ has already been presented in Section 8.2.4 and will now be demonstrated numerically, with focus on the impact of different stochastic models for $\mathbf{P}_u$ on the solution $\mathbf{e}$. Therefore, we consider the following four different adjustment problems in order to estimate $\mathbf{e}$:

The detailed calculation of the results in Table 9-4 can be found in Appendix A.

1. Using the 24 displacement measurements as observations.
2. Using the coefficients $\mathbf{u}$ as observations and under consideration of correlations $\Rightarrow \mathbf{P}_u = \mathbf{A}_\phi^T \mathbf{P}_{disp} \mathbf{A}_\phi$.
3. Using the coefficients $\mathbf{u}$ as observations and without consideration of correlations $\Rightarrow \mathbf{P}_u = \mathbf{diag}(\mathbf{A}_\phi^T \mathbf{P}_{disp} \mathbf{A}_\phi)$.
4. Using the coefficients $\mathbf{u}$ as observations and without explicit stochastic model $\Rightarrow \mathbf{P}_u = \mathbf{I}$.

The results of the four different estimations for $\mathbf{e}$ are given in Table 9-4.

Table 9-4: Resulting coefficients $\mathbf{e}$ of the unknown solution based on the 24 displacement measurements of high precision listed in Table 9-3 for four different adjustments. Differences in the values to the 1. solution are shown in red.

Estimated coefficients $\mathbf{e}$ in $[GPa^{-1}]$ according to			
1.	2.	3.	4.
0.014 306 766 300 151	0.014 306 766 300 212	0.014 172 412 374 338	0.014 343 935 390 659
0.000 080 971 277 957	0.000 080 971 277 841	0.000 318 308 581 172	0.000 016 728 279 048
−0.000 183 237 594 773	−0.000 183 237 594 699	−0.000 354 862 279 467	−0.000 158 897 874 031
0.000 048 179 060 970	0.000 048 179 060 954	0.000 090 003 822 607	0.000 043 401 985 193
0.014 284 158 519 764	0.014 284 158 519 764	0.014 286 234 410 083	0.014 279 231 576 483
0.000 103 484 603 866	0.000 103 484 603 859	0.000 143 530 605 680	0.000 114 461 350 024
0.000 065 238 799 878	0.000 065 238 799 878	0.000 062 758 301 860	0.000 076 174 257 866
−0.000 006 766 328 528	−0.000 006 766 328 524	−0.000 020 400 392 386	−0.000 004 223 296 544
0.013 057 831 082 907	0.013 057 831 082 851	0.013 176 983 814 449	0.012 944 001 628 930
−0.002 246 518 605 775	−0.002 246 518 605 880	−0.002 018 366 780 776	−0.002 498 454 983 944
−0.001 034 809 078 185	−0.001 034 809 078 253	−0.000 855 944 393 495	−0.001 182 342 165 776
−0.000 176 574 984 482	−0.000 176 574 984 498	−0.000 132 716 723 507	−0.000 205 529 440 730

As already presented in Section 8.2.4, the integrated analysis with discrete measurements as observations provides the same results as the integrated analysis with functions as observations, in case the correct stochastic model was considered. As the first two columns of Table 9-4 show, the coefficients of both adjustments only differ in the range of $\approx 10^{-13}$, which mainly results from the solution of the normal equation system. As soon as a simplified stochastic model is applied and the correlations between the coefficients $\mathbf{u}$ are neglected, the results already differ in the fourth decimal place, as can be seen in the last two columns of Table 9-4. Nevertheless, these differences in the

coefficients **e** only have a minor impact on the resulting function $E(x)$ for the elastic modulus, as can be seen in Figure 9-2.

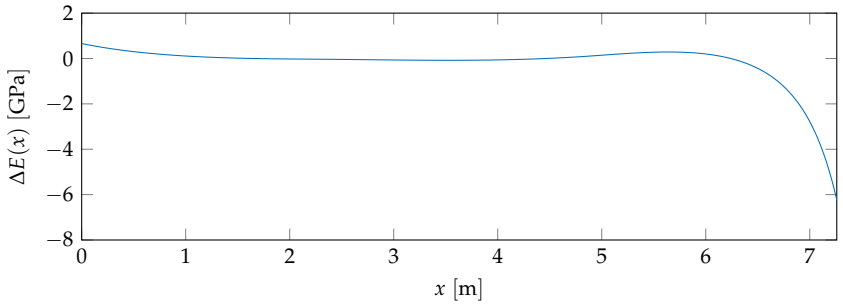

Figure 9-2: Difference $\Delta E(x)$ between the elastic modulus $E(x)$ resulting from the coefficients **e** of the inverse elastic modulus $E^*(x)$ in column 1 and 4 listed in Table 9-4.

The difference $\Delta E(x)$ between the elastic modulus $E(x)$ resulting from the coefficients **e** of the inverse elastic modulus $E^*(x)$ using the 24 displacement measurements as observations and using the coefficients **u** as observations without explicit stochastic model is depicted in Figure 9-2. Over almost the entire beam this difference is below 1 GPa, only at the right bearing larger differences up to ≈ 6 GPa occur. Consequently, an explicit stochastic model can be omitted if no information about the variances and covariances of the observations are available. For further analyses, however, the impact of a simplified stochastic model must be quantified and evaluated. That the largest deviation occurs close to the bearing is not a coincidence and will be discussed in detail in the following sections. As an integrated analysis with functions as observations is equivalent to an integrated analysis with discrete measurements as observations we will only consider the latter case for further studies.

9.2 SENSITIVITY ANALYSIS

Similar results were also partially published in (BECKER *et al.* 2015), but based on a FEM as functional model for the IA.

To get in insight into the difficulties of the determination of $E(x)$ from displacement, inclination and strain measurements and to answer the previously asked questions we perform a Monte Carlo simulation (MCS). The general workflow for the applied MCS is shown in Programme 9-1.

Programme 9-1: Pseudo code for Monte Carlo Simulation.

1: $\tilde{L}_{\text{type}} \leftarrow$ solving (7-29) for $\tilde{E}(x) = 70\,\text{GPa}$
2: $\sigma_{L_{\text{type}}} \leftarrow$ from Table 9-2
3: **for** $i = 1 : 10^3$ **do**
4: $\quad L_{\text{type}} \leftarrow \tilde{L}_{\text{type}} + N(0, \sigma_{L_{\text{type}}})$
5: $\quad E^*(x) \leftarrow$ solving (8-30)
6: $\quad E(x) \leftarrow E^*(x)$ according to Section 3.3.1
7: **end for**

9.2.1 *Impact of sensor position on the precision of* $E(x)$

A minimal configuration.

First of all, we will analyse the impact of the position and precision of a single measurement on the unknown function $E(x)$. Therefore, we consider $E(x)$ as a constant function and choose 726 equally spaced sensor positions x_{obs_i} along the beam. For each position we perform a MCS and estimate $E(x)$ and σ_E from

one single measurement, while the true function is given by $\tilde{E}(x) = 70\,\text{GPa}$. The result of the MCS for displacement measurements is shown in Figure 9-3.

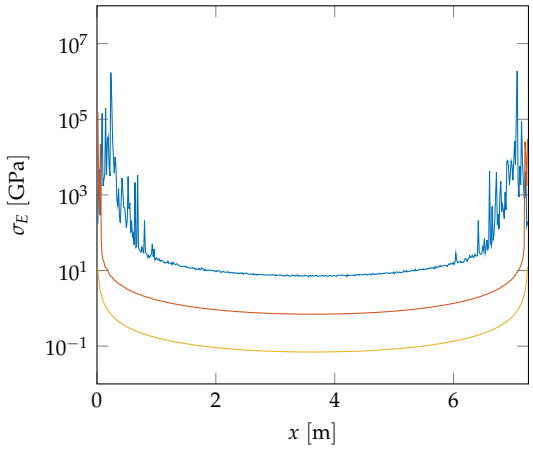

Figure 9-3: Logarithmic plot of the standard deviation σ_E of the estimated elastic modulus depending on the position of a single displacement measurement along the beam and for low (blue), medium (red) and high (yellow) sensor precision.

As was to be expected, the determination of $E(x)$ from displacement measurements in the middle of beam yields the most precise results, while for measurements close to the bearings the estimation $E(x)$ is very inaccurate. The blue line in Figure 9-3 represents the expected standard deviation σ_E of the unknown elastic modulus for displacement measurements of low precision. In the middle of the beam we can expect to estimate an adjusted elastic modulus of about $E \approx 70\,\text{GPa}$ with a standard deviation $\sigma_E \approx 7\,\text{GPa}$, while for measurements close to the bearings a meaningful result for the adjusted elastic modulus E can not be expected. This is caused by the fact that displacement measurements close to the bearings are very small in comparison to their precision, which results in incredible high standard deviation of roughly $\sigma_E \approx 10^5\,\text{GPa}$. For measurements of medium (red) and high (yellow) precision this effect is only limited to positions very close to the bearings. In summary, a poor signal-to-noise ratio gives a very poor result for the estimated elastic modulus E. The result for the MCS using inclination and strain measurements are depicted in Figure 9-4 and 9-5.

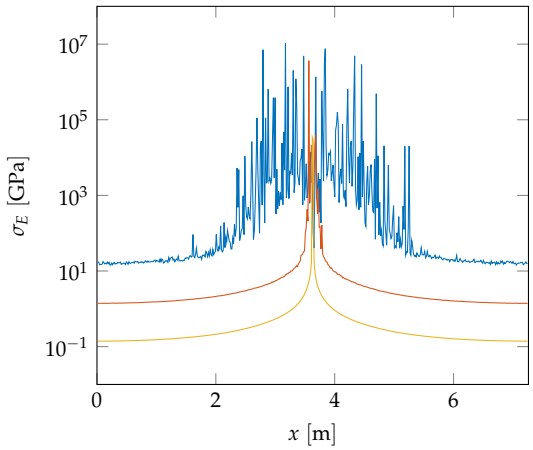

Figure 9-4: Logarithmic plot of the standard deviation σ_E of the estimated elastic modulus depending on the position of a single inclination measurement along the beam and for low (blue), medium (red) and high (yellow) sensor precision.

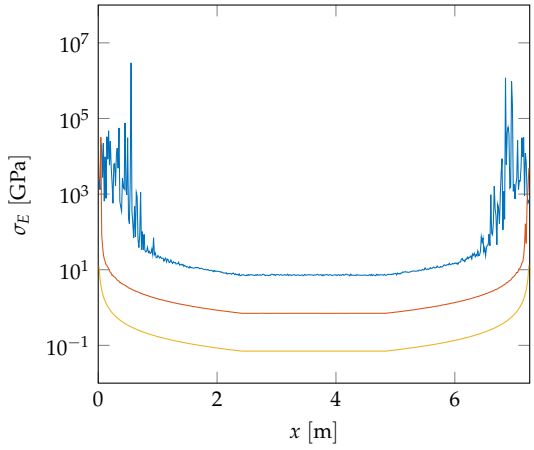

Figure 9-5: Logarithmic plot of the standard deviation σ_E of the estimated elastic modulus depending on the position of a single strain measurement along the beam and for low (blue), medium (red) and high (yellow) sensor precision.

Based on the conclusion for displacement measurements and the true solution depicted in Figure 9-1, we obtain similar results for inclination and strain measurements. To determine the elastic modulus $E(x)$ as precise as possible, inclination should be measured at the bearings and strain in the middle of the beam. The expected standard deviation σ_E for each type of measurement observed at the best position and for low, medium and high precision are summarized in Table 9-5.

Table 9-5: Mean standard deviation σ_E for the estimated elastic modulus $E(x)$ in [GPa] of the best position according to Figure 9-3 – Figure 9-5 for each type of observation and different sensor precisions $\sigma_{L_{\text{type}}}$

	σ_E in [GPa] for $\sigma_{L_{\text{type}}}$ equal		
	low	medium	high
Displacement	6.768	0.7013	0.069 94
Inclination	6.844	0.7017	0.069 92
Strain	6.742	0.7026	0.070 34

As Table 9-5 clearly reveals, we can expect to estimate the elastic modulus E with nearly the same precision for all three types of observations for each sensor precision. These numerical studies were also carried out by (Wu 2020, Chapter 5.1.4), while the numerical solution of the Euler-Bernoulli beam equation (7-1) is based on FEM, but with the same conclusion.

9.2.2 *Impact of measurement noise on $E(x)$*

It is an overdetermined adjustment problem with 10 observations, 12 unknowns and 6 constraints.

To analyse the impact of measurement noise on the elastic modulus $E(x)$, the MCS is based on measurements of 10 sensors equally distributed over the entire beam and a polynomial degree $p_e = 3$ for the unknown solution ${}^{\zeta}E^*(x)$ of each element. Five randomly chosen solutions for $E(x)$ using displacement measurements of low, medium and high precision are depicted in Figure 9-6.

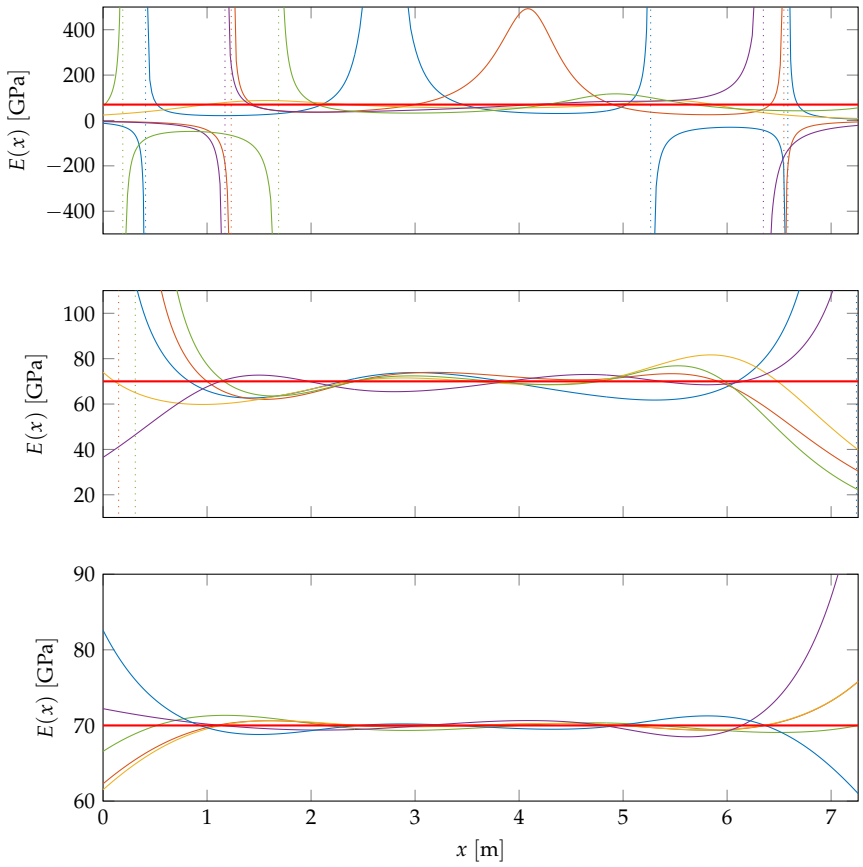

Figure 9-6: Derived $E(x)$ from the estimated $E^*(x)$ for 5 MCS using 10 displacement measurements with low (top), medium (middle) and high (bottom) precision. The horizontal red line in all plots is the true function $\tilde{E}(x) = 70\,\text{GPa}$.

The top plot in Figure 9-6 shows five random solutions for $E(x)$ derived from the estimation $E^*(x)$ using 10 displacement measurements of low precision, while the horizontal red line is the true function $\tilde{E}(x) = 70\,\text{GPa}$ we are looking for. The vertical dotted lines are indicating poles due to roots in the solution $E^*(x)$. As one can easily see, the solutions for $E(x)$ are meaningless and can take any arbitrary numerical value and is not at all identical with the true function $\tilde{E}(x)$. Different noise in the measurement usually results in a completely different solution for $E(x)$. The result for displacement measurements of medium precision (middle) is much better and only yields a poor approximation of $E(x)$ close to the bearings. For displacement measurements of high precision (bottom) the result is quite satisfying and the true function $\tilde{E}(x)$ can usually be estimated within several GPa, only revealing larger deviations close to the bearings. The result for inclination measurements is illustrated in Figure 9-7.

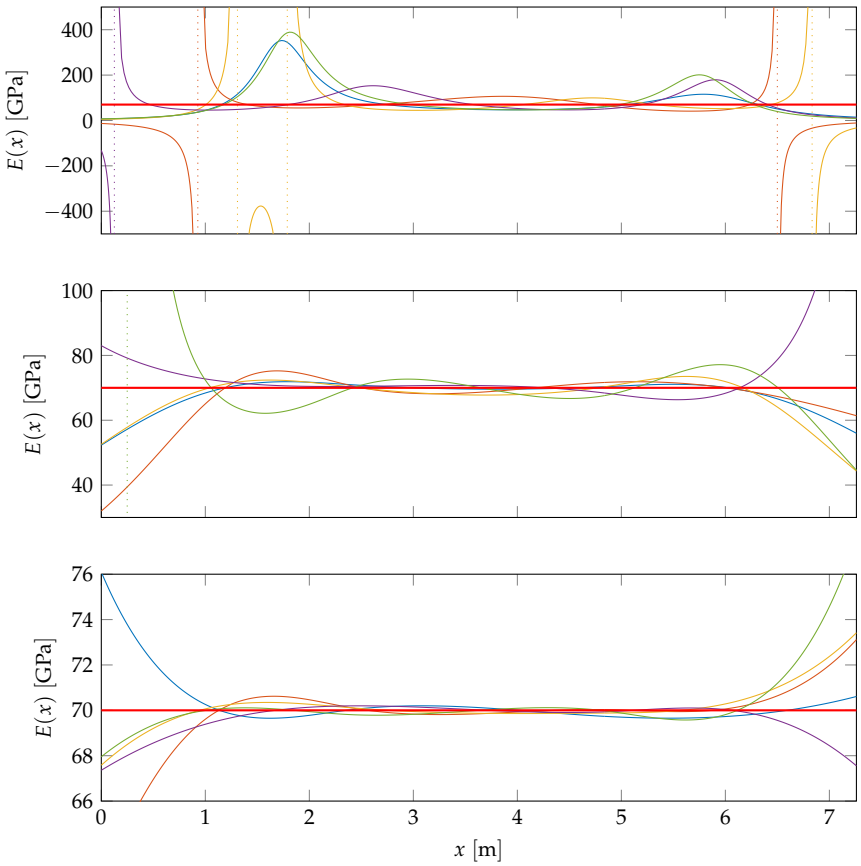

Figure 9-7: Derived $E(x)$ from the estimated $E^*(x)$ for 5 MCS using 10 inclination measurements with low (top), medium (middle) and high (bottom) precision. The horizontal red line in all plots is the true function $\tilde{E}(x) = 70\,\text{GPa}$.

As for displacements, the solutions for $E(x)$ based on inclination measurements of low precision in Figure 9-7 (top) are generally meaningless, while the solutions for medium (middle) and high (bottom) precision are quite satisfying, with often only minor deviations at the bearings. In general, the results seem to be better for inclination than for displacement measurements. For strain measurements the results are even better and are depicted in Figure 9-8.

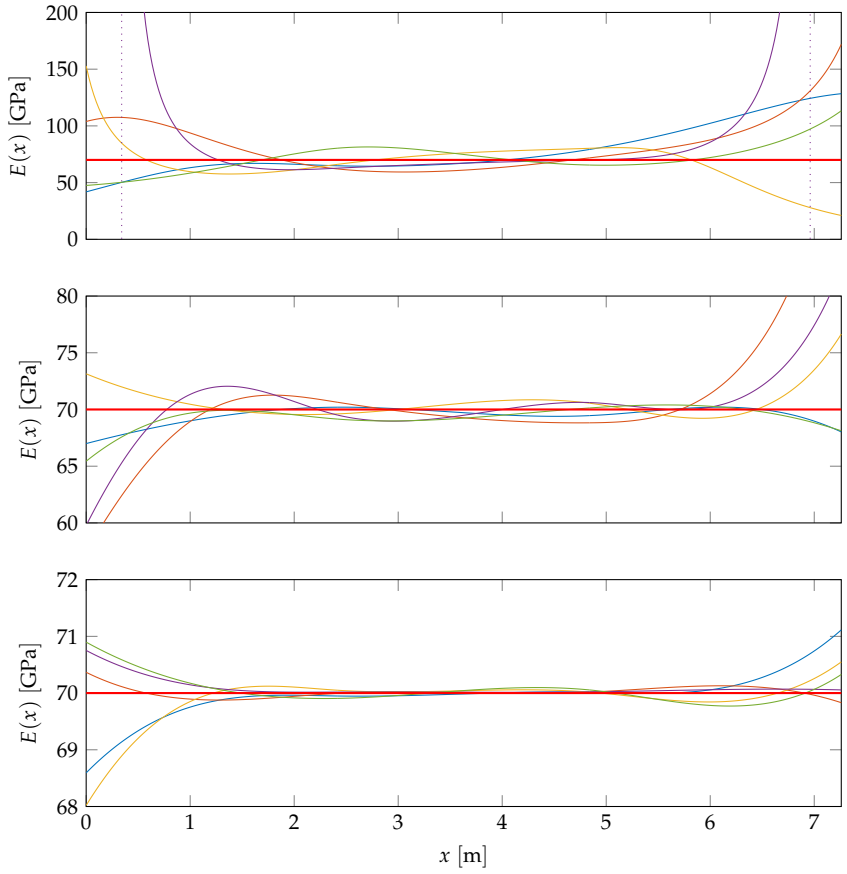

Figure 9-8: Derived $E(x)$ from the estimated $E^*(x)$ for 5 MCS using 10 strain measurements with low (top), medium (middle) and high (bottom) precision. The horizontal red line in all plots is the true function $\tilde{E}(x) = 70\,\text{GPa}$.

Even for strain measurements of low precision in Figure 9-8 (top), the solutions between the bearings are reasonable and even quite good for medium precision (middle). The result for strain measurements of high precision are really good and the true function $\tilde{E}(x)$ can usually be approximated within 1 GPa.

In Section 9.2.1 we introduced $E(x)$ as a constant value and we could estimate this value with nearly the same precision for all three types of observations. But now $E(x)$ is a polynomial of low degree and not a constant function any more. Based on Figure 9-6 – 9-8, now it really matters which type of observations we chose in order to estimate $E(x)$ as precisely as possible. To get a better insight on how precise the function $E(x)$ can be approximated for each type of measurement, the mean standard deviation σ_E of all MCS for low, medium and high precision are listed in Table 9-6.

	Mean σ_E in [GPa] for $\sigma_{L_{\text{type}}}$		
	low	medium	high
Displacement	11 897.63	131.39	7.59
Inclination	7023.55	9.46	0.94
Strain	26.32	2.45	0.24

Table 9-6: Mean standard deviation σ_E for the elastic modulus $E(x)$ for each type of observation and different sensor precisions $\sigma_{L_{\text{type}}}$. Numbers in red are only rough values, as σ_E can be extremely large for some MCS.

Table 9-6 clearly confirms that the elastic modulus $E(x)$ can be determined most precisely by strain measurements. Even for displacement measurements of high precision the result is three times worse than for strain measurements of medium precision. That the solutions for $E(x)$ by strain measurements are most precise is no surprise, because strain is directly related to the elastic modulus. In contrast to inclination and displacement measurements, which

are linked to the elastic modulus by their derivatives. For these studies strain measurements are the clear winner before inclination and displacement measurements.

9.2.3 *Impact of number of measurements on $E(x)$*

In the previous section we gained an impression on the expected precision of the elastic modulus $E(x)$ in dependence of the measurement noise, while the approximation is only based on 10 measurements. In the following we will analyse to what extent the approximation can be improved if more observations are available. Therefore, we will iteratively increase the number of measurements from 10 to 500 and for each iteration we distribute the sensors equally over the entire beam. As before, we choose a polynomial degree $p_e = 3$ for the unknown solution ${}^{\zeta}E^*(x)$ and perform a MCS for each type and every number of measurements. However, we only consider medium sensor precision, as the conclusion for low and high precision is similar. The result is illustrated in Figure 9-9.

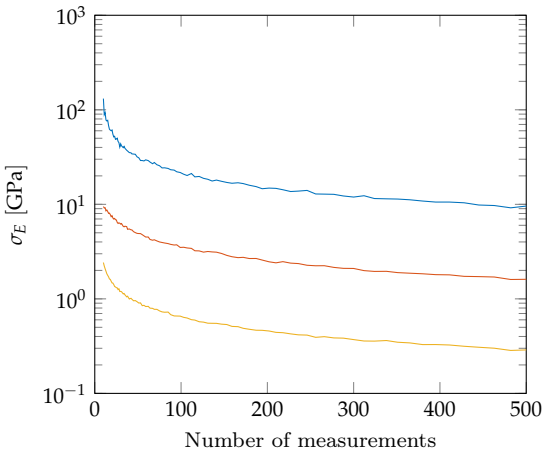

Figure 9-9: Logarithmic plot of the standard deviation σ_E of the derived elastic modulus $E(x)$ for displacement (blue), inclination (red) and strain (yellow) measurements depending on the number of measurements and for medium sensor precision

Based on graphs in Figure 9-9, we can generally conclude that the elastic modulus $E(x)$ can be determined more precisely if more measurements are available. But only to a certain extent, since the gain in accuracy must be obtained by more and more observations, as the decreasing curves indicate. The approximation will only be slightly more precise for 200 than for 100 measurements.

9.2.4 *Impact of the polynomial degree of $E^*(x)$ on $E(x)$*

So far we have gained an insight into the impact of noise and different numbers of sensors on the approximation $E(x)$. However, the polynomial degree p_e also has a significant influence on the approximation, which will be demonstrated in the following. For each type of measurements we always use the same 100 equally distributed observations of high precision and determine $E(x)$ for a different polynomial degrees p_e for the unknown solution ${}^{\zeta}E^*(x)$. The resulting approximations for displacement measurements are shown in Figure 9-10.

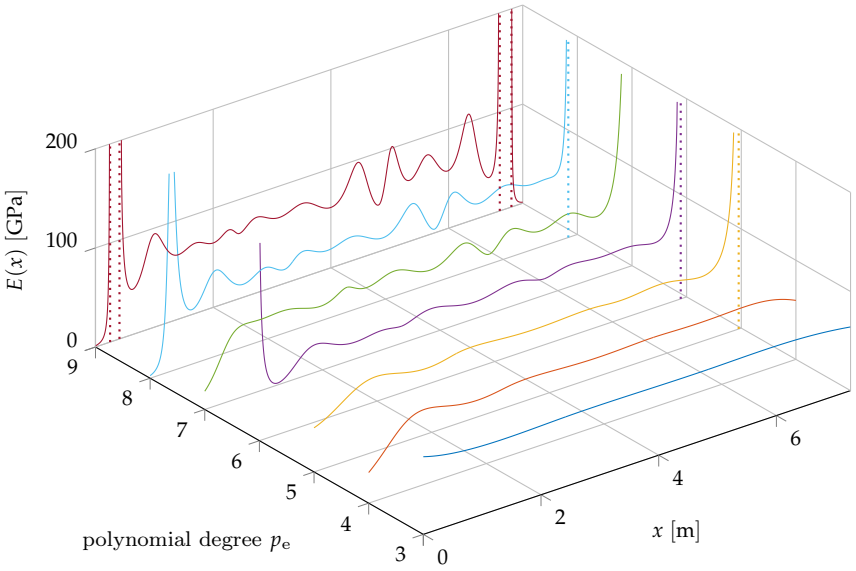

Figure 9-10: Derived $E(x)$ using 100 displacement measurements of high precision for 7 different polynomial degrees p_e for the unknown solution $\zeta E^*(x)$.

The blue curve for $p_e = 3$ in Figure 9-10 approximates the true function $\tilde{E}(x)$ within less than 1 GPa, while we can already recognize larger deviations at the bearings for $p_e = 4$ (red). The approximation for $p_e = 5$ (yellow) already reveals a pole (dotted line) at the right bearing for $x = 7.26\,\mathrm{m}$. A further increase of the polynomial degree p_e leads to a more unstable solution for the unknown solution $E(x)$. The condition number of the extended normal matrix in (8-30) increases and is nearly $\approx 3 \cdot 10^{14}$ for $p_e = 9$. The solution of $E(x)$ for larger polynomial degree are useless although we have used 100 measurements of high precision. The choice of equidistant measurement points is not causing the numerical instabilities, it also exists even if we would have chosen Chebyshev points. Besides the functional model described by (8-30) also the constraints (8-29) having a huge impact on the condition number. The result for inclination measurements of high precision is depicted in Figure 9-11 and is slightly better than for displacements.

It is perhaps worth mentioning that the target function Ω really becomes smaller with increasing polynomial degree.

Rescaling each row in $\mathbf{C}_{\text{conti}}$ improves the condition number.

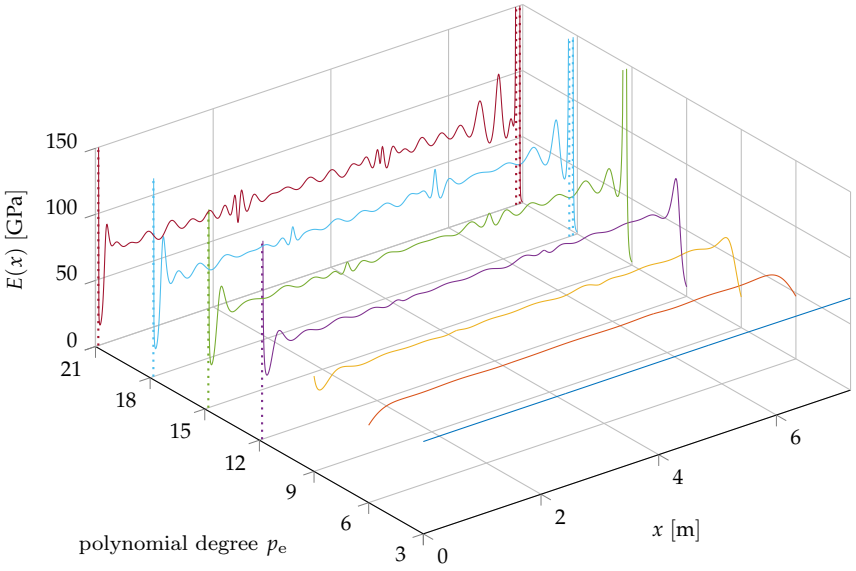

Figure 9-11: Derived $E(x)$ using 100 inclination measurements of high precision for 7 different polynomial degrees p_e for the unknown solution $\zeta E^*(x)$.

As shown in Figure 9-11, the influence of the polynomial degree p_e on the approximation of $E(x)$ for inclination measurements is not as detrimental as

for displacements. The approximation only becomes unstable for a polynomial degree $p_e \geq 20$. However, poles can also occur at the bearings for smaller polynomial degrees, as can be seen on the violet curve for $p_e = 12$. The impact of the polynomial degree p_e on the unknown solution $E(x)$ using strain measurements of high precision is somewhat lower and is illustrated in Figure 9-12.

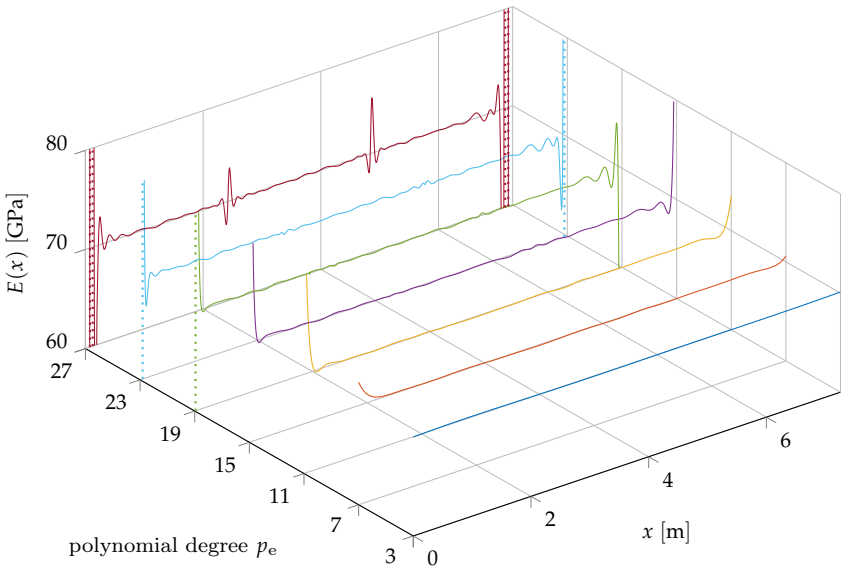

Figure 9-12: Derived $E(x)$ using 100 strain measurements of high precision for 7 different polynomial degrees p_e for the unknown solution ${}^{\zeta}E^*(x)$.

The determination of the approximation $E(x)$ using strain measurements of high precision becomes unstable for a polynomial degree $p_e \geq 27$. As before, poles can also occur at the bearings for smaller polynomial degrees. In general, the resulting approximation is much smoother in between the bearings than for displacement or inclination measurements. Once again, for these studies strain measurements are the clear winner followed by inclination and displacement.

Perhaps these peaks are also caused by the GIBBS phenomenon, while the first derivative of the bending moment $M(x)$ has two jump discontinuities at the inner nodes and also the solution $u(x)$ is only C^2 continuous.

However, Figure 9-12 also reveals a problem that was already apparent in Figure 9-11 but not really in Figure 9-10. The approximation for $p_e = 27$ shows two larger peaks at the two inner nodes for $x \approx 2.5\,\mathrm{m}$ and $x \approx 4.8\,\mathrm{m}$ corresponding to the points where the force is applied. This is caused by the introduced constraints (8-29) for a C^2 continuous approximation of $E(x)$, which can have a unfavourable impact on the solution, that will be discussed in the following section.

9.2.5 *Analysis of Residuals*

Polynomial regression.

In general, the estimation of $E(x)$ from measurements is equivalent to the problem of finding the best fit polynomial to a set of data points. Consequently, there must exist a polynomial $E(x)$ interpolating the measurements, resulting in $\mathbf{v} = \mathbf{0}$. The impact of the constraints (8-29) will be shown on the resulting interpolating polynomial for $E(x)$ with and without constraints. Therefore, we consider 15 equidistant displacement measurements of high precision, excluding the bearings. This results in 5 observations for each element. The degree of the interpolating polynomial without continuity at the inner nodes is $p_e = 4$ and $p_e = 6$ for the C^2 continuous interpolation. Figure 9-13 shows

how the constraints (8-29) for C^2 continuity at the inner nodes only can have minor impact on the solution.

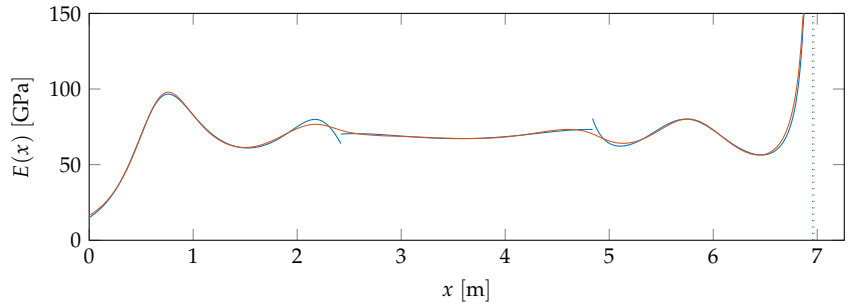

Figure 9-13: Small impact of the constraints. Non-continuous (blue) and C^2 continuous (red) interpolating polynomial for $E(x)$ based in the same 15 displacement measurements of high precision.

Both curves in Figure 9-13 are resulting in residuals for the 15 displacement measurements which are zero within machine precision. The largest deviations between both curves occur at the two inner nodes, but in general they are quite similar. The introduced constraints only have a small impact on the estimation of the polynomial and actually enforce only what they're supposed to, namely a C^2 continuous approximation. However, this is not often the case and the constraints usually have a large impact on the approximation as illustrated by Figure 9-14.

Ω is always a bit smaller for the non-continuous approximation.

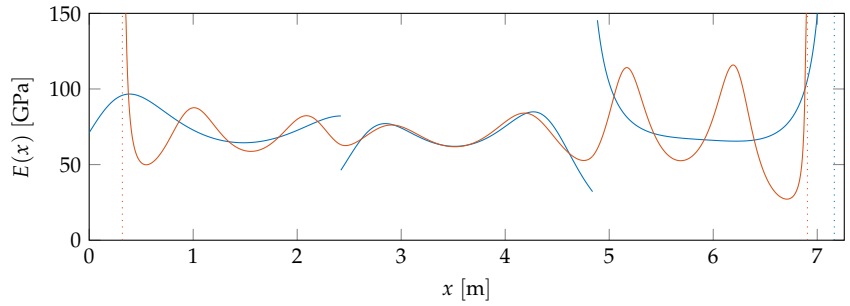

Figure 9-14: Large impact of the constraints. Non-continuous (blue) and C^2 continuous (red) interpolating polynomial for $E(x)$ based on the same 15 displacement measurements of high precision.

While for the element in the middle in Figure 9-14 both curves are quite similar, which is not the case for the first and last element and both curves are very different. Quite often the C^2 continuous approximation is completely different from the non-continuous one. Nevertheless, both curves in Figure 9-14 are resulting in residuals for the 15 displacement measurements which are zero within machine precision. Furthermore, both curves for the elastic modulus $E(x)$ yield almost the same solution for the bending line $u(x)$, with deviations in µm range, as depicted in Figure 9-15.

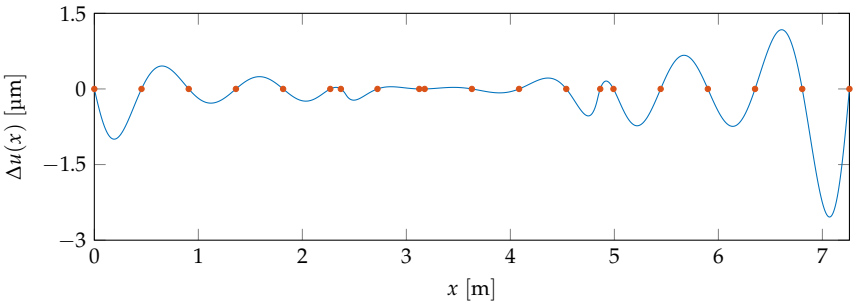

Figure 9-15: Difference $\Delta u(x)$ between the resulting bending line $u(x)$ from the non-continuous and C^2 continuous interpolating polynomial for $E(x)$ from Figure 9-14. The roots of $\Delta u(x)$ are indicated by red dots.

As Figure 9-15 shows, the difference between $u(x)$ based on the non-continuous and C^2 continuous elastic modulus $E(x)$ from Figure 9-14 are within $\approx 2.5\,\mu m$ which is about three times the standard deviation of the displacement measurements. The difference $\Delta u(x)$ has a total of 20 roots (red dots) where 15 exactly match the position of the measurements. Unfortunately, the approximation for $E(x)$ can be extremely different and still describe nearly the same bending line $u(x)$.

9.2.6 *Summary and Conclusion*

As we have seen from this sensitivity analysis, the accuracy of the estimated elastic modulus $E(x)$ depends on several factors, with the measurement noise having the largest impact. The determination of $E(x)$ based in displacement measurements is a highly unstable adjustment problem. Small differences in the measured values usually yield a completely different solution for $E(x)$. So far, it seems that strain measurements are best suited for the determination of $E(x)$, followed by inclination measurement and displacements yield by far the worst result. Due to the curve of the internal bending moment depicted in Figure 7-2, however, the larger oscillations of $E(x)$ always occur at the bearings, regardless of which measurement type, sensor precision or how many measurements we use. In the best case, this indeterminacy at the bearings has only a small influence on the estimation of $E(x)$, but it can also completely spoil it.

Besides the functional model there are also problems with the elementwise approximation using polynomials as shown in the previous section. The introduced constraints for a C^2 continuous approximation of $E(x)$ can have a detrimental impact on the solution which is additionally magnified by the oscillatory behaviour of polynomials. In addition to the aforementioned GIBBS phenomenon, it can be assumed that we also face the RUNGE phenomenon under certain circumstances. In this context, the number of measurement points, point distribution and polynomial degree p_e play an important role. However, using Chebyshev points as measurement positions has not significantly improved the results of the numerical studies and has therefore not been presented in this chapter.

9.3 DAMAGE ANALYSIS

In the following we will discuss the impact of damage on the measurements in order to gain an insight into the extent to which damage can be reconstructed from measurements. Therefore, we have to clarify how damage can be modelled in the particular case. As already mentioned in Section 7.2, damages caused by changes in the material or geometry are represented by the elastic modulus $E(x)$. However, it is usually easier to assess the extent of damage caused by geometry changes, such as a cut in the beam, than by material deterioration. Therefore, the cubic polynomial in Figure 9-16 provides a rough idea of the relationship between damage caused by a cut or material deterioration represented by the elastic modulus $E(x)$.

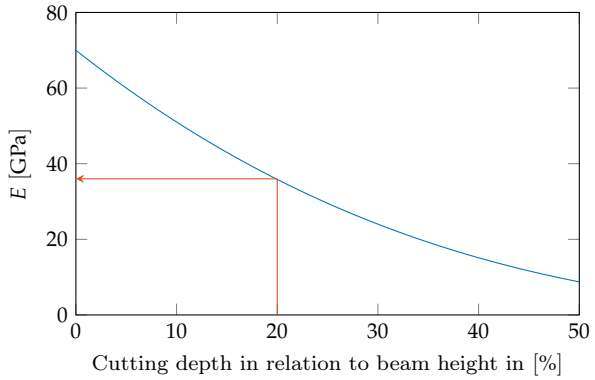

Figure 9-16: Relationship between damage caused by a cut or material deterioration.

As the red arrow in Figure 9-16 illustrates, damage caused by a cut with a depth of 20 % of the beam height results in the same deformation as a reduced elastic modulus of $E \approx 35\,\text{GPa}$ over the same width as the cut. For the current physical model shown in Section 7.1 and the specification of the four-point bending set-up in Table 9-1, a huge cut with a width of 20 cm and a depth of 7.2 cm can be described mathematically by the elastic modulus $E(x)$ illustrated by the blue curve in Figure 9-17.

Just as a rule of thumb.

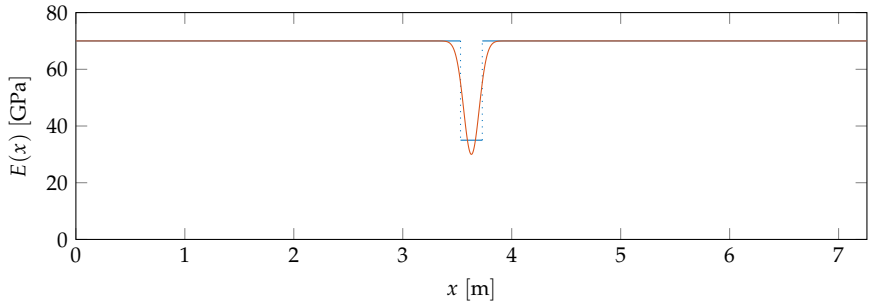

Figure 9-17: Elastic modulus $E(x)$ representing a huge cut with a width of 20 cm and a depth of 7.2 cm in blue and its approximation in red.

As can be clearly seen in Figure 9-17, the blue curve for $E(x)$ has two jump discontinuities which hardly can be approximated by Chebyshev polynomials without introducing new nodes at these two positions. For a proper approximation of the blue curve we would need a very high polynomial degree and for this reason we want to approximate damage by a smooth function as shown by the red curve in Figure 9-17. Consequently, damage will be represented by the contrived function

$$D(x) = h_\text{D} \exp\big(-w_\text{D}(x - x_\text{D})^2\big), \tag{9-1}$$

with h_D being the height, w_D the width and x_D the position of the damage. In the following we will clarify the impact of such damage on the three different types of measurements.

9.3.1 *Impact of damage on the measurements*

Let us consider the huge damage represented by the red line in Figure 9-17, which is given by

$$E_\text{D}(x) = 70 - 40 \exp\big(-500(x - 3.63)^2\big). \tag{9-2}$$

The impact of this damage on displacements is illustrated in Figure 9-18.

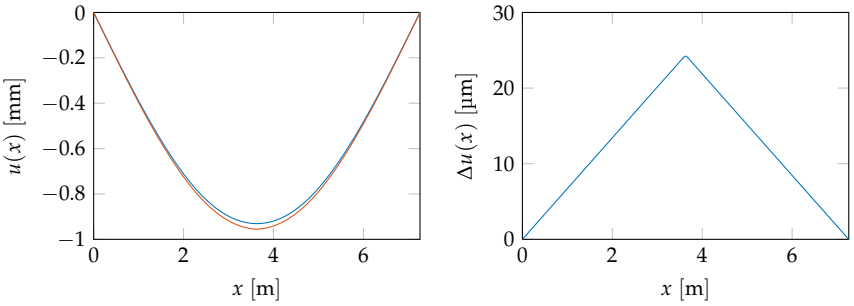

Figure 9-18: Displacements $u(x)$ without damage for $E(x) = 70\,\text{GPa}$ in blue and with damage for $E_\text{D}(x)$ given by (9-2) in red (left). Difference $\Delta u(x)$ between displacements with and without damage (right).

As shown in Figure 9-18, a huge cut in the middle of the beam at $x = 3.63\,\text{m}$ simulated by (9-2) has only a small impact on the displacements. The largest deviations can be found exactly where the damage is located and are in the range of $\approx 25\,\mu\text{m}$ (right), which is about 2.6 % of the maximum displacement without damage. With increasing distance from the position of the damage, the difference $\Delta u(x)$ decreases linearly. The impact of damage given by (9-2) on the inclination is depicted in Figure 9-19.

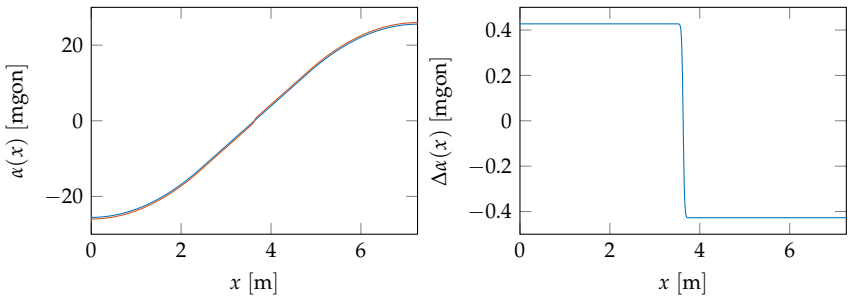

Figure 9-19: Inclination $\alpha(x)$ without damage for $E(x) = 70\,\text{GPa}$ in blue and with damage for $E_\text{D}(x)$ given by (9-2) in red (left). Difference $\Delta\alpha(x)$ between inclination with and without damage (right).

As can be seen in Figure 9-19 (left), the impact of the huge cut in the middle of the beam on the inclination is also quite small. In contrast to the displacements, the largest deviations $\Delta\alpha(x)$ of $\approx 0.4\,\text{mgon}$ do not occur at the location of the damage, but are constant along the beam outside the damaged area. The largest deviations are only about 1.7 % of the maximum inclination without damage. However, the position of the damage can be clearly seen in the curve by the sudden change of sign in Figure 9-19 (right). For strain, the situation is quite different, as Figure 9-20 reveals.

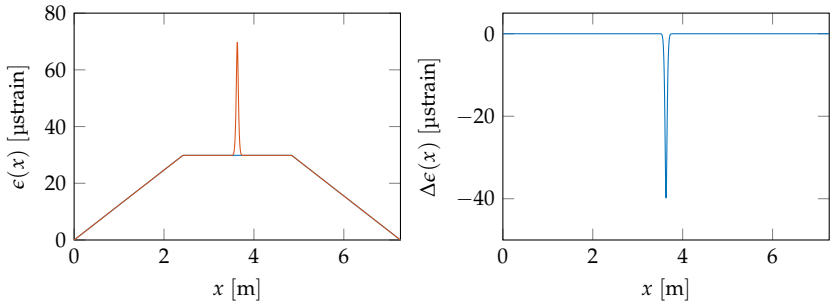

Figure 9-20: Strain $\epsilon(x)$ without damage for $E(x) = 70\,\text{GPa}$ in blue and with damage for $E_\text{D}(x)$ given by (9-2) in red (left). Difference $\Delta\epsilon(x)$ between strain with and without damage (right).

Due to the functional relationship (7-1) between strain and $E(x)$, it is not surprising that $\Delta\epsilon(x)$ in Figure 9-20 (right) represents the damage itself. The largest deviations are in the range of $\approx 40\,\mu\text{strain}$ (right), which is about 134 % of the maximum strain without damage. As we have seen, damage affects

displacements and inclinations over the entire beam, however only to a small extent. In contrast to strain, which only changes locally to damage, but on a large scale. Therefore, if only a few discrete strain measurements are available, we can only detect and localize damage if it occurs in the vicinity of the measurement position. Otherwise, we will not be able to detect any damage from these strain measurements.

9.3.2 *Ambiguities*

As we have seen in the previous section, the huge damage represented by (9-2) has only a minor impact on the displacement and inclination, but a large one on strain, however, only locally. Therefore, and because usually only discrete measurements are available, another problem arises. In Section 9.3 we have decided that we simulate damage by the smooth function (9-1) and the magnitude of a damage depends on the height h_D and width w_D representing for example the depth and width of a cut. However, different combinations of these two parameters lead to a similar magnitude of the damage and thus to a similar impact on the measurements. To illustrate this issue, we consider the following four different types of damages $E_{\mathrm{D}_i}(x)$

$$\begin{aligned} E_{\mathrm{D}_1}(x) &= 70 - 9.2550 \exp\big(-10(x-3.63)^2\big), \\ E_{\mathrm{D}_2}(x) &= 70 - 18.2955 \exp\big(-50(x-3.63)^2\big), \\ E_{\mathrm{D}_3}(x) &= 70 - 23.9015 \exp\big(-100(x-3.63)^2\big), \\ E_{\mathrm{D}_4}(x) &= 70 - 32.7145 \exp\big(-250(x-3.63)^2\big), \end{aligned} \tag{9-3}$$

which are also depicted in Figure 9-21.

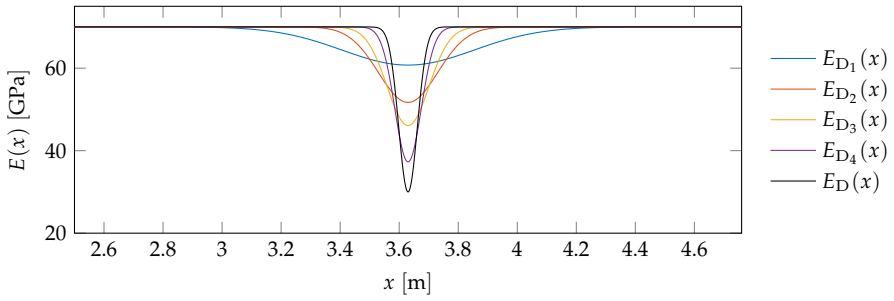

Figure 9-21: Different damages of similar magnitude.

Although these four damages clearly differ, they still result in almost the same deformation of the beam and thus to almost the same displacements and inclinations. The differences $\Delta u(x)$ between the displacements for damage $E_\mathrm{D}(x)$ from (9-2) and for damages $E_{\mathrm{D}_i}(x)$ from (9-3) are shown in Figure 9-22.

At this point we disregard strain, as damage has a direct impact on it anyway.

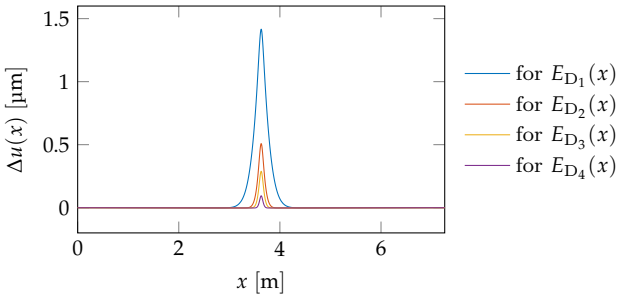

Figure 9-22: Differences $\Delta u(x)$ between displacements for damage $E_\mathrm{D}(x)$ and for damages $E_{\mathrm{D}_i}(x)$.

As Figure 9-22 clearly reveals, the displacements derived for damage $E_D(x)$ and $E_{D_i}(x)$ hardly differ from each other over almost the entire beam. Outside the damaged area these differences can be in the nm range or less and are usually smaller than 1 µm within this area. Thus, deviations can occur which correspond to less than 0.1 % of the maximum displacement of the beam. The situation is slightly different for inclination, as can be seen in Figure 9-23.

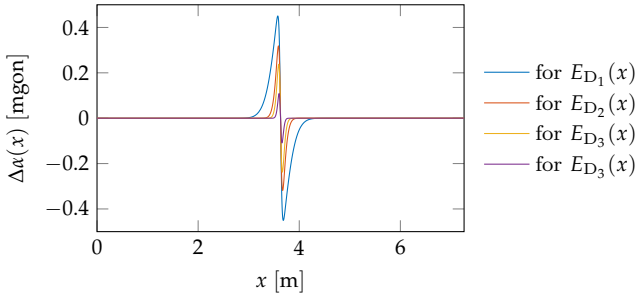

Figure 9-23: Differences $\Delta\alpha(x)$ between inclinations resulting for damage $E_D(x)$ from (9-2) and for damages $E_{D_i}(x)$ from (9-3).

Although the inclination derived for damage $E_D(x)$ and $E_{D_i}(x)$ also hardly differs outside the damaged area, differences of up to 0.4 mgon can occur within this area, which already represents about 1.7 % of the maximum inclination. Nevertheless, no matter for which type of observation, damage can only be quantified in this case if a sufficient number of measurements with appropriate accuracy are available within the damaged area.

9.3.3 *Impact of the position of damage on the measurements*

Moreover, we want to analyse to what extent the position of a damage affects the measurements. Therefore we move the position x_D in (9-1) for the damage in (9-2) along the beam, calculate the difference $\Delta(x)$ as shown in Figure 9-18 – 9-20 (right) and determine the maximum absolute value of this difference. The resulting impact of the damage position on displacements is shown in Figure 9-24.

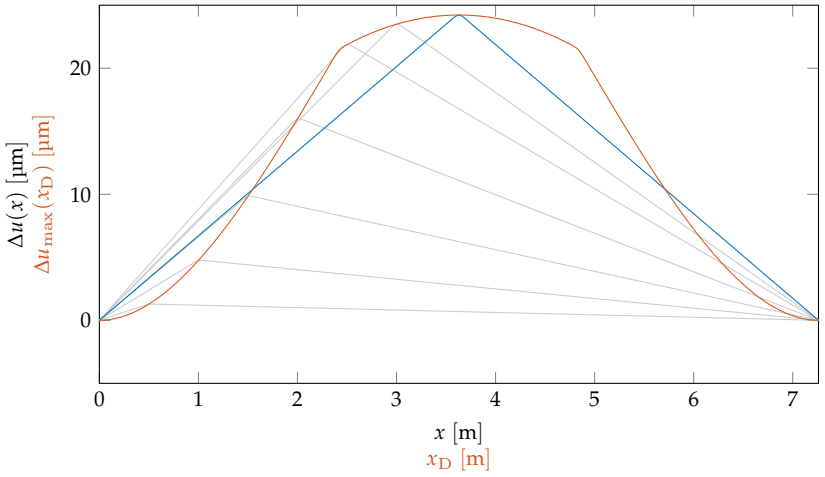

Figure 9-24: Maximum absolute difference $\Delta u_{max}(x_D)$ between displacements with and without damage as a function of the damage position $x_D \in [0, l]$ in red. Difference $\Delta u(x)$ from Figure 9-18 (right) in blue and for $x_D = [0.5, 1, 1.5, 2, 2.5, 3, 3.5]$ in grey.

The blue curve in Figure 9-24 shows the difference $\Delta u(x)$ from Figure 9-18 (right), where the damage is exactly in the middle of the beam. The grey curves are illustrating the resulting differences $\Delta u(x)$ for the same damage

but for different positions $x_D = [0.5, 1, 1.5, 2, 2.5, 3, 3.5]$. As already mentioned, the maximum impact of a damage on displacements always occurs exactly at the position of the damage and if we draw more such curves for additional damage positions $x_D \in [0, l]$ and connect their peaks with each other we obtain the red curve in Figure 9-24. In general, damage in exactly the middle of the beam has the largest impact on displacements than at any other position and decreases only slightly within the two points where the force is applied. Outside these two points for $x_D < 2.42$ and $x_D > 4.84$, however, the impact of a damage decreases rapidly the closer it is to the two bearings. In a similar way, the impact of the damage position on the inclination was determined and is depicted in Figure 9-25.

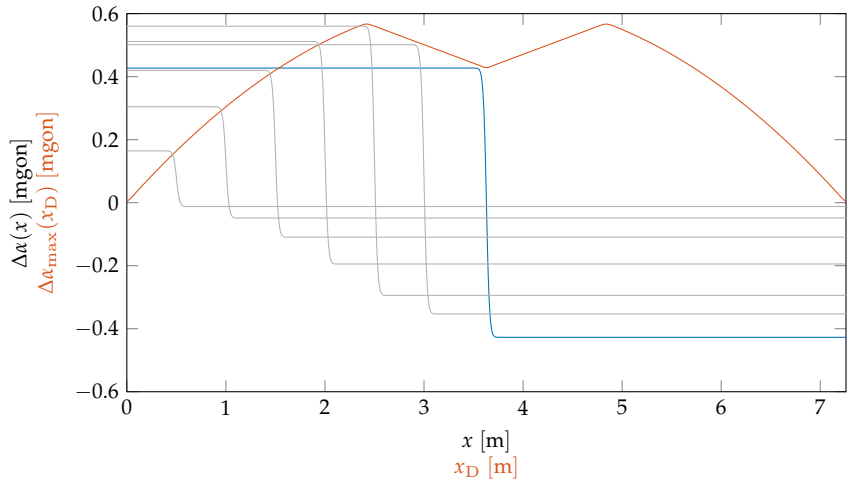

Figure 9-25: Maximum absolute difference $\Delta\alpha_{max}(x_D)$ between inclinations with and without damage as a function of the damage position $x_D \in [0, l]$ in red. Difference $\Delta\alpha(x)$ from Figure 9-19 (right) in blue and for $x_D = [0.5, 1, 1.5, 2, 2.5, 3, 3.5]$ in grey.

As before, the blue curve in Figure 9-25 shows the difference $\Delta\alpha(x)$ from Figure 9-19 (right) and the grey curves are the resulting differences $\Delta\alpha(x)$ for damages at $x_D = [0.5, 1, 1.5, 2, 2.5, 3, 3.5]$. The red curve in Figure 9-25 represents the impact $\Delta\alpha_{max}(x_D)$ of a damage on the inclination in accordance to its position x_D. In contrast to displacements, the largest impact on the inclination occurs exactly at the two points where the force is applied. In between these two points the impact drops a bit and also decreases almost linearly towards the bearings and thus by far not as fast as for the displacements. Due to the functional relationship (7-1) between strain and $E(x)$ the impact of the damage position on strain corresponds to the bending moment from Figure 7-2. For illustrative reasons, however, the maximum impact of the damage position is shown with negative signs in Figure 9-26.

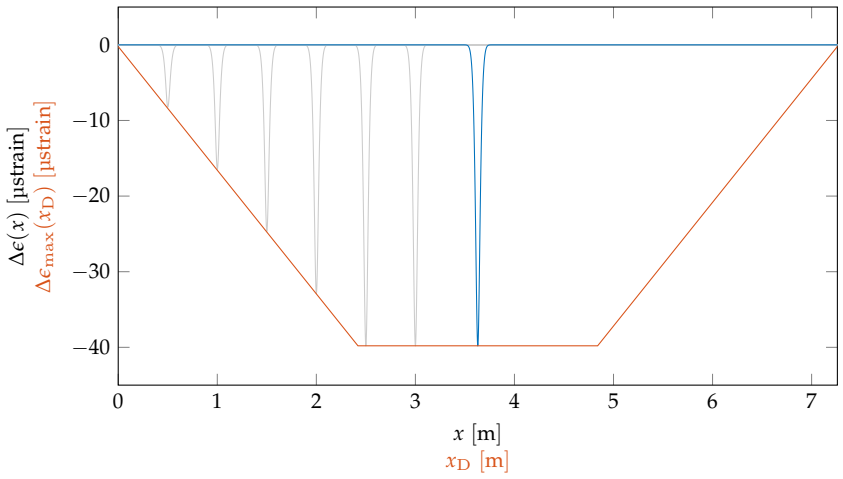

Figure 9-26: Maximum absolute difference $\Delta\epsilon_{\max}(x_D)$ between strain with and without damage as a function of the damage position $x_D \in [0, l]$ with negative signs in red. Difference $\Delta\epsilon(x)$ from Figure 9-20 (right) in blue and for $x_D = [0.5, 1, 1.5, 2, 2.5, 3, 3.5]$ in grey.

As already mentioned, the red curve in Figure 9-26 represents the impact $\Delta\epsilon_{\max}(x_D)$ of the damage position on the strain measurements with negative signs and corresponds to the curve of the internal bending moment in Figure 7-2. Therefore, $\Delta\epsilon_{\max}(x_D)$ is constant between the two points at which the force is applied and decreases linearly towards the bearings. In general, the impact of the position of a damage outside the two points where the force is applied is worst for displacements and somewhat more favourable for inclinations because it decreases slightly more slowly than linearly. Within these two points, the impact for displacements and inclination changes only marginally.

9.3.4 *Impact of the magnitude of damage on the measurements*

Another aspect that we would like to clarify briefly is the relationship between the magnitude of a damage and its maximum absolute impact on the measurements. As discussed in Section 9.3.2, the magnitude of the simulated damage (9-1) depends on the height h_D and width w_D, where different combinations of these two parameters can lead to a similar magnitude of the damage. Hence, we will now consider w_D as constant and describe the magnitude only by h_D. For strain, the impact can simply be derived from Equation (7-5) and with (9-1) it reads for $x = x_D$

$$\Delta\epsilon_{\max}(h_D) = \underbrace{-\frac{M(x)}{I}}_{=\text{const.}} \frac{1}{70 - h_D \underbrace{\exp\left(-w_D(x - x_D)^2\right)}_{=\text{const.}}} \tag{9-4}$$

and is also illustrated in Figure 9-27, where, for reasons of comparability, it is shown relative to the impact for the maximum magnitude of $h_D = 60$.

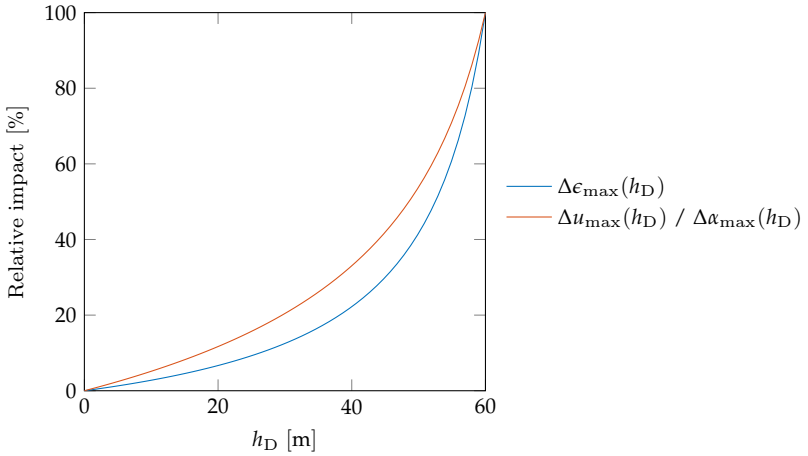

Figure 9-27: Impact of the magnitude of damage h_D on the maximum absolute difference for strain $\Delta\epsilon_{max}(h_D)$ in blue and for displacements $\Delta u_{max}(h_D)$ and inclination $\Delta\alpha_{max}(h_D)$ in red.

The blue curve in Figure 9-27 shows the relative impact of the magnitude of damage on the maximum absolute difference for strain $\Delta\epsilon_{max}(h_D)$. For small damages, this impact is almost linear, whereas for larger damages it rapidly increases. In addition, the impact of the magnitude of damage on the maximum absolute difference for displacements $\Delta u_{max}(h_D)$ and inclinations $\Delta\alpha_{max}(h_D)$ was determined numerically. Since the relative impact for both types of measurements are almost the same, both are represented by the red line and differ only slightly from the relative impact for strain.

9.3.5 *Summary and Conclusion*

As we have seen from this study, the impact of damage on the displacements and inclination is unfortunately rather small. Even the huge cut with a width of 20 cm and a depth of 7.2 cm, represented by (9-2), has only a small impact of about $\approx 2\,\%$ on the displacements and inclinations and is much lower for small damages. Due to the functional relationship (7-1) between strain and $E(x)$, damage has a direct and large impact on strain measurements, however only locally. The main conclusions are summarised in Table 9-7.

	Displacements	Inclination	Strain
Impact	small	small	large
Indicator	global	global	local

Table 9-7: Summary of the studies on the impact of damage on displacements, inclinations and strains.

For a damage detection and localisation via MeMoS it is of course useful if damage has a large and global impact on the measurements, unfortunately none of the three types has this property, as can be seen in Table 9-7. However, the results from the studies in Sections 9.2 and 9.3 clearly favour strains for damage detection and localisation due to existing sensors such as FOS, see e.g. (LIENHART 2007, p. 36 ff.), (LOPEZ-HIGUERA *et al.* 2011) or (WU 2020). However, scattered strain measurements are quite useless if the damage is not in the vicinity of a measuring point.

10 DAMAGE ANALYSIS VIA MEMOS

In the numerical studies in Chapter 9 we have seen which problems occur in the estimation of $E(x)$ and that even huge damages have hardly any influence on the displacements and inclinations. Except for almost continuous strain measurements, a structural analysis via MeMoS does not seem to be very promising at first glance. To show to which extent damage can still be detected and localized by MeMoS, we first present some tools.

Since for the presented four-point bending test damage has a direct and local impact on strain measurements, a structural analysis with strain corresponds in principle to a conventional deformation analysis in geodesy. Accordingly, existing approaches for deformation analysis of point clouds, such as (Schill 2018) or (Wujanz 2016), can also be used for strain measurement using e.g. FOS. As this is another challenge and since no strain measurements are available for the experimental studies, the following tools were essentially designed for displacement and inclination measurements only. However, this does not generally mean that these tools are not suitable for analysing strain measurements. But, in general, it is recommended to use a different methodological approach for the damage analysis of strain measurements, as also the results of the numerical studies in Section 10.2 will illustrate.

10.1 TOOLBOX

For damage detection and localisation via MeMoS, some tools have been developed. Several of them are based on statistical tests and methods known from the literature and some were developed particularly for this application. These tools are referred to as

- Parameter Sifter (PS),
- Global Identifier (GI),
- Local Indicator (LI),
- Local Smoother (LS),
- Damage Sniffer (DS),
- Damage Modeller (DM)

and are described in the following sections.

10.1.1 *Parameter Sifter*

As a result of the Integrated Analysis (IA) from Chapter 8, the unknown parameters e_j and their standard deviations s_{e_j} are available, see Chapter 2. Based on these values, the Parameter Sifter (PS) iteratively removes unknown

parameters from the IA, which are not significant different from zero. Thus, the null hypothesis reads

$$H_0 : |e_j| = 0 \tag{10-1}$$

and the alternative hypothesis results in

$$H_A : |e_j| > 0\,. \tag{10-2}$$

t–test

The test statistic for each unknown parameter e_j is given by

$$t_j = \frac{|e_j|}{s_{e_j}} \tag{10-3}$$

and the critical value of the t–distribution for a degree of freedom f and error level α is denoted by $t_{f,\alpha}$. The null hypothesis H_0 will be rejected in favour of the alternative hypothesis H_A if

$$t_j > t_{f,\alpha}\,. \tag{10-4}$$

This iterative removal of the unknown parameters tends to result in a highly smoothed solution for the unknown function, which in some cases even fails to reveal larger damage. To reduce this problem an error level of $\alpha = 1\,\%$ was chosen and f corresponds to the redundancy of the adjustment problem within the Integrated Analysis. The general workflow of the PS is shown in Programme 10-1.

Programme 10-1: Pseudo code for the Parameter Sifter (PS).

1: e_j and $s_{e_j} \leftarrow$ from IA according to Chapter 8.
2: $t_j = \frac{|e_j|}{s_{e_j}} \quad \forall j$
3: **while** min $(t_j) < t_{f,\alpha}$ **do**
4: $\quad e_k \leftarrow$ parameter with smallest t_j value.
5: $\quad e_j$ and $s_{e_j} \leftarrow$ from IA without e_k.
6: $\quad t_j = \frac{|e_j|}{s_{e_j}} \quad \forall j$
7: **end while**

The elimination of all non-significant parameters at once is not effective, since this procedure neglects the correlations between the unknown parameters and thus leads to false results. If a repeated solution of the normal equation system needs to be avoided, it is recommended to use the approach according to (SCHWINTZER 1984). Thereby, the significance of all parameters e_j is determined under consideration of the correlations, but without solving the normal equation system again.

10.1.2 *Global Identifier*

In this context, deformation can also be considered as damage.

The Global Identifier (GI) is based on the well known *congruency test* used for the deformation analysis of geodetic networks, see e.g. (HEUNECKE *et al.* 2013, Chapter 11) or (NIEMEIER 2008, Chapter 13). Thereby, the solutions of two epochs are compared by a statistical test in order to determine whether deformation is present or not. However, it turned out that a direct comparison of the estimated parameters **e** of two epochs by a *congruency test* is not feasible, as the type-I error is much larger than the chosen error level α. Both, the type-I and type-II error can be up to 50 % or more, so that a reliable

For further information about type-I and type-II error please refer to standard literature, such as (GENTLE 2009, p. 52 ff.) or (DEKKING *et al.* 2005, p. 377 ff.).

damage detection is no longer possible. By transferring the *congruency test* to continuous functions, much more reliable results could be achieved. Therefore, we will now consider the solution of the Integrated Analysis as a continuous function, which of course is always represented by its Chebyshev coefficients. Based on the solutions of two epochs

$$\begin{aligned} &\text{Epoch I:} && E_{\mathrm{I}}(x)\,, && s_{E_{\mathrm{I}}}(x)\,, && s^2_{0_{\mathrm{I}}}\,, && f_{\mathrm{I}}\,, && \Omega_{\mathrm{I}} \\ &\text{Epoch II:} && E_{\mathrm{II}}(x)\,, && s_{E_{\mathrm{II}}}(x)\,, && s^2_{0_{\mathrm{II}}}\,, && f_{\mathrm{II}}\,, && \Omega_{\mathrm{II}}\,, \end{aligned} \tag{10-5}$$

and in case

$$\boldsymbol{\mathcal{E}}\{s^2_{0_{\mathrm{I}}}\} = \boldsymbol{\mathcal{E}}\{s^2_{0_{\mathrm{II}}}\}\,, \tag{10-6}$$

with $\boldsymbol{\mathcal{E}}\{\cdot\}$ being the expectation operator, a common empirical variance factor for both epochs can be introduced and results in

$$s^2_0 = \frac{\Omega_{\mathrm{I}} + \Omega_{\mathrm{II}}}{f_{\mathrm{I}} + f_{\mathrm{II}}}\,. \tag{10-7}$$

The null hypothesis of the statistical test for the GI reads

$$H_0 : \boldsymbol{\mathcal{E}}\{\Theta^2\} = \boldsymbol{\mathcal{E}}\{s^2_0\} \tag{10-8}$$

with

$$\Theta^2 = \frac{1}{l} \int_0^l \frac{\Big(E_{\mathrm{I}}(x) - E_{\mathrm{II}}(x)\Big)^2}{q^2_{E_{\mathrm{I}}}(x) + q^2_{E_{\mathrm{II}}}(x)}\,\mathrm{d}x \tag{10-9}$$

and

$$\begin{aligned} q^2_{E_{\mathrm{I}}}(x) &= \frac{s^2_{E_{\mathrm{I}}}(x)}{s^2_{0_{\mathrm{I}}}}\,, \\ q^2_{E_{\mathrm{II}}}(x) &= \frac{s^2_{E_{\mathrm{II}}}(x)}{s^2_{0_{\mathrm{II}}}}\,. \end{aligned} \tag{10-10}$$

Hence, the alternative hypothesis is given by

$$H_A : \boldsymbol{\mathcal{E}}\{\Theta^2\} > \boldsymbol{\mathcal{E}}\{s^2_0\} \tag{10-11}$$

and the test statistics results in

F–test

$$F = \frac{\Theta^2}{s^2_0}\,. \tag{10-12}$$

The null hypothesis H_0 will be rejected in favour of the alternative hypothesis H_A if

$$F > F_{f_1, f_2, \alpha}\,, \tag{10-13}$$

with $f_1 = 1$ and $f_2 = \infty$. Based on numerical studies an error level $\alpha = 5\,\%$ was chosen and the critical value yields $F_{1,\infty,0.05} \approx 3.8$.

So far, the assumption that the integrated quantity Θ^2 follows the χ^2 distribution is based only on empirical studies and has not yet been proven methodically.

10.1.3 *Local Indicator*

The Local Indicator (LI) compares the solution of two epochs by a statistical test to determine in which regions they differ significantly from each other. As for the Global Identifier (GI) we will also consider the solution of the Integrated Analysis as a continuous function. Given are the solutions of two epochs

$$\begin{aligned} &\text{Epoch I:} && E_{\mathrm{I}}(x)\,, && s_{E_{\mathrm{I}}}(x) \\ &\text{Epoch II:} && E_{\mathrm{II}}(x)\,, && s_{E_{\mathrm{II}}}(x) \end{aligned} \tag{10-14}$$

and the null hypothesis reads

$$H_0 : E_{\mathrm{I}}(x) - E_{\mathrm{I}}(x) = 0\,. \tag{10-15}$$

Hence, the alternative hypothesis yields

$$H_A : E_{\mathrm{I}}(x) - E_{\mathrm{I}}(x) \neq 0\,. \tag{10-16}$$

continuous t-test

In this case, the test statistic is a function of x and is given by

$$t(x) = \frac{E_{\mathrm{I}}(x) - E_{\mathrm{II}}(x)}{\sqrt{s^2_{E_{\mathrm{I}}}(x) + s^2_{E_{\mathrm{II}}}(x)}}\,. \tag{10-17}$$

The new critical value has been determined by an Monte Carlo simulation (MCS).

Numerical investigations have shown, however, that $t(x)$ does not follow the t–distribution and therefore a new critical value needs to be determined, which apparently depends on the type of measurement and configuration. For 30 equidistant displacement measurements of high precision and an error level $\alpha = 5\,\%$, the critical value results in $t_{\mathrm{critical}} = \pm 3.5$. The null hypothesis H_0 will be rejected in favour of the alternative hypothesis H_A for certain positions x if

$$t(x) < t_{\mathrm{critical}} \qquad \text{or} \qquad t(x) > t_{\mathrm{critical}}\,. \tag{10-18}$$

To illustrate this in more detail, we will consider two arbitrary solutions for $E(x)$, which are shown in Figure 10-1.

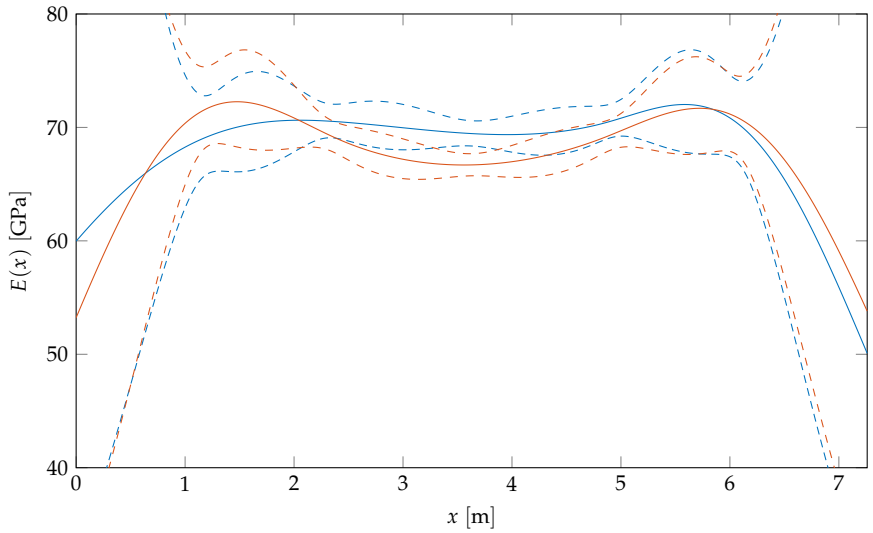

Figure 10-1: Two solutions for $E(x)$ (solid line) and their corresponding 3σ error bounds (dashed line) determined by their standard deviation $s_E(x)$.

Based on these two solutions and their standard deviations, which are shown as 3σ error bounds in the Figure 10-1 (dashed line), we want to analyse where both solutions may differ significantly from each other or not. Therefore we calculate the test statistic $t(x)$ according to Equation (10-17), which is shown in Figure 10-2.

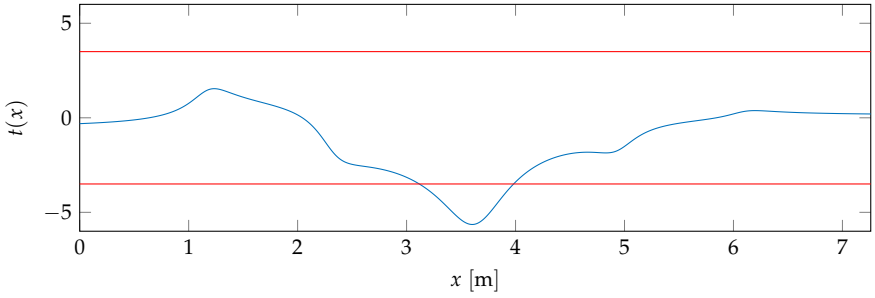

Figure 10-2: Local Indicator in blue for the two solutions depicted in Figure 10-1 according to Equation (10-17). The critical value $t_{\mathrm{critical}} = \pm 3.5$ in red.

As can be seen in the Figure 10-2, both functions differ significantly from each other within $x \in [3.1, 4]$, since $t(x)$ is smaller than the critical value in this range. In all other regions it can be assumed that the difference between both solutions is caused by the measurement noise.

10.1.4 *Local Smoother*

Due to the problems described in the numerical studies in Chapter 9, it is sometimes advantageous to stabilize the solution and, for instance, to reduce the oscillations occurring at the bearings. For the Local Smoother (LS) this is done by introducing the regularisation term

$$w_{\text{reg}} \int_0^l \left(W(x) \frac{\mathrm{d}^\beta E^*(x)}{\mathrm{d}x^\beta} \right)^2 \mathrm{d}x \,, \tag{10-19}$$

whereby the areas in which the unknown function $E^*(x)$ is smoothed are specified by the weighting function $W(x)$ and β defines the type of smoothing, where with $\beta = 1$ the slope and $\beta = 2$ the curvature of $E^*(x)$ is reduced. The intensity of smoothing is regulated by w_{reg}. Before we embed this term into the Integrated Analysis, we write (10-19) in matrix notation, in which both functions $E^*(x)$ and $W(x)$ are represented by their Chebyshev coefficients $\mathbf{e}$ and $\mathbf{w}$. According to Section 5.1.2 and 7.3 the regularisation term in the Chebyshev basis reads

$$w_{\text{reg}} \int_{-1}^{1} \left(\boldsymbol{\phi} \boldsymbol{\mathcal{M}} \boldsymbol{\mathcal{L}} \, \mathbf{e} \right)^2 \mathrm{d}t \,. \tag{10-20}$$

The local smoothing of the unknown function $E^*(x)$ is done by adding (10-20) to (2-12) and minimizing the following target function

$$\Omega(\mathbf{e}) = \mathbf{v}^\mathsf{T} \mathbf{P} \, \mathbf{v} + w_{\text{reg}} \int_{-1}^{1} \left(\boldsymbol{\phi} \boldsymbol{\mathcal{M}} \boldsymbol{\mathcal{L}} \, \mathbf{e} \right)^2 \mathrm{d}t \rightarrow \min \,. \tag{10-21}$$

Analogous to Section 2.3, the following normal equation system results for the target function (10-21)

$$\left(\mathbf{N} + w_{\text{reg}} \mathbf{N}_{\text{reg}} \right) \mathbf{e} = \mathbf{n} \,, \tag{10-22}$$

with

$$\begin{aligned} \mathbf{N}_{\text{reg}} &= \boldsymbol{\mathcal{L}}^\mathsf{T} \boldsymbol{\mathcal{M}}^\mathsf{T} \int_{-1}^{1} \boldsymbol{\phi}^\mathsf{T} \boldsymbol{\phi} \, \mathrm{d}t \, \boldsymbol{\mathcal{M}} \boldsymbol{\mathcal{L}} \,, \\ &= \boldsymbol{\mathcal{L}}^\mathsf{T} \boldsymbol{\mathcal{M}}^\mathsf{T} \mathbf{N}_\phi \, \boldsymbol{\mathcal{M}} \boldsymbol{\mathcal{L}} \,, \end{aligned} \tag{10-23}$$

and since we have 3 elements the matrices in (10-23) are as follows

$$\boldsymbol{\mathcal{L}} = \begin{bmatrix} {}^1J^\beta \boldsymbol{\mathcal{L}}_{\text{x}}^\beta & \mathbf{0} & \mathbf{0} \\ \mathbf{0} & {}^2J^\beta \boldsymbol{\mathcal{L}}_{\text{x}}^\beta & \mathbf{0} \\ \mathbf{0} & \mathbf{0} & {}^3J^\beta \boldsymbol{\mathcal{L}}_{\text{x}}^\beta \end{bmatrix} \,, \tag{10-24}$$

$$\boldsymbol{\mathcal{M}} = \begin{bmatrix} \boldsymbol{\mathcal{M}}[{}^1\mathbf{w}] & \mathbf{0} & \mathbf{0} \\ \mathbf{0} & \boldsymbol{\mathcal{M}}[{}^2\mathbf{w}] & \mathbf{0} \\ \mathbf{0} & \mathbf{0} & \boldsymbol{\mathcal{M}}[{}^3\mathbf{w}] \end{bmatrix} \tag{10-25}$$

and

$$\mathbf{N}_\phi = \begin{bmatrix} {}^1\mathbf{N}_\phi & \mathbf{0} & \mathbf{0} \\ \mathbf{0} & {}^2\mathbf{N}_\phi & \mathbf{0} \\ \mathbf{0} & \mathbf{0} & {}^3\mathbf{N}_\phi \end{bmatrix} \,, \tag{10-26}$$

with ${}^{\zeta}\mathbf{N}_{\phi}$ being the same normal matrix as in (5-68). To reduce the oscillations at the bearings, the following contrived weighting function $W(x)$ has been used

$$W(x) = \exp\left(-50x^2\right) + \exp\left(-50(x-l)^2\right), \tag{10-27}$$

which is also depicted in Figure 10-3.

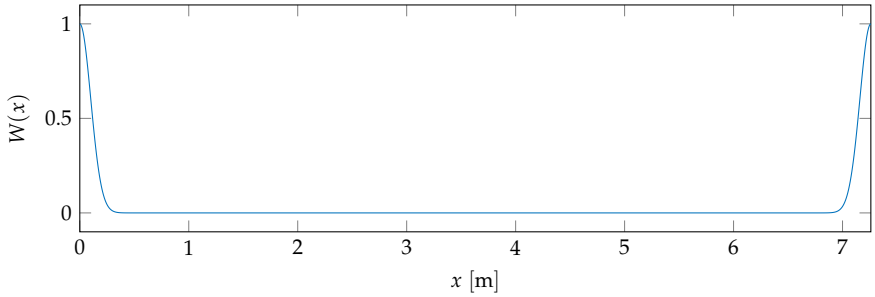

Figure 10-3: Weighting function $W(x)$ to reduce the oscillations at the bearings.

All weighting functions were chosen in such a way that they can be approximated by a few parameters in the Chebyshev basis and still fulfil their objective.

The weighting function (10-27) shown in Figure 10-3 is non-zero only in the vicinity of the bearings, which ensures that the unknown function $E^*(x)$ is only smoothed in these areas and nowhere else.

10.1.5 *Damage Sniffer*

Before we have a closer look at the Damage Sniffer (DS), let us first consider the following example depicted in Figure 10-4.

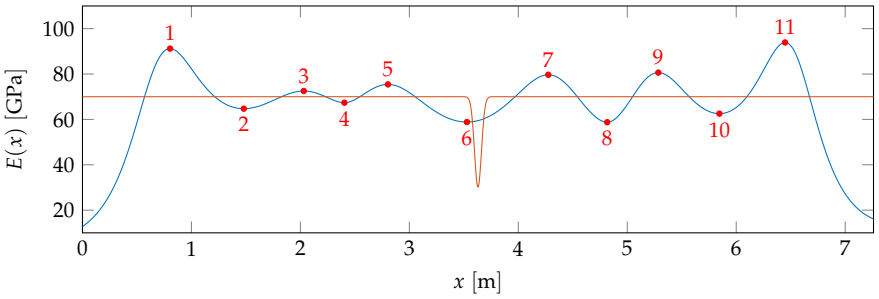

Figure 10-4: Derived $E(x)$ from the estimated $E^*(x)$ for polynomial degree $p_e = 6$ using the 30 displacement measurements of high precision listed in Table B-1 in blue. The true damage $E_D(x)$ given by (9-2) in red. The red dots are the extrema of $E(x)$.

The red curve in Figure 10-4 is the true damage (9-2) we want to determine, with a clear peak at $l/2$. For this damage we derived 30 equidistant displacement measurements of high precision, which are listed in Table B-1 and based on these measurements we estimated $E^*(x)$. The blue curve shows the solution for $E(x)$ derived from the estimation $E^*(x)$ and it is easy to see that the blue curve is by far not similar to the red curve. The true damage (9-2) could only be derived from the measurements insufficiently. Out of a total of 11 extrema (red dots) of the blue curve, the local minimum 6 corresponds most closely to the true position of the damage. Unfortunately, this is only recognizable in direct comparison with the true damage, which is not possible for real applications. However, based on numerical studies and the conclusions from Chapter 9, it can be assumed that the local minimum 6 is mainly resulting from the damage and that all others are only due to the measurement noise, the indeterminacy at the bearings and the characteristics of a polynomial approximation itself.

Polynomial approximations tend to oscillate.

With aid of the DS we want to analyse the extrema of the solution $E^*(x)$ in order to decide whether they might be caused by damage or not. Principally, the DS is based on the Local Smoother (LS), with the main difference that the entire solution is smoothed by using the weighting function $W_{GS}(x) = 1$ and for different intensities $w_{GS} \in [0,1]$. Consequently, there is not only one smoothed solution for $E^*(x)$ but several. For our previous example from Figure 10-4, we will now compute several different smoothed curves for $E^*(x)$, choosing $\beta = 2$ and 29 logarithmically spaced values between 0 and 1 for w_{GS}, where 0 corresponds to none and 1 to maximal smoothing. The smoothed solutions for 29 different values w_{GS} are depicted in Figure 10-5.

For the implementation we use 10^{-15} instead of 0.

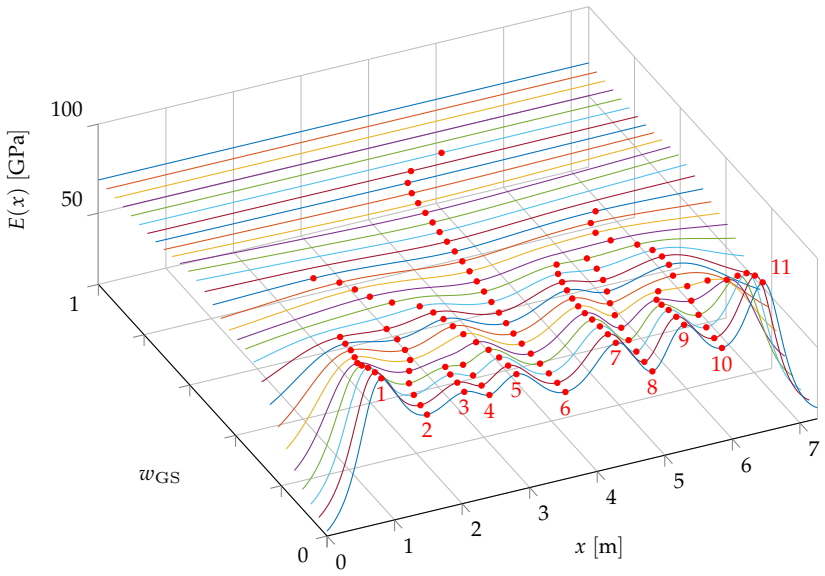

Figure 10-5: 29 smoothed solutions for $E(x)$ for different intensities w_{GS} using the 30 displacement measurements of high precision listed in Table B-1. The red dots are the extrema of $E(x)$.

The blue curve in Figure 10-5 for $w_{GS} = 1$ is the solution with maximum smoothing, which is only a straight line. Decreasing w_{GS} changes the solution slowly and an extremum arises which in principle corresponds to the local minimum 6. With w_{GS} getting smaller and smaller, more and more extrema are appearing up to 11 for the unsmoothed curve from Figure 10-4. The blue curve in Figure 10-5 for $w_{GS} = 0$ is the exactly the same as in Figure 10-4. In a direct comparison of all extrema, the local minimum 6 is the most dominant of all. To make this clearer, we first make a surface out of all the curves in Figure 10-5 , which is shown in Figure 10-6.

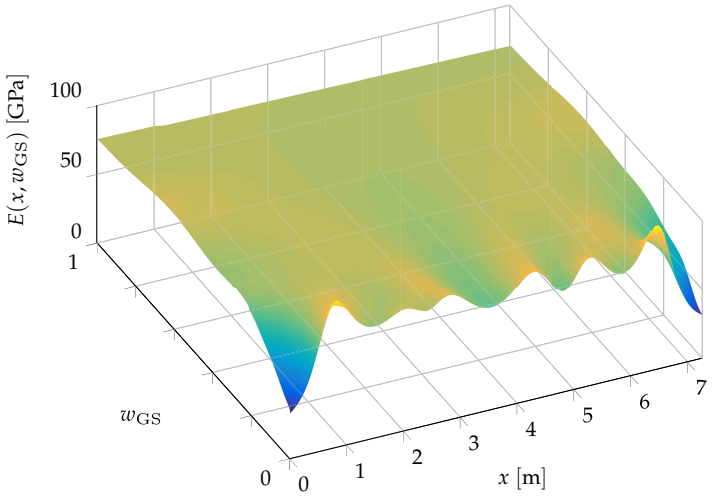

Figure 10-6: Resulting surface $E_{surf}(x, w_{GS})$ from the smoothed solutions $E(x)$ illustrated in Figure 10-5.

To distinguish between maxima and minima we reduce the mean of the straight line for $w_{GS} = 1$ in Figure 10-5 from the surface $E_{surf}(x, w_{GS})$. The resulting reduced surface is illustrated as a filled contour plot in Figure 10-7.

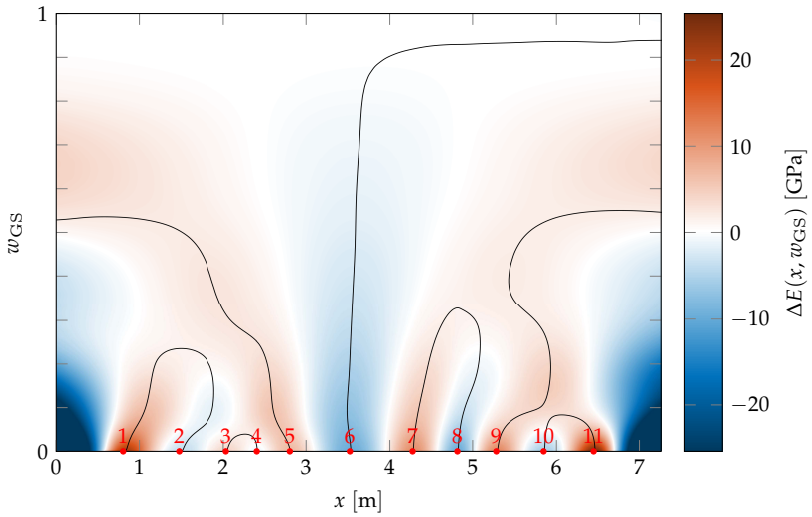

Figure 10-7: Resulting reduced surface $\Delta E_{surf}(x, w_{GS})$. The black lines are the roots of $\frac{\partial \Delta E_{surf}(x, w_{GS})}{\partial x}$ and hence representing the extrema from Figure 10-4 (red dots).

The reduced surface $\Delta E_{surf}(x, w_{GS})$ in Figure 10-7 clearly shows how dominant the local minimum 6 actually is. To remove this minimum from the solution, it must be smoothed in such a way that only a straight line remains. In contrast to the two extrema 3 and 4, which are only mutually dependent with small amplitude and already disappear when the solution is smoothed only slightly. It can be assumed that these two extrema are caused only by measurement noise and do not exist in the unknown solution $E(x)$. Therefore, the unknown solution $E(x)$ can be smoothed locally at the position of the two extrema 3 and 4 and the whole procedure can be repeated. The weighting function $W_{LS}(x)$ for the Local Smoother and the resulting solution for $E(x)$ is depicted in Figure 10-8.

We call the connection of the two extrema a loop.

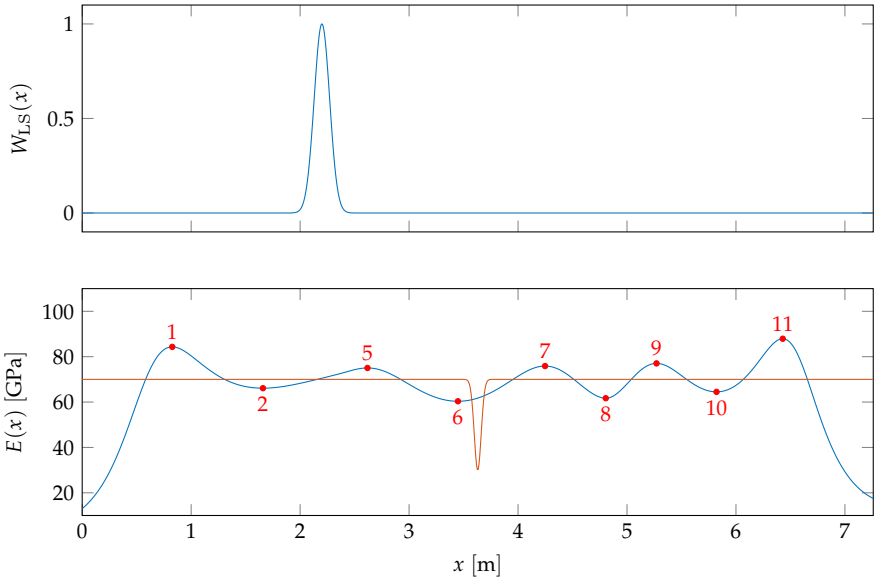

Figure 10-8: Weighting function $W_{LS}(x)$ for the Local Smoother to remove the extrema 3 and 4 (top). Locally smoothed solution $E(x)$ for polynomial degree $p_e = 6$ using the 30 displacement measurements of high precision listed in Table B-1 in blue (bottom). The true damage $E_D(x)$ given by (9-2) in red. The red dots are the extrema of $E(x)$.

As can easily be seen in the Figure 10-8 (bottom), the two extrema 3 and 4 are removed from the solution by the Local Smoother using the weighting function depicted in Figure 10-8 (top). The position of the remaining extrema has changed slightly, but the locally smoothed solution $E(x)$ is basically the same as the unsmoothed one in Figure 10-4. Based on this locally smoothed solution for $E(x)$, a reduced surface can again be derived according to the procedure described above, which is shown in Figure 10-9.

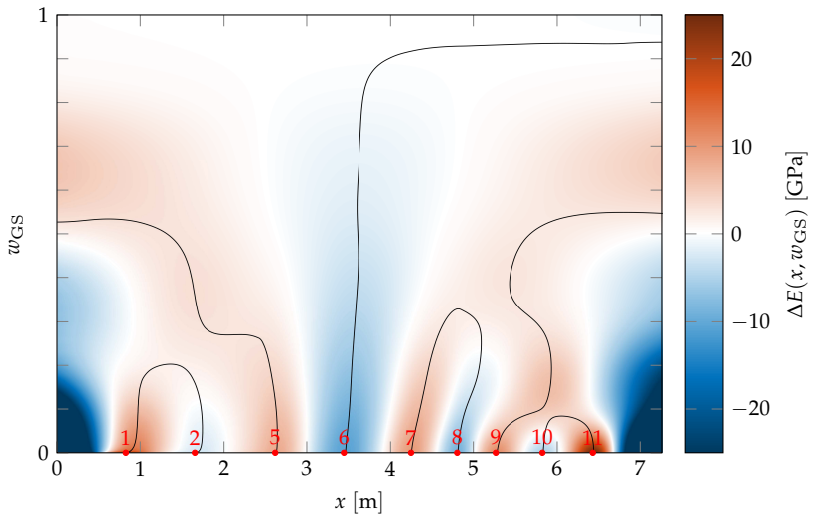

Figure 10-9: Resulting reduced surface $\Delta E_{surf}(x, w_{GS})$. The black lines are the roots of $\frac{\partial \Delta E_{surf}(x, w_{GS})}{\partial x}$ and hence representing the extrema from Figure 10-8 (bottom) (red dots).

The reduced surface $\Delta E_{surf}(x, w_{GS})$ in Figure 10-9 with local smoothing is also just slightly different from that shown in Figure 10-7 without local smoothing. In the following, the solution can be further smoothed locally at extrema that are most likely caused only by measurement noise or by the characteristics of a polynomial approximation itself and not by damage. In this case this would be for example extremum 10. However, the polynomial degree must be carefully increased with increasing local smoothing, otherwise the solution will be smoothed too much and only a straight line remains. It is also not advisable to use a high polynomial degree right from the start, since the solution will only follow the measurement noise and the numerous extrema can usually

no longer be distinguished. The whole iterative process of local smoothing and increasing the polynomial degree is extremely sensitive and must be done carefully. In this example, the position of the damage is already clearly visible in the first step depicted in Figure 10-7, but unfortunately that is not always the case, especially not for small damages. For this reason, the described iterative procedure with local smoothing and increase of the polynomial degree is proposed, whereby the position of damages can be localized more reliably.

This is an essential aspect, and I assume that the reliability of the damage localisation can be increased significantly by selecting further suitable features.

However, there remains one point to be clarified as to how the dominance of an extremum can be expressed. Based on a large number of numerical examples, it has been observed that the dominance can be adequately described by combining the following three features

- The arc length of the roots of $\frac{\partial \Delta E_{\text{surf}}(x, w_{\text{GS}})}{\partial x}$ (the black lines in Figure 10-7).
- The relative amplitude of the extrema for $w_{\text{GS}} = 0$.
- The largest value w_{GS} for which an extremum appears.

The described procedure is implemented in the Damage Sniffer as shown in Programme 10-2.

As a result of the DS, we obtain the extremum with the largest dominance, from which we assume that its position x_{DS_k} is the most likely location for possible damage. For the presented example above, the resulting weighting function for local smoothing and the solution for $E(x)$ from the last iteration step of the DS is depicted Figure 10-10.

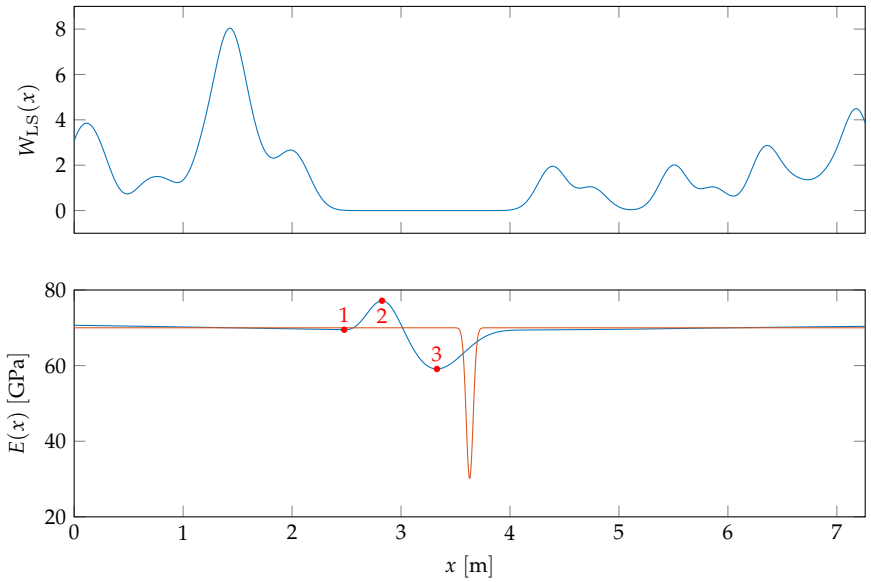

Figure 10-10: Resulting weighting function $W_{\text{LS}}(x)$ for local smoothing in the last iteration step of the DS (top). Final locally smoothed solution $E(x)$ for polynomial degree $p_{\text{e}} = 15$ using the 30 displacement measurements of high precision listed in Table B-1 in blue (bottom). The true damage $E_{\text{D}}(x)$ given by (9-2) in red. The red dots are the extrema of $E(x)$.

As can be seen from the weighting function $W_{\text{LS}}(x)$ in the Figure 10-10 (top), the solution $E(x)$ was not smoothed within the range between $x \in [2.5, 4]$, but everywhere else. Hence, the solution $E(x)$ in Figure 10-10 (bottom) is very smooth and has only 3 extrema. According to the result of the DS, the extrema 3 at $x_{\text{DS}_k} = 3.3296\,\text{m}$ is by far the most dominant one with $D_k \gg D_j \quad \forall j \neq k$ and corresponds to extremum 6 from Figure 10-4. In direct comparison, the result of the DS may be disappointing and the extremum 3 is even further away from the actual damage than extremum 6 before. But now we know that if there is any damage, it is probably near extremum 3, which we did

This is a very important conclusion that we gain from the DS.

not know before. Furthermore, we should be aware that the damage in this example is very large and the DS is also designed for much smaller damage, which can no longer be localized so easily. Therefore, the DS only provides an approximate position at which any damage may be present. This position then serves as the starting point for the Damage Modeller (DM), which will be presented in the next section.

Programme 10-2: Pseudo code for the Damage Sniffer (DS).

$p_{e_{\max}} = 10$ ▷ Maximum polynomial degree for $E^*(x)$
$p_e = 6$ ▷ Starting polynomial degree for $E^*(x)$
$n_{ex_{\min}} = 4$ ▷ Minimum number of extrema
$n_{GS} = 100$ ▷ Number of different intensities w_{GS_i} for global smoothing
$W_{LS}(x) \leftarrow$ from (10-27) ▷ Weighting function for local smoothing
$W_{GS}(x) = 1$ ▷ Weighting function for global smoothing
$w_{LS} = 10^{-5}$ ▷ Intensity of local smoothing
$w_{GS_i} \leftarrow n_{reg}$ logarithmically spaced values $\in [0, 1]$
$\mathbf{N}_{GS} \leftarrow$ from (10-23) with $W_{GS}(x)$ and $\beta = 2$
$\mathbf{N}_{slope} \leftarrow$ from (10-23) with $W_{LS}(x)$ and $\beta = 1$
$n_{ex} = \infty$ ▷ Initialization for the loop
while $p_e \leq p_{e_{\max}}$ and $n_{ex} \geq n_{ex_{\min}}$ **do**
  $\mathbf{N}_{LS} \leftarrow$ from (10-23) with $W_{LS}(x)$ and $\beta = 2$
  Solve $\left(\mathbf{N} + w_{LS}\mathbf{N}_{LS} + 10^{-9}\mathbf{N}_{slope}\right)\mathbf{e} = \mathbf{n}$
  Determine the number of extrema n_{ex}
  if $n_{ex} < n_{ex_{\min}}$ **then**
    $p_e = p_e + 1$
  else
    for $i = 1$ **to** n_{GS} **do**
      Solve $\left(\mathbf{N} + w_{GS_i}\mathbf{N}_{GS} + w_{LS}\mathbf{N}_{LS} + 10^{-9}\mathbf{N}_{slope}\right)\mathbf{e}_i = \mathbf{n}$
    end for
    Compute $E_{surf}(x, w_{reg})$ from $\mathbf{e}_i$
    for $j = 1$ **to** n_{ex} **do**
      $D_{1_j} \leftarrow$ calculate the arc length of the root for extremum j
      $D_{2_j} \leftarrow$ determine the relative amplitude of extremum j
      $D_{3_j} \leftarrow$ determine largest w_{GS_i} for which extremum j appears
      $D_j = D_{1_j} \cdot D_{2_j} \cdot D_{3_j}$ ▷ Dominance of extremum j
      if Extremum j is a loop **then**
        $D_j = 1/2 D_j$
      end if
    end for
    $x_k \leftarrow$ position of extremum with smallest dominance D_k.
    $W_{LS}(x) = W_{LS}(x) + \exp\left(-50(x - x_k)^2\right)$
  end if
end while
x_{DS_j} and D_j $\forall j \leftarrow$ position and dominance of all remaining extrema.
$x_{DS_k} \leftarrow$ position of extremum with largest dominance D_k.

10.1.6 *Damage Modeller*

The solution $E(x)$ of the Damage Sniffer in Figure 10-10 (bottom) approximates the true damage $E_D(x)$ only insufficiently, but it provides us an approximate position where we can look for damage. Therefore, the Damage Modeller (DM) uses this position to reconstruct the possible damage in its near

surroundings. Like the Damage Sniffer, the Damage Modeller is also based on the Local Smoother, but with the following contrived window function as weighting function

$$W_{\mathrm{DM}}(x) = \frac{1}{2}\Big(2 - \tanh\big(10(x - x_{\mathrm{DS}} + 0.5)\big) + \tanh\big(10(x - x_{\mathrm{DS}} - 0.5)\big)\Big). \quad (10\text{-}28)$$

The most dominant extremum cannot be clearly identified.

In the case that the most dominant extrema have similar values for the dominance D_j, it can happen that the wrong extremum is identified as a possible position x_{DS_k} of a damage. Therefore, the DM uses the position x_{DS_j} of all remaining extrema and selects the one that finally provides the smallest value for the target function Ω. The general workflow of the Damage Modeller is shown in Programme 10-3.

Programme 10-3: Pseudo code for the Damage Modeller (DM).

1: x_{DS_j} and $n_{\mathrm{ex}} \leftarrow$ from DS according to Section 10.1.5.
2: **for** $j = 1$ **to** n_{ex} **do**
3: $\quad x_{\mathrm{old}} = \infty$ ▷ Initialization for the loop
4: $\quad$ **while** $|x_{\mathrm{DS}_j} - x_{\mathrm{old}}| > 1\,\mathrm{cm}$ **do**
5: $\quad\quad W_{\mathrm{DM}}(x) \leftarrow$ from (10-28) with x_{DS_j}
6: $\quad\quad E(x) \leftarrow$ from LS with $W_{\mathrm{DM}}(x)$ and $p_{\mathrm{e}} = 200$
7: $\quad\quad x_{\mathrm{old}} = x_{\mathrm{DS}_j}$
8: $\quad\quad x_{\mathrm{DS}_j} \leftarrow$ new position of the extrema
9: $\quad$ **end while**
10: $\quad$ calculate Ω_j
11: **end for**
12: $x_{\mathrm{DM}} \leftarrow$ position of extremum with smallest value Ω_k

For the example from the previous Section 10.1.5, with the initial position for a possible damage $x_{\mathrm{DS}_k} = 3.3296\,\mathrm{m}$ from the DS, we obtain the following solution from the DM depicted in Figure 10-11.

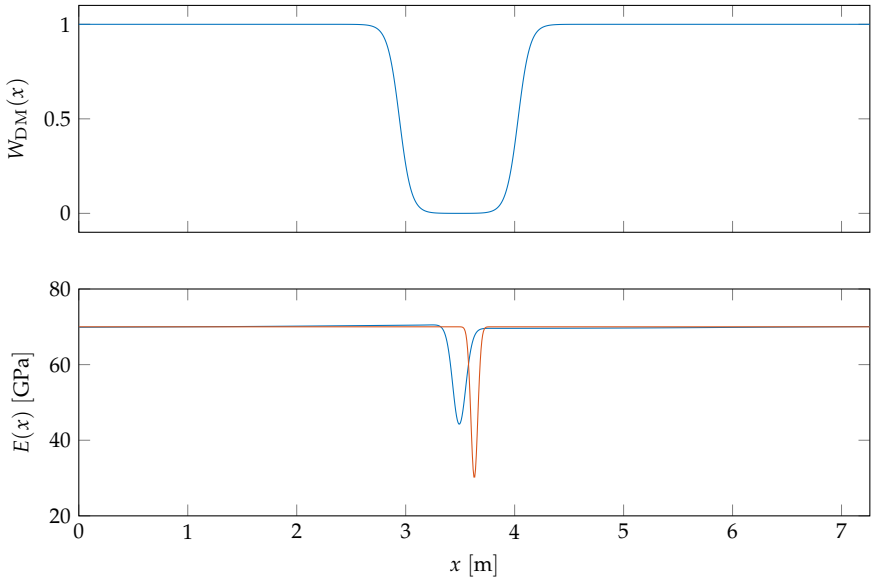

Figure 10-11: Resulting weighting function $W_{\mathrm{DM}}(x)$ for local smoothing in the last iteration step of the Damage Modeller (top). Final locally smoothed solution $E(x)$ for polynomial degree $p_{\mathrm{e}} = 200$ using the 30 displacement measurements of high precision listed in Table B-1 in blue (bottom). The true damage $E_{\mathrm{D}}(x)$ given by (9-2) in red.

The weighting function $W_{\mathrm{DM}}(x)$ in Figure 10-11 (top) is zero only for a small area in the middle of the beam and enforces a smoothed solution for $E(x)$ everywhere else, as the blue curve in Figure 10-11 (bottom) shows. The final

result for $E(x)$ of the DM is mainly revealing the true damage $E_D(x)$ (red curve) except for a small offset of $\approx 14\,\text{cm}$ as the position for a possible damage results in $x_{DM} = 3.49\,\text{m}$. Considering the already discussed problem of ambiguities from Section 9.3.2 and the large impact of measurement noise, the true damage $E_D(x)$ could be reconstructed very well. Surely many assumptions were made for the solution and this reflects only a best case scenario. In general, the Damage Sniffer and Damage Modeller can provide more detailed information on possible damage, especially for small damages, which can no longer be determined so easily. The extent to which damage can be detected and located will be discussed in the following sections.

10.2 NUMERICAL STUDIES

In order to gain a better understanding of how damage can be detected and localised, we will conduct some numerical studies. Like in Chapter 9, the presented numerical studies are based on the specification of the four-point bending test set-up and beam specimen listed in Table 9-1.

Similar results were also partially published in (BECKER *et al.* 2015), but based on a FEM as a functional model for the IA.

10.2.1 *Damage detection*

First we want to investigate how often a damage according to Equation (9-1) can be detected with the Global Identifier (GI) in dependence of its position x_D and magnitude h_D. Due to the described ambiguities in Section 9.3.2, we keep the width of the damage constant for all studies with $w_D = 500$. Again we use 30 equidistant measurements of high precision and perform a MCS with 500 simulations. Each time we estimate the unknown solution $E(x)$ using the Parameter Sifter with $p_e = 3$. The result of the damage detection for displacement measurements is shown in Figure 10-12.

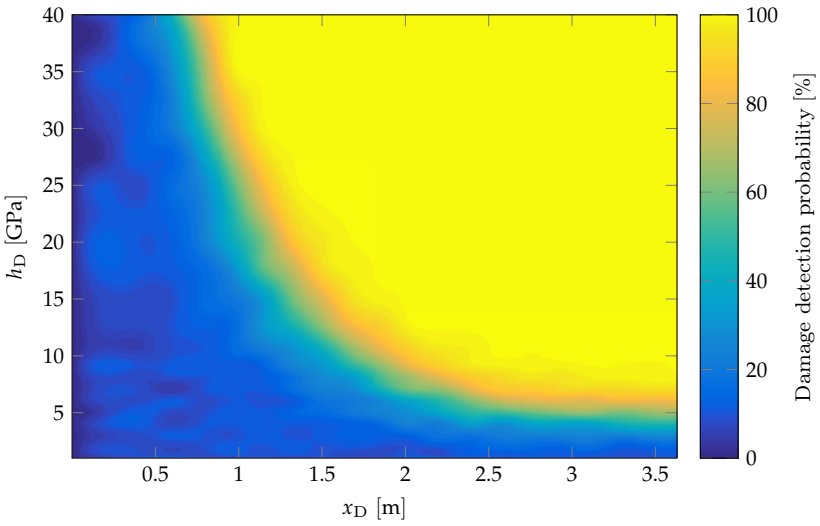

Figure 10-12: The probability that a damage at position x_D and magnitude h_D can be detected by the GI using 30 equidistant displacement measurements of high precision. Due to the symmetry only the left half of the beam is shown.

It can be seen from Figure 10-12 that for displacement measurements a damage at a position $x_D = 2\,\text{m}$ and with a magnitude of $h_D = 10\,\text{GPa}$ can be successfully detected with a probability of $\approx 80\,\%$. If the damage is only slightly larger it can in general always be detected within $2\,\text{m} \leq x_D \leq l - 2.0\,\text{m}$. In contrast, even an extremely large damage with a magnitude of $h_D = 40\,\text{GPa}$

can not be detected close to the bearing at $x_D = 0.25\,\text{m}$. The result is very similar for the inclination measurements, as can be seen in Figure 10-13.

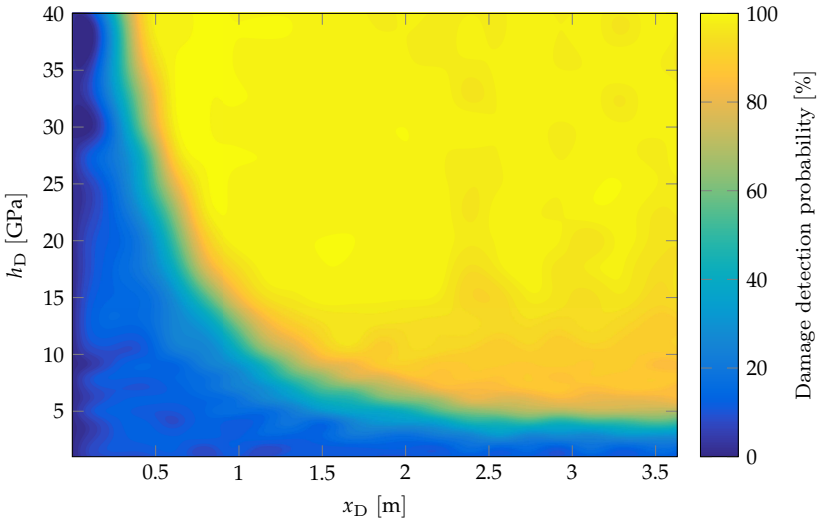

Figure 10-13: The probability that a damage at position x_D and magnitude h_D can be detected by the GI using 30 equidistant inclination measurements of high precision. Due to the symmetry only the left half of the beam is shown.

On the one hand, it is noticeable in Figure 10-13 that even very large damages with a magnitude of $h_D = 40\,\text{GPa}$ can be detected with a probability of $\approx 50\,\%$ close to the bearings with $x_D = 0.25\,\text{m}$. On the other hand, it also turns out that even this large damage can only be detected with a probability $\approx 90\,\%$ in the middle of the beam within $2\,\text{m} \leq x_D \leq l - 2\,\text{m}$. In contrast to the result of the displacements in Figure 10-12, where damage with a magnitude of $h_D > 15\,\text{GPa}$ and within this region can be detected up to 100 %.

As we already discussed, damage has a direct and only local impact on the strain measurements, see Figure 9-20 (right). Since the maximum damage for this study corresponds to a cut of $\approx 20\,\text{cm}$ width and we only consider 30 equidistant measurements, so one measurement every $\approx 25\,\text{cm}$, the damage usually affects only one single measurement. This in turn means that the impact of the damage on the solution $E(x)$ of the PS is very small and can therefore hardly be detected with the GI, as can be seen in Figure 10-14.

In adjustment calculation this observation would usually be considered as an outlier.

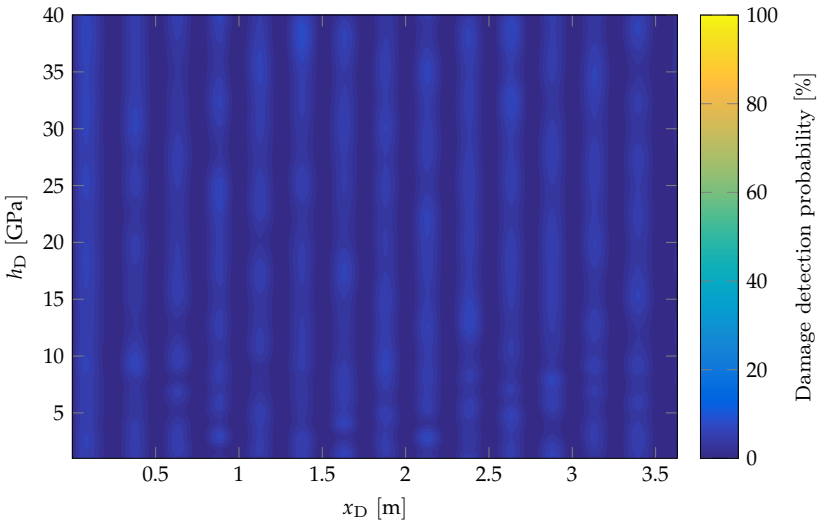

Figure 10-14: The probability that a damage at position x_D and magnitude h_D can be detected by the GI using 30 equidistant strain measurements of high precision. Due to the symmetry only the left half of the beam is shown.

The dark blue vertical stripes in Figure 10-14 correspond to the sensor positions and indicate that damage in their vicinity cannot be detected with this approach. The probability that damage can be detected close to the sensor positions is equal to zero. In contrast, damage located between two sensors can only be detected with a probability of $\approx 5\,\%$, which is indicated by the light blue stripes and only corresponds to the chosen error level α. This is still negligibly small, but does not depend on whether the damage is near the bearings or in the middle of the beam, as long as it is only between two sensors.

In this case, two measurements are slightly affected.

In direct comparison with the results for displacement and inclination measurements, damage detection using the GI for sparse strain measurements is quite pointless.

10.2.2 *Damage localisation*

As we now have an understanding of the extent to which damage can be detected with MeMoS depending on its position and magnitude, we want to analyse in more detail to which extent damage can also be localised. In Section 10.1 we developed two tools that are suitable for this purpose, namely

1. the Local Indicator (LI) and
2. the Damage Sniffer (DS) with the Damage Modeller (DM).

While the numerical studies for damage localisation using the LI can be done in the same extent as for damage detection, this is currently hardly feasible for the DS and DM as the computational time would take several months. Therefore, the potential of the DS and DM for localising damage is not further considered here and is only demonstrated in the experimental studies.

The source code of DS and DM has not yet been optimised and it is expected that the performance can be significantly improved.

The numerical studies for damage localisation are performed in the same way as described in Section 10.2.1, while this time the unknown solution $E(x)$ is estimated using the IA with $p_e = 4$. These changes are necessary because otherwise the spatial resolution would be too low for a proper localisation. The result of the damage localisation for displacement measurements using the LI is shown in Figure 10-15 and is not very promising.

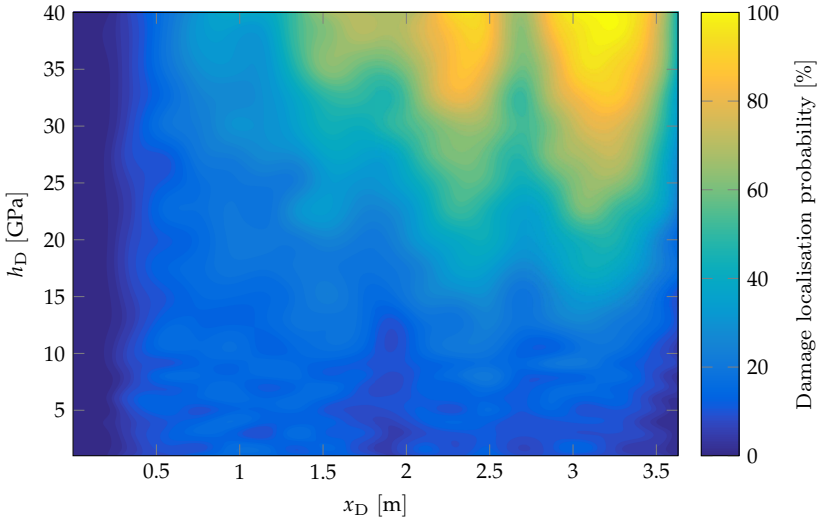

Figure 10-15: The probability that a damage at position x_D and magnitude h_D can be localised within $\pm 5\,\%$ of the beam length by the LI using 30 equidistant displacement measurements of high precision. Due to the symmetry only the left half of the beam is shown.

As Figure 10-15 shows and also was to be expected, the damage must be very large and must occur between the bearings in order to be localised reliably. A damage at a position $x_D = 3\,m$ and with a magnitude of $h_D = 20\,GPa$ can only be localised with a probability of $\approx 40\,\%$ and a huge damage at the same location with a magnitude of $h_D = 40\,GPa$ can always be localised. However, it is also noticeable that the same huge damage at $x_D = 2.6\,m$ or $x_D = 3.6\,m$ can only be localised with a probability of $\approx 50\,\%$. The problem in this case arises from the already discussed characteristics of the solution $E(x)$ and its standard deviation $s_E(x)$, which results mainly from the measurement noise, the selected polynomial degree and the introduced constraints between two elements. Therefore, it occurs that the LI provides two possible solutions for certain damage positions. To clarify this issue, the results of all 500 MCS for a damage at $x_D = 2.6\,m$ and a magnitude of $h_D = 40\,GPa$ are visualised as a histogram in Figure 10-16.

An influence of the sensor positions in relation to the damage position could not be detected so far.

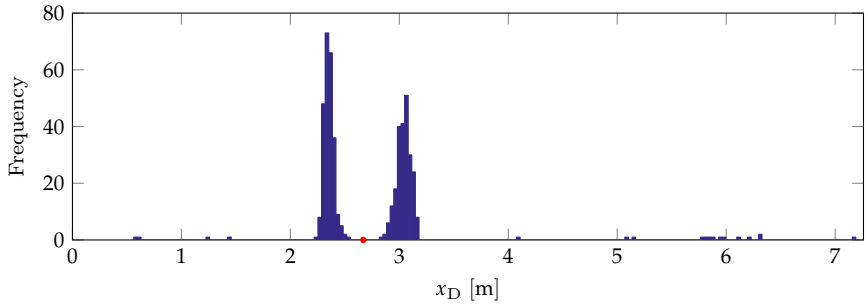

Figure 10-16: Histogram of the 500 MCS for localising a damage at $x_D = 2.6\,m$ and magnitude $h_D = 40\,GPa$ using the LI. The red dot indicates the true position of the damage.

As Figure 10-16 shows, it is not possible to locate the huge damage at $x_D = 2.6\,m$ using the LI, instead there are two solutions directly next to the true position, where the distance mainly depends on the chosen polynomial degree. For the same huge damage at $x_D = 2.3\,m$, however, the result of the MCS is quite different, as Figure 10-17 illustrates.

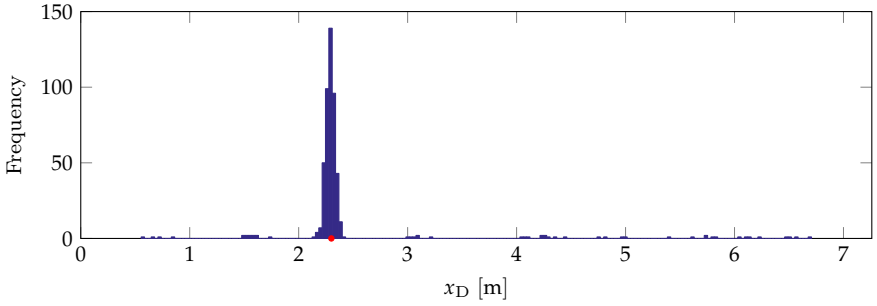

Figure 10-17: Histogram of the 500 MCS for localising a damage at $x_D = 2.3\,m$ and magnitude $h_D = 40\,GPa$ using the LI. The red dot indicates the true position of the damage.

The histogram in Figure 10-17 shows that in this case there is only one solution and the huge damage at $x_D = 2.3\,m$ can be clearly localized using the LI. The described problem also occurs for inclination measurements, however, the distance between two possible solutions is significantly shorter and consequently the damage can still be reliably localised, as illustrated by Figure 10-18.

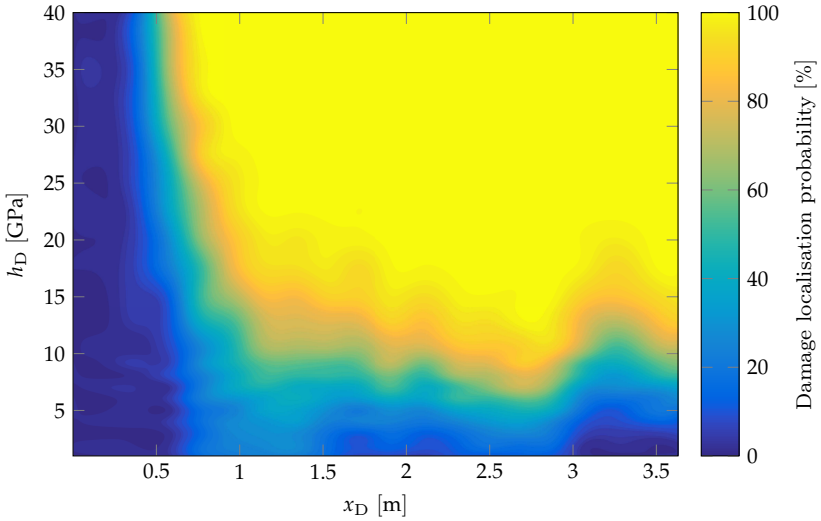

Figure 10-18: The probability that a damage at position x_D and magnitude h_D can be localised within ±5 % of the beam length by the LI using 30 equidistant inclination measurements of high precision. Due to the symmetry only the left half of the beam is shown.

In general, Figure 10-18 reveals that the localisation of damage using the LI for inclination measurements is very reliable and even smaller damages near the bearings at $x_D = 1\,\text{m}$ with a magnitude of $h_D = 20\,\text{GPa}$ can already be localised with a probability of ≈ 85 %. The result of the damage localisation for strains corresponds roughly to that of the damage detection, with the major difference that even small damages in the vicinity of sensors can always be localized and damages between two sensors basically never, which is depicted in Figure 10-19.

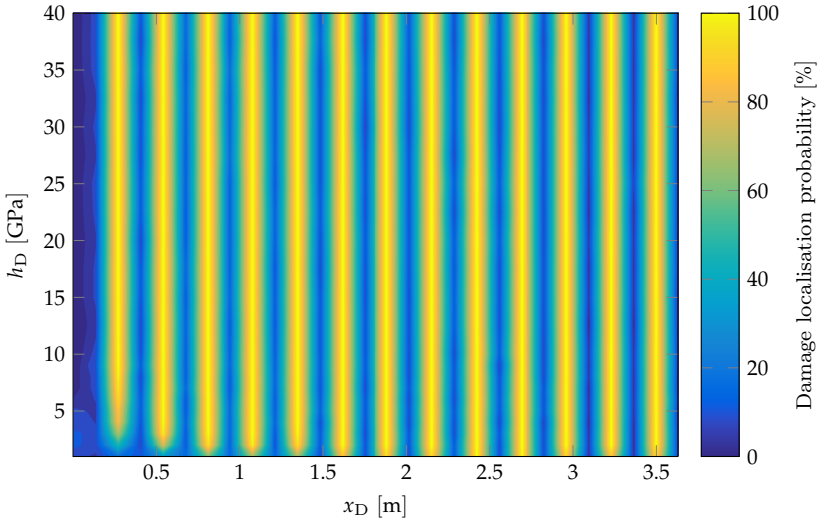

Figure 10-19: The probability that a damage at position x_D and magnitude h_D can be localised within ±5 % of the beam length by the LI using 30 equidistant strain measurements of high precision. Due to the symmetry only the left half of the beam is shown.

In addition, Figure 10-19 shows that even minor damages close to the bearings can be located reliably, as long as it is only close to a sensor. In principle, these results for damage localisation using strain measurements only reflect the conclusions of Chapter 9 and demonstrate again that discrete strain measurements are not suitable for damage analysis using MeMoS.

The results of these numerical studies only provide an insight into the possibilities of a damage analysis with MeMoS. For real-world problems, there are usually some additional issues that can have a negative impact on the damage analysis, which will be explained in more detail in the next section.

10.3 EXPERIMENTAL STUDIES

For the experimental studies we use the data of a four-point bending test, which was carried out by Cheng-Chieh Wu as part of his doctorate at the Institute of Geodesy and Geoinformation Science at TU Berlin, shown in Figure 10-20.

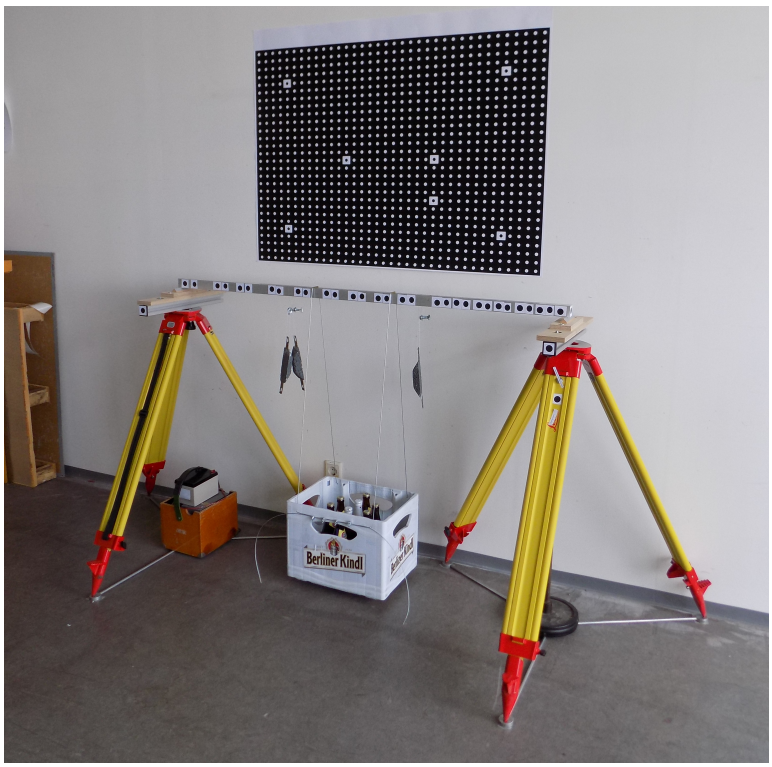

Figure 10-20: A four/six-point bending test apparatus for an aluminium beam specimen (Wu 2020, Figure 5.30). The photogrammetric calibration field on the wall with more than 1000 white markers was used to calibrate the camera and to determine the position of the black markers on the beam. More markers have been placed on the right side of the beam where the damage is located than on the other side. Due to limited resources at the institute only a rather less professional setup could be realised.

The aim of the bending test was to detect and localise damage to an aluminium beam using MeMoS based on FEM. For this purpose, the displacements of 31 measuring points (black markers) along the beam for different loads and damage levels was recorded by photogrammetry. A detailed description of the specimen and measuring setup can be found in (Wu 2020, Chapter 5.3) and is summarised in Table 10-1.

beam length l	1.48 m	loading position a	0.59 m
beam width w	3.5 cm	beam height h	3.5 cm

Table 10-1: Specification of the four-point bending test setup and beam specimen for the experimental studies.

Unfortunately, the results of the load test were not very promising for the implemented approach of MeMoS according to (Wu 2020, Chapter 5). Only in cases where the damage is very large it could be reliably detected and localized, see (Wu 2020, Table 5.5). In addition to the setup itself, the load test was not carried out under optimal conditions, as unfortunately only an office with windows facing north was available at that time. We noticed that changes in light conditions during the day had a considerable influence on the detection of the markers on the beam. At this point, we assumed that this influence on the detection of the markers was more random and could be interpreted as an increased measurement noise. In the end a standard deviation for the displacements of $\sigma_u = 9\,\mu\text{m}$ resulted, see (Wu 2020, Equation 5.35), which is

not optimal for a damage analysis with this setup and which can only lead to such results as presented in (Wu 2020, Table 5.5).

But a review of the derived displacements in 2019 revealed inconsistencies in the position of the markers used in (Wu 2020, Chapter 5.3). Furthermore, it became apparent that some of the markers had deviations that were rather systematic than random. In 2017, the marker positions were determined by fitting an ellipse in the greyscale image and according to (Ouellet and Hébert 2009) this intensity-based approach is sensitive to non-uniform illumination, which we also observed as already mentioned. Ouellet and Hébert (2009) also points out that gradient-based approaches are less sensitive to non-uniform illumination. Since the raw data is still available, this encouraged us to re-evaluate the more than 12 000 images from the bending test. This time the ellipses were estimated by a gradient-based approach and the determination of the position of the markers on the beam was corrected in the software.

10.3.1 *Remaining problems*

However, one important aspect could not be finally solved during the re-evaluation of the raw data. This concerns the transfer of the experimental setup and the markers into a common reference framework. On the one hand, the beam has its own 2D coordinate system, which is defined by the two bearings. The markers, on the other hand, refer to the 3D coordinate system from the bundle block adjustment, which is defined by the white markers of the calibration field, see Figure 10-20. The problem is now, that the functional model of the Integrated Analysis (IA) refers to the coordinate system of the beam and the observations refer to the coordinate system of the bundle block adjustment. Nevertheless, it is still possible to reduce the 3D coordinates of the markers into the 2D coordinate system of the beam, however, a small offset and scaling factor remains that cannot be determined any more. For the determination of the displacements this problem has hardly any influence, since these are only relative quantities. In contrast to this, the $x-$coordinates of the markers x_{disp_i} in the coordinate system of the beam are used as absolute quantities in the functional model of the adjustment, see Equation (8-7). More detailed analyses have shown that this systematic error is depending on the position of the marker along the beam, with largest deviations in the middle of $\approx 0.1\,\text{mm}$. Although this error is quite small, it still has a significant influence on the estimation of $E(x)$.

For further information about bundle block adjustment, see (Luhmann *et al.* 2011, Chapter 4.3)

In addition to the systematically falsified sensor positions x_{disp_i}, further assumptions were made which do not correspond to reality, see Section 8.1.2. These assumptions are:

- The geometry of the beam is fixed and hence, the width w, height h and length l are error free values.
- The force F is an error free value.
- The positions the forces are applied to the beam are error free values, hence a is a fixed value.
- No movements at the bearings.

To consider the uncertainties of these variables when estimating $E(x)$, the geometry of the beam as the force F and its position a can be introduced as observations in the functional model of the IA. Since this model is derived from the Euler-Bernoulli beam equation (7-1), uncertainties in the geometry of the beam have the effect of an additional scaling factor in the estimation of $E(x)$. Consequently, the functional model of the IA becomes a bit more complex without obtaining a better solution for $E(x)$, which is more suitable for a structural analysis via MeMoS. Therefore, we still consider the width w, height h and length l of the beam as error free values.

For uncertainties in the force F and its position a, the situation is a bit different. Theoretically it would make sense to introduce these quantities as observations, but this would lead to a very complex non-linear functional model for the IA. In this case not only all entries in $\boldsymbol{\mathcal{M}}[\mathbf{m}]$ of Equation (7-11) would be observations but also the coordinates of the nodes in Table 7-1. Since the Chebyshev coefficients of both functions $M(x)$ and $E(x)$ are directly depending on these nodes, the position a cannot be estimated simultaneously with the coefficients for $M(x)$ and $E(x)$. This results in a highly non-linear adjustment problem, which is not only very computational intensive, but may not even converge. In addition, the systematically falsified sensor positions x_{disp_i} have a similar influence on the determination of $E(x)$ as the uncertainties in the force F and its position a. Therefore, we still consider the force F and its position a as error free values and prefer a different approach, which will be described in the following section.

What remains is the assumption that the bearings will not move. However, it has already been stated in (Wu 2020, Chapter 5.3) that this assumption does not hold true for this experiment and that the bearings subsided differently for each of the 31 load test. Nevertheless, this is not an issue since the different subsidence of the bearings can easily be estimated within the IA. As in (Wu 2020, Equation 5.28), only the right hand side of the two boundary conditions (7-20) have to be introduced in the functional model as additional unknown parameters. Therefore, the constraints for the boundary condition (7-23) will be rewritten as follows

$$\mathbf{C}_{\mathrm{BC}}\,\mathbf{u} = \mathbf{u}_{\mathrm{BC}}\,, \tag{10-29}$$

with the two additional unknowns $\mathbf{u}_{\mathrm{BC}}$ representing the subsidence of the bearings. Introducing (10-29) and (7-28) into (7-29) yields

$$\begin{bmatrix} \boldsymbol{\mathcal{L}} & \mathbf{C}_{\mathrm{BC}}^{\mathsf{T}} & \mathbf{C}_{\mathrm{conti}}^{\mathsf{T}} \\ \mathbf{C}_{\mathrm{BC}} & \mathbf{0} & \mathbf{0} \\ \mathbf{C}_{\mathrm{conti}} & \mathbf{0} & \mathbf{0} \end{bmatrix} \begin{bmatrix} \mathbf{u} \\ \boldsymbol{\lambda}_{\mathrm{BC}} \\ \boldsymbol{\lambda}_{\mathrm{conti}} \end{bmatrix} = \begin{bmatrix} -\frac{1}{l}\boldsymbol{\mathcal{M}}\mathbf{e} \\ \mathbf{u}_{\mathrm{BC}} \\ \mathbf{0} \end{bmatrix}. \tag{10-30}$$

Extracting the unknowns $\mathbf{e}$ and $\mathbf{u}_{\mathrm{BC}}$ from the right hand side in (10-30) results in

$$\begin{bmatrix} \boldsymbol{\mathcal{L}} & \mathbf{C}_{\mathrm{BC}}^{\mathsf{T}} & \mathbf{C}_{\mathrm{conti}}^{\mathsf{T}} \\ \mathbf{C}_{\mathrm{BC}} & \mathbf{0} & \mathbf{0} \\ \mathbf{C}_{\mathrm{conti}} & \mathbf{0} & \mathbf{0} \end{bmatrix} \begin{bmatrix} \mathbf{u} \\ \boldsymbol{\lambda}_{\mathrm{BC}} \\ \boldsymbol{\lambda}_{\mathrm{conti}} \end{bmatrix} = \begin{bmatrix} -\frac{1}{l}\boldsymbol{\mathcal{M}} & \mathbf{0} \\ \mathbf{0} & \mathbf{I} \\ \mathbf{0} & \mathbf{0} \end{bmatrix} \begin{bmatrix} \mathbf{e} \\ \mathbf{u}_{\mathrm{BC}} \end{bmatrix}, \tag{10-31}$$

with $\mathbf{I}$ being the identity matrix. As described in Chapter 8, the solution of the extended equation system (10-31) can be used to derive the functional model for the IA with the two additional unknowns $\mathbf{u}_{\mathrm{BC}}$. For each of the 31 bending tests, the subsidence of the bearings was determined in this way.

10.3.2 *Measurements*

The measurement data designation of the 31 bending tests with corresponding weights according to (WU 2020, Table 5.5) are summarised in Table 10-2.

designation	$\mathbf{u}_i$	m [kg]
exp	0	3.565
	1	7.120
	2	10.668
	3	17.825
	4	5.491
	5	9.068
exp4mm	6	17.819
	7	3.563
	8	7.134
	9	3.564
	10	7.135
	11	17.818
exp8mm	12	17.820
	13	10.709
	14	3.593
	15	3.593
exp10mm	16	3.569
exp3L	17	3.578
exp3L2	18	3.545
	19	7.121
	20	10.698
exp_Y	21	3.546
	22	7.125
	23	10.703
	24	14.248
exp_K	25	7.114
exp_Z	26	10.695
	27	3.561
	28	7.128
	29	10.690
	30	14.241
	31	17.808

Table 10-2: Measurement data designation and corresponding weights for each measurement set $\mathbf{u}_i$ according to (WU 2020, Table 5.5). The sets with the designation exp correspond to the bending tests with undamaged beam. Sets in red are referring to a six-point bending test and are not considered in this thesis.

The derived 31 displacement measurements for each of the 31 bending tests are listed in Table C-1 – C-6. As with measurements in general, we must assume that outliers are present in the data sets. To identify possible outliers, we need not only the stochastic properties of the measurements, but also the correct functional model, which is not known anyway due to systematic errors in the marker positions and later damage to the beam. Accordingly, we have the following issues:

- The standard deviation of the displacement measurements is not known.
- The correct functional model for the adjustment is not known.
- Outliers may be present in the observations.

In-depth analyses of the measurements for the undamaged beam $\mathbf{u}_0 - \mathbf{u}_3$ have shown that a standard deviation of $\sigma_{\text{disp}} = 0.92\,\mu\text{m}$ can be assumed for the observations, which is about 10 times smaller than for the observations used in (WU 2020, Chapter 5.3). Furthermore, some outliers could be detected in parallel, which are highlighted in Table C-1 – C-6. However, the identified outliers must be viewed with some scepticism due to the problems previously described.

By using a gradient based approach for marker detection, the systematic deviations due to different illumination could be significantly reduced.

10.3.3 *Model calibration*

The model calibration is based on the sets of measurements for the undamaged beam $\mathbf{u}_0 - \mathbf{u}_3$ listed in Table C-1 and the previously determined standard deviation σ_{disp}. Furthermore, we assume that the observations are uncorrel-

ated. An Integrated Analysis of these measurements with $p_e = 3$ yields the following solution for $E(x)$, which is shown in Figure 10-21.

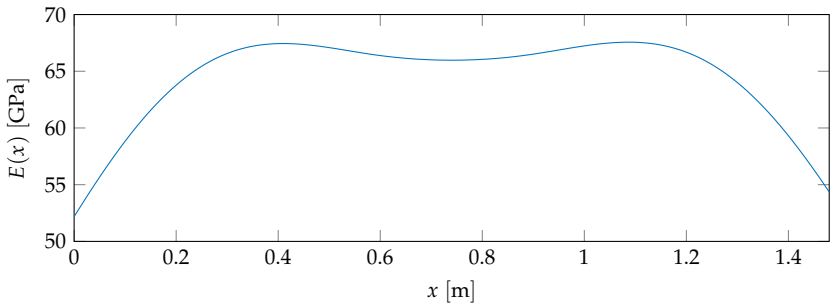

Figure 10-21: Solution $E(x)$ for polynomial degree $p_e = 3$ using the 4 sets of displacement measurements $\mathbf{u}_0 - \mathbf{u}_3$ listed in Table C-1.

Under optimal conditions, a solution for $E(x)$ can be expected that corresponds rather to a constant value than to the curve of $E(x)$ depicted in Figure 10-21. But detailed analyses have shown that this curve of $E(x)$ mainly results from the systematic influences described in Section 10.3.1, since it tends to occur for all 31 sets. For a damage analysis, however, these systematic influences must be taken into account, since otherwise the solution for $E(x)$ is strongly falsified and consequently a damage detection and localization will fail.

We call this approach, to take these systematic influences into account, model calibration and proceed as follows. From the solution $E(x)$ in Figure 10-21 we derive a correction function $C(x)$ by which the bending moment $M(x)$ must be corrected, in order to get a solution for $E(x)$, which is only a constant value. This approach for a model calibration is described in Programme 10-4.

Programme 10-4: Pseudo code for model calibration.

1: $\mathbf{L} \leftarrow$ from $\mathbf{u}_0 - \mathbf{u}_3$ listed in Table C-1
2: $C(x) = 1$ ▷ Initialization of the correction function
3: $M_c(x) = M(x)$ ▷ Initialization of the corrected bending moment
4: $\sigma_E = \infty$ ▷ Initialization for the loop
5: **while** $\sigma_E > 10^{-3}$ GPa **do**
6: $E \leftarrow$ constant value for $E(x)$ from IA with $\mathbf{L}$, $M_c(x)$ and $p_e = 0$
7: $E(x) \leftarrow$ from IA with $\mathbf{L}$, $M_c(x)$ and $p_e = 3$
8: $C(x) = E\,\frac{C(x)}{E(x)}$ ▷ Updating the correction function
9: $M_c(x) = M(x)C(x)$ ▷ Correction of the bending moment
10: $\sigma_E \leftarrow$ standard deviation of $E(x)$
11: **end while**

As a result from the model calibration we obtain the correction function $C(x)$ which is shown in Figure 10-22.

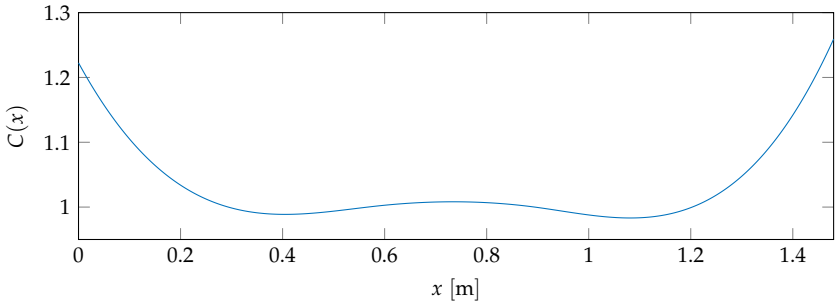

Figure 10-22: Resulting correction function $C(x)$ from the model calibration.

The systematic influences are taken into account when estimating $E(x)$ by correcting the bending moment $M(x)$ with $C(x)$ from Figure 10-22 as follows

$$M_c(x) = M(x)C(x)\,. \tag{10-32}$$

The evaluation of all load tests is always carried out with the corrected bending moment $M_c(x)$.

In addition, the adjusted elastic modulus for the undamaged beam results in

$$\hat{E} = 66.52\,\text{GPa} \qquad \text{with} \qquad \sigma_{\hat{E}} = 0.02\,\text{GPa} \tag{10-33}$$

and corresponds to the value for aluminium from the literature of 66.6 GPa, see e.g. (BENDER and GÖHLICH 2020, p. 604). The resulting residuals v and standardised residuals NV for the displacements $\mathbf{u}_0$ – $\mathbf{u}_3$ are shown in Figure 10-23.

Figure 10-23: Residuals v and standardised residuals NV after model calibration for the observations $\mathbf{u}_0$ – $\mathbf{u}_3$.

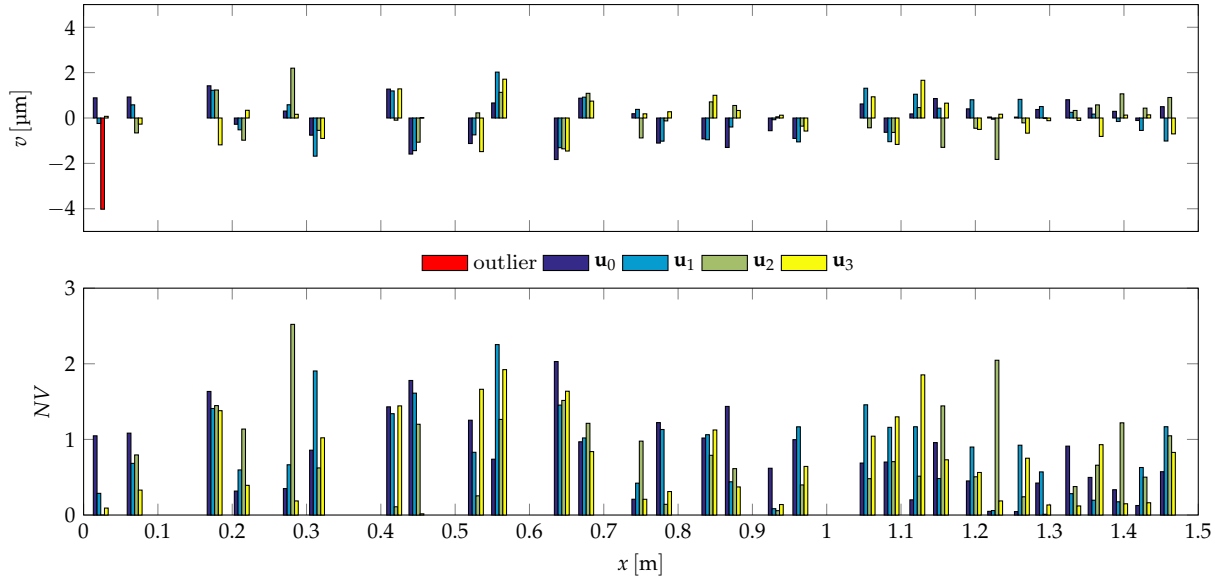

In general it can be seen that observations for markers on the right side of the beam usually have smaller residuals than for markers on the left side. Furthermore, they also seem to have a rather random negative or positive sign, especially in contrast to the observations at $x_{\text{disp}_{11}} = 0.64\,\text{m}$ or $x_{\text{disp}_{12}} = 0.67\,\text{m}$,

During the experiment we installed an additional spotlight, which mainly illuminated the left side of the beam, while the right side was mainly illuminated by daylight.

which are all either negative or positive. It seems as if the observations on the left side of the beam still show systematic influences, which presumably are based on a different illumination of the beam.

The largest residual of $\approx 4\,\mu m$ refers to the first observation of $\mathbf{u}_2$ which was previously detected as an outlier, see Table C-1. Although the outlier is still present in the adjustment, it has in this case no impact on the estimation of $E(x)$ or its standard deviation. All other residuals are usually much smaller than $2\,\mu m$ and also the standardised residuals NV are usually smaller than 2.5, which indicates that no further outliers can be detected. Particularly since the redundancy numbers of the observations are usually larger than 70 % and are therefore very well controlled, see Section 2.5.1.

In all upcoming cases, the redundancy numbers are usually larger than 70 %.

As the functional model is usually not correct for the damaged case, the global test is not considered any further.

Also the test statistic for the global test $T_{\chi^2} = 110.8$ is smaller than the critical value $\chi^2_{\alpha,r} = 134.4$ for redundancy $r = 109$ and error level $\alpha = 5\,\%$. We can summarize that the adjustment is consistent and the chosen stochastic and functional model corresponds to the given observations $\mathbf{u}_0 - \mathbf{u}_3$.

Based on these results, the data sets for the damaged beam will be evaluated in the following sections for a detailed damage analysis via MeMoS.

10.3.4 *Damage detection*

In accordance with the test designations from Table 10-2, the beam was gradually damaged at the approximate position

$$x_{\text{damage}} = 1.107\,\text{m}\,. \tag{10-34}$$

Starting from a small hole of 4 mm (exp4mm), through 3 closely placed holes of 10 mm diameter (exp3L) up to an additional cut of 15 mm depth (exp_Z), see also (Wu 2020, Chapter 5.3). In the following, we will analyse to what extent we can detect the damage based on the sets of observations for these different tests listed in Appendix C.

To gain a better insight, damage detection is done in two different ways, which are as follows:

1. via Integrated Analysis (IA) with $p_e = 0$,
2. via Parameter Sifter (PS) with $p_e = 4$.

In the first case, we estimate only a constant value for $E(x)$, which is definitely the wrong functional model, especially for larger damages. In the second case, at least smaller local variations in $E(x)$ can be considered, which at least allows a rough approximation of the damage. Subsequently, the Global Identifier (GI) is used to statistically compare these solutions with the one from the model calibration in Equation (10-33). The result for all sets of the undamaged and damaged scenarios are listed in Table 10-3.

Table 10-3: Result of the damage detection. Correct decisions of the Global Identifier (GI) in green and wrong in red.

			IA with $p_e = 0$				PS with $p_e = 4$	
designation	$\mathbf{u}_i$	m [kg]	F_i	$F_i > F_{1,\infty,\alpha}$	$\hat{E}$ [GPa]	$\sigma_{\hat{E}}$ [GPa]	F_i	$F_i > F_{1,\infty,\alpha}$
exp	0	3.565	7.7	true	66.88	0.11	7.7	true
	1	7.120	0.1	false	66.55	0.07	0.1	false
	2	10.668	0.6	false	66.57	0.05	0.6	false
	3	17.825	0.8	false	66.49	0.02	0.8	false
exp4mm	6	17.819	0.6	false	66.55	0.04	5.0	true
	7	3.563	2.0	false	66.34	0.10	2.0	false
	8	7.134	2.8	false	66.41	0.08	2.8	false
	9	3.564	8.5	true	66.90	0.10	8.5	true
	10	7.135	0.0	false	66.53	0.10	0.0	false
	11	17.818	7.8	true	66.63	0.04	7.8	true
exp8mm	12	17.820	6.0	true	66.43	0.04	13.7	true
	13	10.709	0.2	false	66.50	0.06	0.2	false
	14	3.593	0.0	false	66.54	0.11	0.0	false
	15	3.593	18.8	true	67.09	0.11	18.8	true
exp10mm	16	3.569	0.5	false	66.43	0.09	3.1	false
exp3L	17	3.578	197.4	true	64.55	0.15	197.4	true
exp3L2	18	3.545	117.0	true	68.04	0.15	117.0	true
	19	7.121	11.4	true	66.25	0.12	13.3	true
	20	10.698	28.8	true	66.18	0.10	24.2	true
exp_Y	21	3.546	38.3	true	65.66	0.16	22.4	true
	22	7.125	30.7	true	66.07	0.11	13.4	true
	23	10.703	54.4	true	66.09	0.08	48.0	true
	24	14.248	22.4	true	66.03	0.19	22.4	true
exp_K	25	7.114	200.7	true	64.18	0.32	120.9	true
exp_Z	26	10.695	256.6	true	59.16	0.83	300.0	true
	27	3.561	287.9	true	59.29	0.82	335.9	true
	28	7.128	278.9	true	59.25	0.83	190.7	true
	29	10.690	251.6	true	59.25	0.83	285.4	true
	30	14.241	217.6	true	59.28	0.83	373.7	true
	31	17.808	189.4	true	59.20	0.83	444.4	true

Columns 8 and 9 in Table 10-3 show the results of the GI for the solution $E(x)$ estimated by the PS. Apart from an incorrect detection for the undamaged experiment 0, it is usually possible to detect damage for larger loads. Which is obvious, since the impact of the measurement noise on the estimation of $E(x)$ decreases with increasing deflection of the beam. It is hardly surprising that, as damage increases, it is always possible to detect it even for smaller loads, which is the case from experiment 17 onwards. This result is a bit better than that of (WU 2020, Table 5.5), where damage could only be reliably detected from experiment 23 onwards.

The results of the GI for the solution $E(x)$ of the IA with $p_e = 0$ can be found in columns 4 to 7. Apart from a different decision for experiment 6, the result of the damage detection using IA is identical to that of the PS. This is quite astonishing as the functional model is incorrect especially for larger damage. In addition, the estimated elastic modulus $\hat{E}$ and its standard deviation $\sigma_{\hat{E}}$ are given in the columns 6 and 7. It is quite remarkable how slightly this value changes even though the beam is heavily damaged. For several large

The functional model of the PS is also wrong, but slightly better than the one of the IA.

holes in the beam (exp3L2), the estimated elastic modulus $\hat{E}$ in principle still corresponds to the value for the undamaged case (exp). Only after a larger cut (exp_K) this value changes significantly. From this point on, the standard deviation $\sigma_{\hat{E}}$ also increases, since the functional model is incorrect and thus the residuals have noticeable systematic characteristics. To clarify this in more detail, the resulting residuals v and standardised residuals NV for the displacements $\mathbf{u}_6$, $\mathbf{u}_8$, $\mathbf{u}_{10}$ and $\mathbf{u}_{11}$ of the experiment exp4mm are shown in Figure 10-24.

Figure 10-24: Residuals v and standardised residuals NV of the Integrated Analysis (IA) with $p_e = 0$ for some sets of observations from experiment exp4mm.

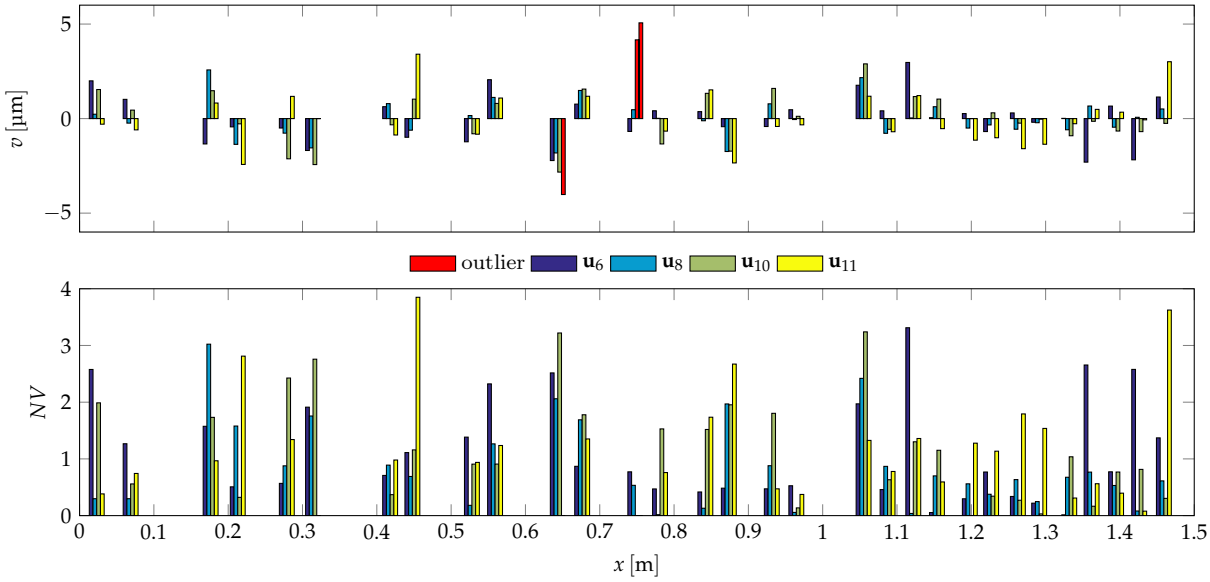

In general, the distribution of the residuals in Figure 10-24 (top) is similar to those from the model calibration in Figure 10-23, but with slightly larger values of up to $\approx 3\,\mu\text{m}$. Unfortunately, systematic errors due to the damage are not noticeable. Also the standardised residuals in Figure 10-24 (bottom) have slightly larger values with up to 3.8 for $\mathbf{u}_{11}$ at $x_{\text{disp}_8} = 0.45\,\text{m}$, which is not considered as an outlier. However, it is not possible to draw any further conclusions from the standardised residuals. With increasing damage, the distribution of residuals changes only slightly, as Figure 10-25 reveals.

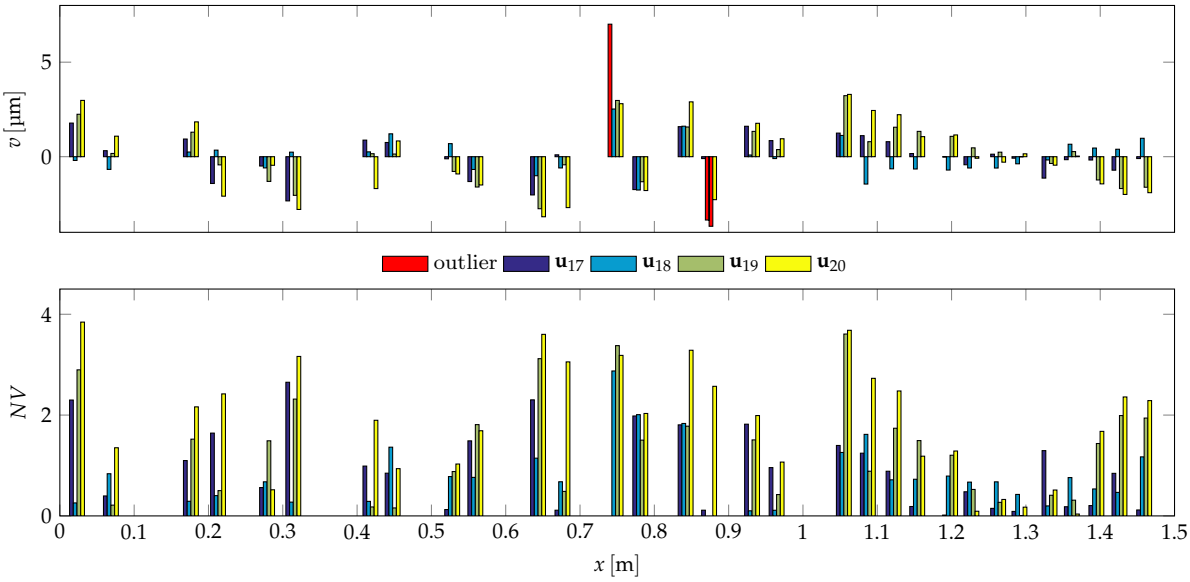

Figure 10-25: Residuals v and standardised residuals NV of the Integrated Analysis (IA) with $p_e = 0$ for the sets of observations from experiments exp3L and exp3L2.

Figure 10-25 shows the resulting residuals v and standardised residuals NV for the displacements $\mathbf{u}_{17} - \mathbf{u}_{20}$ of the experiments with 3 closely placed holes of 10 mm diameter. Although the damage to the beam is already very large, this is hardly noticeable in the residuals, which have values of up to $\approx 3\,\mu m$ and thus correspond to those in Figure 10-24 (top). However, small systematic errors are now visible for residuals on the right side of the beam. Especially for the observations $\mathbf{u}_{19}$ (green) and $\mathbf{u}_{20}$ (yellow), the residuals decrease linearly from $x_{\mathrm{disp}_{19}} = 1.05\,m$ onwards and show hardly any random character. In addition, it should be noted that the standardised residuals NV in Figure 10-25 (bottom) for the observations of the bending test with largest weight $\mathbf{u}_{20}$ generally are larger than for smaller loads. But as before, the standardised residuals are all below 4 and therefore do not allow any further conclusions.

From this level of damage on, the functional model of the IA is no longer able to adequately describe the measurements, so that the previously described systematic errors appear in the residuals. However, these influences are rather small and maybe hardly visible in the residuals. Only with an additional deeper cut the damage is clearly recognizable in the residuals, as Figure 10-26 reveals.

Figure 10-26: Residuals v and standardised residuals NV of the Integrated Analysis (IA) with $p_e = 0$ for some sets of observations from experiments exp_Y, exp_K and exp_Z.

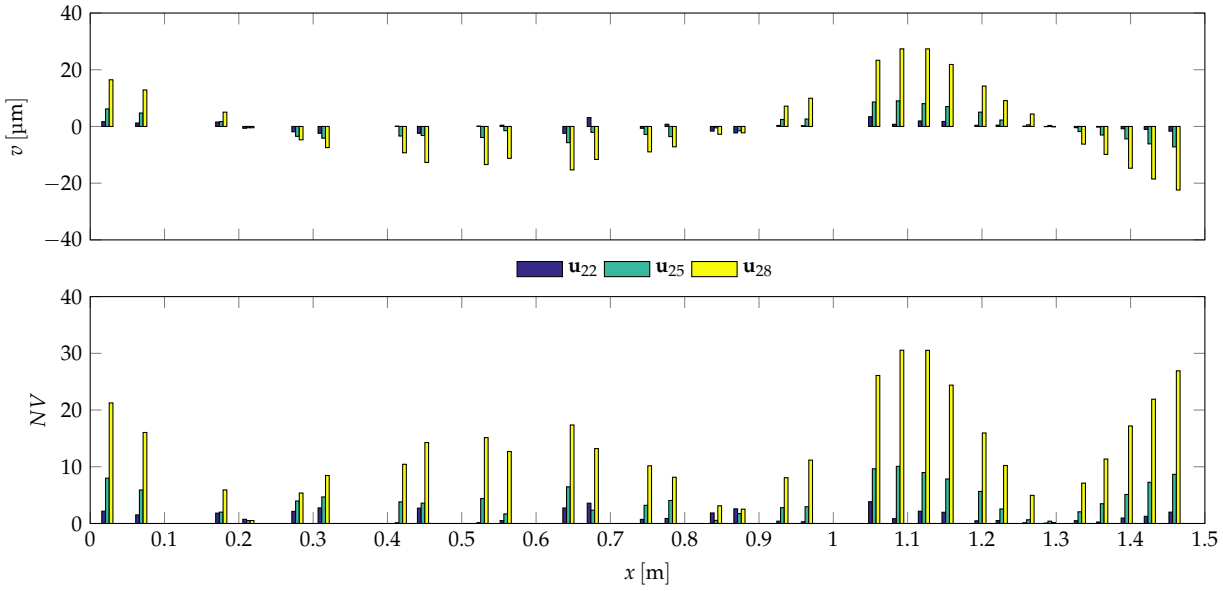

For better comparability of the results, Figure 10-26 shows the residuals v and standardised residuals NV for the displacements of the experiments exp_Y to exp_Z under the same load. As v and NV for the observations $\mathbf{u}_{22}$ for a small cut nearly correspond to those from Figure 10-25 without cut, this changes significantly for the observations of the last two damage levels. The residuals of the observations $\mathbf{u}_{28}$ for maximum damage in Figure 10-26 (top) are extremely large and take values up to $\approx 30\,\mu\text{m}$ and are highly systematically falsified. Only after a considerable damage do systematic errors in the residuals occur very clearly. So far we have only estimated a constant value for $E(x)$ and this functional model of the IA is not applicable for these damage levels. This is also confirmed by the considerably changed value for $E(x)$ from Table 10-3 in column 6. Furthermore, it can be seen that the damage can not only be detected but also localized by the standardised residuals NV. For the two experiments $\mathbf{u}_{25}$ and $\mathbf{u}_{28}$, the largest values for the NV result for observations near the damage at $x_{\text{damage}} = 1.107\,\text{m}$. This can also be seen in the result presented in (Wu 2020, Chapter 5.3).

However, this only applies to damage that is extremely large and can already be seen with the naked eye, which is not useful.

We also want to take a closer look at the solutions derived by the PS. In the case that F_i in column 8 has the same value as in column 4 for the solution of the IA with $p_e = 0$, the PS has also found a constant value as a solution and all other coefficients were not significantly different from zero. With a few exceptions, this is always the case up to and including experiment 18. However, to compare the results of the PS with those of the IA, we will limit ourselves to the sets of observations used for Figure 10-26. The solution for $E(x)$ of the PS for some sets of observations from experiments exp_Y, exp_K and exp_Z are depicted in Figure 10-27.

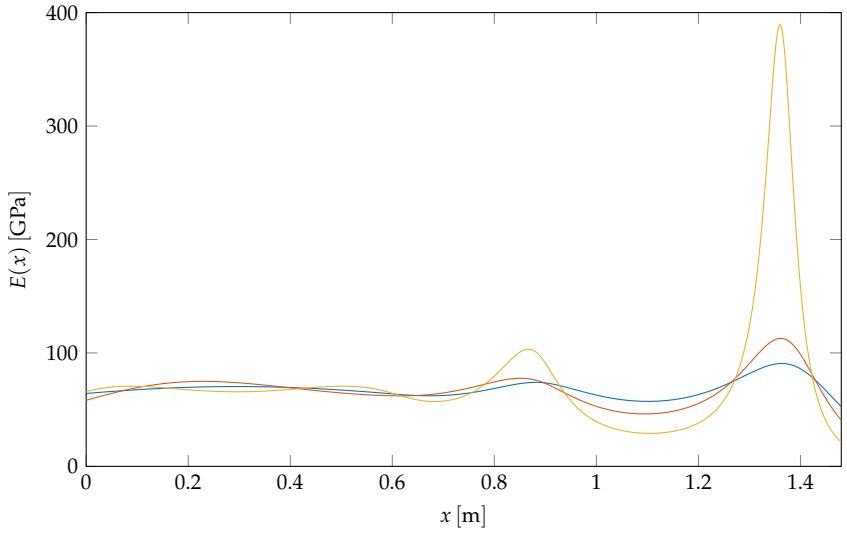

Figure 10-27: Solution $E(x)$ for the PS with $p_e = 4$ and displacements $\mathbf{u}_{22}$ (blue), $\mathbf{u}_{25}$ (red) and $\mathbf{u}_{28}$ (yellow).

All three solutions in Figure 10-27 are relatively smooth on the left side of the beam and show larger oscillations on the right side where the damage is located. In addition, all three solutions have a local minimum close to the damage at $x_{\text{damage}} = 1.107\,\text{m}$, but none of them can be clearly identified as the damage position since the global extremum in all curves is always at $x \approx 1.35\,\text{m}$ with a very large magnitude compared to the other extrema. The resulting residuals v and standardised residuals NV for the displacements $\mathbf{u}_{22}$, $\mathbf{u}_{25}$ and $\mathbf{u}_{28}$ are shown in Figure 10-28.

Within 1 cm.

Figure 10-28: Residuals v and standardised residuals NV of the Parameter Sifter (PS) with $p_e = 4$ for some sets of observations from experiments exp_Y, exp_K and exp_Z.

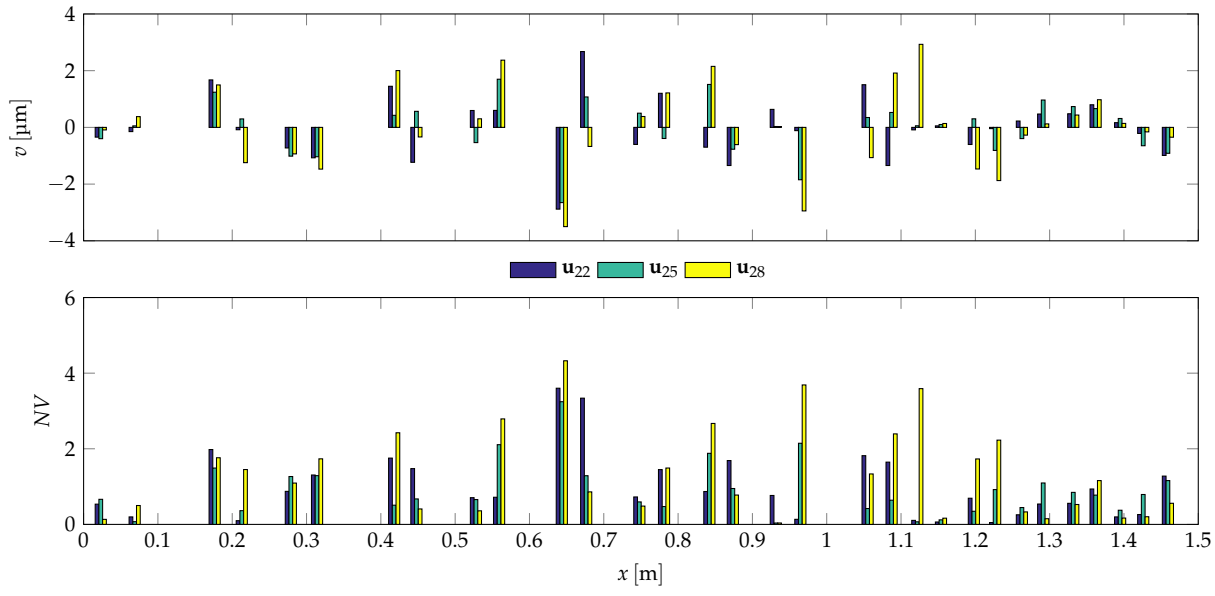

Although the functional model for the PS is wrong for this degree of damage, the residuals in Figure 10-28 (top) do not show any systematic errors. Even the

small oscillation of the residuals from $x = 1.2\,\mathrm{m}$ onwards cannot be identified as a systematic error due to the small number of observations. In general, the distribution of the residuals is similar to those from exp4mm depicted in Figure 10-24, with values of up to $\approx 3.5\,\mu\mathrm{m}$. For all three sets the largest residuals always occur at $x_{\mathrm{disp}_{11}} = 0.64\,\mathrm{m}$. Also the standardised residuals in Figure 10-28 (bottom) are the largest for these observations and for $\mathbf{u}_{28}$ even over 4. But since the functional model is not correct in any case and this observation in general has no impact on the solution $E(x)$, we decided at this point not to eliminate this observation as an outlier. A direct comparison of the results with those in Figure 10-26 shows that the estimated solutions for $E(x)$ in Figure 10-27 do not describe the damage at all, but represent its impact on the observations very well. The extent to which these solutions can be used to localise the damage is discussed in the next section.

10.3.5 *Damage localisation*

So far we have got an insight into the problem of damage detection and now we want to analyse in more detail to which extent the damage can also be localised. In Figure 10-27 we have already seen that at least for large damages a local minimum at the damage position in the solution $E(x)$ appears.

The localisation of the damage is analysed in more detail in the following two ways:

1. via the Local Indicator (LI),
2. via the Damage Sniffer (DS) and Damage Modeller (DM).

Both ways are discussed in more detail in the following sections.

10.3.5.1 *Local Indicator*

A purely data–driven approach.

In the first case, we want to analyse to which extent damage can be localised solely on the solution $E(x)$ and its standard deviation $s_E(x)$. Therefore, we determine the solution for each set of observations by the IA with $p_e = 3$ and compare it with the solution from the model calibration in Equation (10-33) using the LI. In this case, no further conditions are imposed on the solution $E(x)$, e.g. smoothness at the bearings, etc. The solutions $E(x)$ for the displacements $\mathbf{u}_6$ – $\mathbf{u}_{11}$ of the damage level exp4mm are shown in Figure 10-29.

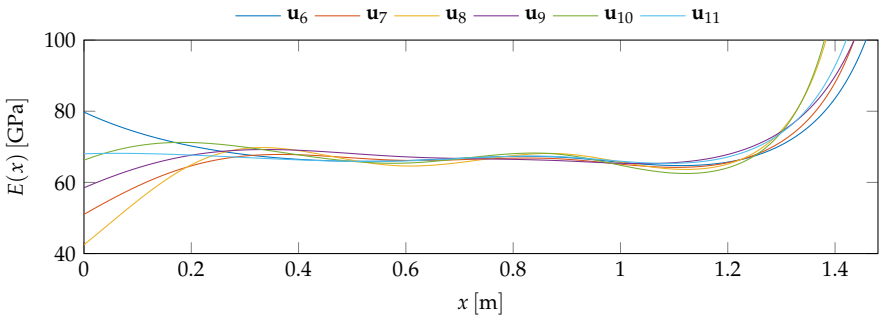

Figure 10-29: Solutions $E(x)$ of the IA with $p_e = 3$ for displacements $\mathbf{u}_6$ – $\mathbf{u}_{11}$ of exp4mm.

As Figure 10-29 shows, the solutions $E(x)$ for all sets of displacement measurements of experiment exp4mm are very similar, apart from larger deviations at the bearings. Each of these solutions for $E(x)$ with their corresponding standard deviations $s_E(x)$ is compared with the solution (10-33) from the model calibration using the LI. The resulting $t(x)$ from the LI for all solutions $E(x)$ for the displacements $\mathbf{u}_6$ – $\mathbf{u}_{11}$ of damage level exp4mm are shown in Figure 10-30.

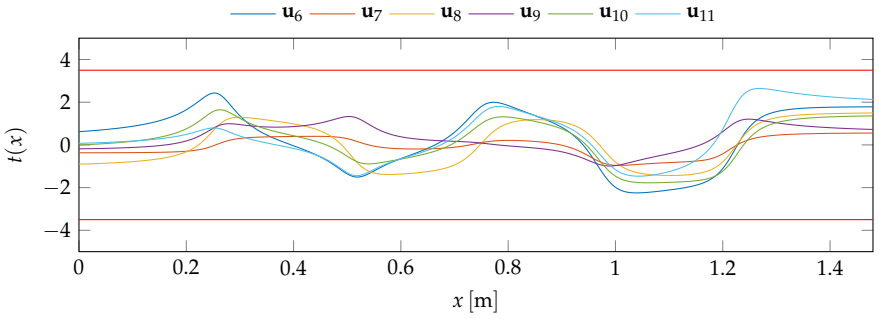

Figure 10-30: Results $t(x)$ of the LI for the solutions $E(x)$ of exp4mm from Figure 10-29. The critical value $t_{\text{critical}} = \pm 3.5$ in red.

As can easily be seen in Figure 10-30, all results for $t(x)$ of the LI are lying within the critical value $t_{\text{critical}} = \pm 3.5$ (horizontal red line) and thus no region can be identified for any of the solutions $E(x)$ that might indicate the damage position. Although damage has been detected for the displacements $\mathbf{u}_9$ and $\mathbf{u}_{11}$, it cannot be localised with the LI. The solutions $E(x)$ for the displacements $\mathbf{u}_{12}$ – $\mathbf{u}_{17}$ of damage levels exp8mm – exp3L are depicted in Figure 10-29.

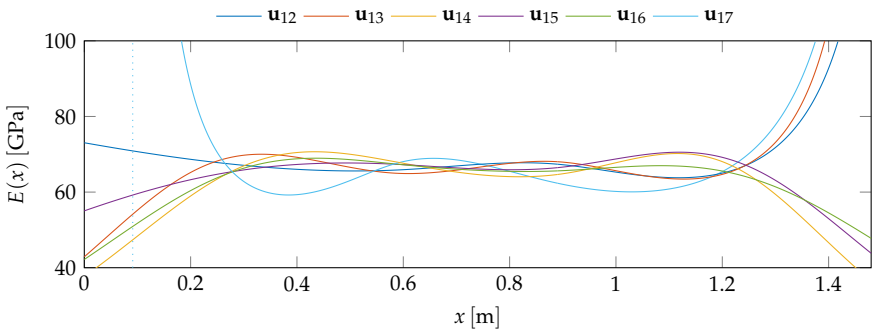

Figure 10-31: Solutions $E(x)$ of the IA with $p_e = 3$ for displacements $\mathbf{u}_{12}$ – $\mathbf{u}_{17}$ of exp8mm – exp3L.

First of all, it is noticeable that the solutions $E(x)$ in Figure 10-31 of damage levels exp8mm – exp3L are no longer as uniform as those for damage level exp4mm previously shown in Figure 10-29. The solution $E(x)$ for $\mathbf{u}_{17}$ (light blue) even has pole at $x \approx 0.1$ (dotted light blue). In general, this is also reflected in $t(x)$ from the LI, as shown in Figure 10-32.

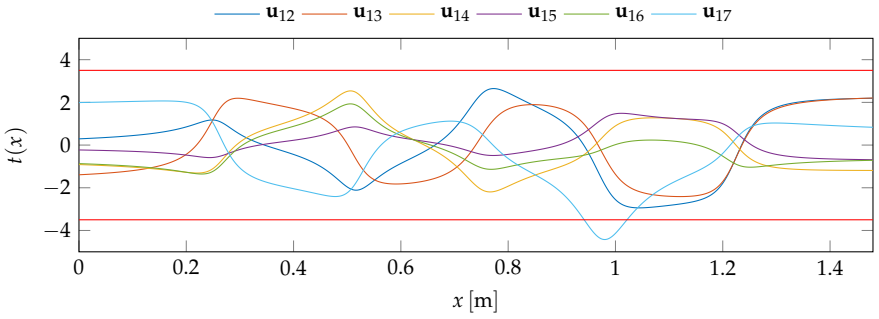

Figure 10-32: Results $t(x)$ of the LI for the solutions $E(x)$ of exp8mm – exp3L from Figure 10-31. The critical value $t_{\text{critical}} = \pm 3.5$ in red.

As Figure 10-32 shows, $t(x)$ is larger than the critical value only for $\mathbf{u}_{17}$ with a maximum value at $x_{\text{LI}} \approx 0.98\,\text{m}$. For this load test, the damage could be localised within $\approx 13\,\text{cm}$, but in all other cases a damage localization with the LI is not possible. The damage already has a large impact on the solution $E(x)$ and enforces larger oscillations, whereby more and more poles (dotted lines) occur close to the bearings, as $E(x)$ for damage levels exp3L2 and exp_Y in Figure 10-33 reveals.

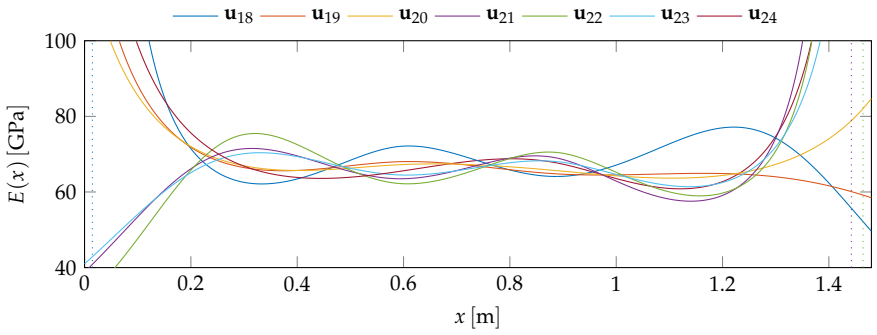

Figure 10-33: Solutions $E(x)$ of the IA with $p_{\text{e}} = 3$ for displacements $\mathbf{u}_{18}$ – $\mathbf{u}_{24}$ of exp3L2 and exp_Y.

All solutions $E(x)$ for $\mathbf{u}_{21}$ – $\mathbf{u}_{24}$ in Figure 10-33 show a minimum near the damage, only $E(x)$ for $\mathbf{u}_{18}$ oscillates in the opposite direction and has a maximum at $x \approx 1.2\,\text{m}$. However, only for $\mathbf{u}_{22}$ the damage can be localized at $x_{\text{LI}} \approx 1.18\,\text{m}$, as $t(x)$ in Figure 10-34 shows. For all other solutions no damage can be localised with the LI, since $t(x)$ is always within the critical value.

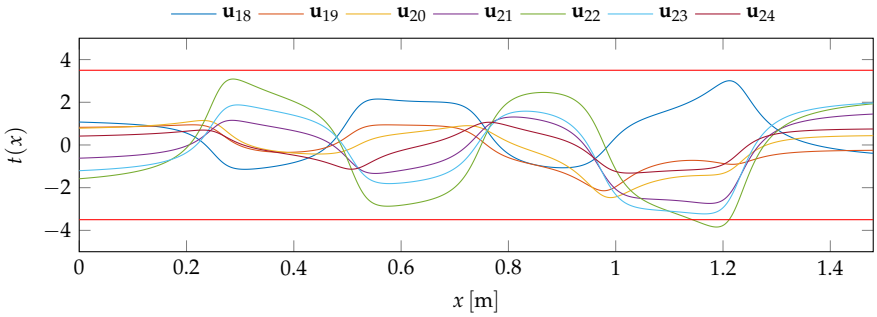

Figure 10-34: Results $t(x)$ of the LI for the solutions $E(x)$ of exp3L2 and exp_Y from Figure 10-33. The critical value $t_{\text{critical}} = \pm 3.5$ in red.

For the last two damage levels, the situation is completely different. Now the impact of damage on the solution $E(x)$ is so large that for the IA it is necessary to increase the polynomial degree to $p_{\text{e}} = 4$, otherwise the functional model is not able to represent the damage at all. The solutions $E(x)$ for the displacements $\mathbf{u}_{25}$ – $\mathbf{u}_{31}$ of the damage levels exp_K and exp_Z are shown in Figure 10-35.

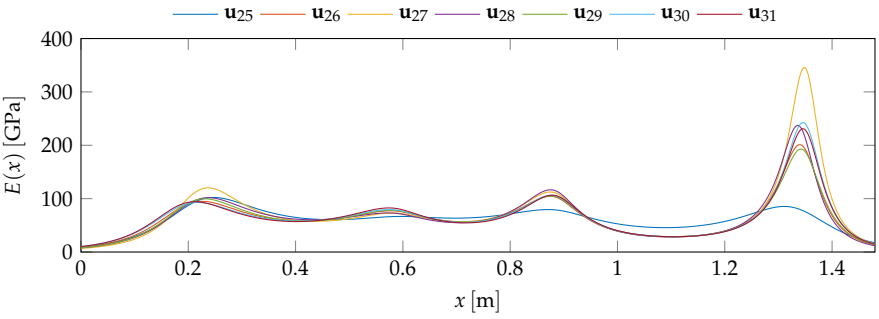

Figure 10-35: Solutions $E(x)$ of the IA with $p_{\text{e}} = 4$ for displacements $\mathbf{u}_{25}$ – $\mathbf{u}_{31}$ of exp_K and exp_Z.

All solutions $E(x)$ in Figure 10-35 for experiments exp_K and exp_Z show a very clear maximum at $x \approx 1.35\,\mathrm{m}$, which actually has nothing to do with the damage itself. The position of the damage cannot be clearly determined from the solution $E(x)$ alone. However, this can be done without any problems using the result $t(x)$ of the LI, as can be seen in the Figure 10-36.

This maximum is mainly caused by the very wide minimum at the damage position.

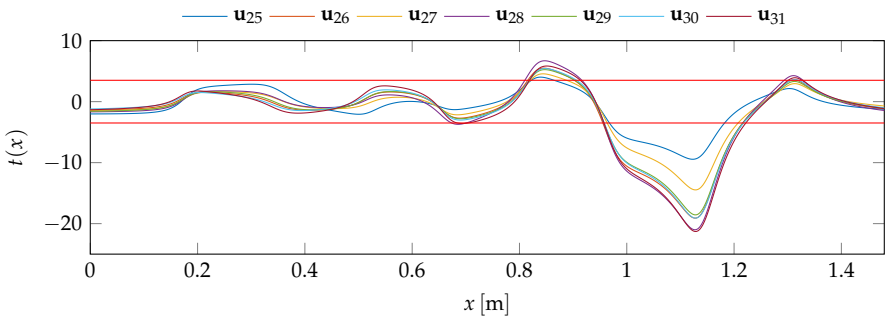

Figure 10-36: Results $t(x)$ of the LI for the solutions $E(x)$ of exp_K and exp_Z from Figure 10-35. The critical value $t_{\mathrm{critical}} = \pm 3.5$ in red.

For all results $t(x)$ in Figure 10-36 of damage levels exp_K and exp_Z, the position of the damage can be determined within 2 cm, since the largest value for all $t(x)$ occurs at $x_{\mathrm{LI}} \approx 1.127\,\mathrm{m}$. In addition, it can be seen that $t(x)$ for the maximum at $x \approx 1.35\,\mathrm{m}$ is usually smaller than the critical value or only a just slightly larger. Therefore, this maximum cannot be interpreted as damage, but is rather caused only by the minimum of the actual damage. From a statistical point of view, this maximum hardly differs from adjusted elastic modulus for the undamaged beam in (10-33), although it takes very large values.

The damage localisation with the Local Indicator has shown that it only works reliably if the damage is very large. For the presented example, the damage could always be localised from experiment 25 onwards, which in principle corresponds to the result of (Wu 2020, Table 5.5). In addition, the position of the damage can already be clearly seen in the residuals of an IA with $p_{\mathrm{e}} = 0$ as shown in Figure 10-26. If enough measurements are available at different positions, the LI unfortunately does not provide any further information which cannot already be obtained by estimating a constant value for $E(x)$. To which extent damage can still be localised is addressed in the next section.

10.3.5.2 *Damage Sniffer and Damage Modeller*

As we have seen in the previous section, a damage localisation based on a pure data–driven approach using an IA with a subsequent LI is unfortunately not effective. In particular, the measurement noise has a considerable influence on the solution $E(x)$ and thus also on the localisation of the damage. Furthermore, due to the indeterminacy at the bearings, large oscillations can occur in the solution $E(x)$ with possibly extreme values at the bearings. All these effects have a large influence and considerably falsify the damage localisation. The extent to which these effects can be separated from the actual damage using the DS will be shown in more detail for some sets of measurements of the experiment exp4mm.

To reduce the influence of the indeterminacy on the bearings, the solution is always smoothed in this area with the LS.

Minimal damage – minimal load

Since the impact of damage on the displacements is directly related to the magnitude of the load, we first consider the measurements $\mathbf{u}_9$ of experiment

exp4mm for minimal load of 3.564 kg in more detail. The reduced surface $\Delta E_{\text{surf}}(x, w_{\text{GS}})$ of the DS for the first iteration is depicted in Figure 10-37.

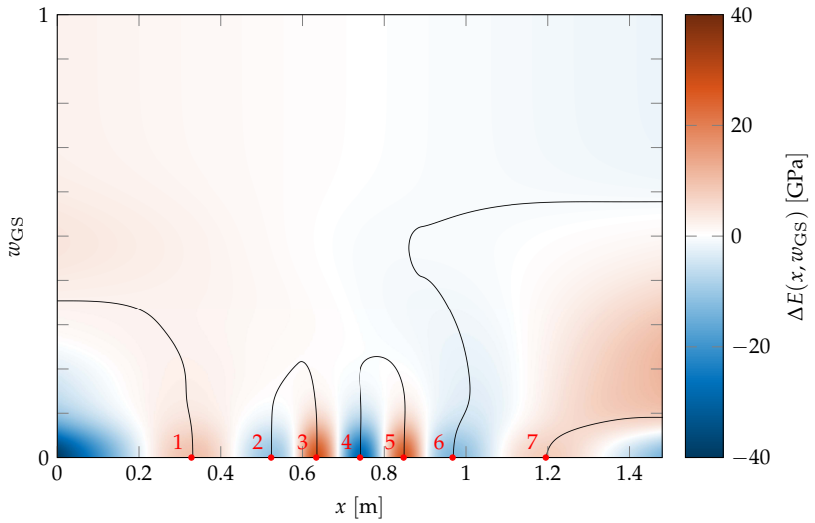

Figure 10-37: Reduced surface $\Delta E_{\text{surf}}(x, w_{\text{GS}})$ of the first iteration of the DS for the measurements $\mathbf{u}_9$.

As Figure 10-37 reveals, 7 extrema occur in the solution, with larger deviations of up to ≈ 40 GPa in the middle of the beam for $w_{\text{GS}} = 0$. First of all, it is noticeable that extrema $2 - 5$ are probably only caused by measuring noise and do not occur in the solution itself. Only minimum 6 differs clearly from the others and may be considered as damage position, since it also has the largest values for dominance of $D_6 = 61.3\,\%$, as Table 10-4 shows.

Table 10-4: Resulting dominance D_j of the Damage Sniffer for the measurements $\mathbf{u}_9$.

		Extrema j						
		1	2	3	4	5	6	7
D_j [%]	first iteration	8.5	3.9	7.1	10.4	7.9	61.3	0.9
	last iteration	12.3					87.7	

In direct comparison of the values D_j for all other extrema, the minimum 6 is by far the most dominant one and this even in the first iteration. The last iteration of the DS is shown in Figure 10-38.

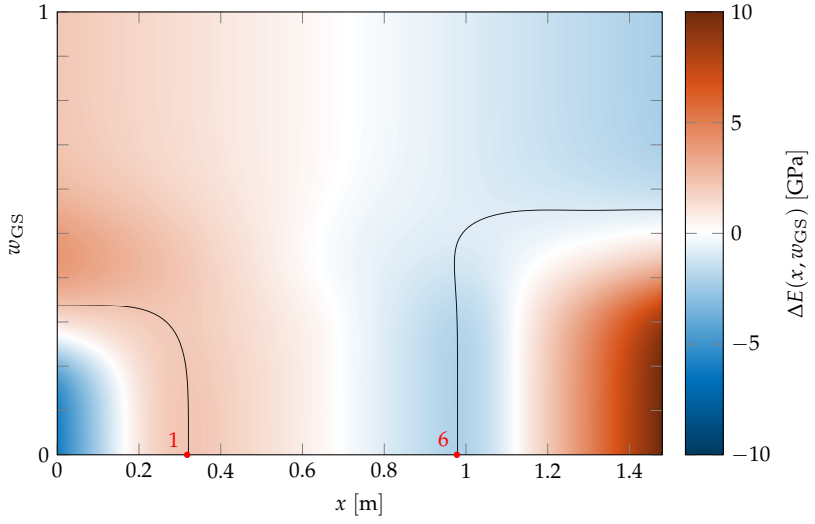

Figure 10-38: Reduced surface $\Delta E_{\text{surf}}(x, w_{\text{GS}})$ of the last iteration of the DS for the measurements $\mathbf{u}_9$.

The result of the DS in Figure 10-38 differs significantly from that of the first iteration in Figure 10-37. Not only that a total of 5 extrema have been removed from the solution, the deviations of $\approx 10\,\text{GPa}$ are much smaller than those of the first iteration. As Table 10-4 shows, the minimum 6 at $x_{\text{DS}} \approx 0.98\,\text{m}$ has always the largest value for the dominance and it also correspond to the true damage position except for $\approx 13\,\text{cm}$. This is also confirmed by the DM, which also locates the damage at $x_{\text{DM}} \approx 0.98\,\text{m}$. For comparison, the two solutions of the DS for $w_{\text{GS}} = 0$ from Figure 10-37 and Figure 10-38 and the one of the DM are shown in the Figure 10-39.

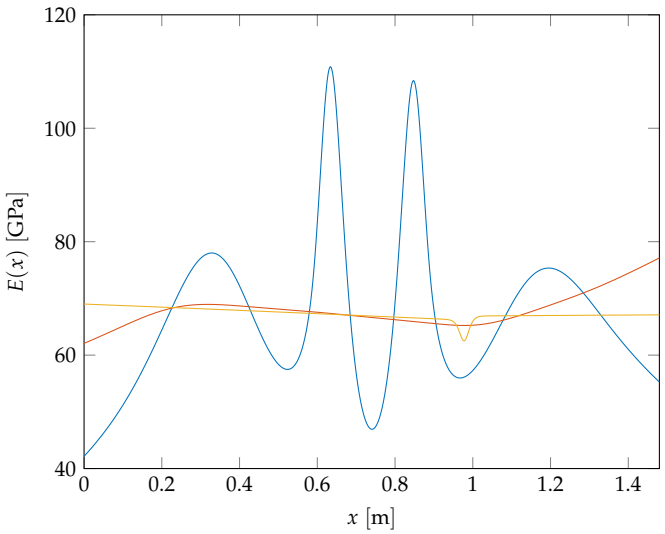

Figure 10-39: Solutions $E(x)$ of the DS for $w_{\text{GS}} = 0$ using the measurements $\mathbf{u}_9$ for the first iteration in blue and for the last iteration in red. Solution $E(x)$ of the DM in yellow.

Most noticeable in Figure 10-39 is the solution $E(x)$ of the first iteration of the DS (blue), with large oscillations in the middle of the beam. However, a direct comparison with the solution $E(x)$ of the last iteration (red) shows that these oscillations are essentially caused by the measurement noise and do not occur in the actual solution. As already mentioned, the result of the DS (red) and the DM (yellow) is consistent and both of them indicate damage at $x_{\text{DM}} \approx 0.98\,\text{m}$, which corresponds roughly to the true position. For this data set the damage could be detected and localised within $\approx 13\,\text{cm}$, see Table 10-3.

Minimal damage – medium load

Next, we will consider the the measurements $\mathbf{u}_{10}$ of experiment exp4mm for a load of $7.135\,\text{kg}$. According to Table 10-3, damage could not be detected for this case and also in the result of the DS no clear extremum can be identified in the first iteration, as can be seen in Figure 10-40 and Table 10-5.

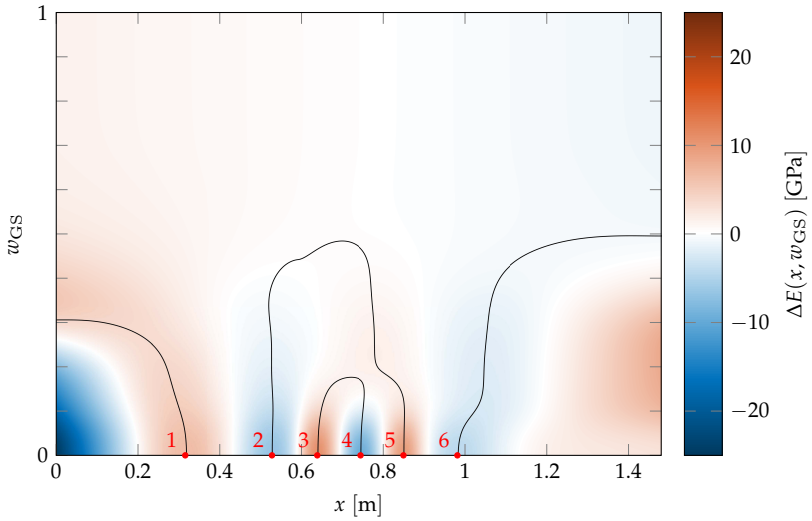

Figure 10-40: Reduced surface $\Delta E_{surf}(x, w_{GS})$ of the first iteration of the DS for the measurements $\mathbf{u}_{10}$.

Of the 6 extrema in total, the minimum 6 near the damage position is visually somewhat prominent, but cannot be clearly identified as a possible damage position, like the values for dominance in Table 10-5 reveal. Accordingly, the two extrema 2 and 5 could also be considered as possible damage positions, since all three extrema have very similar values for dominance between 25.7 % and 28.2 %.

Table 10-5: Resulting dominance D_j of the Damage Sniffer for the measurements $\mathbf{u}_{10}$.

		Extrema j					
		1	2	3	4	5	6
D_j [%]	first iteration	10.2	25.7	4.2	4.6	28.2	27.1
	last iteration	36.9					63.1

In the last iteration of the DS, however, this is quite different, as Figure 10-41 reveals.

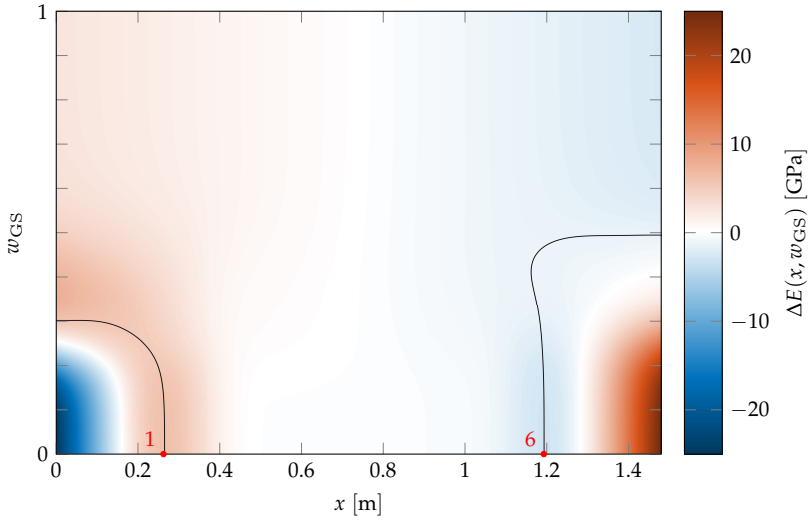

Figure 10-41: Reduced surface $\Delta E_{surf}(x, w_{GS})$ of the last iteration of the DS for the measurements $\mathbf{u}_{10}$.

Figure 10-41 shows that extrema 2–5 have been removed from the solution one after the other and only extrema 1 and 6 are left. Also, the position of the minimum 6 has clearly shifted from $x = 0.98\,\text{m}$ to $x = 1.19\,\text{m}$. The position

of maximum 1, on the other hand, changed only slightly. According to the values for the dominance D_j in Table 10-5, the DS identifies minimum 6 as a possible damage position, but its value $D_6 = 63.1\,\%$ is not strikingly larger than $D_1 = 36.9\,\%$ for maximum 1. This aspect is also reflected in the result of the DM, which finally identifies maximum 1 as a possible damage position with $x_{\mathrm{DM}} \approx 0.26\,\mathrm{m}$. The desired solution, however, would have been $x_{\mathrm{DM}} \approx 1.18\,\mathrm{m}$ for the minimum 6, which corresponds to the true damage position except for $\approx 8\,\mathrm{cm}$. For comparison and in order to point out a possible reason for this problem, the two solutions of the DS for $w_{\mathrm{GS}} = 0$ from Figure 10-40 and Figure 10-41 and the one of the DM are shown in the Figure 10-42.

In contrast to the values for the last iteration in Table 10-4, where D_6 is more than 7 times larger than D_1.

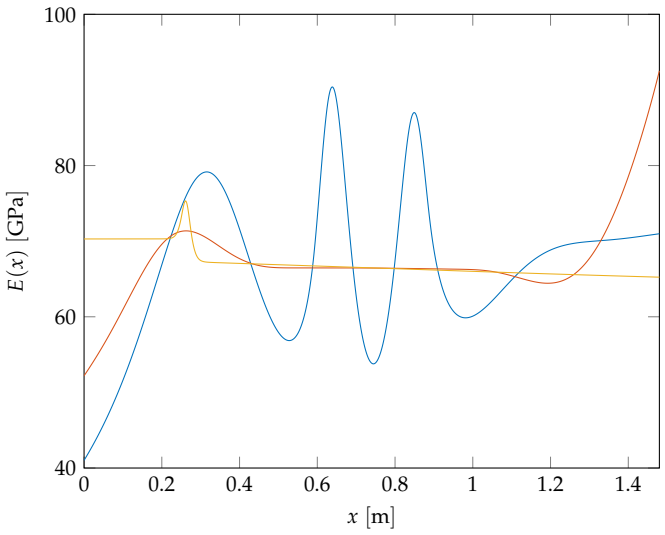

Figure 10-42: Solutions $E(x)$ of the DS for $w_{\mathrm{GS}} = 0$ using the measurements $\mathbf{u}_{10}$ for the first iteration in blue and for the last iteration in red. Solution $E(x)$ of the DM in yellow.

If we now compare the solution $E(x)$ of the first iteration of the DS in Figure 10-42 (blue) with that for the measurements $\mathbf{u}_9$ from Figure 10-39 (blue), then we can see clear similarities between these two curves. This means that both solutions for $E(x)$ are not mainly caused by measurement noise but rather by systematic errors in the observations, which is probably also the main reason for the incorrect identification of the damage position. This fact has already been mentioned in Section 10.3.3 when we discussed the residuals of the model calibration. Unfortunately, it has not yet been possible to consider the remaining systematic errors in the observations in a suitable way, which considerably falsifies the damage analysis. Furthermore, Figure 10-42 shows also the solution $E(x)$ for the last iteration of the DS and for the DM, with wrongly identified damage at $x_{\mathrm{DM}} \approx 0.26\,\mathrm{m}$.

The smaller the load, the larger the impact of this problem on the damage analysis.

Minimal damage – maximum load

As a last example, we will have a closer look at the measurements $\mathbf{u}_{11}$ of the experiment exp4mm for a load of 17.818 kg. The reduced surface $\Delta E_{\mathrm{surf}}(x, w_{\mathrm{GS}})$ of the DS for the first iteration is depicted in Figure 10-43.

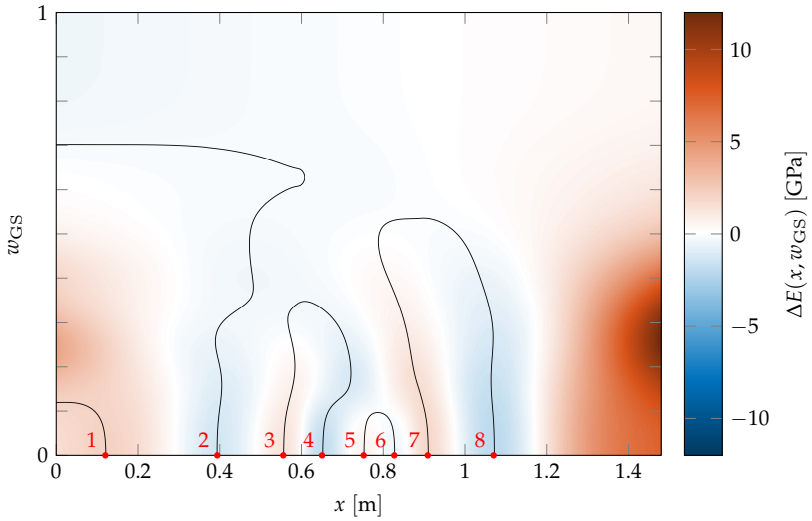

Figure 10-43: Reduced surface $\Delta E_{surf}(x, w_{GS})$ of the first iteration of the DS for the measurements $\mathbf{u}_{11}$.

As Figure 10-43 reveals, 8 extrema occur in the solution, with some deviations of up to $\approx 12\,\text{GPa}$ at the right bearing of the beam. Of all extrema, minimum 2 is clearly different from all others and, according to Table 10-6, also has the largest value for the dominance with $D_2 = 41\,\%$. In this case, however, minimum 8 at $x_{DM} \approx 1.07\,\text{m}$ with a dominance of $D_8 = 22.7\,\%$ represents the true damage, which is also only just a few centimetres from the true position of the damage.

Table 10-6: Resulting dominance D_j of the Damage Sniffer for the measurements $\mathbf{u}_{11}$.

		Extrema j							
		1	2	3	4	5	6	7	8
D_j [%]	first iteration	1.7	41.0	5.7	8.6	0.2	0.2	19.9	22.7
	last iteration		60.4					16.0	23.5

Although the impact of a damage on the observations actually increases with increasing load, the correct extremum could not be identified within the first iteration. In comparison to Figure 10-37, however, this was possible without any problems for the measurements $\mathbf{u}_9$ for minimum load. Even after the last iteration this does not really change, as Figure 10-44 shows.

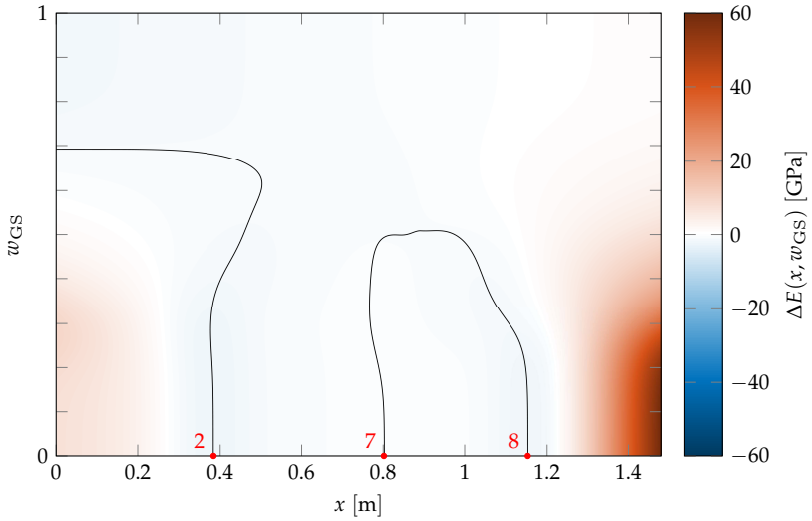

Figure 10-44: Reduced surface $\Delta E_{surf}(x, w_{GS})$ of the last iteration of the DS for the measurements $\mathbf{u}_{11}$.

As Figure 10-44 shows, the extrema 1 and 3 – 6 were removed from the solution, but the DS still identifies minimum 2 as a possible damage position with $D_2 = 60.4\,\%$. However, the DM finally identifies the correct minimum 8 and finds the right position of the damage up to $\approx 5\,\text{cm}$. The two solutions of the DS for $w_{\text{GS}} = 0$ from Figure 10-43 and Figure 10-44 and the one of the DM are shown in the Figure 10-45.

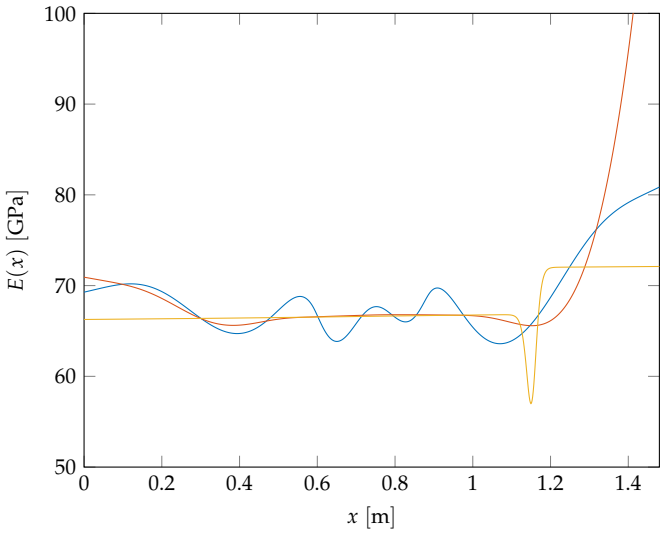

Figure 10-45: Solutions $E(x)$ of the DS for $w_{\text{GS}} = 0$ using the measurements $\mathbf{u}_{11}$ for the first iteration in blue and for the last iteration in red. Solution $E(x)$ of the DM in yellow.

Also for this data set the damage could be detected and localised within $\approx 4\,\text{cm}$, see Table 10-3. How well this worked for the other data sets is discussed in the following.

All data sets

As before, damage localisation using the DS and DM was also done for all other data sets and the results are summarised in Table 10-7. In the final solution of the DS up to 3 extrema can occur and as we have seen in Table 10-6 the extrema with the largest value for the dominance is not necessarily the solution we are looking for. Therefore, Table 10-7 lists two extrema, where $x_{1^{\text{st}}}$ is the position of the extremum with the largest and $x_{2^{\text{nd}}}$ is the position with the second largest value for the dominance. Whether the position of the actual damage $x_{\text{damage}} = 1.107\,\text{m}$ is approximately represented by one of the two extrema is given in column 6. In addition, the solution of the DM is given in column 5 and whether the damage could be localized is given in the last column. The colour coding in Table 10-7 is to be interpreted as follows:

If an extremum corresponds to the damage is not only determined by its position, but also if it is a minimum.

- The damage position is not represented by one of the two extrema and/or could not be localised with $|\Delta x| \geq 12\,\text{cm}$.
- The damage position is represented by one of the two extrema and/or could be located, but not accurately with $6\,\text{cm} \leq |\Delta x| \leq 12\,\text{cm}$.
- The damage position is represented by one of the two extrema and/or could be located accurately with $|\Delta x| \leq 6\,\text{cm}$.

Table 10-7: Result of the damage localisation using the DS and DM.

designation	$\mathbf{u}_i$	m [kg]	DS $x_{1^{st}}$ [m]	DS $x_{2^{nd}}$ [m]	DS x_{damage} contained?	DM x_{DM} [m]	DM Damage localised?
exp	0	3.565	0.80	0.71	● ○ ○	0.71	● ○ ○
	1	7.120	0.86	0.33	● ○ ○	0.79	● ○ ○
	2	10.668	0.40	0.89	● ○ ○	0.89	● ○ ○
	3	17.825	0.35	1.11	○ ○ ●	0.35	● ○ ○
exp4mm	6	17.819	1.13	0.46	○ ○ ●	1.13	○ ○ ●
	7	3.563	0.69	0.99	○ ● ○	0.99	○ ● ○
	8	7.134	0.51	0.29	● ○ ○	0.36	● ○ ○
	9	3.564	0.98	0.32	○ ● ○	0.98	○ ● ○
	10	7.135	1.19	0.26	○ ● ○	0.26	● ○ ○
	11	17.818	0.38	1.15	○ ○ ●	1.15	○ ○ ●
exp8mm	12	17.820	1.05	0.51	○ ○ ●	1.05	○ ○ ●
	13	10.709	0.53	0.29	● ○ ○	0.29	● ○ ○
	14	3.593	0.60	1.12	○ ○ ●	0.72	● ○ ○
	15	3.593	0.61	1.13	○ ○ ●	0.71	● ○ ○
exp10mm	16	3.569	0.35	0.59	● ○ ○	0.36	● ○ ○
exp3L	17	3.578	0.98	0.46	○ ● ○	0.98	○ ● ○
exp3L2	18	3.545	0.63	0.76	● ○ ○	0.76	● ○ ○
	19	7.121	0.59	0.46	● ○ ○	0.46	● ○ ○
	20	10.698	0.48	1.09	○ ○ ●	0.47	● ○ ○
exp_Y	21	3.546	1.19	0.64	○ ● ○	1.20	○ ● ○
	22	7.125	0.87	1.03	○ ● ○	0.73	● ○ ○
	23	10.703	0.29	1.20	○ ● ○	0.29	● ○ ○
	24	14.248	0.37	1.09	○ ○ ●	1.09	○ ○ ●
exp_K	25	7.114	1.10	0.63	○ ○ ●	1.03	○ ○ ●
exp_Z	26	10.695	1.10	0.90	○ ○ ●	1.10	○ ○ ●
	27	3.561	1.11	0.92	○ ○ ●	0.91	● ○ ○
	28	7.128	1.09	0.90	○ ○ ●	0.89	● ○ ○
	29	10.690	1.10	0.90	○ ○ ●	1.10	○ ○ ●
	30	14.241	1.11	0.92	○ ○ ●	1.11	○ ○ ●
	31	17.808	1.13	0.75	○ ○ ●	1.13	○ ○ ●

As can be seen in Table 10-7 column 6, the damage is very often present in the solution of the DS, but not always exactly at the actual position. Apart from the experiments exp for undamaged beam, only in 5 out of 26 cases the damage is not included in the solution of the DS. In these cases the impact of the remaining systematic errors and/or of the measurement noise on the solution is probably larger than the impact of the damage itself. Besides, it cannot be excluded that outliers are still present in these sets of measurements.

In general, it can be seen that the DS is very well suited to limit the possible position of damage. Even for experiments with minimal damage of a small vertical hole with a diameter of 4 mm, its position could be determined very accurately for the measurements $\mathbf{u}_6$ and $\mathbf{u}_{11}$. From experiment 20 onwards, the damage is always present in the solution of the DS, but unfortunately it cannot always be correctly identified with the DM, like in the case of $\mathbf{u}_{27}$ and $\mathbf{u}_{28}$. The decision criterion of the DM is probably not the best one, but unfortunately no better one could be found that always identifies the correct position. In comparison to the results of the damage localisation using the Local Indicator

in Section 10.3.5.1, the DS and DM provide much better results. However, one further point is noticeable, the DS has also found the position of the damage for the measurements $\mathbf{u}_3$, although the beam has not yet been damaged at all. But a closer look at the residuals for these measurements revealed that they are larger at $x_{\text{disp}_{20}} = 1.09\,\text{m}$ and $x_{\text{disp}_{21}} = 1.12\,\text{m}$ than the residuals for measurements in the surroundings. Since this is usually not the case for the other sets of measurements, it is therefore assumed that the damage position in the solution of the DS for the measurements $\mathbf{u}_3$ occurs only by accident.

10.3.6 *Summary and Conclusion*

For the damage analysis of the presented four-point bending test some tools were developed, whereby particularly the Damage Sniffer proved to be very useful. In general, the damage could already be successfully detected and even localised for much smaller damage levels than in (WU 2020, Table 5.5), whose analysis was mainly falsified by large systematic errors in the measurements. The results of the presented damage analysis for the four-point bending test are summarized in Table 10-8. As already discussed, damage localisation using the Local Indicator (LI) only works reliably for very large damages and consequently it could only be localised accurately from experiment 25 onwards, see column 5 in Table 10-8. In contrast, a damage localisation with the DS and DM is very promising, while even for small damages like for experiment 6 and 11 it could be localised very accurately, see column 6. So far the DS is only based on three features and it is assumed that the reliability of the damage localisation can be significantly increased by choosing further suitable features. In addition, the selection of the most significant extremum in the DM is based on the target function Ω and, as already mentioned, the correct extremum cannot always be identified by this decision criteria. It can also be assumed in this case that the result of the DM can be significantly increased by choosing a better decision criteria. Nevertheless, it is essential that a damage has been detected before, otherwise the result of the DS and DM has no meaning. As a direct comparison of the estimated parameters $\mathbf{e}$ under consideration of their stochastic properties is not effective, the damage detection of the Global Identifier (GI) is based on the solution $E(x)$ as a continuous function and its standard deviation $s_E(x)$. However, also this approach still has some drawbacks, since especially for small levels of damage it could often not be detected, compare column 4 in Table 10-8. In summary, the result of the damage analysis with MeMoS is very promising and it was even possible to successfully detect and localise the minimal damage of a small vertical hole with a diameter of 4 mm, see results for experiments 6, 9 and 11 in Table 10-8.

Table 10-8: Result of the damage detection and localisation with MeMoS. Correct damage detection of the Global Identifier (GI) in green and wrong in red. Since the Damage Modeller (DM) always provides a damage position, even if there is no damage, the results for the experiments exp are always marked red.

designation	$\mathbf{u}_i$	m	Detection	Localisation	
		[kg]	GI	LI	DM
exp	0	3.565	🔴 ⚪		🔴 ⚪ ⚪
	1	7.120	⚪ 🟢		🔴 ⚪ ⚪
	2	10.668	⚪ 🟢		🔴 ⚪ ⚪
	3	17.825	⚪ 🟢		🔴 ⚪ ⚪
exp4mm	6	17.819	⚪ 🟢		⚪ ⚪ 🟢
	7	3.563	🔴 ⚪		⚪ 🟡 ⚪
	8	7.134	🔴 ⚪		🔴 ⚪ ⚪
	9	3.564	⚪ 🟢		⚪ 🟡 ⚪
	10	7.135	🔴 ⚪		🔴 ⚪ ⚪
	11	17.818	⚪ 🟢		⚪ ⚪ 🟢
exp8mm	12	17.820	⚪ 🟢		⚪ ⚪ 🟢
	13	10.709	🔴 ⚪		🔴 ⚪ ⚪
	14	3.593	🔴 ⚪		🔴 ⚪ ⚪
	15	3.593	⚪ 🟢		🔴 ⚪ ⚪
exp10mm	16	3.569	🔴 ⚪		🔴 ⚪ ⚪
exp3L	17	3.578	⚪ 🟢	⚪ 🟡 ⚪	⚪ 🟡 ⚪
exp3L2	18	3.545	⚪ 🟢		🔴 ⚪ ⚪
	19	7.121	⚪ 🟢		🔴 ⚪ ⚪
	20	10.698	⚪ 🟢		🔴 ⚪ ⚪
exp_Y	21	3.546	⚪ 🟢		⚪ 🟡 ⚪
	22	7.125	⚪ 🟢	⚪ 🟡 ⚪	🔴 ⚪ ⚪
	23	10.703	⚪ 🟢		🔴 ⚪ ⚪
	24	14.248	⚪ 🟢		⚪ ⚪ 🟢
exp_K	25	7.114	⚪ 🟢	⚪ ⚪ 🟢	⚪ ⚪ 🟢
exp_Z	26	10.695	⚪ 🟢	⚪ ⚪ 🟢	⚪ ⚪ 🟢
	27	3.561	⚪ 🟢	⚪ ⚪ 🟢	🔴 ⚪ ⚪
	28	7.128	⚪ 🟢	⚪ ⚪ 🟢	🔴 ⚪ ⚪
	29	10.690	⚪ 🟢	⚪ ⚪ 🟢	⚪ ⚪ 🟢
	30	14.241	⚪ 🟢	⚪ ⚪ 🟢	⚪ ⚪ 🟢
	31	17.808	⚪ 🟢	⚪ ⚪ 🟢	⚪ ⚪ 🟢

EPILOGUE

SUMMARY AND CONCLUSION

This thesis resulted from a research project in cooperation with my colleague Cheng-Chieh Wu from the Bundesanstalt für Materialforschung und -prüfung (BAM), called Measurement– and Model–based Structural Analysis (MeMoS). Initially, we focused on a combined adjustment of spatially distributed hybrid measurements based on a structural model represented by an FEM and using the method of least squares, which already allowed to detect damage to the structure under investigation. By introducing a local material parameter using the concept of observed unknowns, well known in adjustment calculation, a damage localisation within the structure could be conducted. This approach was to some extent successfully applied in two experimental test set-ups, see (Wu 2020, Chapter 5). To evaluate the results of an adjustment, however, it is always necessary to understand the characteristics of the chosen functional model in all detail, especially for highly non-linear models. Unfortunately, this was not the case at that time and it remained unclear which part of the solution was due to the measurement noise and which was due to the functional model of the adjustment, which is in fact an *inverse problem*. In addition, the influence of the approximation of the structural behaviour by FEM on the estimated material parameters could also not be assessed in all detail. Thus, a falsification of the solution could not be entirely excluded. Therefore, it was necessary to get a detailed understanding on the approximation of functions in general and to obtain a direct influence on the solution of the adjustment problem in order to eliminate all undesired effects caused by the functional model as far as possible. These aspects, thus, lead to the two main research topics addressed within this thesis.

1. About the characteristics of basis functions on the approximation of functions.

2. About the impact of random errors on the damage analysis using MeMoS.

In Part ii we have thoroughly examined the approximation of univariate functions using different sets of basis functions and discussed the main advantages and disadvantages. We have also shown how approximations can be transformed between different sets of basis function and addressed some general problems that arise for the approximation of multivariate functions. With regard to the planned examinations in the second research topic and also for the approximation of Lipschitz continuous univariate functions in general, the Chebyshev basis is excellent. In general, it is possible to approximate any Lipschitz continuous function with arbitrary accuracy using this set of basis functions and, therefore, we can ensure that the approximation error is always zero within machine precision. In addition, the identification of the optimal polynomial degree is solely based on its coefficients and the approximation error can be determined from the absolute values of the last coefficients. Furthermore, an approximation in the Chebyshev basis also offers the possibility to easily and quickly perform numerical computations with functions, such as computing derivatives, integrals or root finding. Whereby many arithmetic operations are available in matrix notation and, thus, can directly be embedded in the least squares adjustment, if necessary. These were the main reasons why we have chosen the Chebyshev basis for the investigations in Part iii.

elementwise vs. global approach

Just to make it clear again, it was never the intention to replace the general approach of the FEM by a spectral method using Chebyshev polynomials.

Since the investigations of the second research topic provide a fundamental framework for understanding a damage analysis using MeMoS, the simple example of a statically bended Euler-Bernoulli beam was chosen in Part iii. At first, the mechanical model of a four-point bending test apparatus was derived and its analytical solution was approximated in the Chebyshev basis. The approximation was directly embedded as the functional model for an Integrated Analysis (IA) of static measurements such as displacements, inclinations and strains. In this example, we have introduced the elastic modulus as a continuous function along the beam $E(x)$ and the whole process of damage detection and localisation is based on a detailed analysis of the estimated function $E(x)$. In addition, it was also shown how functions can be used as observation within the IA, which consequently provides an easy way for the evaluation of quasi continuous measurements using for example TLS, FOS or photogrammetry. Numerical studies have demonstrated in detail the impact of measurement noise on the estimation of the unknown function $E(x)$ and revealed the actual nature of the *inverse problem* at hand. Furthermore, we gained an insight into the extent to which damage can be reconstructed from measurements using MeMoS, while we addressed the impact of damage on the measurements in all detail. In this thesis, we only considered static discrete measurements such as displacements, inclinations and strains and in principle none of these types of measurements are suitable for a damage analysis based purely on the presented IA using the method of least squares. Either damage can only be detected in the direct vicinity of the measuring point, as for strain, or the impact of damage is so small that for real problems, in principle, it can only be detected with highly precise sensor technology at very few measuring points, as for displacements or inclinations. However, the localisation of damage using MeMoS is negatively affected if only measurements from a few measuring points are available.

Apart from quasi-continuous strain measurements via FOS.

If we consider the former aim of MeMoS, namely to detect and localise damage to a structure, based on a rigorous and direct solution for the system parameters by an Integrated Analysis (IA) of spatially distributed hybrid measurements using the method of least squares, then these insights are quite disillusioning. Although damage can be detected to a certain extent, it can basically not be localised, apart from perhaps huge damages. Unfortunately, the measurement noise has a way larger impact on the unknown solution $E(x)$ than the damage itself. At this point, the nature of the *inverse problem* prevents a damage assessment using well established geodetic deformation analysis methods.

At least for discrete static measruements.

This conclusion only refers to displacement and inclination measurements.

Through extensive numerical investigations, however, it became apparent that the solution of the unknown function $E(x)$ was not only randomly disturbed by the measurement noise, but also contained a systematic component due to the damage, which also occurs in its vicinity. The challenge now was to separate this systematic influence within $E(x)$ from the random disturbance, which resulted in the development of the Damage Sniffer (DS) and Damage Modeller (DM). Therefore, features were identified manually in different regularised solutions for $E(x)$ and a strategy for localisation was developed, which proved to be also effective in the experimental studies in Section 10.3. As has been demonstrated, the DS is in some cases also capable to localise minor damage precisely. Besides this, a further approach for the localisation of damage was presented, which is based on a statistical comparison of $E(x)$ from two epochs. This so-called Local Indicator (LI) relies on a t-test, which has been transferred to continuous functions. Since this approach for damage localisation only

works reliably for very large damages, it can only be used to a limited extent. Nevertheless, the methodological concept of the LI can also be used for other problems, such as a deformation analysis of parameterised point clouds, which, however, is a different problem. In addition, the well known *congruency test* for the detection of deformation in geodetic networks of different epochs was adopted for damage detection and transferred to continuous functions, which is referred to as Global Identifier (GI). Apart from a still slightly larger Type-I error, this test quantity as a global indicator has proven to be very promising as a first approach for the detection of damage.

In summary, the results of an damage analysis using MeMoS have thus proved to be very promising, although the established methods for a geodetic deformation analysis cannot be directly applied to a damage analysis based on an *inverse problem*. Only by transferring statistical tests to continuous functions as well as the development of novel approaches for the localisation of damage enables a reliable damage analysis based on an Integrated Analysis (IA) of spatially distributed hybrid measurements using the method of least squares. This thesis at hand provides a fundamental framework for understanding the problem of a Measurement– and Model–based Structural Analysis from a geodetic point of view and consequently provides a technological contribution for Structural Health Monitoring.

OUTLOOK

In order to investigate the general nature of the *inverse problem* and consequently the actual challenges of a Measurement– and Model–based Structural Analysis, a simple *static model* was chosen. Accordingly, only static measurements, such as displacements, inclinations or strains, could be evaluated with the presented IA. From these limitations, the following step-by-step extensions of the model's complexity already result:

- A simple *dynamic model*.

  Following the presented derivation of an IA for static measurements, the functional model for least squares adjustment of spatially and temporally distributed hybrid measurements using a simple 1D dynamic model can be derived, which enables the combined evaluation of static and vibration measurements from a geodetic point of view.

- A complex *static model*.

  Although a complex 3D structure was already investigated in (WU 2020), the damage analysis was based on a first preliminary concept of MeMoS. In addition, only displacements were used. Consequently, the current concept of MeMoS can be transferred to more complex 3D structures for the evaluation of hybrid static measurements.

- A complex *dynamic model*.

  Once both of the previous points have been dealt with in detail, MeMoS can finally be extended to complex 3D dynamic models, which represent the behaviour of real structures best. An IA based on such a model enables a combined evaluation of static and vibration measurements for real world structures. Consequently, MeMoS can be applied for the first time for real monitoring tasks.

Apart from this, there are other aspects that could be further addressed in future work.

- The damage localisation via DS is currently based on only 3 features, which were identified manually in a very time-consuming way, and it can be assumed that the damage localisation can be further improved when more features are available for evaluation. Therefore, additional features need to be identified with machine learning algorithms and/or novel approaches to extract damage from the solution of an IA need to be developed.

- For real monitoring tasks, the environmental conditions, such as temperature or humidity, play an essential role and must be taken into account in the deformation/damage analysis. This implies for the example discussed in this thesis, that the unknown solution $E(x)$ is also a function of the environmental conditions, which have to be considered in the IA as additional measurements and new additional unknown parameters have to be introduced accordingly.

BIBLIOGRAPHY

BIBLIOGRAPHY

Ádám, J. (1982): "A detailed study of the duality relation for the least squares adjustment in euclidean spaces". In: *Journal of Geodesy* 56.3, pp. 180–195.

Adrian, R. (1809): "Research concerning the probabilities of the errors which happen in making observations, etc". In: *Analyst Math. Museum* 1, pp. 93–109.

Ahmed, N. and Fisher, P. S. (1970): "Study of algorithmic properties of chebyshev coefficients". In: *International Journal of Computer Mathematics* 2.1-4, pp. 307–317.

Atkinson, K. E. and Han, W., eds. (2009): Theoretical Numerical Analysis: A Functional Analysis Framework. 3rd ed. Vol. 39. Texts in Applied Mathematics. Dordrecht: Springer.

Baarda, W. (1968): A testing procedure for use in geodetic networks. Vol. N.S. 2,5. Publications on geodesy. Delft.

Bathe, K.-J. (2014): Finite element procedures. Second edition. Watertwon, MA, USA: Klaus-Jürgen Bathe.

Battles, Z. and Trefethen, L. N. (2004): "An Extension of MATLAB to Continuous Functions and Operators". In: *SIAM Journal on Scientific Computing* 25.5, pp. 1743–1770.

Becker, T., Weisbrich, S., Wu, C.-C. and Neitzel, F. (2015): "Advances in structural monitoring by an integrated analysis of sensor measurements and 3D building model". In: *3D Geoinformation science - The selected papers of the 3D GeoInfo 2014*. Ed. by M. Breunig, M. Al-Doori, E. Butwilowski, P. V. Kuper, J. Benner and K. H. Haefele. Lecture Notes in Geoinformation and Cartography. Springer, pp. 141–156.

Bender, B. and Göhlich, D. (2020): Dubbel Taschenbuch für den Maschinenbau 1: Grundlagen und Tabellen. Berlin, Heidelberg: Springer Berlin Heidelberg.

Boljen, J. (1983): "Ein dynamisches Deformationsmodell". In: *Deformationsanalysen '83*. Ed. by W. Welsch. Vol. 9. Schriftenreihe des Instituts für Geodäsie der Hochschule der Bundeswehr München, pp. 43–66.

Boller, C., Chang, F.-K. and Fujino, Y., eds. (2009): Encyclopedia of structural health monitoring. Chichester (G.B.): Wiley.

Borre, K. (2006): Mathematical Foundation of Geodesy: Selected Papers of Torben Krarup. Berlin, Heidelberg: Springer.

Borrmann, A., König, M., Koch, C. and Beetz, J. (2015): Building Information Modeling. Wiesbaden: Springer Fachmedien Wiesbaden.

Boyd, J. P. (2002): Chebyshev and Fourier spectral methods. Dover books on mathematics. Mineola: Dover.

Brandes, K., Neitzel, F., Weisbrich, S. and Daum, W. (2012): "Lagrange-Multiplikatoren (LM) der Ausgleichungsrechnung als Indikator für Strukturschäden". In: *tm - Technisches Messen* 79.7-8, pp. 348–358.

Bronshtein, I. N., Semendjajew, K. A., Musiol, G. and Mühlig, H. (2007): Handbook of mathematics. 5th ed. Berlin and New York: Springer.

Buhmann, M. D. (2003): Radial basis functions: Theory and implementations. Vol. 12. Cambridge monographs on applied and computational mathematics. Cambridge and New York: Cambridge University Press.

Burden, R. L. and Faires, J. D. (2011): Numerical Analysis. 9. ed. Belmont, Calif.: Brooks/Cole.

Carrera, E., Giunta, G. and Petrolo, M. (2011): Beam structures: Classical and advanced theories. 1st ed. Hoboken, N.J: Wiley.

Chebfun (2021): Chebfun – numerical computing with functions. URL: http://www.chebfun.org/ (Accessed on 27th Jan. 2022).

Chen, H.-P. and Ni, Y.-Q. (2018): Structural health monitoring of large civil engineering structures. Hoboken, NJ: John Wiley & Sons.

Czichos, H., ed. (2013): Handbook of Technical Diagnostics: Fundamentals and application to structures and systems. Heidelberg etc.: Springer.

Daum, W. (2013): "Principles, Concepts and Assessment of Structural Health Monitoring". In: *Handbook of Technical Diagnostics*. Ed. by H. Czichos. Heidelberg etc.: Springer, pp. 413–424.

Dekking, F. M., Kraaikamp, C., Lopuhaä, H. P. and Meester, L. E. (2005): A Modern Introduction to Probability and Statistics: Understanding Why and How. Springer Texts in Statistics. London: Springer.

Dermanis, A. (1976): Probabilistic and deterministic aspects of linear estimation in geodesy. Reports of the Department of Geodetic Science 244. Columbus, Ohio: Ohio State University.

Eichhorn, A. (2005): Ein Beitrag zur Identifikation von dynamischen Strukturmodellen mit Methoden der adaptiven Kalman-Filterung. Doctoral Thesis. Vol. C. No. 585. München: Deutsche Geodätische Kommision (DGK).

Ezhov, N., Neitzel, F. and Petrovic, S. (2018): "Spline approximation, Part 1: Basic methodology". In: *Journal of Applied Geodesy* 12.2, pp. 139–155.

Farrar, C. R. and Worden, K. (2013): Structural health monitoring: A machine learning perspective. West Sussex: John Wiley & Sons Ltd.

Friswell, M. I. and Mottershead, J. E. (2011): Finite element model updating in structural dynamics. Vol. 38. Solid mechanics and its applications. Dordrecht and London: Springer.

Gander, W. (2005): "Change of basis in polynomial interpolation". In: *Numerical Linear Algebra with Applications* 12.8, pp. 769–778.

Gauss, C. F. (1809): Theoria motus corporum coelestium in sectionibus conicis solem ambientium. Hamburg: sumtibus Frid. Perthes et I. H. Besser.

Gentle, J. E. (2009): Computational Statistics. New York, NY: Springer New York.

Gere, J. M. and Goodno, B. J. (2013): Mechanics of materials. 8th edition – SI edition. Stamford, CT: Cengage Learning.

Ghilani, C. D. (2018): Adjustment computations: Spatial data analysis. 6th ed. Hoboken, N.J.: John Wiley & Sons.

Harter, H. L. (1974a): "The Method of Least Squares and Some Alternatives: Part I". In: *International Statistical Review / Revue Internationale de Statistique* 42.2, pp. 147–174.

Harter, H. L. (1974b): "The Method of Least Squares and Some Alternatives: Part II". In: *International Statistical Review / Revue Internationale de Statistique* 42.3, pp. 235–282.

Harter, H. L. (1975a): "The Method of Least Squares and Some Alternatives: Part III". In: *International Statistical Review / Revue Internationale de Statistique* 43.1, pp. 1–44.

Harter, H. L. (1975b): "The Method of Least Squares and Some Alternatives: Part IV". In: *International Statistical Review / Revue Internationale de Statistique* 43.2, pp. 125–190.

Harter, H. L. (1975c): "The Method of Least Squares and Some Alternatives: Part V". In: *International Statistical Review / Revue Internationale de Statistique* 43.3, pp. 269–272.

Hartley, R. and Zisserman, A. (2003): Multiple view geometry in computer vision. 2nd ed. Cambridge, UK and New York: Cambridge University Press.

Heunecke, O., Kuhlmann, H., Welsch, W., Eichhorn, A. and Neuner, H. (2013): Auswertung geodätischer Überwachungsmessungen. 2., neu bearb. und erw. Aufl. Handbuch Ingenieurgeodäsie / Möser et al. (Hrsg.) Berlin u.a.: Wichmann.

Higham, N. J. (2002): Accuracy and stability of numerical algorithms. 2nd ed. Philadelphia: Society for Industrial and Applied Mathematics.

Karbhari, V. M. and Ansari, F. (2011): Structural health monitoring of civil infrastructure systems. Woodhead Publishing in materials. Cambridge, UK and Boca Raton, FL: Woodhead Pub.

Koo, K. Y., Brownjohn, J. M. W., List, D. I. and Cole, R. (2013): "Structural health monitoring of the Tamar suspension bridge". In: *Structural Control and Health Monitoring* 20.4, pp. 609–625.

Kopriva, D. A. (2009): Implementing spectral methods for partial differential equations: Algorithms for scientists and engineers. Scientific computation. Dordrecht: Springer.

Kuhlmann, H., Schwieger, V., Wieser, A. and Niemeier, W. (2014): "Engineering Geodesy - Definition and Core Competencies". In: *Journal of Applied Geodesy* 8.4, pp. 327–334.

Künzel, A. (2016): "Parameteridentifikation auf Basis faseroptisch gemessener quasi-kontinuierlicher Dehnungssignale". Doctoral Thesis. Berlin: Technische Universität Berlin.

Lancaster, P. and Salkauskas, K. (1988): Curve and surface fitting: An Introduction. London - San Diego etc: Academic Press.

Langtangen, H. P. (2016a): Approximation of functions. URL: http://hplgit.github.io/num-methods-for-PDEs/doc/pub/approx/sphinx/index.html (Accessed on 27th Jan. 2022).

Langtangen, H. P. (2016b): Approximation of functions. URL: http://hplgit.github.io/num-methods-for-PDEs/doc/pub/approx/pdf/approx-4print-A4-2up.pdf (Accessed on 27th Jan. 2022).

Legendre, A. M. (1806): Nouvelles méthodes pour la détermination des orbites des comètes: Avec un supplément contenant divers perfectionnemens de ces méthodes et leur application aux deux comètes de 1805. Courcier.

Lenzmann, L. and Lenzmann, E. (2004): "Strenge Auswertung des nichtlinearen Gauß-Helmert-Modells". In: *avn - Allgemeine Vermessungsnachrichten* 111, pp. 68–73.

Lienhart, W. (2007): "Analysis of Inhomogeneous Structural Monitoring Data". Doctoral Thesis. Graz: Graz University of Technology.

Lienhart, W., Ehrhart, M. and Grick, M. (2017): "High frequent total station measurements for the monitoring of bridge vibrations". In: *Journal of Applied Geodesy* 11.1, pp. 1–8.

Ljung, L. (1998): "System Identification". In: *Signal Analysis and Prediction*. Ed. by A. Procházka, J. Uhlíř, P. W. J. Rayner and N. G. Kingsbury. Applied and Numerical Harmonic Analysis. Boston, MA and s.l.: Birkhäuser Boston, pp. 163–173.

Logg, A., Mardal, K.-A. and Wells, G. (2012): Automated Solution of Differential Equations by the Finite Element Method: The FEniCS Book. 2012th ed. Vol. 84. Lecture Notes in Computational Science and Engineering. Berlin, Heidelberg: Springer.

Lopez-Higuera, J. M., Rodriguez Cobo, L., Quintela Incera, A. and Cobo, A. (2011): "Fiber Optic Sensors in Structural Health Monitoring". In: *Journal of Lightwave Technology* 29.4, pp. 587–608.

Luhmann, T., Robson, S., Harley, I. and Kyle, S. (2011): Close range photogrammetry: Principles, techniques and applications. Dunbeath and Hoboken, NJ: Whittles and Distributed in North America by J. Wiley & Sons.

Ma, Q. (2019): "Identification of singularities in the displacement field for damage detection in structures". Doctoral Thesis. Sevilla: Universidad de Sevilla.

Mason, J. C. and Handscomb, D. C. (2003): Chebyshev polynomials. Boca Raton, Fla.: Chapman & Hall/CRC.

Meng, X., Roberts, G. W., Dodson, A. H., Cosser, E., Barnes, J. and Rizos, C. (2004): "Impact of GPS satellite and pseudolite geometry on structural deformation monitoring: analytical and empirical studies". In: *Journal of Geodesy* 77.12, pp. 809–822.

Merriman, M. (1877): "On the History of the Method of Least Squares". In: *The Analyst* 4.2, p. 33.

Mikhail, E. M. and Ackermann, F. E. (1976): Observations and least squares. IEP series in civil engineering. New York: IEP.

Montgomery, D. C. and Runger, G. C. (2011): Applied statistics and probability for engineers. 5th ed. Hoboken, NJ: Wiley.

Moritz, H. and Sünkel, H. (1978): Approximation Methods in Geodesy: Band 10. 1. Auflage. Karlsruhe: Wichmann.

Müller, W. H. and Ferber, F. (2012): Technische Mechanik für Ingenieure. 4., aktualisierte Aufl. München: Fachbuchverl. Leipzig im Carl-Hanser-Verl.

Natke, H. G. (1992): Einführung in Theorie und Praxis der Zeitreihen- und Modalanalyse. Wiesbaden: Vieweg+Teubner Verlag.

Neitzel, F. (2010): "Generalization of total least-squares on example of unweighted and weighted 2D similarity transformation". In: *Journal of Geodesy* 84.12, pp. 751–762.

Neitzel, F., Niemeier, W., Weisbrich, S. and Lehmann, M. (2012): "GBSAR, TLS und Beschleunigungsmessungen für Schwingungsuntersuchungen". In: *Interdisziplinäre Messaufgaben im Bauwesen – Weimar 2012. Beiträge zum 115. DVW-Seminar am 25. und 26. September 2012 in Weimar*. Vol. DVW-Schriftenreihe Band 68/2012. Wißner-Verlag, pp. 121–148.

Neitzel, F., Resnik, B., Weisbrich, S. and Friedrich, A. (2011): "Vibration monitoring of bridges". In: *Reports on Geodesy No.1 (90), Proceedings of the X-th Scientific and Technical Conference on Current Problems in Engineering Surveying, Warsaw, Poland, March 24-25*, pp. 331–340.

Neitzel, F., Weisbrich, S. and Wu, C.-C. (2014): "Integration der Finite-Elemente-Methode in die Ausgleichungsrechnung zur Parameteridentifikation". In: *Ingenieurvermessung 14*. Ed. by A. Wieser. Berlin: Wichmann, H, pp. 301–310.

Niemeier, W. (2008): Ausgleichungsrechnung: Statistische Auswertemethoden. 2., überarb. und erw. Aufl. De Gruyter Lehrbuch. Berlin [u.a.]: De Gruyter.

Öchsner, A. (2021): Classical Beam Theories of Structural Mechanics. Cham: Springer International Publishing.

Olver, S. and Townsend, A. (2013): "A Fast and Well-Conditioned Spectral Method". In: *SIAM Review* 55.3, pp. 462–489.

Omidalizarandi, M., Herrmann, R., Kargoll, B., Marx, S., Paffenholz, J.-A. and Neumann, I. (2020): "A validated robust and automatic procedure for vibration analysis of bridge structures using MEMS accelerometers". In: *Journal of Applied Geodesy* 14.3, pp. 327–354.

Orszag, S. A. (1971): "Accurate solution of the Orr–Sommerfeld stability equation". In: *Journal of Fluid Mechanics* 50.04, p. 689.

Ouellet, J.-N. and Hébert, P. (2009): "Precise ellipse estimation without contour point extraction". In: *Machine Vision and Applications* 21.1, pp. 59–67.

Piegl, L. and Tiller, W. (1997): The NURBS book. 2nd ed. Berlin: Springer.

Plackett, R. L. (1972): "Studies in the History of Probability and Statistics. XXIX: The Discovery of the Method of Least Squares". In: *Biometrika* 59.2, pp. 239–251.

Quarteroni, A. and Rozza, G., eds. (2014): Reduced order methods for modeling and computational reduction. Vol. volume 9. MS&A: Modeling, simulation & applications. Cham: Springer.

Radhakrishna Rao, C. and Toutenburg, H. (1999): Linear Models: Least Squares and Alternatives. Second Edition. Springer Series in Statistics. New York: Springer-Verlag.

Reimer, M. (2003): Multivariate Polynomial Approximation. Vol. 144. International Series of Numerical Mathematics. Basel: Birkhäuser.

Rivlin, T. J. (1974): The Chebyshev polynomials. Pure and applied mathematics. New York: Wiley.

Schaback, R. (2015): "Multivariate Approximation". In: *Encyclopedia of applied and computational mathematics*. Ed. by B. Engquist. Berlin and Heidelberg: Springer, pp. 1014–1017.

Schill, F. J. (2018): Überwachung von Tragwerken mit Profilscannern. Doctoral Thesis. Vol. C. No. 844. München: Ausschuss Geodäsie der Bayerischen Akademie der Wissenschaften (DGK).

Schwintzer, P. (1984): "Zur Bestimmung von signifikanten Parametern in Approximationsfunktion". In: *Beiträge aus dem Institut für Geodäsie*. Ed. by W. Caspary, A. Schödlbauer and W. Welsch, pp. 71–91.

Shampine, L. F. (2008): "Vectorized adaptive quadrature in MATLAB". In: *Journal of Computational and Applied Mathematics* 211.2, pp. 131–140.

Sheynin, O. (2014): "C.F. Gauss and the method of least squares". In: *Śląski Przegląd Statystyczny* 12 (18).

Šolin, P. (2006): Partial differential equations and the finite element method. Pure and applied mathematics. Hoboken, N.J.: Wiley-Interscience.

Stephan, C. (2016): Entwicklung eines Verfahrens zur photogrammetrischen Verformungsmessung mittels handelsüblicher Digitalkamera und Systemidentifikation mit der Methode der inversen finiten Elemente. Wuppertal: Universitätsbibliothek Wuppertal.

Stigler, S. M. (1981): "Gauss and the Invention of Least Squares". In: *The Annals of Statistics* 9.3.

Structural Vibration Solutions A/S (2021): ARTeMIS Modal. Ed. by Structural Vibration Solutions A/S. url: https://svibs.com/artemis-modal/ (Accessed on 27th Jan. 2022).

Süli, E. and Mayers, D. F. (2003): An Introduction to Numerical Analysis. Cambridge and New York: Cambridge University Press.

Tesky, F. W. (1988): Integrierte Analyse geodätischer und geotechnischer Daten sowie physikalischer Modelldaten zur Beschreibung des Deformationsverhaltens großer Erddämme unter statischer Belastung. Docotral Thesis. Vol. C. No. 341. München: Deutsche Geodätische Kommision (DGK).

Teunissen, P. J. G. (2000): Adjustment theory: An introduction. Series on mathematical geodesy and positioning. Delft: Delft University Press.

Townsend, A. (2014): "Computing with functions in two dimensions". PhD Thesis. University of Oxford.

Townsend, A. and Olver, S. (2015): "The automatic solution of partial differential equations using a global spectral method". In: *Journal of Computational Physics* 299, pp. 106–123.

Trefethen, L. N. (2008): Spectral methods in MATLAB. 3rd repr. Software, environments, tools. Philadelphia: SIAM.

Trefethen, L. N. (2013): Approximation theory and approximation practice. Philadelphia, Pa.: SIAM.

Trefethen, L. N. and Bau, D. (1997): Numerical linear algebra. Philadelphia: Society for Industrial and Applied Mathematics.

Weisbrich, S. and Neitzel, F. (2014): "Einsatz von Evolutionsstrategien in der Zeitreihenanalyse". In: *Zeitabhängige Messgrößen – Ihre Daten haben (Mehr-)Wert. Beiträge zum 129. DVW-Seminar am 26. und 27. Februar 2014 in Hannover*. Vol. DVW-Schriftenreihe Band 74. Wißner-Verlag, pp. 271–293.

Wendland, H. (2004): Scattered Data Approximation. Vol. no. 17. Cambridge monographs on applied and computational mathematics. Cambridge: Cambridge University Press.

Wenzel, H. (2009): Health monitoring of bridges. Chichester: Wiley.

Wenzel, H. and Pichler, D. (2005): Ambient vibration monitoring. Chichester: Wiley.

Wolfram Research, Inc. (2021): Wolfram|Alpha. Ed. by Wolfram Research, Inc. Champaign, Illinois. URL: https://www.wolframalpha.com/ (Accessed on 27th Jan. 2022).

Worden, K., Farrar, C. R., Manson, G. and Park, G. (2007): "The fundamental axioms of structural health monitoring". In: *Proceedings of the Royal Society A: Mathematical, Physical and Engineering Sciences* 463.2082, pp. 1639–1664.

Wu, C.-C. (2020): The Measurement- and Model-based Structural Analysis for Damage Detection. Doctoral Thesis. Vol. C. No. 844. München: Ausschuss Geodäsie der Bayerischen Akademie der Wissenschaften (DGK).

Wu, C.-C., Weisbrich, S. and Neitzel, F. (2016): "Inverse Finite Element Adjustment of Material Parameters from Integrated Analysis of Displacement Field Measurement". In: *Materials Today: Proceedings* 3.4, pp. 1211–1215.

Wu, C.-C., Weisbrich, S. and Neitzel, F. (2017): "Approximate model for geometrical complex structures". In: *Materials Today: Proceedings* 4.5, pp. 5995–6000.

Wujanz, D. (2016): Terrestrial laser scanning for geodetic deformation monitoring. Doctoral Thesis. Vol. C. No. 775. München: Ausschuss Geodäsie der Bayerischen Akademie der Wissenschaften (DGK).

Zienkiewicz, O. C., Taylor, R. L. and Zhu, J. Z. (2013): The finite element method: Its basis and fundamentals. 7th ed. Kidlington, Oxford, UK and Waltham, MA: Butterworth-Heinemann.

APPENDIX

A

DISCRETE MEASUREMENTS VS. FUNCTIONS

In the following we will present the detailed calculation of the comparison from Section 9.1 for the specification of the four-point bending test set-up and beam specimen which was used for the numerical studies and is given again in Table A-1.

beam length l	7.26 m	beam elastic modulus	70 GPa
beam width w	0.20 m	load F	7460 N
beam height h	0.36 m	loading position a	2.42 m

Table A-1: Specification of the four-point bending set-up and beam specimen for the numerical studies.

The unique identifier for the nodes ν and elements ζ for this specification are listed Table A-2.

ν	x_ν
1	0.00
2	2.42
3	4.84
4	7.26

and

ζ	ν_1	ν_2
1	1	2
2	2	3
3	3	4

Table A-2: Coordinates for all nodes ν and the nodes for all three elements ζ for specification of the four-point bending test set-up in Table A-1.

Furthermore, the 24 equidistant and uncorrelated displacement measurements of high precision of the example from Section 9.1 are again listed in Table A-3, with 8 measurements for each of the three elements according to the beam specification.

1st element			2nd element			3rd element		
i	x_i [m]	L_{disp_i} [µm]	i	x_i [m]	L_{disp_i} [µm]	i	x_i [m]	L_{disp_i} [µm]
1	0.0000	−0.6	9	2.5252	−829.7	17	5.0504	−765.4
2	0.3157	−125.2	10	2.8409	−878.5	18	5.3661	−683.7
3	0.6313	−251.2	11	3.1565	−912.9	19	5.6817	−587.4
4	0.9470	−371.4	12	3.4722	−927.9	20	5.9974	−481.8
5	1.2626	−484.5	13	3.7878	−930.1	21	6.3130	−370.6
6	1.5783	−589.0	14	4.1035	−911.3	22	6.6287	−249.9
7	1.8939	−683.0	15	4.4191	−879.3	23	6.9443	−124.7
8	2.2096	−763.4	16	4.7348	−829.4	24	7.2600	1.6

Table A-3: 24 equidistant displacement measurements of high precision.

Before we can determine the unknown solution $\mathbf{e}$ for the inverse of the elastic modulus $E^*(x)$ based on these measurements, we have to map them onto the interval $[-1,1]$ of the corresponding element by applying (8-6) with the nodes according to Table A-2. For the first element this mapping reads

$$t = f_t\left(x, {}^{\zeta}x_{\nu_1}, {}^{\zeta}x_{\nu_2}\right) = \frac{2x - {}^{\zeta}x_{\nu_1} - {}^{\zeta}x_{\nu_2}}{{}^{\zeta}x_{\nu_2} - {}^{\zeta}x_{\nu_1}}$$
$$= \frac{2x - 0.00 - 2.42}{2.42 - 0.00} = \frac{2x - 2.42}{2.42} \tag{A-1}$$

For the sake of clarity, we will omit the units for all values in formulas in this chapter.

and for the other two elements, the functions for mapping the positions on $[-1, 1]$ can be derived in the same way. The mapped positions t_i of the 24 equidistant displacement measurements are listed in Table A-4.

Table A-4: Mapped position t_i of the 24 equidistant displacement measurements of high precision from Table A-3.

1st element			2nd element			3rd element		
i	x_i [m]	t_i	i	x_i [m]	t_i	i	x_i [m]	t_i
1	0.0000	−1.0000	9	2.5252	−0.9130	17	5.0504	−0.8261
2	0.3157	−0.7391	10	2.8409	−0.6522	18	5.3661	−0.5652
3	0.6313	−0.4783	11	3.1565	−0.3913	19	5.6817	−0.3043
4	0.9470	−0.2174	12	3.4722	−0.1304	20	5.9974	−0.0435
5	1.2626	0.0435	13	3.7878	0.1304	21	6.3130	0.2174
6	1.5783	0.3043	14	4.1035	0.3913	22	6.6287	0.4783
7	1.8939	0.5652	15	4.4191	0.6522	23	6.9443	0.7391
8	2.2096	0.8261	16	4.7348	0.9130	24	7.2600	1.0000

In the following we use these measurements to determine the unknown solution $\mathbf{e}$ for each element and we choose a polynomial degree $p_\mathrm{e} = 3$. Consequently, we choose a polynomial degree $p_\mathrm{u} = 5$ for each element of the unknown solution of the bending line $u(x)$.

At first, we approximate the displacements according to the first step in Section 8.2.4 and the functional model is already given by (8-55). For the measurements and their mapped positions given in Table A-3 and A-4 the functional model for each element ζ results in

$$ {}^{\zeta}\mathbf{L}_\mathrm{disp} = {}^{\zeta}\mathbf{A}_\phi \, {}^{\zeta}\mathbf{u} \tag{A-2} $$

and explicitly reads for the first element

$$ {}^{1}\mathbf{L}_\mathrm{disp} = \begin{bmatrix} -0.0000006 \\ -0.0001252 \\ -0.0002512 \\ -0.0003714 \\ -0.0004845 \\ -0.0005890 \\ -0.0006830 \\ -0.0007634 \end{bmatrix}, \quad {}^{1}\mathbf{u} = \begin{bmatrix} {}^{1}u_0 \\ {}^{1}u_1 \\ {}^{1}u_2 \\ {}^{1}u_3 \\ {}^{1}u_4 \\ {}^{1}u_5 \end{bmatrix} \tag{A-3} $$

and

$$ {}^{1}\mathbf{A}_\phi = \begin{bmatrix} 1 & -1 & 1 & -1 & 1 & -1 \\ 1 & -0.739130434782609 & 0.092627599243857 & 0.602202679378646 & -0.982840255716639 & 0.850691611680733 \\ 1 & -0.478260869565217 & -0.542533081285444 & 0.997205556012164 & -0.411315711421843 & -0.603773136391271 \\ 1 & -0.217391304347826 & -0.905482041587902 & 0.611079148516478 & 0.639795455276389 & -0.889251085593170 \\ 1 & 0.043478260869565 & -0.996219281663516 & -0.130106024492479 & 0.984905714316344 & 0.215749999650423 \\ 1 & 0.304347826086956 & -0.814744801512288 & -0.800279444398783 & 0.327618183182594 & 0.999699208075145 \\ 1 & 0.565217391304348 & -0.361058601134215 & -0.973370592586504 & -0.739273373094007 & 0.137670257784583 \\ 1 & 0.826086956521739 & 0.364839319470700 & -0.223308950439713 & -0.733784541936313 & -0.989030727542022 \end{bmatrix}. \tag{A-4} $$

Since the vector of observations ${}^{\zeta}\mathbf{L}_\mathrm{disp}$ and vector of unknowns ${}^{\zeta}\mathbf{u}$ for the second and third element can be set up analogous to (A-3), the corresponding design matrices ${}^{\zeta}\mathbf{A}_\phi$ for the remaining two elements are

$$
{}^{2}\mathbf{A}_{\phi} = \begin{bmatrix}
1 & -0.913043478260870 & 0.667296786389414 & -0.305498479493712 & -0.109429997748721 & 0.505327171034855 \\
1 & -0.652173913043478 & -0.149338374291116 & 0.846963096901456 & -0.955396099928173 & 0.399205729091812 \\
1 & -0.391304347826087 & -0.693761814744801 & 0.934248376756801 & -0.037389088804000 & -0.904987350736279 \\
1 & -0.130434782608696 & -0.965973534971645 & 0.382427878688255 & 0.866209740531230 & -0.608395637087706 \\
1 & 0.130434782608696 & -0.965973534971645 & -0.382427878688255 & 0.866209740531230 & 0.608395637087708 \\
1 & 0.391304347826087 & -0.693761814744802 & -0.934248376756801 & -0.037389088803999 & 0.904987350736280 \\
1 & 0.652173913043479 & -0.149338374291114 & -0.846963096901454 & -0.955396099928174 & -0.399205729091817 \\
1 & 0.913043478260870 & 0.667296786389413 & 0.305498479493713 & -0.109429997748721 & -0.505327171034856
\end{bmatrix}, \tag{A-5}
$$

and

$$
{}^{3}\mathbf{A}_{\phi} = \begin{bmatrix}
1 & -0.826086956521739 & 0.364839319470700 & 0.223308950439713 & -0.733784541936313 & 0.989030727542022 \\
1 & -0.565217391304348 & -0.361058601134216 & 0.973370592586505 & -0.739273373094007 & -0.137670257784585 \\
1 & -0.304347826086956 & -0.814744801512288 & 0.800279444398782 & 0.327618183182596 & -0.999699208075144 \\
1 & -0.043478260869565 & -0.996219281663516 & 0.130106024492478 & 0.984905714316344 & -0.215749999650421 \\
1 & 0.217391304347825 & -0.905482041587902 & -0.611079148516477 & 0.639795455276391 & 0.889251085593168 \\
1 & 0.478260869565218 & -0.542533081285443 & -0.997205556012164 & -0.411315711421845 & 0.603773136391269 \\
1 & 0.739130434782609 & 0.092627599243857 & -0.602202679378646 & -0.982840255716639 & -0.850691611680733 \\
1 & 1 & 1 & 1 & 1 & 1
\end{bmatrix}. \tag{A-6}
$$

The three equation systems (A-2) can be combined into

$$
\begin{bmatrix} {}^{1}\mathbf{L}_{\text{disp}} \\ {}^{2}\mathbf{L}_{\text{disp}} \\ {}^{3}\mathbf{L}_{\text{disp}} \end{bmatrix} = \begin{bmatrix} {}^{1}\mathbf{A}_{\phi} & \mathbf{0} & \mathbf{0} \\ \mathbf{0} & {}^{2}\mathbf{A}_{\phi} & \mathbf{0} \\ \mathbf{0} & \mathbf{0} & {}^{3}\mathbf{A}_{\phi} \end{bmatrix} \begin{bmatrix} {}^{1}\mathbf{u} \\ {}^{2}\mathbf{u} \\ {}^{3}\mathbf{u} \end{bmatrix}, \tag{A-7}
$$

or in short

$$
\mathbf{L}_{\text{disp}} = \mathbf{A}_{\phi}\,\mathbf{u}\,. \tag{A-8}
$$

The standard deviation of the 24 uncorrelated displacement measurements of high precision according to Table 9-2 is given by $\sigma_{L_{\text{disp}}} = 0.93\,\mu\text{m}$ and choosing the same value for the theoretical reference standard deviation σ_0 results in an identity matrix $\mathbf{I}$ for the weight matrix

$$
\mathbf{P}_{\text{disp}} = \begin{bmatrix} {}^{1}\mathbf{P}_{\text{disp}} & \mathbf{0} & \mathbf{0} \\ \mathbf{0} & {}^{2}\mathbf{P}_{\text{disp}} & \mathbf{0} \\ \mathbf{0} & \mathbf{0} & {}^{3}\mathbf{P}_{\text{disp}} \end{bmatrix} = \mathbf{I}\,. \tag{A-9}
$$

The normal equation system for a least squares adjustment according to (2-17) results in

$$
\begin{aligned}
\mathbf{N}\,\mathbf{u} &= \mathbf{n} \\
\mathbf{A}_{\phi}^{\mathsf{T}}\,\mathbf{P}_{\text{disp}}\,\mathbf{A}_{\phi}\,\mathbf{u} &= \mathbf{A}_{\phi}^{\mathsf{T}}\,\mathbf{P}_{\text{disp}}\,\mathbf{L}_{\text{disp}}
\end{aligned} \tag{A-10}
$$

and introducing the constraints (7-24) at the two inner nodes in Table A-2 for a C^2 continuous approximation of the displacements yields the extended normal equation system

$$
\begin{bmatrix} \mathbf{A}_{\phi}^{\mathsf{T}}\,\mathbf{P}_{\text{disp}}\,\mathbf{A}_{\phi} & \mathbf{C}_{\text{conti}}^{\mathsf{T}} \\ \mathbf{C}_{\text{conti}} & \mathbf{0} \end{bmatrix} \begin{bmatrix} \mathbf{u} \\ \boldsymbol{\lambda} \end{bmatrix} = \begin{bmatrix} \mathbf{A}_{\phi}^{\mathsf{T}}\,\mathbf{P}_{\text{disp}}\,\mathbf{L}_{\text{disp}} \\ \mathbf{0} \end{bmatrix}, \tag{A-11}
$$

with

$$\mathbf{C}_{\text{conti}} = \begin{bmatrix} 1 & 1 & 1 & 1 & 1 & 1 & -1 & 1 & -1 & 1 & -1 & 1 & 0 & 0 & 0 & 0 & 0 & 0 \\ 0 & 0 & 0 & 0 & 0 & 0 & 1 & 1 & 1 & 1 & 1 & 1 & -1 & 1 & -1 & 1 & -1 & 1 \\ 0 & 0.04 & 0.16 & 0.36 & 0.64 & 1 & 0 & -0.04 & 0.16 & -0.36 & 0.64 & -1 & 0 & 0 & 0 & 0 & 0 & 0 \\ 0 & 0 & 0 & 0 & 0 & 0 & 0 & 0.04 & 0.16 & 0.36 & 0.64 & 1 & 0 & -0.04 & 0.16 & -0.36 & 0.64 & -1 \\ 0 & 0 & 0.02 & 0.12 & 0.4 & 1 & 0 & 0 & -0.02 & 0.12 & -0.4 & 1 & 0 & 0 & 0 & 0 & 0 & 0 \\ 0 & 0 & 0 & 0 & 0 & 0 & 0 & 0 & 0.02 & 0.12 & 0.4 & 1 & 0 & 0 & -0.02 & 0.12 & -0.4 & 1 \end{bmatrix}, \tag{A-12}$$

where each line has been normalized to ± 1. Solving (A-11) yields the unknown coefficients $\mathbf{u}$ of a C^2 continuous approximation of the displacements, which are

$${}^1\mathbf{u} = \begin{bmatrix} -0.000\,435\,174\,747\,739 \\ -0.000\,409\,714\,903\,599 \\ 0.000\,030\,873\,625\,874 \\ 0.000\,005\,246\,075\,917 \\ -0.000\,000\,502\,460\,158 \\ 0.000\,000\,135\,802\,966 \end{bmatrix}, \; {}^2\mathbf{u} = \begin{bmatrix} -0.000\,870\,244\,681\,219 \\ -0.000\,000\,364\,653\,125 \\ 0.000\,060\,489\,091\,286 \\ -0.000\,000\,283\,890\,813 \\ 0.000\,000\,054\,112\,415 \\ 0.000\,000\,083\,673\,159 \end{bmatrix} \text{ and } {}^3\mathbf{u} = \begin{bmatrix} -0.000\,434\,651\,922\,078 \\ 0.000\,410\,976\,779\,215 \\ 0.000\,030\,151\,025\,497 \\ -0.000\,004\,966\,110\,086 \\ 0.000\,000\,271\,896\,800 \\ 0.000\,000\,026\,679\,387 \end{bmatrix}. \tag{A-13}$$

A.1 SOLUTION OF THE BVP IN THE CHEBYSHEV BASIS

The functional model for the integrated analysis is based on the solution (8-3) of the BVP in the Chebyshev basis for the specification of the four-point bending test set-up listed in Table A-1 and reads

$$\begin{bmatrix} \mathbf{U} \\ \mathbf{\Lambda} \end{bmatrix} = \begin{bmatrix} \boldsymbol{\mathcal{L}} & \mathbf{C}^{\mathsf{T}} \\ \mathbf{C} & \mathbf{0} \end{bmatrix}^{-1} \begin{bmatrix} -\frac{1}{I}\boldsymbol{\mathcal{M}} \\ \mathbf{0} \end{bmatrix}, \tag{A-14}$$

with area moment of inertia

$$I = \frac{1}{12} w h^3 = 0.0007776\,. \tag{A-15}$$

According to Section 7.3, the matrices in (A-14) result in

$$\boldsymbol{\mathcal{L}} = \begin{bmatrix} {}^1J^2\boldsymbol{\mathcal{L}}_{\text{xx}} & \mathbf{0} & \mathbf{0} \\ \mathbf{0} & {}^2J^2\boldsymbol{\mathcal{L}}_{\text{xx}} & \mathbf{0} \\ \mathbf{0} & \mathbf{0} & {}^3J^2\boldsymbol{\mathcal{L}}_{\text{xx}} \end{bmatrix}, \tag{A-16}$$

with

$${}^\zeta J = \frac{2}{{}^\zeta x_{\nu_2} - {}^\zeta x_{\nu_1}} = \frac{1}{1.21}, \tag{A-17}$$

for all ζ, see Section 3.2. The differential operator according to Section 5.1.2 yields

$$\boldsymbol{\mathcal{L}}_{\text{xx}} = \begin{bmatrix} 0 & 0 & 4 & 0 & 32 & 0 \\ 0 & 0 & 0 & 24 & 0 & 120 \\ 0 & 0 & 0 & 0 & 48 & 0 \\ 0 & 0 & 0 & 0 & 0 & 80 \\ 0 & 0 & 0 & 0 & 0 & 0 \\ 0 & 0 & 0 & 0 & 0 & 0 \end{bmatrix} \tag{A-18}$$

and the multiplication operator for the bending moment in the Chebyshev basis reads

$$\boldsymbol{\mathcal{M}} = \begin{bmatrix} \boldsymbol{\mathcal{M}}[{}^1\mathbf{m}] & \mathbf{0} & \mathbf{0} \\ \mathbf{0} & \boldsymbol{\mathcal{M}}[{}^2\mathbf{m}] & \mathbf{0} \\ \mathbf{0} & \mathbf{0} & \boldsymbol{\mathcal{M}}[{}^3\mathbf{m}] \end{bmatrix}, \tag{A-19}$$

with

$${}^1\mathbf{m} = \begin{bmatrix} 4513.3 \\ 4513.3 \\ 0.0 \\ 0.0 \\ 0.0 \\ 0.0 \end{bmatrix}, \quad {}^2\mathbf{m} = \begin{bmatrix} 9026.6 \\ 0.0 \\ 0.0 \\ 0.0 \\ 0.0 \\ 0.0 \end{bmatrix} \quad \text{and} \quad {}^3\mathbf{m} = \begin{bmatrix} 4513.3 \\ -4513.3 \\ 0.0 \\ 0.0 \\ 0.0 \\ 0.0 \end{bmatrix}. \tag{A-20}$$

Matrix $\mathbf{C}$ in (A-14) reads according to (7-27)

$$\mathbf{C} = \begin{bmatrix} \mathbf{C}_{\text{BC}} \\ \mathbf{C}_{\text{conti}} \end{bmatrix}, \tag{A-21}$$

with

$$\mathbf{C}_{\text{BC}} = \begin{bmatrix} 1 & -1 & 1 & -1 & 1 & -1 & 0 & 0 & 0 & 0 & 0 & 0 & 0 & 0 & 0 & 0 & 0 & 0 \\ 0 & 0 & 0 & 0 & 0 & 0 & 0 & 0 & 0 & 0 & 0 & 0 & 1 & 1 & 1 & 1 & 1 & 1 \end{bmatrix} \tag{A-22}$$

and $\mathbf{C}_{\text{conti}}$ is given by (A-12). Solving (A-14) yields

$$\mathbf{U} = \begin{bmatrix} {}^1\mathbf{U} \\ {}^2\mathbf{U} \\ {}^3\mathbf{U} \end{bmatrix}, \tag{A-23}$$

with

$$\begin{aligned} {}^1\mathbf{U} &= \begin{bmatrix} {}^{11}\mathbf{U} & {}^{12}\mathbf{U} & {}^{13}\mathbf{U} \end{bmatrix}, \\ {}^2\mathbf{U} &= \begin{bmatrix} {}^{21}\mathbf{U} & {}^{22}\mathbf{U} & {}^{23}\mathbf{U} \end{bmatrix}, \\ {}^3\mathbf{U} &= \begin{bmatrix} {}^{31}\mathbf{U} & {}^{32}\mathbf{U} & {}^{33}\mathbf{U} \end{bmatrix}. \end{aligned} \tag{A-24}$$

The 9 submatrices in (A-24) are

$${}^{11}\mathbf{U} = \begin{bmatrix} -10345715.58964359 & -4887031.872427874 & 2082379.446525393 & 3307235.088281441 & 1779483.857843914 & -573458.3488636302 \\ -8718318.051372554 & -4941499.047028706 & 735532.0188756472 & 2741790.777259978 & 1572984.722444413 & -549468.6618478659 \\ 2015939.950204016 & 245556.0419178382 & -1524827.866368344 & -983976.1455636623 & -256349.4856115345 & 124857.480980551 \\ 399437.6556318913 & 399437.6556318913 & -43158.32143965364 & -519234.2318691599 & -232117.3169278467 & 110619.2462357254 \\ -24905.31096108862 & 63613.88445322034 & 152133.0798675295 & 6811.53977183243 & -106793.1495909436 & -12047.6264363625 \\ -35800.55466000026 & -35800.55466000027 & 17310.96258858512 & 107513.9370987938 & 75473.81712486954 & -21799.07870730117 \end{bmatrix}, \tag{A-25}$$

$${}^{12}\mathbf{U} = \begin{bmatrix} -15242032.16875645 & 2306829.070937842 & 7418881.85730664 & -714626.1325372444 & -2487919.576577622 & 526735.0815575167 \\ -15118040.56665488 & 2144847.933009133 & 7542873.459408216 & -876607.2704659516 & -2279008.861741687 & 446467.3687312375 \\ 83417.41103458252 & -133624.0684442123 & 83417.41103458584 & -133624.0684442107 & 285087.9465154848 & -123904.1692700929 \\ -54983.93684446609 & 35737.81110484458 & -54983.93684446609 & 35737.81110484459 & 119006.3290606252 & -66762.94382223717 \\ 24173.16059043959 & -25637.4613317378 & 24173.16059043946 & -25637.46133173782 & 5884.411049279352 & 1202.714796797653 \\ 38582.90636791472 & -33018.20295208581 & 38582.90636791472 & -33018.20295208582 & -36944.68633179535 & 24329.20217522113 \end{bmatrix}, \tag{A-26}$$

$$
{}^{13}\mathbf{U} = \begin{bmatrix}
-4862855.464122241 & 2974445.961950317 & -330672.6589096251 & -687304.3788272543 & 646008.0019119057 & 121108.1093380563 \\
-4843860.696208674 & 2955451.19403675 & -311677.890996057 & -698636.0621000712 & 642013.5159032156 & 129851.2873251376 \\
25103.32870481401 & -25103.32870481402 & 25103.32870481536 & -13872.13997947222 & -8590.237471218481 & 14866.0696474215 \\
9623.062869810752 & -9623.062869810752 & 9623.062869810745 & -4124.65743734581 & -6872.15342758403 & 9277.919145036705 \\
732.1503706491042 & -732.1503706491382 & 732.1503706491128 & -702.85313809734 & 644.2586729937631 & -461.2210803314819 \\
-2782.351707914459 & 2782.35170791446 & -2782.351707914454 & 881.3475925931538 & 2920.660638049427 & -3616.248565028034
\end{bmatrix}, \quad \text{(A-27)}
$$

$$
{}^{21}\mathbf{U} = \begin{bmatrix}
-13451815.44146978 & -7786586.934954012 & 144732.9741680761 & 2825271.685150603 & 1954597.749948288 & -630938.3215258291 \\
3507872.339619947 & 1619462.837448024 & -1024310.465592675 & -1620977.27628399 & -737060.4452775045 & 368801.4470980304 \\
218994.2416099797 & 218994.2416099799 & 218994.2416099795 & 180157.128684736 & 102482.9028342489 & 47734.34243175392 \\
35737.81110484458 & 35737.81110484461 & 35737.8111048446 & 7756.283179347966 & -48206.77267164475 & -57141.22544785592 \\
41120.26441236397 & 41120.26441236395 & 41120.26441236398 & 26521.04059910193 & -2677.407027422099 & -12957.47313051308 \\
-25949.18537090776 & -25949.18537090776 & -25949.18537090776 & -14970.11744014057 & 6988.018421393717 & 13475.31476412066
\end{bmatrix}, \quad \text{(A-28)}
$$

$$
{}^{22}\mathbf{U} = \begin{bmatrix}
-33997575.56210501 & 0.000000001862645 & 18051711.34150867 & -0.000000006053596 & -4797164.896054927 & 0.000000001979060 \\
0.000000001818065 & -5022865.897106128 & 0.000000005454197 & 2577982.349135872 & -0.000000000681774 & -987831.3894498016 \\
3810932.896666873 & -0.000000000140862 & -3270602.736477847 & -0.000000000281725 & 462938.3860689035 & -0.000000000246509 \\
-0.000000000121745 & 779629.1855241609 & -0.000000000194792 & -990754.7227620186 & 0.000000000048698 & 220550.8940127617 \\
-82240.52882472797 & -0.000000000008285 & 271836.2528325081 & 0.000000000020713 & -59667.92803969242 & 0.000000000021749 \\
0.000000000011451 & -51898.37074181549 & 0.000000000011451 & 160547.698252526 & -0.000000000005326 & -40786.75873140126
\end{bmatrix}, \quad \text{(A-29)}
$$

$$
{}^{23}\mathbf{U} = \begin{bmatrix}
-13451815.44146978 & 7786586.934954009 & 144732.9741680729 & -2825271.685150594 & 1954597.749948289 & 630938.321525828 \\
-3507872.339619949 & 1619462.837448022 & 1024310.465592674 & -1620977.276283992 & 737060.4452775029 & 368801.4470980299 \\
218994.24160998 & -218994.2416099797 & 218994.2416099794 & -180157.1286847354 & 102482.9028342491 & -47734.34243175387 \\
-35737.81110484424 & 35737.81110484451 & -35737.81110484464 & 7756.28317934779 & 48206.77267164487 & -57141.2254478559 \\
41120.26441236394 & -41120.26441236395 & 41120.26441236397 & -26521.04059910202 & -2677.407027422129 & 12957.47313051308 \\
25949.18537090773 & -25949.18537090775 & 25949.18537090774 & -14970.11744014053 & -6988.018421393731 & 13475.31476412066
\end{bmatrix}, \quad \text{(A-30)}
$$

$$
{}^{31}\mathbf{U} = \begin{bmatrix}
-4862855.464122242 & -2974445.961950318 & -330672.6589096229 & 687304.3788272609 & 646008.001911904 & -121108.1093380565 \\
4843860.696208675 & 2955451.194036751 & 311677.8909960556 & -698636.062100076 & -642013.5159032145 & 129851.2873251379 \\
25103.32870481451 & 25103.32870481453 & 25103.32870481453 & 13872.13997947037 & -8590.237471217933 & -14866.06964742157 \\
-9623.06286981075 & -9623.062869810758 & -9623.062869810758 & -4124.657437345821 & 6872.153427584026 & 9277.91914503672 \\
732.1503706491261 & 732.1503706491278 & 732.1503706491278 & 702.8531380973415 & 644.2586729937652 & 461.221080331482 \\
2782.35170791446 & 2782.351707914463 & 2782.351707914463 & 881.3475925931648 & -2920.660638049421 & -3616.248565028039
\end{bmatrix}, \quad \text{(A-31)}
$$

$$
{}^{32}\mathbf{U} = \begin{bmatrix}
-15242032.16875646 & -2306829.070937841 & 7418881.857306645 & 714626.1325372359 & -2487919.576577623 & -526735.0815575151 \\
15118040.56665488 & 2144847.933009131 & -7542873.45940822 & -876607.2704659452 & 2279008.861741689 & 446467.3687312357 \\
83417.41103458381 & 133624.0684442129 & 83417.41103458381 & 133624.0684442129 & 285087.946515485 & 123904.169270093 \\
54983.93684446609 & 35737.81110484458 & 54983.93684446609 & 35737.81110484459 & -119006.3290606252 & -66762.94382223711 \\
24173.1605904395 & 25637.46133173776 & 24173.1605904395 & 25637.46133173776 & 5884.411049279331 & -1202.714796797666 \\
-38582.90636791472 & -33018.20295208581 & -38582.90636791472 & -33018.20295208581 & 36944.68633179535 & 24329.20217522111
\end{bmatrix} \quad \text{(A-32)}
$$

$$
{}^{33}\mathbf{U} = \begin{bmatrix}
-10345715.58964359 & 4887031.872427871 & 2082379.44652539 & -3307235.088281438 & 1779483.857843913 & 573458.3488636292 \\
8718318.051372554 & -4941499.047028704 & -735532.0188756455 & 2741790.777259975 & -1572984.722444412 & -549468.6618478651 \\
2015939.950204017 & -245556.0419178376 & -1524827.866368342 & 983976.1455636612 & -256349.4856115345 & -124857.4809805508 \\
-399437.6556318913 & 399437.6556318913 & 43158.32143965364 & -519234.2318691599 & 232117.3169278467 & 110619.2462357253 \\
-24905.31096108862 & -63613.88445322036 & 152133.0798675294 & -6811.539771832358 & -106793.1495909436 & 12047.6264363625 \\
35800.55466000027 & -35800.55466000026 & -17310.96258858512 & 107513.9370987938 & -75473.81712486953 & -21799.07870730116
\end{bmatrix}. \quad \text{(A-33)}
$$

Thus everything is available for an integrated analysis of the 24 displacement measurements.

A.2 SOLUTION FOR DISCRETE MEASUREMENTS AS OBSERVATIONS

The functional model for an integrated analysis of displacement measurements is given by (8-7) and results for this example in

$$\begin{aligned} L_{\text{disp}_i} &= \sum_{j=0}^{5} {}^{\zeta}u_j \; T_j\Big(f_{\text{t}}\Big(x_{\text{disp}_i}, {}^{\zeta}x_{\nu_1}, {}^{\zeta}x_{\nu_2}\Big)\Big) = \sum_{j=0}^{5} {}^{\zeta}u_j \; T_j(t_{\text{disp}_i}) \\ &= \boldsymbol{\phi}(t_{\text{disp}_i})\,{}^{\zeta}\mathbf{u}\,. \end{aligned} \tag{A-34}$$

As the polynomial degree $p_{\text{e}} < p_{\text{u}}$, we have to remove the last two columns of the 9 submatrices in (A-25) – (A-33). According to (Olver and Townsend 2013), this can be done by applying the $(p_{\text{e}}+1)\times(p_{\text{u}}+1)$ truncation operator given by

$$\boldsymbol{\mathcal{P}}_{p_{\text{e}}+1} = \begin{bmatrix} \mathbf{I}_{p_{\text{e}}+1} & \mathbf{0} \end{bmatrix} = \begin{bmatrix} 1 & 0 & 0 & 0 & 0 & 0 \\ 0 & 1 & 0 & 0 & 0 & 0 \\ 0 & 0 & 1 & 0 & 0 & 0 \\ 0 & 0 & 0 & 1 & 0 & 0 \end{bmatrix}. \tag{A-35}$$

Since our problem has 3 elements, the truncation operator reads

$$\boldsymbol{\mathcal{P}} = \begin{bmatrix} \boldsymbol{\mathcal{P}}_{p_{\text{e}}+1} & \mathbf{0} & \mathbf{0} \\ \mathbf{0} & \boldsymbol{\mathcal{P}}_{p_{\text{e}}+1} & \mathbf{0} \\ \mathbf{0} & \mathbf{0} & \boldsymbol{\mathcal{P}}_{p_{\text{e}}+1} \end{bmatrix} \tag{A-36}$$

and the functional model (A-34) can be written as

$$\begin{aligned} L_{\text{disp}_i} &= \boldsymbol{\phi}(t_{\text{disp}_i})\,{}^{\zeta}\mathbf{u} \\ &= \boldsymbol{\phi}(t_{\text{disp}_i})\,{}^{\zeta}\mathbf{U}\boldsymbol{\mathcal{P}}^{\mathsf{T}}\mathbf{e}\,. \end{aligned} \tag{A-37}$$

Introducing (8-57) the functional model (A-37) of all observations for each element ζ results in

$${}^{\zeta}\mathbf{L}_{\text{disp}} = {}^{\zeta}\mathbf{A}_{\boldsymbol{\phi}}\,{}^{\zeta}\mathbf{U}\boldsymbol{\mathcal{P}}^{\mathsf{T}}\mathbf{e}\,. \tag{A-38}$$

and can be combined into

$$\begin{bmatrix} {}^{1}\mathbf{L}_{\text{disp}} \\ {}^{2}\mathbf{L}_{\text{disp}} \\ {}^{3}\mathbf{L}_{\text{disp}} \end{bmatrix} = \begin{bmatrix} {}^{1}\mathbf{A}_{\boldsymbol{\phi}} & \mathbf{0} & \mathbf{0} \\ \mathbf{0} & {}^{2}\mathbf{A}_{\boldsymbol{\phi}} & \mathbf{0} \\ \mathbf{0} & \mathbf{0} & {}^{3}\mathbf{A}_{\boldsymbol{\phi}} \end{bmatrix} \begin{bmatrix} {}^{1}\mathbf{U} \\ {}^{2}\mathbf{U} \\ {}^{3}\mathbf{U} \end{bmatrix} \boldsymbol{\mathcal{P}}^{\mathsf{T}} \begin{bmatrix} {}^{1}\mathbf{e} \\ {}^{2}\mathbf{e} \\ {}^{3}\mathbf{e} \end{bmatrix} \tag{A-39}$$

or in short

$$\mathbf{L}_{\text{disp}} = \mathbf{A}_{\boldsymbol{\phi}}\,\mathbf{U}\,\boldsymbol{\mathcal{P}}^{\mathsf{T}}\,\mathbf{e}\,, \tag{A-40}$$

with $\mathbf{A}_{\boldsymbol{\phi}}$ given by (A-7) and $\mathbf{U}$ by (A-23). Finally, Equation (A-40) can be simplified to

$$\mathbf{L}_{\text{disp}} = \mathbf{A}_{\text{disp}}\,\mathbf{e}\,, \tag{A-41}$$

with

$$\mathbf{A}_{\text{disp}} = \mathbf{A}_{\boldsymbol{\phi}}\,\mathbf{U}\,\boldsymbol{\mathcal{P}}^{\mathsf{T}}\,. \tag{A-42}$$

The least squares approximation of the 24 displacement measurements according to Section 8.1.3 and with the weight matrix (A-9) and (A-12) results in the extended normal equation system

$$\begin{bmatrix} \mathbf{A}_{\text{disp}}^{\mathsf{T}}\,\mathbf{P}_{\text{disp}}\,\mathbf{A}_{\text{disp}} & \mathbf{C}_{\text{conti}}^{\mathsf{T}} \\ \mathbf{C}_{\text{conti}} & \mathbf{0} \end{bmatrix} \begin{bmatrix} \mathbf{e} \\ \boldsymbol{\lambda} \end{bmatrix} = \begin{bmatrix} \mathbf{A}_{\text{disp}}^{\mathsf{T}}\,\mathbf{P}_{\text{disp}}\,\mathbf{L}_{\text{disp}} \\ \mathbf{0} \end{bmatrix}. \tag{A-43}$$

Solving (A-43) yields the unknown coefficients $\mathbf{e}$ of a Chebyshev series for each element representing the inverse of elastic modulus $E(x)$ as a C^2 continuous function along the beam, which are

$$ {}^1\mathbf{e} = \begin{bmatrix} 0.014\,306\,766\,300\,151 \\ 0.000\,080\,971\,277\,957 \\ -0.000\,183\,237\,594\,773 \\ 0.000\,048\,179\,060\,970 \end{bmatrix}, \; {}^2\mathbf{e} = \begin{bmatrix} 0.014\,284\,158\,519\,764 \\ 0.000\,103\,484\,603\,866 \\ 0.000\,065\,238\,799\,878 \\ -0.000\,006\,766\,328\,528 \end{bmatrix} \text{ and } {}^3\mathbf{e} = \begin{bmatrix} 0.013\,057\,831\,082\,907 \\ -0.002\,246\,518\,605\,775 \\ -0.001\,034\,809\,078\,185 \\ -0.000\,176\,574\,984\,482 \end{bmatrix}. \quad \text{(A-44)} $$

These values are already listed in the first column of Table 9-4.

A.3 SOLUTION FOR FUNCTIONS AS OBSERVATIONS

The functional model for an integrated analysis of displacements as functions is given by (8-32) and with the truncation operator (A-36) it reads

$$ \mathbf{L}_\mathrm{u} = \mathbf{A}_\mathrm{u}\,\mathbf{e}\,, \quad \text{(A-45)} $$

with

$$ \mathbf{L}_\mathrm{u} = \begin{bmatrix} {}^1\mathbf{u} \\ {}^2\mathbf{u} \\ {}^3\mathbf{u} \end{bmatrix} \quad \text{(A-46)} $$

from (A-13) and

$$ \mathbf{A}_\mathrm{u} = \mathbf{U}\,\boldsymbol{\mathcal{P}}^\mathsf{T}. \quad \text{(A-47)} $$

The least squares approximation of the displacement measurements represented as a function $\mathbf{u}$ according to Section 8.2.3 results in the extended normal equation system

$$ \begin{bmatrix} \mathbf{A}_\mathrm{u}^\mathsf{T}\,\mathbf{P}_\mathrm{u}\,\mathbf{A}_\mathrm{u} & \mathbf{C}_\mathrm{conti}^\mathsf{T} \\ \mathbf{C}_\mathrm{conti} & \mathbf{0} \end{bmatrix} \begin{bmatrix} \mathbf{e} \\ \boldsymbol{\lambda} \end{bmatrix} = \begin{bmatrix} \mathbf{A}_\mathrm{u}^\mathsf{T}\,\mathbf{P}_\mathrm{u}\,\mathbf{L}_\mathrm{u} \\ \mathbf{0} \end{bmatrix}. \quad \text{(A-48)} $$

According to Section 9.1, we estimate $\mathbf{e}$ in the following sections for 3 different stochastic models:

- Using the coefficients $\mathbf{u}$ as observations and under consideration of correlations $\Rightarrow \mathbf{P}_\mathrm{u} = \mathbf{A}_\phi^\mathsf{T}\,\mathbf{P}_\mathrm{disp}\,\mathbf{A}_\phi$.
- Using the coefficients $\mathbf{u}$ as observations and without consideration of correlations $\Rightarrow \mathbf{P}_\mathrm{u} = \mathrm{diag}\left(\mathbf{A}_\phi^\mathsf{T}\,\mathbf{P}_\mathrm{disp}\,\mathbf{A}_\phi\right)$.
- Using the coefficients $\mathbf{u}$ as observations and without explicit stochastic model $\Rightarrow \mathbf{P}_\mathrm{u} = \mathbf{I}$.

A.3.1 *With correlations*

First of all, we estimate $\mathbf{e}$ under consideration of correlations using the following stochastic model

$$ \mathbf{P}_\mathrm{u} = \mathbf{A}_\phi^\mathsf{T}\,\mathbf{P}_\mathrm{disp}\,\mathbf{A}_\phi \quad \text{(A-49)} $$

and with (A-7) and (A-9) the stochastic model (A-49) can be written as

$$\begin{aligned}\mathbf{P}_{\mathrm{u}} &= \begin{bmatrix} {}^{1}\mathbf{P}_{\mathrm{u}} & \mathbf{0} & \mathbf{0} \\ \mathbf{0} & {}^{2}\mathbf{P}_{\mathrm{u}} & \mathbf{0} \\ \mathbf{0} & \mathbf{0} & {}^{3}\mathbf{P}_{\mathrm{u}} \end{bmatrix} \\ &= \begin{bmatrix} {}^{1}\mathbf{A}_{\phi}^{\mathsf{T}}\,{}^{1}\mathbf{P}_{\mathrm{disp}}\,{}^{1}\mathbf{A}_{\phi} & \mathbf{0} & \mathbf{0} \\ \mathbf{0} & {}^{2}\mathbf{A}_{\phi}^{\mathsf{T}}\,{}^{2}\mathbf{P}_{\mathrm{disp}}\,{}^{2}\mathbf{A}_{\phi} & \mathbf{0} \\ \mathbf{0} & \mathbf{0} & {}^{3}\mathbf{A}_{\phi}^{\mathsf{T}}\,{}^{3}\mathbf{P}_{\mathrm{disp}}\,{}^{3}\mathbf{A}_{\phi} \end{bmatrix}, \end{aligned} \tag{A-50}$$

with

$${}^{1}\mathbf{P}_{\mathrm{u}} = \begin{bmatrix} 8 & -0.695652173913043 & -2.162570888468808 & -0.916577628010191 & 0.085105470606525 & -1.278243872335579 \\ -0.695652173913043 & 2.918714555765596 & -0.806114900961617 & -1.038732708931141 & -1.097410750172885 & 0.427729413642389 \\ -2.162570888468808 & -0.806114900961617 & 4.042552735303262 & -0.986948023124311 & -0.696108765895277 & -1.228413060553586 \\ -0.916577628010191 & -1.038732708931141 & -0.986948023124311 & 4.385176678339127 & -1.117950333505012 & -0.374453822727150 \\ 0.085105470606525 & -1.097410750172885 & -0.696108765895277 & -1.117950333505012 & 4.706831621507255 & -0.992718837868885 \\ -1.278243872335579 & 0.427729413642389 & -1.228413060553586 & -0.374453822727150 & -0.992718837868885 & 4.922067160516348 \end{bmatrix}, \tag{A-51}$$

$${}^{2}\mathbf{P}_{\mathrm{u}} = \begin{bmatrix} 8 & 0 & -2.283553875236295 & 0 & -0.472010891899328 & 0 \\ 0 & 2.858223062381852 & 0 & -1.377782383567812 & 0 & -0.576511605236483 \\ -2.283553875236295 & 0 & 3.763994554050336 & 0 & -1.482283096904966 & 0 \\ 0 & -1.377782383567812 & 0 & 3.659493840713180 & 0 & -1.788829156182099 \\ -0.472010891899328 & 0 & -1.482283096904966 & 0 & 3.352947781436048 & 0 \\ 0 & -0.576511605236483 & 0 & -1.788829156182099 & 0 & 3.207736240291689 \end{bmatrix}, \tag{A-52}$$

$${}^{3}\mathbf{P}_{\mathrm{u}} = \begin{bmatrix} 8 & 0.695652173913045 & -2.162570888468808 & 0.916577628010190 & 0.085105470606528 & 1.278243872335575 \\ 0.695652173913045 & 2.918714555765596 & 0.806114900961618 & -1.038732708931140 & 1.097410750172883 & 0.427729413642388 \\ -2.162570888468808 & 0.806114900961618 & 4.042552735303264 & 0.986948023124311 & -0.696108765895281 & 1.228413060553588 \\ 0.916577628010190 & -1.038732708931140 & 0.986948023124311 & 4.385176678339123 & 1.117950333505014 & -0.374453822727146 \\ 0.085105470606528 & 1.097410750172883 & -0.696108765895281 & 1.117950333505014 & 4.706831621507259 & 0.992718837868888 \\ 1.278243872335575 & 0.427729413642388 & 1.228413060553588 & -0.374453822727146 & 0.992718837868888 & 4.922067160516345 \end{bmatrix}. \tag{A-53}$$

Solving (A-48) under consideration of correlations between the observations $\mathbf{u}$ by the stochastic model (A-49), yields the unknown coefficients $\mathbf{e}$

$${}^{1}\mathbf{e} = \begin{bmatrix} 0.014\,306\,766\,300\,212 \\ 0.000\,080\,971\,277\,841 \\ -0.000\,183\,237\,594\,699 \\ 0.000\,048\,179\,060\,954 \end{bmatrix}, \; {}^{2}\mathbf{e} = \begin{bmatrix} 0.014\,284\,158\,519\,764 \\ 0.000\,103\,484\,603\,859 \\ 0.000\,065\,238\,799\,878 \\ -0.000\,006\,766\,328\,524 \end{bmatrix} \text{ and } {}^{3}\mathbf{e} = \begin{bmatrix} 0.013\,057\,831\,082\,851 \\ -0.002\,246\,518\,605\,880 \\ -0.001\,034\,809\,078\,253 \\ -0.000\,176\,574\,984\,498 \end{bmatrix}. \tag{A-54}$$

These values are already listed in the second column of Table 9-4.

A.3.2 *Without correlations*

Now we estimate $\mathbf{e}$ without consideration of correlations between the observations $\mathbf{u}$. The stochastic model (A-50) simplifies to

$$\mathbf{P}_{\mathrm{u}} = \begin{bmatrix} {}^{1}\mathbf{P}_{\mathrm{u}} & \mathbf{0} & \mathbf{0} \\ \mathbf{0} & {}^{2}\mathbf{P}_{\mathrm{u}} & \mathbf{0} \\ \mathbf{0} & \mathbf{0} & {}^{3}\mathbf{P}_{\mathrm{u}} \end{bmatrix} = \operatorname{diag}\left(\mathbf{A}_{\phi}^{\mathsf{T}}\,\mathbf{P}_{\mathrm{disp}}\,\mathbf{A}_{\phi}\right), \tag{A-55}$$

with

$$
{}^{1}\mathbf{P}_{\mathrm{u}} = \begin{bmatrix}
8 & 0 & 0 & 0 & 0 & 0 \\
0 & 2.918714555765596 & 0 & 0 & 0 & 0 \\
0 & 0 & 4.042552735303262 & 0 & 0 & 0 \\
0 & 0 & 0 & 4.385176678339127 & 0 & 0 \\
0 & 0 & 0 & 0 & 4.706831621507255 & 0 \\
0 & 0 & 0 & 0 & 0 & 4.922067160516348
\end{bmatrix}, \tag{A-56}
$$

$$
{}^{2}\mathbf{P}_{\mathrm{u}} = \begin{bmatrix}
8 & 0 & 0 & 0 & 0 & 0 \\
0 & 2.858223062381852 & 0 & 0 & 0 & 0 \\
0 & 0 & 3.763994554050336 & 0 & 0 & 0 \\
0 & 0 & 0 & 3.659493840713180 & 0 & 0 \\
0 & 0 & 0 & 0 & 3.352947781436048 & 0 \\
0 & 0 & 0 & 0 & 0 & 3.207736240291689
\end{bmatrix}, \tag{A-57}
$$

$$
{}^{3}\mathbf{P}_{\mathrm{u}} = \begin{bmatrix}
8 & 0 & 0 & 0 & 0 & 0 \\
0 & 2.918714555765596 & 0 & 0 & 0 & 0 \\
0 & 0 & 4.042552735303264 & 0 & 0 & 0 \\
0 & 0 & 0 & 4.385176678339123 & 0 & 0 \\
0 & 0 & 0 & 0 & 4.706831621507259 & 0 \\
0 & 0 & 0 & 0 & 0 & 4.922067160516345
\end{bmatrix}. \tag{A-58}
$$

Solving (A-48) without consideration of correlations between the observations $\mathbf{u}$ by the stochastic model (A-55), yields the unknown coefficients $\mathbf{e}$

$$
{}^{1}\mathbf{e} = \begin{bmatrix} 0.014\,172\,412\,374\,338 \\ 0.000\,318\,308\,581\,172 \\ -0.000\,354\,862\,279\,467 \\ 0.000\,090\,003\,822\,607 \end{bmatrix}, \; {}^{2}\mathbf{e} = \begin{bmatrix} 0.014\,286\,234\,410\,083 \\ 0.000\,143\,530\,605\,680 \\ 0.000\,062\,758\,301\,860 \\ -0.000\,020\,400\,392\,386 \end{bmatrix} \text{ and } {}^{3}\mathbf{e} = \begin{bmatrix} 0.013\,176\,983\,814\,449 \\ -0.002\,018\,366\,780\,776 \\ -0.000\,855\,944\,393\,495 \\ -0.000\,132\,716\,723\,507 \end{bmatrix}. \tag{A-59}
$$

These values are already listed in the third column of Table 9-4.

A.3.3 *Without explicit stochastic model*

Lastly, we estimate E without explicit stochastic model, which reads

$$
\mathbf{P}_{\mathrm{u}} = \mathbf{I}. \tag{A-60}
$$

Solving (A-48) without explicit stochastic model for the observations $\mathbf{u}$ by (A-60), yields the unknown coefficients $\mathbf{e}$

$$
{}^{1}\mathbf{e} = \begin{bmatrix} 0.014\,343\,935\,390\,659 \\ 0.000\,016\,728\,279\,048 \\ -0.000\,158\,897\,874\,031 \\ 0.000\,043\,401\,985\,193 \end{bmatrix}, \; {}^{2}\mathbf{e} = \begin{bmatrix} 0.014\,279\,231\,576\,483 \\ 0.000\,114\,461\,350\,024 \\ 0.000\,076\,174\,257\,866 \\ -0.000\,004\,223\,296\,544 \end{bmatrix} \text{ and } {}^{3}\mathbf{e} = \begin{bmatrix} 0.012\,944\,001\,628\,930 \\ -0.002\,498\,454\,983\,944 \\ -0.001\,182\,342\,165\,776 \\ -0.000\,205\,529\,440\,730 \end{bmatrix}. \tag{A-61}
$$

These values are already listed in the fourth column of Table 9-4.

B

DAMAGE SNIFFER

The measurements for the example in Section 10.1.5 are based on the true solution of (7-5) for the huge damage (9-2). The 30 equidistant displacement measurements of high precision are given in Table B-1.

Table B-1: 30 equidistant displacement measurements of high precision for damage according to (9-2).

i	x_i [m]	L_{disp_i} [µm]
1	0.000 000 000 000 000	−0.1
2	0.250 344 827 586 207	−104.3
3	0.500 689 655 172 414	−202.6
4	0.751 034 482 758 621	−301.8
5	1.001 379 310 344 828	−397.3
6	1.251 724 137 931 034	−488.6
7	1.502 068 965 517 242	−575.2
8	1.752 413 793 103 448	−653.4
9	2.002 758 620 689 655	−726.0
10	2.253 103 448 275 862	−789.5
11	2.503 448 275 862 069	−841.8
12	2.753 793 103 448 276	−885.4
13	3.004 137 931 034 483	−919.4
14	3.254 482 758 620 690	−940.8
15	3.504 827 586 206 897	−954.1
16	3.755 172 413 793 103	−952.3
17	4.005 517 241 379 311	−939.8
18	4.255 862 068 965 517	−918.4
19	4.506 206 896 551 724	−884.9
20	4.756 551 724 137 931	−844.7
21	5.006 896 551 724 138	−788.7
22	5.257 241 379 310 345	−726.4
23	5.507 586 206 896 551	−653.7
24	5.757 931 034 482 758	−574.9
25	6.008 275 862 068 966	−489.4
26	6.258 620 689 655 173	−396.8
27	6.508 965 517 241 379	−302.1
28	6.759 310 344 827 585	−204.4
29	7.009 655 172 413 793	−102.8
30	7.260 000 000 000 000	−0.3

C

EXPERIMENTAL STUDIES

The resulting 31 displacement measurements for each of the 31 bending tests are listed in Table C-1 – C-6.

Table C-1: 31 displacements of the bending test exp with undamaged beam. Measurements in red are detected as outliers. The set of displacements $\mathbf{u}_4$ and $\mathbf{u}_5$ are excluded since both refer to a six-point bending test, which is not considered in this thesis.

i	x_{disp_i}	Displacements in [mm]			
	[m]	$\mathbf{u}_0$	$\mathbf{u}_1$	$\mathbf{u}_2$	$\mathbf{u}_3$
1	0.023 096	−0.0229	−0.0523	−0.0877	−0.1202
2	0.068 709	−0.0480	−0.1039	−0.1657	−0.2457
3	0.176 352	−0.1058	−0.2210	−0.3385	−0.5332
4	0.212 851	−0.1227	−0.2569	−0.3916	−0.6280
5	0.278 871	−0.1552	−0.3230	−0.4899	−0.7885
6	0.314 151	−0.1702	−0.3534	−0.5350	−0.8683
7	0.417 935	−0.2144	−0.4423	−0.6609	−1.0827
8	0.447 853	−0.2220	−0.4612	−0.6912	−1.1344
9	0.527 959	−0.2463	−0.5110	−0.7635	−1.2536
10	0.559 127	−0.2556	−0.5291	−0.7864	−1.2944
11	0.643 514	−0.2673	−0.5558	−0.8261	−1.3639
12	0.676 329	−0.2732	−0.5649	−0.8378	−1.3823
13	0.747 849	−0.2747	−0.5701	−0.8420	−1.3940
14	0.781 092	−0.2723	−0.5670	−0.8392	−1.3888
15	0.842 090	−0.2668	−0.5567	−0.8226	−1.3620
16	0.873 664	−0.2616	−0.5483	−0.8080	−1.3380
17	0.931 494	−0.2505	−0.5259	−0.7715	−1.2791
18	0.964 512	−0.2416	−0.5084	−0.7453	−1.2361
19	1.055 018	−0.2139	−0.4540	−0.6572	−1.0929
20	1.087 295	−0.2004	−0.4278	−0.6202	−1.0301
21	1.121 913	−0.1871	−0.4024	−0.5790	−0.9631
22	1.153 746	−0.1741	−0.3749	−0.5359	−0.8940
23	1.197 998	−0.1534	−0.3357	−0.4760	−0.7925
24	1.226 644	−0.1393	−0.3080	−0.4335	−0.7250
25	1.262 643	−0.1215	−0.2739	−0.3815	−0.6355
26	1.291 306	−0.1072	−0.2448	−0.3377	−0.5632
27	1.331 778	−0.0863	−0.2028	−0.2742	−0.4576
28	1.361 852	−0.0698	−0.1710	−0.2259	−0.3766
29	1.394 834	−0.0517	−0.1353	−0.1723	−0.2881
30	1.425 921	−0.0341	−0.1012	−0.1202	−0.2027
31	1.459 129	−0.0162	−0.0644	−0.0651	−0.1100

Table C-2: 31 displacements of the bending test exp4mm with damaged beam. Measurements in red are detected as outliers.

i	x_{disp_i}	Displacements in [mm]					
	[m]	$\mathbf{u}_6$	$\mathbf{u}_7$	$\mathbf{u}_8$	$\mathbf{u}_9$	$\mathbf{u}_{10}$	$\mathbf{u}_{11}$
1	0.023 096	−0.1542	−0.0281	−0.0585	0.0037	−0.0468	−0.1258
2	0.068 709	−0.2778	−0.0527	−0.1080	−0.0207	−0.0958	−0.2503
3	0.176 352	−0.5611	−0.1132	−0.2251	−0.0778	−0.2117	−0.5379
4	0.212 851	−0.6543	−0.1306	−0.2581	−0.0963	−0.2471	−0.6272
5	0.278 871	−0.8132	−0.1626	−0.3223	−0.1269	−0.3092	−0.7901
6	0.314 151	−0.8919	−0.1794	−0.3535	−0.1431	−0.3410	−0.8690
7	0.417 935	−1.1039	−0.2222	−0.4397	−0.1846	−0.4275	−1.0783
8	0.447 853	−1.1545	−0.2343	−0.4592	−0.1960	−0.4499	−1.1350
9	0.527 959	−1.2728	−0.2592	−0.5074	−0.2203	−0.4959	−1.2499
10	0.559 127	−1.3130	−0.2667	−0.5230	−0.2266	−0.5124	−1.2889
11	0.643 514	−1.3793	−0.2805	−0.5482	−0.2403	−0.5374	−1.3549
12	0.676 329	−1.3977	−0.2854	−0.5576	−0.2450	−0.5481	−1.3758
13	0.747 849	−1.4067	−0.2872	−0.5606	−0.2477	−0.5552	−1.3907
14	0.781 092	−1.4018	−0.2875	−0.5577	−0.2461	−0.5474	−1.3793
15	0.842 090	−1.3728	−0.2823	−0.5458	−0.2408	−0.5387	−1.3530
16	0.873 664	−1.3479	−0.2776	−0.5344	−0.2346	−0.5261	−1.3253
17	0.931 494	−1.2879	−0.2667	−0.5127	−0.2248	−0.5056	−1.2677
18	0.964 512	−1.2457	−0.2584	−0.4945	−0.2158	−0.4871	−1.2251
19	1.055 018	−1.1003	−0.2313	−0.4376	−0.1879	−0.4314	−1.0808
20	1.087 295	−1.0374	−0.2175	−0.4099	−0.1736	−0.4035	−1.0178
21	1.121 913	−0.9694	−0.2041	−0.3823	−0.1600	−0.3771	−0.9495
22	1.153 746	−0.8976	−0.1904	−0.3552	−0.1467	−0.3495	−0.8793
23	1.197 998	−0.7965	−0.1703	−0.3133	−0.1259	−0.3081	−0.7778
24	1.226 644	−0.7268	−0.1575	−0.2858	−0.1129	−0.2809	−0.7095
25	1.262 643	−0.6383	−0.1395	−0.2496	−0.0949	−0.2447	−0.6198
26	1.291 306	−0.5644	−0.1257	−0.2204	−0.0803	−0.2156	−0.5470
27	1.331 778	−0.4581	−0.1047	−0.1772	−0.0587	−0.1722	−0.4420
28	1.361 852	−0.3748	−0.0891	−0.1459	−0.0435	−0.1407	−0.3621
29	1.394 834	−0.2876	−0.0695	−0.1085	−0.0261	−0.1042	−0.2722
30	1.425 921	−0.1987	−0.0543	−0.0744	−0.0079	−0.0698	−0.1861
31	1.459 129	−0.1094	−0.0323	−0.0376	0.0097	−0.0333	−0.0970

Table C-3: 31 displacements of the bending tests exp8mm and exp10mm with damaged beam. Sets $\mathbf{u}_{12}$ – $\mathbf{u}_{15}$ are referring to exp8mm and $\mathbf{u}_{16}$ to exp10mm. Measurements in red are detected as outliers.

i	x_{disp_i}	Displacements in [mm]				
	[m]	$\mathbf{u}_{12}$	$\mathbf{u}_{13}$	$\mathbf{u}_{14}$	$\mathbf{u}_{15}$	$\mathbf{u}_{16}$
1	0.023 096	−0.1265	−0.0871	−0.0273	−0.0267	−0.0090
2	0.068 709	−0.2509	−0.1613	−0.0522	−0.0515	−0.0340
3	0.176 352	−0.5389	−0.3353	−0.1111	−0.1097	−0.0911
4	0.212 851	−0.6285	−0.3885	−0.1282	−0.1267	−0.1094
5	0.278 871	−0.7908	−0.4832	−0.1605	−0.1595	−0.1396
6	0.314 151	−0.8700	−0.5295	−0.1758	−0.1740	−0.1549
7	0.417 935	−1.0809	−0.6588	−0.2189	−0.2174	−0.1979
8	0.447 853	−1.1360	−0.6884	−0.2279	−0.2268	−0.2061
9	0.527 959	−1.2527	−0.7616	−0.2518	−0.2501	−0.2301
10	0.559 127	−1.2933	−0.7845	−0.2603	−0.2581	−0.2381
11	0.643 514	−1.3590	−0.8247	−0.2739	−0.2707	−0.2500
12	0.676 329	−1.3787	−0.8346	−0.2773	−0.2746	−0.2536
13	0.747 849	−1.3879	−0.8374	−0.2821	−0.2788	−0.2564
14	0.781 092	−1.3842	−0.8393	−0.2779	−0.2740	−0.2546
15	0.842 090	−1.3526	−0.8189	−0.2731	−0.2696	−0.2480
16	0.873 664	−1.3286	−0.8053	−0.2674	−0.2634	−0.2431
17	0.931 494	−1.2716	−0.7704	−0.2567	−0.2528	−0.2312
18	0.964 512	−1.2289	−0.7441	−0.2463	−0.2419	−0.2216
19	1.055 018	−1.0847	−0.6578	−0.2176	−0.2140	−0.1912
20	1.087 295	−1.0218	−0.6192	−0.2037	−0.2007	−0.1791
21	1.121 913	−0.9524	−0.5772	−0.1906	−0.1869	−0.1649
22	1.153 746	−0.8824	−0.5357	−0.1765	−0.1725	−0.1509
23	1.197 998	−0.7796	−0.4736	−0.1563	−0.1531	−0.1304
24	1.226 644	−0.7113	−0.4317	−0.1414	−0.1384	−0.1149
25	1.262 643	−0.6216	−0.3786	−0.1243	−0.1211	−0.0978
26	1.291 306	−0.5482	−0.3349	−0.1090	−0.1063	−0.0827
27	1.331 778	−0.4418	−0.2695	−0.0881	−0.0852	−0.0607
28	1.361 852	−0.3615	−0.2221	−0.0716	−0.0692	−0.0447
29	1.394 834	−0.2711	−0.1670	−0.0533	−0.0509	−0.0261
30	1.425 921	−0.1842	−0.1150	−0.0350	−0.0335	−0.0078
31	1.459 129	−0.0933	−0.0606	−0.0166	−0.0147	0.0109

Table C-4: 31 displacements of the bending tests exp3L and exp3L2 with damaged beam. Set $\mathbf{u}_{17}$ refers to exp3L and $\mathbf{u}_{18}$– $\mathbf{u}_{20}$ to exp3L2. Measurements in red are detected as outliers.

i	x_{disp_i}	Displacements in [mm]			
	[m]	$\mathbf{u}_{17}$	$\mathbf{u}_{18}$	$\mathbf{u}_{19}$	$\mathbf{u}_{20}$
1	0.023 096	−0.0469	−0.0056	−0.0366	−0.0601
2	0.068 709	−0.0711	−0.0292	−0.0846	−0.1335
3	0.176 352	−0.1304	−0.0852	−0.2003	−0.3068
4	0.212 851	−0.1470	−0.1031	−0.2356	−0.3587
5	0.278 871	−0.1805	−0.1329	−0.2985	−0.4564
6	0.314 151	−0.1951	−0.1491	−0.3298	−0.5023
7	0.417 935	−0.2413	−0.1895	−0.4161	−0.6301
8	0.447 853	−0.2518	−0.2005	−0.4370	−0.6642
9	0.527 959	−0.2752	−0.2227	−0.4837	−0.7341
10	0.559 127	−0.2815	−0.2284	−0.4976	−0.7559
11	0.643 514	−0.2950	−0.2415	−0.5247	−0.7969
12	0.676 329	−0.3002	−0.2448	−0.5333	−0.8067
13	0.747 849	−0.3090	−0.2496	−0.5408	−0.8186
14	0.781 092	−0.2988	−0.2441	−0.5341	−0.8104
15	0.842 090	−0.2959	−0.2415	−0.5253	−0.7977
16	0.873 664	−0.2891	−0.2318	−0.5103	−0.7780
17	0.931 494	−0.2781	−0.2233	−0.4912	−0.7459
18	0.964 512	−0.2683	−0.2146	−0.4730	−0.7191
19	1.055 018	−0.2380	−0.1869	−0.4168	−0.6330
20	1.087 295	−0.2250	−0.1722	−0.3897	−0.5950
21	1.121 913	−0.2099	−0.1592	−0.3621	−0.5522
22	1.153 746	−0.1949	−0.1456	−0.3342	−0.5096
23	1.197 998	−0.1735	−0.1257	−0.2932	−0.4485
24	1.226 644	−0.1588	−0.1123	−0.2650	−0.4058
25	1.262 643	−0.1406	−0.0948	−0.2288	−0.3516
26	1.291 306	−0.1251	−0.0806	−0.1991	−0.3078
27	1.331 778	−0.1018	−0.0599	−0.1559	−0.2429
28	1.361 852	−0.0859	−0.0448	−0.1240	−0.1945
29	1.394 834	−0.0671	−0.0270	−0.0863	−0.1386
30	1.425 921	−0.0486	−0.0100	−0.0513	−0.0862
31	1.459 129	−0.0299	0.0075	−0.0141	−0.0304

Table C-5: 31 displacements of the bending tests exp_Y and exp_K with damaged beam. Sets $\mathbf{u}_{21}$– $\mathbf{u}_{24}$ are referring to exp_Y and $\mathbf{u}_{25}$ to exp_K. Due to the large damage, no outliers could be detected reliably.

i	x_{disp_i}	Displacements in [mm]				
	[m]	$\mathbf{u}_{21}$	$\mathbf{u}_{22}$	$\mathbf{u}_{23}$	$\mathbf{u}_{24}$	$\mathbf{u}_{25}$
1	0.023 096	−0.0313	−0.0633	−0.0942	−0.1240	−0.0574
2	0.068 709	−0.0554	−0.1130	−0.1683	−0.2217	−0.1083
3	0.176 352	−0.1126	−0.2281	−0.3422	−0.4560	−0.2251
4	0.212 851	−0.1318	−0.2630	−0.3955	−0.5178	−0.2617
5	0.278 871	−0.1615	−0.3257	−0.4914	−0.6608	−0.3255
6	0.314 151	−0.1778	−0.3573	−0.5374	−0.7210	−0.3585
7	0.417 935	−0.2201	−0.4440	−0.6650	−0.8828	−0.4476
8	0.447 853	−0.2305	−0.4625	−0.6967	−0.9424	−0.4699
9	0.527 959	−0.2546	−0.5126	−0.7696	−1.0280	−0.5195
10	0.559 127	−0.2612	−0.5277	−0.7925	−1.0587	−0.5376
11	0.643 514	−0.2753	−0.5531	−0.8325	−1.1124	−0.5639
12	0.676 329	−0.2809	−0.5648	−0.8454	−1.1367	−0.5744
13	0.747 849	−0.2775	−0.5651	−0.8455	−1.1245	−0.5791
14	0.781 092	−0.2800	−0.5640	−0.8482	−1.1438	−0.5763
15	0.842 090	−0.2737	−0.5498	−0.8271	−1.1057	−0.5684
16	0.873 664	−0.2679	−0.5394	−0.8135	−1.0901	−0.5578
17	0.931 494	−0.2564	−0.5177	−0.7784	−1.0452	−0.5378
18	0.964 512	−0.2482	−0.5002	−0.7516	−1.0118	−0.5207
19	1.055 018	−0.2202	−0.4441	−0.6646	−0.8960	−0.4673
20	1.087 295	−0.2047	−0.4166	−0.6271	−0.8451	−0.4427
21	1.121 913	−0.1924	−0.3892	−0.5847	−0.7913	−0.4131
22	1.153 746	−0.1779	−0.3613	−0.5416	−0.7341	−0.3840
23	1.197 998	−0.1563	−0.3190	−0.4793	−0.6508	−0.3408
24	1.226 644	−0.1428	−0.2913	−0.4369	−0.5946	−0.3100
25	1.262 643	−0.1239	−0.2548	−0.3830	−0.5228	−0.2718
26	1.291 306	−0.1092	−0.2250	−0.3385	−0.4630	−0.2416
27	1.331 778	−0.0867	−0.1817	−0.2733	−0.3777	−0.1959
28	1.361 852	−0.0705	−0.1492	−0.2248	−0.3135	−0.1616
29	1.394 834	−0.0518	−0.1122	−0.1693	−0.2396	−0.1234
30	1.425 921	−0.0348	−0.0773	−0.1170	−0.1698	−0.0865
31	1.459 129	−0.0153	−0.0393	−0.0607	−0.0974	−0.0476

Table C-6: 31 displacements of the bending test exp_Z with damaged beam. Due to the large damage, no outliers could be detected reliably.

i	x_{disp_i}	Displacements in [mm]					
	[m]	$\mathbf{u}_{26}$	$\mathbf{u}_{27}$	$\mathbf{u}_{28}$	$\mathbf{u}_{29}$	$\mathbf{u}_{30}$	$\mathbf{u}_{31}$
1	0.023 096	−0.0673	0.0041	−0.0079	−0.0293	−0.0535	−0.0778
2	0.068 709	−0.1470	−0.0220	−0.0612	−0.1084	−0.1589	−0.2103
3	0.176 352	−0.3344	−0.0821	−0.1839	−0.2938	−0.4055	−0.5180
4	0.212 851	−0.3917	−0.1010	−0.2206	−0.3501	−0.4802	−0.6134
5	0.278 871	−0.4962	−0.1338	−0.2891	−0.4538	−0.6208	−0.7883
6	0.314 151	−0.5474	−0.1512	−0.3230	−0.5032	−0.6881	−0.8734
7	0.417 935	−0.6893	−0.1961	−0.4174	−0.6433	−0.8712	−1.1043
8	0.447 853	−0.7235	−0.2080	−0.4381	−0.6776	−0.9198	−1.1616
9	0.527 959	−0.8050	−0.2341	−0.4922	−0.7583	−1.0254	−1.2957
10	0.559 127	−0.8326	−0.2444	−0.5116	−0.7857	−1.0625	−1.3401
11	0.643 514	−0.8819	−0.2564	−0.5409	−0.8329	−1.1254	−1.4231
12	0.676 329	−0.8978	−0.2625	−0.5522	−0.8478	−1.1472	−1.4476
13	0.747 849	−0.9115	−0.2659	−0.5610	−0.8622	−1.1653	−1.4730
14	0.781 092	−0.9133	−0.2661	−0.5608	−0.8633	−1.1664	−1.4737
15	0.842 090	−0.9045	−0.2621	−0.5534	−0.8525	−1.1533	−1.4564
16	0.873 664	−0.8914	−0.2555	−0.5437	−0.8393	−1.1349	−1.4360
17	0.931 494	−0.8656	−0.2469	−0.5273	−0.8124	−1.0996	−1.3901
18	0.964 512	−0.8445	−0.2397	−0.5114	−0.7898	−1.0703	−1.3532
19	1.055 018	−0.7673	−0.2144	−0.4607	−0.7128	−0.9683	−1.2250
20	1.087 295	−0.7357	−0.2011	−0.4378	−0.6796	−0.9228	−1.1701
21	1.121 913	−0.6895	−0.1859	−0.4067	−0.6338	−0.8634	−1.0939
22	1.153 746	−0.6351	−0.1684	−0.3709	−0.5794	−0.7914	−1.0050
23	1.197 998	−0.5579	−0.1408	−0.3187	−0.5017	−0.6866	−0.8741
24	1.226 644	−0.5060	−0.1239	−0.2832	−0.4490	−0.6181	−0.7887
25	1.262 643	−0.4396	−0.1016	−0.2390	−0.3828	−0.5290	−0.6759
26	1.291 306	−0.3849	−0.0825	−0.2021	−0.3275	−0.4552	−0.5839
27	1.331 778	−0.3063	−0.0555	−0.1489	−0.2480	−0.3501	−0.4528
28	1.361 852	−0.2475	−0.0357	−0.1095	−0.1889	−0.2717	−0.3541
29	1.394 834	−0.1810	−0.0132	−0.0648	−0.1224	−0.1830	−0.2436
30	1.425 921	−0.1178	0.0081	−0.0230	−0.0592	−0.0987	−0.1377
31	1.459 129	−0.0517	0.0304	0.0218	0.0084	−0.0102	−0.0265